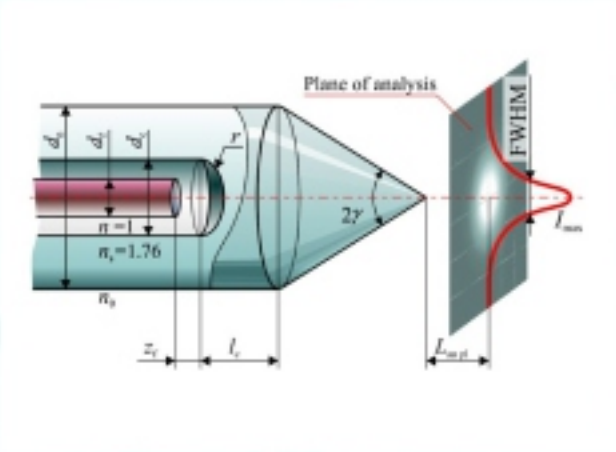
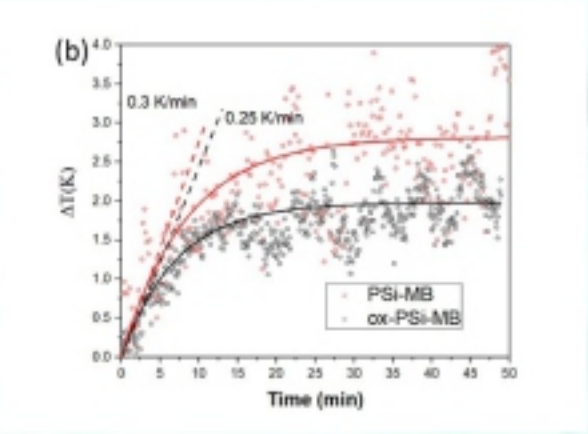
Volume 10 | Issue 4 |2024

Journal of Biomedical Photonics & Engineering





Special Issue Editors:
Elina Genina and Valery Zakharov

Editor-In-Chief:
Valery Tuchin

©2024 J-BPE

Journal of Biomedical Photonics & Engineering

by Samara National Research University

Volume 10, Issue 4 (September 2024)

Special Section
Advanced Technologies in Biophotonics: the 80th anniversary of Professor Valery Tuchin

Special Section Editor

Prof. Elina A. Genina
Department of Optics and Biophotonics
Saratov State University
Saratov, Russian Federation

Prof. Valery P. Zakharov
Department of Laser and Biotechnical Systems
Samara National Research University
Samara, Russian Federation

Editor-In-Chief

Valery V. Tuchin − Saratov State University, Russian Federation;
Institute of Precision Mechanics and Control RAS, Russian Federation; a corr.-member of RAS

Deputy Editor-In-Chief

Valery P. Zakharov − Samara National Research University, Russian Federation

© 2024 J-BPE

Postal address:
39B Lukacheva st., room #301
Samara 443086, Russian Federation

Used Figures from this issue on the Cover

Irina A. Shikunova et al., Radiation Patterns Formed by Sapphire Capillary Needles with Different Shapes of Internal Channels, 040315, Fig. 2.

Alexandr A. Bubnov et al., Laser-Stimulated Release of Methylene Blue from Porous Silicon Nanocontainers, 040305, Fig. 5b.

© 2024 J-BPE

 doi: 10.18287/JBPE24.10.040101

Foreword to Advanced Technologies in Biophotonics: the 80th anniversary of Professor Valery Tuchin

Dear Colleagues,



On February 4, 2024, Valery V. Tuchin turned 80 years old. He is a Doctor of Sciences, professor, head of the Optics and Biophotonics Department of the Physical Institute of Saratov University, corresponding member of the Russian Academy of Sciences, author of fundamental world-class scientific works in the field of biophotonics, winner of numerous prizes in the field of science.

Valery V. Tuchin, one of the world's leading experts in biophotonics, was born in Saratov. In 1966, he graduated from the Department of Radiophysics and Electronics of the Physics Department of Saratov State University.

In the 1960s, there was a scientific breakthrough associated with the creation of an optical quantum generator, which did not bypass the Department of Optics of Saratov University. Laser became the main focus of scientific research of postgraduate student Valery Tuchin. His interests concerned fluctuations in laser radiation, dynamic processes in gas-discharge lasers, and modulation characteristics of lasers. Valery defended his PhD thesis (1974) and doctoral dissertation (1982) on this topic.

In the mid-1980s, Prof. Tuchin began creating his own scientific school in the field of biotissue optics, which eventually grew into an interdisciplinary science – biophotonics, and pioneered "tissue optical clearing" as a new direction.

Valery Tuchin is a man of amazing scientific intuition. He generously shares ideas with colleagues, connecting Saratov University with scientific groups around the world. His authority and charisma, as well as energy and efficiency allow him to implement large international projects, conferences and symposiums, both in Russia and abroad.

For almost 30 years now, the Saratov Fall Meeting (SFM) has been hosting international events annually at Saratov University, attended by leading and young scientists from different countries. The organizer and inspirer of this widely known event in the scientific world is V. V. Tuchin. Our journal regularly publishes special sections with articles based on the materials of the reports presented at SFM. In addition to SFM, Valery is a co-chairman of well-known international conferences held within the framework of Photonics West in the USA, International Conference on Photonics and Imaging in Biology and Medicine (PIBM) in China and SPIE Photonics Europe in France.

Professor Valery Tuchin is a unique example of an outstanding scientist, a talented teacher, and organizer of the scientific process. He has created a scientific school known all over the world. His fruitful scientific and educational activities have marked by the awarding of medals, orders, honorary titles and prizes from the State and various scientific communities, as SPIE, OPTICA, Laser Association of the Russian Federation and others. In 2024, Valery Tuchin became a laureate of the "Vyzov" Award in the "Scientist of the Year" nomination.

 doi: 10.18287/JBPE24.10.040101

This special issue is a tribute from students and colleagues to a brilliant scientist, an outstanding teacher and just a wonderful person. Congratulations to Valery Tuchin on his anniversary and wish him good health, creative inspiration and great success in his multifaceted activities!

Special Issue Editors:

Elina A. Genina, PhD, DSc
Department of Optics and Biophotonics
Saratov State University
E-mail: eagenina@yandex.ru

Valery P. Zakharov, PhD, DSc
Department of Laser and Biotechnical Systems, Samara National Research University, Russia
E-mail: zakharov@ssau.ru

Contents

Special Section

Passive and Active Tumor Targeting in Photodynamic Therapy of Cancer: Mini-Review 040201
Blassan P. George and Heidi Abrahamse

Visualizing Nucleic Acid Loci with the CRISPR-Cas System: Current Approaches 040203
Gerel A. A. Abushinova, Victoria V. Zherdeva, Ekaterina M. Vassina, and Liliya G. Maloshenok

Optical Clearing for Deep Skin Imaging with Optical Methods 040204
Maxim E. Darvin and Jürgen Lademann

Inhibition of Lung Cancer Stem Cell Migration and Growth Through Nano-Photodynamic Therapy 040301
Anine Crous and Heidi Abrahamse

Possibility of Measuring of Erythrocyte Size Distribution Parameters by Laser Diffractometry of a Blood Smear 040302
Sergey Yu. Nikitin, Evgeniy G. Tsybrov, Maria S. Lebedeva, Andrei E. Lugovtsov, and Alexander V. Priezzhev

Enhanced Optical Imaging of Proximal Human Interphalangeal Joints Using Skin Optical Clearing 040303
Elina A. Genina, Ekaterina A. Kolesnikova, Viacheslav G. Artyushenko, Evgeny Berik, and Valery V. Tuchin

Therapeutic and Diagnostic Algorithm for Patients with Obstructive Jaundice Based on the Estimation of the Optical Characteristics of the Liver and Bile 040304
Elena V. Potapova, Ksenia Y. Kandurova, Vadim N. Prizemin, Dmitry S. Sumin, and Andrian V. Mamoshin

Study of the Effect of Formaldehyde Fixation on Collagen Optical Properties in the Terahertz Frequency Range 040306
Anastasia I. Knyazkova, Oksana D. Kuzminykh, Yury V. Kistenev, and Alexey V. Borisov

Silica Microspheres with Adsorbed Gold Nanostars for Single Cell SERS Detection of Formazan 040308
Olga A. Inozemtseva, Ekaterina S. Prikhozhdenko, Olga I. Gusliakova, Yulia A. Tyunina, Mariia S. Saveleva, Daniil N. Bratashov, Andrey M. Burov, and Boris N. Khlebtsov

Preparation of Fluorescently Labeled Bacteria via Biogenic Synthesis of Orange-Red Emitting Gold Nanoclusters 040309
Daniil S. Chumakov, Stella S. Evstigneeva, and Nikolai G. Khlebtsov

Estimating the Porosity of Nickel-Titanium (NiTi) Implants Using Optical Coherence Tomography and Machine Learning 040310
Viktor V. Nikolaev, Tatiana B. Lepekhina, Georgii V. Malkin, Alexander S. Garin, Ekaterina S. Marchenko, Alexander V. Dubrov, Maxim D. Khomenko, and Yury V. Kistenev

Optical Properties of Fluorescent Tags Based on Gold Nanoparticles at Physiological Salt Content: *In Vitro* and *In Vivo* Study 040312
Andrei Demenshin, Maria Istomina, and Elena Solovyeva

 © 2024 J-BPE

Effects of Illumination Angle and Different Light Sources on Acousto-Optic-based Sensing of Focused Ultrasound 040313
Mohammadreza Omidali, Triana Rahayu, Zuomin Zhao, Sadegh Moradi, and Teemu Myllylä

Nanocomposites Based on Gold Nanostars with a Hollow Silica Shell for Controlled-Release Drug Delivery 040314
Andrey V. Simonenko, Andrey M. Burov, and Vitaly A. Khanadeev

Radiation Patterns Formed by Sapphire Capillary Needles with Different Shapes of Internal Channels 040315
Irina A. Shikunova, Dmitry O. Stryukov, Julia N. Zubareva, Anna S. Kucheryavenko, Vladimir N. Kurlov, and Irina N. Dolganova

Phase Separation of L-Menthol an Aqueous Dispersion of Biologically Active Nanoparticles of Chitosan L- and D-Aspartate 040316
Xenia M. Shipenok, Aliya M. Mazhikenova, Evgeny G. Glukhovskoy, and Anna B. Shipovskaya

Non-Contact Automatic Respiratory Rate Monitoring for Newborns Using Digital Camera Technology and Deep Learning 040317
Huda Ali Hashim

Light Dose and Fluorescence Imaging Depth in Dual-Wavelength PDT: a Numerical Study for Various Photosensitizer Distributions in a Layered Biotissue 040318
Daria Kurakina, Ekaterina Sergeeva, Aleksandr Khilov, and Mikhail Kirillin

Comparison of Machine Learning Methods for the Analysis of Serum Raman Spectra in the Detection of Chronic Heart Failure 040319
Yulia Khristoforova, Elena Sorokina, Ivan Bratchenko, Maria Skuratova, Petr Lebedev, and Valery Zakharov

Reviews

Modern Optical Microscopy. Part 2 040202
Darya V. Prokopova and Svetlana P. Kotova

Articles

Laser-Stimulated Release of Methylene Blue from Porous Silicon Nanocontainers 040305
Alexandr A. Bubnov, Gleb N. Abrashitov, and Victor Yu. Timoshenko

Evaporation Peculiarities of Soft Biological Tissues in the Process of Automated 2D-Scanning of CO_2 Laser Radiation 040307
Alexander K. Dmitriev, Alexey N. Konovalov, Vladimir N. Kortunov, and Valery A. Ulyanov

Inactivation of Bacteria in Biofilms by Shock Waves 040311
Sergey Letuta, Azamat Ishemgulov, Olga Davydova, and Maxim Grigoriev

 © 2024 J-BPE

Passive and Active Tumor Targeting in Photodynamic Therapy of Cancer: Mini-Review

Blassan P. George and Heidi Abrahamse*
Laser Research Centre, Faculty of Health Sciences, University of Johannesburg, PO Box 17011, Johannesburg 2028, South Africa
*e-mail: habrahamse@uj.ac.za

Abstract. Photodynamic therapy (PDT) is a minimally invasive treatment procedure that utilizes a light of specific wavelength and a chemically nontoxic drug photosensitizer (PS) to generate reactive oxygen species (ROS) that can selectively destroy cancer cells or other targeted tissues. However, to increase the efficiency and application of PDT, several issues still need to be resolved. One of the main challenges in PDT is ensuring that the photosensitizing agent accumulates specifically in cancer cells and not in healthy tissues. This is particularly challenging for solid tumors, which have a complex microenvironment and poor vascularization. Passive and active targeting are two strategies in PDT that aim to improve treatment outcomes by enhancing the selective accumulation of PS in tumors thereby improving the cancer therapeutic outcome. These strategies play a critical role in optimizing the efficacy and safety of PDT for cancer treatment. Passive and active targeting strategies have their advantages and limitations. In this mini-review, we focus on the advantages and disadvantages of each method and discuss the role of stimuli-responsive changes in PS delivery. © 2024 Journal of Biomedical Photonics & Engineering.

Keywords: passive and active targeting; photosensitizers; photodynamic therapy; stimuli-response; cancer.

Paper #9100 received 15 Apr 2024; revised manuscript received 28 May 2024; accepted for publication 4 Jun 2024; published online 3 Aug 2024. doi: 10.18287/JBPE24.10.040201.

1 Introduction

Photodynamic Therapy (PDT) has been used as an alternative therapeutic option to treat various diseases including cancer. Oscar Raab discovered PDT more than a hundred years ago; however, the photodynamic reaction term was first coined by Von Tappeiner [1]. Even though PDT was discovered a hundred years ago, its widespread use started in late 1970s [2]. PDT works based on the utilization of light-sensitive photochemical molecules they are nontoxic in the dark and are called photosensitizers (PSs). The other two important components of PDT are light and oxygen. Due to their specific photochemical properties and cellular uptake efficiency, only a limited number of PSs have received approval to be used in clinics [3]. PS are photoactive molecules that aid their wide use as therapeutic agents in PDT as well as possess fluorescence, which properly enables their use in imaging and photodiagnosis of tumor cells. PDT-induced cell destruction involves different mechanisms of action [3, 4]. The extent of tissue damage and cell death mechanisms are dependent on various factors, such as the type of PS used, doses, subcellular localization, etc. PSs absorb specific wavelengths of light, triggering photochemical or photophysical reactions. A high degree of chemical purity, high photochemical reactivity, stability at room temperature, minimal dark toxicity, easy solubility, availability, and high selectivity for cancer cells are the important characteristics of an ideal PS. Ideal PS also should have minimum absorption in the range of 400 nm to 600 nm and a light absorption maximum between 600 nm and 800 nm [5−7].

In 1970s, Dougherty introduced PSs for the treatment on a commercial scale with the use of hematoporphyrin derivative (HpD). HpD is considered as a first-generation PS, obtained by purification and chemical modification

of the hematoporphyrin which is the first porphyrin used as PS. The first-generation PSs show minimal chemical purity and tissue penetration which leads to the accumulation in skin. These disadvantages lead to the development of second-generation PS with better chemical purity, higher singlet oxygen production, and better tissue penetration. Still, the low water solubility is a limiting factor. The third generation PS invention solves many of these drawbacks by developing PS with high affinity to tumor with reduced damage to nearby healthy tissues. Third generation PS developed by conjugation of second-generation PS with targeting entities or moieties [8, 9].

One of the biggest challenges in PDT is ensuring that the photosensitizing agent accumulates specifically in cancer cells and not in healthy tissues. This is particularly challenging for solid tumors, which have a complex microenvironment and poor vascularization [10−12]. Recently the drug delivery has become an important aspect of cancer research. Compared to the conventional drugs, nanoparticles-based drugs enhance the efficacy of drug delivery process due to its easy preparation, minimal toxicity and tumor targeting efficacies. Passive and active targeting are two ways to enhance the consequent PDT outcomes. Furthermore, passive and active targeting are two complementary approaches in PDT that aim to improve treatment outcomes by enhancing the selective accumulation of PSs in tumor tissues. These strategies play an important role in optimizing the efficacy and safety of PDT for cancer treatment [12−14]. In this mini-review we focus on advantages and disadvantages of each method and we also highlighted the limitations and recent developments in the area of tumor targeting.

2 Drug Delivery in Nanotechnology

Nanoparticles are typically designed to carry drugs and release them in a controlled manner, allowing for targeted and efficient drug delivery. There are various types of nanoparticles used in drug delivery, including liposomes, polymeric nanoparticles, dendrimers, and carbon nanotubes [15, 16]. These nanoparticles can be engineered to have specific properties such as size, shape, surface charge, and surface functionalization, which can influence their interactions with cells and tissues. One of the key advantages of using nanotechnology for drug delivery is the ability to enhance the therapeutic efficacy of drugs while minimizing their side effects [17]. Nanoparticles can improve drug solubility, stability, and bioavailability, allowing for better drug absorption and distribution in the body. Additionally, nanoparticles can be designed to target specific cells or tissues, such as tumor cells, by incorporating targeting ligands on their surfaces [18, 19]. This targeted drug delivery approach can increase drug accumulation at the desired site while reducing systemic toxicity. Nanoparticles can also be engineered to release drugs in a controlled manner, either through passive diffusion or by responding to specific stimuli such as pH, temperature, or enzymes. This controlled release mechanism can prolong the drug's therapeutic effect and reduce the frequency of drug administration [20−22].

2.1 Passive and Active Targeting

Recent research has shifted towards targeted drugs, which offer significantly improved efficiency in cancer treatment compared to traditional chemotherapeutic drugs, thus becoming the mainstream therapy for cancer. Imatinib, the first tyrosine kinase inhibitor, was approved by the Food and Drug Administration (FDA) in 2001. Since then, increased number of small molecules for targeting chemotherapeutic drugs have been established for various types of cancer treatments. Targeted chemotherapeutic drugs can be small molecules or macromolecules such as antibody, peptide, antibody drug conjugate, nucleic acid etc. [23].

The advantages of targeted drug delivery systems include safeguarding healthy cells from drug molecules that can cause cytotoxicity, a reduction in dose-limiting unpleasant side effects, and killing of tumor cells that are resistant to treatment and relapse. Because of the specific cellular uptake mechanisms, nanoparticles (NPs) act as drug delivery systems to the targeted sites in active form, in adequate doses and reduce the levels that settle down in healthy cells [24−26].The tumor update increased due to Enhanced Permeability and Retention (EPR) effect, that refers to the increased permeability of abnormal tumor blood vessels, allowing for enhanced drug delivery to tumor tissues while reducing systemic side effects, thereby achieving the improved PDT efficacy. The lack of normal lymphatic drainage in cancer cells leads to the retaining of NPs in cancer cells. Small molecule medicines, which have a short circulation time and quick clearance from cancer tissue. As a result, encapsulating small molecule drugs in nanosized drug carriers improves their pharmacokinetic characteristics to extend systemic circulation, provides cancer selectivity, and lowers the adverse side effects. Although it lacks a ligand for precise tissue binding, this sort of passive tumor targeting depends on the features of carrier molecules, such as size, circulation time, and tumor biology [27, 28].

Active targeting has the potential to greatly improve the amount of drug delivered to the target cells as compared to free drug or passively targeted nanocarriers. This can be achieved by the modification/addition of the nanocarrier sides with ligands binding to specific receptors upregulated on the cancer cells. This method will enhance the affinity of NPs to cancer cell surface and increase the drug diffusion. Most of the tumor cell targeting is achieved using nanocarriers that enhance the drug penetration. Numerous peptides, antibodies, and other small molecules are utilized often in targeted therapies [29]. In Fig. 1, it has been demonstrated how PS delivery can be targeted passively and actively with special reference to liposome mediated drug delivery. Fig. 1 also depicts three different drug loading strategies.

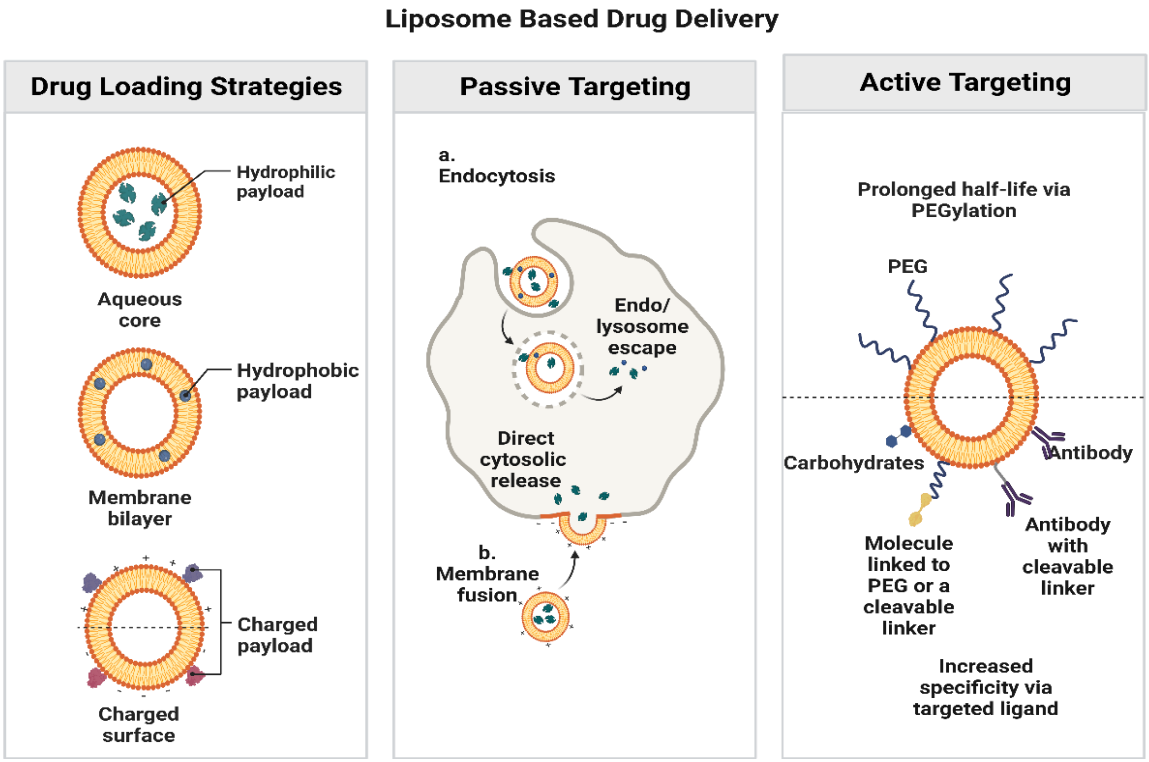


Fig. 1 Schematic representation of the hydrophilic and hydrophobic drugs loading on liposome for passive and active targeting application in cancer cells during PDT. During passive targeting liposomes can merge into cells via (a) Endocytosis and (b) Membrane fusion, while during active targeting, conjugating ligands and antibody can increase specificity of drug delivery in cells.

Recent studies in PDT have directed on many innovative methods to enhance the targeting of cancer cells using anticancer drugs and photosensitizers. An essential strategy involves combining a photosensitizing agent with folic acid (FA), potentially enhancing the targeting efficiency of folate receptors, which are often excessively expressed on the surface of numerous tumor cells. Stallivieri et al, synthesized different folic acid (oligo(ethylene glycol)) OEG conjugated photosensitisers and studied the photophysical properties for possible *in vitro* and *in vivo* applications. They found that introducing an OEG does not notably enhance the hydrophilicity of the FA-porphyrin. However, all FA-targeted photosensitizers synthesized exhibit favorable to excellent photophysical characteristics, with Chlorin e6 (Ce6) emerging as the most promising option [30]. Yan et al. conducted a study showcasing polydopamine (PDA)-FA-PS nanomedicine as an exceptionally potent and targeted anticancer solution. Additionally, they proposed a strategy to mitigate the metabolic and specificity challenges associated with clinical photosensitizers [31].

2.2 In Vitro and in Vivo Studies in PDT

Photosensitizers (PSs) have been loaded in various methods such as physical loading in self-assembled NPs for hydrophobic drugs and chemical conjugating of PSs to drug delivery and each procedure has advantages and drawbacks [32, 33]. In passive targeting the size and surface properties play critical role to PS delivery, while NPs have been coated with a number of ligands that attach to cell surface receptors to enable active targeting [34−36]. Tumor vascular network in contrast to normal tissue, has leakage endothelial layer and impairment of lymphatic drainage, so during passive targeting intravenous injection of PSs leads to accumulation in tumor [36]. In this area, Huang et al. examined human serum albumin (HSA) NP loading paclitaxel and sinoporphyrin as PS on 4T1 breast cancer cells. Their findings showed albumin has excellent potential to PS delivery, more uptake and long half-time in blood circulation [37]. A similar study in passive targeting area conducted by Gong et al, used hyaluronidase (HAase) which breaks down hyaluronan by extracellular matrix of tumor in chlorine e6 (NM-Ce6) nanocomplex on 4T1 cells *in vitro* and *in vivo*. They found that tumor uptake increased due to the EPR effect, thereby leads to improved PDT efficacy [38].

Several studies regarding active targeting therapy in PDT have been carried out. For instance, Naidoo et al., designed and synthesized an antibody-metallated phthalocyanine-polyethylene glycol-gold NP drug conjugate in PDT of A375 melanoma cells *in vitro*. They showed that the bio-active antibody PS drug targeting enhanced the PDT efficiency in A375 cancer cells [39] Moreover, Yoo et al. reported some ligands such as proteins, polysaccharides, aptamers, peptides can be employed in active targeting of NPs stature [40].

Table 1 Some studies in passive and active targeting of PSs agents in PDT.

References	Year	Nanocomplex or drug	Passive/Active targeting	Cell line	*In vitro*/*in vivo*
Y. Zhang et al. [37]	2020	HSA-NPs	Passive targeting via increasing temperature and cells permeability	4T1	*In vitro* and *in vivo*
H. Gong et al. [38]	2016	chlorine e6 (NM-Ce6)	Passive targeting (enhanced permeability and retention (EPR) effect)	4T1	*In vitro* and *in vivo*
C. Naidoo et al. [39]	2019	ZnPcS4 PS	Active targeting via conjugating specific antibody on gold nanoparticles	A375	*In vitro*
T. Qi et al. [41]	2019	TPP-PS	Passive targeting via pH-activatable of nanoparticle in tumor environment and increasing cell uptake	HO8910	*In vivo*
N. Iqbal et al. [42], J. Koval' et al. [43]	2014, 2010	hypericin (HY)	Active targeting via HY delivery by conjugating of Human epidermal growth factor receptor 2 (HER2) inhibitor	SKBR-3 cells	*In vitro*
H. J. Hah et al. [44]	2011	MB-conjugated PAA	Active targeting via coating with F3 peptides on PAA photosensitizer	9L, MDA-MB-435, and F98	*In vitro*
L. Zeng et al. [45]	2015	FA-NPs-DOX	Passive targeting via DOX-loaded on $NaYF_4$:Yb/Tm–TiO_2 (FA-NPs-DOX)	MCF-7	*In vitro*
Gavrina et al. [46]	2018	Ce6-PVA	Passive targeting via permeability of cells and cell uptake	CT26	*In vitro* and *in vivo*

Qi et al. reported that pH-activatable and mitochondria-targeted of Pyropheophorbide-a (PPa) conjugated with triphenyl phosphonium (TPP-NH2) shows high contrast in tumor imaging and remarkable suppress of HO8910-tumor progression without obvious toxicity *in vivo*. They concluded that the active targeting of PPa conjugated with TTP increases the enhanced uptake of the photosensitizer drug [41]. Human epidermal growth factor receptor 2 (HER2) in some cancers including breast and gastric has been targeted for active therapy [42]. Koval' et al. for the first time showed hypericin (HY) in combination with AG 825 can target HER2 in SKBR-3 breast cancer cells *in vitro* and increased apoptotic cell death and total degradation of HER2 via the high uptake of HY[43]. Another study by Hah et al., synthesised Methylene blue(MB)-conjugated polyacrylamide (PAA) NPs for PDT aimed on various cell lines such as 9L, MDA-MB-435, and F98. They coated the NPs with F3 peptides, which give specific targeting for 9L, MDA-MB-435, and F98 cancer cells *in vitro*. Finally they reported high uptake of NPs in all cell lines lead to increase the PDT efficiency with minimum cytotoxicity [44]. Furthermore, Zeng et al. synthesized Doxorubicin (Dox)-loaded NaYF4:Yb/Tm-TiO2 inorganic PSs (FA-NPs-Dox) to overcome resistant MCF-7/ADR cells in PDT. Their findings indicated that the presence of folic acid (FA) in FA-NPs-Dox facilitated the targeted cellular uptake and rapid release of Dox in drug-sensitive MCF-7 cells [45]. Some studies about passive and active targeting of PS agents in PDT have been summarized in Table 1.

Gavrina et al. investigated the effectiveness of PDT utilizing chlorin e6 (Ce6) formulated with polyvinyl alcohol (PVA) compared to Ce6 alone and the clinical drug Photodithazine *in vivo*. Their research indicated that encapsulating Ce6 in PVA shows promise in enhancing selectivity and PDT efficacy. They delved into the photoactivity of Ce6-PVA through a tryptophan oxidation model reaction, examined polymer-Ce6 interaction using fluorescence spectroscopy and atomic-force microscopy, and assessed phototoxicity *in vitro*. Fluorescence imaging *in vivo* revealed that injecting Ce6 in a PVA formulation into mice resulted in a higher tumor-to-normal ratio and more significant photobleaching compared to Ce6 alone or Photodithazine. Tumor growth analysis and histological

examination of CT26 tumors demonstrated rapid, consistent tumor regression and increased necrosis following PDT with Ce6-PVA. The heightened photoactivity of the Ce6-PVA complex was validated in a tryptophan oxidation model reaction and in cultured cells [46].

3 Advantages and Disadvantages of Passive and Active Targeting in PDT

Active targeting and passive targeting are two different approaches used in PDT to deliver PSs to the desired site for effective treatment. A comparison between active and passive targeting and highlights their advantages and disadvantages are shown in Table 2. Active targeting involves the use of specific ligands or antibodies that can recognize and bind to specific receptors or biomarkers on the surface of target cells or tissues. Ligands or antibodies are usually attached to the PS, allowing for selective delivery to the desired site. Passive targeting takes advantage of the unique characteristics of tumor tissues, such as leaky blood vessels and impaired lymphatic drainage. PSs are designed to have certain physicochemical properties that allow them to accumulate passively in tumor tissues through EPR effect [47, 48].

The decision between passive and active targeting procedures depends on the application and properties of the target tissue, both of which have advantages and disadvantages.

4 Role of Stimuli-Responsive Changes in PS Delivery

Ramin et al. conducted an extensive review focusing on stimuli-responsive drug delivery systems for active and/or passive targeted cancer chemotherapy, activated by physical and chemical cues. These systems represent a new paradigm in disease understanding at the molecular level, classified into physical and chemical categories. Stimuli-responsive materials undergo alterations in response to external triggers, offering precise control over drug release. This approach holds significant promise in nanomedicine and nanotechnology, facilitating controlled and targeted drug delivery. Stimuli-responsive drug delivery systems serve as innovative tools for oncotargeted therapy, enabling drug release through mechanisms such as EPR, interaction with overexpressed oncoreceptors, and theranostic applications [56].

Stimuli-responsive changes in PS delivery play an important role in drug release and enhancement of PDT outcomes. These changes involve the use of stimuli, such as light, temperature, pH, or enzymes, to trigger the release or activation of PSs at the target site [57, 58]. For instance, Yang et al. created hypoxia-responsive HSA based NPs for PDT. In this study, they described how to create a special kind of hypoxia-responsive HSA-based nanosystem (HCHOA) by cross-linking the PS, Ce6-conjugated HSA (HC), and oxaliplatin prodrug-conjugated HSA (HO) molecules of hypoxia-sensitive azobenzene groups. Their findings showed with a size of 100–150 nm, the HCHOA nanosystem is stabl under ambient oxygen partial pressure. When exposed to the hypoxic tumor microenvironment, the nanosystem can quickly split into ultrasmall HC and HO therapeutic NPs with a diameter less than 10 nm, considerably enhancing their improved intratumoral penetration. However, with the help of this straightforward approach, it is possible to boost tumor penetration and therapeutic impact by dissociating the hypoxic-responsive nanosystem [59].

Table 2 Advantages and disadvantages of passive and active targeting in PS delivery.

Types of PS delivery	Advantages	Disadvantages	References
Passive delivery	Relatively simple and does not require specific ligands or antibodies. It relies on the natural properties of tumor tissues, making it applicable to a wide range of tumors.	Passive targeting may not achieve high specificity compared to active targeting. The EPR effect can vary among different tumors and even within the same tumor, leading to inconsistent accumulation of PSs. Normal tissues may also accumulate PSs to some extent, potentially causing side effects.	[47−52]
Active targeting	Active targeting offers higher specificity and selectivity. This approach can enhance the accumulation of PSs at the target site, leading to improved therapeutic outcomes.	Achieving high targeting specificity while maintaining stability and functionality of the PS can be challenging. The biological environment is complex, and potential interactions with non-targeted components may affect the efficacy of active targeting.	[53−55]

Moreover, Zhang and colleagues in another study utilized a ROS-responsive linker for the managed release of PSs [60]. They created a block copolymer that reacts to $^1O_2$ (POEGMA-b-P(MAA-co-VSPpaMA)) to improve PDT by precisely controlled release of PSs. Pyropheophorbide-a (Ppa) could be controllably released via the trigger of $^1O_2$ generated by a short duration light irradiation once NPs synthesized by the block copolymer were accumulated in tumor and taken up by cancer cells. By controlling the release of Ppa with Near Infrared (NIR) illumination to enhance the sensitization of Ppa, a self-amplified PDT could be effectively realized by taking advantage of the $^1O_2$-responsiveness of POEGMA-b-P(MAA-co-VSPpaMA) block copolymer. This may offer new insight into the design of precise PDT. Some key points regarding the role of stimuli-responsive changes in PS delivery have been discussed here:

1. *Controlled release*: Stimuli-responsive systems can be designed to encapsulate PSs and release them in a controlled manner upon exposure to specific stimuli. For example, light-responsive systems can be designed to release PSs when illuminated with a specific wavelength of light. This allows for precise control over the timing and location of PS release, improving treatment outcomes.
2. *Enhanced selectivity*: Stimuli-responsive changes can help improve the selectivity of PS delivery by ensuring that the release or activation occurs only at the desired site. For instance, pH-responsive systems can be designed to release PSs in the acidic environment typically found in tumor tissues, minimizing off-target effects and reducing side effects on healthy tissues.
3. *Overcoming biological barriers*: Stimuli-responsive changes can also help overcome biological barriers that may hinder effective PS delivery. For instance, temperature-responsive systems can be designed to undergo phase transitions in response to mild hyperthermia, which can enhance the penetration and accumulation of PSs in tumor tissues.
4. *Combination therapy*: Stimuli-responsive changes can be combined with other therapeutic modalities to achieve synergistic effects. For example, combining PDT with chemotherapy or radiation therapy can enhance the overall treatment efficacy. Stimuli-responsive systems can be designed to release PSs in response to specific conditions created by these combination therapies, further improving treatment outcomes.

Overall, stimuli-responsive changes in PS delivery offer opportunities to improve the effectiveness and selectivity of PDT. By utilizing these changes, researchers and clinicians can enhance the therapeutic potential of PDT and contribute to the development of more targeted and personalized cancer treatments.

5 Future perspectives

Recent developments in enhancing passive and active targeting delivery of PSs in PDT have focused on the use of nanocarriers, active targeting ligands, stimuli-responsive systems, and multifunctional platforms. These advancements hold great promise for improving the efficacy and specificity of PDT in cancer treatment. Passive targeting relies on integrating the therapeutic agent into a macromolecule or nanoparticle, allowing it to reach the target organ passively. The efficacy of passive targeting hinges on the drug's circulation time, which is attained by enveloping the nanoparticle with a coating of some form. The active targeting strategy involves the binding of the antitumor agent, either covalently or non-covalently, to a molecule capable of selectively interacting with specific molecules on the surface of target cells. Here, we have summarized some suggestions and strategies to develop passive and active targeting of PSs.

1) Exploration of novel nanocarriers, 2) Targeting ligand optimization: Further research can be conducted to identify and optimize specific ligands or antibodies that have high affinity and selectivity for cancer cell receptors, 3) Combination therapies, 4) Personalized medicine approaches: Tailoring the passive and active targeting strategies to individual patients' specific tumor characteristics can improve treatment outcomes. 5) To overcome biological barriers, research efforts may target obstacles like the extracellular matrix or the blood-brain barrier, which could impede the efficient delivery of photosensitizers. 6) Combination of multiple targeting strategies: Combining passive and active targeting approaches can potentially enhance the overall delivery efficiency and specificity of PSs, 7) Combination of multiple targeting strategies: Combining passive and active targeting approaches can potentially enhance the overall delivery efficiency and specificity of PSs, 8) Long-term stability and safety: Ensuring the long-term stability and safety of the nanocarriers and PSs is crucial for their clinical application, 9) Stimuli-responsive nanocarriers: Designing nanocarriers that respond to specific stimuli in the tumor microenvironment, such as pH, temperature, or enzyme activity, can improve the targeted release of PSs, 10) Combination of physical and chemical targeting: Combining physical targeting strategies, such as passive accumulation through the EPR effect, with active targeting using ligands or antibodies can enhance the overall delivery efficiency and specificity of PSs, 11) Nanoscale drug delivery systems: Investigating the use of nanoscale drug delivery systems, such as liposomes, polymeric NPs, or exosomes, can improve the stability and pharmacokinetics of PSs. These systems can also be engineered to enhance cellular uptake and intracellular release of PSs.

6 Conclusion

In conclusion, both passive and active targeting of PSs have shown potential in improving PDT efficiency. Passive targeting takes advantage of the EPR effect to accumulate PSs in tumor tissues, while active targeting uses ligands or antibodies to specifically target cancer cells. Additionally, there are some key points regarding the role of stimuli-responsive changes in PS delivery and controlled release of drugs.

In the future, it will be important to continue developing and optimizing targeted delivery systems for PSs. This includes exploring new ligands or antibodies that can specifically recognize different types of cancer cells and developing multifunctional delivery systems that can carry both PSs and imaging agents for real-time monitoring. Furthermore, the integration of other emerging technologies, such as nanotechnology and immunotherapy, could further improve the PDT outcomes. NPs can be used as carriers for PSs, allowing the controlled release and improved delivery to tumors. Immunotherapy approaches, such as immune checkpoint inhibitors, can be combined with PDT to enhance the immune response against cancer cells. It seems, the future of targeted delivery of PSs in PDT looks promising. Continued research and development in this field will undoubtedly lead to improved therapeutic outcomes and better patient care. Additionally, the stimuli-responsive changes in PS delivery have the potential to significantly enhance the effectiveness of PDT. By designing systems that can release or activate PSs in response to specific stimuli, researchers can achieve controlled release, improve selectivity, overcome biological barriers, and combine therapies for synergistic therapeutic outcomes.

Acknowledgments

The authors sincerely thank the South African Research Chairs initiative of the Department of Science and Technology and the National Research Foundation (NRF) of South Africa, South African Medical Research Council (SAMRC), and Laser Research Centre (LRC), University of Johannesburg. The research reported in this review article was supported by the South African Medical Research Council (SAMRC) through its Division of Research Capacity Development under the Research Capacity Development Initiative from funding received from the South African National Treasury. The content and findings reported/illustrated are the sole deduction, view, and responsibility of the researchers and do not reflect the official position and sentiments of the SAMRC. The figures are created using BioRender.com website.

Funding

This work is based on the research funded by the South African Research Chairs initiative of the Department of science and technology and National Research Foundation (NRF) of South Africa (Grant No. 98337), South African Medical Research Council (Grant No. SAMRC EIP007/2021), as well as grants received from the NRF Research Development Grants for Y-Rated Researchers (Grant No: 137788), University Research Committee (URC), African Laser Centre (ALC), University of Johannesburg, and the Council for Scientific Industrial Research (CSIR)-National Laser Centre (NLC).

Disclosures

The authors declare that they have no conflict of interest.

References

1. The Lancet, "GLOBOCAN 2018: counting the toll of cancer," The Lancet 392(10152), 985 (2018).
2. H. Abrahamse, M. R. Hamblin, "New photosensitizers for photodynamic therapy," Biochemical Journal 473(4), 347–364 (2016).
3. K. Moloudi, H. Abrahamse, and B. P. George, "Photodynamic therapy induced cell cycle arrest and cancer cell synchronization: review," Frontiers in Oncology 13, 1225694 (2023).
4. K. Moloudi, P. Sarbadhikary, H. Abrahamse, and B. P. George, "Understanding the Photodynamic Therapy Induced Bystander and Abscopal Effects: A Review," Antioxidants 12(7), 1434 (2023).
5. M. M. Van Veen, J. J. S. Kooij, A. M. Boonstra, M. C. M. Gordijn, and E. J. W. Van Someren, "Delayed Circadian Rhythm in Adults with Attention-Deficit/Hyperactivity Disorder and Chronic Sleep-Onset Insomnia," Biological Psychiatry 67(11), 1091–1096 (2010).
6. B. Ortel, C. R. Shea, and P. Calzavara-Pinton, "Molecular mechanisms of photodynamic therapy," Frontiers in Bioscience 14(11), 4157−4172 (2009).
7. D. Sharma, S. Singh, P. Kumar, G. K. Jain, G. Aggarwal, W. H. Almalki, and P. Kesharwani, "Mechanisms of photodynamic therapy," Chapter 2 in Nanomaterials for Photodynamic Therapy, P. Kesharwani (Ed.), Elsevier, 41–54 (2023).
8. L. B. Josefsen, R. W. Boyle, "Photodynamic therapy: novel third-generation photosensitizers one step closer?," British Journal of Pharmacology 154(1), 1−3 (2008).
9. N. Plekhova, O. Shevchenko, O. Korshunova, A. Stepanyugina, I. Tananaev, and V. Apanasevich, "Development of Novel Tetrapyrrole Structure Photosensitizers for Cancer Photodynamic Therapy," Bioengineering 9(2), 82 (2022).
10. H. O. Alsaab, M. S. Alghamdi, A. S. Alotaibi, R. Alzhrani, F. Alwuthaynani, Y. S. Althobaiti, A. H. Almalki, S. Sau, and A. K. Iyer, "Progress in Clinical Trials of Photodynamic Therapy for Solid Tumors and the Role of Nanomedicine," Cancers 12(10), 2793 (2020).
11. M. Lan, S. Zhao, W. Liu, C. Lee, W. Zhang, and P. Wang, "Photosensitizers for Photodynamic Therapy," Advanced Healthcare Materials 8(13), 1900132 (2019).

12. H. Montaseri, C. A. Kruger, and H. Abrahamse, "Review: Organic nanoparticle based active targeting for photodynamic therapy treatment of breast cancer cells," Oncotarget 11(22), 2120–2136 (2020).
13. W. T. Li, "Nanotechology-based strategies to enhance the efficacy of photodynamic therapy for cancers," Current Drug Metabolism 10(8), 851−860 (2009).
14. A. M. Bugaj, "Targeted photodynamic therapy — a promising strategy of tumor treatment," Photochemical & Photobiological Sciences 10(7), 1097–1109 (2011).
15. A. Narmani, R. Jahedi, E. Bakhshian-Dehkordi, S. Ganji, M. Nemati, R. Ghahramani-Asl, K. Moloudi, S. M. Hosseini, H. Bagheri, P. Kesharwani, A. Khani, B. Farhood, and A. Sahebkar, "Biomedical applications of PLGA nanoparticles in nanomedicine: advances in drug delivery systems and cancer therapy," Expert Opinion on Drug Delivery 20(7), 937–954 (2023).
16. Y.-C. Lin, Z.-R. Lin, L.-W. Tsai, E. Perevedentseva, A. Karmenyan, and C.-L. Cheng, "Spectral Analysis of Nanodiamond-Berberine Complex Interaction with Living Cells for Nanoparticle Mediated Drug Delivery," Journal of Biomedical Photonics & Engineering 3(1), 010305 (2017).
17. A. Agrawal, S. Rellegadla, and S. Jain, "Biomedical applications of PLGA particles," Chapter 4 in Materials for Biomedical Engineering, A.-M. Holban, A. M. Grumezescu (Eds.), Elsevier, 87–129 (2019).
18. M. R. Gigliobianco, C. Casadidio, R. Censi, and P. Di Martino, "Nanocrystals of Poorly Soluble Drugs: Drug Bioavailability and Physicochemical Stability," Pharmaceutics 10(3), 134 (2018).
19. N. A. Charoo, Z. Rahman, and M. A. Khan, "Nanoparticles for improvement in oral bioavailability," Chapter 11 in Nanoarchitectonics in Biomedicine, A. M. Grumezescu (Ed.), Elsevier, 371–410 (2019).
20. N. C. Shinde, N. J. Keskar, and P. D. Argade, "Nanoparticles: Advances in drug delivery systems," Research Journal of Pharmaceutical, Biological and Chemical Sciences 3(1), 922−929 (2012).
21. D. Mishra, J. R. Hubenak, and A. B. Mathur, "Nanoparticle systems as tools to improve drug delivery and therapeutic efficacy," Journal of Biomedical Materials Research Part A: An Official Journal of The Society for Biomaterials 101(12), 3646–3660 (2013).
22. A. Z. Wilczewska, K. Niemirowicz, K. H. Markiewicz, and H. Car, "Nanoparticles as drug delivery systems," Pharmacological Reports 64(5), 1020–1037 (2012).
23. L. Zhong, Y. Li, L. Xiong, W. Wang, M. Wu, T. Yuan, W. Yang, C. Tian, Z. Miao, T. Wang, and S. Yang, "Small molecules in targeted cancer therapy: advances, challenges, and future perspectives," Signal Transduction and Targeted Therapy 6(1), 201 (2021).
24. S. Parveen, R. Misra, and S. K. Sahoo, "Nanoparticles: a boon to drug delivery, therapeutics, diagnostics and imaging," Nanomedicine: Nanotechnology, Biology and Medicine 8(2), 147−166 (2012).
25. Y. Herdiana, N. Wathoni, S. Shamsuddin, I. M. Joni, and M. Muchtaridi, "Chitosan-Based Nanoparticles of Targeted Drug Delivery System in Breast Cancer Treatment," Polymers 13(11), 1717 (2021).
26. K. Moloudi, A. Khani, M. Najafi, R. Azmoonfar, M. Azizi, H. Nekounam, M. Sobhani, S. Laurent, and H. Samadian, "Critical parameters to translate gold nanoparticles as radiosensitizing agents into the clinic," Wiley Interdisciplinary Reviews: Nanomedicine and Nanobiotechnology 15(6), e1886 (2023).
27. M. F. Attia, N. Anton, J. Wallyn, Z. Omran, and T. F. Vandamme, "An overview of active and passive targeting strategies to improve the nanocarriers efficiency to tumour sites," Journal of Pharmacy and Pharmacology 71(8), 1185–1198 (2019).
28. V. Torchilin, "Tumor delivery of macromolecular drugs based on the EPR effect," Advanced Drug Delivery Reviews 63(3), 131–135 (2011).
29. X. Wang, S. Li, Y. Shi, X. Chuan, J. Li, T. Zhong, H. Zhang, W. Dai, B. He, and Q. Zhang, "The development of site-specific drug delivery nanocarriers based on receptor mediation," Journal of Controlled Release 193, 139–153 (2014).
30. A. Stallivieri, L. Colombeau, G. Jetpisbayeva, A. Moussaron, B. Myrzakhmetov, P. Arnoux, S. Acherar, R. Vanderesse, and C. Frochot, "Folic acid conjugates with photosensitizers for cancer targeting in photodynamic therapy: Synthesis and photophysical properties," Bioorganic & Medicinal Chemistry 25(1), 1–10 (2017).
31. S. Yan, Q. Huang, J. Chen, X. Song, Z. Chen, M. Huang, P. Xu, and J. Zhang, "Tumor-targeting photodynamic therapy based on folate-modified polydopamine nanoparticles," International Journal of Nanomedicine 14, 6799−6812 (2019).
32. G. Yi, S. H. Hong, J. Son, J. Yoo, C. Park, Y. Choi, and H. Koo, "Recent advances in nanoparticle carriers for photodynamic therapy," Quantitative Imaging in Medicine and Surgery 8(4), 433–443 (2018).
33. J. Son, D. Lee, J. Yoo, C. Park, and H. Koo, "A comparative study of the effect of drug hydrophobicity on nanoparticle drug delivery in vivo using two photosensitizers," Nanomedicine: Nanotechnology, Biology and Medicine 24, 102151 (2020).
34. R. A. Petros, J. M. DeSimone, "Strategies in the design of nanoparticles for therapeutic applications," Nature Reviews Drug Discovery 9(8), 615–627 (2010).
35. R. H. Fang, C.-M. J. Hu, K. N. H. Chen, B. T. Luk, C. W. Carpenter, W. Gao, S. Li, D.-E. Zhang, W. Lu, and L. Zhang, "Lipid-insertion enables targeting functionalization of erythrocyte membrane-cloaked nanoparticles," Nanoscale 5(19), 8884 (2013).

36. J. D. Byrne, T. Betancourt, and L. Brannon-Peppas, "Active targeting schemes for nanoparticle systems in cancer therapeutics," Advanced Drug Delivery Reviews 60(15), 1615–1626 (2008).
37. Y. Zhang, Y. Wan, Y. Chen, N. T. Blum, J. Lin, and P. Huang, "Ultrasound-Enhanced Chemo-Photodynamic Combination Therapy by Using Albumin "Nanoglue"-Based Nanotheranostics," ACS Nano 14(5), 5560–5569 (2020).
38. H. Gong, Y. Chao, J. Xiang, X. Han, G. Song, L. Feng, J. Liu, G. Yang, Q. Chen, and Z. Liu, "Hyaluronidase To Enhance Nanoparticle-Based Photodynamic Tumor Therapy," Nano Letters 16(4), 2512–2521 (2016).
39. C. Naidoo, C. A. Kruger, and H. Abrahamse, "Targeted photodynamic therapy treatment of in vitro A375 metastatic melanoma cells," Oncotarget 10(58), 6079–6095 (2019).
40. J. Yoo, C. Park, G. Yi, D. Lee, and H. Koo, "Active Targeting Strategies Using Biological Ligands for Nanoparticle Drug Delivery Systems," Cancers 11(5), 640 (2019).
41. T. Qi, B. Chen, Z. Wang, H. Du, D. Liu, Q. Yin, B. Liu, Q. Zhang, and Y. Wang, "A pH-Activatable nanoparticle for dual-stage precisely mitochondria-targeted photodynamic anticancer therapy," Biomaterials 213, 119219 (2019).
42. N. Iqbal, N. Iqbal, "Human Epidermal Growth Factor Receptor 2 (HER2) in Cancers: Overexpression and Therapeutic Implications," Molecular Biology International 2014, 1–9 (2014).
43. J. Kovaľ, J. Mikeš, R. Jendželovský, M. Kello, P. Solár, and P. Fedoročko, "Degradation of HER2 Receptor Through Hypericin-mediated Photodynamic Therapy," Photochem & Photobiology 86(1), 200−205 (2010).
44. H. J. Hah, G. Kim, Y. K. Lee, D. A. Orringer, O. Sagher, M. A. Philbert, and R. Kopelman, "Methylene Blue-Conjugated Hydrogel Nanoparticles and Tumor-Cell Targeted Photodynamic Therapy," Macromolecular Bioscience 11(1), 90−99 (2011).
45. L. Zeng, Y. Pan, Y. Tian, X. Wang, W. Ren, S. Wang, G. Lu, and A. Wu, "Doxorubicin-loaded NaYF4:Yb/Tm–TiO2 inorganic photosensitizers for NIR-triggered photodynamic therapy and enhanced chemotherapy in drug-resistant breast cancers," Biomaterials 57, 93–106 (2015).
46. A. I. Gavrina, M. V. Shirmanova, N. A. Aksenova, D. V. Yuzhakova, L. B. Snopova, A. B. Solovieva, P. S. Timashev, V. V. Dudenkova, and E. V. Zagaynova, "Photodynamic therapy of mouse tumor model using chlorin e6- polyvinyl alcohol complex," Journal of Photochemistry and Photobiology B: Biology 178, 614–622 (2018).
47. D. Lee, S. Kwon, S. Jang, E. Park, Y. Lee, and H. Koo, "Overcoming the obstacles of current photodynamic therapy in tumors using nanoparticles," Bioactive Materials 8, 20–34 (2022).
48. S. Moghassemi, A. Dadashzadeh, R. B. Azevedo, O. Feron, and C. A. Amorim, "Photodynamic cancer therapy using liposomes as an advanced vesicular photosensitizer delivery system," Journal of Controlled Release 339, 75–90 (2021).
49. S. Md, S. Haque, T. Madheswaran, F. Zeeshan, V. S. Meka, A. K. Radhakrishnan, and P. Kesharwani, "Lipid based nanocarriers system for topical delivery of photosensitizers," Drug Discovery Today 22(8), 1274–1283 (2017).
50. S. Marchal, G. Dolivet, H.-P. Lassalle, F. Guillemin, and L. Bezdetnaya, "Targeted photodynamic therapy in head and neck squamous cell carcinoma: heading into the future," Lasers in Medical Science 30(9), 2381–2387 (2015).
51. J. C. S. Simões, S. Sarpaki, P. Papadimitroulas, B. Therrien, and G. Loudos, "Conjugated Photosensitizers for Imaging and PDT in Cancer Research," Journal of Medicinal Chemistry 63(23), 14119–14150 (2020).
52. A. Dhaliwal, G. Zheng, "Improving accessibility of EPR-insensitive tumor phenotypes using EPR-adaptive strategies: Designing a new perspective in nanomedicine delivery," Theranostics 9(26), 8091–8108 (2019).
53. A. Gumala, S. Sutriyo, "Active Targeting Gold Nanoparticle for Chemotherapy Drug Delivery: A Review," Pharmaceutical Sciences 28(3), 342−354 (2021).
54. L. Lin, L. Xiong, Y. Wen, S. Lei, X. Deng, Z. Liu, W. Chen, and X. Miao, "Active Targeting of Nano-Photosensitizer Delivery Systems for Photodynamic Therapy of Cancer Stem Cells," Journal of Biomedical Nanotechnology 11(4), 531–554 (2015).
55. O. C. Didamson, R. Chandran, and H. Abrahamse, "A Gold Nanoparticle Bioconjugate Delivery System for Active Targeted Photodynamic Therapy of Cancer and Cancer Stem Cells," Cancers 14(19), 4558 (2022).
56. M. A. Rahim, N. Jan, S. Khan, H. Shah, A. Madni, A. Khan, A. Jabar, S. Khan, A. Elhissi, Z. Hussain, H. C. Aziz, M. Sohail, M. Khan, and H. E. Thu, "Recent Advancements in Stimuli Responsive Drug Delivery Platforms for Active and Passive Cancer Targeting," Cancers 13(4), 670 (2021).
57. J. Tian, C. Xiao, B. Huang, C. Wang, and W. Zhang, "Janus macromolecular brushes for synergistic cascade-amplified photodynamic therapy and enhanced chemotherapy," Acta Biomaterialia 101, 495–506 (2020).
58. W. Yu, R. Liu, Y. Zhou, and H. Gao, "Size-Tunable Strategies for a Tumor Targeted Drug Delivery System," ACS Central Science 6(2), 100–116 (2020).
59. G. Yang, S. Z. F. Phua, W. Q. Lim, R. Zhang, L. Feng, G. Liu, H. Wu, A. K. Bindra, D. Jana, Z. Liu, and Y. Zhao, "A Hypoxia-Responsive Albumin-Based Nanosystem for Deep Tumor Penetration and Excellent Therapeutic Efficacy," Advanced Materials 31(25), 1901513 (2019).
60. Z. Liu, T. Cao, Y. Xue, M. Li, M. Wu, J. W. Engle, Q. He, W. Cai, M. Lan, and W. Zhang, "Self-Amplified Photodynamic Therapy through the $^1O_2$ -Mediated Internalization of Photosensitizers from a Ppa-Bearing Block Copolymer," Angewandte Chemie International Edition 59(9), 3711−3717 (2020).

Visualizing Nucleic Acid Loci with the CRISPR-Cas System: Current Approaches

Gerel A. Abushinova[1,2], Victoria V. Zherdeva[2], Ekaterina M. Vassina[1], and Liliya G. Maloshenok[1,2*]

[1] Vavilov Institute of General Genetics Russian Academy of Sciences, 3 Gubkina str., 119333 Moscow, Russian Federation

[2] Bach Institute of Biochemistry, Research Center of Biotechnology of the Russian Academy of Sciences, 33 Leninsky pr., build. 2, Moscow 119071, Russian Federation

[*]e-mail: maloshenoklg@gmail.com

Abstract. The visualization of genomic loci in living cells is crucial for detecting mutations and observing the spatial proximity of DNA regions in the 3D nuclear environment. One of the primary applications of the clustered regularly interspaced short palindromic repeats–CRISPR-associated protein 9 (CRISPR/Cas9) system is the non-invasive, real-time labeling of DNA loci in living cells, enabled by its unique characteristics. Visualization of genomic loci has been made possible by the use of an endonuclease-inactive form of the Cas9 protein (dCas9) and sgRNA in combination with fluorescent molecules. However, using CRISPR/Cas9 for targeting DNA regions has certain limitations, the most significant being suboptimal signal-to-noise ratio, the need for multiplexed labeling, and the large size of the Cas fluorescent reporter sytem, which impacts the complex's functionality and complicates its delivery. Current variations of the method using CRISPR/dCas9 overcome these limitations in different ways. This review examines the evolution of genome locus visualization methods based on CRISPR/Cas9 from the initial use of the system to the present. © 2024 Journal of Biomedical Photonics & Engineering.

Keywords: CRISPR/Cas9; genome locus visualization; endonuclease-inactive Cas9 protein; nucleic acids.

Paper #9176 received 9 Oct 2024; revised manuscript received 27 Nov 2024; accepted for publication 27 Nov 2024; published online 29 Dec 2024. doi: 10.18287/JBPE24.10.040203.

1 Introduction

The function of the clustered regularly interspaced short palindromic repeats (CRISPR)- CRISPR associated (Cas) system is based on the ability of the Cas protein to bind with a guide RNA that is complementary to a specific target DNA sequence. Additionally, the protein recognizes a specific sequence of 3-6 nucleotide adjacent to the target DNA, enhancing the overall specificity of the system [1]. While the primary function of the CRISPR-Cas system is to induce double-strand breaks in target DNA, leading to deletions or replacements in the genome, it has been adapted for many other applications. Many of these are based on the mutagenic inactivation of the endonuclease activity of the Cas protein, known as dCas [2]. Despite losing the ability to induce DNA breaks, dCas retains its capacity to bind to guide RNA and target DNA. Proteins linked to dCas via a linker (dCas-X) are known to maintain their activity, thereby expanding their range of applications, such as methylation and demethylation of specific DNA loci [3, 4], activation (CRISPRa) and inactivation (CRISPRi) of transcription in specific DNA regions [5, 6], base editing using adenosine deaminases [7], and analysis of chromatin remodeling factors via biotinylation (CAPTURE - CRISPR affinity purification in situ of regulatory elements, CasID) [8−10]. However, one of the earliest methods using dCas9 is the visualization of genomic loci with molecules, where dCas9 is fused to fluorescent protein (dCas9-FP). Today, this method has undergone numerous modifications aimed at optimizing labeling for key tasks such as marking loci in living cells and tracking them in real time. This is essential for better understanding the molecular mechanisms underlying chromatin dynamics. Beyond its

role in fundamental research, this technique also shows significant potential in medical diagnostics, particularly for detecting hereditary disorders. Currently, diseases caused by microdeletions and microduplications are predominantly diagnosed using Multiplex Ligation-dependent Probe Amplification (MLPA) − a technically challenging, multi-step technique requiring sample denaturation. Moreover, interpreting MLPA results can be complicated by factors such as mosaicism, contamination with normal tissue, and mutation heterozygosity [11]. Therefore, the CRISPR-Cas9 system offers a transformative alternative, enabling direct visualisation of genomic loci, overcoming many of the limitations of traditional diagnostic methods.

2 Visualization of Genomic Loci in Living Cells Using the CRISPR-Cas System

The non-invasive introduction of CRISPR-Cas components into cells, without the need for DNA fixation or denaturation, enables the dynamic visualization of genomic loci throughout the cell's life cycle. Currently, there are four CRISPR-Cas systems that can potentially be used for visualizing DNA or RNA loci. These include Class 2 CRISPR/Cas systems: CRISPR/Cas9, CRISPR/Cas12a, CRISPR/Cas13, and CRISPR/Cas12f (also known as CRISPR/Cas14). The Cas proteins in these systems have the ability to bind to guide RNA and target DNA, as well as introduce breaks in nucleic acids (NA). This makes them applicable in higher eukaryotic cells since these systems require fewer components than Class 1 CRISPR/Cas systems, simplifying their delivery [12].

At present, endonuclease-inactive forms of the Cas protein (dCas) have been developed for all these systems, with mutations in the HNH and RuvC domains, preserving all functions except for introducing breaks in NA [13, 14]. Comparing the mechanisms of different systems within Class 2, we see that CRISPR/Cas9 and CRISPR/Cas12a differ in two key aspects that are crucial for their application in higher eukaryotic cells. Specifically, Cas9 recognizes GC-rich protospacer adjacent motif (PAM) sequences and creates double-strand breaks in DNA, leaving blunt ends. In contrast, Cas12a requires recognition of AT-rich PAM sequences, resulting in the formation of sticky ends in DNA [15, 16]. Therefore, when visualizing DNA loci, the only relevant difference lies in the nucleotide composition of the PAM, which can be effectively addressed by using various Cas9 orthologues or modifying its PI domain. The other two Class 2 CRISPR/Cas systems show greater functional diversity. For instance, Cas13 recognizes and cleaves RNA sequences [17], making it suitable for labeling RNA molecules. Cas12f, discovered in 2018 and initially named Cas14, is distinct from previously identified Class 2 CRISPR/Cas proteins. The main distinguish due to its significantly smaller size (400−700 amino acids, compared to 1,250, 1,300, and 1,368 amino acids for Cas13, Cas12a, and Cas9, respectively) and operates as a dimer to introduce double-strand breaks in DNA, although its monomeric form can cleave single-stranded DNA [18−20]. Additionally, Cas12f does not require recognition of a PAM sequence when targeting a specific DNA fragment using a 36-nucleotide guide RNA. Despite these advantages, Cas12f remains the least studied system. Therefore, the only two CRISPR/Cas systems currently used for labeling nucleic acid sequences are Cas9 and Cas13.

3 DNA Labelling

The first DNA locus labeling using the dCas9 protein fused to a fluorescent protein (EGFP) was demonstrated by Chen et al. [21]. This study showcased the method's capability for real-time analysis of chromatin behavior and conformation, offering potential insights into telomere length, gene copy number, and interactions between different loci. However, the existing limitations – such as the inability to simultaneously labeling of multiple loci in a single living cell, the need to introducinge numerous guide RNAs, and a low signal-to-noise ratio (SNR) – emphasized the need for further method optimization.

The first issue (labeling multiple NA loci simultaneously) was addressed by using several dCas9 orthologs, each recognising different PAM sequences and targeting distinct DNA loci, along with fluorescent proteins of different colours. For instance, Chen et al. used two Cas9 orthologs (SpdCas9 and SadCas9) to label two loci at once [22], and Ma et al. utilised NmdCas9 and StdCas9 [23]. One key drawback of the dCas9-FP system was its SNR. To tackle this, researchers increased the number of fluorescent components in the reporter system. Tanenbaum et al. introduced the SunTag peptide scaffold, which can bind to an scFv antibody fused with GCN4 peptide and EGFP, allowing recruitment of up to 24 EGFP molecules. Using this system to label telomeres significantly increased signal intensity [24].

Later, Ye et al. [25] applied the SunTag approach with a brighter fluorescent protein, Neon Green, reducing the number of guide RNAs needed for labeling. However, issues remained, particularly with the size of the construct and high background fluorescence levels. To mitigate background fluorescence, Ye et al. [26] proposed a system where fluorescence is only activated in the complete ribonucleoprotein complex (dCas9-sgRNA). They enhanced the signal by attaching multiple copies of fluorescent protein fragments to the system's components, enabling the simultaneous visualization of up to three DNA loci. The individual components were fused to the N- and C-terminal parts of the yellow fluorescent protein Venus, as described previously. Through bimolecular fluorescence complementation (BiFC), Venus regained its full structure upon the formation of the ribonucleoprotein complex. This method eliminated background fluorescence from free dCas9 protein bound to the fluorescent molecule or guide RNA recruiting fluorescent proteins. Additionally, this study demonstrated signal enhancement by using alternative fluorescent proteins, such as mCherry and Clover, to label genomic loci, reducing background noise and improving signal strength. However, several limitations remain, primarily due to the bulkiness of the construct. Currently, signal enhancement

can be achieved not only by increasing the number of fluorescent molecules but also by improving their brightness and photostability. Organic dyes exhibit significantly greater brightness and photostability compared to the fluorescent proteins typically used in dCas systems. Furthermore, some of them have the added advantage of being able to penetrate cells. Grimm and colleagues were the first to create fluorescent dyes that maintained their spectroscopic characteristics while being capable of cell penetration by modifying tetramethylrhodamine [27]. This structural alteration of the dye allowed Deng et al. [28] to use Halo Tag labels linked to dCas9 proteins and fluorescent dyes as markers for visualising genomic loci in the nucleus. Additionally, molecular beacons (MBs), oligonucleotides complementary to target sequences equipped with fluorescent tags and quenchers, present a viable alternative. The quencher is attached in such a way that it suppresses fluorescence when the beacon is not bound to its target sequence. Wu et al. applied MBs in conjunction with the CRISPR-Cas9 system for DNA visualization, where MBs bind to guide RNA loops, thereby enhancing the signal while minimizing background fluorescence by preventing emission from unbound MBs [29]. Mao et al. further modified sgRNAs to interact with two distinct molecular beacons simultaneously, thereby expanding the diversity of color labels available for targeting specific DNA sequences [30].

All the methods discussed significantly improve the SNR and enable the labeling of various DNA sequences using fewer guide RNAs. However, in recent years, systems based on the Casilio method have shown even better results. This method uses Pumilio RNA-binding proteins that recognize specific 8-mer PUF-binding sequences (PBS), which are typically integrated into the guide RNA. By extending the guide RNA, more fluorescent proteins can be recruited, enabling complex multimerization and labeling of non-repetitive sequences. This system employs proteins such as Clover and Ruby, which are significantly brighter than commonly used GFP and mCherry, reducing the required number of guide RNAs to just one per non-repetitive sequence [31]. However, in this system, increasing signal intensity also raises background fluorescence due to the recruitment of fluorescent proteins by the tag molecule. This issue was mitigated by using the t-Deg peptide, which makes fluorescent proteins fluorogenic. These proteins are normally degraded through the proteasomal pathway via ubiquitination, but when a Pepper RNA aptamer is present, the t-Deg peptide binds to it, preventing degradation. By integrating this mechanism with the CRISPR-Cas9 system, Zhang et al. developed a fluorogenic CRISPR system that incorporates the Pepper aptamer into the guide RNA, recruiting a fluorogenic protein through a degron [32]. Since all fluorescent proteins not bound to the aptamer are degraded, this system significantly reduces background fluorescence and effectively visualizes both high-copy (e.g., telomeres) and low-copy DNA sequences. Additionally, the system can label sequences using two fluorescent proteins simultaneously, enhancing the signal by recruiting multiple fluorescent proteins, one of which is tagged with the tDeg peptide. Interestingly, each guide RNA can recruit up to 12 fluorescent proteins to both of its loops. These proteins do not fluoresce when attached individually because the system removes 1–10 β-strands from the fluorescent proteins attached to one loop and the 11th β-strand from the proteins bound to the second loop. This approach enhances the signal without increasing background fluorescence and allows for the labeling of non-repetitive DNA sequnces [33]. Compared to the Casilio method and two other new approaches, which also aim at visualising non-repetitive DNA sequences, this method features simpler guide RNA engineering and a less bulky fluorescent reporter system. For example, the CRISPR FISHer ((CRISPR-mediated) fluorescence *in situ* hybridisation amplifier) method utilises a system for local signal amplification by binding sgRNA through two PP7 aptamers to a foldon (C-terminal domain of T4 fibritin) complex made up of GFP, the PCP coat protein, and the trimeric motif of T4 fibritin. It was shown that attaching up to eight aptamers to the guide RNA and adding purified foldons to the system led to exponential complex assembly and local accumulation at the guide RNA targeting locus [34]. Peng et al. developed the Simultaneous Imaging and Manipulation of genomic loci by Biomolecular Assemblies (SIMBA) method to enhance signal strength during genomic locus labeling by leveraging multivalent interactions between HP1α and SunTag repeats. In this approach, FRB-mCherry-HP1α molecules are recruited to dCas9, which is fused to 24 SunTag repeats, and activated using rapamycin. To reduce background fluorescence, the Venus fluorescent protein is split across different guide RNA loops, while signal enhancement is achieved through the recruitment of large numbers of FRB-mCherry-HP1α molecules [35]. These methods not only reduce background fluorescence but also enable the labeling of non-repetitive sequences and can even detect DNA breaks. This opens up the possibility of using these approaches to observe chromatin integrity and its dynamic changes in living cells. Additionally, they hold potential for monitoring genome editing processes by active Cas proteins. Nearly all the cited studies emphasise that background fluorescence affects target point detection and, consequently, any associated measurements − typically involving fluorescence intensity, photostability, and fluorophore lifetime. Several factors contribute to background fluorescence, including the nature of the effector molecule, the induction mechanism for transgene expression, and the delivery method. Studies highlight the advantages of lentiviral transduction over transient transfection for delivering constructs, as well as the impact of viral titer ratios on the various components involved. Excessive amounts of fluorescent products or bulky constructs can induce cytotoxic and phototoxic effects in cells. To mitigate transgene toxicity, some methods rely on inducible systems such as Tet-On,

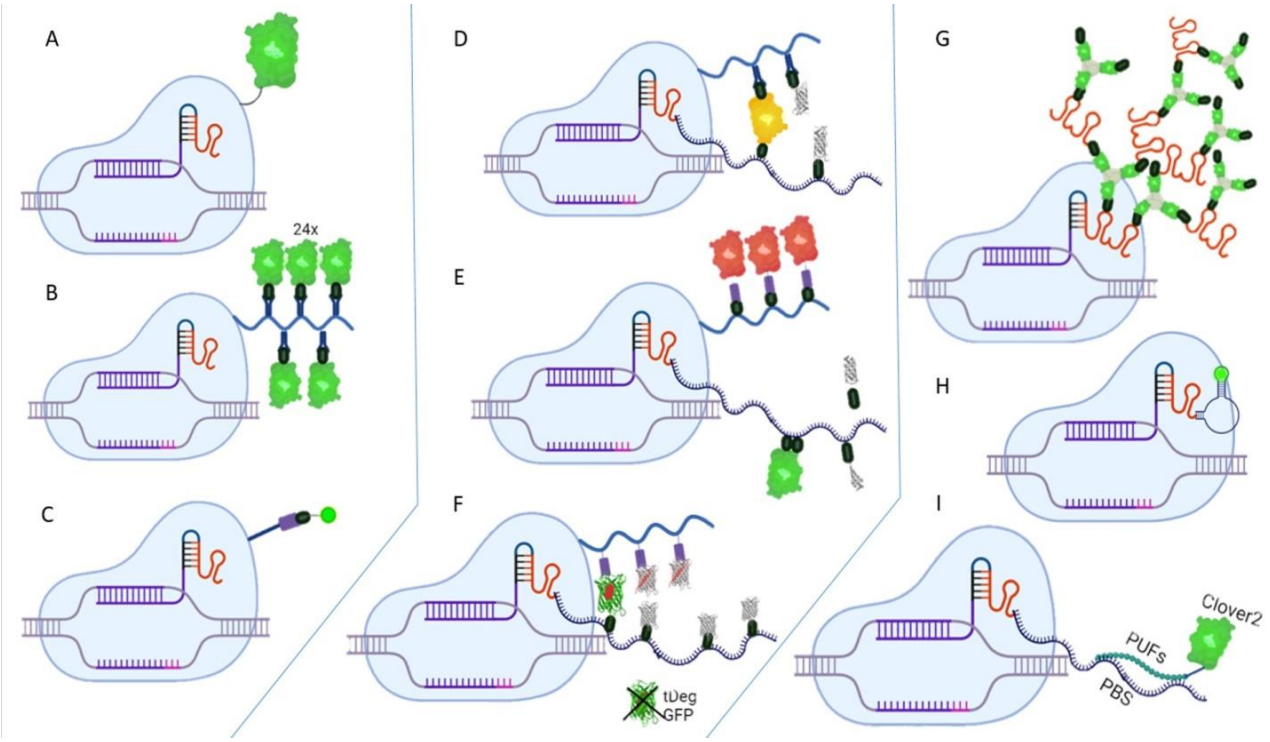


Fig. 1 Methods for labeling DNA loci using the CRISPR/Cas9 system. Methods based on the modification of dCas9: (A) dCas9-FP, (B) dCas9-SunTag, (C) dCas9-HaloTag. Methods based on the modification of both dCas9 and sgRNA: (D) dCas9-BiFC-sgRNA, (E) SIMBA, (F) dCas9-tDeg-sgRNA-Pepper. Methods based on the modification of sgRNA: (G) FISHer, (H) sgRNA-aptamer, (I) Casilio.

where delayed component introduction or fluorescent protein degradation mechanisms are often employed. Additionally, splitting fluorescent proteins into two non-fluorescent parts can help reduce background noise.

Therefore, among the methods described, the CRISPR-Cas9 approach utilizing fluorogenic split proteins remains the most promising for DNA labeling in living cells. Fig. 1 provides an overview of the techniques used for labeling genomic loci with these methods.

4 RNA Labelling

Even before the discovery of dCas13 and its ability to label RNA sequences, dCas9 was modified to recognise RNA sequences instead of DNA [36]. This was achieved by replacing the PAM-recognition domain with an oligonucleotide called PAMmer, which hybridises with the target RNA, allowing the new RdCas9 to target sequences in RNA. This protein is also smaller, making it easier to deliver the coding sequences compared to the original constructs used for DNA labelling. In subsequent work [37], Batra and colleagues demonstrated that RdCas9-EGFP could not only visualise microsatellite expansions of repeats but also eliminate such repeats in human RNA, leading to positive molecular changes in the cell. This could be considered a potential therapeutic approach for treating certain diseases.

A few years later, Sun et al. combined the RNA locus labelling system RdCas9-EGFP with the SunTag approach to label non-repetitive sequences in RNA [38]. They developed a fluorescent RNA aptamer called Pepper, which has high photostability and brightness compared to its analogs. This monomeric aptamer features a wide range of emission maxima from blue to red, allowing for reliable visualisation of RNA in living cells. The study also demonstrated the ability to target the Pepper aptamer using the CRISPR/Cas9 system [39].

Subsequent approaches for visualising RNA loci have primarily relied on the CRISPR-Cas13 system, which targets RNA. Similar to Cas9, an endonuclease-inactive form of Cas13 was created and later fused with a fluorescent protein [40]. This method is user-friendly, does not require complex genetic manipulations, and effectively visualises both repetitive and non-repetitive RNA regions.

Further development led to the dCas13a-NF (Negative-Feedback) approach, which incorporates the KRAB repression domain. This modification reduces background fluorescence and allows for precise targeting of non-repetitive sequences [41]. Similar results have been observed when combining the dCas13 system with RNA aptamers [42].

Tang and his team achieved more accurate visualisation of RNA loci by using dCas13 linked to the Tat peptide, which interacts with fluorescent RNA aptamers via the trans-activation response (TAR) hairpin structure [43]. This design is flexible, smaller, and provides pinpoint signals, optimising the signal-to-noise ratio. Today, this method is considered the most effective for multiplexed visualisation of non-repetitive RNA sequences.

As seen in the Table 1, various DNA locus labeling systems have been developed to visualise highly repetitive sequences (such as telomeric, centromeric, and pericentromeric regions, as well as the exon of the MUC4 oncogene) and repetitive sequences (e.g., the intron of the MUC4 oncogene and the 5S rDNA gene). However, only a few studies have optimized these systems to label unique sequences and improve the signal-to-noise ratio (Table 1). This often increases the complexity of the fluorescent tag, complicating its delivery or functionality. Additionally, it is important to note that the main method for visualisation remains confocal fluorescence microscopy.

Table 1 Advantages and Limitations of CRISPR/Cas-Based Visualisation Methods.

Visualization method	Cas protein	Fluorescent reporter system	Target	Advantages	Limitations	Microscopy method	Ref.
Visualization of chromatin/genomic loci							
Fluorescent Protein Based	dCas 9	dCas9-EGPF	Telomeres*, MUC4 gene**	A simple and versatile tool for DNA visualization	Low signal-to-noise ratio (SNR), low labeling efficiency.	Fluorescent confocal microscopy	[21]
	dCas 9	dSaCas9-EGFP, dSpCas9-mCherry	Telomeres*, centromeres*, MUC4* gene*, 5S rDNA gene** and unique tandem repeats on chromosomes 1, 7, and 17**	Two-Color Image of CRISPR	Relatively weak fluorescence signal and low signal-to-noise ratio	Fluorescent Widefield Microscopy	[22]
	dCas 9	dSt1Cas9-EGFP, dSpCas9-EGFP, dNmCas9-mCherry	Telomeres*	Tet-on expression, highly specific detection based on the fluorescent protein's lifetime	A preliminary assessment of the dynamics of inducible expression of labeled orthologs is required	Fluorescent confocal microscopy	[44]
	dCas 9	dCas 9/ sgRNA-aptamer-FP	Telomeres* and unique tandem repeats on chromosomes 1, 3, 7, 13, 14, and X**	Simultaneous labeling of six genetic loci	Complex sgRNA design; an effective delivery system is required	Fluorescent Phase-Contrast Microscopy	[45]
	dCas 9	dCas9-SunTag-scFv-GCN4-sfGFP	Telomeres*	Enhancing fluorescence intensity improves SNR, enabling the labeling of rare motifs	The large size of the reporter molecule impacts functionality of Cas9	Fluorescent confocal microscopy	[24]

Table 1 Cont.

	dCas 9	dCas9-SunTag-FRB-mCherry-HP1α	Telomeres*, MUC4 gene**, MUC4.1gene***, IL-1B gene****	Enhancing fluorescence intensity improves SNR, enabling the labeling of rare motifs	The large size of the reporter molecule impacts functionality of Cas9 and gene activity	Fluorescent confocal microscopy	[35]
	dCas 9	dCas9/sgRNA-PP7-PCP-T4 fibritin foldon-GFP	Telomeres*, Chr3Rep*, Chr13q34*, PPP1R2 locus***, SOX1 gene***, TOP3 gene***, TOP1gene***, BAGE gene***, TPTE gene***	Signal amplification enhances detection directly at the recognition site, improves the SNR and enables labeling of unique sequences	The large size of the reporter molecule complicates the its delivery.	Fluorescent confocal microscopy	[34]
Based on the BiFC Fluorescent Protein system	dCas 9	dCas9-N-Venus/sgRNA-C-Venus	Telomeres*, MUC4*, repetitive sequence on chromosome 3**, EMX-1 gene***	Improved signal-to-noise ratio, use of smaller amounts of guide RNA, high specificity	Low SNR, complex sgRNA design, and too large reporter molecule for labeling non-repetitive sequences	Fluorescent confocal microscopy	[26]
Based on organic dyes	dCas 9	dCas9-HaloTag/sgRNA	Telomeres*, centromeres*, major satellites*	Cost-effective, efficient	Altered cell physiology	Fluorescent confocal microscopy	[28]
	dCas 9	sgRNA-MTS-MB	Telomeres*, satellites*	Flexible combinations of fluorophore/cleavage agent pairs and MB/MTS sequences	MBS are costly	Fluorescent confocal microscopy	[29]
	dCas 9	dCas 9/3sgMUC4-dual-MTS-MB	Telomeres*, MUC4 gene*	Dynamic visualisation of unique genomic motifs using only three distinct sgRNAs. High sensitivity	MBS are costly. Simultaneous visualization of multiple genomic motifs is impossible	Fluorescent confocal microscopy	[30]
Fluorescent Protein Based	dCas 9	dCas9/SgRNA-Pepper-tdTomato-Tdeg	Telomeres*, centromeres*, MUC4 gene**, sequences on chromosomes 13*, 3, 9, 13, and 19*.	Efficient labeling of two repetitive sequences and labeling of a unique sequence with a single guide RNA. Reduced background signal	Complex sgRNA design, background signal retention, and use of multiple guide RNA	Fluorescent confocal microscopy	[32]

Table 1 Cont.

Fluorescent Protein Based		dCas9/SgRNA-Pepper-split12xGFP-Tdeg	Telomeres*, centromeres*, sequence on chromosome 3*, IDR1 **, IDR3** (intergenic DNA regions (IDRs)), FBN3 gene**, IL-1B gene***	Efficient labeling of two repetitive sequences and labeling of a unique sequence with a single guide RNA. Reduced background signal	Complex sgRNA design	Fluorescent confocal microscopy	[33]
RNA Visualization							
Fluorescent Protein Based	dCas 9	dCas9-FP	(CTG) repeats***, (CCTG) repeats**, and (CAG) repeats***	RNA Visualization	Limited visualization of low abundance mRNA	Fluorescent confocal microscopy	[37]
	dCas 9	dCas9-EGFP	HBG1 mRNA transcripts	Enables efficient visualization of mRNA	The large size of the reporter tag	Fluorescent confocal microscopy	[38]
Organic dyes based	dCas 9	dCas9/sgRNA-Pepper530	CAP31 and TMED2 mRNA transcripts	High fluorescence intensity and its rapid induction	The detailed structure-activity relationship of Pepper is poorly studied	Fluorescence confocal microscopy, two-photon excitation microscopy, Structured Illumination Microscopy (SIM)	[39]
Fluorescent Protein Based	dCas13a	dCas13a-EGFP/sgRNA	Transcripts of the SatIII, MUC4, GCN4, and NEAT1 genes*	RNA Visualization	Currently, no established guidelines exist for designing effective gRNAs targeting the RNA of interest	Fluorescence confocal microscopy, two-photon excitation microscopy, Structured Illumination Microscopy (SIM)	[40]
Fluorescent Protein Based	dCas13a	dCas13a-msfGFP-ZF-KRAB	Transcripts of the KRAS and CXC4 genes*	Optimised SNR	Visualization of intranuclear RNA is currently not possible	Fluorescent confocal microscopy	[41]
Fluorescent Protein Based	dCas13b	CRISPR-TRA-tag	Transcripts of the GCN4, MUC4, and SatIII lncRNA genes*	Flexibility of the modular design, smaller size and more precise fluorescent signal	Complex tag design?	Fluorescent confocal microscopy	[43]

* Highly repetitive sequences (350−500 binding sites).
** Repetitive sequences (40−100 binding sites).
*** Unique sequences (1−20 binding sites).
**** Unique sequences in heterochromatin regions.

5 Labeling DNA Sequences in Cells of Other Organisms

In addition to labelling sequences in human cells, research has also been conducted in other organisms. For example, dynamic labelling of DNA loci using various CRISPR/dCas9 methodologies has been demonstrated in mice, plants, and viruses. The systems used for different eukaryotic organisms remain unchanged; for example, dCas9 fused with GFP [46] and dCas9 with the Halo-ligand system [27, 47] have been employed for labelling DNA loci in mouse cells. Meanwhile, the first signal amplification method, which utilised three GFPs fused with dCas9 [48], and the tagging of two loci with two orthologs of dCas9 and a second red fluorescent protein, Ruby2 [49], were used for visualising DNA fragments in plant cells. Since both mouse and plant cells are eukaryotic, the principle of the system remains unchanged; only the delivery method varies, which subsequently affects the plasmid vector carrying the necessary construct and the promoter used for expression in specific organisms or their tissues. Thus, repeated telomeric and pericentric sequences have been visualised in mouse and plant cells, leading to a likely focus on human cells in further studies.

An intriguing approach involves labelling the nucleic acids of the pseudorabies virus (PRV) using quantum dots. These quantum dots are characterised by their high brightness, photostability, and unique emission properties, making them among the best fluorescent markers available [50]. The quantum dots were fused with dCas, which binds to the target nucleic acid via sgRNA, and were subsequently encapsulated within the virus during virion assembly [51]. This method opens up possibilities for visualising the nucleic acids of various viruses and for in-depth studies of the infection processes they induce in cells. However, it is essential to note the need for further research in this area to enhance signal compactness and improve the signal-to-background ratio.

6 Challenges in Using CRISPR/Cas Systems for Visualizing Genomic Loci in Living Organisms

One of the primary limitations of employing the CRISPR/Cas system in living organisms is the low signal brightness and inadequate signal-to-noise ratio. These issues can hinder the detection of fluorescent labels throughout entire organisms or within specific organs. One potential solution is to generate stable cell lines that express all components of the CRISPR system, which can then be introduced into the organism. However, it is crucial to consider the necessity of specific animal models and the immunogenicity of these interventions. Additionally, careful selection of tag molecules with detectable fluorescence is vital for successful visualisation [52].

7 Visualization Techniques

Confocal microscopy is the primary method for detecting fluorescent signals generated by CRISPR-Cas-based imaging techniques. There are two main types of confocal microscopes: laser-scanning and spinning-disk. Both systems enable optical sectioning of samples but rely on different technologies. Laser-scanning confocal microscopes generate images by sequentially capturing individual points along the Z-plane within the selected region, compiling them into a complete image. In contrast, spinning-disk confocal microscopes utilise a high-speed rotating disk perforated with multiple pinholes to scan the sample, providing a full image in real time. Both laser-scanning and spinning-disk microscopy enhance signal-to-noise ratios and facilitate visualisation of deeper cellular and tissue layers. However, spinning-disk systems offer superior speed, quantum efficiency, and signal-to-noise ratios while requiring lower laser power. Wide-field fluorescence microscopy is another commonly used method for visualisation. This technique captures all light emitted by the sample, regardless of focus, which can increase background fluorescence and complicate imaging of samples thicker than 50 μm [53]. Additionally, phase-contrast microscopy is employed for imaging, offering high-contrast visualisation by creating significant phase differences between sample structures. However, a notable limitation of this method is the appearance of bright halos, which can obscure adjacent structures [54]. Advanced imaging techniques, such as two-photon microscopy, structured illumination microscopy (SIM), and fluorescence lifetime imaging microscopy (FLIM), are particularly useful for detecting fluorescent labels in live cells and organisms and monitoring their dynamics. Two-photon microscopy uses near-infrared fluorescent proteins, which reduce light scattering in tissues, making it ideal for deep-tissue imaging [55]. SIM improves both lateral and axial resolution by enabling optical imaging near the diffraction limit [56]. FLIM measures the spatial distribution of fluorescent labels based on their fluorescence lifetime, effectively distinguishing target fluorescence from autofluorescence and reducing background interference [57]. Together, these methods provide high-resolution detection of fluorescent labels in live cells and organisms while minimising background fluorescence.

8 Conclusion

The development of new nucleic acid locus labelling methods using the CRISPR/Cas system opens unique opportunities not only for visualising the dynamics of chromatin loci but also for studying the interactions between specific genomic regions. These methods can facilitate the correction of genetic errors associated with the expansion of short repeats, which can have severe consequences for the organism, manifesting in various neurodegenerative and inherited disorders, such as Huntington's chorea, Kennedy disease, and others [37].

Using the CRISPR/Cas method, it is possible to determine the length of repetitive sequences [32] and identify different types of mutations (beyond single-nucleotide substitutions) [31]. These advancements hold significant potential for both fundamental research into the four-dimensional structure of the nucleome and practical medical applications, including the diagnosis of hereditary diseases, offering an alternative to the existing MLPA (Multiplex Ligation-dependent Probe Amplification) method, which has its own limitations [33]. Thus, the application of CRISPR/Cas can greatly improve the accuracy and reliability of diagnostics, which is especially critical in the context of inherited diseases.

Acknowledgments

This work was supported by the Russian Science Foundation, agreement No. 221400205. https://rscf.ru/project/22-14-00205/

Disclosures

The authors declare no conflict of interest.

References

1. J. M. Jinek, K. Chylinski, I. Fonfara, M. Hauer, J. A. Doudna, and E. Charpentier, "A Programmable Dual-RNA–Guided DNA Endonuclease in Adaptive Bacterial Immunity," Science 337(6096), 816–821 (2012).
2. L. S. Qi, M. H. Larson, L. A. Gilbert, J. A. Doudna, J. S. Weissman, A. P. Arkin, and W. A. Lim, "Repurposing CRISPR as an RNA-Guided Platform for Sequence-Specific Control of Gene Expression," Cell 152(5), 1173–1183 (2013).
3. A. Vojta, P. Dobrinić, V. Tadić, L. Bočkor, P. Korać, B. Julg, M. Klasić, and V. Zoldoš, "Repurposing the CRISPR-Cas9 system for targeted DNA methylation," Nucleic Acids Research 44(12), 5615–5628 (2016).
4. P. Bashtrykov, N. Rajaram, and A. Jeltsch, "Efficient Targeted DNA Methylation with dCas9-Coupled DNMT3A-DNMT3L Methyltransferase," in Epigenomics, I. Hatada and T. Horii (Eds.), Springer US, 2577, 177–188 (2023).
5. H. O'Geen, S. L. Bates, S. S. Carter, K. A. Nisson, J. Halmai, K. D. Fink, S. K. Rhie, P. J. Farnham, and D. J. Segal, "Ezh2-dCas9 and KRAB-dCas9 enable engineering of epigenetic memory in a context-dependent manner," Epigenetics & Chromatin 12(1), 26 (2019).
6. A. Chavez, M. Tuttle, B. W. Pruitt, B. Ewen-Campen, R. Chari, D. Ter-Ovanesyan, S. J. Haque, R. J. Cecchi, E. J. K. Kowal, J. Buchthal, B. E. Housden, N. Perrimon, J. J. Collins, and G. Church, "Comparison of Cas9 activators in multiple species," Nature Methods 13(7), 563–567 (2016).
7. A. C. Komor, Y. B. Kim, M. S. Packer, J. A. Zuris, and D. R. Liu, "Programmable editing of a target base in genomic DNA without double-stranded DNA cleavage," Nature 533(7603), 420–424 (2016)..
8. X. Liu, Y. Zhang, Y. Chen, M. Li, F. Zhou, K. Li, H. Cao, M. Ni, Y. Liu, Z. Gu, K. E. Dickerson, S. Xie, G. C. Hon, Z. Xuan, M. Q. Zhang, Z. Shao, and J. Xu, "In Situ Capture of Chromatin Interactions by Biotinylated dCas9," Cell 170(5), 1028-1043.e19 (2017).
9. E. Schmidtmann, T. Anton, P. Rombaut, F. Herzog, and H. Leonhardt, "Determination of local chromatin composition by CasID," Nucleus 7(5), 476–484 (2016).
10. J. Duan, G. Lu, Y. Hong, Q. Hu, X. Mai, J. Guo, X. Si, F. Wang, and Y. Zhang, "Live imaging and tracking of genome regions in CRISPR/dCas9 knock-in mice," Genome Biology 19(1), 192 (2018).
11. L. G. Maloshenok, G. A. Abushinova, A. Yu. Ryazanova, S. A. Bruskin, and V. V. Zherdeva, "Visualizing the Nucleome Using the CRISPR–Cas9 System: From in vitro to in vivo," Biochemistry Moscow 88(S1), S123–S149 (2023).
12. L. Stuppia, I. Antonucci, G. Palka, and V. Gatta, "Use of the MLPA Assay in the Molecular Diagnosis of Gene Copy Number Alterations in Human Genetic Diseases," International Journal of Molecular Sciences 13(3), 3245–3276 (2012).
13. X. Xu, L. S. Qi, "A CRISPR–dCas Toolbox for Genetic Engineering and Synthetic Biology," Journal of Molecular Biology 431(1), 34–47 (2019).
14. T. A. Kazi, S. R. Biswas, "CRISPR/dCas system as the modulator of gene expression," in Progress in Molecular Biology and Translational Science, Elsevier, 178, 99–122 (2021).
15. B. Paul, G. Montoya, "CRISPR-Cas12a: Functional overview and applications," Biomedical Journal 43(1), 8–17 (2020).
16. D. Singh, J. Mallon, A. Poddar, Y. Wang, R. Tippana, O. Yang, S. Bailey, and T. Ha, "Real-time observation of DNA target interrogation and product release by the RNA-guided endonuclease CRISPR Cpf1 (Cas12a)," Proceedings of the National Academy of Science 115(21), 5444–5449 (2018).
17. L. Liu, D.-S. Pei, "Insights Gained from RNA Editing Targeted by the CRISPR-Cas13 Family," International Journal of Molecular Sciences 23(19), 11400 (2022).
18. T. Karvelis, G. Bigelyte, J. K. Young, Z. Hou, R. Zedaveinyte, K. Budre, S. Paulraj, V. Djukanovic, S. Gasior, A. Silanskas, Č. Venclovas, and V. Siksnys, "PAM recognition by miniature CRISPR–Cas12f nucleases triggers programmable double-stranded DNA target cleavage," Nucleic Acids Research 48(9), 5016–5023 (2020).

19. R. Xiao, Z. Li, S. Wang, R. Han, and L. Chang, "Structural basis for substrate recognition and cleavage by the dimerization-dependent CRISPR–Cas12f nuclease," Nucleic Acids Research 49(7), 4120–4128 (2021).
20. T. Wu, C. Liu, S. Zou, R. Lyu, B. Yang, H. Yan, M. Zhao, and W. Tang, "An engineered hypercompact CRISPR-Cas12f system with boosted gene-editing activity," Nature Chemical Biology 19(11), 1384–1393 (2023).
21. B. Chen, L. A. Gilbert, B. A. Cimini, J. Schnitzbauer, W. Zhang, G.-W. Li, J. Park, E. H. Blackburn, J. S. Weissman, L. S. Qi, and B. Huang, "Dynamic Imaging of Genomic Loci in Living Human Cells by an Optimized CRISPR/Cas System," Cell 155(7), 1479–1491 (2013).
22. B. Chen, J. Hu, R. Almeida, H. Liu, S. Balakrishnan, C. Covill-Cooke, W. A. Lim, and B. Huang, "Expanding the CRISPR imaging toolset with Staphylococcus aureus Cas9 for simultaneous imaging of multiple genomic loci," Nucleic Acids Research 44(8), e75–e75 (2016).
23. H. Ma, A. Naseri, P. Reyes-Gutierrez, S. A. Wolfe, S. Zhang, and T. Pederson, "Multicolor CRISPR labeling of chromosomal loci in human cells," Proceedings of the National Academy of Sciences 112(10), 3002–3007 (2015).
24. M. E. Tanenbaum, L. A. Gilbert, L. S. Qi, J. S. Weissman, and R. D. Vale, "A Protein-Tagging System for Signal Amplification in Gene Expression and Fluorescence Imaging," Cell 159(3), 635–646 (2014).
25. H. Ye, Z. Rong, and Y. Lin, "Live cell imaging of genomic loci using dCas9-SunTag system and a bright fluorescent protein," Protein & Cell 8(11), 853–855 (2017).
26. Y. Hong, G. Lu, J. Duan, W. Liu, and Y. Zhang, "Comparison and optimization of CRISPR/dCas9/gRNA genome-labeling systems for live cell imaging," Genome Biology 19(1), 39 (2018).
27. J. B. Grimm, B. P. English, J. Chen, J. P. Slaughter, Z. Zhang, A. Revyakin, R. Patel, J. J. Macklin, D. Normanno, R. H. Singer, T. Lionnet, and L. D. Lavis, "A general method to improve fluorophores for live-cell and single-molecule microscopy," Nature Methods 12(3), 244–250 (2015).
28. W. Deng, X. Shi, R. Tjian, T. Lionnet, and R. H. Singer, "CASFISH: CRISPR/Cas9-mediated in situ labeling of genomic loci in fixed cells," Proceedings of the National Academy of Sciences 112(38), 11870–11875 (2015).
29. X. Wu, S. Mao, Y. Yang, M. N. Rushdi, C. J. Krueger, and A. K. Chen, "A CRISPR/molecular beacon hybrid system for live-cell genomic imaging," Nucleic Acids Research 46(13), e80–e80 (2018).
30. S. Mao, Y. Ying, X. Wu, C. J. Krueger, and A. K. Chen, "CRISPR/dual-FRET molecular beacon for sensitive live-cell imaging of non-repetitive genomic loci," Nucleic Acids Research 47(20), e131–e131 (2019). doi:.
31. P. A. Clow, M. Du, N. Jillette, A. Taghbalout, J. J. Zhu, and A. W. Cheng, "CRISPR-mediated multiplexed live cell imaging of nonrepetitive genomic loci with one guide RNA per locus," Nature Communications 13(1), 1871 (2022).
32. Z. Zhang, X. Rong, T. Xie, Z. Li, H. Song, S. Zhen, H. Wang, J. Wu, S. R. Jaffrey, and X. Li, "Fluorogenic CRISPR for genomic DNA imaging," Nature Communications 15(1), 934 (2024).
33. M. Chen, X. Huang, Y. Shi, W. Wang, Z. Huang, Y. Tong, X. Zou, Y. Xu, and Z. Dai, "CRISPR/Pepper-tDeg: A Live Imaging System Enables Non-Repetitive Genomic Locus Analysis with One Single-Guide RNA," Advanced Science 11(32), 2402534 (2024).
34. X.-Y. Lyu, Y. Deng, X.-Y. Huang, Z.-Z. Li, G.-Q. Fang, D. Yang, F.-L. Wang, W. Kang, E.-Z. Shen, and C.-Q. Song, "Correction: CRISPR FISHer enables high-sensitivity imaging of nonrepetitive DNA in living cells through phase separation-mediated signal amplification," Cell Research 32(12), 1133–1133 (2022).
35. Q. Peng, Z. Huang, K. Sun, Y. Liu, C. W. Yoon, R. E. S. Harrison, D. L. Schmitt, L. Zhu, Y. Wu, I. Tasan, H. Zhao, J. Zhang, S. Zhong, S. Chien, and Y. Wang, "Engineering inducible biomolecular assemblies for genome imaging and manipulation in living cells," Nature Communications 13(1), 7933 (2022).
36. D. A. Nelles, M. Y. Fang, M. R. O'Connell, J. L. Xu, S. J. Markmiller, J. A. Doudna, and G. W. Yeo, "Programmable RNA Tracking in Live Cells with CRISPR/Cas9," Cell 165(2), 488–496 (2016).
37. R. Batra, D. A. Nelles, E. Pirie, S. M. Blue, R. J. Marina, H. Wang, I. A. Chaim, J. D. Thomas, N. Zhang, V. Nguyen, S. Aigner, S. Markmiller, G. Xia, K. D. Corbett, M. S. Swanson, and G. W. Yeo, "Elimination of Toxic Microsatellite Repeat Expansion RNA by RNA-Targeting Cas9," Cell 170(5), 899-912.e10 (2017).
38. N.-H. Sun, D.-Y. Chen, L.-P. Ye, G. Sheng, J.-J. Gong, B.-H. Chen, Y.-M. Lu, and F. Han, "CRISPR-Sunspot: Imaging of endogenous low-abundance RNA at the single-molecule level in live cells," Theranostics 10(24), 10993–11012 (2020).
39. X. Chen, D. Zhang, N. Su, B. Bao, X. Xie, F. Zuo, L. Yang, H. Wang, L. Jiang, Q. Lin, M. Fang, N. Li, X. Hua, Z. Chen, C. Bao, J. Xu, W. Du, L. Zhang, Y. Zhao, L. Zhu, J. Loscalzo, and Y. Yang, "Visualizing RNA dynamics in live cells with bright and stable fluorescent RNAs," Nature Biotechnology 37(11), 1287–1293 (2019).
40. L.-Z. Yang, Y. Wang, S.-Q. Li, R.-W. Yao, P.-F. Luan, H. Wu, G. G. Carmichael, and L.-L. Chen, "Dynamic Imaging of RNA in Living Cells by CRISPR-Cas13 Systems," Molecular Cell 76(6), 981-997.e7 (2019).
41. O. O. Abudayyeh, J. S. Gootenberg, P. Essletzbichler, S. Han, J. Joung, J. J. Belanto, V. Verdine, D. B. T. Cox, M. J. Kellner, A. Regev, E. S. Lander, D. F. Voytas, A. Y. Ting, and F. Zhang, "RNA targeting with CRISPR–Cas13," Nature 550(7675), 280–284 (2017).
42. H. Tang, J. Peng, S. Peng, Q. Wang, X. Jiang, X. Xue, Y. Tao, L. Xiang, Q. Ji, S.-M. Liu, X. Weng, and X. Zhou, "Live-cell RNA imaging using the CRISPR-dCas13 system with modified sgRNAs appended with fluorescent RNA aptamers," Chemical Science 13(47), 14032–14040 (2022).

43. H. Tang, J. Peng, X. Jiang, S. Peng, F. Wang, X. Weng, and X. Zhou, "A CRISPR-Cas and Tat Peptide with Fluorescent RNA Aptamer System for Signal Amplification in RNA Imaging," Biosensors 13(2), 293 (2023).
44. L. Maloshenok, G. Abushinova, N. Kazachkina, A. Bogdanov, and V. Zherdeva, "Tet-Regulated Expression and Optical Clearing for In Vivo Visualization of Genetically Encoded Chimeric dCas9/Fluorescent Protein Probes," Materials 16(3), 940 (2023).
45. H. Ma, L.-C. Tu, A. Naseri, M. Huisman, S. Zhang, D. Grunwald, and T. Pederson, "Multiplexed labeling of genomic loci with dCas9 and engineered sgRNAs using CRISPRainbow," Nature Biotechnology 34(5), 528–530 (2016).
46. T. Anton, S. Bultmann, H. Leonhardt, and Y. Markaki, "Visualization of specific DNA sequences in living mouse embryonic stem cells with a programmable fluorescent CRISPR/Cas system," Nucleus 5(2), 163–172 (2014).
47. S. C. Knight, L. Xie, W. Deng, B. Guglielmi, L. B. Witkowsky, L. Bosanac, E. T. Zhang, M. El Beheiry, J.-B. Masson, M. Dahan, Z. Liu, J. A. Doudna, and R. Tjian, "Dynamics of CRISPR-Cas9 genome interrogation in living cells," Science 350(6262), 823–826 (2015).
48. S. Fujimoto, S. Matsunaga, "Visualization of Chromatin Loci with Transiently Expressed CRISPR/Cas9 in Plants," CYTOLOGIA 82(5), 559–562 (2017).
49. S. Dreissig, S. Schiml, P. Schindele, O. Weiss, T. Rutten, V. Schubert, E. Gladilin, M. F. Mette, H. Puchta, and A. Houben, "Live-cell CRISPR imaging in plants reveals dynamic telomere movements," The Plant Journal 91(4), 565–573 (2017).
50. U. Resch-Genger, M. Grabolle, S. Cavaliere-Jaricot, R. Nitschke, and T. Nann, "Quantum dots versus organic dyes as fluorescent labels," Nature Methods 5(9), 763–775 (2008).
51. Z.-G. Wang, S.-L. Liu, and D.-W. Pang, "Quantum Dots: A Promising Fluorescent Label for Probing Virus Trafficking," Accounts of Chemical Research 54(14), 2991–3002 (2021).
52. S. P. B. Van Beljouw, J. Sanders, A. Rodríguez-Molina, and S. J. J. Brouns, "RNA-targeting CRISPR–Cas systems," Nature Reviews Microbiology 21(1), 21–34 (2023).
53. A. D. Elliott, "Confocal Microscopy: Principles and Modern Practices," Current Protocols in Cytometry 92(1), e68 (2020).
54. Z. Yin, T. Kanade, and M. Chen, "Understanding the phase contrast optics to restore artifact-free microscopy images for segmentation," Medical Image Analysis 16(5), 1047–1062 (2012).
55. R. K. P. Benninger, D. W. Piston, "Two-Photon Excitation Microscopy for the Study of Living Cells and Tissues," Current Protocols in Cell Biology 59(1), (2013).
56. X. Chen, S. Zhong, Y. Hou, R. Cao, W. Wang, D. Li, Q. Dai, D. Kim, and P. Xi, "Superresolution structured illumination microscopy reconstruction algorithms: a review," Light: Science & Applications 12(1), 172 (2023).
57. R. Datta, T. M. Heaster, J. T. Sharick, A. A. Gillette, and M. C. Skala, "Fluorescence lifetime imaging microscopy: fundamentals and advances in instrumentation, analysis, and applications," Journal of Biomedical Optics 25(07), 1 (2020).

Optical Clearing for Deep Skin Imaging with Optical Methods

Maxim E. Darvin[1*] and Jürgen Lademann[2]
[1] Independent Researcher, Berlin 10178, Germany
[2] Center of Experimental and Applied Cutaneous Physiology, Department of Dermatology, Venerology and Allergology, Charité – Universitätsmedizin Berlin, corporate member of Freie Universität Berlin and Humboldt-Universität zu Berlin, 1 Charitéplatz, Berlin 10117, Germany
[*]e-mail: maxim.darvin@protonmail.com

Abstract. Skin imaging with optical methods is always limited in depth mainly due to the strong scattering of the excitation and emission light, which significantly reduces the contrast of the images and the probing depth. One of the reasons for the scattering is the mismatch in refractive indices between the skin components, which can be minimized using an optical clearing procedure – the topical application of immersion liquid on the skin. Professor Valery V. Tuchin is a well-known scientist who plays a major role in the field of determination and maintenance of the optical properties of biological objects, including skin, and was a driving force in the development of the optical clearing method. In addition, Professor Valery V. Tuchin can be considered the "Father of Biophotonics in Russia" due to his long-standing, highly effective and globally recognized work in the field of biophotonics, biomedical optics and laser medicine. The following article provides an overview of the work carried out at the Charité – Universitätsmedizin Berlin, Department of Dermatology, Center of Experimental and Applied Cutaneous Physiology, in cooperation with Professor Valery V. Tuchin, on the improvement of image contrast and the increase of probing depth in the skin using exemplary optical methods in combination with optical clearing.
© 2024 Journal of Biomedical Photonics & Engineering.

Keywords: Raman spectroscopy; confocal Raman microspectroscopy; two-photon tomography; second harmonic generation; two-photon excited autofluorescence; epidermis; dermis; deep tissue imaging.

Paper #9197 received 11 Dec 2024; revised manuscript received 17 Dec 2024; accepted for publication 18 Dec 2024; published online 29 Dec 2024. doi: 10.18287/JBPE24.10.040204.

1 Introduction

Optical microscopic and spectroscopic methods are widespread in dermatology to image the hidden structures and substances in the skin. These include linear optics-based methods such as laser scanning microscopy in reflectance and fluorescence mode, confocal Raman micro spectroscopy, optical coherence tomography; and non-linear optics-based methods such as two-photon tomography, coherent anti-Stokes Raman scattering, stimulated Raman scattering – comprehensively reviewed in Refs. [1−7]. The primary limitation of all optical methods used in dermatology is their low imaging depth, which is generally limited to a few hundred μm and considerably restricts skin diagnostics. The reason for the imaging limitation is a strong scattering of the skin – the light is reflected multiple times within the skin components with different refractive indices (n_{lipids} = 1,47; $n_{collagen}$ = 1.47; n_{nuclei} = 1.39; n_{water} = 1.33; n_{blood} = 1.4; n_{air} = 1.00) [4, 8]. The greater the refractive index mismatch along the light propagation, the stronger the scattering.

To minimize the mismatch of reflective indices, the immersion optical clearing (OC) method was introduced by Professor Valery V. Tuchin in 1997 [9], who is a pioneer of this development and of further research on biological objects using optical methods in combination with OC [8, 10−14]. The basic idea of the OC method for

the skin is the topical application of a non-toxic optical clearing agent (OCA) with a refractive index comparable to the refractive index of the main skin components (proteins and lipids), with the ability to squeeze out interstitial fluid (mainly water) and replace it with an OCA [8, 9, 15]. The most frequently used OCAs are glycerol (n = 1.47 at 785 nm) [16], glycerol in water 60%/40% (n = 1.41 at 785 nm) [16], glucose and fructose (n = 1.46–1.48) [17], propylene glycol (n = 1.43) [17], iohexol (n = 1.43 at 760 nm) [15], polyethylene glycol (n = 1.46 at 930 nm) [18], their mixtures and solutions in water. Topical application of OCA minimizes the mismatch of the refractive indices considerably, reduces the scattering and thus increases the probing depth. However, the OC method has a few limitations when used *in vivo* – not every OCA is biocompatible with the skin and can induce irreversible changes to skin components at the micro level, so the concentration used and the application time should be considered [17].

Since many scientific groups worldwide are following the development of OC and the successful combination of optical methods with OC has been demonstrated for decades [10, 14, 17, 19−22], we summarize below the results in this field achieved in the past by the authors of this manuscript, previously employed at the Center of Experimental and Applied Cutaneous Physiology, Department of Dermatology, Charité – Universitätsmedizin Berlin, in cooperation with Professor Valery V. Tuchin. These results include application of OC using confocal Raman micro spectroscopy and two-photon tomography in dermatological research.

2 Results and Discussion

2.1 Optical Clearing of the Skin – Important Application Features

The stratum corneum (SC), the outermost layer of the epidermis, consists of denucleated cells (corneocytes) embedded in a structurally organized lipid matrix, is hardly permeable and maintains the skin barrier function [23−25]. Consequently, the topically applied OCA is mainly stored in the superficial SC depth and does not penetrate the deeper skin layers. To realize the OC method efficiently, OCA should permeate the SC. Therefore, in most studies, OCA penetration is facilitated by removing part or all of the SC by means of tape stripping, creation of micropores, micro ablation, etc. [8]. Another option is to mix a target OCA with penetration enhancers, such as ethanol, dimethyl sulfoxide, thiazone, linoleic and oleic acids [8]. Thus, OC is always associated with the influence on the SC with its complete or partial destruction – it is classified as a low-invasive method. *In vivo* applications are not too common compared to the widely used *ex vivo* investigations to improve probing depth by imaging methods [18, 19, 26–31]. For *in vivo* OC, mixtures of glycerol/dimethyl sulfoxide or propylene glycol/water with a proportion of ≈70/(5–20)/(10–25)% are popular, but not limited to these OCAs. *In vivo* skin OC has its action time – it reaches its maximum 10–15 min after treatment, the effect lasts about 45 min and then slowly decreases due to the substitution of OCA by interstitial fluid.

2.2. Confocal Raman Micro Spectroscopy (CRM)

CRM is a non-invasive spectroscopic method that provides depth-resolved information about skin composition with chemical sensitivity down to a depth of ≈50 μm [32, 33]. CRM is very popular in skin research and is used to study structural and physiological features of the skin *in vivo* and *ex vivo* [32, 34, 35]. CRM helps to determine penetration depth of topically applied substances [32, 36, 37] and to evaluate their influence on the skin [38, 39], to identify changes in the SC between healthy and non-malignant diseased skin [40−43], and to determine cancerous tissue [44−50].

The enhanced probing depth by combining CRM and OC methods [51−53] was confirmed by Sdobnov et al. [54] using porcine ear skin with destroyed SC *ex vivo* and 70/30% glycerol/water and 100% iohexol as OCAs. The results show a significant increase in Raman band intensities (increment factor >1) 30–60 min after topical treatment of the skin with glycerol (for 40–240 μm depth) and iohexol (for 160–240 μm depth) compared to untreated skin. Superficial skin areas show no OC efficiency (increment factor <1), which is due to the presence of OCA in these skin depths. The authors demonstrated that OCAs penetrate into the dermis, provide an OC and cause a significant dehydration of the collagen, which is more pronounced after application of glycerol than iohexol. Comparable results were obtained by Jaafar et al. for porcine dura mater *ex vivo* (glycerol/water solution in different proportions as OCA) [55] and for porcine lung tissue *ex vivo* (e-cigarette liquid as OCA) [56] using a combination of CRM with OC.

In addition, Yanina et al. [16] investigated OC on intact porcine skin *ex vivo* without disturbing the SC by applying a mixture of glycerol and dimethyl sulfoxide and found that a solution of 80/20% glycerol/dimethyl sulfoxide for 15–45 min was optimal to permeate the SC and reach the viable epidermis.

It is known that the contact of OCA with a biological object leads to its dehydration, but the question of the changes in water mobility states after OCA treatment was open. Based on the decomposition of Raman spectra and determination of water mobility states, Sdobnov et al. [57, 58] studied the interaction of 70/30% glycerol/water and 100% iohexol on water homeostasis in porcine skin with the removed SC *ex vivo*. Fig. 1 shows that glycerol induced the highest water displacement from the epidermis and dermis (depths 0–200 μm) and a decrease in the concentrations of all water mobility states (tightly-, strongly-, weakly-bound, and unbound water), while the hydrogen bonding state of the water (ratio of weakly bound to strongly bound water) did not change significantly (0–200 μm) after the OCA treatment. It is concluded that the weakly bound and strongly bound

water mobility states, which are most prevalent in the skin, are preferentially involved in OCA-induced water flux in the skin, and are thus mainly responsible for OC efficiency [57]. Treatment with both OCAs leads to a significant decrease in the fluorescence intensity of the Raman spectra at a depth of 0–50 μm, which is explained by the presence of the OCAs in this skin region due to penetration [15, 58].

The main limitation of using a combination of CRM and OC is the strong overlapping of skin- and OCA-related Raman bands in a broad spectral range, which hinders the calculation of some structural and physiological features of the skin. Another aspect is an *in vivo* application – here the safety of the applied OCA and the doses should be confirmed.

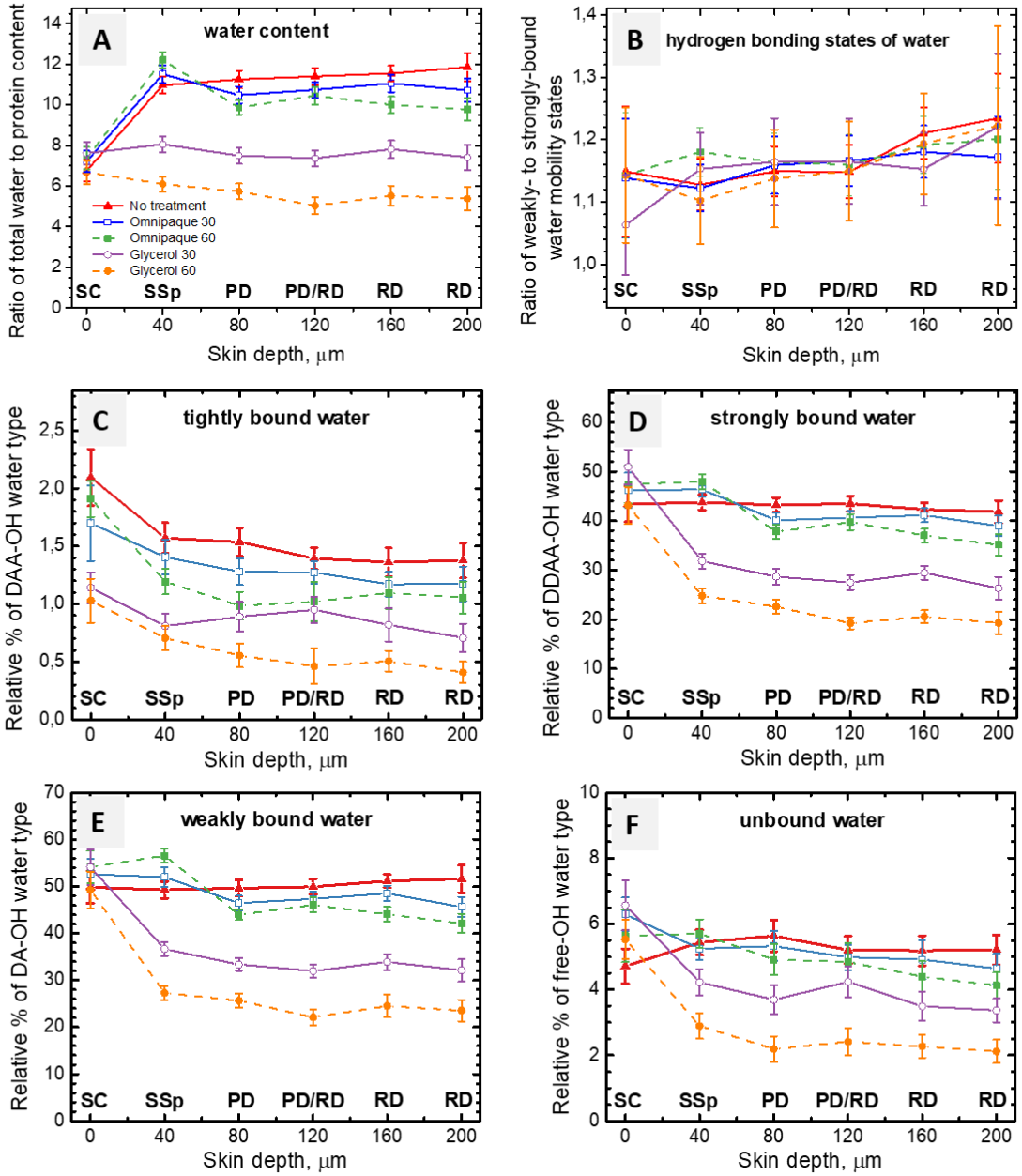


Fig 1. Skin depth profiles of (A) total water content (determined by the ratio of total water to proteins content), (B) hydrogen bonding state of water molecules (determined by the ratio of weakly bound to strongly bound water), (C) concentration of tightly bound water, (D) concentration of strongly bound water, (E) concentration of weakly bound water, and (F) concentration of unbound water determined on porcine ear skin *ex vivo* using CRM (excitation at 671 nm, detection at 3000–3750 cm^{-1}). Thick red line – untreated skin; blue solid line/green dotted line – skin treated with Iohexol (Omnipaque) for 30/60 min; purple solid line/orange dotted line – skin treated with glycerol for 30/60 min. SC – stratum corneum; SSp – stratum spinosum; PD – papillary dermis, RD – reticular dermis. Reproduced with permission from Ref. [57].

2.3. Two-Photon Tomography (TPT)

TPT is a non-invasive imaging method that enables depth-resolved visualization of skin structures by measuring two-photon excited autofluorescence, fluorescence lifetime imaging (TPE-FLIM) and second harmonic generation (SHG) to a depth of ≈150 µm. TPT is used in skin research with a focus on the visualization of epidermal and dermal structures including cells of different types [59−62], tattoos [63], collagen and elastin in the dermis [64−66], for the determination of the penetration of topically applied substances in the skin [2, 67, 68], and in clinical research (mainly in skin cancer diagnostics) [69−72] both *in vivo* and *ex vivo*. Compared to methods based on linear optics, TPT offers excellent subcellular axial (<2 µm) and lateral (<0.6 µm) resolution and the highest imaging depth. Despite the high resolution, the images in the dermis at a depth exceeding 80 µm are partially blurred [60, 61, 63] and can still be improved. The selectivity of TPT to different substances (measured with SHG and TPE-FLIM) is unique in *in vivo* skin imaging.

Skin scattering reduces image quality and probing depth, so the combination of TPT with OC may be useful to minimize these limitations. Cicchi et al. [73] were the first to show that the OCAs glycerol, propylene glycol and glucose at high concentrations effectively improve image contrast and probing depth in TPT of human skin *ex vivo*. Sdobnov et al. [74] investigated porcine skin *ex vivo* and found up to a 2-fold enhancement in autofluorescence intensity at 30–100 µm and up to a 7-fold enhancement in second harmonic generation intensity at 130–180 µm after using 40–100% glycerol in water solution. The use of iohexol also leads to an enhancement in signal intensity, but to a much lesser extent than with glycerol [15, 74, 75]. Fig. 2 demonstrates structural horizontal TPT images of porcine ear skin *ex vivo* (autofluorescence/SHG are shown in red/green) for various depths (5–165 µm) after application of 100% iohexol (Omnipague), glycerol in water solutions, as well as for an untreated skin sample.

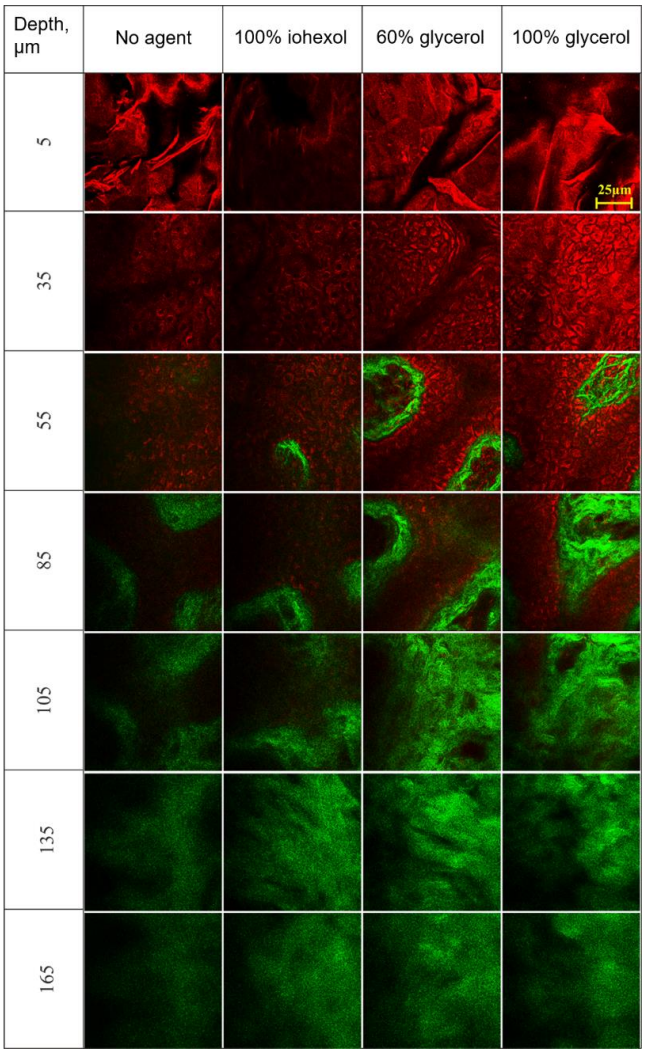


Fig. 2 Exemplary TPT images of different skin layers obtained *ex vivo* for porcine ear skin samples using different iohexol (Omnipaque) and glycerol solutions as OCAs. The red colour corresponds to two-photon-excited autofluorescence and the green colour corresponds to SHG intensities. The image size is 100 µm × 100 µm. Reproduced with permission from Ref. [74].

These results show that both glycerol and iohexol solutions increase the probing depth and image quality in the skin so that the deep-located regions can be examined. Glycerol is more effective than iohexol at the concentration and application time values used. However, since iohexol (Omnipaque) is a radiocontrast agent used *in vivo* in X-ray microscopy and an approved pharmaceutic agent for topical or systemic use with no known impact on the skin, it is more promising than glycerol for *in vivo* application.

One of the future prospects for reducing the influence of scattering on image quality and probing depth may be the combination of OC with a TPT device upgraded with adaptive optics elements, in particular spatial light modulators, used for wavefront correction [76–78], similar to what Yu et al. [79] showed for optical coherence tomography.

3 Conclusions

The effect of OC is generally observed in all biological objects investigated using optical methods and is here presented for CRM and TPT used for skin diagnostics. The improvement in image quality and probing depth due to a reduced scattering using optical methods is clearly pronounced after OC and is consistent with the results presented by other authors. The effectiveness of OC depends on the type of OCA, its concentration, and the application time. Although many OCAs are already used *in vivo*, an important limitation of OC method is still its application *in vivo*, as not all OCAs are biocompatible with the skin and can potentially cause irreversible changes in skin components. Therefore, future studies should be considered for the optimization of the composition and concentration of OCAs with the aim of achieving fast OC effect and rapid recovery with no or minimal effects on skin components.

Disclosures

The authors declare no conflict of interest.

References

1. J. Lademann, A. Patzelt, M. Darvin, H. Richter, C. Antoniou, W. Sterry, and S. Koch, "Application of optical non-invasive methods in skin physiology," Laser Physics Letters 5(5), 335–346 (2008).
2. M. E. Darvin, "Optical Methods for Non-Invasive Determination of Skin Penetration: Current Trends, Advances, Possibilities, Prospects, and Translation into In Vivo Human Studies," Pharmaceutics 15(9), 2272 (2023).
3. M. E. Darvin, M. C. Meinke, W. Sterry, and J. Lademann, "Optical methods for noninvasive determination of carotenoids in human and animal skin," Journal of Biomedical Optics 18(6), 061230 (2013).
4. B. Limcharoen, S. Wanichwecharungruang, W. Banlunara, and M. E. Darvin, "Seeing through the skin: Optical methods for visualizing transdermal drug delivery with microneedles," Advanced Drug Delivery Reviews 217, 115478 (2025).
5. M. A. Calin, S. V. Parasca, R. Savastru, M. R. Calin, and S. Dontu, "Optical techniques for the noninvasive diagnosis of skin cancer," Journal of Cancer Research and Clinical Oncology 139(7), 1083–1104 (2013).
6. K. M. Hanson and C. J. Bardeen, "Application of Nonlinear Optical Microscopy for Imaging Skin†," Photochemistry and Photobiology 85(1), 33–44 (2009).
7. L. Rey-Barroso, S. Peña-Gutiérrez, C. Yáñez, F. J. Burgos-Fernández, M. Vilaseca, and S. Royo, "Optical Technologies for the Improvement of Skin Cancer Diagnosis: A Review," Sensors 21(1), 252 (2021).
8. A. Yu. Sdobnov, M. E. Darvin, E. A. Genina, A. N. Bashkatov, J. Lademann, and V. V. Tuchin, "Recent progress in tissue optical clearing for spectroscopic application," Spectrochimica Acta Part A: Molecular and Biomolecular Spectroscopy 197, 216–229 (2018).
9. V. V. Tuchin, "Light propagation in tissues with controlled optical properties," Journal of Biomedical Optics 2(4), 401 (1997).
10. D. Zhu, K. V. Larin, Q. Luo, and V. V. Tuchin, "Recent progress in tissue optical clearing," Laser & Photonics Reviews 7(5), 732–757 (2013).
11. V. V. Tuchin (Ed.), Tissue Optics Light scattering methods and instruments for medical diagnostics, 3 ed., SPIE Press, Bellingham, Washington, USA (2015).
12. V. V. Tuchin, "Optical clearing of tissues and blood using the immersion method," Journal of Physics D: Applied Physics 38(15), 2497–2518 (2005).
13. V. V. Tuchin (Ed.), Handbook of Optical Sensing of Glucose in Biological Fluids and Tissues, CRC Press, Boca Raton (2008).
14. T. Yu, X. Zhong, D. Li, J. Zhu, V. V. Tuchin, and D. Zhu, "Delivery and kinetics of immersion optical clearing agents in tissues: Optical imaging from ex vivo to in vivo," Advanced Drug Delivery Reviews 215, 115470 (2024).
15. A. Yu. Sdobnov, J. Lademann, M. E. Darvin, and V. V. Tuchin, "Methods for Optical Skin Clearing in Molecular Optical Imaging in Dermatology," Biochemistry Moscow 84(S1), 144–158 (2019).
16. I. Yu. Yanina, J. Schleusener, J. Lademann, V. V. Tuchin, and M. E. Darvin, "The Effectiveness of Glycerol Solutions for Optical Clearing of the Intact Skin as Measured by Confocal Raman Microspectroscopy," Optics and Spectroscopy 128(6), 759–765 (2020).

17. I. Costantini, R. Cicchi, L. Silvestri, F. Vanzi, and F. S. Pavone, "In-vivo and ex-vivo optical clearing methods for biological tissues: review," Biomedical Optics Express 10(10), 5251 (2019).
18. E. A. Genina, A. N. Bashkatov, G. S. Terentyuk, and V. V. Tuchin, "Integrated effects of fractional laser microablation and sonophoresis on skin immersion optical clearing in vivo," Journal of Biophotonics 13(7), e202000101 (2020).
19. Q. Xia, D. Li, T. Yu, J. Zhu, and D. Zhu, "In vivo skin optical clearing for improving imaging and light-induced therapy: a review," Journal of Biomedical Optics 28(06), (2023).
20. L. Fernandes, H. Silva, I. Martins, S. Carvalho, I. Carneiro, R. Henrique, V. V. Tuchin, and L. M. Oliveira, "Tissue Spectroscopy and Optical Clearing of Colorectal Mucosa in the Pursuit of New Cancer Diagnostic Approaches," Journal of Biomedical Photonics & Engineering 7(4), 040302 (2021).
21. L. R. Oliveira, M. R. Pinheiro, D. K. Tuchina, P. A. Timoshina, M. I. Carvalho, L. M. Oliveira, "Light in evaluation of molecular diffusion in tissues: discrimination of pathologies," Advanced Drug Delivery Reviews 212, 115420 (2024).
22. T. Yu, J. Zhu, D. Li, and D. Zhu, "Physical and chemical mechanisms of tissue optical clearing," iScience 24(3), 102178 (2021).
23. J. A. Bouwstra, M. Ponec, "The skin barrier in healthy and diseased state," Biochimica et Biophysica Acta (BBA) - Biomembranes 1758(12), 2080–2095 (2006).
24. J. Caussin, G. S. Gooris, M. Janssens, and J. A. Bouwstra, "Lipid organization in human and porcine stratum corneum differs widely, while lipid mixtures with porcine ceramides model human stratum corneum lipid organization very closely," Biochimica et Biophysica Acta (BBA) - Biomembranes 1778(6), 1472–1482 (2008).
25. F. Damien, M. Boncheva, "The Extent of Orthorhombic Lipid Phases in the Stratum Corneum Determines the Barrier Efficiency of Human Skin In Vivo," Journal of Investigative Dermatology 130(2), 611–614 (2010).
26. M. S. Saveleva, R. A. Verkhovskii, P. A. Demina, Y. I. Surkov, R. A. Anisimov, E. S. Prikhozhdenko, P. S. Pidenko, I. A. Serebryakova, S. M. Zaytsev, V. V. Tuchin, and Y. I. Svenskaya, "Biodegradable calcium carbonate carriers for the topical delivery of clobetasol propionate," Journal of Materials Chemistry B 12(20), 4867–4881 (2024).
27. M. V. Novoselova, T. O. Abakumova, B. N. Khlebtsov, T. S. Zatsepin, E. N. Lazareva, V. V. Tuchin, V. P. Zharov, D. A. Gorin, and E. I. Galanzha, "Optical clearing for photoacoustic lympho- and angiography beyond conventional depth limit in vivo," Photoacoustics 20, 100186 (2020).
28. D. Zhu, V. Tuchin, "Tissue Optical Clearing Imaging from Ex vivo toward In vivo," BME Front 5, 0058 (2024).
29. I. Yu. Yanina, Y. Tanikawa, E. A. Genina, P. A. Dyachenko, D. K. Tuchina, A. N. Bashkatov, L. E. Dolotov, Y. V. Tarakanchikova, G. S. Terentuk, N. A. Navolokin, A. B. Bucharskaya, G. N. Maslyakova, Y. Iga, S. Takimoto, and V. V. Tuchin, "Immersion optical clearing of adipose tissue in rats: ex vivo and in vivo studies," Journal of Biophotonics 15(7), e202100393 (2022).
30. E. A. Genina, E. A. Kolesnikova, V. G. Artyushenko, E. Berik, and V. V. Tuchin, "Enhanced Optical Imaging of Proximal Human Interphalangeal Joints Using Skin Optical Clearing," Journal of Biomedical Photonics & Engineering 10(4), 040303 (2024).
31. S. M. Zaytsev, M. Amouroux, V. V. Tuchin, E. A. Genina, and W. Blondel, "In vivo skin optical clearing efficacy quantification of clinically compatible agents using line-field confocal optical coherence tomography," Journal of Biomedical Optics 28(05), (2023).
32. P. J. Caspers, H. A. Bruining, G. J. Puppels, G. W. Lucassen, and E. A. Carter, "In Vivo Confocal Raman Microspectroscopy of the Skin: Noninvasive Determination of Molecular Concentration Profiles," Journal of Investigative Dermatology 116(3), 434–442 (2001).
33. R. J. H. Richters, D. Falcone, N. E. Uzunbajakava, B. Varghese, P. J. Caspers, G. J. Puppels, P. E. J. Van Erp, and P. C. M. Van De Kerkhof, "Sensitive Skin: Assessment of the Skin Barrier Using Confocal Raman Microspectroscopy," Skin Pharmacology and Physiology 30(1), 1–12 (2017).
34. M. E. Darvin, J. Schleusener, J. Lademann, and C.-S. Choe, "Current Views on Noninvasive in vivo Determination of Physiological Parameters of the Stratum Corneum Using Confocal Raman Microspectroscopy," Skin Pharmacology and Physiology 35(3), 125–136 (2022).
35. B. P. Yakimov, A. V. Venets, J. Schleusener, V. V. Fadeev, J. Lademann, E. A. Shirshin, and M. E. Darvin, "Blind source separation of molecular components of the human skin in vivo : non-negative matrix factorization of Raman microspectroscopy data," Analyst 146(10), 3185–3196 (2021).
36. D. Lunter and R. Daniels, "Confocal Raman microscopic investigation of the effectiveness of penetration enhancers for procaine delivery to the skin," Journal of Biomedical Optics 19(12), 126015 (2014).
37. M. A. Maciel Tabosa, P. Vitry, P. Zarmpi, A. L. Bunge, N. A. Belsey, D. Tsikritsis, T. J. Woodman, K. A. J. White, M. B. Delgado-Charro, and R. H. Guy, "Quantification of Chemical Uptake into the Skin by Vibrational Spectroscopies and Stratum Corneum Sampling," Molecular Pharmaceutics 20(5), 2527–2535 (2023).
38. C. Choe, J. Schleusener, J. Lademann, and M. E. Darvin, "In vivo confocal Raman microscopic determination of depth profiles of the stratum corneum lipid organization influenced by application of various oils," Journal of Dermatological Science 87(2), 183–191 (2017).

39. M. E. Darvin, A. Salazar, J. Schleusener, J. Lademann, and J. Von Hagen, "Topical Peroxisome Proliferator-Activated Receptor Agonist Induces Molecular Alterations Enhancing Barrier Function and Water-Holding Capacity of the Human Stratum Corneum In Vivo," Cosmetics 11(2), 44 (2024).
40. M. Zolotas, J. Schleusener, J. Lademann, M. C. Meinke, G. Kokolakis, and M. E. Darvin, "Atopic Dermatitis: Molecular Alterations between Lesional and Non-Lesional Skin Determined Noninvasively by In Vivo Confocal Raman Microspectroscopy," International Journal of Molecular Sciences 24(19), 14636 (2023).
41. M. Zolotas, J. Schleusener, J. Lademann, M. C. Meinke, G. Kokolakis, and M. E. Darvin, "Altered structure indicating reduced barrier function of lesional compared to non-lesional psoriatic skin − A non-invasive in vivo study of the human stratum corneum with confocal Raman micro-spectroscopy," Experimental Dermatology 32(10), 1763–1773 (2023).
42. U. S. Dinish, Y. W. Yew, K. Vinod Ram, R. Bi, A. B. E. Attia, V. Teo Xinhui, P. Rajarahm, H. H. Oon, S. T. G. Thng, and M. Olivo, "Non-invasive biochemical analysis and comparison of atopic dermatitis and psoriasis skin using handheld confocal Raman spectroscopy," Journal of Biophotonics 16(12), e202300191 (2023).
43. M. Wu, B. Gao, and X. Wei, "Recent advances in Raman spectroscopy for skin diagnosis," Journal of Innovative Optical Health Sciences 16(03), 2330003 (2023).
44. E. M. Barroso, R. W. H. Smits, C. G. F. Van Lanschot, P. J. Caspers, I. Ten Hove, H. Mast, A. Sewnaik, J. A. Hardillo, C. A. Meeuwis, R. Verdijk, V. Noordhoek Hegt, R. J. Baatenburg De Jong, E. B. Wolvius, T. C. Bakker Schut, S. Koljenović, and G. J. Puppels, "Water Concentration Analysis by Raman Spectroscopy to Determine the Location of the Tumor Border in Oral Cancer Surgery," Cancer Research 76(20), 5945–5953 (2016).
45. I. A. Bratchenko, L. A. Bratchenko, Y. A. Khristoforova, A. A. Moryatov, S. V. Kozlov, and V. P. Zakharov, "Classification of skin cancer using convolutional neural networks analysis of Raman spectra," Computer Methods and Programs in Biomedicine 219, 106755 (2022).
46. Y. Khristoforova, I. Bratchenko, L. Bratchenko, A. Moryatov, S. Kozlov, O. Kaganov, and V. Zakharov, "Combination of Optical Biopsy with Patient Data for Improvement of Skin Tumor Identification," Diagnostics 12(10), 2503 (2022).
47. H. Lui, J. Zhao, D. McLean, and H. Zeng, "Real-time Raman Spectroscopy for In Vivo Skin Cancer Diagnosis," Cancer Research 72(10), 2491–2500 (2012).
48. I. A. Matveeva, A. I. Komlev, O. I. Kaganov, A. A. Moryatov, and V. P. Zakharov, "Multidimensional Analysis of Dermoscopic Images and Spectral Information for the Diagnosis of Skin Tumors," Journal of Biomedical Photonics & Engineering 10(1), 010307 (2024).
49. D. N. Artemyev, L. A. Bratchenko, I. A. Matveeva, V. I. Kukushkin, D. V. Lystsev, A. I. Ishchenko, A. A. Ishchenko, V. M. Zuev, and V. P. Zakharov, "Differential Rapid Diagnosis of Endometrial Cancer and Its Benign Pathological Conditions Using Surface-Enhanced Raman Spectroscopy," Journal of Biomedical Photonics & Engineering 10(2), 020307 (2024).
50. E. Rimskaya, A. Gorevoy, S. Shelygina, E. Perevedentseva, A. Timurzieva, I. Saraeva, N. Melnik, S. Kudryashov, and A. Kuchmizhak, "Multi-Wavelength Raman Differentiation of Malignant Skin Neoplasms," International Journal of Molecular Sciences 25(13), 7422 (2024).
51. D. Huang, W. Zhang, H. Zhong, H. Xiong, X. Guo, and Z. Guo, "Optical clearing of porcine skin tissue in vitro studied by Raman microspectroscopy," Journal of Biomedical Optics 17(1), 015004 (2012).
52. P. Liu, Y. Huang, Z. Guo, J. Wang, Z. Zhuang, and S. Liu, "Discrimination of dimethyl sulphoxide diffusion coefficient in the process of optical clearing by confocal micro-Raman spectroscopy," Journal of Biomedical Optics 18(2), 020507 (2013).
53. M. E. Darvin, J. Schleusener, F. Parenz, O. Seidel, C. Krafft, J. Popp, and J. Lademann, "Confocal Raman microscopy combined with optical clearing for identification of inks in multicolored tattooed skin in vivo," Analyst 143(20), 4990–4999 (2018).
54. A. Y. Sdobnov, V. V. Tuchin, J. Lademann, and M. E. Darvin, "Confocal Raman microscopy supported by optical clearing treatment of the skin—influence on collagen hydration," Journal of Physics D: Applied Physics 50(28), 285401 (2017).
55. A. Jaafar, M. E. Darvin, V. V. Tuchin, and M. Veres, "Confocal Raman Micro-Spectroscopy for Discrimination of Glycerol Diffusivity in Ex Vivo Porcine Dura Mater," Life 12(10), 1534 (2022).
56. A. Jaafar, A. Albarazanchi, M. J. Kadhim, M. E. Darvin, T. Váczi, V. V. Tuchin, and M. Veres, "Impact of e-cigarette liquid on porcine lung tissue − Ex vivo confocal Raman micro-spectroscopy study," Journal of Biophotonics e202300336 (2023).
57. A. Y. Sdobnov, M. E. Darvin, J. Schleusener, J. Lademann, and V. V. Tuchin, "Hydrogen bound water profiles in the skin influenced by optical clearing molecular agents—Quantitative analysis using confocal Raman microscopy," Journal of Biophotonics 12(5), e201800283 (2019).
58. A. Yu. Sdobnov, J. Schleusener, J. Lademann, V. V. Tuchin, and M. E. Darvin, "Water migration at skin optical clearing," in Handbook of Tissue Optical Clearing, V. V. Tuchin, D. Zhu, E. A. Genina (Eds.), 1st ed., CRC Press, Boca Raton, 167–184 (2022). ISBN: 9781003025252.
59. K. König, "Multiphoton microscopy in life sciences," Journal of Microscopy 200(2), 83–104 (2000).

60. M. Kröger, J. Scheffel, E. A. Shirshin, J. Schleusener, M. C. Meinke, J. Lademann, M. Maurer, and M. E. Darvin, "Label-free imaging of M1 and M2 macrophage phenotypes in the human dermis in vivo using two-photon excited FLIM," eLife 11, e72819 (2022).
61. M. Kröger, J. Scheffel, V. V. Nikolaev, E. A. Shirshin, F. Siebenhaar, J. Schleusener, J. Lademann, M. Maurer, and M. E. Darvin, "In vivo non-invasive staining-free visualization of dermal mast cells in healthy, allergy and mastocytosis humans using two-photon fluorescence lifetime imaging," Scientific Reports 10(1), 14930 (2020).
62. L. Deng, Z. Fan, B. Chen, H. Zhai, H. He, C. He, Y. Sun, Y. Wang, and H. Ma, "A Dual-Modality Imaging Method Based on Polarimetry and Second Harmonic Generation for Characterization and Evaluation of Skin Tissue Structures," International Journal of Molecular Sciences 24(4), 4206 (2023).
63. M. Kröger, J. Schleusener, J. Lademann, M. C. Meinke, S. Jung, and M. E. Darvin, "Tattoo Pigments Are Localized Intracellularly in the Epidermis and Dermis of Fresh and Old Tattoos: In vivo Study Using Two-Photon Excited Fluorescence Lifetime Imaging," Dermatology 239(3), 478–493 (2023).
64. M. J. Koehler, K. König, P. Elsner, R. Bückle, and M. Kaatz, "In vivo assessment of human skin aging by multiphoton laser scanning tomography," Optics Letters 31(19), 2879 (2006).
65. S. Springer, M. Zieger, A. Böttcher, J. Lademann, and M. Kaatz, "Examination of wound healing after curettage by multiphoton tomography of human skin in vivo," Skin Research and Technology 23(4), 452–458 (2017).
66. A.-M. Pena, T. Baldeweck, E. Decencière, S. Koudoro, S. Victorin, E. Raynaud, B. Ngo, P. Bastien, S. Brizion, and E. Tancrède-Bohin, "In vivo multiphoton multiparametric 3D quantification of human skin aging on forearm and face," Scientific Reports 12(1), 14863 (2022).
67. F. Stracke, B. Weiss, C.-M. Lehr, K. König, U. F. Schaefer, and M. Schneider, "Multiphoton Microscopy for the Investigation of Dermal Penetration of Nanoparticle-Borne Drugs," Journal of Investigative Dermatology 126(10), 2224–2233 (2006).
68. M. S. Roberts, Y. Dancik, T. W. Prow, C. A. Thorling, L. L. Lin, J. E. Grice, T. A. Robertson, K. König, and W. Becker, "Non-invasive imaging of skin physiology and percutaneous penetration using fluorescence spectral and lifetime imaging with multiphoton and confocal microscopy," European Journal of Pharmaceutics and Biopharmaceutics 77(3), 469–488 (2011).
69. M. Klemp, M. C. Meinke, M. Weinigel, H. Röwert-Huber, K. König, M. Ulrich, J. Lademann, and M. E. Darvin, "Comparison of morphologic criteria for actinic keratosis and squamous cell carcinoma using in vivo multiphoton tomography," Experimental Dermatology 25(3), 218–222 (2016).
70. M. J. Koehler, M. Speicher, S. Lange-Asschenfeldt, E. Stockfleth, S. Metz, P. Elsner, M. Kaatz, and K. König, "Clinical application of multiphoton tomography in combination with confocal laser scanning microscopy for in vivo evaluation of skin diseases," Experimental Dermatology 20(7), 589–594 (2011).
71. K. König, "Clinical multiphoton tomography," Journal of Biophotonics 1(1), 13–23 (2008).
72. K. König, H. G. Breunig, A. Batista, A. Schindele, M. Zieger, and M. Kaatz, "Translation of two-photon microscopy to the clinic: multimodal multiphoton CARS tomography of in vivo human skin," Journal of Biomedical Optics 25(01), 1 (2020).
73. R. Cicchi, F. S. Pavone, D. Massi, and D. D. Sampson, "Contrast and depth enhancement in two-photon microscopy of human skin ex vivo by use of optical clearing agents," Optics Express 13(7), 2337 (2005).
74. A. Sdobnov, M. E. Darvin, J. Lademann, and V. Tuchin, "A comparative study of ex vivo skin optical clearing using two-photon microscopy," Journal of Biophotonics 10(9), 1115–1123 (2017).
75. A. Yu. Sdobnov, J. Lademann, V. V. Tuchin, and M. Darvin, "Nonlinear Optics of Skin: Enhancement of Autofluorescence and Second Harmonic Generation Signals by Immersion Optical Clearing," Journal of Biomedical Photonics & Engineering 030201 (2023).
76. C. Rodríguez, A. Chen, J. A. Rivera, M. A. Mohr, Y. Liang, R. G. Natan, W. Sun, D. E. Milkie, T. G. Bifano, X. Chen, and N. Ji, "An adaptive optics module for deep tissue multiphoton imaging in vivo," Nature Methods 18(10), 1259–1264 (2021).
77. Z. Qin, Z. She, C. Chen, W. Wu, J. K. Y. Lau, N. Y. Ip, and J. Y. Qu, "Deep tissue multi-photon imaging using adaptive optics with direct focus sensing and shaping," Nature Biotechnology 40(11), 1663–1671 (2022).
78. M. J. Booth, "Adaptive optics in microscopy," Philosophical Transactions of the Royal Society A: Mathematical, Physical and Engineering Sciences 365(1861), 2829–2843 (2007).
79. H. Yu, P. Lee, Y. Jo, K. Lee, V. V. Tuchin, Y. Jeong, and Y. Park, "Collaborative effects of wavefront shaping and optical clearing agent in optical coherence tomography," Journal of Biomedical Optics 21(12), 121510 (2016).

Inhibition of Lung Cancer Stem Cell Migration and Growth Through Nano-Photodynamic Therapy

Anine Crous and Heidi Abrahamse*
Laser Research Centre, Faculty of Health Sciences, University of Johannesburg, PO Box 17011, Johannesburg 2028, South Africa
*e-mail: habrahamse@uj.ac.za

Abstract. Recurrence and post-treatment spreading of lung cancer signify the existence of drug-resistant cancer stem cells (CSCs) that withstand current therapies. The development of metastases and secondary tumors is a primary contributor to mortality. CSCs play a pivotal role in driving cellular invasion and have a critical impact on prognosis. Enhancing treatment outcomes involves the targeted elimination of CSCs while preserving healthy tissue. In this laboratory-based investigation, Photodynamic Therapy (PDT), a minimally invasive treatment, was employed alongside a nano drug carrier for lung cancer. PDT operates by inducing light-triggered cell death using a photosensitizing drug. When coupled with gold nanoparticles, this nano-mediated PDT facilitated cell death specifically in lung CSCs. The study's objective was to assess the impact on normal lung cells and isolated CSCs, considering aspects such as cellular structure, migratory ability, proliferation, toxicity, doubling time, and the cell cycle. The results revealed minimal effects on normal lung cells, a reduction in CSC migration and invasion, the initiation of cell cycle arrest, and a decrease in CSC proliferation. Utilizing a drug nano carrier like AuNPs significantly enhanced the efficacy of PDT, with a specific focus on curtailing CSC-mediated dissemination in lung cancer, ultimately leading to an improved prognosis. © 2024 Journal of Biomedical Photonics & Engineering.

Keywords: gold nano sensitizer; photodynamic therapy; dissemination; lung cancer stem cells.

Paper #9086 received 27 Mar 2024; revised manuscript received 24 Apr 2024; accepted for publication 24 Apr 2024; published online 30 May 2024. doi: 10.18287/JBPE24.10.040301.

1 Introduction

Photodynamic therapy (PDT) is a promising cancer treatment. PDT produces reactive oxygen species (ROS) upon photoactivation of a photosensitizer (PS). Cancer stem cells (CSCs) are inhibited by oxygen-dependent exogenous ROS. PDT may also raise ROS levels by influencing metabolism, endoplasmic reticulum stress, or mitochondrial membrane potential. PDT induced ROS have a short half-life, are highly reactive, and have limited diffusion. Thus, PDT's photodynamic action is seen at the subcellular level, which aids in understanding how PDT affects CSC characteristics such as differentiation, self-renewal, apoptosis, autophagy, and immunogenicity. Excess ROS disrupts the redox system, oxidizes DNA, alters mitochondrial permeability, and activates the unfolded protein response, autophagy, and the CSC resting state. Thus, understanding the molecular mechanism by which ROS affect CSCs improves PDT and prevents tumor recurrence and dissemination [1]. Gold nanoparticles have gained attention in cancer therapy due to their unique physicochemical properties and potential applications in PDT. Gold nano-sensitizers have been utilized as promising agents in PDT to enhance the efficiency of light-based treatments by amplifying the generation of ROS and improving the therapeutic outcomes [2].

Evaluating the effects of nanoPDT using gold nanoparticles (AuNPs) as drug delivery vehicle on lung CSC proliferation, invasion, and migration is significant

due to the unique characteristics and role of CSCs in cancer progression and treatment resistance. CSCs are a small subset of cells within tumors that possess self-renewal capabilities and have been associated with tumor initiation, relapse, and dissemination [3]. Traditional cancer therapies often target the bulk of tumor cells but may fail to effectively eliminate CSCs, leading to tumor recurrence and treatment failure. Therefore, it is crucial to develop therapeutic strategies that can specifically target and eradicate CSCs to achieve long-term remission and improve patient outcomes.

The current state of research on nanoPDT using AuNPs on lung CSC proliferation, invasion, and migration is still an emerging field with limited studies available, where related research on the topic has only been reviewed. However, related, and preliminary research suggests promising potential for using gold nano-sensitizers in PDT to target and inhibit the behaviors of lung CSCs. Previous research on A549 lung cancer using AlPcS4Cl and AuNPs indicated that the compound can prevent lung cancer migration and invasion, induce cell cycle arrest and reduce its proliferative abilities [4]. These results only related to lung cancer alone and not the effects of the compound on the side population of CSCs and normal lung cells. Mkhobongo et al. (2022) investigated the effects of PDT on melanoma cells (A375) and their stem cell population using AlPcS4Cl and AuNPs. The study found that the drug delivery vehicle (AuNPs) increased PS uptake and localization in mitochondria and lysosomes, resulting in a dose-dependent decrease in melanoma viability [5]. Researchers investigated the efficiency of a nanoparticle conjugate loaded with Indocyanine green and Protoporphyrin IX on cobalt ferrite superparamagnetic nanoparticles as a multifunctional compound for nanoPDT in another study on A375 CSCs. The study found that ROS and cell death were effectively increased [6].

These studies provide preliminary evidence supporting the use of nanoPDT for inhibiting CSC proliferation, invasion, and migration. However, further research is required to validate these findings and optimize the treatment protocols. It is important to note that the field of gold nano-sensitizer PDT on lung CSCs is still evolving, and more studies are needed to fully understand its potential and establish its clinical relevance.

By evaluating the effects of nanoPDT on lung CSCs, researchers aim to investigate the potential of this treatment modality in specifically targeting and suppressing the proliferation, invasion, and migration abilities of CSCs. The study intends to shed light on the effectiveness of nanoPDT as a novel therapeutic approach in overcoming CSC-related challenges in lung cancer treatment. Understanding the impact of using AuNPs as PS deliver vehicle during PDT on lung CSCs' behavior is essential for developing personalized and targeted therapies that can eradicate CSCs and prevent cancer recurrence and dissemination. This research may provide valuable insights into the development of innovative treatment strategies for lung cancer patients, ultimately improving their prognosis and quality of life.

The study assessed the photodynamic effects of gold nano-sensitizer PDT on normal lung epithelium and isolated lung CSCs by evaluating the morphological and biochemical effects on normal lung cells and determining the effects on CSC migration, proliferation, and invasion.

2 Methods

2.1 Cell Culture and CSC Separation

Normal lung epithelial cells (HBEC3-KT (ATCC® CRL-4051™)) were cultured in Airway Epithelial Cell Basal Medium (ATCC PCS-300-030) and Bronchial Epithelial Cell Growth Kit (ATCC PCS-300-040). Cancer cells were cultured in Rosewell Park Memorial Institute 1640 medium (RPMI-1640) (Sigma-Aldrich, R8758) supplemented with 5% fetal bovine serum (FBS) (Biochrom, S0615) and 0.5% penicillin/ streptomycin (Sigma-Aldrich, P4333) and 0.5% amphotericin B (Sigma-Aldrich, A2942). A side population of CSCs were sorted using a magnetic bead isolation kit (Miltenyi Biotec, QuadroMACS™ separation unit 130-091-051) and characterized using flow cytometry. CSCs enriched for the respective markers were maintained at a passage between 4 and 8 for all experimental purposes. All cultures were maintained and incubated at 37 °C in 5% CO_2 and 85% humidity.

2.2 Immunophenotyping of Lung CSCs

The protein expression of the CSC markers CD133, CD44 and CD56 (CD133 Antibody (3F10), NovusBio, NBP2-3774 / CD44 Antibody (8E2F3), NovusBio, NBP1-47386 / CD56 Monoclonal Anti-N Cam, Sigma-Aldrich, C9672) was identified using the secondary antibody identification technique. Suspension cells were labelled with primary human anti-mouse and identified with secondary fluorescent Goat anti-Mouse (NovusBio, NB720-F-1 mg; NovusBio, NB7602; NovusBio, NB7594). Antigenic expression was examined by flow cytometry (BD Accuri Flow Cytometer C6).

2.3 Photodynamic Therapy

The gold nano-sensitizer in this study was synthesized and characterized as described in previous research [7] by loading Al (III) Phthalocyanine Chloride Tetra sulfonic Acid ($AlPcS_4Cl$) (Frontier Scientific, AlPcS-834) onto gold nanoparticles (AuNPs) (Sigma-Aldrich, 765465). Lung CSCs were cultured and seeded at a total of 5×10^5 cells per petri dish in complete media and allowed to attach for 24 h before irradiation. Cultures were divided into 4 study groups. Group 1 was the control and received no PDT, group 2 received PBM alone and was irradiated at 10 J/cm^2. Group 3 received PDT treatment with 10 J/cm^2 photoactivation and 20 μM $AlPcS_4Cl$ and group 4 received the gold nano-sensitizer and 10 J/cm^2 photoactivation. All samples were incubated for 24 h after PDT treatment followed by

morphological and physiological analysis. For migration studies cells were incubated for 24- and 48-h post irradiation. The concentrations of the sensitizers and laser parameters used are indicated in Table 1.

2.4 Morphology: Inverted Light Microscopy

Morphological differences were observed and examined 24 h after irradiation using an inverted light microscope (OLYMPUS, CKX41). The microscope was equipped with a digital camera (OLYMPUS, SC30) connected to it, allowing the capture of images. The Olympus cellSens Software was utilized for image acquisition and analysis.

2.5 Cell Migration: "Central Scratch Test" Method

The migration of cells was assessed using the "central scratch" technique. The cells were cultured in 35 mm petri dishes and incubated overnight at 37 °C and 5% CO2. Before irradiation, a central scratch was created using a sterile P-200 pipette tip. The movement of the cells was observed using specific positions and focal planes on an Inverted Microscope (Wirsam, Olympus CKX41) and documented using a digital camera (SC30 Olympus Camera). Images were captured at 0 h, 24 h, and 48 h after irradiation. Velocity (v) a vector quantity that measures displacement (or change in position, Δs) over the change in time (Δt) was calculated using the following Eq.: $\bar{v} = \frac{\Delta x}{\Delta t}$, where the distance that the cells travelled was measured and the mean cell velocity (μm/h) tabulated. Area migration was quantified by calculating the area of the image covered by cells using Image J analysis software, which converts the cell population image to a mean grey value and calibrates the area measured using the image's scale bar.

2.6 Cell Proliferation and Deterioration

The Cell Titer-Glo test (Promega, G7573) was used to detect cell proliferation as a marker of metabolically active cells. The assay produces a bright signal indicating the presence of ATP production in metabolically active or developing cells. The ATP test takes advantage of luciferase's characteristics to provide a sustained luminous signal while preventing endogenous ATP release during cell lysis. To induce cell lysis, equal amounts of reconstituted reagent and cell suspension were introduced and stirred. The luminous signal was quantified in Relative Light Units using a luminometer (Perkin Elmer, Victor3) (RLU).

The release of LDH from the cytosol, resulting from induced membrane disruption, was utilized to quantify the deterioration of cells. The CytoTox96® nonradioactive cytotoxicity test (Promega, G400) was employed for this purpose. In this test, LDH interacts with a tetrazolium salt (present in the reconstituted reagent) in its oxidized form, leading to the formation of a measurable red formazan product in its reduced form. This chemical reaction is dependent on NADH. The absorbance of the resulting color was measured spectrophotometrically at 490 nm using a multi-label Counter (Perkin Elmer, VICTOR3TM, 1420).

2.7 Cell Viability-Proliferation Kinetics: Population Doubling Time

To detect live and dead cells, a Trypan Blue Stain (0.4%) assay was performed (Invitrogen™, T10282). This assay relies on the principle of color exclusion. An Automated Cell Counter (ThermoFischer, AMQAX1000) was used to quantify the number of viable cells. The doubling time represents the duration required for a given quantity to double in size or value, assuming a constant growth rate.

To calculate the population doubling time of the samples, the following Eq. was utilized:

$$gr = \frac{\ln(N(t)/N(0))}{t},$$

$$dt = \frac{ln2}{gr}.$$

The growth rate was determined by dividing the number of cells by the initial seeding density. Subsequently, the doubling time was calculated as an exponential rate, taking into account the viable cell count at seeding ($N(0)$), the viable cell count at harvest ($N(t)$), and the time interval (t) in hours between seeding and harvest. The viability of cells was determined using trypan blue exclusion method.

Table 1 Gold nano-sensitizer and irradiation parameters.

PDT Parameters	
AlPcS4Cl Concentration (μM)	20
AuNPs Concentration (ppm)	20
Wavelength (nm)	659.4
Type	LED Well plate illuminator
PSU	Keithley 2200-32-3
Power density (mW/cm^2)	117.17
Fluence (J/cm^2)	10
Time of irradiation (s)	85.4

2.8 Cell Cycle Analysis: PI

Flow cytometry was utilized for cell cycle analysis, which involved quantifying the DNA content. In this analysis, a stoichiometric dye called PI (propidium iodide) was employed, which binds to DNA in proportion to its amount within the cells. The experimental procedure involved harvesting the cells and washing them with PBS (phosphate-buffered saline). Subsequently, the cells were fixed by treating them with 70% ethanol for 30 min at 4 °C. After two additional washes with PBS, the cells were treated with 50 µl of a 100 µg/ml stock solution of RNase. Following that, the cells were stained with 50 µg/ml of PI.

2.9 Statistical Analysis

Statistical examinations were carried out on datasets sourced from no fewer than three independent experiments. The comparison between two groups was conducted using Student's *t*-test, while simultaneous comparisons among multiple groups were performed using one-way ANOVA. These analyses were executed utilizing SigmaPlot software version 12, which automates mathematical transformations and statistical analyses. It is noteworthy that both Student's *t*-test and one-way ANOVA assume data normality, a condition verified using the Shapiro-Wilk test. Quantitative analysis of migration morphology data was performed using Image J, a publicly available image processing program based on Java (National Institute of Health, Bethesda, MD, USA). The results are presented as the mean ± standard error (SE). Statistical differences were indicated in tables and graphs using the symbols $P < 0.05$ (*), $P < 0.01$ (**), and $P < 0.001$ (***), while dispersion bars were used to represent the standard error.

3 Results

3.1 Synthesis and Characterization of NanoPDT

Synthesis and characterization of this work has been already published in 2020 [7]. Synthesis of nanoPDT was done using a centrifugation process. Since the average size of the nanoPDT was 61.99 nm, the composite can still be categorized as a nano-structure because nanostructures are material configurations with a size between 1 and 100 nm. The nanoPDT suspension appeared to be polydisperse with a modest size distribution based on the polydispersity index (PdI) value of 0.477. The AuNP-PEG-COOH showed O-H stretching at 3422 cm^{-1}, which was caused by the compound being suspended in water, C=C stretching at 1642 cm^{-1}, PEG functionalization-related O-H bending at 1413.9–1468.5 cm^{-1}, carboxylic acid-related O-H bending, and C-O stretching at 1100 cm^{-1} due to the polyether structure in PEG. $AlPcS_4Cl$-AuNP-PEG-COOH also had O-H stretching at 3422 cm^{-1}, C=C stretching at 1642 cm^{-1}, C-H bending at 1471 cm^{-1}, O-H stretching at 1430 cm^{-1}, and S=O stretching at 1308.8 cm^{-1} and 1072 cm^{-1} from the sulphate functionalized PS. AuNP-PEG-COOH and $AlPcS_4Cl$ both have 520 nm and 676 nm absorption spectra, respectively, as shown by ultraviolet-visible spectroscopy (UV-Vis) of the individual molecules.

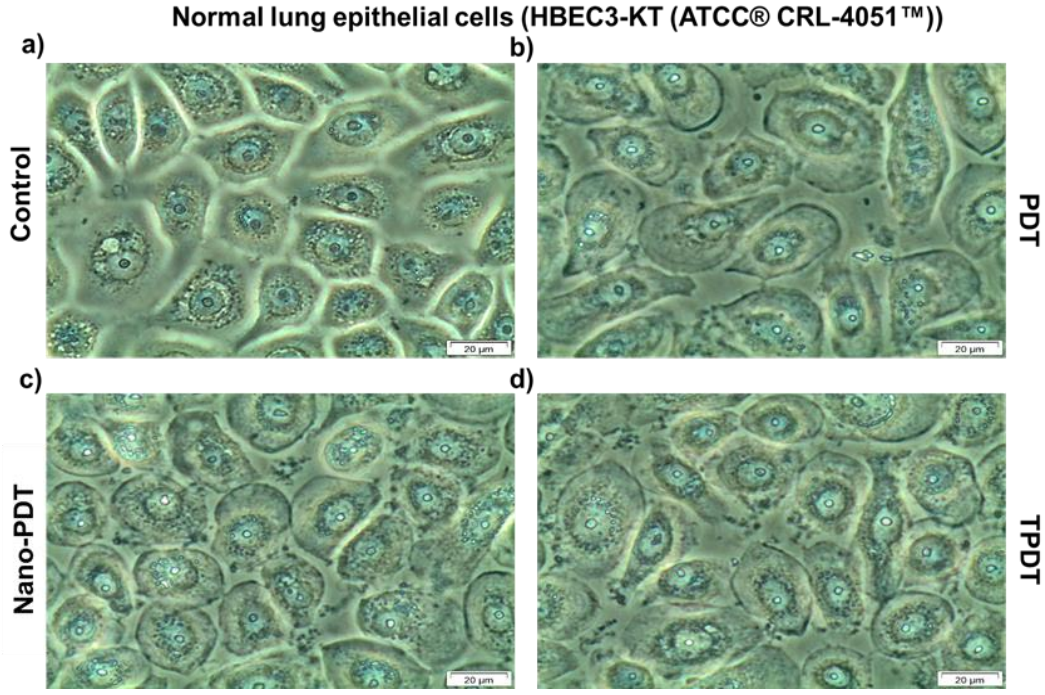


Fig. 1 Morphology of normal lung cells post PDT. Results show normal lung epithelial morphology of the (a) control cells that received no treatment, (b) cells that received PDT treatment, (c) cells that received nanoPDT treatment, and (d) TPDT treated cells, 24 h post PDT treatments.

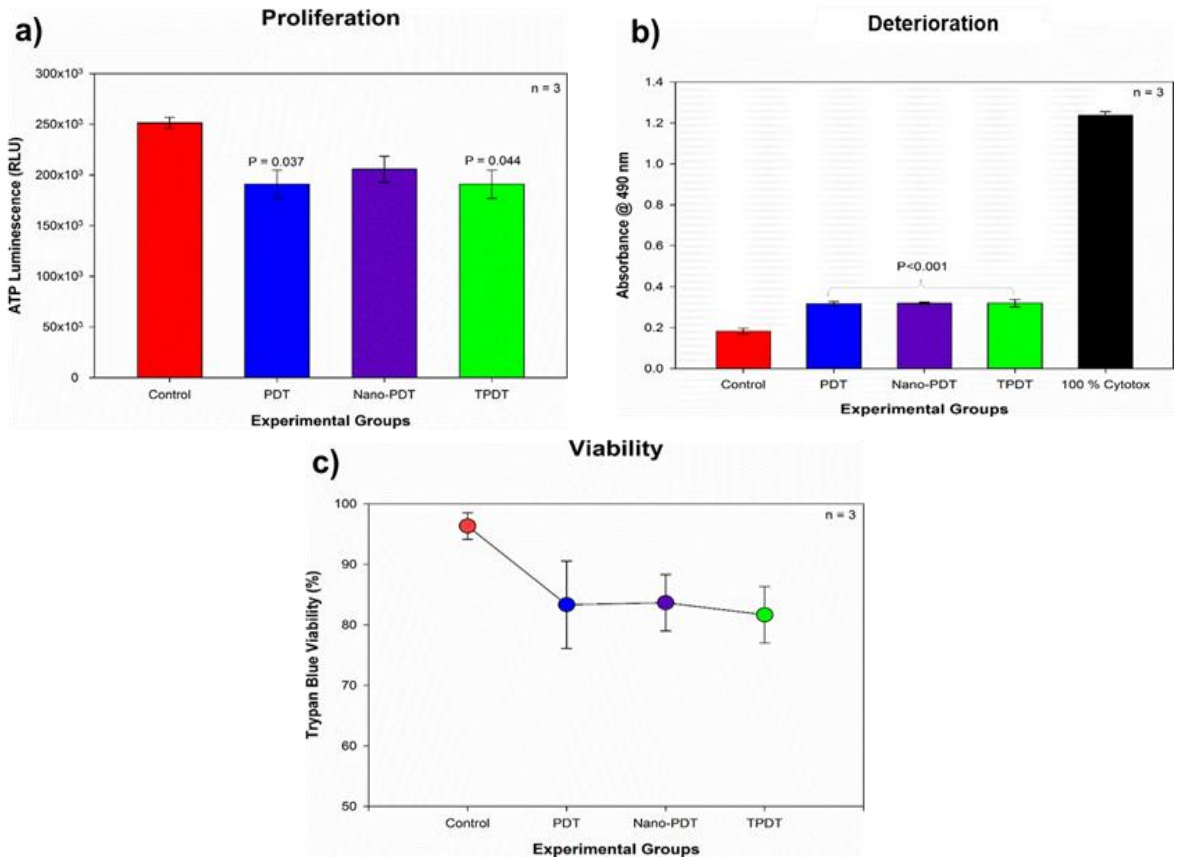


Fig. 2 Biochemical analysis of normal lung cells post PDT treatment. Results show (a) a significant decrease in proliferation of P = 0.037 when comparing PDT treated samples to the control and P = 0.044 when comparing TPDT treated samples to the control, (b) a significant increase of P < 0.001 in cytotoxicity for all PDT treated samples compared to the control and (c) an insignificant decrease in viability post PDT treatments.

The concentration distributions of the AuNPs and the PS in relation to their corresponding dependent absorbance were both linear. Each molecule's linear regression was determined, and the regression coefficients were computed [7].

3.2 Effects of NanoPDT on Normal Lung Cells

3.2.1 Morphology of Normal Lung Cells Post NanoPDT Treatment

The morphology findings (Fig. 1) of normal lung cells at a 24-h interval following photodynamic therapy (PDT) treatments demonstrate that various treatment modalities, including PDT utilizing the photosensitizer (PS) alone with photoactivation, nanoPDT involving PS conjugated to gold nanoparticles, and targeted-PDT (TPDT) incorporating PS conjugated to gold nanoparticles along with an attached antibody, exhibit cellular morphology comparable to that observed in the control experiment with no treatments administered. The observed cellular structures exhibit preserved cell membranes, minimal vacuolization, and a compact monolayer arrangement. There is a lack of substantial alteration in morphology.

3.2.2 Biochemical Examination of Normal Lung Cells Following NanoPDT Treatment

The biochemical findings presented in Fig. 2 indicate a reduction in proliferation among the experimental groups. Specifically, the samples treated with PDT and TPDT demonstrate a statistically significant decrease in proliferation compared to the control group. However, it is important to note that these results are not as significant as the findings presented in Fig. 7(a), which demonstrate a minimum 50% decrease in proliferation among CSCs when subjected to PDT. There is a notable rise in the occurrence of membrane damage, resulting in the leakage of lactate dehydrogenase (LDH) into the surrounding medium across all photodynamic therapy (PDT) groups, as compared to the control group. However, this lack of significance is observed when comparing the results obtained regarding the cytotoxic effects induced in the CSCs (Fig. 7(b)), as well as when comparing it to the positive control, which serves as an indicator of complete cytotoxicity. In a similar vein, the findings pertaining to viability indicate a decline in the percentage of viability. Nevertheless, it is important to note that these results do not exhibit statistical significance. In addition to the morphological findings, the data indicate that the PS exhibits potential in selectively inducing apoptosis in tumor cells while preserving the viability of normal cells.

3.3 Effects of NanoPDT on Lung CSCs

3.3.1 Immunophenotyping of Lung CSCs

Antigenic detection was performed on the separated cells to determine their stem-ness using the BD AccuriTM C6 Flow Cytometer. Indirect antibody labelling enabled the detection of antigen-antibody conjugation fluorescently. Flow cytometry analysis revealed that the separated cells exhibited the markers CD133, CD44, and CD56 (Fig. 3).

3.3.2 Morphology: Inverted Light Microscopy

The morphology of lung CSCs was examined 24 h after PDT treatment. The treated samples were compared to a control sample that did not undergo photoactivation. The results are presented in Fig. 4, which illustrates the appearance of lung CSCs under different conditions. In Fig. 4(a)), untreated lung CSC morphology is shown. In Fig. 4(b)), lung CSCs treated with photobiomodulation (PBM) exhibit no significant changes in morphology compared to the control sample. These results indicate that the cells maintain their viability and ability to proliferate, as evidenced by a dense monolayer of cells. Figs. 4(c) and 4(d) represent samples that underwent PDT and nanoPDT treatment, respectively. In both cases, these samples demonstrate notable morphological alterations compared to the control sample. These changes include cell shrinkage, condensation of chromatin, cancer cell blebbing, cytoplasmic vacuolization, as well as loss of cellular shape, detachment, and the presence of free-floating cells. These observed changes collectively indicate cell death [8], translating into a decrease in cell dissemination as cell death limits the invasion and dissemination of cancer cells [9].

3.3.3 Cell Migration

The evaluation of migration was conducted on the morphological samples. Figs. 5(a) and 5(b) illustrate the migration patterns of control cells and cells subjected to photobiomodulation (PBM), revealing a similar trend where the cells migrate towards the central scratch. In contrast, Figs. 5(c) and 5(d) demonstrate the effects of PDT and nanoPDT treatment on CSCs. After PDT treatment, the migration rate of the cells decreased, and they were unable to close the scratch over time. This impaired migration can be attributed to cell arrest induced by PDT.

The findings presented in Fig. 6(a) reveal a significant decrease in velocity when comparing the samples treated with PDT and nanoPDT to the control. Table 2 further demonstrates that the mean cell velocity of the PDT and nanoPDT treated samples was significantly lower compared to both the control and PBM samples. Among the treated samples, CSCs treated with nanoPDT exhibited the slowest velocity, although this difference did not reach statistical significance when compared to the samples treated with PDT. In terms of area migration, as depicted in Fig. 6(b), it represents the extent of cell coverage 48 h after irradiation. The results indicate a statistically significant distinction between the PBM, PDT, and nanoPDT treated samples when compared to the control. PBM treatment resulted in a significant increase in area coverage, while both PDT and nanoPDT treatments led to a significant decrease in area coverage. Notably, the two PDT-treated samples displayed notable differences, with nanoPDT showing the greatest reduction in area migration.

Table 2 Mean cell velocity of lung CSCs post irradiation.

	Mean cell velocity (µm/h)
Control	5.96 ± 0.5
PBM	5.16 ± 0.47
PDT	0.22 ± 0.37
nanoPDT	0.08 ± 0.11

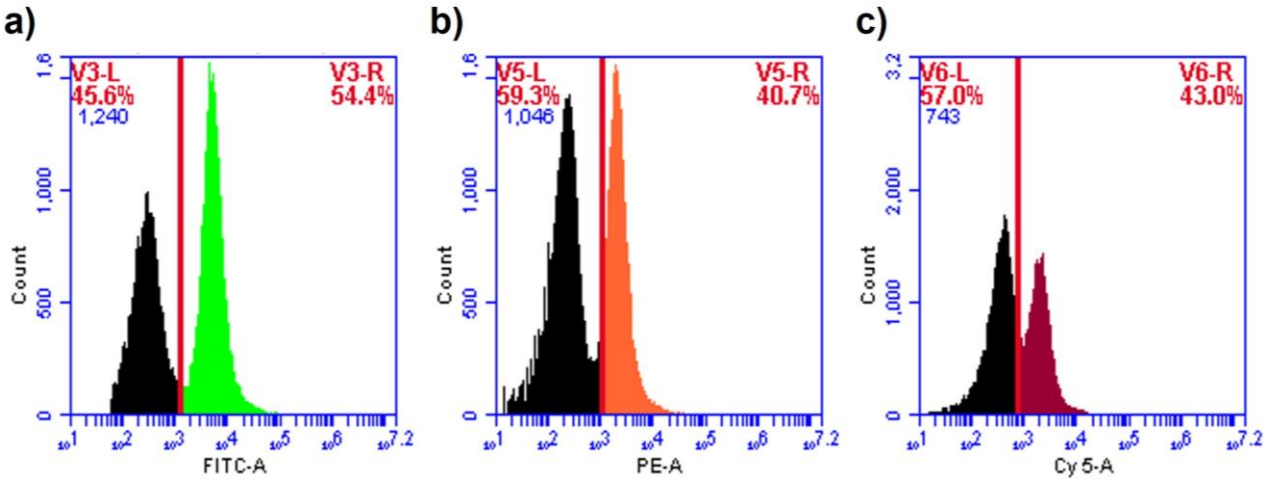


Fig. 3 Flow cytometry expression of stem cell markers (a) CD 133, (b) CD 44, and (c) CD 56 of sorted lung cancer cells.

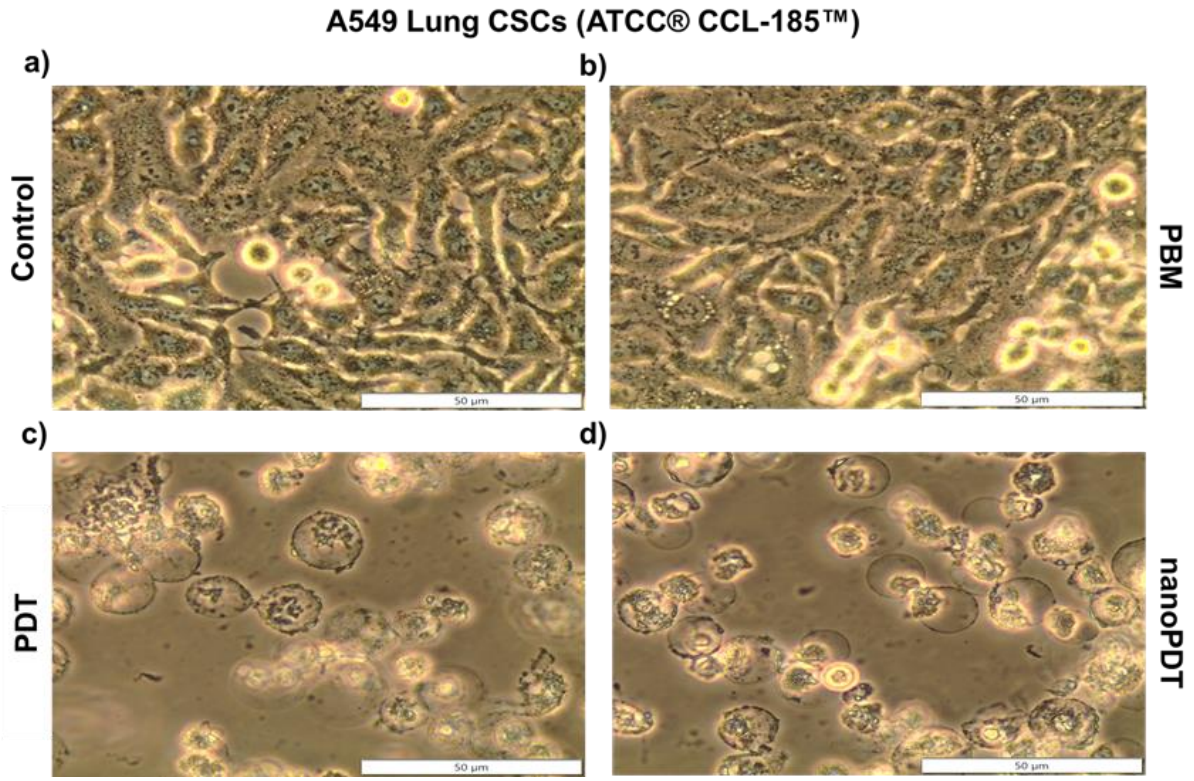


Fig. 4 Morphology of lung CSCs 24 h post PDT treatment. (a) Untreated control cells, (b) CSCs receiving PBM treatment (c) cells receiving PDT treatment, and (d) cells treated using nanoPDT.

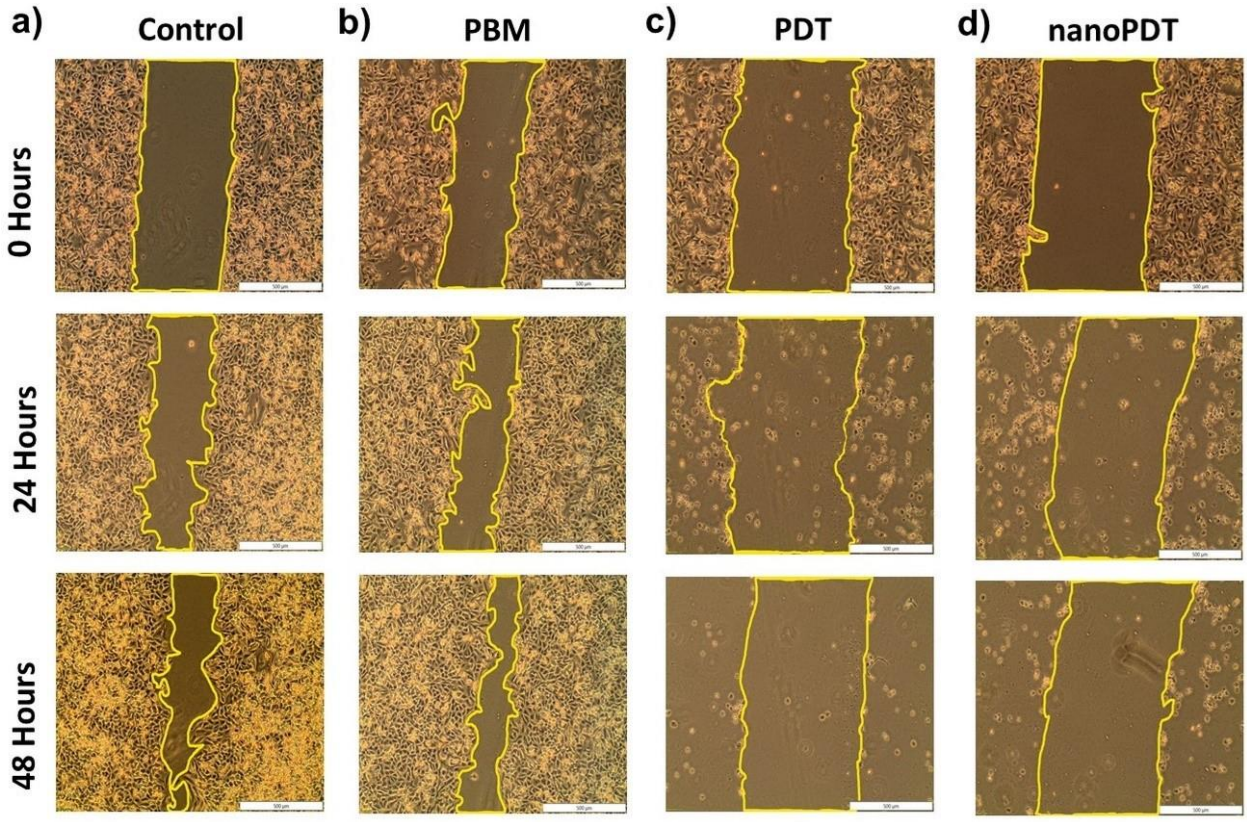


Fig. 5 Morphology of lung CSCs migration 0-, 24- and 48-h post PDT treatment. (a) Control cells that have not received any treatment, (b) CSCs that received only 660 nm PBM at 10 J/cm^2, (c) cells that received PDT treatment with 20 µM $AlPcS_4Cl$ and 660 nm photoactivation at 10 J/cm^2, and (d) cells that received nanoPDT treatment with 20 ppm AuNPs and 660 nm photoactivation at 10 J/cm^2.

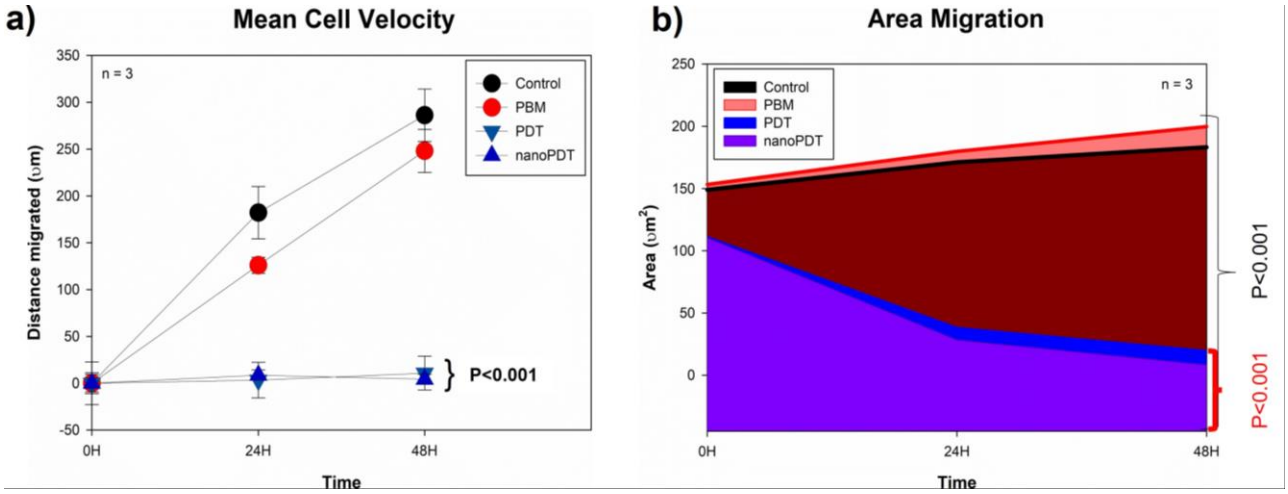


Fig. 6 Lung CSC velocity and area migration 0, 24, and 48 h post irradiation. (a) Mean cell velocity, where PDT and nanoPDT treated samples had a significant ($P < 0.001$) decrease in MCV and (b) area migration, where PBm treated samples had a significant increase ($P < 0.001$) in area migritation, and PDT and nanoPDT samples had a significant ($P< 0.001$) decrease.

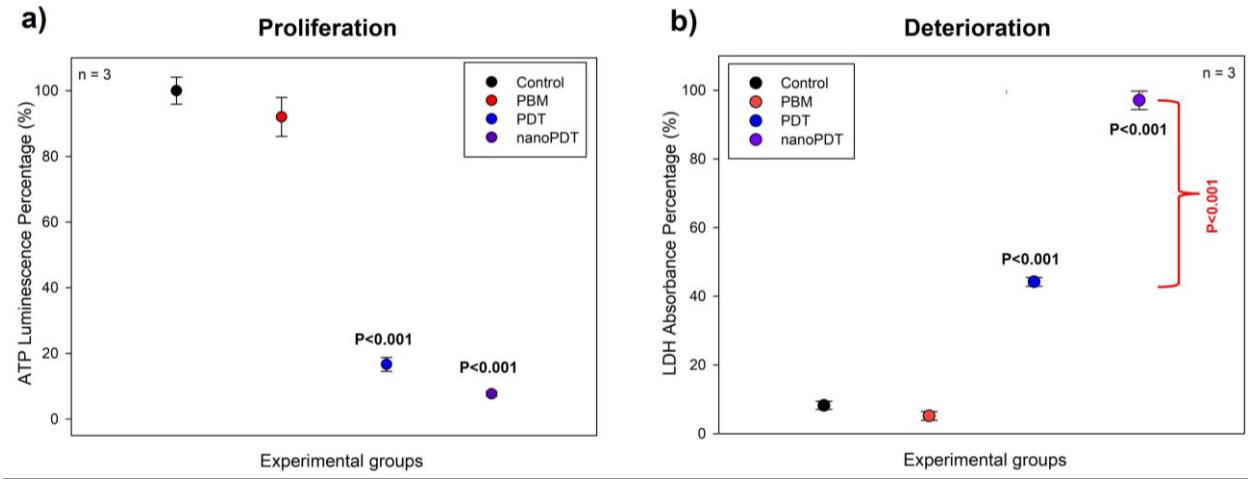


Fig. 7 Lung CSC (a) proliferation, where PDT and nanoPDT had a significant ($P < 0.001$) decrease compared to the control, and (b) deterioration, where PDT and nanoPDT had a significant ($P < 0.001$) increase compared to the control and furthermore a significant increase ($P < 0.001$) was seen in nanoPDT compared to PDT alone, 24 h post irradiation.

3.3.4 Cell Proliferation and Deterioration

The impact of PDT and nanoPDT on lung CSCs was evaluated by measuring intracellular adenosine triphosphate (ATP) levels and LDH release. The quantification of cell proliferation, depicted in Fig. 7(a), was performed by measuring relative light units and converting them into a percentage value using ATP luminescence. The proliferation of CSCs treated with PDT and nanoPDT exhibited a significant reduction compared to both control cells and CSCs treated with PBM alone. Although there was a slight decrease in the number of CSCs treated with nanoPDT compared to PDT, this difference did not reach statistical significance.

The assessment of cell deterioration, presented in Fig. 7(b), was conducted by measuring the absorbance of released LDH resulting from cellular damage and converting it into a percentage value. Control cells and samples treated with PBM demonstrated minimal LDH release into the surrounding environment. In contrast, CSCs treated with PDT and nanoPDT both exhibited significant LDH release. Notably, it was observed that nanoPDT-induced disruption of the cell membrane led to a significant increase in LDH release when compared to the PDT-treated samples.

The objective of the study was to assess the proliferation and growth rates of lung CSCs before and after irradiation treatment, aiming to determine the effectiveness of PDT in inhibiting growth and inducing cellular degradation. The results, as depicted in Fig. 8, demonstrate that prior to irradiation, all samples exhibited a linear increase in growth rate. However, following irradiation, control and PBM samples displayed a steady increase in growth rate, whereas PDT samples exhibited a significant decrease.

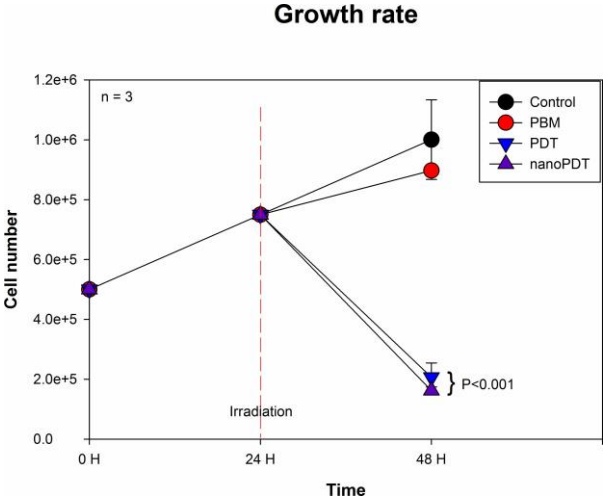


Fig. 8 Growth rate of lung CSCs prior and post PDT treatment. PDT and nanoPDT treated samples showed a significant ($P < 0.001$) decrease in growth rate compared to the control.

Table 3 Population doubling time of lung CSCs 48 h after PDT treatment.

	Ave cell number @ 48 h	**Doubling time (h)**
Control	1×10^6	47.9 ± 2.82
PBM	8.97×10^5	56.89 ± 3.44
PDT	2.07×10^5	-37.72 ± 3.08
nanoPDT	1.62×10^5	-29.57 ± 3.54

The doubling times, calculated and presented in Table 3, provide insights into the rate at which the cell population would double. For the control and PBM samples, the doubling times indicate that the cell population would double after approximately 48 h and 56 h, respectively. In contrast, the PDT-treated samples exhibited negative doubling times, indicating cellular decay. Specifically, the calculated values suggest that the cell population would be depleted after approximately 37 h for PDT-treated samples and after 29 h for nanoPDT-treated samples. These findings imply that the population of cells treated with nanoPDT would deplete at a faster rate compared to the cells treated with PDT.

3.3.5 Cell Cycle

The cell cycle is a sequential process consisting of four stages that contribute to cell proliferation. These stages include the G1 (Gap 1) phase, where cells mature; the S phase, during which DNA is replicated; the G2 phase, where cells prepare for division and undergo DNA checks; and the M phase, involving mitosis. Cells in the S phase possess more DNA compared to cells in the G1 phase. These S phase cells exhibit a higher uptake of dye and fluorescence until their DNA content has doubled. Cells in the G2 phase appear approximately twice as bright as cells in the G1 phase. The results presented in Fig. 9 demonstrate that control cells and those treated with PBM predominantly reside in the G1 and S phases. PBM-treated cells show a shift towards the S phase, indicating that PBM stimulates DNA synthesis and cell proliferation. On the other hand, PDT-treated samples in Figs. 9(c) and 9(d) display a significant number of cells entering the G0 phase, resulting in a decreased percentage of cells in G1 and a reduction of cells transitioning out of the S phase. Notably, cells treated with nanoPDT exhibit greater cell cycle arrest compared to PDT-treated samples that were not conjugated to AuNPs.

4 Discussion and Conclusion

In cancer therapy, including PDT, targeting not only the bulk of cancer cells but also CSCs are crucial for achieving long-term treatment success and preventing recurrence. CSCs are a subset of cells within a tumor that are thought to play a role in tumor initiation, growth, dissemination, and resistance to therapy. Because of their unique properties, CSCs are often more resistant to traditional cancer treatments, making them a significant challenge in achieving complete remission. PDT has the potential to target both cancer cells and CSCs while sparing normal cells due to its localized and selective nature [10]. CSCs are highly tolerant to conventional cancer treatments and resilient due to their capacity to migrate and metastasize [11]. Eliminating lung CSCs during therapy is critical because it can prevent CSC proliferation, cancer relapse, and secondary tumor formation. It is consequently critical to know whether a tumor contains a population of cells that exhibit certain stem cell-like characteristics to predict the treatment's prognosis. The isolated cells expressed markers associated with stem cell maintenance, tumor migration and progression, and decreased anti-tumor response. Thus, they are suitable for evaluating drug efficacy, particularly in this case, the enhancement of PDT using AuNPs as a delivery vehicle for the inhibition of lung CSC proliferation and migration. The utilization and investigation of gold nanoparticles as drug delivery vehicles in the context of PDT have been explored. Although gold nanoparticles do not possess inherent photodynamic activity, they can function as vehicles for photosensitizing chemicals [7].

NanoPDT bears promise as a possible strategy to targeting lung cancer stem cells, which are a subpopulation of cancer cells capable of self-renewal and tumor formation. It is critical to target lung cancer stem cells since they are assumed to be responsible for tumor initiation, development, dissemination, and resistance to conventional therapy [12]. Nanoparticles utilized in nanoPDT can be functionalized with specific ligands or antibodies, allowing them to actively target surface indicators or receptors overexpressed on lung cancer stem cells. These ligands or antibodies can promote the selective binding of nanoparticles to lung cancer stem cells, improving photosensitizer uptake and

retention [13]. Active targeting techniques allow for more effective and selective elimination of lung cancer stem cells while causing the least amount of harm to healthy cells [14]. The enhanced permeability and retention (EPR) effect is a feature of tumor tissues, particularly lung cancer stem cells, in which leaky blood arteries and decreased lymphatic outflow lead to increased nanoparticle accumulation in the tumor microenvironment. After intravenous delivery, this action permits nanoparticles to passively collect in tumor tissues [15]. NanoPDT can selectively distribute photosensitizers to the tumor and target lung cancer stem cells within the tumor mass by utilizing the EPR effect [16]. Nanoparticle size and surface charge can alter cellular absorption and dispersion within tumor tissues. Furthermore, surface charge can influence nanoparticle interactions with cancer cells [17]. NanoPDT may be adjusted to increase its' specificity for targeting lung cancer stem cells by carefully manipulating the size and surface features of nanoparticles [7]. Additionally, nanoPDT can be coupled with other stem cell-targeted therapies to improve therapeutic specificity and effectiveness. Therapies that target signaling pathways or molecular markers associated with lung cancer stem cells can be combined with nanoPDT to create a synergistic impact that results in a more successful lung CSC elimination [18]. However, nanoPDT for targeting lung CSCs is still in the early stages of development. While preclinical investigations have yielded encouraging findings, more research, including in vitro, in vivo, and clinical trials, is required to evaluate the selectivity and therapeutic efficacy of nanoPDT for lung CSCs.

Because most cancer fatalities are caused by metastases, the greatest significant gains in morbidity and mortality will come from preventing or eliminating such disseminated illness [19]. As a result, preventing dissemination is critical for improving patient prognosis. We examined the impact of PDT and its enhanced form utilizing AuNPs as a drug delivery vehicle on lung CSC dissemination. To begin, we examined the migratory impacts of PDT and nanoPDT. Both types of PDT decreased lung CSCs' migratory and invasion potential. NanoPDT significantly decreased cell migration more than PDT alone. It has been proven that PDT can decrease lung cancer dissemination [20]. Additionally, new research indicates that AuNPs can inhibit cancer cell migration/invasion and reduce metastases [21]. Thus, it is hypothesized that combining PDT with nanoparticles would have a greater effect on reducing lung cancer and CSC migration, as demonstrated in this study by a decline in mean cell velocity and a significant reduction in area migration when comparing PDT to nanoPDT.

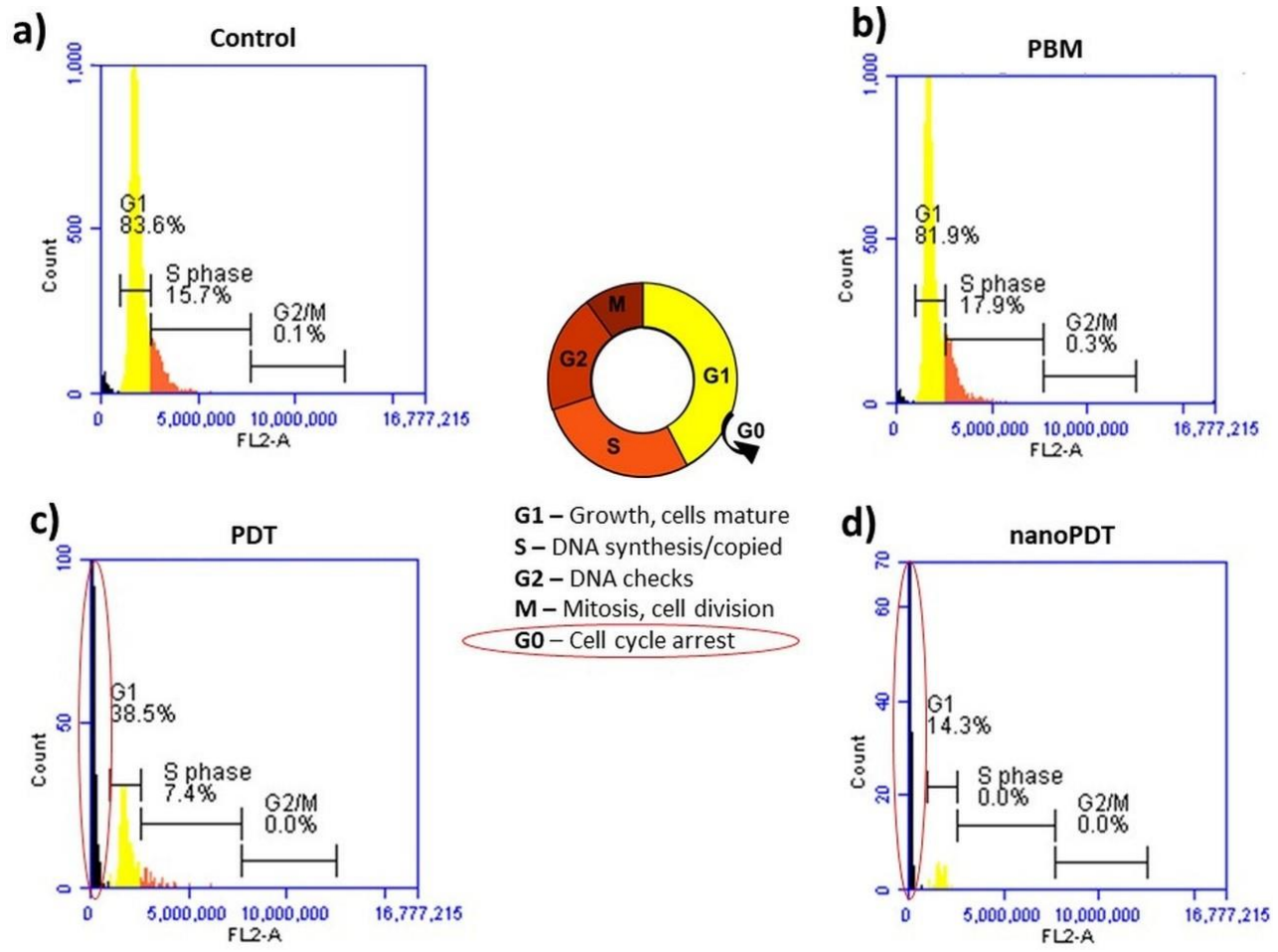


Fig. 9 Cell cycle analysis of CSCs 24 h post PDT treatment. (a) Control cells receiving no treatment. (b) Cells receiving PBM treatment. (c) Cells receiving PDT treatment. (d) Cells receiving nanoPDT treatment.

The amount of ATP in cells can be utilized as a marker for proliferation [22]. Lung cancer cell metabolism is regulated by their mitochondria via aerobic glycolysis in ATP synthesis [23]. Furthermore cancer cell energy metabolism is associated with tumor proliferation and migration [24]. This correlation implies that the altering of lung cancer metabolism through its mitochondrial activity is proportional to lung cancer migration [25], where decreased ATP production is indicative of decreased cell dissemination. Damaged or compromised membranes release the enzyme LDH into the surrounding extracellular space. The quantified amount of LDH is then proportional to the amount of deteriorating cells [26]. CSCs' drug resistance and metastatic potential are a result of their improved capacity to withstand physical stressors that typically result in cell membrane destruction. As a result, circumventing the cell's ability to mend its membrane may result in metastatic inhibition [27]. Effective cytotoxicity can lead to cell regression and death caused by a loss of plasma/cellular membrane integrity or cytoplasmic shrinking. The mechanism through which PDT is harmful is by photosensitized oxidation of biomolecules. Protein and membrane damage is critical for optimizing the cytotoxic efficacy of PDT. Indeed, PSs that accumulate more readily in cell and/or organelle membranes are typically more cytotoxic [28]. PDT has proven successful in decreasing CSC proliferation and increasing membrane damage [7, 29−32], we had previously determined the effects of AlPcS4Cl – PDT and AlPcS4Cl – nanoPDT on lung CSC proliferation and cytotoxicity [7], we replicated these experiments in this study to evaluate the two methods of PDT, statistically demonstrating that nanoPDT improved the efficacy of PDT in causing anti-proliferative and metastatic abilities in lung CSCs.

The rate of cell proliferation is a measure of mitosis, and rapid cancer cell division indicates tumor progression and aggressiveness. Proliferation kinetics is frequently utilized for prognosis and can be used to measure the therapeutic effects of various treatment methods [33] such as PDT. Effective treatment of metastatic cancer frequently necessitates the treatment of both primary tumors and systemic disease undetectable at the time of diagnosis. PDT studies have shown to control primary and metastatic tumor growth and enhances anti-tumor immunity [34]. These outcomes are of importance when considering the abilities of CSCs to metastasize and cause tumor progression. Results indicate that nanoPDT can induce cell cycle arrest in CSCs, disrupting their proliferation and potentially leading to cell death. This arrest can be achieved by the following mechanisms, the PS photoactivation generating ROS causing cellular damage, where the ROS initiate a cascade of cellular responses, including DNA damage, lipid peroxidation, and protein oxidation, which can trigger signaling pathways involved in cell cycle regulation [35]. The damage inflicted by ROS activates cell cycle checkpoints, such as the DNA damage checkpoint and the G2/M checkpoint. These checkpoints serve as surveillance mechanisms that temporarily halt the cell cycle to allow time for DNA repair and prevent the transmission of damaged DNA to daughter cells [36]. One key regulator of cell cycle arrest is the tumor suppressor protein p53. Activated in response to DNA damage, p53 can upregulate the expression of p21, a cyclin-dependent kinase inhibitor. Elevated p21 levels inhibit cyclin-dependent kinase activity, specifically CDK2 and CDK4, which are essential for cell cycle progression [37]. The activation of cell cycle checkpoints and the induction of p21 can lead to G1 and G2 phase arrest, respectively. G1 arrest prevents damaged cells from entering the S phase, where DNA replication occurs. G2 arrest prevents cells from progressing to mitosis [38]. Depending on the extent of damage, arrested CSCs may either undergo cellular senescence (a state of irreversible growth arrest) or apoptosis (programmed cell death) [39]. These outcomes contribute to limiting the proliferation and survival of CSCs.

The results of this study indicate that PDT have the potential to inhibit tumor progression and dissemination by slowing CSC development, with greater effects observed when nanoPDT is used. The exact mechanism as to why PDT or nanoPDT affect CSCs differently than they do normal cells is unclear. However, the difference in how PDT affects CSCs and normal cells is primarily due to the unique properties and vulnerabilities of CSCs compared to normal cells. CSCs and normal cells may have different rates of photosensitizer uptake due to variations in their metabolic activities and expression of surface receptors. CSCs' distinct properties, such as altered signaling pathways and stem cell markers, can influence their ability to take up photosensitizing agents differently from normal cells. This differential uptake can lead to preferential accumulation of PSs within CSCs, making them more susceptible to PDT-induced damage [29]. CSCs and normal cells may have variations in DNA repair mechanisms and cellular survival pathways. PDT has the potential to target the self-renewal pathway of CSCs indirectly by inducing oxidative stress and cellular damage. While PDT itself does not directly target specific molecular pathways, its effects on cellular processes can disrupt the self-renewal capabilities of CSCs, which are often driven by specific signaling pathways [40]. PDT can trigger an immune response by inducing inflammation and cell death. Immune cells can recognize and target CSCs, further inhibiting their self-renewal capacity [41]. Cancer cells often have higher metabolic rates and more active cellular processes than normal cells. As a result, they may take up photosensitizing agents more readily [42]. Normal cells possess efficient DNA repair mechanisms [43] that may help them recover from DNA damage caused by PDT.

The *in vitro* results obtained indicate a difference in use of PDT versus nanoPDT for CSC destruction. This is of importance when considering *in vivo* and clinical application where the use of PDT can be enhanced by using nanoparticles. The drug delivery capabilities of the

system are highly precise, exhibiting a high level of accuracy. Additionally, the system demonstrates a proficient and effective reaction to visual stimuli, as well as a notable resistance to hypoxia. Additionally, the utilization of nano-photosensitizers (nano-PSs) has been explored to boost the effectiveness of photodynamic therapy (PDT) by increasing the production of ROS. Furthermore, the utilization of nano-sized polymer spheres (nano-PSs) in combination with additive or synergistic medicines has great importance in both ongoing preclinical research and potential future clinical applications. This is due to their capacity to enhance therapeutic efficacy to a significant extent while minimizing the risk associated with systemic drug administration [44]. Furthermore the use of AuNPs have been found to be biocompatible and comparatively less toxic [45], where AuNPs accumulate preferentially in organs like the liver, lung and spleen, where accumulation had been seen to be size dependent [46]. The reticuloendothelial system (RES) plays a key role in the excretion of gold nanoparticles. RES, composed of specialized cells in the liver and spleen, recognizes and engulfs foreign particles, including gold nanoparticles, from the bloodstream. Once engulfed, these nanoparticles become sequestered within RES cells [47]. Over time, the engulfed gold nanoparticles undergo processes such as degradation or transformation. Depending on the nanoparticle's properties, degradation products or transformed forms may be released from the RES cells into the bloodstream. Subsequently, these altered nanoparticles or degradation products can be eliminated from the body through routes like urine or feces. The RES-mediated excretion of gold nanoparticles is a crucial aspect of their pharmacokinetics and biocompatibility, impacting their potential use in biomedical applications [48]. This study showed that PDT directly affects lung CSC viability and proliferation [29], and so indirectly its metastatic abilities of migration and growth rate, where AuNPs significantly enhanced the PDT effects, similarly results indicated that PDT treatment effectivity was improved using nanomaterials [49, 50].

Future perspectives and limitations of this study include that the findings shed light on promising avenues for future research in cancer therapy, particularly in the context of targeting CSCs using PDT and its enhanced form with nanoparticles (nanoPDT). Further exploration is warranted to elucidate the exact mechanisms underlying the differential effects of PDT and nanoPDT on CSCs compared to normal cells. Understanding these mechanisms will be crucial for optimizing treatment strategies and enhancing therapeutic outcomes. Additionally, investigating the use of specific ligands or antibodies for active targeting of nanoparticles to CSCs could improve the selectivity and efficacy of nanoPDT. Moreover, the combination of nanoPDT with other stem cell-targeted therapies holds promise for synergistically inhibiting CSC proliferation and metastasis. However, it's essential to recognize that nanoPDT for targeting CSCs is still in its early stages of development, and further research, including preclinical and clinical trials, is necessary to validate its selectivity and therapeutic efficacy. Despite the promising findings, several limitations should be considered when interpreting the results of this study. Firstly, the research primarily relied on *in vitro* experiments, which may not fully recapitulate the complex tumor microenvironment and interactions between different cell types observed *in vivo*. Therefore, future studies should incorporate *in vivo* models to better assess the efficacy and safety of nanoPDT for targeting CSCs in a more physiologically relevant setting. Additionally, while the use of AuNPs as drug delivery vehicles shows potential advantages, such as biocompatibility and low toxicity, their pharmacokinetics and biodistribution need further investigation to ensure their safe and effective utilization in clinical applications. Moreover, the study focused on lung CSCs, and extrapolating these findings to other types of CSCs or cancers may require additional validation. Finally, while PDT and nanoPDT demonstrated promising results in inhibiting CSC proliferation and migration, their long-term effects on tumor recurrence and patient survival remain to be evaluated through rigorous clinical trials. Therefore, caution should be exercised when translating these findings into clinical practice until further evidence is gathered.

In conclusion, the primary goal of photodynamic treatment (PDT) is to selectively eliminate cancer cells while preserving healthy cells. The results of this study demonstrate that the application of PDT to normal lung cells led to some toxicity and reduced growth. However, these effects were less pronounced compared to the impact on cancer cells, which were completely eradicated. Importantly, normal lung cells maintained favorable morphological characteristics and exhibited high viability despite exposure to PDT. Considering the role of cancer stem cells (CSCs) in cancer recurrence and dissemination, it is crucial for cancer treatments to effectively target and suppress their abilities. The results of PDT and nanoPDT on the proliferation and migration of CSCs revealed significant reductions in cell migration, velocity, population doubling time, and cell cycle progression. Notably, nanoPDT demonstrated enhanced effects, suggesting a substantial inhibition of CSC mobility. However, before suggesting nanoPDT as a therapeutic treatment for cancer, the current findings must be verified utilizing pre-clinical animal and human clinical investigations.

Acknowledgments

The authors would like to acknowledge the University of Johannesburg and the Laser Research Centre for their facilities. This research was funded by the National Research Foundation of South Africa Thuthuka Instrument, grant number TTK2205035996; the Department of Science and Innovation (DSI) funded African Laser Centre (ALC), grant number HLHA23X task ALC-R007; the University Research Council, grant number 2022URC00513; the Department of Science and

Technology's South African Research Chairs Initiative (DST-NRF/SARChI), grant number 98337.

Disclosures

The authors declare that they have no conflict of interest.

References

1. Z.-J. Zhang, K.-P. Wang, J.-G. Mo, L. Xiong, and Y. Wen, "Photodynamic therapy regulates fate of cancer stem cells through reactive oxygen species," World Journal of Stem Cells 12(7), 562–584 (2020).
2. A. M. Itoo, M. Paul, S. G. Padaga, B. Ghosh, and S. Biswas, "Nanotherapeutic Intervention in Photodynamic Therapy for Cancer," ACS Omega 7(50), 45882–45909 (2022).
3. A. Z. Ayob, T. S. Ramasamy, "Cancer stem cells as key drivers of tumour progression," Journal of Biomedical Science 25(1), 20 (2018).
4. A. Crous, H. Abrahamse, "Photodynamic Therapy with an AlPcS4Cl Gold Nanoparticle Conjugate Decreases Lung Cancer's Metastatic Potential," Coatings 12(2), 199 (2022).
5. Targeted photodynamic therapy of metastatic melanoma cancer and cancer stem cells.
6. B. K. Najafabad, N. Attaran, M. Mahmoudi, and A. Sazgarnia, "Effect of photothermal and photodynamic therapy with cobalt ferrite superparamagnetic nanoparticles loaded with ICG and PpIX on cancer stem cells in MDA-MB-231 and A375 cell lines," Photodiagnosis and Photodynamic Therapy 43, 103648 (2023).
7. A. Crous, H. Abrahamse, "Effective Gold Nanoparticle-Antibody-Mediated Drug Delivery for Photodynamic Therapy of Lung Cancer Stem Cells," International Journal of Molecular Sciences 21(11), 3742 (2020).
8. U. Ziegler, P. Groscurth, "Morphological Features of Cell Death," Physiology 19(3), 124–128 (2004).
9. Z. Su, Z. Yang, Y. Xu, Y. Chen, and Q. Yu, "Apoptosis, autophagy, necroptosis, and cancer metastasis," Molecular Cancer 14(1), 48 (2015).
10. P. Gierlich, A. I. Mata, C. Donohoe, R. M. M. Brito, M. O. Senge, and L. C. Gomes-da-Silva, "Ligand-Targeted Delivery of Photosensitizers for Cancer Treatment," Molecules 25(22), 5317 (2020).
11. J. Sleeman, P. S. Steeg, "Cancer metastasis as a therapeutic target," European Journal of Cancer 46(7), 1177–1180 (2010).
12. B. Bao, A. Ahmad, A. S. Azmi, S. Ali, and F. H. Sarkar, "Overview of Cancer Stem Cells (CSCs) and Mechanisms of Their Regulation: Implications for Cancer Therapy," Current Protocols in Pharmacology 61(1), (2013).
13. U. Chitgupi, Y. Qin, and J. F. Lovell, "Targeted Nanomaterials for Phototherapy," Nanotheranostics 1(1), 38–58 (2017).
14. R. Bazak, M. Houri, S. El Achy, S. Kamel, and T. Refaat, "Cancer active targeting by nanoparticles: a comprehensive review of literature," Journal of Cancer Research and Clinical Oncology 141(5), 769–784 (2015).
15. J. Wu, "The Enhanced Permeability and Retention (EPR) Effect: The Significance of the Concept and Methods to Enhance Its Application," Journal of Personalized Medicine 11(8), 771 (2021).
16. C. Kruger, H. Abrahamse, "Utilisation of Targeted Nanoparticle Photosensitiser Drug Delivery Systems for the Enhancement of Photodynamic Therapy," Molecules 23(10), 2628 (2018).
17. A. Sohrabi Kashani, M. Packirisamy, "Cancer-Nano-Interaction: From Cellular Uptake to Mechanobiological Responses," International Journal of Molecular Sciences 22(17), 9587 (2021).
18. M. Majerník, R. Jendželovský, J. Vargová, Z. Jendželovská, and P. Fedoročko, "Multifunctional Nanoplatforms as a Novel Effective Approach in Photodynamic Therapy and Chemotherapy, to Overcome Multidrug Resistance in Cancer," Pharmaceutics 14(5), 1075 (2022).
19. S. A. Eccles, D. R. Welch, "Metastasis: recent discoveries and novel treatment strategies," The Lancet 369(9574), 1742–1757 (2007).
20. I. O. Lisnjak, V. V. Kutsenok, L. Z. Polyschuk, O. B. Gorobets, and N. F. Gamaleia, "Effect of photodynamic therapy on tumor angiogenesis and metastasis in mice bearing Lewis lung carcinoma," Experimental Oncology 27(4), 333−335 (2005).
21. M. R. K. Ali, Y. Wu, D. Ghosh, B. H. Do, K. Chen, M. R. Dawson, N. Fang, T. A. Sulchek, and M. A. El-Sayed, "Nuclear Membrane-Targeted Gold Nanoparticles Inhibit Cancer Cell Migration and Invasion," ACS Nano 11(4), 3716–3726 (2017).
22. S. P. M. Crouch, R. Kozlowski, K. J. Slater, and J. Fletcher, "The use of ATP bioluminescence as a measure of cell proliferation and cytotoxicity," Journal of Immunological Methods 160(1), 81–88 (1993).
23. K. Vanhove, G.-J. Graulus, L. Mesotten, M. Thomeer, E. Derveaux, J.-P. Noben, W. Guedens, and P. Adriaensens, "The Metabolic Landscape of Lung Cancer: New Insights in a Disturbed Glucose Metabolism," Frontiers in Oncology 9, 1215 (2019).
24. S. Ye, H.-B. Zhou, Y. Chen, K.-Q. Li, S.-S. Jiang, and K. Hao, "Crizotinib changes the metabolic pattern and inhibits ATP production in A549 non-small cell lung cancer cells," Oncology Letters 21(1), 61 (2020).

25. Y. Zhou, F. Tozzi, J. Chen, F. Fan, L. Xia, J. Wang, G. Gao, A. Zhang, X. Xia, H. Brasher, W. Widger, L. M. Ellis, and Z. Weihua, "Intracellular ATP Levels Are a Pivotal Determinant of Chemoresistance in Colon Cancer Cells," Cancer Research 72(1), 304–314 (2012).
26. P. Kumar, A. Nagarajan, and P. D. Uchil, "Analysis of Cell Viability by the Lactate Dehydrogenase Assay," Cold Spring Harbor Protocols 2018(6), pdb.prot095497 (2018).
27. F. Bouvet, M. Ros, E. Bonedeau, C. Croissant, L. Frelin, F. Saltel, V. Moreau, and A. Bouter, "Defective membrane repair machinery impairs survival of invasive cancer cells," Scientific Reports 10(1), 21821 (2020).
28. A. F. Dos Santos, D. R. Q. De Almeida, L. F. Terra, M. S. Baptista, and L. Labriola, "Photodynamic therapy in cancer treatment - an update review," Journal of Cancer Metastasis and Treatment 2019, (2019).
29. E. P. Chizenga, R. Chandran, and H. Abrahamse, "Photodynamic therapy of cervical cancer by eradication of cervical cancer cells and cervical cancer stem cells," Oncotarget 10(43), 4380–4396 (2019).
30. P. Sundaram, H. Abrahamse, "Effective Photodynamic Therapy for Colon Cancer Cells Using Chlorin e6 Coated Hyaluronic Acid-Based Carbon Nanotubes," International Journal of Molecular Sciences 21(13), 4745 (2020).
31. J. Giraud, S. Molina-Castro, L. Seeneevassen, E. Sifré, J. Izotte, C. Tiffon, C. Staedel, H. Boeuf, S. Fernandez, P. Barthelemy, F. Megraud, P. Lehours, P. Dubus, and C. Varon, "Verteporfin targeting YAP1/TAZ-TEAD transcriptional activity inhibits the tumorigenic properties of gastric cancer stem cells," International Journal of Cancer 146(8), 2255–2267 (2020).
32. Y. Peng, G. He, D. Tang, L. Xiong, Y. Wen, X. Miao, Z. Hong, H. Yao, C. Chen, S. Yan, L. Lu, Y. Yang, Q. Li, and X. Deng, "Lovastatin Inhibits Cancer Stem Cells and Sensitizes to Chemo- and Photodynamic Therapy in Nasopharyngeal Carcinoma," Journal of Cancer 8(9), 1655–1664 (2017).
33. E. Mehrara, E. Forssell-Aronsson, H. Ahlman, and P. Bernhardt, "Specific Growth Rate versus Doubling Time for Quantitative Characterization of Tumor Growth Rate," Cancer Research 67(8), 3970–3975 (2007).
34. M. Shams, B. Owczarczak, P. Manderscheid-Kern, D. A. Bellnier, and S. O. Gollnick, "Development of photodynamic therapy regimens that control primary tumor growth and inhibit secondary disease," Cancer Immunology, Immunotherapy 64(3), 287–297 (2015).
35. M. Schieber, N. S. Chandel, "ROS Function in Redox Signaling and Oxidative Stress," Current Biology 24(10), R453–R462 (2014).
36. R.-X. Huang and P.-K. Zhou, "DNA damage response signaling pathways and targets for radiotherapy sensitization in cancer," Signal Transduction and Targeted Therapy 5(1), 60 (2020).
37. T. Ozaki, A. Nakagawara, "Role of p53 in Cell Death and Human Cancers," Cancers 3(1), 994–1013 (2011).
38. L. A. Hoeferlin, N. V. Oleinik, N. I. Krupenko, and S. A. Krupenko, "Activation of p21-Dependent G1/G2 Arrest in the Absence of DNA Damage as an Antiapoptotic Response to Metabolic Stress," Genes & Cancer 2(9), 889–899 (2011).
39. K. Santos-de-Frutos, N. Djouder, "When dormancy fuels tumour relapse," Communications Biology 4(1), 747 (2021).
40. S. Keyvani-Ghamsari, K. Khorsandi, A. Rasul, and M. K. Zaman, "Current understanding of epigenetics mechanism as a novel target in reducing cancer stem cells resistance," Clinical Epigenetics 13(1), 120 (2021).
41. A. Crous, H. Abrahamse, "Photodynamic therapy of lung cancer, where are we?," Frontiers in Pharmacology 13, 932098 (2022).
42. N. Shirasu, S.O. Nam, and M. Kuroki, "Tumor-targeted Photodynamic Therapy," Anticancer Research 33(7), 2823-2831 (2013).
43. G. Cooper, K. Adams, The cell: a molecular approach, 9th ed., Oxford University Press, New York (2023). ISBN: 9780197583913.
44. L. Lin, X. Song, X. Dong, and B. Li, "Nano-photosensitizers for enhanced photodynamic therapy," Photodiagnosis and Photodynamic Therapy 36, 102597 (2021).
45. E. E. Connor, J. Mwamuka, A. Gole, C. J. Murphy, and M. D. Wyatt, "Gold Nanoparticles Are Taken Up by Human Cells but Do Not Cause Acute Cytotoxicity," Small 1(3), 325–327 (2005).
46. G. Sonavane, K. Tomoda, and K. Makino, "Biodistribution of colloidal gold nanoparticles after intravenous administration: Effect of particle size," Colloids and Surfaces B: Biointerfaces 66(2), 274–280 (2008).
47. M. Zhang, S. Gao, D. Yang, Y. Fang, X. Lin, X. Jin, Y. Liu, X. Liu, K. Su, and K. Shi, "Influencing factors and strategies of enhancing nanoparticles into tumors in vivo," Acta Pharmaceutica Sinica B 11(8), 2265–2285 (2021).
48. Q. Gao, J. Zhang, J. Gao, Z. Zhang, H. Zhu, and D. Wang, "Gold Nanoparticles in Cancer Theranostics," Frontiers in Bioengineering and Biotechnology 9, 647905 (2021).
49. S. M. Muramulla, L. S. Chethan, S. S. Kumar, D. Gangodkar, and A. R. Prasad, "PDT treatment techniques using nano-composite material," Materials Today: Proceedings 66, 1211–1215 (2022).
50. D. Zhu, F. Liu, L. Ma, D. Liu, and Z. Wang, "Nanoparticle-Based Systems for T1-Weighted Magnetic Resonance Imaging Contrast Agents," International Journal of Molecular Sciences 14(5), 10591–10607 (2013).

Possibility of Measuring of Erythrocyte Size Distribution Parameters by Laser Diffractometry of a Blood Smear

Sergey Yu. Nikitin, Evgeniy G. Tsybrov*, Maria S. Lebedeva, Andrei E. Lugovtsov, and Alexander V. Priezzhev

M. V. Lomonosov Moscow State University, GSP-1 Leninskie Gory, Moscow 119991, Russian Federation

*e-mail: tsybrovevgeniy@yandex.ru

Abstract. We consider the issues of obtaining information about the distribution of red blood cells in size from the scattering pattern of a laser beam on a wet blood smear. Within this article it is assumed to calculate the first three moments of the size distribution. The analytical model of light diffraction by blood smears was developed, as well as numerical experiments for verification suggested approach were carried out. The possibility of calculating average diameter of erythrocyte, width and asymmetry of size distribution by analyzing the angular distribution of light intensity in the diffraction pattern was shown. © 2024 Journal of Biomedical Photonics & Engineering.

Keywords: light scattering; laser diffractometry; data processing algorithms; red blood cells; size distribution; asymmetry.

Paper #9103 received 28 Apr 2024; revised manuscript received 20 May 2024; accepted for publication 20 May 2024; published online 29 Aug 2024. doi: 10.18287/JBPE24.10.040302.

1 Introduction

In the human circulatory system, the microrheological properties of blood play an important role. The main microrheological parameters include the deformability and aggregation ability of erythrocytes [1]. The size distribution of red blood cells also affects the rheology of blood [2]. The importance of this distribution is evidenced, in particular, by the fact that the width of the erythrocyte size distribution is a reliable predictor of mortality in the general population of adults aged 45 years and older [3]. Typically, red blood cell size distribution is measured using a Coulter counter or flow cytometer [4–6]. Other measurement methods are also being developed, such as digital microscopy [7], hyperspectral holography [8], and laser diffractometry [9–14]. The advantage of the laser diffractometry method is that this method allows one to quickly process large ensembles of red blood cells without requiring complex equipment such as microscopes, microchannels, high-speed electronic circuits, etc.

The laser diffractometry method is based on the effect of scattering of a laser beam on a blood smear or a thin layer of red blood cell suspension. With such scattering, a pattern appears that resembles the pattern of light diffraction by a round aperture (the so-called Airy pattern). The picture has axial symmetry. In its center there is a bright spot, the brightness of which decreases as the scattering angle increases. As a rule, this spot is surrounded by a dark ring, behind which a faint light ring is visible. The task of laser diffractometry is to determine the parameters of an ensemble of red blood cells based on measurements of the characteristics of the diffraction pattern. Note that the quality of the diffraction pattern strongly depends on the method of preparing the blood smear and its quality. For more details on this, see Ref. [15].

Some theoretical aspects of laser diffractometry of erythrocytes were considered in Refs. [16–20]. It is known that the angular size of the first dark ring in the diffraction pattern determines the average size of the red blood cells on the blood smear. The visibility of this ring determines the size distribution width of red blood cells. In this work, we identify the parameters of the diffraction pattern that determine the asymmetry of the size distribution of erythrocytes.

2 Characteristics of the Diffraction Pattern

Fig. 1 shows an example of a diffraction pattern that occurs when a laser beam is scattered on a blood smear, and the angular distribution of light intensity in this pattern $I = I(\theta)$. Normalizing this distribution to the

intensity of the central diffraction maximum $I(0)$, we obtain the function

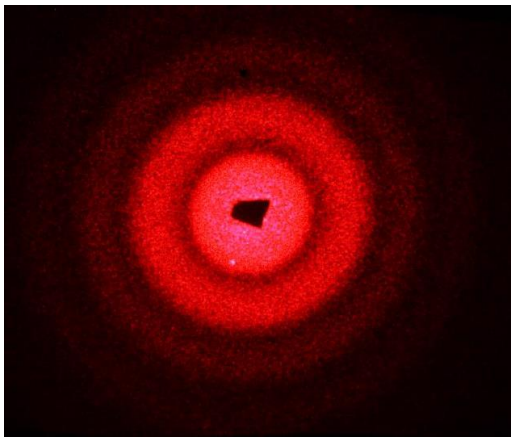
$$f(\theta) = \frac{I(\theta)}{I(0)}.$$

Let us consider a fragment of the diffraction pattern lying near the first minimum of light intensity (the first dark ring). In this region, the function $f(\theta)$ can be approximately represented as

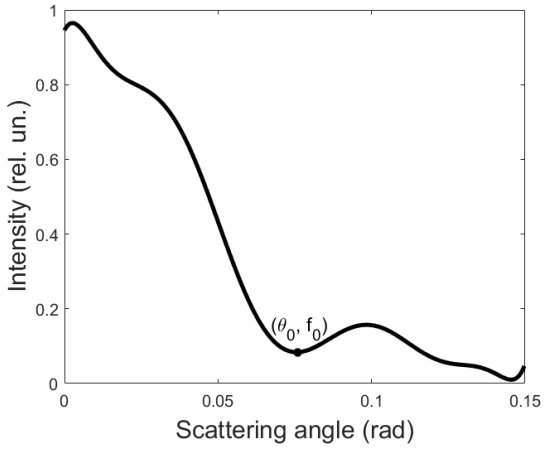
$$f(\theta) = f(\theta_0) + \frac{1}{2} f''(\theta_0) \cdot (\theta - \theta_0)^2. \quad (1)$$

Here θ_0 is the angular coordinate of the first minimum of light intensity in the diffraction pattern, determined by the condition

$$f'(\theta_0) = 0, \quad (2)$$



(a)



(b)

Fig. 1 (a) Diffraction pattern obtained from a wet blood smear and (b) the angular distribution of light intensity in this pattern. Laser wavelength λ = 650 nm.

where $f''(\theta_0)$ is the second derivative of the function f(θ) with respect to the scattering angle, taken at $\theta = \theta_0$. Let us introduce the dimensionless parameter

$$f_2 = f''(\theta_0) \cdot \theta_0^2 \quad (3)$$

and denote

$$f(\theta_0) = f_0. \quad (4)$$

The parameters θ_0 and f_0 are shown in the graph of the function $f(\theta)$ in Fig. 1b. These parameters, as well as the f_2 parameter, can be measured in an experiment on scattering of a laser beam on a blood smear.

3 Parameters of the Erythrocyte Ensemble

We will consider the red blood cells on a blood smear to be round discs and characterize them with radii R. The applicability of this model is justified by the fact that in the region of the diffraction pattern of interest to us, the indicatrix of light scattering by a biconcave disk and a flat disk differ negligibly little from each other [18]. Taking into account the scatter of red blood cells in size, we will consider the radius of the red blood cell to be a random variable and describe it with the following Eq.:

$$R = R_0 \cdot (1 + \varepsilon). \quad (5)$$

Here R_0 is the average radius of red blood cells on a blood smear, ε is a random parameter, the average value of which is considered equal to zero

$$\langle \varepsilon \rangle = 0. \quad (6)$$

The size distribution of red blood cells will be characterized by the parameters

$$\mu = \langle \varepsilon^2 \rangle \quad (7)$$

and

$$\nu = \langle \varepsilon^3 \rangle. \quad (8)$$

The μ value characterizes the width, and the ν value characterizes the asymmetry of the size distribution of erythrocytes. When calculating diffraction patterns, we will use the approximation of a weakly inhomogeneous ensemble of red blood cells. Mathematically, this approximation is expressed by the Eq.:

$$|\varepsilon| \ll 1. \quad (9)$$

For convenience, we also introduce the parameters

$$\mu' = \sqrt{\mu} \quad (10)$$

and

$$\nu' = \sqrt[3]{\nu}. \quad (11)$$

Our task is to express the parameters of erythrocytes R_0, μ, ν through the characteristics of the diffraction

pattern θ_0, f_0, f_2 and to construct an algorithm for measuring the average radius of an erythrocyte, as well as the width and asymmetry of the size distribution of erythrocytes using laser diffractometry of a blood smear.

4 Diffractometric Equations

Following the works [16, 17], we will model red blood cells as transparent flat disks. The angular distribution of light intensity in the diffraction pattern arising when a laser beam is scattered on a blood smear is approximately described by the following Eq.:

$$I(\theta) = \frac{1}{4} I_0 N |\alpha|^2 \left(\frac{k}{z}\right)^2 \langle R^4 G(kR\theta)\rangle. \quad (12)$$

Here I is the light intensity at a given point of the observation screen, R is the radius of a red blood cell, θ is the scattering angle, I_0 is the intensity of the incident laser beam, N is the number of red blood cells on the blood smear illuminated by the laser, z is the distance from the blood smear to the observation screen, $k = 2\pi/\lambda$ is the wave number, λ is the light wavelength, the parameter $|\alpha|^2$ characterizes the thickness and optical density of the red blood cell, angle brackets indicate averaging over the size of the red blood cells. The function G, called the Airy function, is defined by the Eq.:

$$G(x) = \left[\frac{2J_1(x)}{x}\right]^2, \quad (13)$$

where $J_1(x)$ is the first order Bessel function. The Airy function satisfies the condition $G(0) = 1$. Eq. (12) was obtained in the single scattering approximation and describes the distribution of light intensity in the far diffraction zone in that part of the observation screen where the radiation of the direct laser beam does not impinge. Let us represent the normalized distribution of light intensity in the diffraction pattern $f(\theta)$ in the form

$$\langle \rho^4 \rangle f(\theta) = \langle \rho^4 G(\rho\theta)\rangle. \quad (14)$$

Here

$$\rho = kR = 2\pi \frac{R}{\lambda} \quad (15)$$

is red blood cell size parameter.

Let us consider a limited part of the diffraction pattern located near the first minimum of light intensity. Mathematically, this region is determined by the condition $\rho\theta \approx x_0$, where the value x_0 is determined by the equation

$$J_1(x_0) = 0.$$

Here

$$x_0 = 3.8318. \quad (16)$$

Expanding the Bessel function into a Taylor series in the vicinity of the point x_0, we obtain

$$J_1(x) = J_1'(x_0) \cdot (x - x_0) + \frac{1}{2} J_1''(x_0) \cdot (x - x_0)^2 + \\ + \frac{1}{6} J_1'''(x_0) \cdot (x - x_0)^3.$$

In the region $0.5 \le x/x_0 \le 1.3$ the error of this approximation does not exceed 3%. The derivatives of the Bessel function included in this expression can be calculated using the Eqs. [21]:

$$J_0'(x) = -J_1(x), \\ J_1'(x) = J_0(x) - \frac{1}{x} J_1(x). \quad (17)$$

In this approximation, for the function $f(\theta)$ we obtain the expression

$$\langle \rho^4 \rangle f = \langle \rho^4 H(y)\rangle, \quad (18)$$

where

$$y = \frac{\rho\theta}{x_0} \quad (19)$$

is the normalized scattering angle. The function $H(y)$ is defined by the following Eq.:

$$H(y) = \frac{1}{x_0^2}\left[\frac{2\psi(y)}{y}\right]^2,$$

where

$$\psi(y) = x_0 J_1'(x_0) \cdot (y - 1) + \frac{1}{2} x_0^2 J_1''(x_0) \cdot \\ \cdot (y - 1)^2 + \frac{1}{6} x_0^3 J_1'''(x_0) \cdot (y - 1)^3.$$

Using Eqs. (17), we obtain

$$J_1''(x) = -\frac{1}{x} J_0(x) + \left(-1 + \frac{2}{x^2}\right) J_1(x), \\ J_1'''(x) = \left(-1 + \frac{3}{x^2}\right)\left[J_0(x) - \frac{2}{x} J_1(x)\right].$$

Here $J_0(x)$ is the zeroth order Bessel function. In particular, for $x = x_0$

$$J_1'(x_0) = J_0(x_0), \\ J_1''(x_0) = -\frac{1}{x_0} J_0(x_0), \\ J_1'''(x_0) = \left(-1 + \frac{3}{x_0^2}\right) J_0(x_0),$$

Let us denote

$$J_0(x_0) = -\beta. \quad (20)$$

Here

$$\beta = 0.40276. \tag{21}$$

Then

$$J_1'(x_0) = -\beta,$$
$$J_1''(x_0) = \frac{1}{x_0}\beta,$$
$$J_1'''(x_0) = \left(1 - \frac{3}{x_0^2}\right)\beta.$$

The functions $\psi(y)$ and $H(y)$ take the form

$$\psi(y) = ay^3 - by^2 + cy - d$$

and

$$H(y) = c_1y^4 - c_2y^3 + c_3y^2 - c_4y + \\ +c_5 - \frac{c_6}{y} + \frac{c_7}{y^2}, \tag{22}$$

where

$$a = \frac{\beta x_0}{6}(x_0^2 - 3),$$
$$b = \frac{\beta x_0}{6}3(x_0^2 - 4),$$
$$c = \frac{\beta x_0}{6}3(x_0^2 - 7), \tag{23}$$
$$d = \frac{\beta x_0}{6}(x_0^2 - 12)$$

and

$$a^2\frac{4}{x_0^2} = c_1,$$
$$ab\frac{8}{x_0^2} = c_2,$$
$$(2ac + b^2)\frac{4}{x_0^2} = c_3,$$
$$(ad + bc)\frac{8}{x_0^2} = c_4, \tag{24}$$
$$(c^2 + 2bd)\frac{4}{x_0^2} = c_5,$$
$$cd\frac{8}{x_0^2} = c_6,$$
$$d^2\frac{4}{x_0^2} = c_7.$$

Thus, the normalized angular distribution of light intensity in the diffraction pattern is represented as a polynomial relative to the normalized scattering angle. This distribution is expressed by Eqs. (18), (19), (22).

Derivatives of the function $f(\theta)$

$$f^{(n)}(\theta) = \frac{d^n}{d\theta^n}f(\theta)$$

are expressed by the following Eqs.:

$$\langle\rho^4\rangle x_0 f^{(1)}(\theta) = \langle\rho^5 H^{(1)}(y)\rangle,$$
$$\langle\rho^4\rangle x_0^2 f^{(2)}(\theta) = \langle\rho^6 H^{(2)}(y)\rangle$$

where

$$H^{(1)}(y) = \frac{dH}{dy} = 4c_1y^3 - 3c_2y^2 + 2c_3y - c_4 + \frac{c_6}{y^2} - 2\frac{c_7}{y^3},$$
$$H^{(2)}(y) = \frac{d^2H}{dy^2} = 12c_1y^2 - 6c_2y + 2c_3 - 2\frac{c_6}{y^3} + 6\frac{c_7}{y^4}.$$

The functions $f^{(n)}(\theta)$ are also polynomials with respect to the normalized scattering angle.

Let us find the angular coordinate θ_0 of the minimum light intensity in the diffraction pattern. Assuming

$$f^{(1)}(\theta_0) = 0$$

we get the Eq.:

$$\langle\rho^5 H^{(1)}(y_0)\rangle = 0,$$

where

$$y_0 = \rho\frac{\theta_0}{x_0}.$$

From here

$$\langle\rho^5\left(4c_1y_0^3 - 3c_2y_0^2 + 2c_3y_0 - c_4 + \frac{c_6}{y_0^2} - 2\frac{c_7}{y_0^3}\right)\rangle = 0$$

or

$$4c_1\langle\rho^5y_0^3\rangle - 3c_2\langle\rho^5y_0^2\rangle + 2c_3\langle\rho^5y_0\rangle - c_4\langle\rho^5\rangle + \\ +c_6\langle\frac{\rho^5}{y_0^2}\rangle - 2c_7\langle\frac{\rho^5}{y_0^3}\rangle = 0.$$

Here

$$\langle\rho^5y_0^3\rangle = \frac{\theta_0^3}{x_0^3}\langle\rho^8\rangle,$$
$$\langle\rho^5y_0^2\rangle = \frac{\theta_0^2}{x_0^2}\langle\rho^7\rangle,$$
$$\langle\rho^5y_0\rangle = \frac{\theta_0}{x_0}\langle\rho^6\rangle,$$
$$\langle\frac{\rho^5}{y_0^2}\rangle = \frac{x_0^2}{\theta_0^2}\langle\rho^3\rangle,$$
$$\langle\frac{\rho^5}{y_0^3}\rangle = \frac{x_0^3}{\theta_0^3}\langle\rho^2\rangle.$$

Now

$$4c_1\frac{\theta_0^3}{x_0^3}\langle\rho^8\rangle - 3c_2\frac{\theta_0^2}{x_0^2}\langle\rho^7\rangle + 2c_3\frac{\theta_0}{x_0}\langle\rho^6\rangle - c_4\langle\rho^5\rangle + \\ +c_6\frac{x_0^2}{\theta_0^2}\langle\rho^3\rangle - 2c_7\frac{x_0^3}{\theta_0^3}\langle\rho^2\rangle = 0.$$

Let us consider a weakly inhomogeneous ensemble of erythrocytes. From Eqs. (9) and (15) it follows that

$$\rho = \rho_0 \cdot (1 + \varepsilon),$$

where

$$\langle \rho \rangle = \rho_0$$

is the average size of a red blood cell on a blood smear. Let us enter the parameters

$$m_n = \frac{\langle \rho^n \rangle}{\rho_0^n} = \langle (1 + \varepsilon)^n \rangle.$$

Then

$$\langle \rho^n \rangle = m_n \rho_0^n$$

and the equation for the angle θ_0 takes the form

$$4c_1 \frac{\theta_0^3}{x_0^3} m_8 \rho_0^8 - 3c_2 \frac{\theta_0^2}{x_0^2} m_7 \rho_0^7 + 2c_3 \frac{\theta_0}{x_0} m_6 \rho_0^6 - \\ -c_4 m_5 \rho_0^5 + c_6 \frac{x_0^2}{\theta_0^2} m_3 \rho_0^3 - 2c_7 \frac{x_0^3}{\theta_0^3} m_2 \rho_0^2 = 0$$

or

$$4c_1 \frac{\theta_0^3}{x_0^3} m_8 \rho_0^3 - 3c_2 \frac{\theta_0^2}{x_0^2} m_7 \rho_0^2 + 2c_3 \frac{\theta_0}{x_0} m_6 \rho_0 - \\ -c_4 m_5 + c_6 \frac{x_0^2}{\theta_0^2 \rho_0^2} m_3 - 2c_7 \frac{x_0^3}{\theta_0^3 \rho_0^3} m_2 = 0.$$

Let us denote

$$z = \frac{\theta_0}{x_0} \rho_0.$$

Then

$$4c_1 m_8 z^3 - 3c_2 m_7 z^2 + 2c_3 m_6 z - c_4 m_5 + \\ + c_6 m_3 \frac{1}{z^2} - 2c_7 m_2 \frac{1}{z^3} = 0$$

or

$$4c_1 m_8 z^6 - 3c_2 m_7 z^5 + 2c_3 m_6 z^4 - \\ -c_4 m_5 z^3 + c_6 m_3 z - 2c_7 m_2 = 0. \qquad (25)$$

Proceeding in the same way as when deriving Eq. (25), we obtain two more Eqs.:

$$m_4 z^2 f_0 = c_1 m_8 z^6 - c_2 m_7 z^5 + c_3 m_6 z^4 - \\ -c_4 m_5 z^3 + c_5 m_4 z^2 - c_6 m_3 z + c_7 m_2,$$

$$m_4 z^2 f_2 = 12c_1 m_8 z^6 - 6c_2 m_7 z^5 + \\ +2c_3 m_6 z^4 - 2c_6 m_3 z + 6c_7 m_2. \qquad (26)$$

Here the parameters f_0 and f_2 are determined by Eqs. (3), (4). For a weakly inhomogeneous ensemble of erythrocytes, the parameters m_n are related to the values of μ and ν by the relations

$$m_2 = 1 + \mu, \qquad (27)$$

$$m_3 = 1 + 3\mu + \nu,$$
$$m_4 = 1 + 6\mu + 4\nu,$$
$$m_5 = 1 + 10\mu + 10\nu,$$
$$m_6 = 1 + 15\mu + 20\nu,$$
$$m_7 = 1 + 21\mu + 35\nu,$$
$$m_8 = 1 + 28\mu + 56\nu.$$

From Eqs. (23), (24) it follows that there are certain relationships between the coefficients of Eqs. (25), (26). These relations are expressed by the following Eqs.:

$$4c_1 - 3c_2 + 2c_3 - c_4 + c_6 - 2c_7 = 0,$$
$$c_1 - c_2 + c_3 - c_4 + c_5 - c_6 + c_7 = 0, \qquad (28)$$
$$12c_1 - 6c_2 + 2c_3 - 2c_6 + 6c_7 = 8\beta^2.$$

For a weakly inhomogeneous ensemble of erythrocytes, we will look for a solution to Eqs. (25), (26) in the form

$$z = 1 + \alpha, \qquad (29)$$

where

$$|\alpha| \ll 1$$

is a small parameter. Then, in an approximation linear in this parameter

$$z^n = 1 + n\alpha. \qquad (30)$$

Let us introduce the values M_n, defining them by the Eqs.:

$$m_n = 1 + M_n. \qquad (31)$$

From Eq. (27) it follows that

$$|M_n| \ll 1,$$

$$M_2 = \mu, \qquad M_3 = 3\mu + \nu,$$
$$M_4 = 6\mu + 4\nu, \qquad M_5 = 10\mu + 10\nu,$$
$$M_6 = 15\mu + 20\nu, \qquad M_7 = 21\mu + 35\nu, \qquad (32)$$
$$M_8 = 28\mu + 56\nu.$$

Substituting Eqs. (30), (31) into Eqs. (25), (26) and taking into account Eqs. (28), (32), we obtain the following Eqs.:

$$c_{1\alpha}\alpha + c_{1\mu}\mu + c_{1\nu}\nu = 0,$$
$$(1 + 6\mu + 4\nu + 2\alpha) f_0 = c_{2\alpha}\alpha + c_{2\mu}\mu + c_{2\nu}\nu, \qquad (33)$$
$$(1 + 6\mu + 4\nu + 2\alpha) f_2 = 8\beta^2 + c_{3\alpha}\alpha + c_{3\mu}\mu + c_{3\nu}\nu.$$

Here

$$\alpha = \frac{\theta_0}{x_0}\rho_0 - 1. \quad (34)$$

The numbers x_0 and β are defined by Eqs. (16) and (21). The remaining coefficients are determined by the following Eqs.

$$\begin{aligned} c_{1\alpha} &= 24c_1 - 15c_2 + 8c_3 - 3c_4 + c_6, \\ c_{1\mu} &= 112c_1 - 63c_2 + 30c_3 - 10c_4 + 3c_6 - 2c_7, \\ c_{1\nu} &= 224c_1 - 105c_2 + 40c_3 - 10c_4 + c_6, \end{aligned} \quad (35)$$

$$\begin{aligned} c_{2\alpha} &= 6c_1 - 5c_2 + 4c_3 - 3c_4 + 2c_5 - c_6, \\ c_{2\mu} &= 28c_1 - 21c_2 + 15c_3 - 10c_4 + 6c_5 - 3c_6 + c_7, \\ c_{2\nu} &= 56c_1 - 35c_2 + 20c_3 - 10c_4 + 4c_5 - c_6, \end{aligned} \quad (36)$$

$$\begin{aligned} c_{3\alpha} &= 72c_1 - 30c_2 + 8c_3 - 2c_6, \\ c_{3\mu} &= 336c_1 - 126c_2 + 30c_3 - 6c_6 + 6c_7, \\ c_{3\nu} &= 672c_1 - 210c_2 + 40c_3 - 2c_6. \end{aligned} \quad (37)$$

From Eqs. (23), (24), (35) – (37) it follows that

$$\begin{aligned} &c_{1\alpha} = 8\beta^2, \qquad c_{1\mu} = 4\beta^2, \\ &c_{1\nu} = -\frac{16}{3}\beta^2 x_0^2, \\ &c_{2\alpha} = 0, \qquad c_{2\mu} = 4\beta^2, \\ &c_{2\nu} = 4\beta^2, \\ &c_{3\alpha} = -40\beta^2, \qquad c_{3\mu} = -4(4x_0^2 + 3)\beta^2, \\ &c_{3\nu} = -\frac{8}{3}(11x_0^2 - 30)\beta^2. \end{aligned} \quad (38)$$

Substituting Eq. (38) into Eq. (33), we obtain the following Eqs.:

$$8\beta^2\alpha + 4\beta^2\mu - \frac{16}{3}\beta^2 x_0^2\nu = 0,$$

$$(1 + 6\mu + 4\nu + 2\alpha)f_0 = 4\beta^2\mu + 4\beta^2\nu,$$

$$\begin{aligned} &(1 + 6\mu + 4\nu + 2\alpha)f_2 = \\ &= 8\beta^2 - 40\beta^2\alpha - 4(4x_0^2 + 3)\beta^2\mu - \frac{8}{3}(11x_0^2 - 30)\beta^2\nu \end{aligned}$$

or

$$2\alpha + \mu - \frac{4}{3}x_0^2\nu = 0, \quad (39)$$

$$\frac{1}{4\beta^2}(1 + 6\mu + 4\nu + 2\alpha)f_0 = \mu + \nu, \quad (40)$$

$$\begin{aligned} &\frac{1}{8\beta^2}(1 + 6\mu + 4\nu + 2\alpha)f_2 = \\ &= 1 - 5\alpha - \left(2x_0^2 + \frac{3}{2}\right)\mu - \frac{1}{3}(11x_0^2 - 30)\nu. \end{aligned} \quad (41)$$

From Eq. (39) it follows that

$$\alpha = -\frac{\mu}{2} + \frac{2}{3}x_0^2\nu. \quad (42)$$

Substituting Eq. (42) into Eqs. (40), (41), we obtain

$$\begin{aligned} &\frac{1}{4\beta^2}\left[1 + 5\mu + 4\nu\left(1 + \frac{x_0^2}{3}\right)\right]f_0 = \mu + \nu, \\ &\frac{1}{8\beta^2}\left[1 + 5\mu + 4\nu\left(1 + \frac{x_0^2}{3}\right)\right]f_2 = \\ &= 1 - (2x_0^2 - 1)\mu - (7x_0^2 - 10)\nu. \end{aligned} \quad (43)$$

Eqs. (42) and (43) solve the problem. They relate the characteristics of the diffraction pattern θ_0, f_0, f_2 with the parameters of the ensemble of erythrocytes ρ_0, μ, ν. The solution to these equations taking into account Eqs. (16), (21) has the form

$$\mu = \frac{-1.2977 + 233f_0 + f_2}{83.7 + 410f_0 + 18.6f_2}, \quad \nu = \frac{1.2977 - 66.7f_0 - f_2}{83.7 + 410f_0 + 18.6f_2}. \quad (44)$$

5 Measurement Algorithm

The algorithm for measuring parameters μ', ν', ρ_0 is expressed by the Eqs.:

$$\mu' = \sqrt{\frac{-1.2977 + 233f_0 + f_2}{83.7 + 410f_0 + 18.6f_2}}, \quad (45)$$

$$\nu' = \sqrt[3]{\frac{1.2977 - 66.7f_0 - f_2}{83.7 + 410f_0 + 18.6f_2}}, \quad (46)$$

$$\rho_0 = (1 - 0.5\mu + 9.79\nu)\frac{3.83}{\theta_0}. \quad (47)$$

The average diameter of a red blood cell on a blood smear can be found using the following Eq.:

$$D = 1.22\frac{\lambda}{\theta_0} \cdot (1 - 0.5\mu + 9.79\nu). \quad (48)$$

In these Eqs., ρ_0, μ', ν' are the parameters of the size distribution of red blood cells, θ_0, f_0, f_2 are the characteristics of the diffraction pattern that occurs when the laser beam is scattered on a blood smear, λ is the laser wavelength. Namely, ρ_0 is the average size parameter of the erythrocyte, μ' is the relative width of the distribution of erythrocytes along the radii, ν' is the asymmetry coefficient of the distribution of erythrocytes along the radii, θ_0 is the scattering angle at which the first minimum light intensity in the diffraction pattern is achieved, f_0 – relative light intensity in the first minimum, f_2 – relative curvature of the angular distribution of light intensity at the first minimum intensity. The parameters $\lambda, \theta_0, f_0, f_2$ can be measured in an experiment by scattering a laser beam on a blood smear. The indicated values are mathematically determined by Eqs. (1) – (11).

On the stability of the algorithm. Estimates show that for the conditions of interest to us, the denominators of

Eqs. (44) weakly depend on the parameters f_0 and f_2, which are the input data for the algorithm. If we neglect this dependence, then the parameters μ and ν become linear functions of the parameters f_0 and f_2. This means that the relative error in measuring the parameters μ and ν is the same as the relative error in measuring the diffraction pattern parameters f_0 and f_2. Further, by virtue of Eqs. (44) – (46), the relative error in measuring the parameter μ' is two times, and the parameter ν' is three times less than the relative error in measuring the parameters μ and ν. On this basis, we conclude that the measurement algorithm expressed by Eqs. (45), (46) is stable.

6 Verification of the Algorithm in a Numerical Experiment

Let us evaluate the accuracy of the algorithm using a model of a bimodal ensemble of red blood cells. This ensemble contains red blood cells of only two sizes. Let ρ_1 be the size parameter of the first component of the ensemble, ρ_2 be the size parameter of the second component of the ensemble, p be the fraction of particles of the first type. The parameters of the bimodal ensemble are found using the following Eqs.:

$$\begin{aligned}
&\rho_0 = \langle\rho\rangle = p_1\rho_1 + p_2\rho_2,\\
&\rho_1 = \rho_0(1+\varepsilon_1), \qquad \rho_2 = \rho_0(1+\varepsilon_2),\\
&\varepsilon_1 = \frac{\rho_1}{\rho_0} - 1, \qquad \varepsilon_2 = \frac{\rho_2}{\rho_0} - 1, \qquad (49)\\
&\mu = \langle\varepsilon^2\rangle = p_1\varepsilon_1^2 + p_2\varepsilon_2^2,\\
&\nu = \langle\varepsilon^3\rangle = p_1\varepsilon_1^3 + p_2\varepsilon_2^3.
\end{aligned}$$

The angular distribution of light intensity in the diffraction pattern arising when a laser beam is scattered on a bimodal ensemble of erythrocytes is described by the Eq.:

$$f(\theta) = \frac{p_1\rho_1^4 G(\rho_1\theta) + p_2\rho_2^4 G(\rho_2\theta)}{p_1\rho_1^4 + p_2\rho_2^4},$$

where $p_1 = p$, $p_2 = 1-p$, and the function $G(x)$ is determined by Eq. (13). Setting the parameters of the bimodal ensemble ρ_1, ρ_2 and p, through numerical calculations we find the parameters of the diffraction pattern θ_0, f_0 and f_2, determined by Eqs. (2) – (4). The characteristics of bimodal ensembles (BME) and the results of calculations of the parameters of diffraction patterns are presented in Table 1. The numerical values of the erythrocyte size parameters are selected for the laser radiation wavelength $\lambda = 0.63\ \mu m$.

We use the found values of the parameters θ_0, f_0 and f_2 as input data for the algorithm expressed by Eqs. (45) – (47). Using Eqs. (45) – (47), we calculate the parameters of the ensemble of erythrocytes ρ_0, μ', ν' and compare the obtained values with the exact values of the parameters found using Eqs. (10), (11), (49). The calculation results are presented in Table 2. In this table, ρ_{0c}, μ_c', ν_c' are the exact values of the parameters of bimodal ensembles of erythrocytes, found using Eqs. (10), (11), (49). Approximate values of these parameters, found using algorithm (45) – (47), are designated ρ_0, μ', ν'. The errors in determining the parameters of an ensemble of erythrocytes using algorithm (45) – (47) are designated $\delta\rho_0, \delta\mu', \delta\nu'$. These errors are expressed as percentages.

Let us consider, as an example, the problem of reconstructing the parameters of a bimodal ensemble of erythrocytes from laser diffractometry data of a blood smear. The task is to determine the parameters of the bimodal ensemble p, ρ_1, ρ_2 from the measured parameters of the diffraction pattern θ_0, f_0, f_2. Using the following Eqs.:

$$\begin{aligned}
&p\varepsilon_1 + (1-p)\varepsilon_2 = 0,\\
&\mu = p\varepsilon_1^2 + (1-p)\varepsilon_2^2,\\
&\nu = p\varepsilon_1^3 + (1-p)\varepsilon_2^3
\end{aligned}$$

we find [22]

$$\begin{aligned}
&p = \frac{1}{2}\left(1 + \frac{\nu}{\sqrt{\nu^2+4\mu^3}}\right),\\
&\varepsilon_1 = \frac{\nu - \sqrt{\nu^2+4\mu^3}}{2\mu},\\
&\varepsilon_2 = \frac{\nu + \sqrt{\nu^2+4\mu^3}}{2\mu},\\
&\rho_1 = \rho_0 \cdot (1+\varepsilon_1),\\
&\rho_2 = \rho_0 \cdot (1+\varepsilon_2).
\end{aligned} \qquad (50)$$

Table 1 Parameters of diffraction patterns found by numerical experiment.

	BME 1	**BME 2**	**BME 3**	**BME 4**	**BME 5**
$\boldsymbol{\rho_1}$	35	33	32	31	30
$\boldsymbol{\rho_2}$	40	42	43	44	45
$\boldsymbol{p}$	0.4	0.4	0.4	0.4	0.4
$\boldsymbol{\theta_0, rad}$	0.1005	0.0984	0.0968	0.0948	0.0923
$\boldsymbol{f_0}$	0.002501	0.006984	0.009471	0.01181	0.01377
$\boldsymbol{f_2}$	1.141	0.887	0.7777	0.7011	0.680

Table 2 Results on the evaluation of parameters of RBC size distribution, obtained in the numerical experiment.

	BME 1	**BME 2**	**BME 3**	**BME 4**	**BME 5**
$\boldsymbol{\rho_{0c}}$	38	38.4	38.6	38.8	39
$\boldsymbol{\rho_0}$	38	38.5	38.8	39.2	39.8
$\boldsymbol{\delta\rho_0}$, %	0	0.3	0.5	1	2
$\boldsymbol{\mu_c'}$, %	6.45	11.5	14.0	16.4	18.8
$\boldsymbol{\mu'}$, %	6.34	10.9	12.9	14.6	15.9
$\boldsymbol{\delta\mu'}$, %	1.7	5.2	7.9	11	15
$\boldsymbol{\nu_c'}$	−0.0478	−0.085	−0.104	−0.122	−0.140
$\boldsymbol{\nu'}$	−0.0458	−0.081	−0.103	−0.124	−0.144
$\boldsymbol{\delta\nu'}$, %	4.2	4.7	1.0	1.6	2.9
$\boldsymbol{p_c}$	0.4	0.4	0.4	0.4	0.4
$\boldsymbol{p}$	0.41	0.40	0.37	0.35	0.33
$\boldsymbol{\delta p}$, %	2.5	0	7.5	12.5	17.5
$\boldsymbol{\rho_{1c}}$	35	33	32	31	30
$\boldsymbol{\rho_1}$	35.1	34.1	33.6	33.2	33.0
$\boldsymbol{\delta\rho_1}$, %	0.3	3.3	5.0	7.1	10
$\boldsymbol{\rho_{2c}}$	40	42	43	44	45
$\boldsymbol{\rho_2}$	40	42.6	43.9	45.1	46.5
$\boldsymbol{\delta\rho_2}$, %	0	1.4	2.1	2.5	3.3

The calculation results are presented in the same Table 2. In this table, $p_c, \rho_{1c}, \rho_{2c}$ are the exact values of the parameters of bimodal ensembles of erythrocytes. Approximate values of these parameters, found using Eqs. (45) – (47), (50) based on the analysis of diffraction patterns, are designated p, ρ_1, ρ_2 . The errors in determining parameters using algorithm (45) – (47), (50) are designated $\delta p, \delta\rho_1, \delta\rho_2$. These errors are expressed as percentages. Note that it is advisable to test the proposed algorithm on more complex models of red blood cell ensembles.

7 Discussion

In this paper we presented an algorithm to measure parameters of the size distribution of red blood cells on a blood smear. The algorithm is designed to measure the average size, as well as the width and asymmetry of the red blood cell size distribution. In the case of a bimodal ensemble of erythrocytes, these data make it possible to determine the individual size of the ensemble components under consideration, as well as the percentage ratio between them. The solution to the inverse scattering problem is presented in the form of explicit analytical expressions suitable for weakly homogeneous ensembles of erythrocytes. From a mathematical point of view, the possibility of analytically solving the inverse problem of scattering a laser beam on an inhomogeneous ensemble of red blood cells is associated with the use of two approximations. First, this is a polynomial representation of the Bessel function and the Airy function, applicable to a limited part of the diffraction pattern that occurs when a laser beam is scattered on a blood smear. Second, the approximation of a weakly heterogeneous (in size) ensemble of erythrocytes. The first of these approximations makes it possible to write diffractometric equations in terms of elementary functions, the second makes it possible to linearize these equations with respect to small parameters and obtain their analytical solution. Both approximations introduce measurement errors, which we estimated using a numerical experiment. The results show that the error of the algorithm increases with increasing heterogeneity of the ensemble. The corresponding data are shown in Table 2. Thus, with an expansion of the size distribution of erythrocytes $\mu' = 14\%$, the measurement error of the ensemble parameters is not more than 8%, and with $\mu' = 18.8\%$ the measurement error reaches 17.5%. The results obtained can be used to create laser diffractometers of erythrocytes with expanded functionality.

For the practical implementation of the proposed measurement algorithm, several conditions must be met. Red blood cells on a blood smear should have their natural shapes, and their concentration should not be too high so that the condition of single light scattering is met. The laser beam must be sufficiently coherent. The width of the laser spectrum must be much less than its carrier frequency, and the coherence radius must significantly exceed the size of the red blood cell. Finally, the system

for recording diffraction patterns must have a sufficiently high resolution and a sufficiently wide dynamic range for measuring light intensity.

Let us also note the following circumstance. Eq. (48) shows that to accurately determine the average diameter of erythrocytes using laser diffractometry, it is necessary to know the width of the erythrocyte size distribution. This is due to the fact that the contribution of the red blood cell to the light intensity in the diffraction pattern is proportional to the fourth power of the radius of the red blood cell. In other words, the contribution of large erythrocytes dominates over the contribution of small erythrocytes. At a constant average radius of the erythrocyte, this leads to the fact that the scattering of erythrocytes in size shifts the minimum light intensity in the diffraction pattern to the region of small scattering angles. Therefore, the average size of a red blood cell on a blood smear depends not only on the angle θ_0, but also on the width of the red blood cell size distribution.

Our theoretical model is based on the assumption of weak heterogeneity of the erythrocyte ensemble. We call an ensemble weakly heterogeneous for which the scatter of erythrocyte sizes is small compared to the average size of an erythrocyte. For blood samples close to normal, this condition is well met. Mathematically, the condition is expressed by the formula $\mu \ll 1$. In the numerical experiment we use a model of a bimodal ensemble of red blood cells. This model is convenient because it is characterized by a minimum number of parameters. In the case of pathological blood samples (for example, with sickle cell anemia), the visibility of the dark ring in the diffraction pattern can be significantly reduced, which will be interpreted by our algorithm as an abnormally large dispersion of red blood cells in size.

Our algorithm is based on processing the diffraction pattern in the region of the first dark ring. As a rule, there is such a ring. But if it is not there, then this may indicate the presence of a large number of irregularly shaped cells, for example, echinocytes, in the blood sample.

Acknowledgements

The theoretical part, development of theoretical experiment methodology, data analysis were supported by the Russian Science Foundation grant (No. 22-15-00120). Computer simulation of diffraction patterns was supported by the Ministry of Education and Science of the Russian Federation as part of the program of the Moscow Center for Fundamental and Applied Mathematics under the agreement No. 075-15-2022-284.

Disclosures

The authors declare that they have no conflict of interest.

References

1. A. V. Muravyov, P. V. Mikhailov, and I. A. Tikhomirova, "Microcirculation and Hemorheology: points of interaction," Regional blood circulation and microcirculation 16(2), 90−100 (2017). [in Russian]
2. F. I. Ataullakhanov, D. V. Borsakova, E. S. Protasov, E. I. Sinauridze, and A. M. Zeynalov, "Erythrocyte: a bag with hemoglobin, or a living active cell?," Pediatric Hematology/Oncology and Immunopathology 17(1), 108−116 (2018). [in Russian]
3. K. V. Patel, L. Ferrucci, W. B. Ershler, D. L. Longo, and J. M. Guralnik, "Red Blood Cell Distribution Width and the Risk of Death in Middle-aged and Older Adults," Archives of Internal Medicine 169(5), 515 (2009).
4. A. Bogdanova, L. Kaestner, G. Simionato, A. Wickrema, and A. Makhro, "Heterogeneity of Red Blood Cells: Causes and Consequences," Frontiers in Physiology 11, 392 (2020).
5. J. Picot, C. L. Guerin, C. Le Van Kim, and C. M. Boulanger, "Flow cytometry: retrospective, fundamentals and recent instrumentation," Cytotechnology 64(2), 109–130 (2012).
6. R. Green, S. Wachsmann-Hogiu, "Development, History, and Future of Automated Cell Counters," Clinics in Laboratory Medicine 35(1), 1–10 (2015).
7. V. A. Dubrovskii, I. V. Zabenkov, E. P. Karpocheva, and S. O. Torbin, "Identification and Counting of Erythrocytes of Native Human Donor Blood by Digital Optical Microscopy Using Spectral Filtered Illumination," Optics and Spectroscopy 129(3), 315–328 (2021).
8. A. E. Lugovtsov, V. D. Ustinov, G. S. Kalenkov, S. G. Kalenkov, and A. V. Priezzhev, "Hyperspectral Holography and Laser Diffractometry of Erythrocytes," Journal of Biomedical Photonics & Engineering 6(2), 020306 (2020).
9. M. Bessis, "A diffractometric method for the measurement of cellular deformability," Blood Cells 1, 307−313 (1975).
10. Y. Yang, Z. Zhang, X. Yang, J. H. Yeo, L. Jiang, and D. Jiang, "Blood cell counting and classification by nonflowing laser light scattering method," Journal of Biomedical Optics 9(5), 995−1001 (2004).
11. Y. S. Yurchuk, V. D. Ustinov, S. Y. Nikitin, and A. V. Priezzhev, "Scattering of a laser beam on a wet blood smear and measurement of red cell size distribution," Quantum Electronics 46(6), 515–520 (2016).
12. P. S. Vinnikov, V. D. Ustinov, A. E. Shtanko, A. E. Lugovtsov, G. S. Kalenkov, and M. A. Karpilova, "A Mobile Device for Measuring the Size Distribution of Red Blood Cells," Biomedical Engineering 54(1), 6–8 (2020).
13. M. A. Casas-Ramos, G. E. Sandoval-Romero, "Yeast cells characterization through near-forward light scattering," Optical and Quantum Electronics 52(3), 159 (2020).
14. M. J. Berg, S. C. Hill, G. Videen, and K. P. Gurton, "Spatial filtering technique to image and measure two-dimensional near-forward scattering from single particles," Optics Express 18(9), 9486−9495 (2010).

15. M. S. Lebedeva, E. G. Tsybrov, and A. E. Nikandrova, "Experiments on laser diffractometry of blood smears," Proceedings of the XVI International Scientific and Technical Conference "Optical Methods of Flow Investigation", Moscow, 175–182 (2021).
16. S. Y. Nikitin, A. E. Lugovtsov, and A. V. Priezzhev, "On the problem of visibility of the diffraction pattern in laser diffractometry of red blood cells," Quantum Electronics 40(12), 1074–1076 (2010).
17. S. Y. Nikitin, A. E. Lugovtsov, A. V. Priezzhev, and V. D. Ustinov, "Relation between the diffraction pattern visibility and dispersion of particle sizes in an ektacytometer," Quantum Electronics 41(9), 843–846 (2011).
18. S. Yu. Nikitin, A. V. Priezzhev, and A. E. Lugovtsov, "Analysis of laser beam scattering by an ensemble of particles modeling red blood cells in ektacytometer," Journal of Quantitative Spectroscopy and Radiative Transfer 121, 1–8 (2013).
19. V. D. Ustinov, "On inverse reconstruction problems of the erythrocyte size distribution in laser diffractometry," Mathematical Models and Computer Simulations 9(5), 561–569 (2017).
20. G. P. Sarkisyan, Theoretical description of diffraction of laser radiation on erythrocytes monolayer, NAS of Armenia. Reports. Optics. Biophysics 120(1), 45–51 (2020). [in Russian]
21. F. Emde, Tables of higher functions, B. G. Teubner Verlagsgesellschaft, Leipzig, Germany (1960).
22. S. Yu. Nikitin, V. D. Ustinov, S. D. Shishkin, and M. S. Lebedeva, "Line curvature algorithm in laser ektacytometry of red blood cells," Quantum Electronics 50(9), 888–894 (2020).

Enhanced Optical Imaging of Proximal Human Interphalangeal Joints Using Skin Optical Clearing

Elina A. Genina[1,2*], Ekaterina A. Kolesnikova[1], Viacheslav G. Artyushenko[3], Evgeny Berik[4], and Valery V. Tuchin[1,2,5]

[1] Saratov State University, 83 Astrakhanskaya str., Saratov 410012, Russian Federation
[2] Tomsk State University, 36 Lenin av., Tomsk 634050, Russian Federation
[3] art photonics GmbH, 46 Rudower Chaussee, Berlin 12489, Germany
[4] Estla Ltd, Lasers & Laser Systems, 7 Teaduspargi, Tartu 51014, Estonia
[5] Institute of Precise Mechanics and Control, FRC "Saratov Scientific Centre of the Russian Academy of Sciences", 24 Rabochaya str., Saratov 410028, Russian Federation
*e-mail: eagenina@yandex.ru

Abstract. In this study we have analyzed the change in the intensity distribution of three-wavelength transillumination images of human interphalangeal joints under the action of the optical clearing agent. RheumaSens medical scanner prototype with the following wavelengths: 660, 850, and 905 nm, has been tested. A water solution of glycerol (70%) and DMSO (5%) has been used as an optical clearing agent, and sonophoresis has been applied for enhance of skin permeability. Eight healthy volunteers and a volunteer with rheumatoid arthritis have been investigated. As a result, we have obtained an increase in the contrast of joint images within 10 min: 1.2±0.14, 1.16±0.15, and 1.16±0.02 folds at the wavelengths of 660, 850, and 905 nm, respectively. It has been shown an effect of skin optical clearing on the enhancement of the images of joint with rheumatoid arthritis in the transillumination mode. © 2024 Journal of Biomedical Photonics & Engineering.

Keywords: optical clearing; laser transillumination; optical imaging; proximal interphalangeal joints; rheumatoid arthritis.

Paper #9101 received 17 Apr 2024; revised manuscript received 20 Aug 2024; accepted for publication 21 Aug 2024; published online 20 Sep 2024. doi: 10.18287/JBPE24.10.040303.

1 Introduction

The most common cause of severe inflammation of the joints is rheumatoid arthritis (RA). RA is a disease of unknown etiology that results in chronic, systemic inflammation that can affect many organs and tissues. This disease can cause inability to move and painful synovial joints, which in turn can lead to significant loss of function and mobility if not treated properly. Thus, it is vital to diagnose and treat this disease early and aggressively before damage ensues [1, 2].

Diagnosing RA requires a physical exam, blood tests and scans like X-ray, MRI, or ultrasound. Testing for serum antibodies to anti-citrullinated protein antibodies and rheumatoid factor continues to be valuable in the diagnostic evaluation of patients with suspected RA, and these antibodies serve as biomarkers of prognostic significance. Advances in imaging modalities assist clinical decision-making by improving the detection of joint inflammation and monitoring the progression of damage [1]. Conventional radiography is still used as a standard of reference in detecting disease progression and is therefore used as an indicator of prognosis, however X-rays may not show anything abnormal in early arthritis and current inflammatory disease activity [2]. MRI is more sensitive in comparison with conventional radiography in detection of early RA, but its usage may be limited by availability, costs, and workflow consideration [3]. Compared with MRI, ultrasonography is more readily available and less expensive, and therefore it is often used for fast assessment of joint inflammation [4].

Synovium is a highly specialized tissue whose main function is to maintain healthy lubrication and nutrition. The process of RA involves an inflammatory response of

the capsule around the joints secondary to swelling (turgescence) of synovial cells, excess synovial fluid (synovia), and the development of fibrous tissue (pannus) in the synovium [1]. Pathological changes lead to changes in the optical properties of the synovium with an increase in both absorption and scattering compared to healthy tissue. The main variations in absorption and scattering coefficients in sinovia and synovial tissues are observed in red and near-IR spectral region [5]. Therefore, optical imaging is one of the perspective methods for diagnostics of the joint pathologies due to its absolutely safety, high sensitivity, and unique specificity in comparison to other biomedical imaging modalities. Some methods of RA optical detection at an early stage are presented in the literature. For example, a method of deconvolution for laser based images was proposed for monitoring RA in Ref. [6]. In Ref. [7] it was offered to improve the diagnostic sensitivity of RA by using overlapped pseudo-colored images at different wavelengths. The techniques of diffuse optical tomography [8], fluorescence optical imaging [9], and fluorometric imaging using bioengineered targeted agents of the blood vessel, bone, and cartilage in combination with the customized optical fluorescence imaging system [10] were also proposed to diagnose RA at an early stage. It was suggested to distinguish septic arthritis patients from other causes of joint effusion by using mid infrared deported spectroscopy [11]. Authors of Ref. [12] designed a RA system using a ring-array sensor to image human finger vasculature. It was shown that this system has the potential to help visualize abnormal vascularization as an important marker of inflammatory arthritis.

Transillumination can be used successfully for optical imaging of the internal structure of joints. An experimental laser diode based setup for the transillumination of rheumatoid finger joints was described in Refs. [13−15]. However, strong light scattering in tissues causes image blurring. The relatively low contrast and poor spatial resolution of the technique, which do not allow one to find the difference between healthy and pathology joints precisely, could be improved by reduction of skin light scattering at using of optical clearing (OC) technique. Pilot experiments for enhancement of optical imaging of PIP joints were carried out *in vivo* using dehydrated glycerol and hand cream with urea (5%) [16]. It was found that a one-hour glycerol and hand cream topical application resulted in ~1.4 and ~1.1-fold contrast decreasing at 670 nm, respectively. At the wavelengths 820 nm and 904 nm the image contrast increased in ~1.5 and ~1.7 folds, respectively, for glycerol application and in ~1.3 and ~1.1 folds, respectively, for the hand cream application. The contrast rise in the NIR wavelength region was caused by light scattering reduction due to skin optical clearing and, correspondingly, an increase in the intensity of light detected on the opposite side of the finger. Contrast decrease at the wavelength 670 nm during skin optical clearing could be caused by an increase in light absorption by deoxyhemoglobin of venous blood.

As an optical clearing agent (OCA) glycerol is widely used at skin optical clearing [17−22] because of its hyperosmolarity and high refractive index. Glycerol is a highly effective agent providing three major mechanisms of OC: osmotic dehydration of tissue, refractive index matching of scatterers and interstitial fluid, and collagen dissociation [23]. Optical clearing potential of solutions with different concentration of glycerol has been compared theoretically and experimentally [18-22]. Aqueous 70%-glycerol solution has shown the best result due to much low viscosity at dilution by water and still sufficient osmolarity and refractive index.

Dimethyl sulfoxide (DMSO) is an effective enhancer of the diffusion of optical clearing agents through the *stratum corneum* of the epidermis [24, 25]. The mechanism of action of DMSO is due to its ability temporarily and partially dissolve the lipid base of the stratum corneum of the epidermis and create pores in it [26]. Due to this property, DMSO increases the rate of transdermal penetration of both hydrophilic and lipophilic agents. For *in vivo* topical applications, low concentration DMSO is preferred because it has no side effects and has been used for many years to reduce inflammation in arthritis [27]. Also, 10%-DMSO solution has been shown to induce skin edema [28]. Thus, the component ratio of 70%-glycerol/5%-DMSO may provide a safe and effective composition for skin optical clearing.

In addition to DMSO application, sonophoresis (US) as an effective physical enhancer of the OCA diffusion in skin [29, 30], can be used. It was shown in Ref. [29] that the combined use of DMSO, US, and OCA reduces the attenuation coefficient of light in skin by about 31% within 4 min, compared with a decrease of 5% achieved when using a combination of DMSO-OCA for 20 min.

The optimization of the device for transillumination imaging of finger joints and development of an approach to the rapid skin OC *in vivo* are important tasks for potentional implementation of the method into clinical practice.

The goal of this study is developing the approaches to improve transillumination optical images of human finger capsule synovial structures due to the application of OC technique.

2 Materials and Methods

2.1 Object of Study

The experiments were carried out *in vivo* on proximal interphalangeal (PIP) joint of the middle and ring fingers of the left and right hands of eight healthy volunteers (seven males aged 20 years and a female aged 32 years). Average thickness of the investigated PIP joints was 16.8 ± 0.9 мм. The PIP joint of the middle finger (thickness 16 mm) of the right hand of a female volunteer (age 32) with the first degree of RA was also examined.

An authorization for the human skin studies *in vivo* was obtained from the Saratov State Medical University

Ethical Committee (protocol no. 11 by 7 June 2022). All volunteers gave their informed consent for the study.

2.2 Experimental Setup

To assess the condition of the patient's finger joints a prototype of medical scanner RheumaSens (art photonics GmbH, Berlin, Germany) was used. The RheumaSens (Fig. 1a) consists of transparent spherical hand support (1), set of quickly replaceable adjustable hand holders for different hand sizes (2), three-wavelength laser emitter (660 nm: FP-D-660-40P-C-C, 850nm: FP-D-850-40P-E-C, 905nm: FP-D-905-7P-E-C, FLEXPOINT®, Laser Components GmbH, Olching, Germany) moving around on a 2-axis robotic arm (3 and detailed image is in Fig. 1b), computer controls for emitter and arm positioning, NIR extended CCD camera IDS uEye UI-1240ML-NIR-GL (4) with real-time image display on computer screen, automated image registration on each wavelength.

The power of all lasers was set to 5 mW in order to comply with European safety regulations.

The imaging scheme is shown in Fig. 1c. By adjusting the focus and aperture of the camera lens it was possible to adjust the (vertical) position of the recording zone in the joint and the depth of field.

As a result of the experiment, a set of images was obtained (Fig. 1d), which represent two-dimensional maps of the scattered light intensity distribution on the underside of the finger.

2.3 OCA and Experimental Design

A mixture of glycerol (70%), DMSO (5%) and distilled water (25%) was used as the OCA for the testing of the possibility of image improvement of the joints. The spectral dependence of the refractive index was measured using an Abbe multiwave refractometer (Atago DR-M2/1550, Japan) in the range 450−1550 nm and approximated to obtain the following refractive index values at the wavelengths used: 1.4409 (660 nm), 1.4371 (850 nm), and 1.4361 (905 nm).

The OCA was applied topically on the investigated skin site and was not subsequently added. The images of the PIP joints were registered before and for 60 min after the OCA application every 5 min.

To enhance the skin permeability for OCA we used the Dynatron 125 ultrasonic (US) device (Dynatronics, USA) for sonophoresis. The following exposure parameters were selected: power density 1.5 W/cm^2, frequency 1 MHz, exposure time 5 min in pulse mode with a duty cycle of 50%. The diameter of the US probe was 2.2 cm. OCA was used as a contact substance during sonication.

The measurements were obtained before, after the OCA application with sonication, and then for 15 min every 5 min.

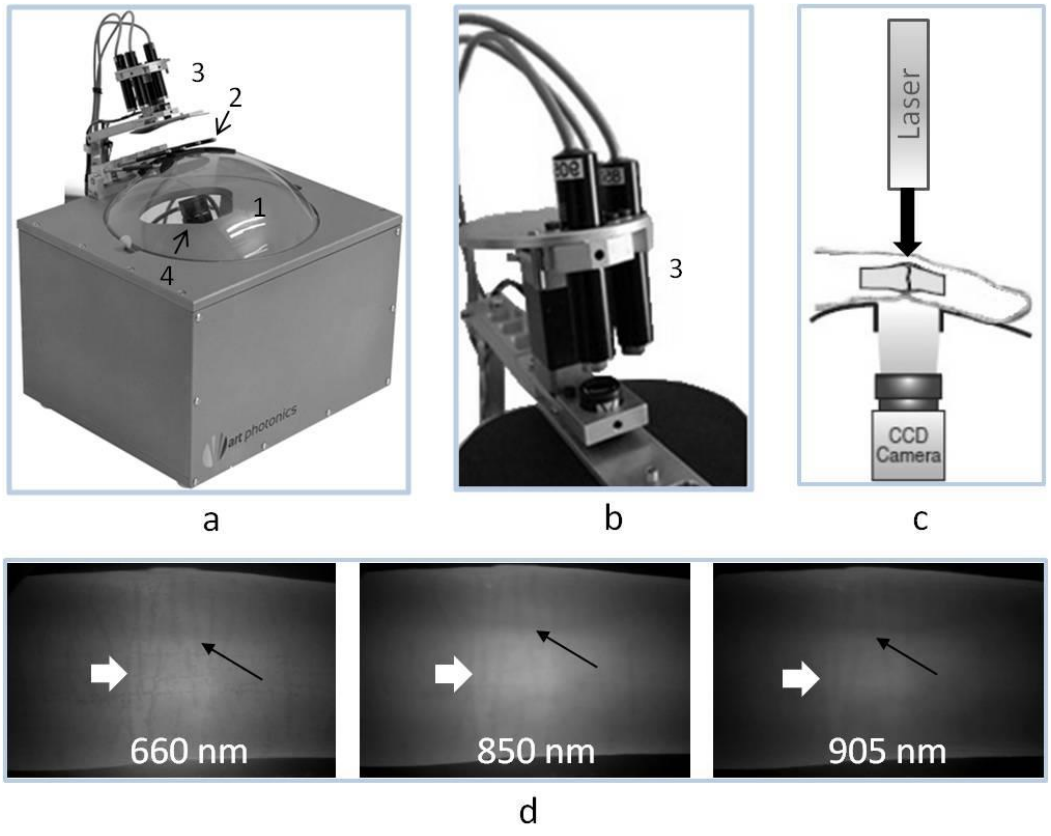


Fig. 1 (a) RheumaSens medical scanner: general view; (b) three-wavelength laser emitter; (c) a scheme for laser illumination of a finger and detection of transmitted light; and (d) images of the interphalangeal joint in transmission mode at three wavelengths: 660 nm, 850 nm and 905 nm. The white arrows point to the joint and the black ones point to the blood vessels.

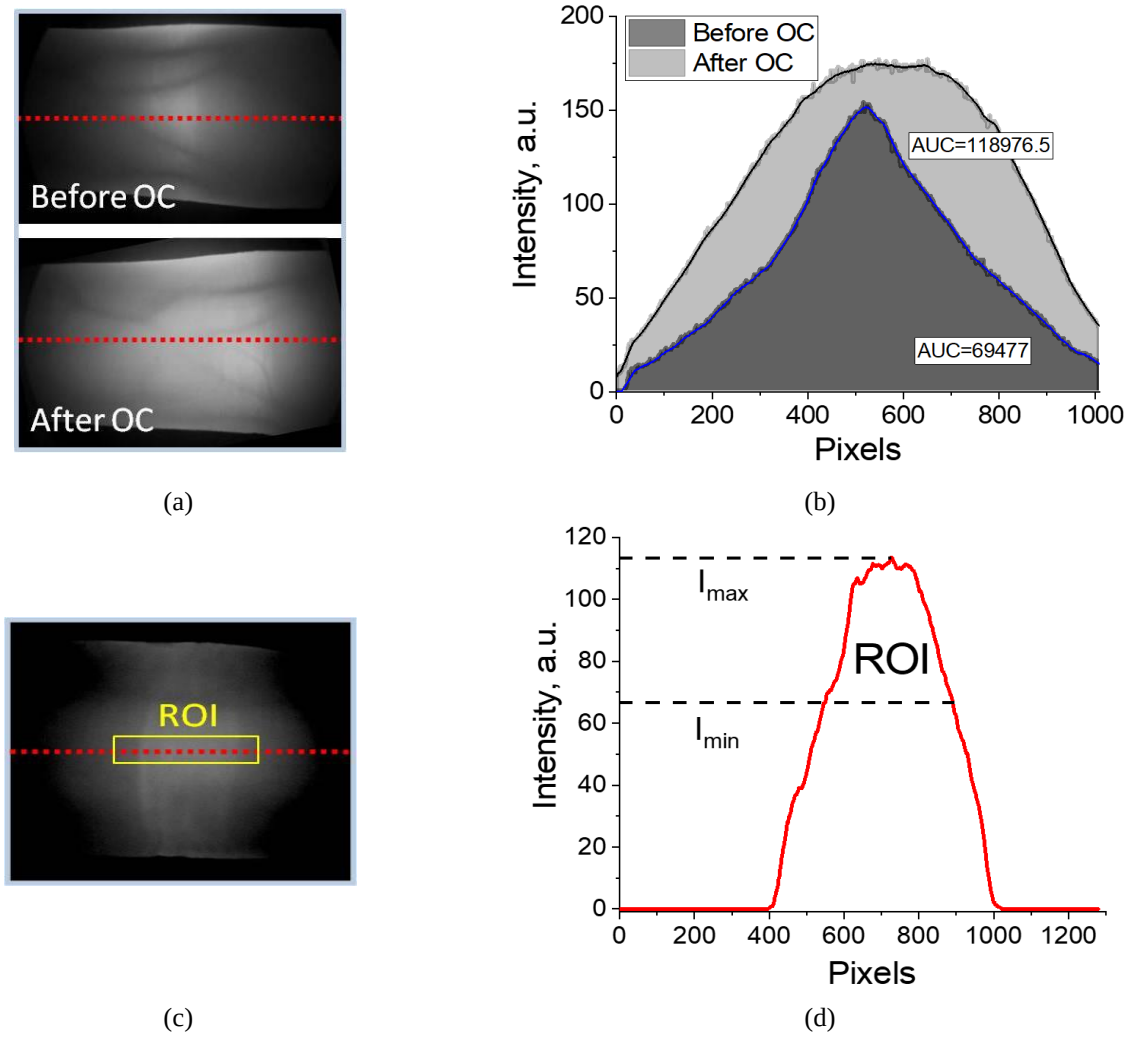


Fig. 2 (a) Images of the finger section in transillumination mode at the wavelength 850 nm and (b) typical profiles of the intensity of the transmitted light with the areas under the curves (AUC), obtained before applying OCA and after 60-min exposure. The parameters were calculated along the red dotted line. (c) The region of interest (ROI) (d) and averaged profile of intensity in the ROI. I_{max} and I_{min} correspond to the maximal and minimal brightness of the pixels in the ROI, respectively.

2.4 Processing of Experimental Data

To evaluate the changes in transillumination images of PIP joint during optical cleaning, the intensity profile of the transmitted light was calculated using the pixel brightness of the finger section images in the range 0–255. The intensity profile was built along the X-axis (red dotted line in Fig. 2a) approximately in the middle of the finger image using the built-in MatLab (The MathWorks, Inc., USA) function. The curves were smoothed by 25 points using the built-in OriginPro (Origin Corp., USA) function "adjacent-averaging". In addition, the area under the curves (AUC) was calculated, as shown in Fig. 2b. All parameters were calculated for similar experiments, normalized to the initial value and averaged.

Processing of the experimental data allowed calculating the contrast in the region of interest (ROI) near the middle of the finger joint (see Fig. 2c). ROI included the intensity profile corresponding to the image of the joint with the adjacent areas on the right and left to calculate the contrast of the joint image compared to its immediate surroundings, since the entire observed section of the finger became brighter during the clearing process. The edges of the image were excluded because the pixel brightness in these areas was always almost zero. The calculation of the contrast was performed using the expression $C = (I_{max}-I_{min})/(I_{max}+I_{min})$, where I_{max} is the maximal brightness and I_{min} is the minimal brightness of the pixels in the ROI (see, Fig. 2d).

3 Results

Fig. 3 shows kinetics of the calculated parameters of the PIP joint images obtained for three wavelengths and normalized on the initial values before OC. It is well seen that 10 min after the OCA application, both the intensity and the AUC lower than in the initial moment. The decrease in both intensity and AUC immediately after application of OCA is apparently explained by a decrease in transmitted light due to an increase in the specularly reflected flow from the skin surface.

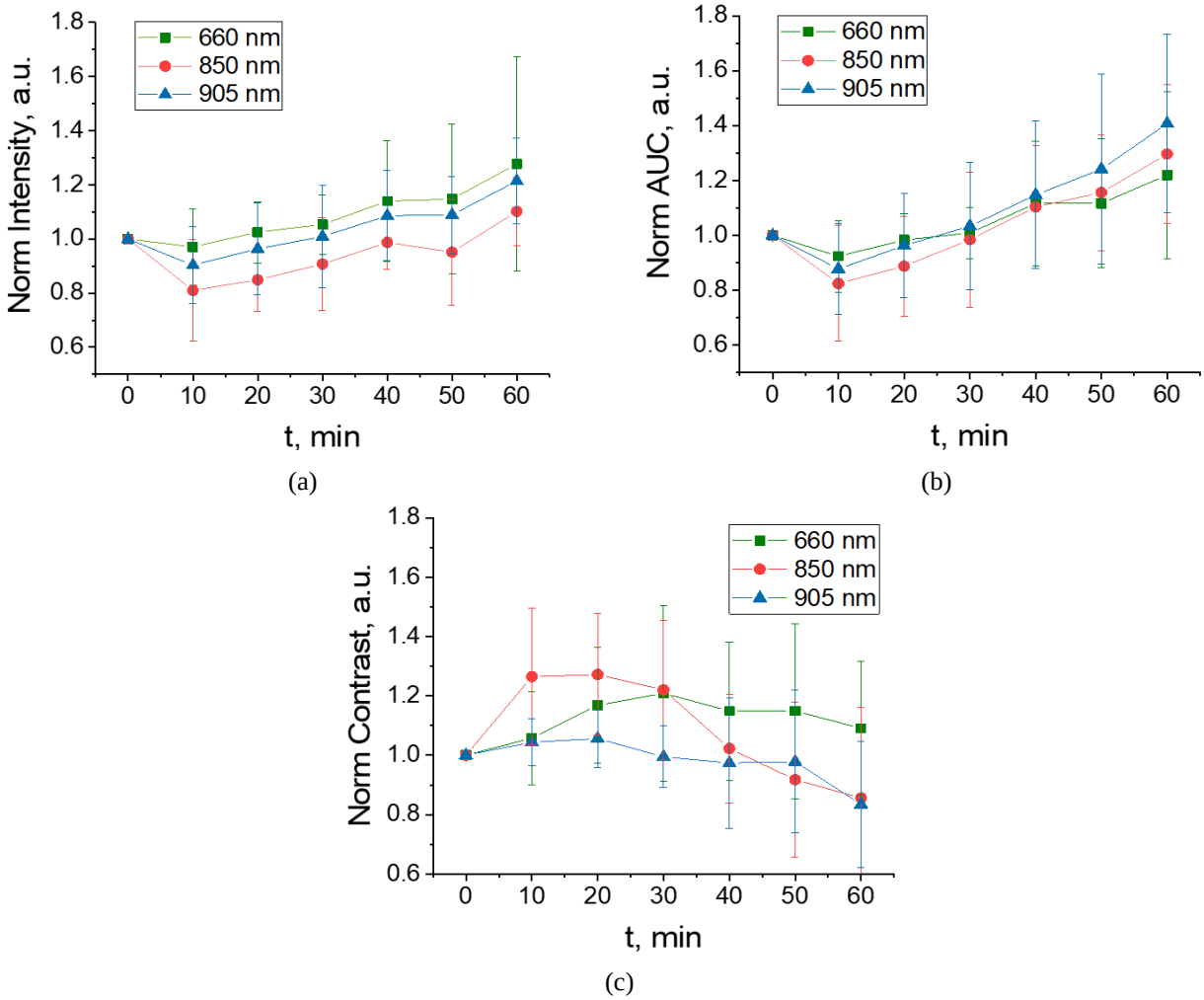


Fig. 3 (a) Kinetics of the normalized maximal intensity of the transmitted light, (b) the area under the curves (AUC) of the intensity, and (c) the contrast of the PIP joint image during optical clearing averaged by seven healthy volunteers.

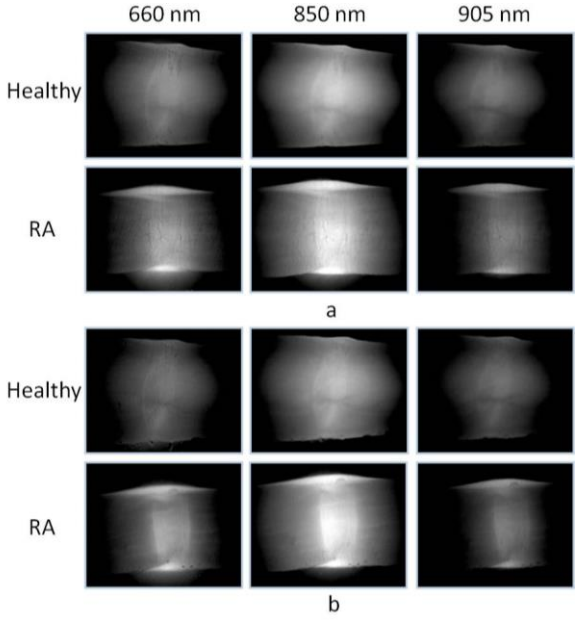


Fig. 4 Images of a healthy joint and an RA joint in the transillumination mode at three wavelengths (a) without optical clearing and (b) 10 min after applying OCA.

However then, the illumination of the opposite surface of the finger gradually increased, which can be seen from an increase in both the brightness of the pixels in the PIP region and the illumination area. The average increase in transmitted light intensity was estimated to be 1.28 ± 0.4, 1.1 ± 0.1, and 1.2 ± 0.2 folds at wavelengths of 660, 850, and 905 nm, respectively. The average AUC increased by 1.22 ± 0.3, 1.3 ± 0.25, and 1.41 ± 0.3 folds at wavelengths of 660, 850, and 905 nm, respectively. The large standard deviation is caused by significant variation in finger thickness.

Kinetics of the contrast of the PIP joint images, on average, demonstrates complex behavior (Fig. 3c). This is caused by the dependence of contrast on the relation of maximum and minimum pixel brightness within the ROI. Thus, to increase the contrast of the image, it is necessary that the brightness of the image of the joint increases, and the brightness outside the joint decreases. However, from Figs. 3a, b it follows that an increase in illumination intensity as a result of optical clearing of the skin leads to an increase in both the maximum brightness and the illumination area in the ROI, therefore, the brightness of pixels outside the junction region also increases.

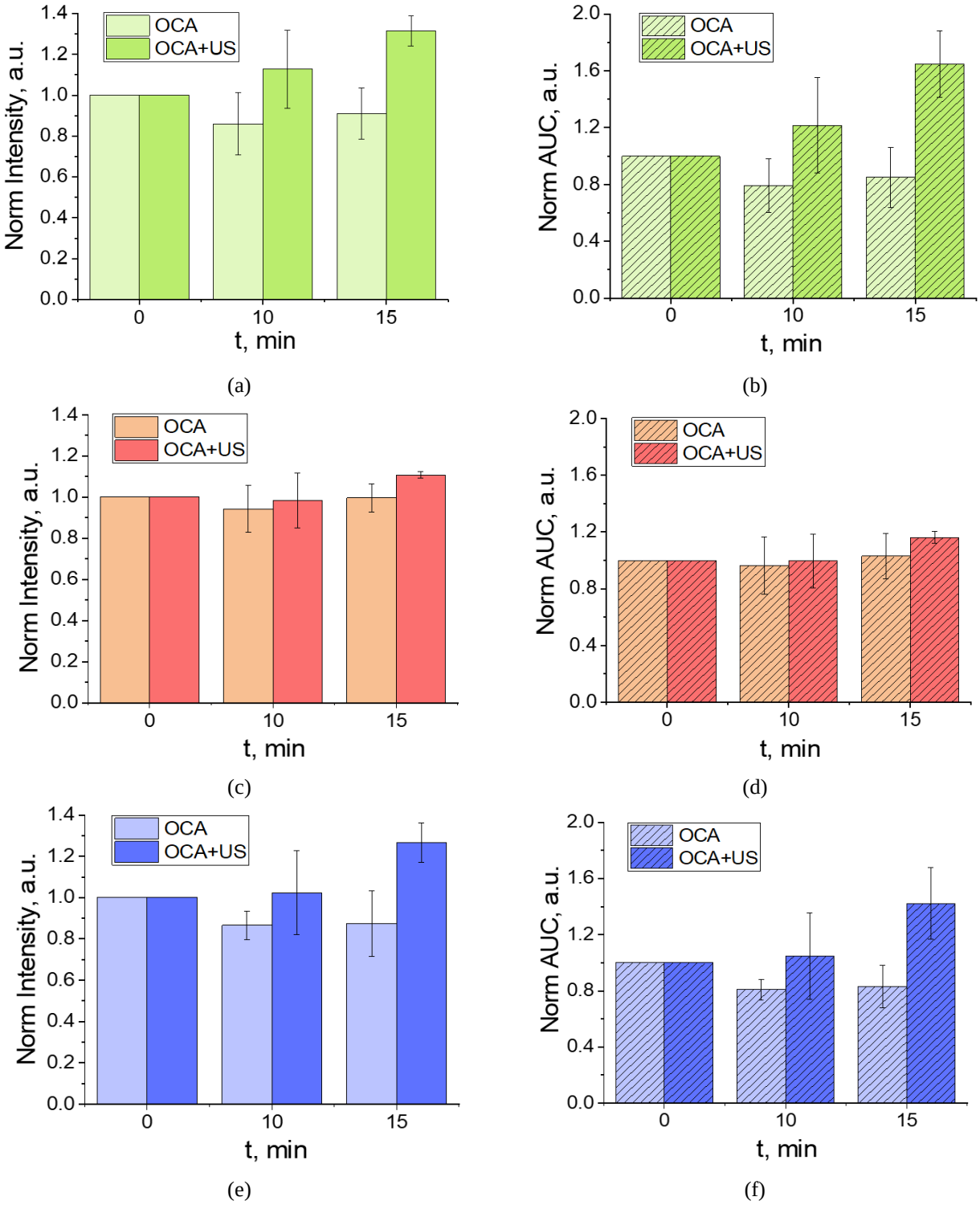


Fig. 5 (a, c, e) Comparative kinetics of the normalized maximal intensity of the transmitted light and (b, d, f) the area under the curves (AUC) of the intensity during optical clearing without/with sonication at the wavelengths: 660 nm (a, b), 850 nm (c, d), and 905 nm (e, f).

The peak contrast value was achieved in different times at the wavelengths used: about 10−20 and 30 min at wavelengths of 850 and 660 nm, respectively. At a wavelength of 905 nm, the contrast tended to decrease within 60 min. On average, the contrast increased by 1.21 ± 0.3 (in 30 min), 1.27 ± 0.2 (in 20 min), and 1.06 ± 0.09 (in 20 min) folds at wavelengths of 660, 850, and 905 nm, respectively.

Fig. 4 presents images of the PIP joints of the middle fingers obtained from a healthy volunteer (female, 32 years) and a volunteer with RA (female, 32 years). The PIP joint looks like a lighter area. The observation time was limited to 10 min, since the images of the joint

with RA had already reached a maximum brightness of 255 pixels at a wavelength of 850 nm. The improvement in the details of the image of the RA joint after the application of OCA is clearly visible. For a healthy joint, the improvement is imperceptible. Apparently, this is caused by differences in the thickness of the fingers in the study area: in healthy volunteers and volunteers with RA, it is 18 and 16 mm, respectively.

For improvement of the joint visualization OCA application was combined with sonophoresis. Fig. 5 shows the normalized intensity and AUC in the group using US to accelerate skin optical clearing. Columns with light shades of color correspond to the values of the studied parameters when OCA has been applied without sonication. During observation, the parameter values generally decreased. When using US (columns with more saturated colors), they increased immediately after the treatment. The exception was images at a wavelength of 850 nm. In this case, the intensity and AUC of the initial images were quite high, and significant changes in parameters were not noticeable.

The images of the same healthy PIP joint and the contrast values are shown in Fig. 6. It is clearly seen that the best visualization of the joint was achieved after optical clearing with sonophoresis during 10 min. It matches with kinetics of the contrast of the joint images.

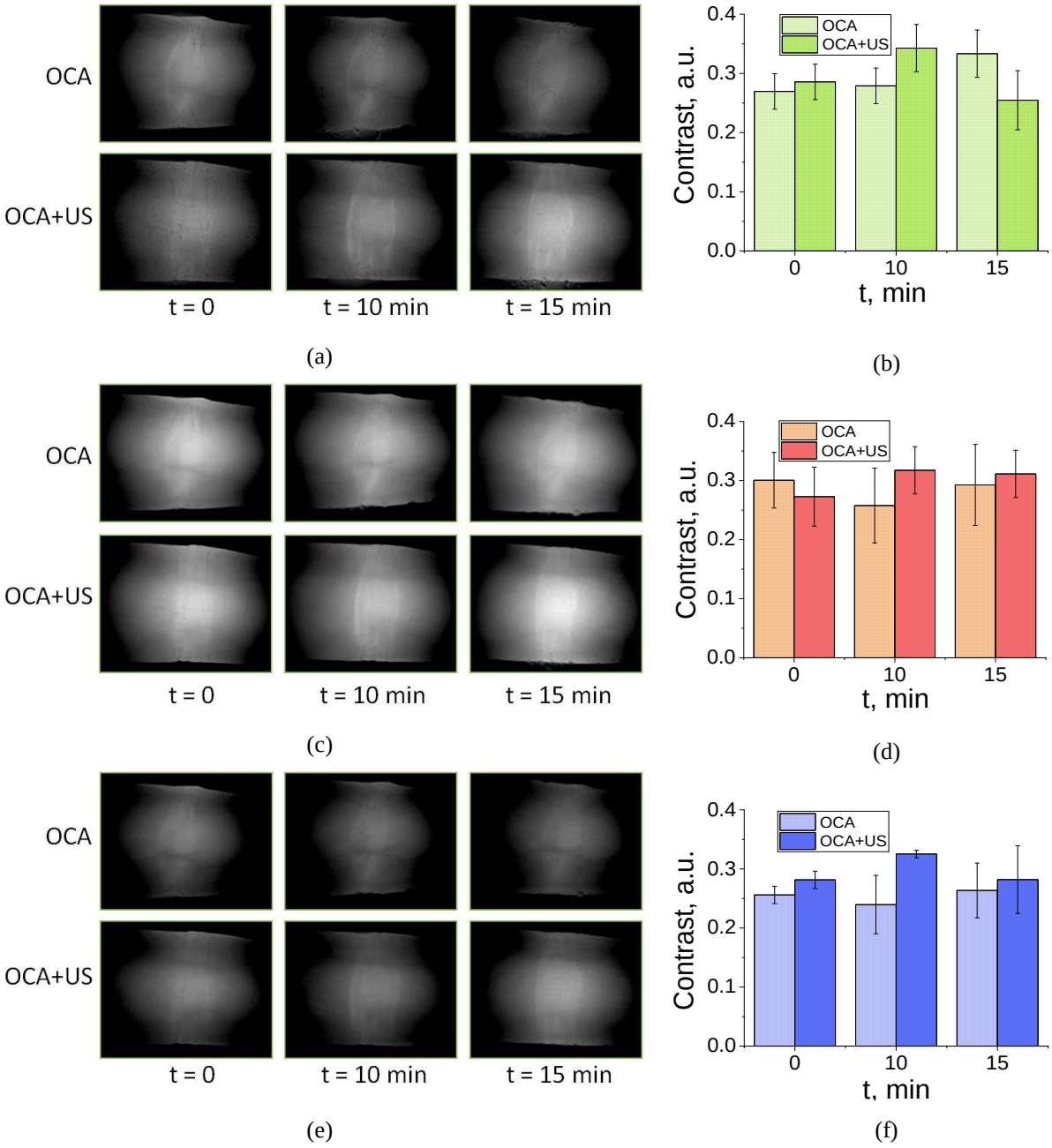


Fig. 6 (a, c, e) Typical images of a healthy joint in transmission mode and (b, d, f) comparative kinetics of the contrast of the joint image during optical clearing without/with sonication at the wavelengths: (a, b) 660 nm, (c, d) 850 nm, and (e, f) 905 nm.

Table 1 Absorption coefficient (μ_a) and reduced scattering coefficient (μ_s') of a healthy and RA diseased human finger joint *ex vivo* at three wavelengths. The data presented in the form of averaged values ± standard deviation are obtained from Ref. [5].

	μ_a, 1/cm (Healthy/RA)			**μ_s', 1/cm (Healthy/RA)**		
	660 nm	**850 nm**	**905 nm**	**660 nm**	**850 nm**	**905 nm**
Synovia	(0.04±0.015)/ **(0.11±0.1)**	(0.025±0.02)/ (0.09±0.07)	(0.065±0.01)/ (0.09±0.01)	(0.06±0.01)/ **(0.13±0.06)**	(0.1±0.03)/ (0.135±0.06)	(0.055±0.006)/ (0.085±0.012)
Synovial tissues	(0.16±0.03)/ **(0.25±0.03)**	(0.1±0.01)/ (0.13±0.1)	(0.17±0.04)/ (0.14±0.01)	(6.0±0.5)/ **(11.5±4.5)**	(5.0±0.8)/ (6.0±1.5)	(3.5±0.8)/ **(6.3±1.8)**

Relative increase in the contrast for the group with US treatment was estimated as 1.2 ± 0.14, 1.16 ± 0.15, and 1.16 ± 0.02 folds at the wavelengths of 660, 850, and 905 nm, respectively. During this time interval in the group without sonophoresis the following increased contrast was achieved: 1.06 ± 0.16, 1.26 ± 0.2, and 1.04 ± 0.08 folds at the wavelengths of 660, 850, and 905 nm, respectively. Thus, significant enhancement in the visualization of the PIP joint due to sonophoresis was observed only for the wavelengths 660 and 905 nm.

4 Discussion

The development of optical methods of RA diagnostics requires knowledge of optical parameters of healthy and pathological PIP joints. Lichter et al. measured the transmission of a set of wavelengths by a healthy finger joint: 650, 710, 730, 830, and 930nm using a multispectral diffuse optical tomographic imaging system [15]. These wavelengths were chosen as optimal for differentiation of main chromophores, which are oxyhemoglobin, deoxyhemoglobin, water, and lipids [31]. The maximum transmission in the center of the joint was obtained at a wavelength of 830 nm [15].

The affected joints of patients with RA are characterized by increased metabolism, which manifests itself in lower local oxygenation (hypoxia) compared to healthy joints [32]. To meet this increased metabolism, the regulation of blood vessel formation (synovial angiogenesis) is also enhanced [33]. The absorption coefficient of deoxygenated blood is an order of magnitude higher than that of oxygenated blood at a wavelength of 660 nm [34]. These pathological changes lead to a significant change in the absorption of the synovium compared to healthy tissue in this spectral range. Spectra of absorption and reduced scattering coefficients of synovialis in a healthy and a pathological state in the range of 630−1100 nm are presented in Ref. [5]. Table 1 shows the values for three wavelengths used in our study.

It is clearly seen that the minimum absorption of healthy joints occurs in the spectral range of about 850 nm. Thus, it is possible to visualize the structure of the joint. However, changes in absorption and scattering caused by the development of pathological processes in the synovial and synovial tissues are insignificant in this area due to the large deviation of values for RA tissues. A significant increase in both absorption and reduced scattering coefficients in the synovia, as well as in synovial tissues, is observed at a wavelength of 660 nm due to the presence of deoxyhemoglobin. A registered increase in scattering is also observed in pathological synovial tissues at a wavelength of 903 nm.

In RA, bone edema (i.e., free water in tissues), detected by MRI, is a marker of inflammation [3, 4, 35]. A prolonged inflammatory process reduces scattering in tissues since the presence of additional water leads to swelling of the collagen fibers of connective tissue and reduces the relative refractive index. Thus, the intensity of red-NIR light transmitted through the joint with RA may be higher than in a healthy joint. This can be seen in Fig. 4a.

However, reliable differentiation of healthy and pathologically altered joints using variations in optical properties and, thus, accurate optical diagnosis of RA is difficult due to the high scattering of surrounding tissues, including skin and muscles. For example, the depth of light penetration into the skin was estimated from 2 to 2.5 mm in the range of 660−900 nm [36]. A comparison of images of healthy joints and RA joints in the transillumination mode shows that the RA joint is visualized worse without optical clearing than a healthy joint. Apparently, this may be caused by increased absorption and scattering of the synovial membrane. Increasing the contrast of images due to optical clearing provides improved visualization of joint details. Using US to accelerate the penetration of OCA into the skin allows achieving maximum contrast within 10 min (Fig. 6).

However, too high illumination of the surrounding tissues can interfere with clear visualization of the joint. Therefore, the use of a specific approach depends on the thickness of the fingers. In particular, in a volunteer with RA, the maximum contrast at the wavelength of 850 nm was obtained after 10 min without the use of sonophoresis (Fig. 4b).

5 Conclusions

In this paper we have demonstrated that topical application of OCA (e.g. water solution of glycerol (70%) with DMSO (5%)) to human skin in area of finger joint allows one to improve the contrast of joint optical transillumination images. It has been found that one-hour

OCA application on the human skin results in the contrast increasing by 1.21 ± 0.3 (in 30 min), 1.27 ± 0.2 (in 20 min) and 1.06 ± 0.09 (in 20 min) folds at wavelengths of 660, 850, and 905 nm, respectively. Further application of the OCA leads to the contrast reducing due to the growth of the illumination of the surrounding tissues. Combination of OCA with sonophoresis accelerates achievement of maximum contrast within 10 min: 1.2 ± 0.14, 1.16 ± 0.15, and 1.16 ± 0.02 folds at the wavelengths of 660, 850, and 905 nm, respectively.

In this study, we only focused on the effect of optical clearing on the joint transillumination images. Although the study involved only one volunteer with early-stage rheumatoid arthritis, the results reliably showed the effect of skin optical clearing on improving transillumination images of such joints. In the future, we plan to expand the group of volunteers with different degrees of rheumatoid arthritis, age and gender to develop a methodology for differentiating pathology. It can be assumed that the combination of all wavelengths accompanied by optical clearing will provide the most complete information about the joint condition and will allow differentiating between diseased and healthy joints using machine learning.

Acknowledgements

The study was supported by RFBR grant No. 20-52-56005.

Disclosures

The authors declare that they have no conflict of interest.

References

1. A. Shah, E. W. St. Clair, "Rheumatoid Arthritis," Chapter 358 in Harrison's Principle of Internal Medicine, 21st Ed., J. Loscalzo, A. Fauci, D. Kasper, S. Hauser, D. Longo, and J. Jameson (Eds.), McGraw Hill, United States, 2751−2765 (2022). ISBN: 9781264268504.
2. B. Shah, "Rheumatoid Arthritis," American College of Rheumatology, 2023 (accessed 10 April 2024). [http://www.rheumatology.org/I-Am-A/Patient-Caregiver/Diseases-Conditions/Rheumatoid-Arthritis].
3. P. Bøyesen, E. A. Haavardsholm, D. van der Heijde, M. Østergaard, H. B. Hammer, S. Sesseng, and T. K. Kvien, "Prediction of MRI erosive progression: a comparison of modern imaging modalities in early rheumatoid arthritis patients," Annals of the Rheumatic Diseases 70(1), 176−179 (2011).
4. M. Boesen, K. Ellegaard, L. Boesen, M. A. Cimmino, P. S. Jensen, L. Terslev, S. Torp-Pedersen, B. Danneskiold-Samsøe, and H. Bliddal, "Ultrasound Doppler score correlates with OMERACT RAMRIS bone marrow oedema and synovitis score in the wrist joint of patients with rheumatoid arthritis," Ultraschall in der Medizin 33(7), E155−E172 (2012).
5. J. Beuthan, U. Netz, O. Minet, A. D. Klose, A. H. Hielscher, A. Scheel, J. Henniger, and G. Muller, "Light scattering study of rheumatoid arthritis," Quantum Electronics 32(11), 945−952 (2002).
6. O. Minet, U. Zabarylo, and J. Beuthan, "Deconvolution of laser-based images for monitoring rheumatoid arthritis," Laser Physics Letters 2(11), 556−563 (2005).
7. O. Minet, P. Scheibe, and U. Zabarylo, "Diagnosis of rheumatoid arthritis using light: correction of motion artefacts and color visualization of multispectral images," Journal of Biophotonics 3(3), 130−137 (2010).
8. D. Lighter, J. Hughes, I. Styles, A. Filer, and H. Dehghani, "Multispectral, non-contact diffuse optical tomography of healthy human finger joints," Biomedical Optics Express 9(4), 1445-1460 (2018).
9. A.-M. Glimm, L. I. Sprenger, I. K. Haugen, U. Mansmann, S. Hermann, Th. Häupl, P. Hoff, G.-R. Burmester, M. Backhaus, L. Le, and S. Ohrndorf, "Fluorescence optical imaging for treatment monitoring in patients with early and active rheumatoid arthritis in a 1-year follow-up period," Arthritis Research & Therapy 21(1), 209 (2019).
10. J. H. Lee, S. Y. Jung, G. K. Park, K. Bao, H. Hyun, G. El Fakhri, and H. S. Choi, "Fluorometric imaging for early diagnosis and prognosis of rheumatoid arthritis," Advanced Science 7(1), 1902267 (2019).
11. J.-D. Albert, V. Monbet, A. Jolivet-Gougeon, N. Fatih, M. Le Corvec, M. Seck, F. Charpentier, G. Coiffier, C. Boussard-Pledel, B. Bureau, P. Guggenbuhl, and O. Loréal, "A novel method for a fast diagnosis of septic arthritis using mid infrared and deported spectroscopy," Joint Bone Spine 83(3), 318−323 (2016).
12. M. Nishiyama, T. Namita, K. Kondo, M. Yamakawa, and T. Shiina, "Ring-array photoacoustic tomography for imaging human finger vasculature," Journal of Biomedical Optics 24(9), 096005 (2019).
13. O. Minet, H. Gajewski, J. A. Griepentrog, and J. Beuthan, "The analysis of laser light scattering during rheumatoid arthritis by image segmentation," Laser Physics Letters 2(11), 556−563 (2007).
14. U. Zabarylo, O. Minet, "Pseudo color visualization of fused multispectral laser scattering images for optical diagnosis of rheumatoid arthritis," Laser Physics Letters 7(1), 73−77 (2010).
15. D. Lighter, J. Hughes, I. Styles, A. Filer, and H. Dehghani, "Multispectral, non-contact diffuse optical tomography of healthy human finger joints," Biomedical Optics Express 9(4), 1445−1460 (2018).
16. E. A. Kolesnikova, A. S. Kolesnikov, U. Zabarylo, O. Minet, E. A. Genina, A. N. Bashkatov, and V. V. Tuchin, "Optical clearing of human skin for the enhancement of optical imaging of proximal interphalangeal joints," Proceedings of SPIE 9031, 90310C (2014).

17. H. Q. Zhong, Z. Y. Guo, H. J. Wei, C. C. Zeng, H. L. Xiong, Y. H. He, and S. H. Liu, "Quantification of glycerol diffusion in human normal and cancer breast tissues in vitro with optical coherence tomography," Laser Physics Letters 7(4), 315−320 (2010).
18. T. Son. B. Jung, "Cross-evaluation of optimal glycerol concentration to enhance optical clearing efficacy," Skin Research and Technology 21(3), 327−332 (2015).
19. V. D. Genin, D. K. Tuchina, A. J. Sadeq, E. A. Genina, V. V. Tuchin, and A. N. Bashkatov, "Ex vivo investigation of glycerol diffusion in skin tissue," Journal of Biomedical Photonics & Engineering 2(1), 010303 (2016).
20. D. K. Tuchina, A. N. Bashkatov, A. B. Bucharskaya, E. A. Genina, and V. V. Tuchin, "Study of glycerol diffusion in skin and myocardium ex vivo under the conditions of developing alloxan-induced diabetes," Journal of Biomedical Photonics & Engineering 3(2), 020302 (2017).
21. K. V. Berezin, K. N. Dvoretskiy, M. L. Chernavina, A. M. Likhter, V. V. Smirnov, I. T. Shagautdinova, E. M. Antonova, E. Yu. Stepanovich, E. A. Dzhalmuhambetova, and V. V. Tuchin, "Molecular modeling of immersion optical clearing of biological tissues," Journal of Molecular Modeling 24, 45 (2018).
22. V. D. Genin, E. A. Genina, V. V. Tuchin, and A. N. Bashkatov, "Glycerol effects on optical, weight and geometrical properties of skin tissue," Journal of Innovative Optical Health Sciences 14(5), 2142006 (2021).
23. T. Yu, D. Zhu, L. Oliveira, E. A. Genina, A. N. Bashkatov, and V. V. Tuchin, "Tissue optical clearing mechanisms," Chapter 1 in Handbook of tissue optical clearing: new prospects in optical imaging, V. Tuchin, D. Zhu, and E. A. Genina (Eds.), CRC Press, Boca Raton, 3−30 (2022).
24. J. Jiang, M. Boese, P. Turner, and R. K. Wang, "Penetration kinetics of dimethyl sulphoxide and glycerol in dynamic optical clearing of porcine skin tissue in vitro studied by Fourier transform infrared spectroscopic imaging," Journal of Biomedical Optics 13(2), 021105 (2008).
25. M. Zimmerley, R. A. McClure, B. Choi, and E. O. Potma, "Following dimethyl sulfoxide skin optical clearing dynamics with quantitative nonlinear multimodal microscopy," Applied Optics 48(10), D79–D81 (2009).
26. J.-M. Andanson, K. L. A. Chan, and S. G. Kazarian, "High-throughput spectroscopic imaging applied to permeation through the skin," Applied Spectroscopy 63(5), 512−517 (2009).
27. I. Elisia, H. Nakamura, V. Lam, E. Hofs, R. Cederberg, J. Cait, M. R. Hughes, L. Lee, W. Jia, H. H. Adomat, E. S. Guns, K. M. McNagny, I. Samudio, and G. Krystal, "DMSO represses inflammatory cytokine production from human blood cells and reduces autoimmune arthritis," PLoS ONE 11(3), e0152538 (2016).
28. V. D. Genin, A. B. Bucharskaya, N. A. Navolokin, G. S. Terentjuk, N. G. Khlebtsov, V. V. Tuchin, and E. A. Genina, "Influence of immersion agents on optical parameters of bio-tissues during laser photothermal therapy of tumor: pilot study," Optics and Spectroscopy 130(6), 678−687 (2022).
29. E. A. Genina, A. N. Bashkatov, E. A. Kolesnikova, M. V. Basco, G. S. Terentyuk, and V. V. Tuchin, "Optical coherence tomography monitoring of enhanced skin optical clearing in rats in vivo," Journal of Biomedical Optics 19(2), 021109 (2014).
30. S. V. Zaitsev, Y. I. Svenskaya, E. V. Lengert, G. S. Terentyuk, A. N. Bashkatov, V. V. Tuchin, and E. A. Genina, "Optimized skin optical clearing for optical coherence tomography monitoring of encapsulated drug delivery through the hair follicles," Journal of Biophotonics 13(4), e201960020 (2020).
31. A. Corlu, R. Choe, T. Turduran, K. Lee, M. Schweiger, S. R. Arridge, E. M. Hillman and A. G. Yodh, "Diffuse optical tomography with spectral constraints and wavelength optimization," Applied Optics 44(11), 2082−2093 (2005).
32. C. T. Ng, M. Biniecka, A. Kennedy, J. McCormick, O. Fitzgerald, B. Bresnihan, D. Buggy, C. T. Taylor, J. O'Sullivan, U. Fearon, and D. J. Veale, "Synovial tissue hypoxia and inflammation in vivo," Annals of the Rheumatic Diseases 69(7), 119776 (2010).
33. K. H. Falchuk, E. J. Goetzl, and J. P. Kulka, "Respiratory gases of synovial fluids: an approach to synovial tissue circulatory-metabolic imbalance in rheumatoid arthritis," The American Journal of Medicine 49(2), 223−231 (1970).
34. S. A. Prahl, "Optical absorption of hemoglobin," OMLC, 1999 (accessed 10 April 2024). [https://omlc.org/spectra/hemoglobin/].
35. F. M. McQueen, "Bone marrow edema and osteitis in rheumatoid arthritis: the imaging perspective," Arthritis Research & Therapy 14(5), 224 (2012).
36. A. N. Bashkatov, E. A. Genina, V. I. Kochubey, and V. V. Tuchin, "Optical properties of human skin, subcutaneous and mucous tissues in the wavelength range from 400 to 2000 nm," Journal of Physics D: Applied Physics 38(15), 2543 (2005).

Therapeutic and Diagnostic Algorithm for Patients with Obstructive Jaundice Based on the Estimation of the Optical Characteristics of the Liver and Bile

Elena V. Potapova[1*], Ksenia Y. Kandurova[1], Vadim N. Prizemin[1], Dmitry S. Sumin[2], and Andrian V. Mamoshin[1,2]

[1] Research and Development Center of Biomedical Photonics, 95 Komsomolskaya str., Orel State University, Orel 302026, Russian Federation

[2] Orel Regional Clinical Hospital, 10 Pobedy Blvd., Orel 302028, Russian Federation

*e-mail: potapova_ev_ogu@mail.ru

Abstract. Timely detection and prognosis of liver failure play an important role in improving treatment outcomes for patients with biliary obstruction. The study describes the use of optical biopsy methods to determine the functional state of the liver in patients with obstructive jaundice syndrome during and after antegrade biliary decompression. Fluorescence spectroscopy method allowed us to detect the patients suffering from severe liver failure during biliary drainage with high sensitivity, specificity, and accuracy (0.88, 0.98, and 0.96) to provide emergency treatment by extracorporeal detoxification methods. Raman spectroscopy method was proposed to be used to obtain additional diagnostic information on the recovery of excretory function of the liver to determine the possibility of transition to the next stage of treatment of the underlying disease. The scheme of treatment and diagnostic algorithm is proposed, which shows the position of optical diagnostic methods in the standard treatment protocol of patients with obstructive jaundice of different etiology. © 2024 Journal of Biomedical Photonics & Engineering.

Keywords: liver; obstructive jaundice; liver failure; decompression of bile ducts; optical biopsy; fluorescence spectroscopy; Raman spectroscopy; bile.

Paper #9149 received 8 Aug 2024; revised manuscript received 18 Sep 2024; accepted for publication 19 Sep 2024; published online 14 Oct 2024. doi: 10.18287/JBPE24.10.040304.

1 Introduction

Diagnosis and treatment of hepatopancreaticoduodenal diseases complicated by biliary obstruction remain an urgent problem in medicine. The number of patients with obstructive jaundice (OJ) of various etiologies is increasing every year, mainly due to changes in lifestyle and diet. OJ is a syndrome that develops as a result of impaired bile outflow through the intrahepatic and extrahepatic biliary ducts to the duodenum [1]. Biliary obstruction can be caused by cholelithiasis, inflammatory processes, benign and malignant diseases of hepatopancreaticoduodenal organs. One of the key factors worsening the prognosis of patients with OJ syndrome is the development of liver disorders based on hepatocyte dysfunction. Disruption of bile flow leads to accumulation of bile acids, bilirubin, and other metabolites in the liver and systemic circulation, resulting in the development of liver failure (LF) [2–4]. Increasing hyperbilirubinemia and functional LF cause pathological disorders in the whole organism, including vital organs and systems such as brain, kidneys, intestines, immune system, and others.

Surgical treatment in the presence of hyperbilirubinemia increases the risk of intra- and postoperative complications, so the treatment of patients with OJ syndrome is usually performed in two stages within the concept of preoperative biliary drainage [5]. In this approach, cholestasis is treated with minimally invasive procedures, followed by radical surgery after bilirubinemia resolves [6]. The placement of external, external-internal, or internal drainage systems is aimed at

early decompression of bile ducts, adequate, predictable, manageable and effective temporary or permanent biliary outflow and is the main way of temporary or definitive treatment of OJ, interruption of LF progression and prevention of complications development [7, 8]. However, LF may progress despite the drainage of the bile ducts in some clinical situations [9]. This is due to the fact that some patients have quite severe LF, and decompression procedures not only do not contribute to a rapid recovery, but actually aggravate the situation and require the use of extracorporeal hemocorrection methods or, in particularly severe cases, immediate intensive therapy for progressive LF. Thus, the success of treatment in patients with OJ syndrome depends significantly on the functional state of the liver [10, 11]. Clinical picture, common laboratory, and instrumental parameters of liver dysfunction developed due to OJ do not always correspond to the degree of liver damage, which requires further search for criteria to assess the severity of the condition of such patients [12].

As mentioned above, the development of biliary hypertension is one of the causes of impaired blood supply to the liver, resulting in damage to the membranes of hepatocytes and cholangiocytes. Accumulation of bilirubin and bile acids leads to inhibition of oxidative phosphorylation and antioxidant defenses of the liver, decrease of bioenergetic processes in mitochondria of hepatocytes [13]. As a result, significant impairment of oxygen utilization by cells is observed, which leads to pronounced tissue hypoxia of the liver. The degree and speed of pathological changes in liver tissue depend on the rate of increase in biliary hypertension, microcirculatory disturbance, tissue hypoxia, presence of inflammation in ducts and duration of disease [14]. It is also known that the composition of bile is closely related to the clinical severity, progression and prognosis of liver diseases, and its components can be reliable diagnostic and prognostic markers of the functional state of the organ [15–18].

Optical methods are characterized by high sensitivity to metabolic and biochemical changes in biological tissues and fluids [19–21]. One of the optical biopsy techniques widely used to monitor cellular and tissue metabolism in the liver parenchyma is fluorescence spectroscopy (FS) [22–26]. In previous work, we have shown that the use of deconvolution analysis of FS spectra allows us to identify the contribution of fluorophores reflecting changes in the liver of OJ patients [27]. Such fluorophores include NAD(P)H, flavins, bilirubin, vitamin A, protoporphyrins, and lipofuscin. Raman spectroscopy (RS) is widely used for highly sensitive physicochemical analysis of biological fluids [28]. Previously, we have shown that the determination of bilirubin concentration in bile obtained through the drainage catheter by RS allowed us to predict the recovery of excretory function of the liver and the dynamics of recovery of OJ patients after antegrade decompression of biliary tracts [29].

The aim of this work was to retrospectively study patients with OJ syndrome, different degrees of LF, and different dynamics of the postoperative period after antegrade biliary decompression, including the assessment of the functional state of the liver parenchyma by FS and bile composition by RS, as well as to develop a therapeutic and diagnostic algorithm including optical diagnostic methods in the standard protocol of treatment of OJ patients.

2 Materials and Methods

2.1 Object of Study

The study included 40 patients (66 ± 13 years) with OJ syndrome of different etiology (malignant tumors of the hepatopancreaticoduodenal area – 30 patients, gallstone disease – 8 patients, pancreatic head cyst with compression of the common bile duct – 2 patients). All patients underwent external percutaneous transhepatic cholangiostomy. According to clinical and laboratory parameters (results of blood biochemical analysis – the level of bilirubin fractions, alkaline phosphatase (ALP), alanine transaminase (ALT), aspartate transaminase (AST), creatinine, urea and total protein) before biliary decompression and the results of dynamic follow-up after the procedure, the patients were retrospectively divided into groups with positive (n=33) and negative (n=7) dynamics of the course of the postoperative period. In addition, it was possible to obtain bile samples from the common bile duct of 3 other patients after surgery for cholelithiasis. These patients did not have OJ syndrome and had a drainage catheter placed, so they could be considered as a control group without violations of the functional state of the liver. All studies were conducted in accordance with the Declaration of Helsinki of 1964 and its subsequent amendments and were approved by the local bioethics committee of Orel State University (Protocol № 28 dated 31.05.2023). All volunteers gave their informed consent for the study.

Fluorescence spectra were recorded at 1 or 2 points in the liver parenchyma near the bile ducts after creating primary access to the biliary tree under ultrasound and X-ray control. The total amount of measured spectra used for further analysis included 40 measurements for the positive dynamics group and 8 measurements for the negative dynamics group. Bile sampling for the study of optical properties by RS was performed during antegrade decompression of the biliary system by puncture needle and then every 3 days through the cholangiostomy drainage catheter. Reference samples for the control group were obtained through the drainage catheter 5 days after surgery.

2.2 Experimental Setup

Fluorescence spectra were recorded using the FS channel of a specially designed optical biopsy device [27]. Autofluorescence was excited at wavelengths of 365 nm and 450 nm. Fluorescence spectra were recorded using a CCD spectrometer in the 350−1000 nm range after attenuation of backscattered radiation from the sources. The optical radiation was transmitted through a small

diameter 1 mm fiber optic probe. The exposure time for measuring a spectrum was 1.5 s. For each patient, 5 fluorescence spectra were recorded at each wavelength at 1−2 study points and then averaged for further processing.

The study of the spectral characteristics of bile by RS was performed using the setup described in Ref. [29]. The volume of sample placed in the measurement cuvette was 5 ml. For each sample, 3 Raman spectra were recorded and averaged. In order to obtain Raman spectra of bile with a high signal-to-noise ratio, an exposure time of 90 s was chosen based on preliminary experiments. To reduce the contribution of fluorescence intensity to the total signal and to avoid photobleaching of the sample, the power of the 785 nm laser source was set to 16.5 mW.

2.3 Processing of Experimental Data

The processing of the signals recorded by FS in the liver parenchyma was performed in several steps. The averaged fluorescence spectra were smoothed with the Savitzky-Golay filter to remove noise but not to affect the shape of the spectra. The smoothed spectra were normalized from 0 to 100. The next step involved a non-linear deconvolution procedure based on the Levenberg-Marquardt algorithm to calculate combinations of Gaussian curves reflecting the contribution of each fluorophore to the total signal obtained from the liver tissue.

The fluorescence spectra were characterized by Gaussian curves related to the fluorescence of the following substances (Fig. 1(a, c)): collagen and elastin (curve 1), NAD(P)H (2) - reduced forms of nicotinamideneadenine dinucleotide (NADN) and nicotinamideneadenine dinucleotide phosphate (NADPH), free fatty acids (3), vitamin A (4), bilirubin (5, 7), flavins (6), lipofuscin (8), and porphyrins (9, 10). The number of curves, their central wavelengths and full width at half maximum values were initially selected from literature data on fluorophores of liver parenchyma [27] and then adjusted empirically to provide the best possible fit to the measured spectra. Parameters analyzed included peak heights and proportions of areas under Gaussian curves in the total area of the fluorescence spectra.

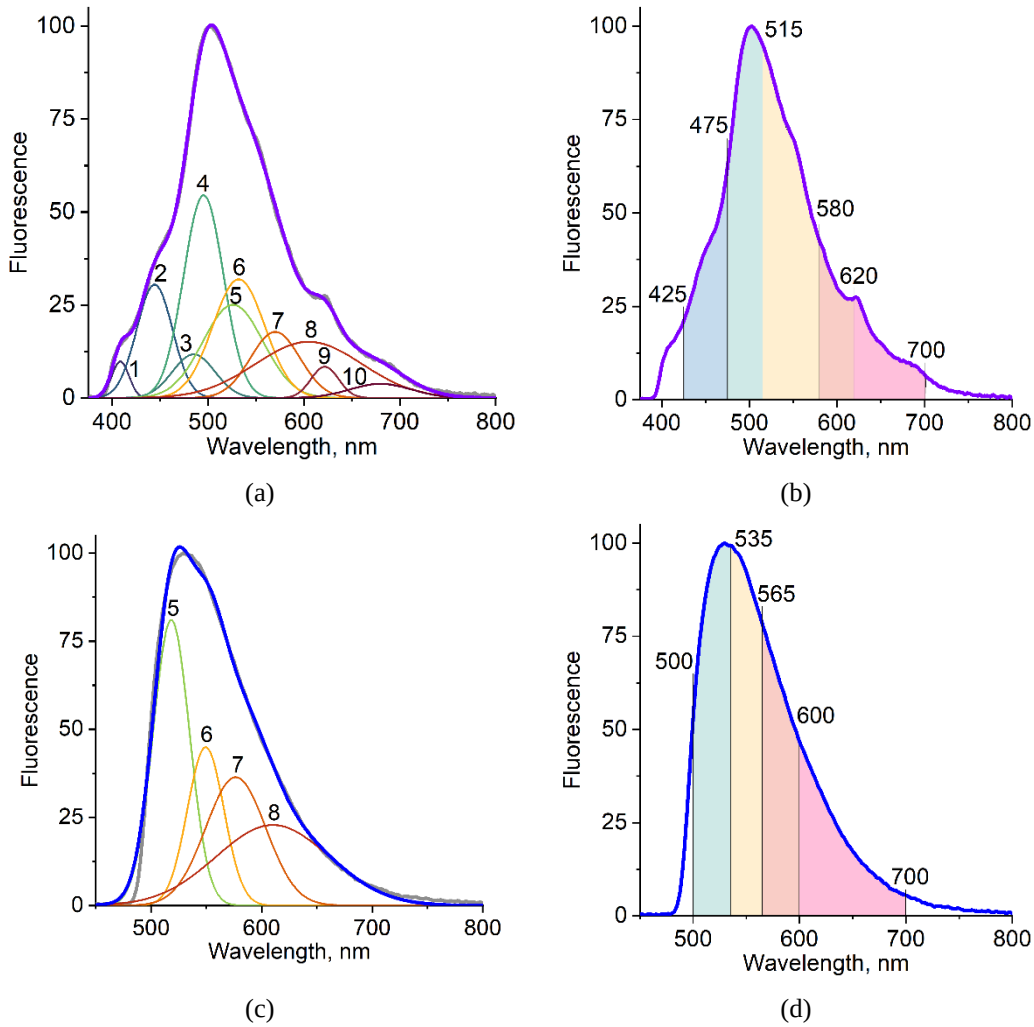


Fig. 1 Fluorescence spectra parameters calculated for analyzing: (a) fluorophores curves for 365 nm excitation wavelength, (b) fluorophores curves for 450 nm excitation wavelength, (c) bands for calculating areas under 365 nm spectrum, (d) bands for calculating areas under 450 nm spectrum.

In addition, the areas under the spectral curves in different spectral bands were calculated to take into account the simultaneous contribution of fluorophores with overlapping fluorescence spectra (Fig. 1(b, d)), as well as the areas of the spectra before and after the average wavelength of maximum fluorescence intensity (425−515 and 515−700 nm for the 365 nm excitation channel; 500−535 and 535−700 nm for the 450 nm excitation channel). Statistical significance of differences between groups was tested using the non-parametric Mann-Whitney *U* test due to limited sample size and lack of confirmed normal distribution of results in all compared samples.

The identified differences were used to select combinations of parameters promising for further development of a classifier to assess the functional state of the liver and identify severe LF in OJ patients. A linear discriminant analysis (LDA) approach was used to build a classification model and identify the features that best separate patients with OJ syndrome according to the expected positive or negative dynamics of the postoperative period after minimally invasive biliary drainage.

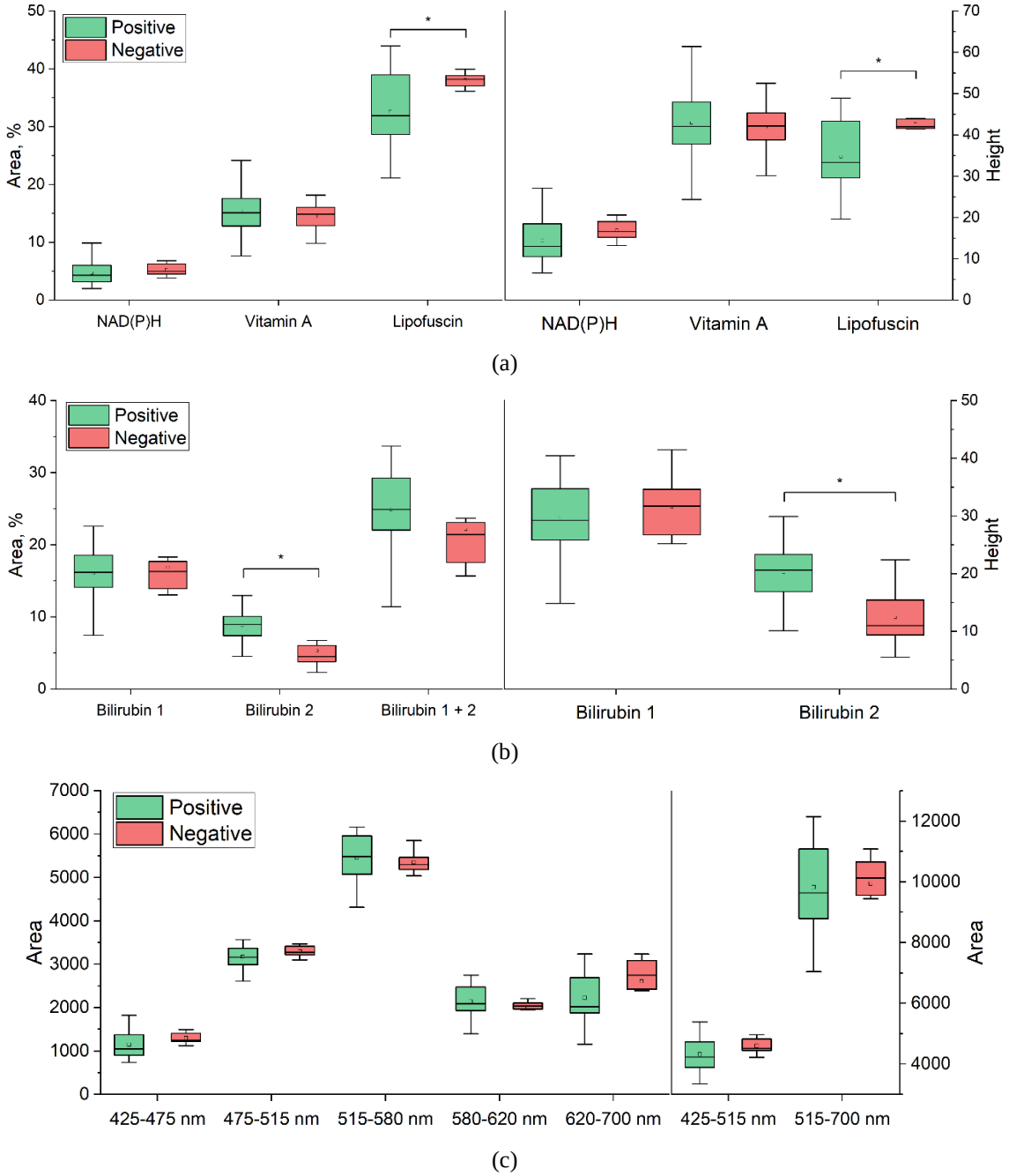
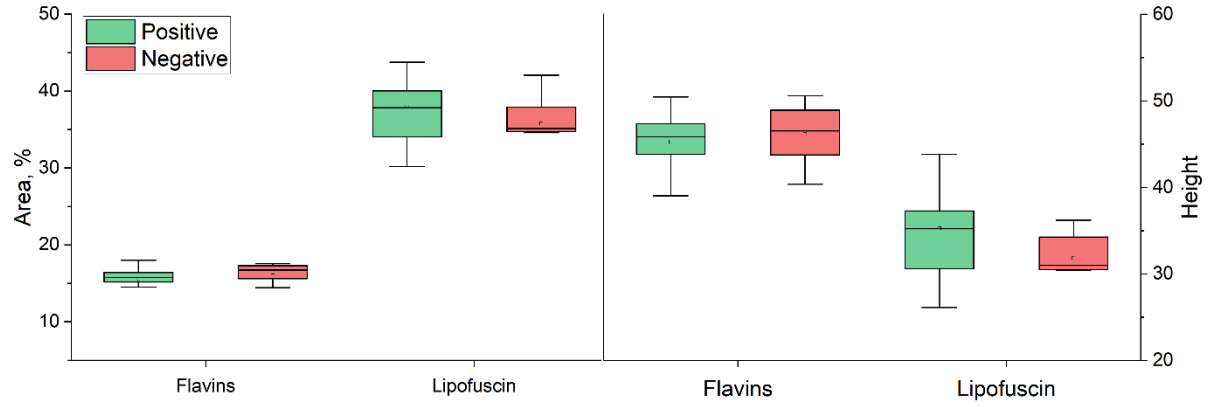
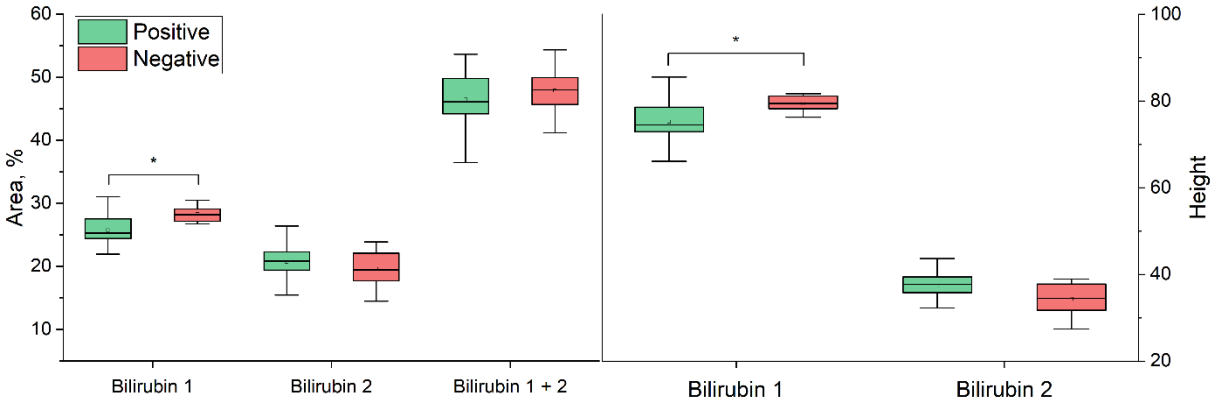


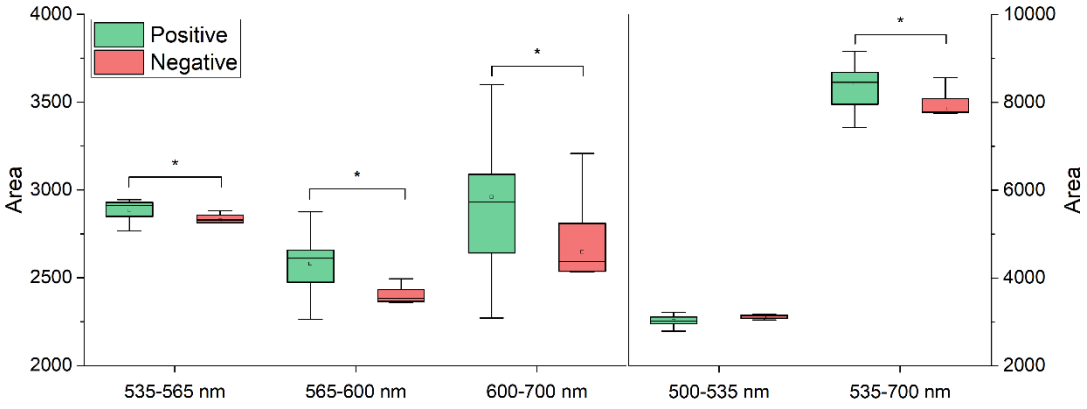
Fig. 2 Comparison of the parameters obtained by FS at 365 nm excitation: (a, b) percentage of the area under the Gaussian curves and their peaks heights for major liver tissue fluorophores, (c) areas under the spectra curve in different wavelength ranges. Statistically significant differences for *p < 0.05.



(a)



(b)



(c)

Fig. 3 Comparison of the parameters obtained by FS at 450 nm excitation: (a, b) percentage of the area under the Gaussian curves and their peaks heights for major liver tissue fluorophores, (c) areas under the spectra curve in different wavelength ranges. Statistically significant differences for *p < 0.05.

The result of LDA is the discriminant function, which should provide high sensitivity and specificity and an acceptable level of type 1 error (probability of a false negative result). The discriminant function is described by the following Eq.:

$$f(x) = \sum_1^n a_i x_i + c,$$

where $X = (x_1,\ldots,x_n)$ – vector of discriminant variables; $a = (a_1,\ldots,a_n)$ – vector of discriminant function coefficients; n – number of variables; c – a constant term.

The diagnostic criterion is a classification model as a discriminant function that allows us to classify the presence or absence of negative dynamics of the patient's condition after biliary decompression. To develop the diagnostic criterion, we calculated the vector of discriminant function coefficients and its constant term for each combination of discriminant variables. To select the most appropriate criterion for this diagnostic task, the sensitivity (proportion of true positive cases of negative dynamics), specificity (proportion of true negative cases), and accuracy (proportion of correctly predicted

cases) were evaluated, as well as the area under the error curve (AUC).

During RS spectra processing, the fluorescence background was removed by fitting the fluorescence spectrum using a polynomial approximation of the obtained data. The polynomial degree was set to 10 to provide the best possible fit according to the literature and empirical adjustments [30, 31]. The spectra were smoothed by the Savitsky-Golay filter with the following filter parameters: 15 number of sliding window points, 3 polynomial degree. The part of the spectrum in the 1000−1800 cm^{-1} range was analyzed. Detection of bilirubin was carried out in the following spectral bands: 1258−1264 cm^{-1} and 1615−1620 cm^{-1} [32].

All data processing was performed using OriginPro 2021 software.

3 Results

Fig. 2 shows the results of the comparison of the calculated fluorescence parameters under excitation at 365 nm for the two groups of patients analyzed. Despite the small number of patients who remained in the most severe condition after biliary decompression, changes in the curves and spectral areas reflecting the content of certain fluorophores were observed mainly in relation to bilirubin and lipofuscin.

The data obtained at 450 nm (Fig. 3) were characterized by statistically significant differences in the areas of the spectrum for almost all bands, which may be due in part to the optical properties of bilirubin, which has a higher absorption at 450 nm.

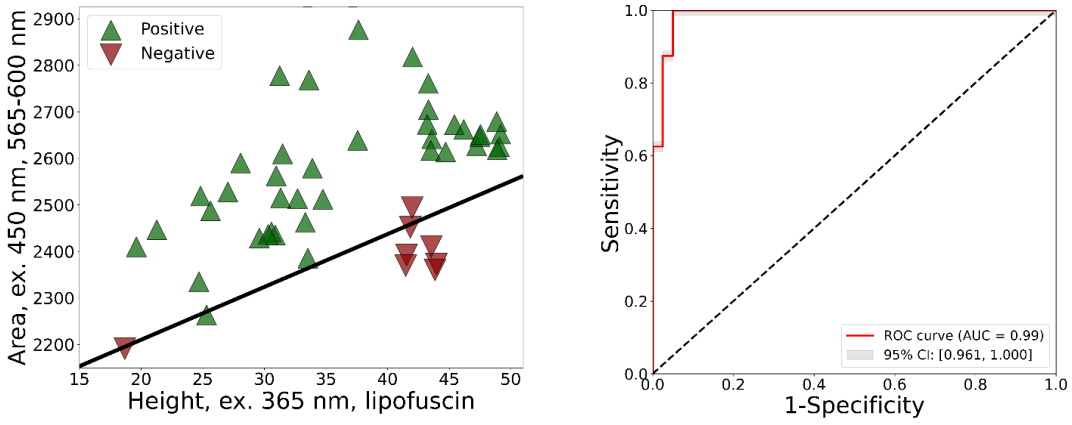
Table 1 shows the results of LDA for dividing the data into two groups (patients with positive and negative state dynamics after biliary decompression) for the pairs of discriminant variables with the highest sensitivity, specificity, and accuracy scores.

In order to achieve the highest sensitivity, specificity, and accuracy for all the methods used, the discriminant function based on the values of the height of the Gaussian curve of lipofuscin in the 365 nm spectrum $H_{lipofuscin}^{365\,nm}$ and the area of the 450 nm spectrum in the range of 565−600 nm $A_{565-600\,nm}^{450\,nm}$ was chosen as the most acceptable. As a result, the discriminant function of the classification model based on the combinations of parameters obtained by the FS method at 365 nm and 450 nm wavelengths is as follows:

$$f(x) = 0.28 \cdot H_{lipofuscin}^{365\,nm} - 0.02 \cdot A_{565-600\,nm}^{450\,nm} + 48.33. \quad (2)$$

Table 1 Sensitivity and specificity values of the obtained discriminant functions.

Parameters	Variables				
	Area, $A_{bilirubin\,2}^{365\,nm}$	**Area,** $A_{bilirubin\,2}^{365\,nm}$	**Area,** $A_{bilirubin\,2}^{365\,nm}$	**Area,** $A_{lipofuscin}^{365\,nm}$	**Height,** $H_{lipofuscin}^{365\,nm}$
	Area, $A_{bilirubin\,1+\,bilirubin\,2}^{450\,nm}$	**Area,** $A_{565-600\,nm}^{450\,nm}$	**Area,** $A_{535-700\,nm}^{450\,nm}$	**Area,** $A_{565-600\,nm}^{450\,nm}$	**Area,** $A_{565-600\,nm}^{450\,nm}$
Sensitivity	0.88	0.88	0.88	0.88	0.88
Specificity	0.95	0.98	0.95	0.95	0.98
Accuracy	0.94	0.96	0.94	0.94	0.96
AUC	0.94	0.97	0.96	0.99	0.99



(a) (b)

Fig. 4 LDA results: (a) scatter plot of selected parameter values, (b) ROC curve with 95% confidence interval to evaluate the performance of the classification model.

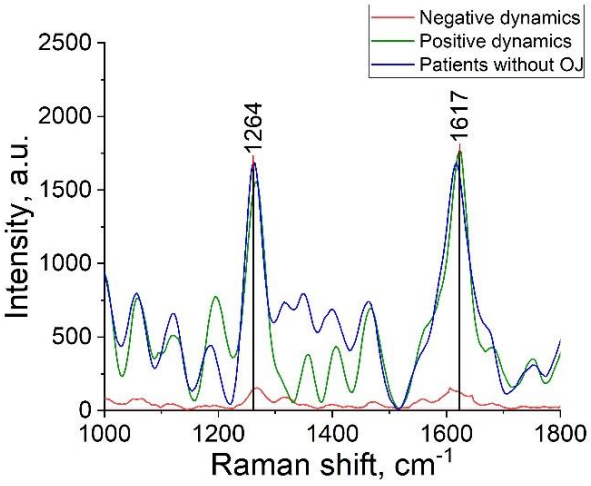
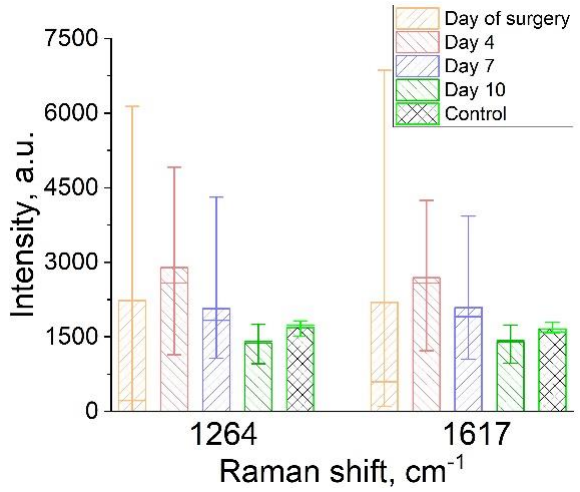
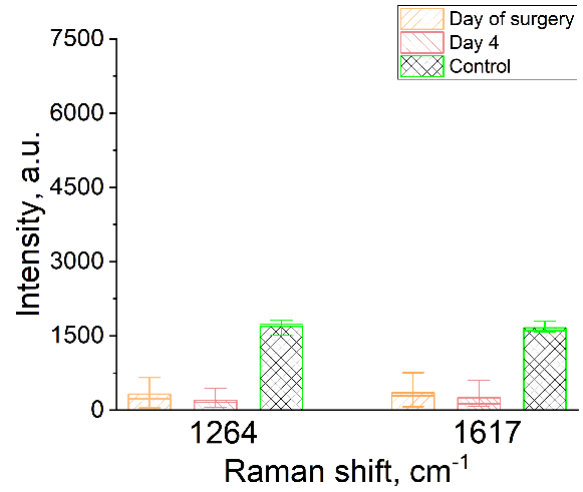


Fig. 5 Examples of Raman spectra of bile from patients without OJ syndrome, patients with negative and positive postoperative dynamics.



(a)



(b)

Fig. 6 Results of RS of patients in dynamics during the treatment: (a) patients with positive postoperative dynamics, (b) patients with negative postoperative dynamics.

Fig. 4 shows the LDA results as a scatter plot with a discriminant line dividing the experimental points into two groups. If the obtained experimental point lies above the discriminant line *f*, it is concluded that the patient will have positive dynamics of the state after biliary decompression, if the experimental point lies below the line *f* - that the patient will have negative dynamics in the postoperative period. Thus, we can conclude that the application of the FS method at 365 nm and 450 nm excitation wavelengths allows us to synthesize the decision rule for identifying patients with positive and negative dynamics of the state after biliary decompression with the probability of false negative results less than 0.2.

Fig. 5 shows typical Raman spectra of the bile samples from the control group as an example of normal bilirubin levels, as well as examples of Raman spectra of patients with suppressed (negative dynamics of the postoperative period) and restored excretory function of the liver (positive dynamics of the postoperative period) after antegrade decompression of biliary tracts. The Raman bands of bilirubin are clearly distinguishable in the spectra, which are caused by the bending and stretching of the C-H bond in the 1260 cm^{-1} wave shift region, and are associated with the bending of the C=H bond in the five-membered carbocycle in the 1615 cm^{-1} wave shift region [33]. Bilirubin peaks were analyzed in the spectral bands 1258−1264 cm^{-1} and 1615−1620 cm^{-1}. The maximum amplitude in the specified range was selected for each patient when processing the statistical data.

Fig. 6 shows Raman spectra of bile from OJ patients with different dynamics of the pathological process in the liver.

On the first day of the study, there was a great variation of data, which was associated with the different functional state of the liver of patients with OJ syndrome admitted to the hospital. Some patients had decreased secretory function due to biliary obstruction, while others had active production of bile in the lumen of biliary capillaries. There were also patients with initially normal excretory function of the liver, which correlated with their rather satisfactory condition according to blood biochemical analysis and general clinical evaluation of the patient's condition by a doctor [29].

Gradually, the patients of the first group showed normalization of Raman peaks in both studied bands (using the present configuration and operating modes of the diagnostic equipment) to the intensities of 1300−1600 a.u. (the level of bilirubin peaks in bile of conditionally healthy volunteers [29]), which correlated with clinical and laboratory data of recovery of liver function and general condition of patients).

The second group of patients showed signs of suppression of hepatic excretory function on the first day of the study. Three days later, it was found that the dynamics of changes in laboratory parameters in these patients indicated an unsatisfactory response of the liver parenchyma to antegrade biliary decompression, and it was necessary to add extracorporeal detoxification methods to the therapy. The patients were transferred to the intensive care unit.

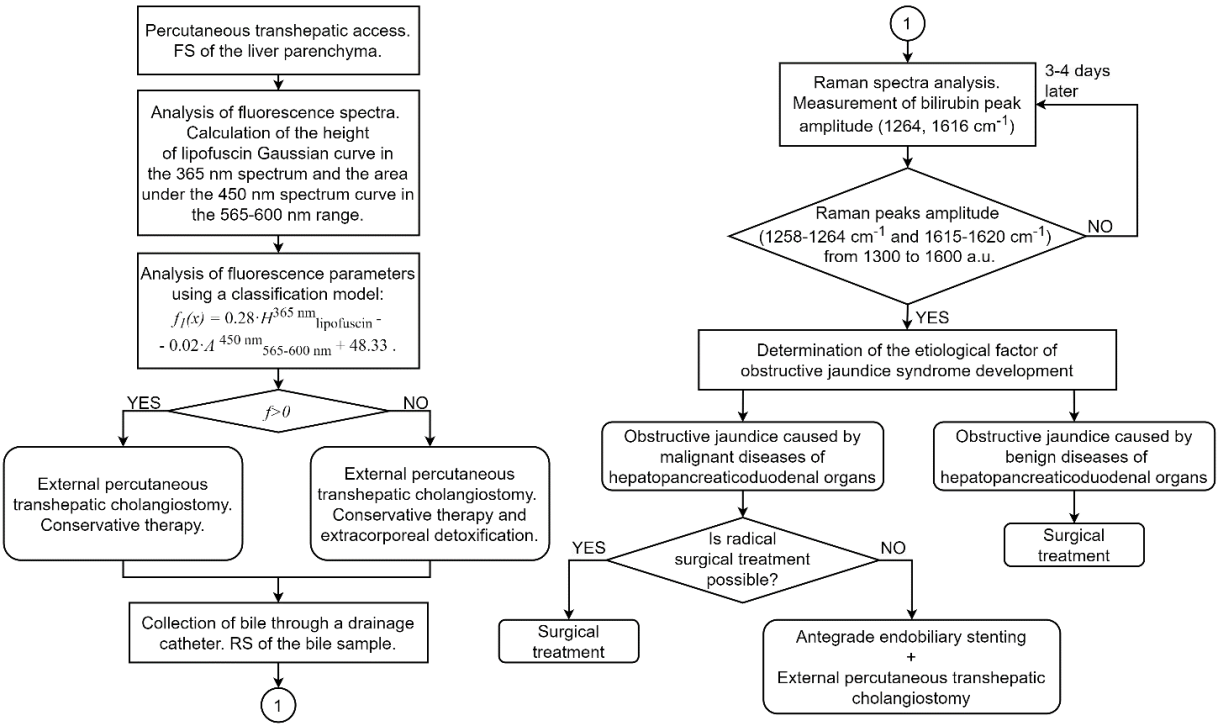


Fig. 7 The scheme of therapeutic and diagnostic algorithm including optical diagnostic methods in the standard treatment protocol for OJ patients.

Based on the retrospective study and established relationships between the course of postoperative period of OJ patients and optical characteristics of liver and bile, detected by optical diagnostic methods, a scheme of therapeutic and diagnostic algorithm was proposed, which shows the place of FS and RS in the standard treatment protocol for patients with OJ syndrome of various etiologies (Fig. 7).

Patients with OJ syndrome underwent standard treatment according to the recommended protocol upon admission to the hospital. During the creation of the primary antegrade transhepatic access, fluorescence spectra are recorded and subsequently processed to calculate diagnostic parameters included in the discriminant function. Based on data analysis, conclusions are drawn about the expected course of postoperative period of patients and the necessity of adding extracorporeal methods of hemocorrection to the therapy. Then, during the postoperative period, bile is collected through a drainage catheter and its optical properties are analyzed by RS method. If the amplitude of bilirubin peaks in spectral bands 1258−1264 cm^{-1} and 1615−1620 cm^{-1} is normalized to the values of 1300−1600 a. u., it is possible, if necessary, to perform additional diagnostic procedures to determine the etiological factor of the development of OJ syndrome and to proceed to the next stage of treatment of the main disease (oncology, gallstone disease, cysts, etc.).

4 Discussion

The retrospective study allowed to find out the relationship between the optical characteristics of the liver and bile with the course of the postoperative period after antegrade biliary decompression.

The assessment of the functional state of the liver using the FS method and the determination of the contributions of individual fluorophores demonstrate the possibility of obtaining new diagnostic information about changes in the structure and metabolic processes in the liver parenchyma. During the deconvolution analysis of the FS spectra, the highest values of fluorescence height were observed for the components characterizing fluorophores with emission spectra closest to the maximum of the whole spectrum, in particular vitamin A and bilirubin. A number of fluorophores, such as structural proteins and fatty acids, porphyrin derivatives (although increases were observed in some cases), made minor contributions to the spectra, but theirfluorescence could influence the area of individual segments that were also evaluated. Previous study has shown statistically significant changes in the fluorescence of NAD(P)H and flavins compared to results from patients without OJ, which is associated with significant impairment of hepatocyte function and development of hypoxia in OJ syndrome [27, 34]. The revealed changes did not show static significance among the groups of OJ patients, but there was a similar tendency of increase of their fluorescence contributions. It is known that with the increase of bilirubin content in liver tissues, oxidative phosphorylation and antioxidant defense disorders progress, and a decrease of bioenergetic processes in mitochondria of hepatocytes is observed, which is reflected in the obtained results [35].

The differences in the metabolic state are not as obvious as in the case of comparison with the patients without OJ, which suggests the search for potential diagnostic criteria among a larger number of fluorophores, which are noted to be used to assess changes in the progression of pathologies. Thus, when analyzing the areas of the fluorophore curves and the areas allocated under the curves of the initial spectrum in a certain range, a significant contribution of lipofuscin was noted, but without statistically significant differences. Lipofuscin, which contributes significantly to the fluorescence spectra, is considered to be a pigment that accumulates as a result of aging [36, 37], but some researchers consider it to be a marker of pathological processes in the liver, the accumulation of which depends on the degree of these processes [38, 39]. Accordingly, the level of this pigment can also be used to assess the metabolic state of cells, like other well-known biomarkers NAD(P)H and flavins [40]. Similarly, the results show an increase in the average contribution of lipofuscin fluorescence in the 365 nm fluorescence spectra for a group of patients with negative postoperative dynamics, which is associated with more severe hepatocyte damage and consequently with LF as a result of prolonged progression of OJ.

A decrease in the relative contribution of lipofuscin to the 450 nm fluorescence spectra may be due to an increase in the total contribution of bilirubin, despite a decrease in the contribution of the second peak of bilirubin fluorescence. Overall, the contribution of these fluorophores can be expected to cause statistically significant changes in the 450 nm fluorescence spectra and high accuracy rates when this parameter is used in various combinations of discriminant variables.

The developed algorithm based on the calculated parameters of FS (the height of the Gaussian curve of lipofuscin in the 365 nm spectrum and the area of the 450 nm spectrum in the range of 565−600 nm) showed high enough values of diagnostic effectiveness of the classifier: sensitivity 0.88, specificity 0.98, and accuracy 0.96 in identifying a group of patients requiring urgent intensive care.

The method of assessing the recovery of hepatic excretory function in patients with OJ syndrome by the intensity of Raman peaks of bilirubin is relatively simple and does not require any additional reagents. Based on the results obtained by RS, we can conclude that normalization of Raman peaks in both areas of the study (using the present configuration and operating modes of the diagnostic equipment) to intensities in the range of 1300−1600 a. u. correlates with clinical and laboratory data on recovery of liver function and general clinical condition of patients. This parameter can be taken into account when deciding on the next stage of OJ treatment.

The developed therapeutic and diagnostic algorithm considers the results of the application of two optical diagnostic methods and allows to develop individual treatment protocols for patients, taking into account the assessment of the functional state of the liver, determined by the optical characteristics of the liver parenchyma and bile. The developed approach may become the basis for improving the results of minimally invasive surgical procedures by identifying patients with severe LF and subjecting them to earlier intensive therapy, as well as by optimally determining the timing of transition to treatment of the patient's underlying disease, for example, lithoextraction in the case of cholelithiasis or tumor removal in the case of oncological etiology.

5 Conclusions

Most surgeons prefer a stepwise approach to surgical tactics in the treatment algorithm for patients with OJ syndrome. Despite numerous data confirming the efficacy of antegrade decompression procedures in resolving OJ syndrome, the question of widespread use of this type of minimally invasive drainage procedure remains controversial. This is due to the fact that in some patients with OJ syndrome with high and prolonged hyperbilirubinemia, removal of the biliary obstruction does not lead to an overall improvement of the condition and LF progression occurs.

The article proposes an approach for obtaining diagnostic information on the optical properties of the liver parenchyma and bile, which includes obtaining quantitative data on the contribution of fluorophores to the fluorescence spectra of liver tissues by decomposing the FS spectra using Gaussian curves and conducting studies on bile samples obtained during percutaneous transhepatic cholangiostomy and dynamically after biliary decompression in patients with OJ. The introduction of optical technologies into the standard algorithm for the treatment of patients with OJ syndrome of various etiologies will reduce the frequency of postoperative complications by identifying patients with severe LF, as well as predict the course of postoperative recovery of the functional state of the liver in order to plan the next stage of treatment.

We assume that this study will form the basis for the development of a point-of-care technology to assess the functional status of the liver and, in the future, lead to a correction of the recommendations for minimally invasive procedures in the biliary tract.

Acknowledgements

The research was supported by the Russian Science Foundation Grant No. 23-25-00487 (https://rscf.ru/en/project/23-25-00487/).

Disclosures

The authors declare that they have no conflict of interest.

References

1. J.-J. Liu, Y.-M. Sun, Y. Xu, H.-W. Mei, W. Guo, and Z.-L. Li, "Pathophysiological consequences and treatment strategy of obstructive jaundice," World Journal of Gastrointestinal Surgery 15(7), 1262–1276 (2023).
2. S.-Y. Cai, X. Ouyang, Y. Chen, C. J. Soroka, J. Wang, A. Mennone, Y. Wang, W. Z. Mehal, D. Jain, and J. L. Boyer, "Bile acids initiate cholestatic liver injury by triggering a hepatocyte-specific inflammatory response," JCI Insight 2(5), (2017).
3. A. Filipović, D. Mašulović, K. Gopčević, D. Galun, A. Igić, D. Bulatović, M. Zakošek, and T. Filipović, "Effect of Percutaneous Biliary Drainage on Enzyme Activity of Serum Matrix Metalloproteinase-9 in Patients with Malignant Hilar Obstructive Hyperbilirubinemia," Medicina 59(2), 336 (2023).
4. E. T. Pavlidis, T. E. Pavlidis, "Pathophysiological consequences of obstructive jaundice and perioperative management," Hepatobiliary & Pancreatic Diseases International 17(1), 17–21 (2018).
5. N. A. Van Der Gaag, J. J. Kloek, S. M. M. De Castro, O. R. C. Busch, T. M. Van Gulik, and D. J. Gouma, "Preoperative Biliary Drainage in Patients with Obstructive Jaundice: History and Current Status," Journal of Gastrointestinal Surgery 13(4), 814–820 (2009).
6. H. Moole, M. Bechtold, and S. R. Puli, "Efficacy of preoperative biliary drainage in malignant obstructive jaundice: a meta-analysis and systematic review," World Journal of Surgical Oncology 14(1), 182 (2016).
7. P. Watanapa, "Recovery patterns of liver function after complete and partial surgical biliary decompression," The American Journal of Surgery 171(2), 230–234 (1996).
8. O. M. Van Delden, J. S. Laméris, "Percutaneous drainage and stenting for palliation of malignant bile duct obstruction," European Radiology 18(3), 448–456 (2008).
9. C. Iacono, A. Ruzzenente, T. Campagnaro, L. Bortolasi, A. Valdegamberi, and A. Guglielmi, "Role of Preoperative Biliary Drainage in Jaundiced Patients Who Are Candidates for Pancreatoduodenectomy or Hepatic Resection: Highlights and Drawbacks," Annals of Surgery 257(2), 191–204 (2013).
10. S. Kumar, S. Masood, U. Srivastava, S. M. Madhavan, S. Chauhan, and A. Pandey, "Factors predicting recovery of liver function after percutaneous drainage in malignant biliary obstruction: the role of hospital-acquired biliary sepsis," Clinical and Experimental Hepatology 6(4), 295–303 (2020).
11. J. Sha, Y. Dong, and H. Niu, "A prospective study of risk factors for in-hospital mortality in patients with malignant obstructive jaundice undergoing percutaneous biliary drainage," Medicine 98(15), e15131 (2019).
12. F. Scheufele, L. Aichinger, C. Jäger, I. E. Demir, S. Schorn, E. Demir, M. Sargut, H. Friess, and G. O. Ceyhan, "INR and not bilirubin levels predict postoperative morbidity in patients with malignant obstructive jaundice," The American Journal of Surgery 222(5), 976–982 (2021).
13. C. Ercin, S. Bagci, Z. Yesilova, A. Aydin, A. Sayal, and G. Erdem, "Oxidative stress in extrahepatic cholestasis," The Anatolian Journal of Clinical Investigation 2(4), 150−154 (2008).
14. M. Tanaka, K. Tanaka, Y. Masaki, M. Miyazaki, M. Kato, K. Kotoh, M. Enjoji, M. Nakamuta, and R. Takayanagi, "Intrahepatic microcirculatory disorder, parenchymal hypoxia and NOX4 upregulation result in zonal differences in hepatocyte apoptosis following lipopolysaccharide- and D-galactosamine-induced acute liver failure in rats," International Journal of Molecular Medicine 33(2), 254–262 (2014).
15. A. Verma, V. Bhatnagar, S. Prakash, and A. Srivastava, "Analysis of bile in various hepatobiliary disease states: A pilot study," Journal of Indian Association of Pediatric Surgeons 19(3), 151−155 (2014).
16. M. L. Shiffman, H. J. Sugerman, J. M. Kellum, and E. W. Moore, "Changes in gallbladder bile composition following gallstone formation and weight reduction," Gastroenterology 103(1), 214–221 (1992).
17. A. P. M. Matton, Y. De Vries, L. C. Burlage, R. Van Rijn, M. Fujiyoshi, V. E. De Meijer, M. T. De Boer, R. H. J. De Kleine, H. J. Verkade, A. S. H. Gouw, T. Lisman, and R. J. Porte, "Biliary Bicarbonate, pH, and Glucose Are Suitable Biomarkers of Biliary Viability During Ex Situ Normothermic Machine Perfusion of Human Donor Livers," Transplantation 103(7), 1405–1413 (2019).
18. I. M. A. Brüggenwirth, R. J. Porte, and P. N. Martins, "Bile composition as a diagnostic and prognostic tool in liver transplantation," Liver Transplantation 26(9), 1177–1187 (2020).
19. S. Palmer, K. Litvinova, A. Dunaev, S. Fleming, D. McGloin, and G. Nabi, "Changes in autofluorescence based organoid model of muscle invasive urinary bladder cancer," Biomedical Optics Express 7(4), 1193−1200 (2016).
20. A. V. Dunaev, V. V. Dremin, E. A. Zherebtsov, I. E. Rafailov, K. S. Litvinova, S. G. Palmer, N. A. Stewart, S. G. Sokolovski, and E. U. Rafailov, "Individual variability analysis of fluorescence parameters measured in skin with different levels of nutritive blood flow," Medical Engineering & Physics 37(6), 574–583 (2015).
21. I. A. Bratchenko, D. N. Artemyev, O. O. Myakinin, Y. A. Khristoforova, A. A. Moryatov, S. V. Kozlov, and V. P. Zakharov, "Combined Raman and autofluorescence ex vivo diagnostics of skin cancer in near-infrared and visible regions," Journal of Biomedical Optics 22(2), 027005 (2017).
22. A. C. Croce, A. Ferrigno, G. Santin, V. M. Piccolini, G. Bottiroli, and M. Vairetti, "Autofluorescence of liver tissue and bile: Organ functionality monitoring during ischemia and reoxygenation," Lasers in Surgery and Medicine 46(5), 412–421 (2014).

23. A. C. Croce, A. Ferrigno, V. Bertone, V. M. Piccolini, C. Berardo, L. G. Di Pasqua, V. Rizzo, G. Bottiroli, and M. Vairetti, "Fatty liver oxidative events monitored by autofluorescence optical diagnosis: Comparison between subnormothermic machine perfusion and conventional cold storage preservation," Hepatology Research 47(7), 668–682 (2017).
24. V. Dremin, E. Potapova, E. Zherebtsov, K. Kandurova, V. Shupletsov, A. Alekseyev, A. Mamoshin, and A. Dunaev, "Optical percutaneous needle biopsy of the liver: a pilot animal and clinical study," Scientific Reports 10(1), 14200 (2020).
25. E. V. Potapova, E. A. Zherebtsov, V. V. Shupletsov, V. V. Dremin, K. Y. Kandurova, A. V. Mamoshin, A. Y. Abramov, and A. V. Dunaev, "Detection of NADH and NADPH levels in vivo identifies shift of glucose metabolism in cancer to energy production," The FEBS Journal 291(12), 2674–2682 (2024).
26. E. A. Zherebtsov, E. V. Potapova, A. V. Mamoshin, V. V. Shupletsov, K. Y. Kandurova, V. V. Dremin, A. Y. Abramov, and A. V. Dunaev, "Fluorescence lifetime needle optical biopsy discriminates hepatocellular carcinoma," Biomedical Optics Express 13(2), 633 (2022).
27. K. Y. Kandurova, D. S. Sumin, A. V. Mamoshin, and E. V. Potapova, "Deconvolution of the fluorescence spectra measured through a needle probe to assess the functional state of the liver," Lasers Surg Med 55(7), 690–701 (2023).
28. K. Kong, C. Kendall, N. Stone, and I. Notingher, "Raman spectroscopy for medical diagnostics — From in-vitro biofluid assays to in-vivo cancer detection," Advanced Drug Delivery Reviews 89, 121–134 (2015).
29. E. V. Potapova, V. N. Prizemin, D. S. Sumin, and A. V. Mamoshin, "Assessment of Bilirubin Concentrations in the Bile of Patients with Obstructive Jaundice by Raman Spectroscopy," Optics and Spectroscopy 132(2), 179–187 (2024).
30. J. Zhao, H. Lui, D. I. McLean, and H. Zeng, "Automated Autofluorescence Background Subtraction Algorithm for Biomedical Raman Spectroscopy," Applied Spectroscopy 61(11), 1225–1232 (2007).
31. L. A. Bratchenko, I. A. Bratchenko, D. N. Artemyev, A. A. Moryatov, J. V. Starikova, E. N. Tupikova, I. A. Platonov, S. V. Kozlov, and V. P. Zakharov, "Conventional Raman and surface-enhanced Raman spectroscopy of ascitic fluid," Journal of Physics: Conference Series 1368(2), 022032 (2019).
32. B. Yang, M. D. Morris, M. Xie, and D. A. Lightner, "Resonance Raman spectroscopy of bilirubins: band assignments and application to bilirubin/lipid complexation," Biochemistry 30(3), 688–694 (1991).
33. L. Ouyang, L. Yao, R. Tang, X. Yang, and L. Zhu, "Biomimetic point-of-care testing of trace free bilirubin in serum by using glucose selective capture and surface-enhanced Raman spectroscopy," Sensors and Actuators B: Chemical 340, 129941 (2021).
34. T. Okaya, K. Nakagawa, F. Kimura, H. Shimizu, H. Yoshidome, M. Ohtsuka, Y. Morita, and M. Miyazaki, "Obstructive jaundice impedes hepatic microcirculation in mice," Hepatogastroenterology 55(88), 2146–2150 (2008).
35. A. C. Croce, A. Ferrigno, C. Berardo, G. Bottiroli, M. Vairetti, and L. G. Di Pasqua, "Spectrofluorometric Analysis of Autofluorescing Components of Crude Serum from a Rat Liver Model of Ischemia and Reperfusion," Molecules 25(6), 1327 (2020).
36. U. T. Brunk, A. Terman, "Lipofuscin: mechanisms of age-related accumulation and influence on cell function," Free Radical Biology and Medicine 33(5), 611–619 (2002).
37. O.-D. Ilie, A. Ciobica, S. Riga, N. Dhunna, J. McKenna, I. Mavroudis, B. Doroftei, A.-M. Ciobanu, and D. Riga, "Mini-Review on Lipofuscin and Aging: Focusing on The Molecular Interface, The Biological Recycling Mechanism, Oxidative Stress, and The Gut-Brain Axis Functionality," Medicina 56(11), 626 (2020).
38. S. G. Hübscher, R. F. Harrison, "Portal lymphadenopathy associated with lipofuscin in chronic cholestatic liver disease," Journal of Clinical Pathology 42(11), 1160–1165 (1989).
39. M. Saif, W. J. Kwanten, J. A. Carr, I. X. Chen, J. M. Posada, A. Srivastava, J. Zhang, Y. Zheng, M. Pinter, S. Chatterjee, S. Softic, C. R. Kahn, K. Van Leyen, O. T. Bruns, R. K. Jain, and M. G. Bawendi, "Non-invasive monitoring of chronic liver disease via near-infrared and shortwave-infrared imaging of endogenous lipofuscin," Nature Biomedical Engineering 4(8), 801–813 (2020).
40. E. I. Lebedzeva, "Histological characteristics of lipofuscin in the liver of rats with experimental cirrhosis," Proceedings of the National Academy of Sciences of Belarus, Medical Series (2), 41–46 (2015). [in Russian]

Study of the Effect of Formaldehyde Fixation on Collagen Optical Properties in the Terahertz Frequency Range

Anastasia I. Knyazkova[1,2*], Oksana D. Kuzminykh[1], Yury V. Kistenev[1,2], and Alexey V. Borisov[1]
[1] Tomsk State University, 36 Lenin ave., Tomsk 634050, Russian Federation
[2] V.E. Zuev Institute of Atmospheric Optics SB RAS, 1 Academician Zuev sq., Tomsk 634055, Russian Federation
[*]e-mail: knyazkova@iao.ru

Abstract. The study investigated the effect of collagen fixation with formaldehyde on optical properties in the THz frequency range. The spectral characteristics transformation of protein solutions occurs due to hydrogen bonds and intermolecular interactions among the various components of the solution. Changes of the optical characteristics of collagen solutions with distilled water, 10% formalin, and 40% formalin in the frequency range from 0.2 THz to 1 THz were studied. © 2024 Journal of Biomedical Photonics & Engineering.

Keywords: terahertz spectroscopy; collagen; formalin.

Paper #9114 received 6 Jun 2024; revised manuscript received 22 Oct 2024; accepted for publication 23 Oct 2024; published online 10 Nov 2024. doi: 10.18287/JBPE24.10.040306.

1 Introduction

Collagen is the main component of the extracellular matrix, which is involved in cell migration and differentiation and accumulates in tissues during oncological processes. The presence of oncological tumors is confirmed by histological examination of tissue biopsy. Histological preparations are usually analyzed using conventional optical microscopy, which does not use information on the molecular composition of the tissue. Combination optical microscopy with spectroscopy can provide more comprehensive information for making a medical decision. However, it is important to understand how the process of formalin fixation during the histological preparation affects the spectral properties of collagen in the tissue. Collagen is the most common protein in mammals (more than 30%). It is a filamentous molecule consisting of three-stranded polypeptides forming a helix. The molecular weight of collagen is about 300 kDa [1].

In histology, during fixation and processing stage, it is essential to minimize post-surgical tissue alterations [2, 3]. Biopsy fixation is the critical initial step to preserve cellular and extracellular material [4]. Aqueous formaldehyde solutions (formalin) are the most commonly employed fixatives [5, 6]. In practice, a neutral solution of 10% formalin is used as a universal fixative.

The treatment of collagen structures with fixing and preservative substances has been demonstrated to enhance collagen resistance to degradation by collagenolytic enzymes, reduces its solubility, and also increases the temperature of hydrothermal contraction [6−8]. Formalin fixation displaces water molecules and introduces new intermolecular interactions between the sample and formalin [9]. Formaldehyde also reversibly forms methanediol, also known as formaldehyde monohydrate or methylene glycol, in the presence of water. Methylene glycol reacts with several side chains of proteins and forms reactive hydroxymethylene groups (−CH_2−OH). A characteristic reaction for formalin fixatives is the formation of intra- and intermolecular methylene cross-links between nucleic acids, as well as between amino acids and nucleic acids [10−14]. Cross-links can form only in the presence of uncharged amino groups, which is possible in neutral solutions.

In the terahertz (THz) spectral range, there are strong absorption lines of many biopolymers, including collagen. Collagen THz absorption spectrum is sensitive to its spatial structure and environment [15−16]. The strong absorption in the THz range of water solutions caused by collective fluctuations in the structure of the network of hydrogen bonds in water makes it possible to control changes in protein conformation in solutions [17]. Moreover, the vibrational, translational and intermolecular collective motions of hydrated water also corresponds to low-frequency THz modes (Fig. 1) [18].

As protein structures break down during unfolding, hydrophobic moieties (amino acid residues), which are otherwise hidden within the native structure are exposed, it influences on the absorption spectrum in the corresponding spectral range.

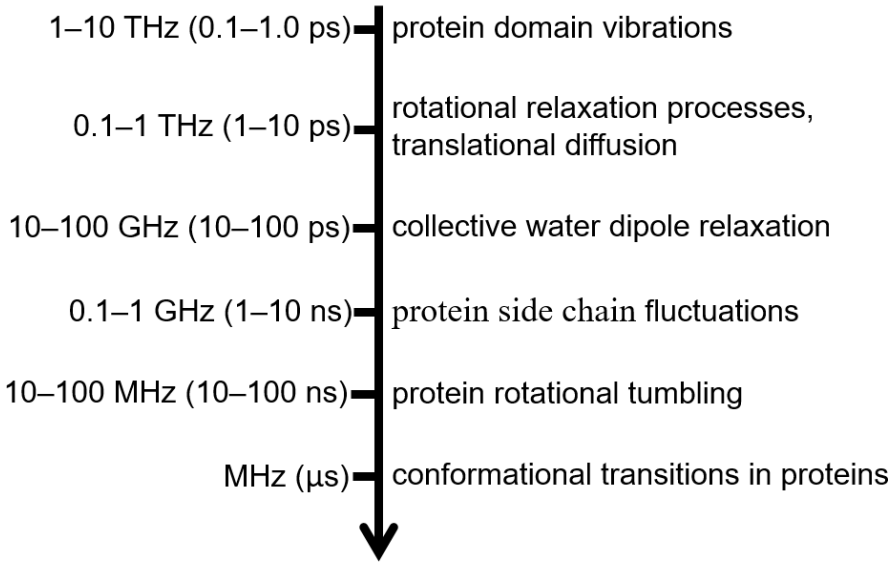


Fig. 1 Hierarchy of time scales for protein motions.

Therefore, analyzing protein THz absorption offers a direct means of assessing structural changes. Havenith et al. investigated the dynamics of protein hydration using THz spectroscopy [19−21]. They established that hydrophobic and hydrophilic protein residues exhibit different THz absorption when interacting with water molecules [19].

The addition of protein molecules to water leads to disruption of the network structure of water hydrogen bonds and the formation of hydrogen bonds between the protein and water molecules. The process of hydration involves not only water molecules directly associated with protein molecules in the primary layer, but also those outside the latter. Therefore, it can be expected significant changes in the collective oscillations of the network structure of hydrogen bonds of water molecules and, consequently, in the THz absorption spectra of protein solutions [22−25]. Manna et al. studied in detail the dependence of the THz absorption of aqueous buffer solutions of the human serum albumin (HSA) protein (up to 2.6 mM protein concentration) on its concentration [23]. The absorption of the solution in the THz range was shown to increase initially, following a clearly linear behavior up to a concentration of $\sim 6 \times 10^{-4}$ mol dm^{-3}, but then gradually decreases with a further increase in the HSA concentration. Such a nonlinear behavior of the change in the absorption of protein solutions in the THz range with increasing protein concentration is explained by the formation of protein aggregates. The critical concentration of collagen aggregation in an aqueous solution was 0.5 mg/ml [26]. R. K. Mitra and D. K. Palit supposed that protein solutions should be considered as three-component systems, where one component is the protein itself, and the other two are water molecules in the hydration layer and bulk water molecules [27].

In the study, we assessed the effect of collagen fixation with formaldehyde on collagen optical properties in the THz frequency range.

2 Materials and Methods

2.1 Sample Preparation

Immersion formalin fixation, a chemical process, significantly alters the molecular structure. This treatment prevents tissue degradation by inhibiting cellular enzymes and decay processes, preserving the vital structure for histological analysis. The principle of fixing liquids is based on the rapid death of cells and protein coagulation. During formalin fixation, collagen can successively lose its quaternary, tertiary and even secondary structure, while the primary structure (amino acid composition) remains intact. Therefore, to describe the process of tissue fixation with formalin when preparing a histological preparation, we will consider a mixture of collagen and water as a simplified model of biological tissue. In this case, it is possible to consider, for example, only hydrolyzed collagen.

Collagen solutions in distilled water, 40% formalin and in 10% formalin were prepared as follows. Dry Collagen Type 1 (Doctor's Best, USA) was weighed on an analytical balance (accuracy 0.001 g) and dissolved in 0.5 ml liquid (i.e. 0.5 ml water, 10% or 40% formalin). Thus, 10 solutions were prepared with a collagen content of 0.026, 0.05, 0.08, 0.125, 0.166, 0.214, 0.27, 0.33, 0.409, 0.5 g, respectively. The amount of components added to the solution and the resulting ratios of the concentrations of collagen (COL), free water (H_2O) and formaldehyde (F) in the prepared solutions of collagen with formalin are shown in Table 1. Sample preparation for dissolving collagen with formaldehyde was carried out as follows: collagen was weighed on an analytical balance GR-120 (AND, Japan) (d = 0.0001 g) and placed in disposable IMEC tubes (volume 2 ml). Formalin was added to each test tube using an ECOHIM single-channel variable volume pipette (ECROSKHIM Co., Ltd, Russia) (100−1000 μl).

Table 1 Percentage ratio of components of collagen solutions with formalin.

	Mass of components, g			Content in solution, %		
	COL	**H_2O**	**F**	**H_2O**	**F**	**COL**
10% formalin	0.026	0.410	0.050	84.4	10.3	5.3
	0.050			80.4	9.8	9.8
	0.080			75.9	9.3	14.8
	0.125			70.1	8.5	21.4
	0.166			65.5	8.0	26.5
	0.214			60.8	7.4	31.8
	0.270			56.2	6.8	37.0
	0.330			51.9	6.3	41.8
	0.409			47.2	5.8	47.1
	0.500			42.7	5.2	52.1
	COL	**H_2O**	**F**	**H_2O**	**F**	**COL**
40% formalin	0.026	0.280	0.180	57.6	37.0	5.3
	0.050			54.9	35.3	9.8
	0.080			51.9	33.3	14.8
	0.125			47.9	30.8	21.4
	0.166			44.7	28.8	26.5
	0.214			41.5	26.7	31.8
	0.270			38.4	24.7	37.0
	0.330			35.4	22.8	41.8
	0.409			32.2	20.7	47.1
	0.500			29.2	18.8	52.1

Mixing of hydrolyzed collagen (in dry form) and formalin was carried out using a Vortex V-1 plus (Biosan, Latvia) at a speed of 2000 rpm until a homogeneous solution was obtained. Ten solutions were prepared for each solvent (distilled water and formalin), with varying concentrations of hydrolyzed collagen ranging from 5 % to 50 % of the total solution volume.

2.2 THz Spectra Acquisition and Analysis

For each individual components of the solutions: dry collagen, distilled water, 10% formalin and 40% formaldehyde, 6 spectra in THz region were obtained. Additionally, 6 spectra were acquired for each collagen concentration (see Section 2.1), representing 60 spectra of collagen solutions with distilled water (6 spectra for each of the 10 concentrations of collagen added to the solution), 60 spectra for solutions with 10% formalin and 60 spectra for solutions with 40% formalin.

Measurements of the absorption and refraction spectra of collagen solutions were carried out using a THz-TDS spectrometer T-spec from EXPLA in transmission mode (Fig. 2) in the frequency range from 0.2 to 1 THz.

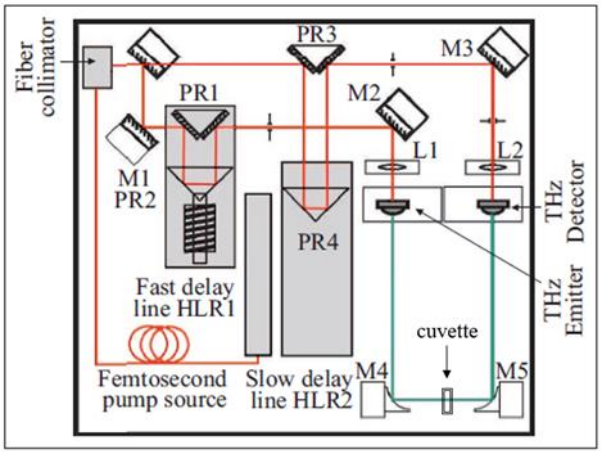


Fig. 2 Scheme of the experimental setup. M1–M5: mirrors; HLR1, HLR2: hollow retro-reflectors; PR1– PR4: prisms; L1, L2: lens.

The studied samples were placed in plastic cuvettes with a thickness of 0.5 mm [28], providing sufficient transparency in the THz spectral range. Scanning with a fast delay line at a frequency of 10 Hz forms a wave front of the electric field of THz radiation (Fig. 3a). The Fourier transform allows us to reconstruct the

dependence of the amplitude of the recorded signal on the frequency, and gives a spectral representation of the THz radiation (Fig. 3b). The obtained values of the signal amplitude allow us to calculate the intensities of the reference I_0 and the signals transmitted through the sample I. Relative transmittance is a measure of how much radiation is attenuated by the material at a given frequency. The intensity of radiation transmitted through the sample (Fig. 3a) can be described using the Bouguer-Lambert-Beer law

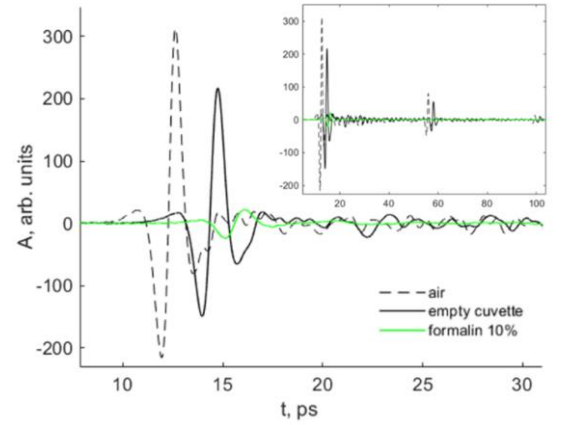
$$I = I_0 e^{-\alpha d}.$$

Here $I_0$is the intensity of the signal generated by the THz emitter, I is the intensity of the signal transmitted through a medium of thickness d, α is the absorption coefficient

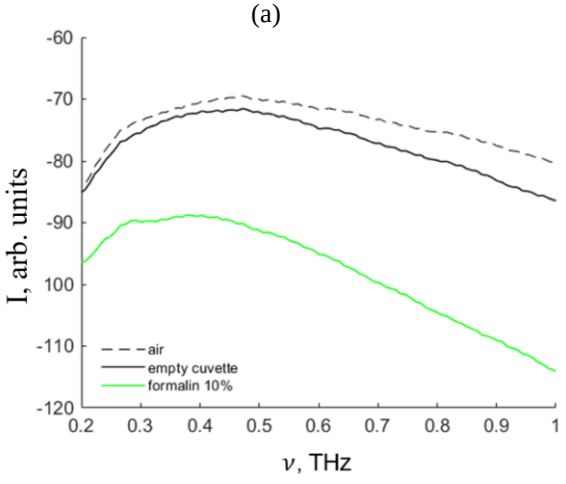
$$\alpha = -\frac{1}{d} ln\left(\frac{I}{I_0}\right).$$

The refractive index through the phase difference has the following form:

$$n = 1 + \frac{c}{\omega d}(\varphi_{samp} - \varphi_{ref}),$$



(a)



(b)

Fig. 3 (a) Incident time-domain THz pulse and (b) frequency domain signal following Fourier transform.

where c is the speed of light, ω is the frequency, d is the thickness of the sample, φ_{sam} and φ_{ref} are the phases of the signal transmitted through the sample and in the absence of the sample, respectively.

The study of solutions was carried out as follows: an empty cuvette was initially placed in the path of the THz radiation beam, as shown in Fig. 2. The THz beam diameter at the focal point was ~3.5−4 mm. The cuvette was placed in the THz spectrometer to ensure the beam passed directly through its center. The THz radiation was focused onto the sample using parabolic mirrors. Then, the reference intensity $I_{ref}(\nu)$ of THz wave passed through an empty cuvette, was recorded (Fig. 3b, black solid line). Next, immediately after mixing the solution, the test sample was placed into the cuvette using a Lenpipet dispenser. The solution was poured evenly along the wall of the cuvette, avoiding the formation of bubbles. Measurement of samples began 5 min after their preparation. The cuvette with the sample was scanned in 2D space with a step of 0.1 mm vertically and horizontally and THz spectra were measured several times in every spatial point. Each intensity $I_{samp}(\nu)$ was averaged over 128 time intervals to obtain a better signal-to-noise ratio. All measurements were carried out at room temperature, 21 ± 1 °C.

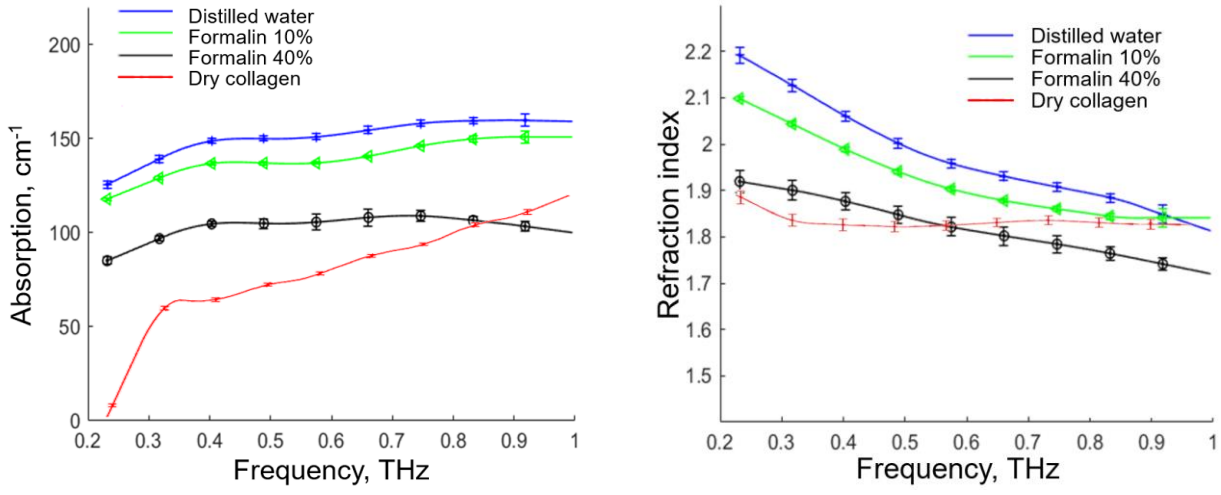
3 Result and Discussion

The averaged THz absorption and refraction spectra of hydrolyzed collagen and the solvents are presented in Fig. 4. The THz spectrum of dry collagen (red line, Fig. 4) shows a sharp rise in absorption in the frequency range from 0.2 to 0.3 THz, followed by a steady increase in the absorption coefficient with increasing THz frequency.

There are no obvious peaks in this spectral range. The THz spectra of distilled water (blue line, Fig. 4) and 10% formalin (green line, Fig. 4) have a similar shape, characterized by a gradual increase in absorption with increasing frequency, with an increase in the presence of dissolved formalin in water (black line, Fig. 4) in absorption becomes less. The refractive index (average in the studied THz frequency range) for hydrolyzed collagen was 1.84 ± 0.06, for distilled water was 1.97 ± 0.02, for 10% and 40% formalin were 1.92 ± 0.02 and 1.82 ± 0.03, respectively.

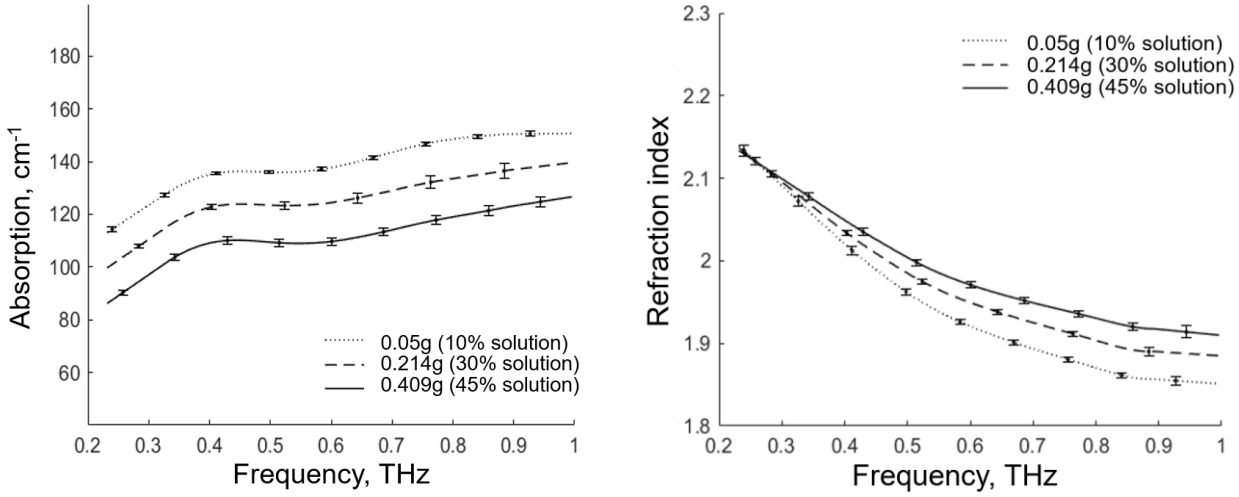
When collagen was added to 10% formalin, the THz absorption spectra of solutions did not have characteristic peaks; for all concentrations of dry collagen in solutions, there was a tendency for absorption to increase with increasing frequency (Fig. 5). As the collagen content of collagen solutions with 10% formalin increases, the total absorption decreases.

Water intermolecular hydrogen bonds vibrations exceed the intramolecular vibrations of the solute, thereby we observed a decrease in the absorption of solutions in the THz range with increasing collagen content. Considering the refractive index spectra for collagen solutions with 10% formalin, it was noted that as the THz frequency increases, the values decrease.



(a) (b)

Fig. 4 (a) Absorption and (b) refraction spectra of dry collagen, 10% and 40% formalin and distilled water.



(a) (b)

Fig. 5 THz (a) absorption and (b) refraction spectra of collagen in 10% formalin.

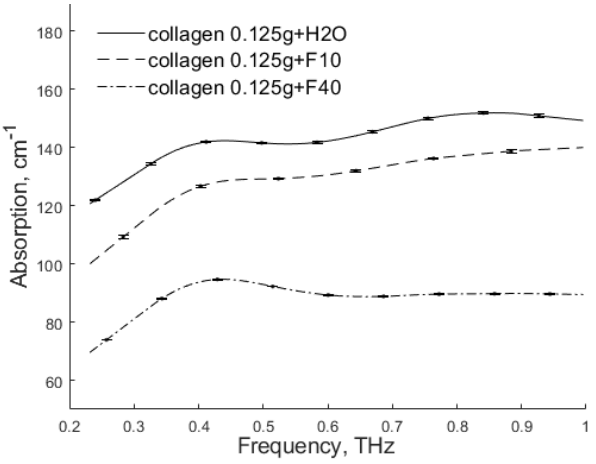


Fig. 6 THz absorption spectra of collagen of 0.125 g weight in water solution (solid line), 10% formalin (dashed line) and 40% formalin (dash-dot line).

The absorption spectra of collagen in an aqueous solution, in 10% formalin and in 40% formalin were examined to assess whether fixation with formaldehyde affects the optical properties of the solution in the THz frequency range. The absorption spectra of solutions containing 0.125 g of collagen dissolved in solvent are shown in Fig. 6. The dependences of the absorption of the studied solutions on the concentration of the components added to the solution (collagen, water and formalin) in percentage terms are shown in Fig. 7.

Since water is replaced by formaldehyde during the fixation process, a corresponding decrease in the absorption coefficient is expected, as shown in Fig. 8. Before fixation (collagen solution in distilled water, Fig. 8a), depending on the mass fraction of collagen added to the test solution, the absorption coefficient was ~140 cm^{-1} at frequencies from 0.6 to 1 THz, and decreased to values of ~90 cm^{-1} at frequencies 0.2 to 0.3 THz. When collagen was fixed with 10% formaldehyde (Fig. 8b), the absorption coefficient

decreased to values of ~80 cm^{-1} with a mass of collagen added to the solution equal to 0.5 g. With an increase in the percentage of formaldehyde content in the solution (Fig. 8c), it was shown that in the frequency range from 0.35 to 0.5 THz, the absorption coefficient remained practically unchanged at a collagen mass fraction from 0.08 to 0.409 g.

Using the distributions shown in Fig. 8, it is possible to evaluate the molecular interactions of formalin with collagen in the THz region of the spectrum in the frequency range from 0.2 to 1 THz. Depending on the proportion of collagen content, the results obtained can be interpreted for different types of tissues and organs.

For a quantitative comparison of spectral profiles, we used the curve proximity factor (CPF) S, similar to the Pearson's correlation coefficient, to compare curves of collagen solutions in distilled water and in formalin [29]:

$$S = \frac{\sum_i |X_i - Y_i|}{\frac{1}{2}\sum_i |X_i + Y_i|},$$

where X_i, Y_i are the absorption coefficients of collagen solutions in distilled water and formalin, respectively.

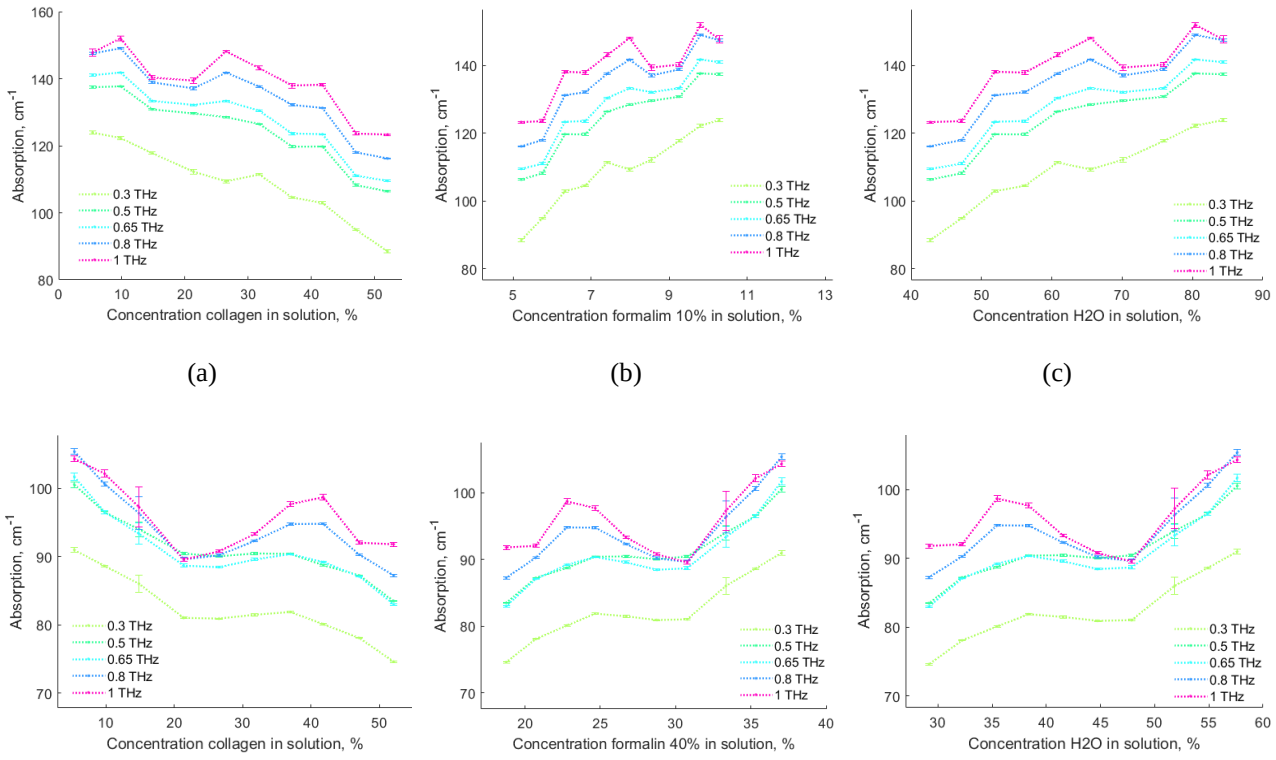


Fig. 7 Dependencies of the absorption of the studied solutions on the concentration of the components added to the solution. Upper images: the content of (a) collagen, (b) formalin and (c) water in a solution with 10% formalin; lower images: the content of (g) collagen, (d) formalin and (e) water in a solution with 40% formalin.

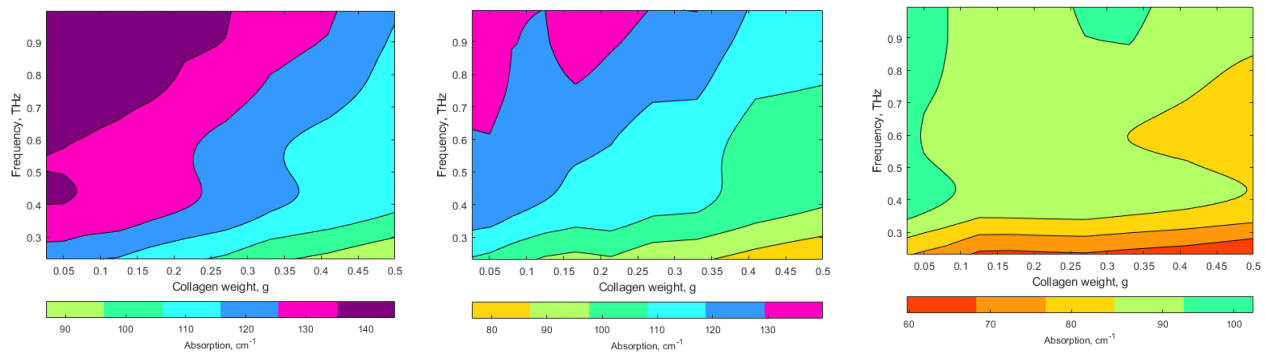


Fig. 8 Distribution of absorption coefficients depending on the mass fraction of collagen added to the solution in (a) aqueous solutions, (b) collagen solutions with 10% formaldehyde, (c) collagen solutions with 40% formaldehyde in the THz frequency range.

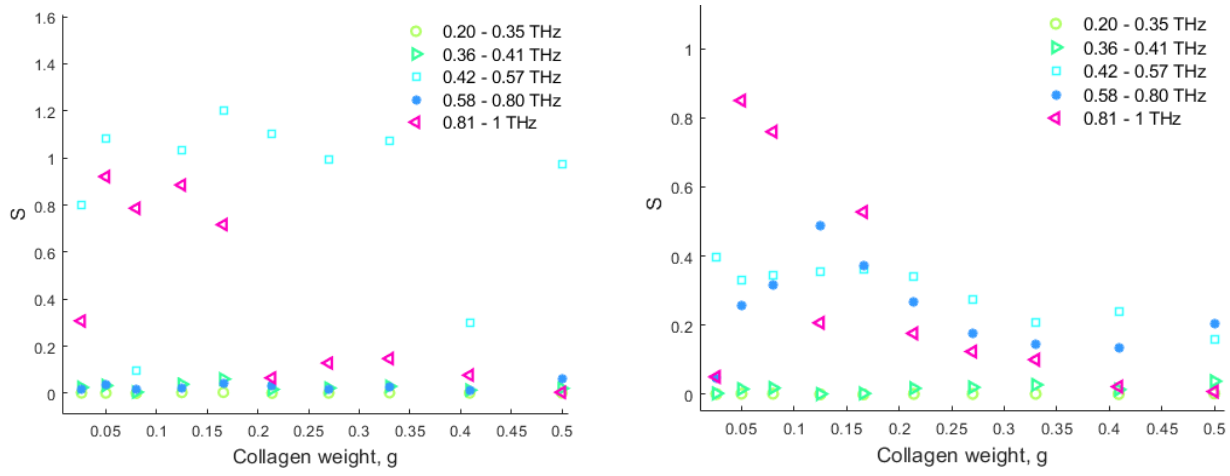


Fig. 9 CPF value (a) for collagen solutions in 10% formalin and (b) for solutions in 40% formalin.

Table 2 CPF values for the studied samples.

	Frequency, THz	Collagen weight, g									
		0.026	**0.05**	**0.08**	**0.125**	**0.166**	**0.214**	**0.27**	**0.33**	**0.409**	**0.5**
10% formalin	0.20−0.35	0.0013	0.0013	0.0002	0.0036	0.0041	0.0007	0.0014	0.0024	0.0013	0.0018
	0.36−0.41	0.0253	0.0330	0.0051	0.0385	0.0606	0.0167	0.0223	0.0295	0.0137	0.0211
	0.42−0.57	0.8009	1.0817	0.0954	1.0334	1.2041	1.1014	0.9946	1.0742	0.3007	0.9745
	0.58−0.80	0.0190	0.0386	0.0162	0.0222	0.0426	0.0333	0.0194	0.0292	0.0116	0.0610
	0.81−1	0.3075	0.9210	0.7865	0.8853	0.7170	0.0655	0.1285	0.1476	0.0770	0.0041
40% formalin	0.20−0.35	0.0009	0.0020	0.0020	0.0002	0.0001	0.0015	0.0013	0.0016	0.0009	0.0028
	0.36−0.41	0.0030	0.0154	0.0184	0.0012	0.0028	0.0176	0.0202	0.0276	0.0140	0.0382
	0.42−0.57	0.3968	0.3288	0.3438	0.3548	0.3636	0.3401	0.2743	0.2064	0.2402	0.1589
	0.58−0.80	0.0475	0.2587	0.3163	0.4865	0.3723	0.2664	0.1759	0.1466	0.1343	0.2049
	0.81−1	0.0507	0.8500	0.7598	0.2070	0.5277	0.1766	0.1238	0.1003	0.0224	0.0083

The lower the CPF value, the closer the collagen solutions in formalin are to the collagen solutions in distilled water (Fig. 9a for solutions in 10% formalin, Fig. 9b for solutions in 40% formalin). CPF values for all groups are shown in Table 2.

As shown in Fig. 8, the CPF value in the low frequency range (0.2−0.4 THz) is small regardless of the concentration of collagen in solutions. Therefore, in this range, collagen fixation in both 10% formalin and 40% formalin, depending on the percentage of formaldehyde does not change their optical characteristics compared to solutions of collagen with distilled water. A similar situation can be observed in the frequency range from 0.8 to 1 THz for solutions with a collagen content of more than 0.2 g.

The dependence of the absorption coefficient on the amount of collagen content in the solutions was analyzed (Fig. 10). It has been shown that with frequency increasing, nonlinear changes in absorption coefficients are observed for solutions of hydrolyzed collagen with 10% formaldehyde. At frequencies ranging from 0.8 THz (Fig. 10) and higher, it can be observed that the absorption coefficient values increase with increasing protein concentration in the range from 10% to 20%, and then decrease almost monotonically. The nonlinear behavior is associated with protein aggregation [23].

In order to evaluate the dependencies of absorption coefficients on protein concentration in solutions, absorption spectra of collagen solutions with distilled water and collagen solutions with 40% formalin were analyzed. When collagen interacts with water (Fig. 10b), linear dependence absorption coefficients on protein concentration in solutions is observed in the 0.2−0.8 THz interval, however, at a frequency of 1 THz, the absorption of aqueous solutions containing collagen from 0.026 g to 0.166 g is less than for the same at a frequency of 0.8 THz.

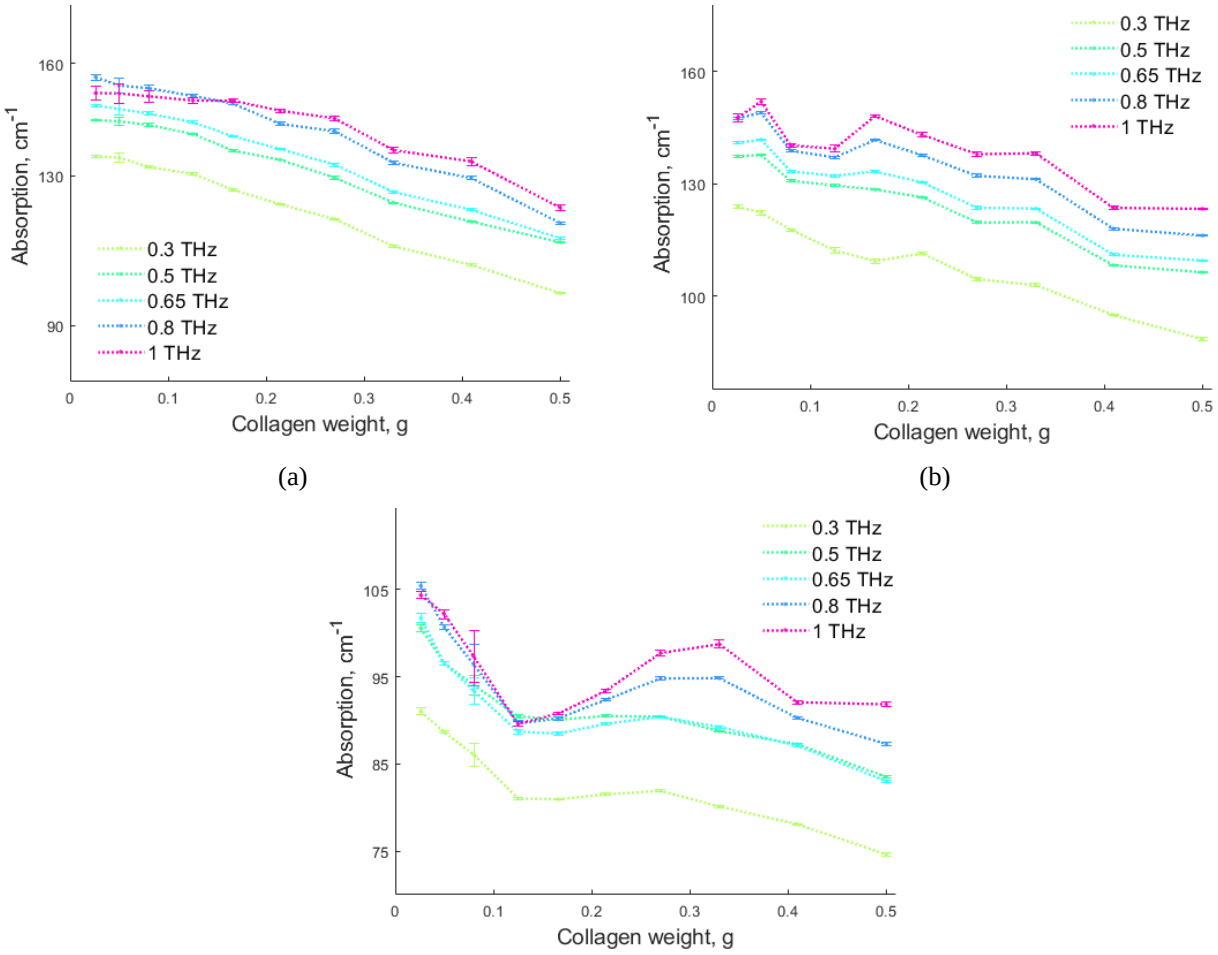


Fig. 10 Dependences of absorption coefficients on collagen content in (a) collagen aqueous solutions, (b) solutions of collagen with 10% formalin, and (c) solutions of collagen with 40% formalin.

The proportion of water in 40% formalin is significantly lower than in 10% formalin. This fact allows us to evaluate the interaction of collagen with formaldehyde in conditions of a small amount of water. As illustrated in Fig. 10c, the absorption spectra of collagen-40% formalin mixtures exhibit a nonlinear relationship at all frequencies between absorption coefficients and protein concentration. This nonlinearity is likely attributed to the decreased water content and increased formaldehyde concentration within the mixture.

The first stage of the interaction of formaldehyde with collagen usually consists of the methylol derivatives formation. Formaldehyde, being a reactive electrophilic substance, easily reacts with various functional groups of biological macromolecules, forming cross-links. Studies indicate that the most common type of cross-link formed by formaldehyde in collagen is between the nitrogen atom at the end of the lysine side chain and the nitrogen atom of the peptide bond, and the number of such cross-links increases over time, which can reach 48 h and more then [5, 30]. The hydroxyl group formed exhibits substantial reactivity and can condense with any atomic group containing active oxygen. This reaction results in the formation of a methylene bridge between amino acids. The interaction between formaldehyde and collagen can be represented by the following scheme:

$$B_1 - NH_2 + HCOH \rightarrow B_1 - NHCH_2OH + H_2N - B_2 - -NHCH_2 - NH - B_2 + H_2O,$$

where B_1 and B_2 are polypeptide chains of collagen.

Collagen treated with formaldehyde contains free methylol groups:

$$B - NH_2 + HCOH - B - NHCH_2OH.$$

For this reason, the formation of additional cross-links in the protein structure continues after processing is completed. At the same time, further polymerization of formaldehyde on the fiber occurs. Also, when treated with formaldehyde, irreversible changes occur as a result of an increase in the number of C–N and C–C bonds.

The use of formalin in histological practice is due to the need to preserve the intravital structure of cells. However, it is essential to determine the optimal formaldehyde concentration that ensures adequate tissue stabilization without compromising the molecular integrity of the samples.

4 Conclusion

In the present study, we assessed the effect of collagen fixation with formaldehyde on optical properties in the THz frequency range. Protein solutions spectral characteristics transformation occurs due to hydrogen bonds and intermolecular interactions among the various components of the solution. The optical properties of real solutions differ significantly from the properties of a model ideal solution. In real solutions, deviations from the linear dependence of the absorption of the solution on the concentration of the solute were observed. To determine the nature of the interaction among the components in solutions of collagen with distilled water, collagen with 10% formalin, and collagen with 40% formalin, spectral characteristics (absorption coefficient and refractive index) of each individual component were measured in the frequency range from 0.2 THz to 1 THz.

Changes in the optical characteristics of collagen solutions with distilled water, collagen solutions with 10% formalin, and collagen solutions with 40% formalin in the frequency range from 0.2 THz to 1 THz were studied. It has been shown that in the frequency range from 0.2 THz to 1 THz, the refractive indices of collagen solutions decrease with frequency increasing. It has been shown that in the frequency range from 0.2 THz to 0.35 THz the optical properties of the solution do not change.

A nonlinear dependence of the absorption coefficient of solutions of formalin with collagen on the content of the latter was established. Nonlinearity is significantly manifested in the interaction of collagen with 10% formalin in the frequency range from 0.8 THz to 1 THz and collagen with 40% formalin at frequencies from 0.2 THz to 1 THz. Nonlinear changes in the absorption of collagen solutions with formaldehyde are characterized by the appearance of another component in the solutions: water associated with collagen.

Funding

The research was supported by the Tomsk State University Development Programme (Priority-2030).

Disclosures

The authors declare that they have no conflict of interest.

References

1. A. Denis, N. Brambati, B. Dessauvages, S. Guedj, C. Ridoux, N. Meffre, and C. Autier, "Molecular weight determination of hydrolyzed collagens," Food Hydrocolloids 22(6), 989–994 (2008).
2. W. E. Grizzle, J. Fredenburgh, and R. B. Myers "Fixation of tissues," Theory and Practice of Histological Techniques 53–74 (2007).
3. W. E. Grizzle, "The use of fixatives in diagnostic pathology," Journal of Histotechnology 24(3), 151–152 (2001).
4. V. Carriel, I. Garzón, M. Alaminos, and M. Cornelissen, "Histological assessment in peripheral nerve tissue engineering," Neural Regeneration Research 9(18), 1657 (2014).
5. R. Thavarajah, V. Mudimbaimannar, J. Elizabeth, U. Rao, and K. Ranganathan, "Chemical and physical basics of routine formaldehyde fixation," Journal of Oral and Maxillofacial Pathology 16(3), 400–405 (2012).
6. B. W. Sutherland, J. Toews, and J. Kast, "Utility of formaldehyde cross-linking and mass spectrometry in the study of protein–protein interactions," Journal of Mass Spectrometry 43(6), 699–715 (2008).
7. T. Tomihata, K. Burczak, K. Shiraki, and Y. Ikada "Cross-linking and biodegradation of native and denatured collagen," ACS Symposium Series, 540, 275−286 (1994).
8. P. Zioupos, J. C. Barbenel, and J. Fisher, "Anisotropic elasticity and strength of glutaraldehyde fixed bovine pericardium for use in pericardial bioprosthetic valves," Journal of Biomedical Materials Research 28(1), 49–57 (1994).
9. Y. Sun, B. M. Fischer, and E. Pickwell-MacPherson, "Effects of formalin fixing on the terahertz properties of biological tissues," Journal of Biomedical Optics 14(6), 064017 (2009).
10. J. A. Kiernan, "Formaldehyde, formalin, paraformaldehyde and glutaraldehyde: what they are and what they do," Microscopy Today 8(1), 8–13 (2000).
11. R. Dapson, "Macromolecular changes caused by formalin fixation and antigen retrieval," Biotechnic & Histochemistry 82(3), 133–140 (2007).
12. M. C. Jamur, C. Oliver, "Cell fixatives for immunostaining," Immunocytochemical Methods and Protocols 588, 55−61 (2010).
13. N. Masuda, T. Ohnishi, S. Kawamoto, M. Monden, and K. Okubo, "Analysis of chemical modification of RNA from formalin-fixed samples and optimization of molecular biology applications for such samples," Nucleic Acids Research 27(22), 4436–4443 (1999).
14. H. Puchtler, S. N. Meloan, "On the chemistry of formaldehyde fixation and its effects on immunohistochemical reactions," Histochemistry 82(3), 201–204 (1985).

15. W.-G. Yeo, N. K. Nahar, C. L. Hitchcock, S. Park, O. Gurel, and K. Sertel, "Real-time THz imaging of human tissue characteristics and cancer margins," in 38th International Conference on Infrared, Millimeter, and Terahertz Waves, Mainz, Germany (2013).
16. S. Y. Huang, Y. X. J. Wang, D. K. W. Yeung, A. T. Ahuja, Y.-T. Zhang, and E. Pickwell-MacPherson, "Tissue characterization using terahertz pulsed imaging in reflection geometry," Physics in Medicine & Biology 54(1), 149–160 (2009).
17. O. Miyashita, P. G. Wolynes, and J. N. Onuchic, "Simple energy landscape model for the kinetics of functional transitions in proteins," The Journal of Physical Chemistry B 109(5), 1959–1969 (2005).
18. Y. Xu, M. Havenith, "Perspective: Watching low-frequency vibrations of water in biomolecular recognition by THz spectroscopy," The Journal of Chemical Physics 143(17), 170901 (2015).
19. M. Heyden, M. Havenith, "Combining THz spectroscopy and MD simulations to study protein-hydration coupling," Methods 52(1), 74–83 (2010).
20. S. Ebbinghaus, S. J. Kim, M. Heyden, X. Yu, M. Gruebele, D. M. Leitner, and M. Havenith, "Protein sequence- and ph-dependent hydration probed by terahertz spectroscopy," Journal of the American Chemical Society 130(8), 2374–2375 (2008).
21. M. Grossman, B. Born, M. Heyden, D. Tworowski, G. B. Fields, I. Sagi, and M. Havenith, "Correlated structural kinetics and retarded solvent dynamics at the metalloprotease active site," Nature Structural & Molecular Biology 18(10), 1102–1108 (2011).
22. J. W. Bye, S. Meliga, D. Ferachou, G. Cinque, J. A. Zeitler, and R. J. Falconer, "Analysis of the hydration water around bovine serum albumin using terahertz coherent synchrotron radiation," The Journal of Physical Chemistry A 118(1), 83–88 (2014).
23. B. Manna, A. Nandi, M. Tanaka, H. Toyokawa, R. Kuroda, and D. K. Palit, "Effect of aggregation on hydration of HSA protein: Steady-state Terahertz absorption spectroscopic study," Journal of Chemical Sciences 132(1), 8 (2020).
24. F. Novelli, S. Ostovar Pour, J. Tollerud, A. Roozbeh, D. R. T. Appadoo, E. W. Blanch, and J. A. Davis, "Time-domain thz spectroscopy reveals coupled protein–hydration dielectric response in solutions of native and fibrils of human lysozyme," The Journal of Physical Chemistry B 121(18), 4810–4816 (2017).
25. S.-H. Chong, S. Ham, "Distinct role of hydration water in protein misfolding and aggregation revealed by fluctuating thermodynamics analysis," Accounts of Chemical Research 48(4), 956–965 (2015).
26. X. Shi, W. Ma, C. Sun, and S. Wu, "The aggregation behavior of collagen in aqueous solution and its property of stabilizing liposomes in vitro," Biomaterials 22(12), 1627–1634 (2001).
27. R. K. Mitra, D. K. Palit, "Probing biological water using terahertz absorption spectroscopy," Terahertz Technology (2021).
28. D. O. Zyatkov, Z. S. Kochnev, A. I. Knyazkova, and A. V. Borisov, "Analysis of the spectral characteristics of promising liquid carriers in the terahertz spectral range," Russian Physics Journal 62(3), 400−405 (2019).
29. Yu. V. Kistenev, V. E. Skiba, V. V. Prischepa, D. A. Vrazhnov, and A. V. Borisov, "Super-resolution reconstruction of noisy gas-mixture absorption spectra using deep learning," Journal of Quantitative Spectroscopy and Radiative Transfer 289, 108278 (2022).
30. G. J. Wilmink, B. L. Ibey, T. Tongue, B. Schulkin, N. Laman, X. G. Peralta, C. C. Roth, C. Z. Cerna, B. D. Rivest, J. E. Grundt, and W. P. Roach, "Development of a compact terahertz time-domain spectrometer for the measurement of the optical properties of biological tissues," Journal of Biomedical Optics 16(4), 047006 (2011).

Silica Microspheres with Adsorbed Gold Nanostars for Single Cell SERS Detection of Formazan

Olga A. Inozemtseva[1,2*], Ekaterina S. Prikhozhdenko[1], Olga I. Gusliakova[2], Yulia A. Tyunina[1,2], Mariia S. Saveleva[1], Daniil N. Bratashov[1], Andrey M. Burov[2], and Boris N. Khlebtsov[2]

[1] Saratov State University, 83 Astrakhanskaya str., Saratov 410012, Russian Federation

[2] Institute of Biochemistry and Physiology of Plants and Microorganisms of the Russian Academy of Sciences – a separate structural subdivision of the Federal State Budgetary Scientific Institution Federal Research Center "Saratov Scientific Center of the Russian Academy of Sciences", 13 Entuziastov ave., Saratov 410049, Russian Federation

[*]e-mail: Inozemtsevaoa@mail.ru

Abstract. In this study we report a rapid and sensitive surface-enhanced Raman spectroscopy (SERS)-based 3-(4, 5-dimethylthiazol-2-yl)-2,5-diphenyltetrazolium bromide (MTT) assay for *in situ* cell viability and proliferation assessment. The developed method based on silica microspheres with adsorbed gold nanostars serves as intracellular SERS platforms for formazan detection. The proposed method has several advantages over traditional MTT assays. Firstly, the formazan concentration can be determined from the SERS signal intensity without extraction and enrichment steps. Secondly, the SERS spectra of formazan can be directly obtained at the level of a single particle internalized by the cell. The SERS-MTT detection method is expected to avoid interference from background substances (such as residual MTT reagent, serum, exogenous drugs) in cell suspensions. Furthermore, the proposed approach not only simplifies the testing procedure, but it is also anticipated to provide more precise results when evaluating the effectiveness of cancer treatments compared to the conventional MTT method. © 2024 Journal of Biomedical Photonics & Engineering.

Keywords: 3-(4, 5-dimethylthiazol-2-yl)-2,5-diphenyltetrazolium bromide (MTT); surface-enhanced Raman spectroscopy (SERS); formazan; gold nanostars.

Paper #9160 received 30 Aug 2024; revised manuscript received 21 Oct 2024; accepted for publication 25 Oct 2024; published online 16 Nov 2024. doi: 10.18287/JBPE24.10.040308.

1 Introduction

Cell viability analysis has attracted much attention as a substitute for animal testing. This is necessary, for example, when screening large numbers of chemicals for their cytotoxicity on various cell types.The traditional quantitative cell viability test involves the addition of exogenous agents such as 3-(4,5-dimethyl-2-thiazolyl)-2,5-diphenyl-2H-tetrazolium bromide (MTT), which has been one of the most commonly used dyes for colorimetric assessment of cell viability since the early 1980s [1]. This assay is now presented as a rapid, accurate, and simple method for the detection of live cells in mammalian cell cultures.

MTT is a yellow water-soluble tetrazolium salt [2] that is converted into a water-insoluble formazan [3, 4] by reductive cleavage of the tetrazolium ring by mitochondrial dehydrogenases in living cells. Since dead cells are unable to produce dehydrogenase during metabolic processes, they do not possess this reductive capacity.

The key steps of the traditional MTT assay include incubation of cells with MTT, removal of the cell culture medium containing formazan crystals from the cells, solubilization of formazan, and measurement of the optical density to determine the amount of formazan using a microplate spectrophotometer [4]. Thus, the assay results depend on the ability of metabolically active cells to reduce MTT to formazan. In other words, the amount of formazan detected spectrophotometrically serves as an indicator of the number of mitochondria, which, in turn, corresponds to the number of living cells in the sample [5, 6].

The MTT assay has been shown to be useful for monitoring cell viability independent of proliferative

activity [1], and for quantifying mitochondrial activity [7]. In addition, MTT assays have been used to study chemosensitivity, radiosensitivity, and toxicity of drugs in human tumor cell lines [8]. Cytotoxic effects of drugs on the development of various forms of cancer have also been reported using the MTT assay [9, 10].

As noted, the conventional MTT method is a robust quantitative method with distinct advantages, such as being time- and cost-effective, and the use of microplate scanning spectrophotometers allows for the processing of large numbers of samples. Nevertheless, it has certain limitations, including significant interference from other substances and a low detection sensitivity (approximately 1.0 μg/mL), as well as the tendency to produce false positive results [11]. The addition of organic solvents to serum-containing medium results in the precipitation of serum proteins, which affects absorbance measurements [12]. In addition, a 4 h incubation period is typically required, which may be extended for low-density cells or cells with a lower metabolic rate, prior to spectrophotometric assessment of their viability [8]. A small amount of formazan can be lost during the removal of the culture medium, which can bias the experimental results. These observations have led to the search for various alternative assays [13]. Increasing the detection sensitivity of MTT assays and simplifying the steps remains an important challenge. Moreover, the precise nature of the interactions between MTT salts and living cells at very low concentrations (ng/mL) in situ needs to be elucidated. To obtain information at such dilute levels, non-destructive assay approaches are needed that combine sensitivity, chemistry, and spatial resolution.

Here we propose a combination of MTT analysis with surface-enhanced Raman spectroscopy (SERS), which can fulfill all of these requirements. SERS combines the advantages of in situ molecular identification [14], offline detection, well-established instrumentation, exceptional sensitivity, non-invasiveness and virtually no sample preparation [15−19]. Advances in both laser and detector technologies, as well as an improved understanding of the SERS mechanism, have led to the application of SERS for single-molecule detection [20]. Beyond this fundamental limit in chemical analysis, SERS has also been employed in various biological applications, such as the identification and classification of viruses or cancer cells [21, 22], as well as in biochemical diagnostics [23, 24], pH sensing [25], and pharmaceutical research [26]. The characteristic Raman bands of biological macromolecules can be used to track the changes of various components before and after apoptosis using Raman imaging. The introduction of the SERS probe into the cell not only increases the sensitivity of Raman imaging, but also enables dynamic observation of intracellular organelle interactions, providing a more convenient and intuitive detection method.

In our work, a novel type of SERS platform, consisting of silica microspheres coated with gold nanostars, was developed and combined with Raman imaging technology and traditional MTT assay to determine the viability of single cells *in situ*. This overcomes the limitations of the traditional MTT method in terms of complex sample pretreatment steps and provides a new method to assess cell apoptosis in situ in real time. Furthermore, Raman spectroscopy-based cell imaging methods have emerged as powerful tools in cell biology because the molecular composition of subcellular compartments can be visualized without the additional labeling [27] and within a relatively short time frame (typically minutes) compared to traditional methods that are typically time-consuming. Thus, the proposed method has great potential for use in highly sensitive and highly efficient cell imaging methods.

2 Materials and Methods

2.1 Formazan Synthesis

To reduce MTT to formazan we added glucose in a 10-fold excess to an aqueous solution of MTT with a concentration of 1 mg/mL and pH = 10. After 2 h, the resulting formazan suspension was washed with water and dried for 2 days at 40 °C.

2.2 Gold Nanostars Synthesis

Gold nanostars were synthesized using a two-step protocol using gold seed particles [28, 29], with minor modifications. In the first step, gold nanospheres with an average diameter of 15 nm were synthesized using the Frens method [30], and used as seeds for the synthesis of gold nanostars. For this, 238 mL of water were boiled in an Erlenmeyer flask while stirring on a magnetic stirrer. 2.5 mL of 1% $HAuCl_4$ solution and 7.75 mL of 1% sodium citrate solution were added. The solution was stirred for 15 min, during which time the color of the solution changed from colorless to red. In the second step, to synthesize nanostars, 46.25 mL of water, 3.75 mL of 10 mM $HAuCl_4$ and 150 μL of 1 M HCl were successively added to 4.5 mL of 15-nm seed particles with a concentration of $1.6 \cdot 10^{12}$ mL^{-1}. Then, 750 μL of 4 mM silver nitrate and 750 μL of ascorbic acid (AA; 100 mM) were added with stirring (700 rpm). The solution was stirred for 30 s, during which its color quickly changed from light red to blue-green. Then, 5 mL of 1% polyvinylpyrrolidone (PVP) solution (10 kDa) in ethanol was added to the colloid with stirring and stirred for additional 10 min. Then, gold nanostars were purified from reaction products by centrifugation (5000 rpm, 10 min) and resuspended in 20 mL of ethanol.

2.3 Concentration vs SERS and Absorbance Calibration Plots

To plot the calibration dependence, a series of successively diluted formazan solutions in a 1:1 mixture of water and isopropyl alcohol were prepared. The calibration dependence of absorption on the concentration of formazan was made by measuring absorption at a wavelength of 560 nm for different concentrations of the reactant. SERS calibration dependence was made as follows. The gold nanostars colloid (100 μL) with an optical density of 1.4 (measured

in 1 cm cuvette) was added to 900 mL of the formazan solutions with different concentrations and the Raman spectra of the resulting mixture were recorded. A PeakSeeker Pro setup (Ocean optics, USA) was used to measure the Raman spectra. The measurements were carried out in 1 cm four-sided quartz cuvettes with excitation at a wavelength of 785 nm. The laser radiation power was 30 mW, the signal accumulation time was 10 s. To reduce the effect of the internal filter, the laser beam was focused near the wall of the cuvette.

2.4 SERS Platform Preparation

To synthesize isodisperse silica microparticles, we used a multistage overgrowth method, described in detail in our work [31]. The number of overgrowth cycles was selected so that the size of the silica particles was about 2 μm.

For the adsorption of gold nanostars, the surface of silica microparticles was functionalized with amino groups by doping with aminopropyltrimethoxysilane. The corresponding silane was added to a colloid of 2 μm silica particles in ethanol in an amount of 1% of the reaction mixture volume. The particle suspension was incubated for 1 h at room temperature with stirring. The resulting aminated particles were centrifuged at 5000 rpm for 1 min and resuspended in ethanol again using ultrasonic treatment.

Next, 1 mL of the colloid of functionalized silica particles was added to 4 mL of concentrated colloid of gold nanostars (Optical density, OD = 20). The resulting mixture was incubated for 24 h with stirring at 500 rpm. The particles were then centrifuged at 5000 rpm for 1 min and resuspended in ethanol.

The extinction spectra were recorded using a Specord S300 spectrophotometer (Analytik Jena, Germany). The measurements were performed in the wavelength range of 320−1100 nm using quartz cuvettes with an optical path length of 2 mm and 10 mm.

The size and electrokinetic potential of gold nanoparticles and silica particles were measured using a Zetasizer ZS setup (Malvern, UK).

Transmission electron microscopy (TEM) images were obtained using a Libra-120 transmission electron microscope (Carl Zeiss, Germany) at the Simbioz Center for the Collective Use of Research Equipment in the Field of Physical Chemical Biology and Nanobiotechnology, IBPPM RAS, Saratov.

Scanning electron microscopic images were obtained using a Mira-II LMU microscope (Tescan, Czech Republic). For analysis, samples of nano- and microparticles were applied to a silicon substrate, the accelerating voltage during the study was 30 kV.

The concentration of silica microparticles was determined gravimetrically by weighing the dry residue after lyophilization of the colloid on an analytical balance. The total weight of particles in 1 mL of the colloid allow us to unambiguously determine the numerical concentration of particles using the following Eq.:

$$N = \frac{3m}{4\rho r R^3},$$

where m is the mass of silica, expressed in mg, ρ is the density of silica, expressed in mg/cm^3, R is the radius of the particles, expressed in centimeters. The mass of the silicate particle with a diameter of 2 μm is the product of the density by the volume of the particle and is $7.12 \cdot 10^{-9}$ mg. The suspension has a concentration of silicate particles of 20 mg/mL or $2.86 \cdot 10^9$ mL^{-1}.

2.5 Metabolic Cells Activity Test

Undifferentiated murine colon carcinoma cell line (CT26.WT) was used in experiments on cytotoxicity, internalization and detection of formazan inside cells. CT26.WT was cultured in Dulbecco's Modified Eagle Medium (DMEM) supplemented with a 10% Fetal bovine serum (FBS), and 1% penicillin / streptomycin.

The relative metabolic activity of CT26.WT cells after incubation with SERS platforms was measured using MTT reagent. Cells were seeded in 96-well plates at a density of 5×10^3 cells per well and left in humidify atmosphere containing 5% CO_2 at 37 °C. The next day, the SERS platforms were added to the wells at predefined concentration (1, 2, 3, 4, 5, 10, 15, 20, 25, 30, and 50 SERS platforms per cell) with fresh media after aspiration of the old media. For control cells group, only medium replacement was performed. Further cell incubation was carried out at 37 °C and in an atmosphere containing 5% CO_2. After 48 h, the media was aspirated and replaced with 90 μL of the fresh media, followed by the addition of MTT reagent (10 μL) dissolved in PBS (5 mg/mL). The culture media from well (75 μL) of were aspirate and 75 μL of Dimethyl sulfoxide (DMSO) were added after 4 h of cells incubation with MTT reagent. The final solution with DMSO in the wells was carefully pipetting, and plate was left at 37 °C for 10 min. Optical density (OD) of formazan solution in the wells was measured at wavelength of 554 nm using CLARIOstar Plus Microplate Reader (BMG Labtech, Germany). Relative metabolic activity was calculated as the ratio of the OD mean value in the wells where cells were incubated with SERS platforms to the OD mean value of the control group, expressed as a percentage.

2.6 Microscopy Study of Particles Internalization

CT26.WT cells were seeded in SPL Confocal Dishes (SPL Life Sciences Co., Ltd.) at a density 300×10^3 cells and left in humidify atmosphere containing 5% CO_2 at 37 °C. The next day, the SERS platforms were added to the Confocal Dishes at concentration of 30 SERS platforms per cell with fresh media after aspiration of the old media. Incubation lasted 48 h at 37 °C and in an atmosphere containing 5% CO_2. After the co-incubation period, the cells were washed with Ca- and Mg-free Dulbecco's Phosphate-Buffered Saline (DPBS), fixed with 2.5% glutaraldehyde for 8 h, and prepared for scanning electron and atomic force microscopy. For this purpose, dehydration was performed by sequential soaking in ethanol/water solutions with increasing alcohol concentrations (50%, 60%, 70%, 80%, 90%, and

99.9%) for 30 min. Drying of the cell layer at the bottom of the Confocal Dishes was accomplished with Hexamethyldisilizane (HMDS). The 99.9% ethanol in the Confocal Dishes was replaced with a 1:2 solution of HMDS: 99.9% ethanol, then with a 2:1 solution of HMDS: 99.9% ethanol, and finally with 100% HMDS. The exposure to solutions containing HMDS lasted 20 min. Cells' layer was exposed to 100% HMDS twice and then left for drying in the fume hood overnight.

To study the morphology and microstructure, dried cell layer with particles were sputtered with gold and imaged with scanning electron microscopes MIRA II LMU at an operating voltage of 15 kV.

Atomic force microscopy (AFM) measurements were performed in tapping mode on an NTEGRA spectra setup (NT-MDT-SI, Zelenograd, Russia) using NSG10 probes. Alignment and artifact correction were performed using Gwiddion 2.6 software.

2.7 Cell Preparation for Raman Spectroscopy

For cell preparation for Raman spectroscopy quartz glasses (15 × 15 mm) were coated with poly-D-lysine (100 μg/mL) preliminary. CT26.WT cells were seeded in Petri Dishes 35 mm (Nunc™ Cell Culture/Petri Dishes, Thermo Scientific) with quartz glass located at the bottom at a density 300×10^3 cells and left in humidify atmosphere containing 5% CO_2 at 37 °C. The next day, the particles were added to the Petri Dishes at concentration of 30 particles per cell with fresh media after aspiration of the old media. Incubation lasted 48 h at 37 °C and in an atmosphere containing 5% CO_2. After the co-incubation period, the cells were washed with Ca- and Mg-free DPBS and MTT solution in complete culture media was added (1 mL). MTT solution consisted of complete culture (90% v/v) and Stock MTT solution in DPBS at concentration 5 mg/mL (10% v/v). The biochemical reaction was stopped by aspirating the MTT solution and washing the cell layer with DPBS without Ca and Mg. For Raman Spectroscopy, 5 mL of DPBS without Ca and Mg was added to the Petri dish. Measurements were taken 20 and 60 min after adding the MTT solution to the cells.

Raman spectra were collected using a Renishaw InVia Raman spectrometer (Renishaw, UK), equipped with a 785 nm laser. Drops of SiO_2 microparticles from the suspension and formazan solution (0.1 mg/mL) in ethanol were deposited onto a quartz substrate. A Raman map of the air-dried mixture was obtained with a 50×/0.5 NA objective (Leica, Germany), using 0.1% (25 μW) laser power and 1 second per single spectrum acquisition time. Raman maps of cells on a quartz substrate were also collected with a Leica 63×/0.9 NA water-immersion objective, using 1% (250 μW) laser power, and 1 s/spectrum acquisition time.

All collected spectra were processed using Renishaw WiRE software version 4.2, which removed cosmic rays and a polynomial baseline fit of order 11. The data were then analyzed using Python 3 in the Jupyter notebook environment. Mean spectra were calculated from data with intensities above 95% percentile for microparticles or 75% percentile for cells.

3 Results

In the first stage of the study we decided to compare the possibility of detecting formazan in solution using spectrophotometry and SERS. It is important to note that a laser with a wavelength of 785 nm is used for SERS experiments, which is most widely used for SERS mapping of biological objects due to the significant penetration depth of near-IR radiation into biological tissues and low autofluorescence of biological tissues [32]. It was previously reported that MTT-formazan has a very low Raman scattering cross-section when irradiated with a 785 nm laser [15].

MTT is a yellow water-soluble tetrazolium salt. MTT is reduced in the mitochondria of metabolically active cells by succinate dehydrogenase to yield a water-insoluble purple formazan crystal [33, 34], which can be spectrophotometrically measured upon solubilization. Outside cells, formazan is formed from MTT by reduction (Fig. 1) with plant extracts [35], tocopherols [36], and flavonoids [37].

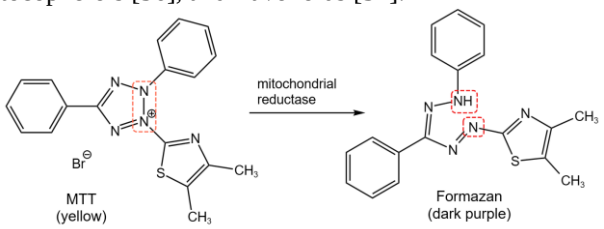


Fig. 1 Scheme of the cleavage proceeding of the MTT salt to formazan. The red dotted line indicates the N-N bond, through which reduction occurs with the opening of the heterocycle.

To reduce MTT to formazan, glucose was used in a 10-fold excess compared to an aqueous solution of MTT with a concentration of 1 mg/mL and pH = 10 (pH was adjusted by the addition of 1 M sodium hydroxide). After 2 h, the resulting formazan suspension was washed with water and dried for 2 days at 40 °C.

Gold nanostars were used as amplifiers of the SERS signal. To obtain gold nanostars, a seed particle protocol was implemented [38, 39], where 15-nm quasi-spherical gold particles were used as nanostars growth centers. In our case, gold was reduced on the seed surface using ascorbic acid, and silver chloride obtained directly in the colloid by reacting silver nitrate with hydrochloric acid was used to create anisotropic growth conditions. By varying the concentration of gold seeds and the amount of gold-containing precursor, it is possible to regulate the size of the stars and the number of "tips" [38, 40].

The synthesized nanoparticles were characterized by transmission electron microscopy. Thus, from the transmission electron microscopy data (Fig. 2a) it is evident that the average size of the core of such particles was about 40 nm, the length of the rays was 15−20 nm and the number of "tips" was from 3 to 10. The data on the size parameters of the nanostars obtained from TEM micrographs are in good agreement with the values determined by the dynamic light scattering (measured in ethanol), which were 68.8 ± 26.2 nm.

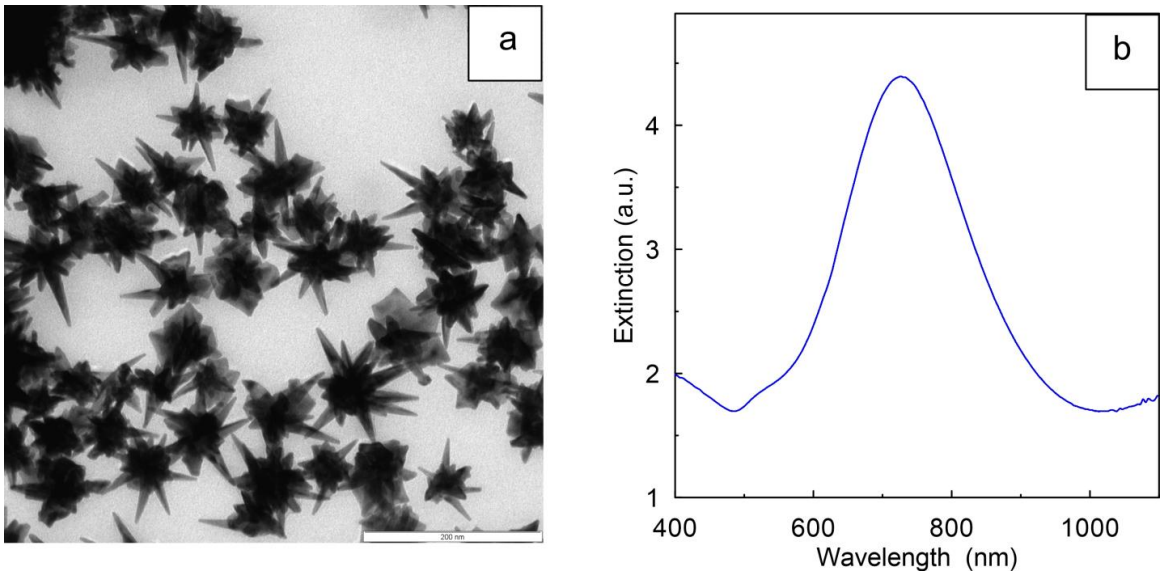


Fig. 2 (a) Electron microscopy images of gold nanostars obtained by reducing the gold-containing precursor with ascorbic acid on the surface of 15-nm "seeds". The scale bar is 200 nm. (b) The extinction spectrum of the synthesized nanoparticles.

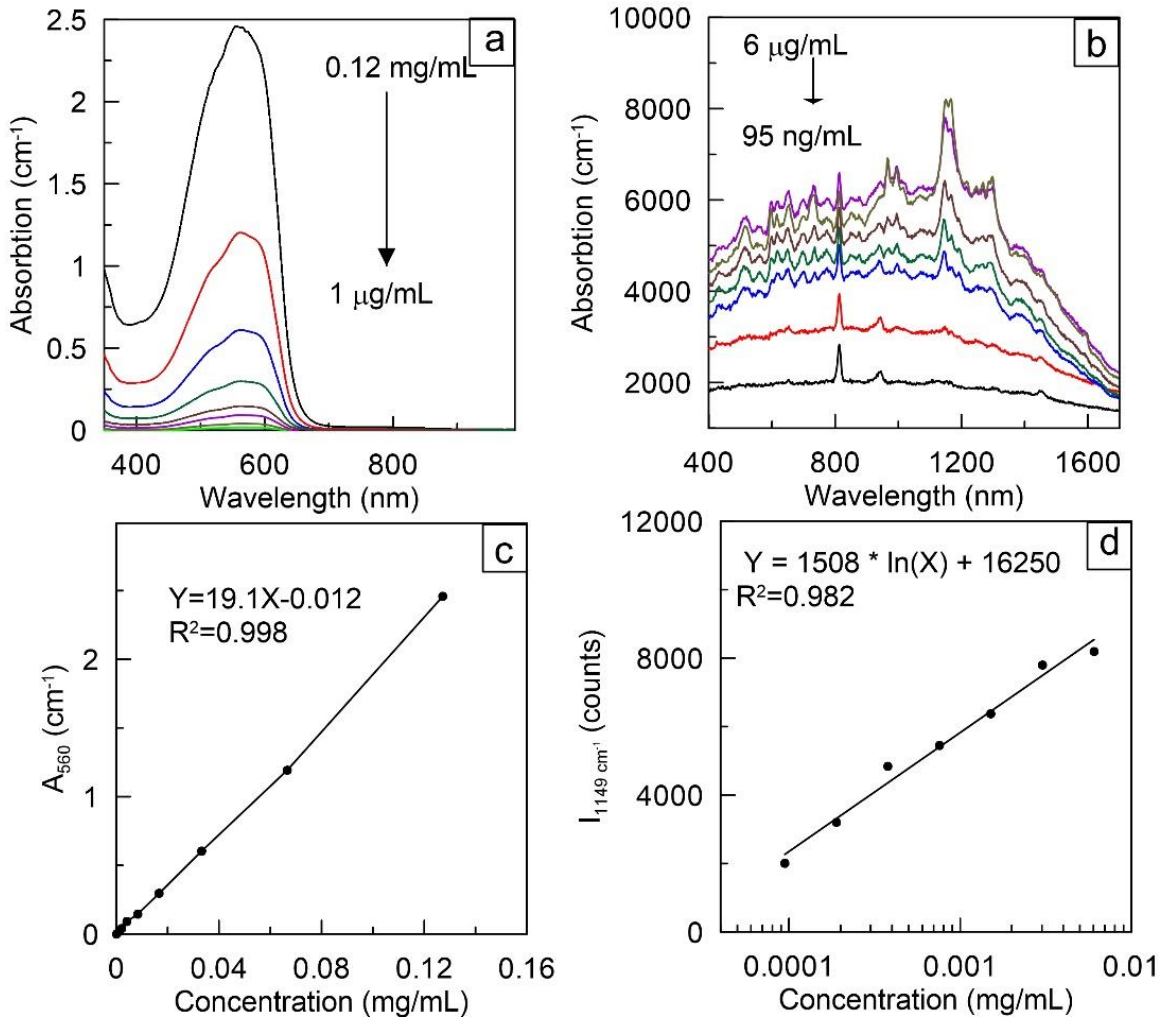


Fig. 3 (a) Absorption spectra of MTT-formazan solutions in isopropyl alcohol with concentrations of 120^{-1} μg/mL. (b) SERS spectra of MTT-formazan on gold nanostars in a colloid. The formazan concentration is 6 μg–95 ng/mL. Calibration curves for determining the formazan concentration in solution by (c) absorption at a wavelength of 560 nm and (d) SERS intensity at 1176 cm^{-1}.

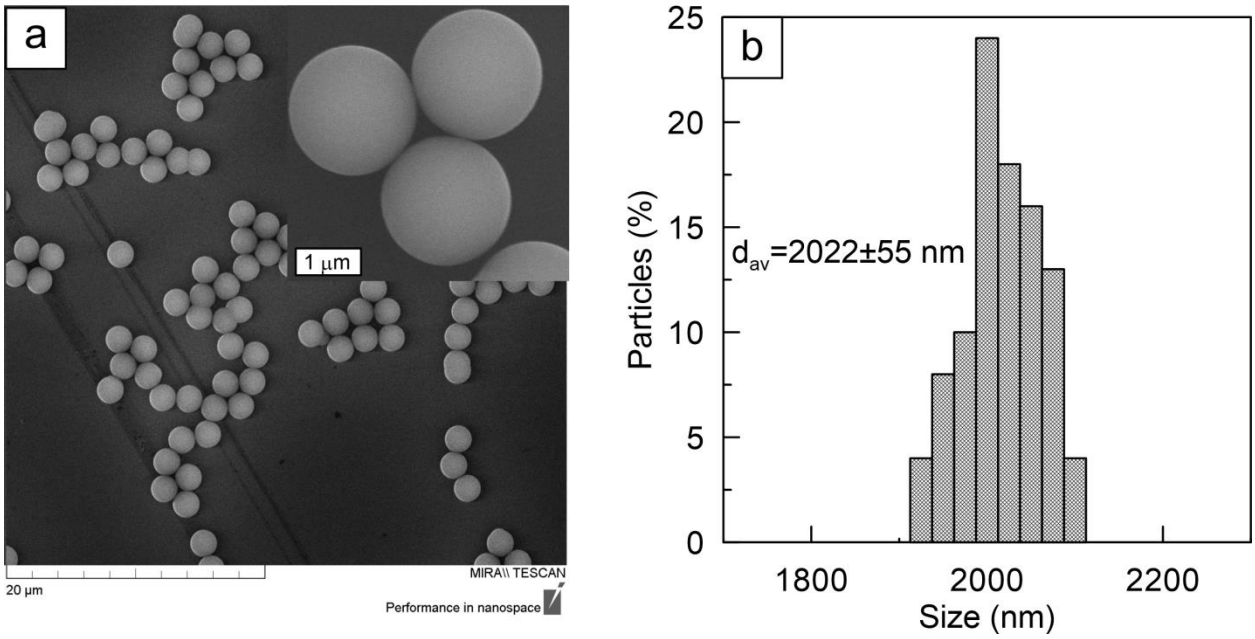


Fig. 4 (a) Scanning electron microscopic image of silicate microparticles. Scale bar is 20 μm. The inset shows an enlarged image of individual particles. Scale bar is 1 μm. (b) Histogram of the size distribution of silicate particles.

Fig. 2b shows the extinction spectra of the gold nanostars colloid. In agreement with our previous studies [41], there is maximum in the extinction spectrum at 720 nm. Also the extinction spectrum has a shoulder in NIR region. These spectral features are typical for nanostars with rough core and thin and sharp tips.

In general, it can be expected that the measured optical properties of the nanoparticles will allow obtaining an enhanced electromagnetic field near the rays when excited by laser radiation in the red and near infrared range.

Fig. 3a shows the absorption spectra of MTT-formazan at concentrations up to 120 μg/mL. It is evident that there is a well-known absorption maximum at 560 nm. The calibration curve in Fig. 3c shows excellent linearity ($R^2 = 0.998$) of the dependence of the formazan absorption intensity on its concentration in solution. The detection limit using a 1 cm cuvette was aproximately 1 μg/mL.

To determine the possibility of detecting formazan by SERS, 1 mL of an aqueous colloid of gold nanostars with an OD of 1.4 (measured in 1 cm cuvette) was mixed with 100 μL of a formazan solution in isopropanol (final concentration of 6 μg − 95 ng/mL). Then, the SERS spectrum of the resulting colloid was measured in a four-sided quartz cuvette.

Fig. 3b shows the measured SERS spectra. A decrease in the SERS intensity with a decrease in the formazan concentration is evident. It should be noted that the spectral lines at 819, 953, and 1454 cm^{-1} are related to isopropanol and have a constant intensity, since its concentration in all samples is the same. These spectral lines can be used as an internal standard, if necessary, to check the same laser focusing for all samples.

To construct a calibration dependence for determining the concentration of MTT-formazan by SERS, the most intense peak of formazan at 1176 cm^{-1} was used. The resulting calibration dependence is shown in Fig. 3d. It should be noted that, unlike the spectrophotometric dependence, it has a semi-logarithmic rather than linear form, which is typical for all SERS calibrations. It worth mentioning that the minimum detection limit of formazan by SERS was almost an order of magnitude lower than using spectrophotometry while maintaining a high correlation coefficient. Thus, formazan can be effectively detected by analyzing the SERS signal excited at 785 nm.

Isodispersed SiO_2 particles were used as a matrix for assembling gold nanostars in SERS active microstructures. Fig. 4a shows scanning electron microscopic images of such particles.

The inset on Fig. 4a shows an enlarged image demonstrating the ideal spherical shape of the SiO_2 particle. Fig. 4b shows a histogram of the size distribution of silicate microparticles, the average diameter 2022 ± 55 nm. For the subsequent adsorption of gold nanostars, silicate microparticles were functionalized with aminopropyltrimethoxysilane to introduce amino groups with a positive charge. The initial silicate microparticles in water had an electrokinetic potential of −33.2 ± 4.6 mV. After the amination procedure, the electrokinetic potential was +13.8 ± 6.2 mV.

In contrast to the commonly used SERS platforms based on individual spherical gold or silver nanoparticles [42−44], in this work, PVP-stabilized gold nanostars were assembled via electrostatic interactions on the surface of positively charged amino-functionalized silica microspheres. The insets in Fig. 5a show scanning electron microscopy (SEM) images of silica microspheres with surface-adsorbed gold nanostars.

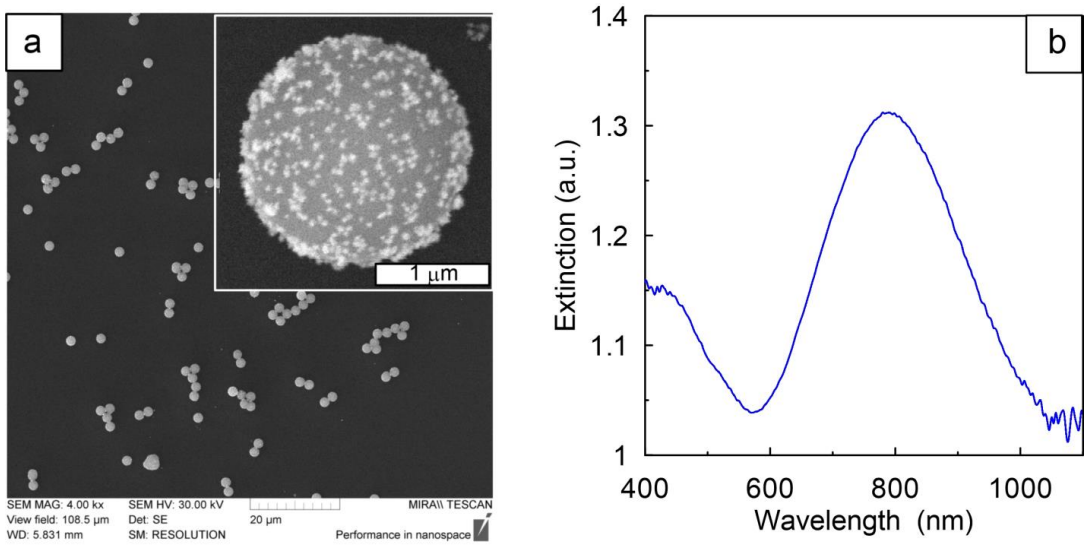
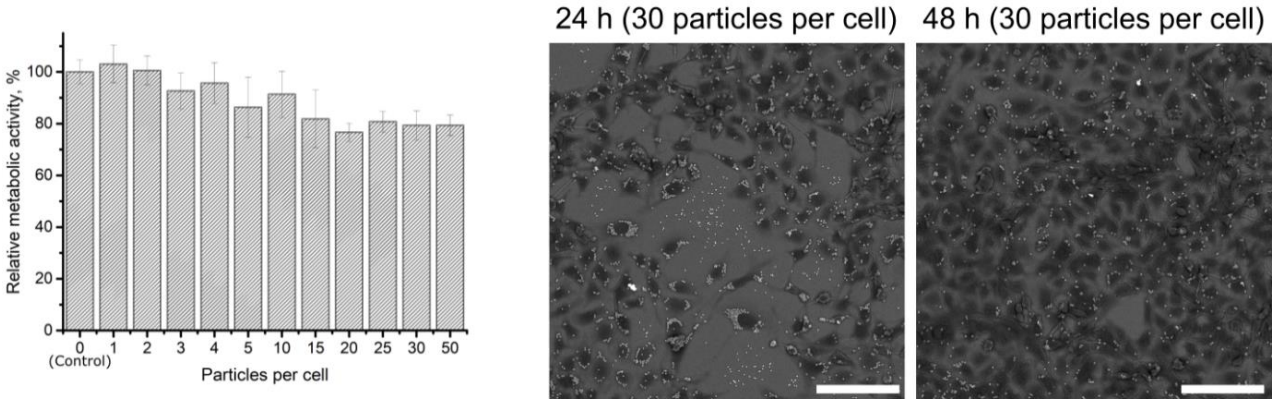


Fig. 5 Panel (a) shows the electron microscopic image of silica microspheres with surface-adsorbed gold nanostars. Scale bars are 20 μm and 1 μm in the insert. Panel (b) shows the extinction spectrum of the synthesized SERS platforms.



(a) (b) (c)

Fig. 6 Study of particles' impact on mouse colorectal carcinoma cells (CT26.WT) during 48 h of co-incubation. (a) Relative metabolic activity of CT26.WT after 48 h of incubation with particles added at different concentrations. Scanning electron microscopy (SEM) images of CT26.WT after (b) 24 h and (c) 48 h of incubation. SEM images obtained in backscattered electron (BSE) mode. Scale bar corresponds to 100 μm.

It is important to note that the silica microparticles after adsorption of gold nanostars retained colloidal stability, were not aggregated, and in the SEM image (Fig. 5a) the microspheres are separated from each other. The extinction spectra SiO_2@AuNst shown in the Fig. 5b demonstrate that the positions of the surface plasmon resonance peaks for stars adsorbed on silica microspheres differ from those for the original colloid. In this case, the plasmon resonance peak broadens and shifts to the near IR region of the spectrum.

The effect of the designed particles on cellular metabolic activity and determination of particle concentrations that exert significant cytotoxic effect were studied on mouse colorectal carcinoma cells (CT26.WT). The study was conducted in a wide range of added particles (Fig. 6a).

The most pronounce decrease in metabolic activity was observed with the addition of 15 or more particles per cell. However, such a decrease did not exceed 24% even for the case of co-incubation of cells and particles at a concentration of 50 particles per cell. Study of cell morphology during co-incubation with particles (30 particles per cell) after 24 and 48 h by scanning electron microscopy did not reveal areas of dead cells (Fig. 6 b, c). After the specified time, the cells had normal morphology (as they were elongated and adhered to the bottom), and their number also increased significantly between 24 and 48 h. Thus, it can be concluded that the developed SERS platform does not have any toxic effects *in vitro*.

In the images obtained by scanning electron and atomic force microscopy spread cells with pseudopodia can be seen (Fig. 7a, b). The constructed surface profiles of the obtained AFM images (Fig. 7c) allow us to distinguish particles adhered to the cell membrane on the cell surface (profile 1) from particles internalized by the cell (profile 2).

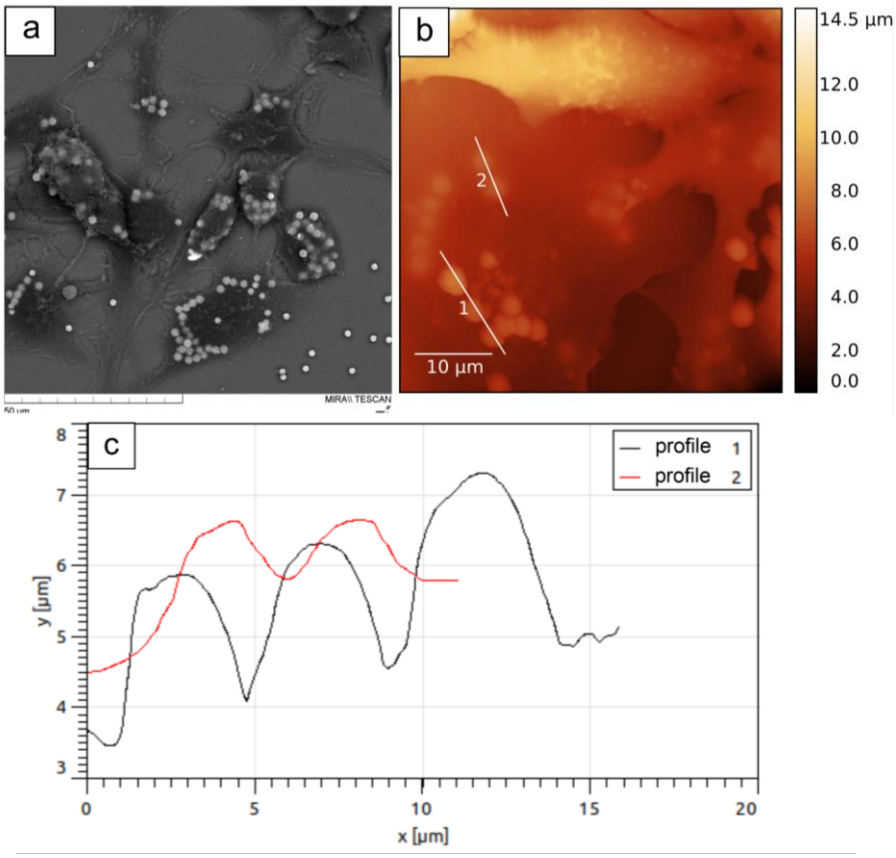


Fig. 7 Particle internalization by CT26.WT cells. (a) Scanning electron microscopy in backscattered electron (BSE) detection mode. Scale bar is 50 µm. (b) AFM of a cell layer after 48 h of incubation with SERS platforms. (c) Surface profile of AFM image.

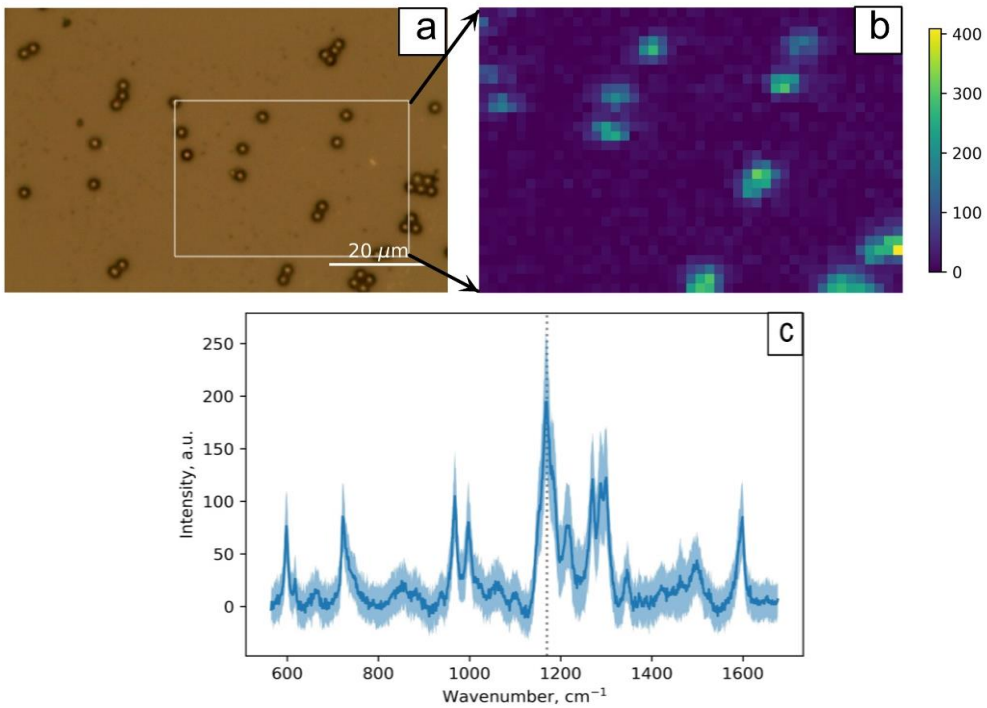


Fig. 8 (a) Microscopic image of SiO_2@AuNst microparticles deposited on quartz glass together with formazan. (b) SERS map of SiO_2@AuNst microparticles deposited on quartz glass together with formazan. (c) Averaged SERS spectrum of different SiO_2@AuNst microparticles and spectrum variations from particle to particle. The image is decoded by the intensity of the characteristic line. Panel (c) shows mean SERS spectrum with standard deviation of the studied microparticles.

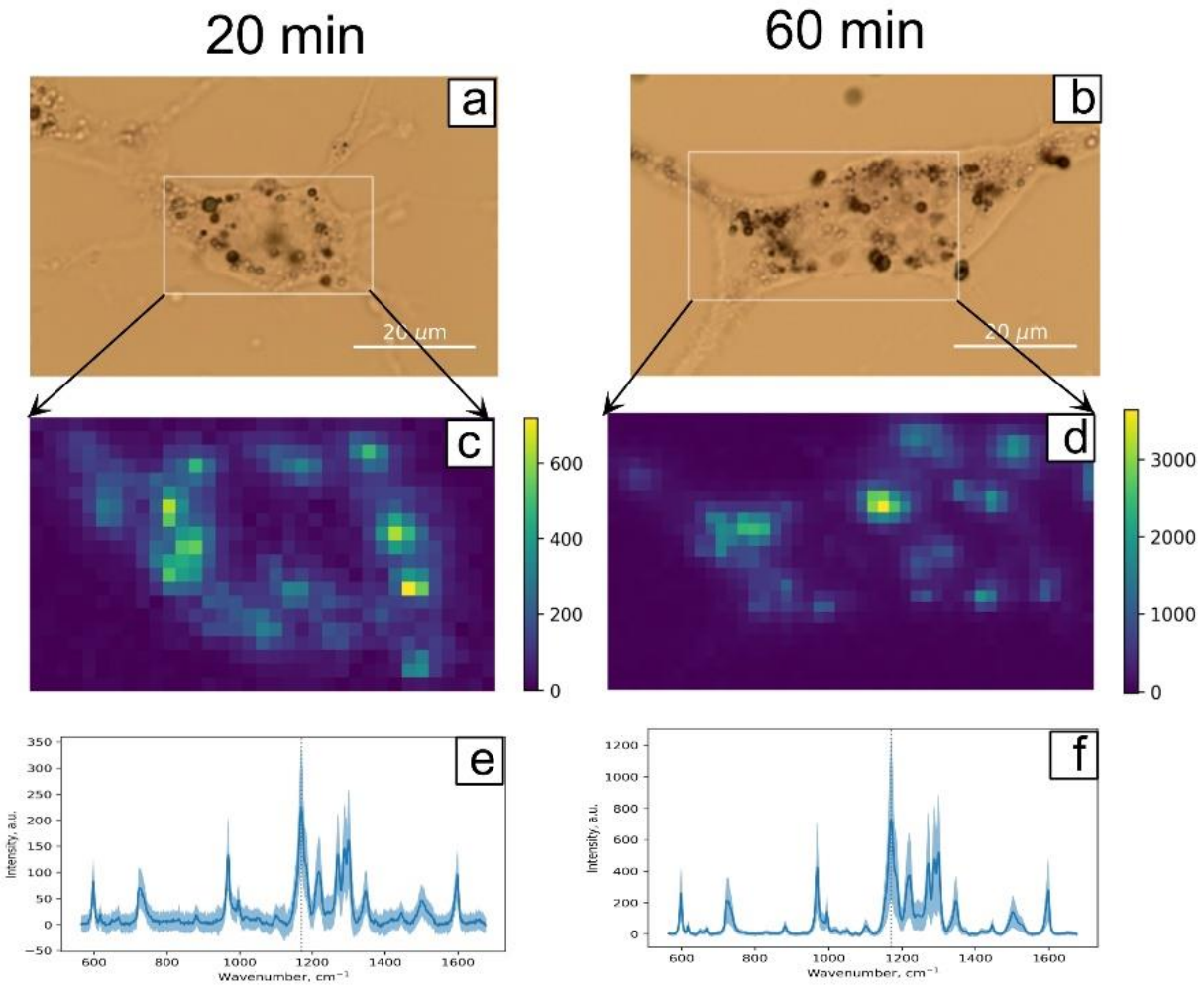


Fig. 9 Microscopic images of CT26.WT cells incubated with SiO_2@AuNst microparticles at a concentration of 30 pieces per cell (a) 20 and (b) 60 min after the addition of formazan. (c, d) SERS mapping of these cells. (e, f) SERS spectra (mean and standard deviation) of formazan inside the cells measured using SiO_2@AuNst microparticles.

Our main goal was to demonstrate the possibility of local detection of formazan using the developed SiO_2@AuNst microplatform. To test the assumption of the possibility of local detection, the platforms were mixed with a formazan solution (0.1 mg/mL) and dried on the surface of quartz glass. Then, SERS mapping of the area containing microparticles and their aggregates was performed, and the signal levels on the microparticles and in the areas where there was only formazan without particles were estimated. Fig. 8a shows a microscopic image of microparticles dried from a mixture with formazan. Due to the 2 μm size, the particles are easily visualized using a conventional optical microscope with a 40× objective. The mapping area is marked with a white rectangle. Mapping was performed with a resolution of 1 μm. The SERS image constructed from the intensity of the most pronounced line at 1176 cm^{-1} (Fig. 8b) shows that the position and number of particles coincide with the optical image, and outside the particles, the signal from formazan is at the noise level. The averaged spectra from different particles and the signal variation are shown in Fig. 8c. The signal level variation within 20% from particle to particle is visible.

To test the possibility of detecting formazan inside cells using the developed SERS platforms, cells were incubated with microparticles and individual living cells were mapped 20 and 60 min after adding MTT.

Fig. 9 a, b shows microscopic images of cells after incubation with microparticles and adding MTT. Microparticles accumulated inside the cells are visible in the optical image. To assess the enzymatic activity, SERS mapping of the cell was performed (Fig. 9c, d). In both cases, formazan accumulation in the cells was observed, and it was especially easily detected in the area of localization of the SERS microplatforms. It should be noted that the absolute signal level after 60 min was 4 times higher than after 20 min (Fig. 9e, f). However, even after 20 min, it is quite detectable. Thus, the developed platforms and SERS detection technique allows one to study enzymatic activity at the level of a single cell based on the level and distribution of the SERS signal from MTT-formazan. An additional advantage is the ability to evaluate these parameters within 20 min

after adding the reagent and the absence of the need to dissolve formazan with dimethyl sulfoxide.

4 Conclusions

A novel type of SERS platform, consisting of silica microspheres coated with gold nanostars, was developed and combined with Raman imaging technology and traditional MTT assay to determine the viability of single cells *in situ*. First, the formazan concentration can be determined from the SERS signal intensity without performing the extraction and enrichment steps. Second, the SERS spectra of formazan can be directly obtained at the level of a single particle internalized by the cell. Based on the characteristics of SERS, the SERS-MTT detection method is expected to avoid interference from background substances (such as residual MTT reagent, serum, exogenous drugs) in cell suspensions. In addition, the proposed approach not only simplifies the testing procedure, but we also expect it to have a higher accuracy in assessing the efficacy of anticancer drugs compared to the traditional MTT method.

Acknowledgment

The study was supported by Russian Science Foundation, grant No. 23-24-00062.

Disclosures

The authors declare that they have no conflict of interest.

References

1. T. Mosmann, "Rapid colorimetric assay for cellular growth and survival: Application to proliferation and cytotoxicity assays," Journal of Immunological Methods 65(1–2), 55–63 (1983).
2. A. M. Mattson, C. O. Jensen, and R. A. Dutcher, "Triphenyltetrazolium chloride as a dye for vital tissues," Science 106(2752), 294–295 (1947).
3. A. S. Shawali, N. A. Samy, "Functionalized formazans: A review on recent progress in their pharmacological activities," Journal of Advanced Research 6(3), 241–254 (2015).
4. F. M. Young, W. Phungtamdet, and B. J. S. Sanderson, "Modification of MTT assay conditions to examine the cytotoxic effects of amitraz on the human lymphoblastoid cell line, WIL2NS," Toxicology in Vitro 19(8), 1051–1059 (2005).
5. F. Denizot, R. Lang, "Rapid colorimetric assay for cell growth and survival," Journal of Immunological Methods 89(2), 271–277 (1986).
6. T. J. M. Patricia Price, Trevor J. McMillan, "Use of the tetrazolium assay in measuring the response of human tumor cells to ionizing radiation," Cancer Research 50(5), 1392–1396 (1990).
7. D. Gerlier, N. Thomasset, "Use of MTT colorimetric assay to measure cell activation," Journal of Immunological Methods 94(1−2), 57−63 (1986).
8. K. Buch, T. Peters, T. Nawroth, M. Sänger, H. Schmidberger, and P. Langguth, "Determination of cell survival after irradiation via clonogenic assay versus multiple MTT Assay - A comparative study," Radiation Oncology 7(1), 1 (2012).
9. E. Ulukaya, F. Ozdikicioglu, A. Y. Oral, and M. Demirci, "The MTT assay yields a relatively lower result of growth inhibition than the ATP assay depending on the chemotherapeutic drugs tested," Toxicology in Vitro 22(1), 232–239 (2008).
10. Z. Chen, G. Liu, M. Chen, B. Xu, Y. Peng, M. Chen, and M. Wu, "Screen anticancer drug in vitro using resonance light scattering technique," Talanta 77(4), 1365–1369 (2009).
11. N. T. H. Nga, T. T. B. Ngoc, N. T. M. Trinh, T. L. Thuoc, and D. T. P. Thao, "Optimization and application of MTT assay in determining density of suspension cells," Analytical Biochemistry 610, 113937 (2020).
12. R. Foldbjerg, D. A. Dang, and H. Autrup, "Cytotoxicity and genotoxicity of silver nanoparticles in the human lung cancer cell line, A549," Archives of Toxicology 85(7), 743–750 (2011).
13. P. Marqués-Gallego, H. den Dulk, C. Backendorf, J. Brouwer, J. Reedijk, and J. F. Burke, "Accurate non-invasive image-based cytotoxicity assays for cultured cells," BMC Biotechnology 10(1), 43 (2010).
14. 14. J. Kneipp, H. Kneipp, and K. Kneipp, "SERS—a single-molecule and nanoscale tool for bioanalytics," Chemical Society Reviews 37(5), 1052 (2008).
15. Z. Mao, Z. Liu, L. Chen, J. Yang, B. Zhao, Y. M. Jung, X. Wang, and C. Zhao, "Predictive value of the surface-enhanced resonance raman scattering-based mtt assay: a rapid and ultrasensitive method for cell viability in situ," Analytical Chemistry 85(15), 7361–7368 (2013).
16. B. Zhang, H. Wang, L. Lu, K. Ai, G. Zhang, and X. Cheng, "Large-area silver-coated silicon nanowire arrays for molecular sensing using surface-enhanced raman spectroscopy," Advanced Functional Materials 18(16), 2348–2355 (2008).
17. A. Musumeci, D. Gosztola, T. Schiller, N. M. Dimitrijevic, V. Mujica, D. Martin, and T. Rajh, "SERS of semiconducting nanoparticles (TiO 2 hybrid composites)," Journal of the American Chemical Society 131(17), 6040–6041 (2009).

18. S. Lee, S. Kim, J. Choo, S. Y. Shin, Y. H. Lee, H. Y. Choi, S. Ha, K. Kang, and C. H. Oh, "Biological imaging of hek293 cells expressing plcγ1 using surface-enhanced raman microscopy," Analytical Chemistry 79(3), 916–922 (2007).
19. J. R. Lombardi, R. L. Birke, "A unified view of surface-enhanced raman scattering," Accounts of Chemical Research 42(6), 734–742 (2009).
20. B. Tolaieb, C. J. L. Constantino, and R. F. Aroca, "Surface-enhanced resonance Raman scattering as an analytical tool for single molecule detection," Analyst 129(4), 337 (2004).
21. S. Shanmukh, L. Jones, Y.-P. Zhao, J. D. Driskell, R. A. Tripp, and R. A. Dluhy, "Identification and classification of respiratory syncytial virus (RSV) strains by surface enhanced Raman spectroscopy and multivariate statistical techniques," Analytical and Bioanalytical Chemistry 390(6), 1551–1555 (2008).
22. X. Qian, X.-H. Peng, D. O. Ansari, Q. Yin-Goen, G. Z. Chen, D. M. Shin, L. Yang, A. N. Young, M. D. Wang, and S. Nie, "In vivo tumor targeting and spectroscopic detection with surface-enhanced Raman nanoparticle tags," Nature Biotechnology 26(1), 83–90 (2008).
23. J.-H. Kim, J.-S. Kim, H. Choi, S.-M. Lee, B.-H. Jun, K.-N. Yu, E. Kuk, Y.-K. Kim, D. H. Jeong, M.-H. Cho, and Y.-S. Lee, "Nanoparticle probes with surface enhanced raman spectroscopic tags for cellular cancer targeting," Analytical Chemistry 78(19), 6967–6973 (2006).
24. K. Hering, D. Cialla, K. Ackermann, T. Dörfer, R. Möller, H. Schneidewind, R. Mattheis, W. Fritzsche, P. Rösch, and J. Popp, "SERS: a versatile tool in chemical and biochemical diagnostics," Analytical and Bioanalytical Chemistry 390(1), 113–124 (2008).
25. Z. Wang, A. Bonoiu, M. Samoc, Y. Cui, and P. N. Prasad, "Biological pH sensing based on surface enhanced Raman scattering through a 2-aminothiophenol-silver probe," Biosensors and Bioelectronics 23(6), 886–891 (2008).
26. R. Stevenson, R. J. Stokes, D. MacMillan, D. Armstrong, K. Faulds, R. Wadsworth, S. Kunuthur, C. J. Suckling, and D. Graham, "In situ detection of pterins by SERS," Analyst 134(8), 1561 (2009).
27. H.-J. Van Manen, Y. M. Kraan, D. Roos, and C. Otto, "Single-cell Raman and fluorescence microscopy reveal the association of lipid bodies with phagosomes in leukocytes," Proceedings of the National Academy of Sciences 102(29), 10159–10164 (2005).
28. B. N. Khlebtsov, A. M. Burov, S. V. Zarkov, and N. G. Khlebtsov, "Surface-enhanced Raman scattering from Au nanorods, nanotriangles, and nanostars with tuned plasmon resonances," Physical Chemistry Chemical Physics 25(45), 30903–30913 (2023).
29. N. Pazos-Perez, L. Guerrini, and R. A. Alvarez-Puebla, "Plasmon tunability of gold nanostars at the tip apexes," ACS Omega 3(12), 17173–17179 (2018).
30. G. Frens, "Controlled nucleation for the regulation of the particle size in monodisperse gold suspensions," Nature Physical Science 241(105), 20–22 (1973).
31. B. N. Khlebtsov, A. M. Burov, "Synthesis of monodisperse silica particles by controlled regrowth," Colloid Journal 85(3), 456–468 (2023).
32. V. Tuchin (Ed.), Tissue optics: light scattering methods and instruments for medical diagnostics, 3rd ed., SPIE Press, Bellingham, USA (2015). ISBN: 9781628415162.
33. H. Garn, H. Krause, V. Enzmann, and K. Dröβler, "An improved MTT assay using the electron-coupling agent menadione," Journal of Immunological Methods 168(2), 253–256 (1994).
34. S. M. Thom, R. W. Horobin, E. Seidler, and M. R. Barer, "Factors affecting the selection and use of tetrazolium salts as cytochemical indicators of microbial viability and activity," Journal of Applied Bacteriology 74(4), 433–443 (1993).
35. M. Shoemaker, I. Cohen, and M. Campbell, "Reduction of MTT by aqueous herbal extracts in the absence of cells," Journal of Ethnopharmacology 93(2–3), 381–384 (2004).
36. S.-W. Lim, H.-S. Loh, K.-N. Ting, T. D. Bradshaw, and Z. N. Allaudin, "Reduction of MTT to purple formazan by vitamin e isomers in the absence of cells," Tropical Life Sciences Research 26(1), 111 (2015).
37. L. Peng, B. Wang, and P. Ren, "Reduction of MTT by flavonoids in the absence of cells," Colloids Surfaces B Biointerfaces 45(2), 108–111 (2005).
38. P. Senthil Kumar, I. Pastoriza-Santos, B. Rodríguez-González, F. Javier García de Abajo, and L. M. Liz-Marzán, "High-yield synthesis and optical response of gold nanostars," Nanotechnology 19(1), 015606 (2008).
39. X. Zou, E. Ying, and S. Dong, "Seed-mediated synthesis of branched gold nanoparticles with the assistance of citrate and their surface-enhanced Raman scattering properties," Nanotechnology 17(18), 4758–4764 (2006).
40. J. Xie, Q. Zhang, J. Y. Lee, and D. I. C. Wang, "The synthesis of SERS-active gold nanoflower tags for in vivo applications," ACS Nano 2(12), 2473–2480 (2008).
41. N. G. Khlebtsov, S. V. Zarkov, V. A. Khanadeev, and Y. A. Avetisyan, "A novel concept of two-component dielectric function for gold nanostars: theoretical modelling and experimental verification," Nanoscale 12(38), 19963–19981 (2020).
42. Y. C. Cao, R. Jin, and C. A. Mirkin, "Nanoparticles with Raman spectroscopic fingerprints for dna and rna detection," Science 297(5586), 1536–1540 (2002).

43. J.-M. Nam, C. S. Thaxton, and C. A. Mirkin, "Nanoparticle-based bio-bar codes for the ultrasensitive detection of proteins," Science 301(5641), 1884–1886 (2003).
44. W. E. Doering, S. Nie, "Spectroscopic tags using dye-embedded nanoparticles and surface-enhanced raman scattering," Analytical Chemistry 75(22), 6171–6176 (2003).

Preparation of Fluorescently Labeled Bacteria via Biogenic Synthesis of Orange-Red Emitting Gold Nanoclusters

Daniil S. Chumakov[1*], Stella S. Evstigneeva[1], and Nikolai G. Khlebtsov[1,2]
[1] Institute of Biochemistry and Physiology of Plants and Microorganisms, Saratov Scientific Centre of the Russian Academy of Sciences (IBPPM RAS), 13 Prospekt Entuziastov, Saratov 410049, Russian Federation
[2] Saratov State University, 83 Astrakhanskaya str., Saratov 410012, Russian Federation
[*]e-mail: laik2012@yandex.ru

Abstract. Whole-cell bacteria-based luminescent probes are crucial for monitoring bacterial interactions with biotic surfaces. The primary approach to developing these probes involves genetic engineering, which is labor-intensive and sophisticated technology. In this study, we created fluorescent probes derived from gram-negative and gram-positive bacteria. This was achieved through the chemical modification of their surfaces with fluorescent glutathione-stabilized gold nanoclusters (bio-GSH-AuNCs) that were synthesized using biogenic approaches. On the other hand, similar nanoclusters produced via traditional chemical reduction approach (ch-GSH-AuNCs) were shown to be ineffective in modifying the bacterial surface. We developed and characterized biofilms of the rhizobacteria *Azospirillum baldaniorum* Sp245 and *Bacillus subtilis* 26D. Notably, this study marks the first report of generating fluorescently labeled bacterial biofilms through the biogenic synthesis of fluorescent gold nanoclusters. The resulting fluorescent bacterial probes, doped with bio-GSH-AuNCs, show significant potential for visualizing the interactions between rhizobacteria and plant root systems. © 2024 Journal of Biomedical Photonics & Engineering.

Keywords: fluorescence; gold nanoclusters; whole-cell probes; biofilms; biogenic synthesis.

Paper #9158 received 30 Aug 2024; revised manuscript received 21 Oct 2024; accepted for publication 30 Oct 2024; published online 25 Nov 2024. doi: 10.18287/JBPE24.10.040309.

1 Introduction

Luminescent technologies hold immense practical significance in analytical chemistry, cell biology, and biomedicine. Luminescent sensors are valued for their simple analytical procedures, high sensitivity, and low background signal. The equipment required to detect luminescent signals is widely available and accessible [1]. Typically, luminescent labels refer to molecular organic dyes or emitting nanomaterials [2, 3]. However, luminescent sensors can also be developed using living cells, particularly promising bacterial cells. One of the most notable advantages of luminescent bacterial probes is their ability to colonize diverse substrates, including the tissues of larger organisms [4]. For instance, intestinal microflora performs essential functions within the host organism [5]. Similarly, plant growth-promoting rhizobacteria (PGPR) form biofilms on root surfaces [6]. Luminescently labeled bacteria offer a means to visualize interactions with biological tissues, providing valuable insights into symbiotic relationships between bacteria and their host organisms. Moreover, luminescent bacterial probes have potential applications in disease diagnostics. Numerous bacteria play a critical role in the microenvironment of malignant tumors. Most of these bacteria are located within the tumor cells [7]. Bacterial biofilms complicate the treatment of chronic wounds [8].

Three main strategies for creating luminescent probes using bacteria are genetic engineering, loading fluorescent tags into bacterial cells, and chemical modification of the bacterial surface [9]. The genetic engineering approach introduces genes encoding fluorescent reporter proteins into the bacterial genome. This can be accomplished by inserting the gene, coding for the fluorescent protein, into a plasmid, which is

subsequently delivered into the bacterial cell. Alternatively, transposons can directly integrate the marker gene into the bacterial chromosome [10]. Cao et al. [11] utilized the probiotic strain *Escherichia coli* Nissle 1917, labeled with the yellow photoactive fluorescent protein FAST, to visualize microflora within the intestines of mice. Similarly, another study employed the *Bacillus subtilis* NCIB 361 strain to express the recombinant red fluorescent protein mKate and track interactions between bacteria and the roots of *Arabidopsis thaliana* [12]. The use of fluorescent proteins in scientific research comes with several limitations. Firstly, they often exhibit a low quantum yield of fluorescence. Additionally, some commonly used fluorescent proteins require dissolved oxygen to fluoresce [13]. In contrast, luciferases are also employed as reporter proteins in developing luminescent whole-cell bacterial probes. However, many luciferase systems necessitate the addition of an external substrate, luciferin, to produce a chemiluminescent signal, typically in the spectral range of 550−570 nm. An exception to this is the LuxCDABE enzymatic system (luxCDABE operon of *Vibrio fischeri*), which is advantageous because it enables the synthesis of luciferin directly within bacterial cells [14]. For example, Matsumoto et al. [15] successfully integrated the luxCDABE operon into the genome of *Pseudomonas syringae* pv. tomato DC3000 using a Tn7 transposon. This genetic modification resulted in luminescent bacterial probes that were used to track bacterial colonization in plant tissues across several plant species. Similarly, Jutras et al. [16] utilized luminescent probes based on *Agrobacterium tumefaciens* to study bacterial interactions with *Nicotiana benthamiana* leaves. Despite these advancements, the genetic engineering approach has its drawbacks. Creating the necessary genetic constructs and transferring them into bacterial cells (a process known as transformation) is labor-intensive. Moreover, transformation is not practical for all bacterial species.

In the second strategy, fluorescent nanomaterials are incorporated into bacterial cells to enable *in vivo* tracking. Tang et al. [17] demonstrated this approach using 3 nm fluorescent green-emitting silicon nanoparticles to track bacteria in animal wound models. The nanoparticles were internalized by the bacterial cells through an ATP-binding transport protein. However, a significant limitation of this strategy is the restricted size range of nanoparticles that bacteria can effectively internalize. Besides, it is essential to note that nanoparticle size is not the sole determinant of penetration through the bacterial cell wall; it is a complex, multifactorial process.

A promising approach for developing luminescent bacterial sensors involves the chemical modification of bacterial surfaces. The bacterial cell wall is composed of many molecules, including peptidoglycan, teichoic acids, proteins, and polysaccharides. These components are rich in various functional groups, such as amino, carboxyl, thiol, and phosphoric acid residues [18]. The functional groups can be utilized to conjugate fluorescent labels onto the bacterial surface. This binding can occur through electrostatic, hydrophobic, or covalent interactions. Studies have demonstrated that bacterial surfaces can be effectively doped with various luminescent materials, including blue-emitting carbon dots [19], luminophores with aggregation-induced emission enhancement (AIE luminophores) [20], persistent luminescent nanoparticles [21], and metallic nanoclusters [22].

Fluorescent gold nanoclusters (AuNCs) are small supramolecular complexes, typically 2−3 nm in size, composed of gold atoms and organic molecules [23]. These nanoclusters exhibit unique optical properties, making them valuable for developing luminescent probes for bacterial detection. The synthesis of AuNCs is straightforward and does not require organic solvents. Key advantages of AuNCs include high photostability, the ability to tune fluorescence emission across a wide spectral range, and a large Stokes shift [24]. Several studies have used AuNCs to chemically modify bacterial surfaces, giving them luminescent properties [25, 26]. However, a limitation of this approach is that chemically synthesized AuNCs cannot bind to individual bacterial cells without specific recognition molecules. Goswami et al. [27, 28] developed fluorescent bacterial probes using *Bacillus cereus* and *E. coli* through bacteria-mediated biogenic synthesis of AuNCs to address this issue. The biosynthesized AuNCs (bio-AuNCs), stabilized by mercaptopropionic acid (MPA), were localized on the bacterial cell surfaces. This “green” synthetic approach eliminates recognition molecules needing to modify bacterial surfaces with fluorescent labels. Despite these advancements, the literature has limited information regarding the biogenic synthesis of AuNCs using bacteria. There are opportunities to develop this technology further. For instance, bio-AuNCs could be synthesized using less toxic ligands than MPA. Additionally, the potential for creating luminescent bacterial biofilms through the biogenic synthesis of AuNCs remains unexplored.

In this study, we developed fluorescent bacterial probes using the rhizobacteria *Azospirillum baldaniorum* and *Bacillus subtilis.* The bacteria were doped with biogenic gold nanoclusters (bio-AuNCs) stabilized by non-toxic glutathione residues (bio-GSH-AuNCs). To the best of our knowledge, we demonstrated the potential for biogenic synthesis of gold nanoclusters by bacterial biofilms for the first time.

2 Materials and Methods

2.1 Bacterial Cultures and Growth Conditions

A baldaniorum Sp245 and *B. subtilis* 26D strains were obtained from the Collection of Rhizosphere Microorganisms at the Institute of Biochemistry and Physiology of Plants and Microorganisms, Russian Academy of Sciences (http://collection.ibppm.ru/catalogue.html). Bacterial cultures were grown to the late exponential phase. Cultivation was conducted with constant agitation on a vibration

rotator at 30 °C. *A. baldaniorum* was cultured in a liquid selective synthetic medium containing sodium malate [29], while *B. subtilis* was grown in LB medium [30]. Light microscopy was employed using a DM2500 microscope (Leica Microsystems, Germany) to ensure the bacterial inoculum's purity. The "crushed drop" method was applied for this purpose (×480 magnification).

2.2 Biofilm Formation

Bacterial biofilms were formed by cultivating overnight bacterial cultures in liquid medium. Bacterial cultures were diluted with sterile media to achieve a 1×10^5 CFU/mL concentration. Following dilution, 2 mL of the bacterial suspensions were dispensed into sterile Petri dishes. The Petri dishes were then incubated under specific temperature conditions. *B. subtilis* 26D strain was incubated for 72 h, whereas *A. baldaniorum* Sp245 strain required an incubation period of 120 h.

2.3 Quantitative Analysis of Biofilm Thickness

Biofilm thickness was assessed using phase-contrast microscopy on a Leica LMD7000 laser microdissector. The equipment was provided by the Simbioz Center for the Collective Use of Research Equipment (IBPPM RAS, Saratov). The sample preparation and result analysis procedure followed the methodology outlined in Ref. [31]. Before microscopy, coverslips with biofilms were inverted so the biofilm faced downward and placed onto a glass slide with a well. To measure the biofilm thickness, the microscope was first focused on the bottom surface of the sample at the glass interface, recording this focal distance as Z_1 in micrometers. Then, the focal distance to the top surface of the biofilm was determined and recorded as Z_2. The biofilm thickness was calculated using the formula: $Z = (Z_2 - Z_1) \times (n / n_1)$, where n is the refractive index of glass (1.5), and n_1 is the refractive index of air (1.0).

2.4 Quantification of Biofilm Biomass

Initially, the biofilms were rinsed three times with phosphate buffer (pH 7.2) to eliminate any planktonic cells. Subsequently, a 1% aqueous solution of crystal violet dye was applied to the biofilms and allowed to incubate at room temperature for 20−30 min. After incubation, excess dye was removed by washing the biofilms three times with phosphate buffer. The adsorbed dye was then desorbed by adding ethanol, followed by gentle shaking and a brief standing period at room temperature, not exceeding 10 min. The optical density of the desorbed dye solution was measured at 590 nm. The optical density values obtained are directly proportional to the biofilm biomass present.

2.5 Scanning Electron Microscopy of Biofilms

The biofilm samples were prepared for scanning electron microscopy (SEM) following the protocol outlined in reference [32]. Initially, the samples were fixed with 3% glutaraldehyde. They were then dehydrated using a graded series of acetone concentrations (50%, 70%, 90%, and 100%) and subsequently dried with hexamethyldisilazane. Once dried, the samples were sputter-coated with gold under vacuum conditions. SEM was performed at the Educational and Scientific Institute of Nanostructures and Biosystems at Saratov State University, utilizing a Mira II LMU field emission scanning electron microscope (TESCAN, Czech Republic). The biofilms were examined at an operating voltage of 30 kV in secondary electron mode, with magnifications ranging from 1000× to 10000×.

2.6 Chemical Synthesis of Fluorescent Gold Nanoclusters

All glassware was first cleaned with aqua regia (HCl/HNO_3 in a 3:1 ratio) and subsequently rinsed with ethanol and water to ensure purity. Following the method described by Luo et al. [33], 1.5 mL of a 100 mM reduced glutathione solution was mixed with 43.5 mL of miliQ H_2O in a glass vial and stirred thoroughly. Subsequently, 5 mL of 20 mM $HAuCl_4$ solution was added to the mixture and stirred for an additional 2 min. The reaction mixture was then incubated at 70 °C without stirring for 24 h.

2.7 Staining of Bacterial Cultures with Chemically Synthesized Fluorescent Gold Nanoclusters

In order to stain bacterial cultures with chemically synthesized fluorescent gold nanoclusters (ch-GSH-AuNCs), overnight cultures were first grown with constant shaking at 100−120 rpm in a shaker-incubator. The cultures were then washed once with phosphate buffer (pH 7.2) and diluted to 1×10^8 CFU/mL. Subsequently, ch-GSH-AuNCs were added to the bacterial suspension to achieve a final concentration of 25 μM. The mixture was incubated at 37 °C for 48 h. Following incubation, the bacterial suspensions were centrifuged at 4000 rpm for 10 min. Finally, the fluorescence of both the cells and the supernatant was evaluated using a transilluminator.

2.8 Biogenic Synthesis of Fluorescent Gold Nanoclusters

The following protocol achieved the biogenic synthesis of fluorescent gold nanoclusters (bio-GSH-AuNCs) with bacterial cells. The cultures were washed with distilled water and diluted to a concentration of 1×10^8 colony CFU/mL. To bacterial suspension, 30 μL of 100 mM glutathione and 100 μL of 20 mM $HAuCl_4$ were added. The mixture was then incubated at 37 °C for 48 h.

In the biofilm-mediated synthesis, mature biofilms grown on cover glasses were transferred to Petri dishes and washed three times with phosphate buffer (pH 7.2)

to eliminate non-adherent planktonic cells. Each dish was supplemented with 2 mL of distilled water, followed by the addition of 60 μL of 100 mM GSH and 200 μL of 20 mM $HAuCl_4$. The dishes were incubated at 37 °C for 48 h. After incubation, the cover glasses were thoroughly washed three times to remove any excess unreacted materials. The bio-GSH-AuNCs were visualized using a DMI6000 B inverted fluorescent microscope (Leica, Germany). Images were captured with a Leica DFC 450 camera, with an excitation light source ranging from 340 to 380 nm.

2.9 Characterization of Fluorescent Gold Nanoclusters

Extinction spectra were recorded using a Specord S600 spectrophotometer (Analytic Jena, Germany) over 300−800 nm wavelengths. Fluorescent properties were assessed with a Cary Eclipse spectrofluorimeter (Agilent Technologies, USA), with a slit width of 10 nm for measurements. Transmission electron microscopy (TEM) analysis was performed using a Libra 120 microscope (Carl Zeiss, Germany) at an accelerating voltage of 120 kV. For TEM sample preparation, the samples were applied to nickel grids coated with formvar and subsequently dried.

2.10 Assessment of Bacterial Viability

The viability of individual bacteria and cells within biofilms was evaluated using a culture-based technique. This assessment followed the biogenic synthesis of bio-AuNCs. The biofilms were detached from cover glass surfaces using 1 mL of sterile phosphate buffer (pH 7.2). Similarly, planktonic cultures were resuspended in 1 mL of the same buffer after the biogenic synthesis of bio-AuNCs. The optical density of bacterial suspensions was adjusted to 0.5 optical units at $\lambda = 600$ nm. Subsequently, the suspensions were serially diluted to 10^4, 10^5, and 10^6 in phosphate buffer and plated onto LB agar nutrient media (100 μL per plate). After incubating at 37 °C for 24−48 h, colony counts were conducted, considering the dilutions.

3 Results and Discussion

Gold nanostructures can be synthesized using various methods, including traditional chemical reduction techniques and biogenic "green" approaches that utilize whole cells or cell extracts for gold reduction [34, 35]. Fig. 1 shows the characterization of ch-GSH-AuNCs. These nanoclusters were obtained through chemical reduction.

The absorption spectrum of these nanoclusters did not exhibit a distinct peak (Fig. 1b), indicating that the synthesized nanoclusters were smaller than 5 nm and that plasmon-resonant nanoparticles were not formed. This was corroborated by electron microscopy, which showed that the ch-GSH-AuNCs had an average size of 1.5 ± 0.5 nm (Fig. 1a). The fluorescence properties of the ch-GSH-AuNCs revealed an excitation maximum at $\lambda = 410$ nm and an emission maximum at $\lambda = 613$ nm (Fig. 1c).

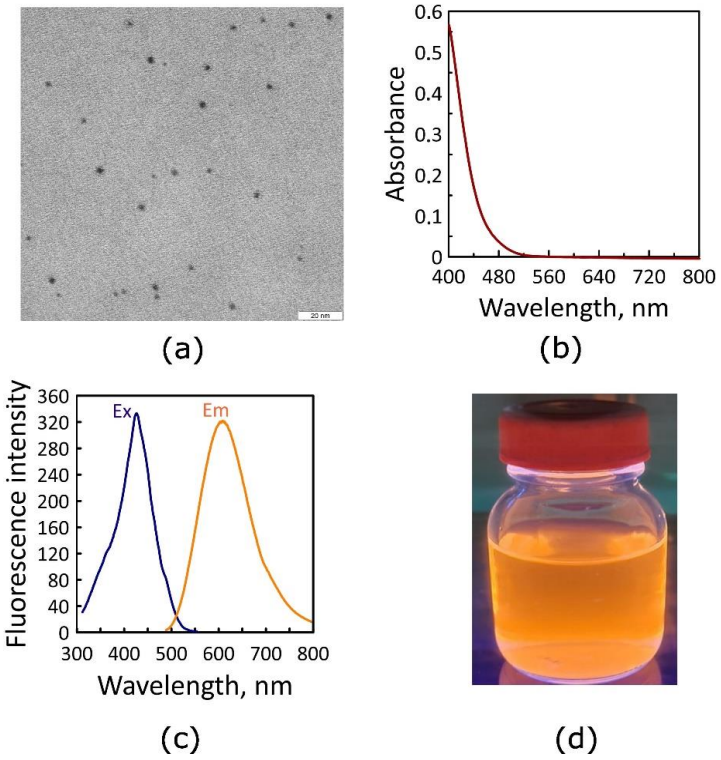


Fig. 1 Characteristics of the ch-GSH-AuNCs: (a) TEM-image of the ch-GSH-AuNCs (scale bar is 20 nm); (b) Absorption spectrum of the ch-GSH-AuNCs; (c) Fluorescence spectra of the ch-GSH-AuNCs; (d) A photograph of the ch-GSH-AuNCs suspension under UV-lamp irradiation $\lambda = 365$ nm).

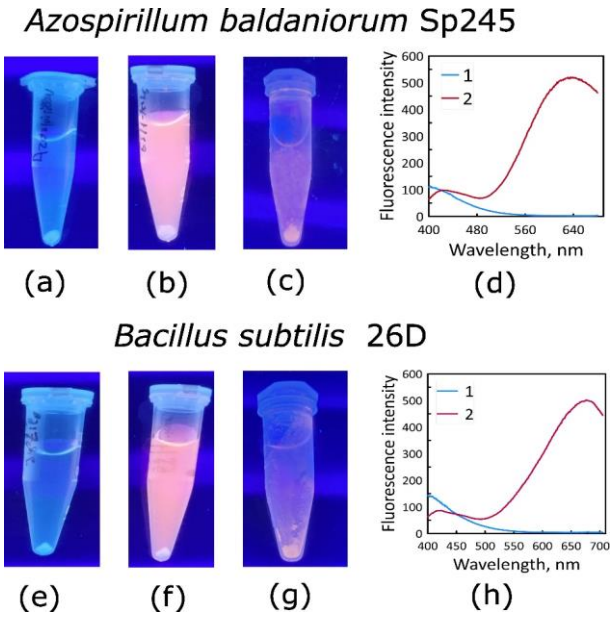


Fig. 2 Characteristics of the bio-GSH-AuNCs: (a) Photograph of the tube with *A. baldaniorum* culture; (b) Photograph obtained after incubation of *A. baldaniorum* bacteria with the ch-GSH-AuNCs for 1 h followed by centrifugation; (c) Photograph obtained after biogenic synthesis of bio-GSH-AuNCs by *A. baldaniorum* bacteria followed by centrifugation; (d) Fluorescence spectra (1 – *A. baldaniorum* culture without AuNCs, 2 – bio-GSH-AuNCs produced by *A. baldaniorum*); (e) Photograph of the tube with *B. subtilis* culture; (f) Photograph obtained after incubation of *B. subtilis* bacteria with the ch-GSH-AuNCs for 1 h followed by centrifugation; (g) Photograph obtained after biogenic synthesis of bio-GSH-AuNCs by *B. subtilis* bacteria followed by centrifugation; (h) Fluorescence spectra (1 – *B. subtilis* culture without AuNCs, 2 – bio-GSH-AuNCs produced by *B. subtilis*).

Fig. 2 presents the characterization of the bio-GSH-AuNCs synthesized biogenically by the bacterial cells of *A. baldaniorum* and *B. subtilis*.

The suspensions were centrifuged after the biogenic synthesis procedure, resulting in fluorescent bacterial pellets (Figs. 2c, g). Notably, nanoclusters were almost absent in the supernatants, indicating that bio-GSH-AuNCs effectively modified the bacterial surface. This observation is supported by the fact that free nanoclusters cannot sediment under the applied centrifugation conditions (4000 rpm). Figs. 2d, h show the fluorescence spectra of both control bacterial suspensions and those containing bio-GSH-AuNCs. The emission peaks of bio-GSH-AuNCs shifted towards the red region compared to chemically synthesized GSH-AuNCs. Specifically, bio-GSH-AuNCs from *A. baldaniorum* had an emission peak at $\lambda = 638$ nm, while those from *B. subtilis* had an emission peak at $\lambda = 662$ nm. The fluorescence spectra of bio-GSH-AuNCs displayed two distinct peaks: one in the red region due to the nanoclusters and another in the blue region from the natural autofluorescence of the bacterial cells. The biosynthesized nanoclusters showed maximum fluorescence when excited by ultraviolet light (365 nm), unlike ch-GSH-AuNCs, which were best excited by blue light. Additionally, when we tested the ability of ch-GSH-AuNCs to label bacterial cells (Figs. 2b, f), we found that the bacterial pellets did not fluoresce after incubation with ch-GSH-AuNCs. The nanoclusters remained in the supernatant, demonstrating that ch-GSH-AuNCs did not effectively bind to bacterial cells.

We have developed fluorescent probes using whole bacterial cells by synthesizing gold nanoclusters (AuNCs) through a biogenic process. This method utilizes rhizobacteria such as *A. baldaniorum* (gram-negative) and *B. subtilis* (gram-positive). These probes are particularly promising for studying how rhizobacteria interact with plant tissues. In contrast to ch-GSH-AuNCs, biogenic nanoclusters can chemically modify the surface of bacterial cells. The fluorescent properties and photostability of the bio-GSH-AuNCs are primarily attributed to glutathione residues, which stabilize the gold core through the formation of -S-Au- bonds. It is likely that the bacterial surface interacts with the functional carboxyl (-COOH) groups of glutathione residues, thereby anchoring the nanoclusters to the bacterial cell wall [28]. Importantly, glutathione, the ligand employed, is highly biocompatible and non-toxic to bacteria. The localization of biosynthesized nanoclusters within bacterial cells is an important area of inquiry. It is known that bacterial cell wall components can bind metal ions and subsequently reduce them to atoms. For example, Banerjee et al. demonstrated the use of *Bacillus anthracis* cell wall polysaccharides to produce copper nanoparticles [36]. Similarly, Goswami et al. showed that biogenic mercaptopropionic acid-stabilized AuNCs specifically formed on the surface of *E. coli* cells, as was confirmed by electron microscopy [28]. Drawing from research literature, we propose that the biogenic glutathione-stabilized bio-AuNCs are likely formed on the bacterial cell surface. This process is likely to be facilitated by cell wall biomolecules.

We conducted an investigation into the potential for biogenic synthesis of nanoclusters utilizing bacterial biofilms, specifically those formed by *A. baldaniorum* and *B. subtilis*. Both bacterial species demonstrated the ability to form biofilms on hydrophilic cover glass surfaces, although the extent of biofilm formation varied between the two species. Biofilms produced by *B. subtilis* were notably thicker, with measurements of 85.3 ± 6.8 μm, in contrast to those produced by *A. baldaniorum*, which measured 67.2 ± 3.4 μm. Correspondingly, the total biomass was observed to be greater in the biofilms of *B. subtilis* than those of *A. baldaniorum*.

We examined the ultrastructural features of biofilms formed by *A. baldaniorum* and *B. subtilis* using SEM (Fig. 3). The biofilms of *A. baldaniorum* displayed a complex spatial organization, characterized by a “mesh structure” with alternating dense and sparse clusters of cells. This matrix framework incorporated compact

fragments of cell debris and high-molecular-weight components, effectively embedding the bacteria within the biofilm. Additionally, fibril-like structures were observed to penetrate the cell layers, creating intercellular "bridges" (Fig. 3c). This structural arrangement likely plays a crucial role in adapting to biofilm formation on plant roots. Areas with higher cell density may be involved in synthesizing phytohormones and other compounds, while the sparse regions forming "channels" could facilitate their transport.

In the biofilms of *B. subtilis*, alternating regions of varying thickness and cell density were observed. Unlike *Azospirillum*, the biofilm matrix of *B. subtilis* did not form a structured framework. Instead, it consisted of a suspension containing macromolecular components and lysed cells with bacteria embedded within. The absence of fibril-like structures in the matrix is likely due to the denser packing of cells within the biofilm. Additionally, the cells of *B. subtilis* exhibited variations in size and shape, suggesting potential differentiation among the bacteria to perform specific functions (Fig. 3d).

Fig. 4 presents fluorescence microscopy images of bacterial biofilms after applying a biogenic synthesis protocol for AuNCs. The images reveal the formation of the bio-GSH-AuNCs, which subsequently modified the biofilm matrix of *A. baldaniorum* and *B. subtilis*. The bio-GSH-AuNCs exhibited fluorescence in the orange spectral range. In contrast, the control images only show the autofluorescence of the biofilm matrix.

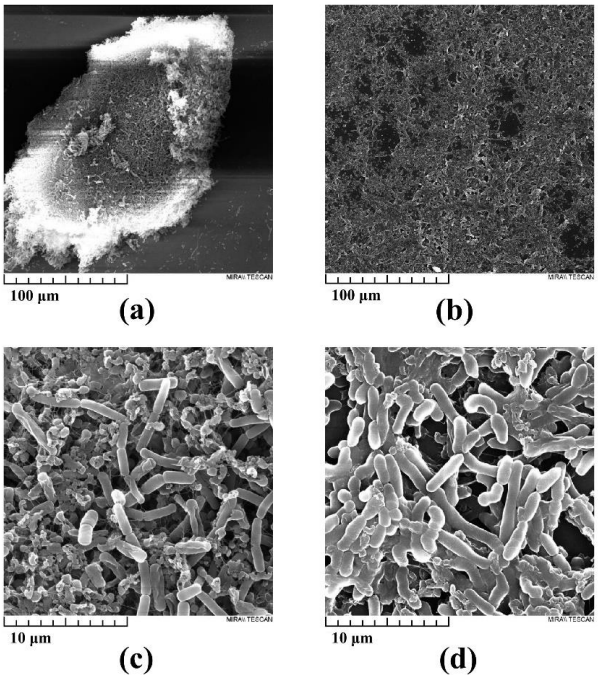


Fig. 3 SEM images of obtained bacterial biofilms: (a) SEM image of *A. baldaniorum* biofilm (× 1000); (b) SEM image of *B. subtilis* biofilm (× 1000); (c) SEM image of *A. baldaniorum* biofilm (× 10000); (d) SEM image of *B. subtilis* biofilm (× 10000).

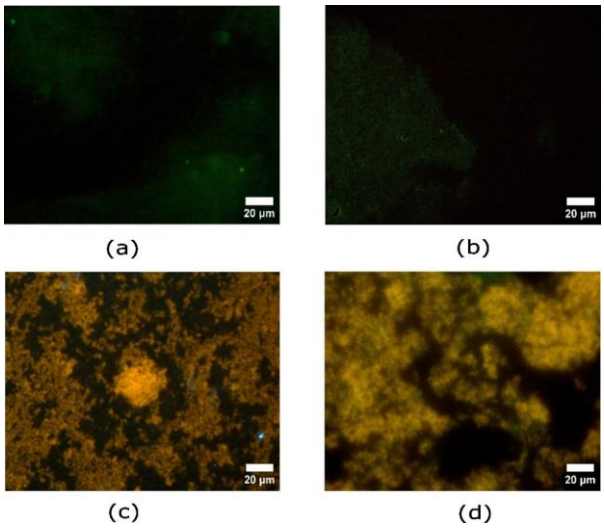


Fig. 4 Microscopic images of bacterial biofilms: (a) *A. baldaniorum* biofilm without AuNCs; (b) *B. subtilis* biofilm without AuNCs; (c) *A. baldaniorum* biofilm obtained after biogenic synthesis of bio-GSH-AuNCs; (d) *B. subtilis* biofilm obtained after biogenic synthesis of bio-GSH-AuNCs.

Preserving bacterial cell viability following the biogenic synthesis of bio-AuNCs is crucial. We conducted further studies to address this concern. We evaluated bacterial viability using *A. baldaniorum* Sp245, as it is more sensitive to environmental factors when compared to *Bacillus* species. Native planktonic bacterial cultures and biofilms that were not exposed to the chemical compounds, required for bio-AuNCs biosynthesis, served as control samples. Fig. 5 shows that both planktonic bacterial cells and biofilms retain viability during the AuNCs biosynthesis process. In planktonic bacterial cultures, the CFU/mL declined from 1.2×10^8 to 1.4×10^6 (Fig. 5a, b). In biofilm cultures, the CFU/mL declined from 5.2×10^8 to 3.1×10^7 (Fig. 5c, d). Biofilms exhibit a greater resistance to the toxic effects of gold ions compared to individual bacterial cells.

In summary, we have successfully produced fluorescent bacterial biofilms by biologically synthesizing gold nanoclusters (AuNCs). This innovative method can be compared with our previous approach [37]. In that earlier study, we demonstrated the selective fluorescent visualization of the biofilm matrix with the ch-GSH-AuNCs. However, a notable limitation of the previous technique was its potential difficulty in visualizing biofilms on biological tissues. Chemically synthesized nanoclusters often tend to aggregate when interacting with the complex structures of biological tissues [38]. In contrast, the biogenic synthesis of fluorescent nanoclusters likely mitigates such aggregation during the detection of biofilms on biological tissue surfaces due to the gradual formation of bio-GSH-AuNCs. Our newly developed approach shows significant promise for detecting rhizobacterial biofilms on root surfaces.

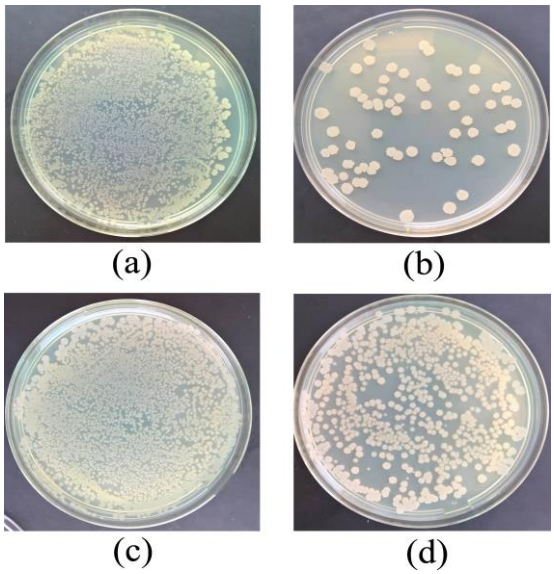


Fig. 5 Determining bacterial colony forming units: (a) native control planktonic cultures of *A. baldaniorum*, 1.2×10^8 CFU/mL; (b) planktonic cultures of *A. baldaniorum* after biosynthesis of bio-AuNCs, 1.4×10^6 CFU/mL; (c) biofilm control cultures of *A. baldaniorum*, 5.2×10^8 CFU/mL; (d) biofilm cultures of *A. baldaniorum* after biosynthesis of bio-AuNCs, 3.1×10^7 CFU/mL.

4 Conclusion

In this study, fluorescent whole-cell probes were developed using the rhizobacteria *A. baldaniorum* and *B. subtilis*. The bacterial surfaces were chemically modified with biogenically synthesized fluorescent glutathione-stabilized gold nanoclusters (bio-GSH-AuNCs). The fluorescently labeled bacteria had an excitation peak at a wavelength of 365 nm. For the bio-GSH-AuNCs-modified *A. baldaniorum*, the emission peak was observed at $\lambda = 638$ nm, whereas for the bio-GSH-AuNCs-modified *B. subtilis*, the emission peak occurred at $\lambda = 662$ nm. Furthermore, fluorescent rhizobacterial biofilms doped with bio-GSH-AuNCs were successfully produced. Research also indicated that bacterial cells and biofilms remained viable during the biosynthesis of bio-AuNCs, although their viability was diminished. A notable distinction was observed between biogenic and chemically synthesized glutathione-stabilized AuNCs (ch-GSH-AuNCs) in their ability to modify bacterial cells. The ch-GSH-AuNCs were unable to bind to the bacterial cells. These findings suggest that biogenic synthesis is an effective method for creating bacteria-based luminescent probes. Such probes hold significant potential for future applications in visualizing interactions between rhizobacteria and plant root systems.

Acknowledgments

The authors thank Victor Galushka (SSU, Saratov, Russia) for scanning electron microscopy measurements using the "Educational and Scientific Institute of Nanostructures and Biosystems" equipment of the Saratov State University.

Funding

This research was supported by the Russian Science Foundation (Project № 23-24-00246).

Disclosures

The authors declare that they have no known competing financial interests or personal relationships that could have appeared to influence the work reported in this paper.

References

1. D. K. Mal, H. Pal, and G. Chakraborty, "A comprehensive review on recent advances in fluorescence-based bio-analytes sensing," TrAC Trends in Analytical Chemistry 171, e117493 (2024).
2. S. Zeng, X. Liu, Y. S. Kafuti, H. Kim, J. Wang, X. Peng, H. Li, and J. Yoon, "Fluorescent dyes based on rhodamine derivatives for bioimaging and therapeutics: recent progress, challenges, and prospects," Chemical Society Reviews 52(16), 5607–5651 (2023).
3. M. J. Ruedas-Rama, J. D. Walters, A. Orte, and E. A. H. Hall, "Fluorescent nanoparticles for intracellular sensing: a review," Analytica Chimica Acta 751, 1−23 (2012).
4. R. Soldan, N. Sanguankiattichai, M. Bach-Pages, I. Bervoets, W. E. Huang, and G. M. Preston, "From macro to micro: a combined bioluminescence-fluorescence approach to monitor bacterial localization," Environmental Microbiology 23(4), 2070–2085 (2021).
5. K. Hou, Z.-X. Wu, X.-Y. Chen, J.-Q. Wang, D. Zhang, C. Xiao, D. Zhu, J. B. Koya, L. Wei, J. Li, and Z.-S. Chen, "Microbiota in health and diseases," Signal Transduction and Targeted Therapy 7(1), e135 (2022).
6. Y. Liu, Z. Xu, L. Chen, W. Xun, X. Shu, Y. Chen, X. Sun, Z. Wang, Y. Ren, Q. Shen, and R. Zhang, "Root colonization by beneficial rhizobacteria," FEMS Microbiology Reviews 48(1), fuad066 (2024).
7. D. Nejman, I. Livyatan, G. Fuks, N. Gavert, Y. Zwang, L. T. Geller, A. Rotter-Maskowitz, R. Weiser, G. Mallel, E. Gigi, A. Meltser, G. M. Douglas, I. Kamer, V. Gopalakrishnan, T. Dadosh, S. Levin-Zaidman, S. Avnet, T. Atlan, Z. A. Cooper, R. Arora, A. P. Cogdill, M. A. W. Khan, G. Ologun, Y. Bussi, A. Weinberger, M. Lotan-Pompan, O. Golani, G. Perry, M. Rokah, K. Bahar-Shany, E. A. Rozeman, C. U. Blank, A. Ronai, R. Shaoul, A. Amit, T. Dorfman, R. Kremer, Z. R. Cohen, S. Harnof, T. Siegal, E. Yehuda-Shnaidman, E. N. Gal-Yam, H. Shapira, N.

Baldini, M. G. I. Langille, A. Ben-Nun, B. Kaufman, A. Nissan, T. Golan, M. Dadiani, K. Levanon, J. Bar, S. Yust-Katz, I. Barshack, D. S. Peeper, D. J. Raz, E. Segal, J. A. Wargo, J. Sandbank, N. Shental, and R. Straussman, "The human tumor microbiome is composed of tumor type-specific intracellular bacteria," Science 368(6494), 973–980 (2020).
8. I. Cavallo, F. Sivori, A. Mastrofrancesco, E. Abril, M. Pontone, E. G. Di Domenico, and F. Pimpinelli, "Bacterial biofilm in chronic wounds and possible therapeutic approaches," Biology 13(2), 109 (2024).
9. H. Jiang, Z. Cao, Y. Liu, R. Liu, Y. Zhou, and J. Liu, "Bacteria-based living probes: preparation and the applications in bioimaging and diagnosis," Advanced Science 11(4), e2306480 (2024).
10. An. Kh. Baymiev, R. S. Yamidanov, R. T. Matniyazov, D. K. Blagova, Al. Kh. Baymiev, and A. V. Chemeris, "Preparation of fluorescent labeled nodule bacteria strains of wild legumes for their detection *in vivo* and *in vitro*," Molecular Biology 45(6), 904–910 (2011).
11. Z. Cao, L. Wang, R. Liu, S. Lin, F. Wu, and J. Liu, "Encoding with a fluorescence-activating and absorption-shifting tag generates living bacterial probes for mammalian microbiota imaging," Materials Today Bio 15, 100311 (2022).
12. H. Massalha, E. Korenblum, S. Malitsky, O. H. Shapiro, and A. Aharoni, "Live imaging of root-bacteria interactions in a microfluidics setup," Proceedings of the National Academy of Sciences of the United States of America 114(17), 4549–4554 (2017).
13. E. S. Swenson, J. G. Price, T. Brazelton, and D. S. Krause, "Limitations of green fluorescent protein as a cell lineage marker," Stem Cells 25(10), 2593–2600 (2007).
14. T. Jiang, X. Bai, and M. Li, "Advances in the development of bacterial bioluminescence imaging," Annual Review of Analytical Chemistry 17(1), 265–288 (2024).
15. A. Matsumoto, T. Schlüter, K. Melkonian, A. Takeda, H. Nakagami, and A. Mine, "A versatile Tn7 transposon-based bioluminescence tagging tool for quantitative and spatial detection of bacteria in plants," Plant Communications 3(1), 100227 (2021).
16. P. V. Jutras, R. Soldan, I. Dodds, M. Schuster, G. M. Preston, and R. A. L. van der Hoorn, "AgroLux: bioluminescent *Agrobacterium* to improve molecular pharming and study plant immunity," The Plant Journal 108(2), 600–612 (2021).
17. J. Tang, B. Chu, J. Wang, B. Song, Y. Su, H. Wang, and Y. He, "Multifunctional nanoagents for ultrasensitive imaging and photoactive killing of Gram-negative and Gram-positive bacteria," Nature Communications 10(1), 4057 (2019).
18. S. Gautam, T. J. Gniadek, T. Kim, and D. A. Spiegel, "Exterior design: strategies for redecorating the bacterial surface with small molecules," Trends in Biotechnology 31(4), 258–267 (2013).
19. J. Yang, X. Zhang, Y.-H. Ma, G. Gao, X. Chen, H.-R. Jia, Y.-H. Li, Z. Chen, and F.-G. Wu, "Carbon dot-based platform for simultaneous bacterial distinguishment and antibacterial applications," ACS Applied Materials & Interfaces 8(47), 32170–32181 (2016).
20. G.-J. Liu, S.-N. Tian, C.-Y. Li, G.-W. Xing, and L. Zhou, "Aggregation-induced-emission materials with different electric charges as an artificial tongue: design, construction, and assembly with various pathogenic bacteria for effective bacterial imaging and discrimination," ACS Applied Materials & Interfaces 9(34), 28331–28338 (2017).
21. L.-X. Yan, L.-J. Chen, X. Zhao, and X.-P. Yan, "pH Switchable nanoplatform for *in vivo* persistent luminescence imaging and precise photothermal therapy of bacterial infection," Advanced Functional Materials 30(14), 1909042 (2020).
22. P.-H. Chan, Y.-C. Chen, "Human serum albumin stabilized gold nanoclusters as selective luminescent probes for Staphylococcus aureus and methicillin-resistant *Staphylococcus aureus*," Analytical Chemistry 84(21), 8952–8956 (2012).
23. M. Zhou, C. Zeng, Q. Li, T. Higaki, and R. Jin, "Gold nanoclusters: bridging gold complexes and plasmonic nanoparticles in photophysical properties," Nanomaterials 9(7), 933 (2019).
24. I. M. Khan, S. Niazi, L. Yue, Y. Zhang, I. Pasha, M. K. Iqbal Khan, W. Akhtar, A. Mohsin, M. F. J. Chughati, and Z. Wang, "Research update of emergent gold nanoclusters: a reinforced approach towards evolution, synthesis mechanism and application," Talanta 241, 123228 (2022).
25. B. Khlebtsov, E. Tuchina, V. Tuchin, and N. Khlebtsov, "Multifunctional Au nanoclusters for targeted bioimaging and enhanced photodynamic inactivation of *Staphylococcus aureus*," RSC Advances 5(76), 61639–61649 (2015).
26. Y. Wang, B. Shen, Z. Zhang, Y. Chen, L. Zhu, Y. Zhang, H. Huang, and L. Jiang, "Multifunctional fluorescent gold nanoclusters with enhanced aggregation-induced emissions (AIEs) and excellent antibacterial effect for bacterial imaging and wound healing," Biomaterials Advances 137, 212841 (2022).
27. U. Goswami, S. Basu, A. Paul, S. S. Ghosh, and A. Chattopadhyay, "White light emission from gold nanoclusters embedded bacteria," Journal of Materials Chemistry C 5(47), 12360–12364 (2017).
28. U. Goswami, A. K. Sahoo, A. Chattopadhyay, and S. S. Ghosh, "*In situ* synthesis of luminescent Au nanoclusters on a bacterial template for rapid detection, quantification, and distinction of kanamycin-resistant bacteria," ACS Omega 3(6), 6113–6119 (2018).

29. S. A. Konnova, O. E. Makarov, I. M. Skvortsov, and V. V. Ignatov, "Isolation, fractionation and some properties of polysaccharides produced in a bound form by *Azospirillum brasilense* and their possible involvement in *Azospirillum*-wheat root interactions," FEMS Microbiology Letters 118(1−2), 93–99 (1994).
30. G. Bertani, "Studies on lysogenesis I: the mode of phage liberation by lysogenic *Escherichia coli*," Journal of Bacteriology 62(3), 293–300 (1951).
31. A. V. Shelud'ko, Y. A. Filip'echeva, E. M. Shumilova, B. N. Khlebtsov, A. M. Burov, L. P. Petrova, and E. I. Katsy, "Changes in biofilm formation in the nonflagellated flhB1 mutant of *Azospirillum brasilense* Sp245," Microbiology 84(2), 144–151 (2015).
32. J. Makovcova, V. Babak, P. Kulich, J. Masek, M. Slany, and L. Cincarova, "Dynamics of mono- and dual-species biofilm formation and interactions between *Staphylococcus aureus* and Gram-negative bacteria," Microbial Biotechnology 10(4), 819–832 (2017).
33. Z. Luo, X. Yuan, Y. Yu, Q. Zhang, D. T. Leong, J. Y. Lee, and J. Xie, "From aggregation-induced emission of Au(I)-thiolate complexes to ultrabright Au(0)@Au(I)-thiolate core-shell nanoclusters," Journal of the American Chemical Society 134(40), 16662–16670 (2012).
34. D. S. Chumakov, A. O. Sokolov, V. A. Bogatyrev, O. I. Sokolov, N. Yu. Selivanov, and L. A. Dykman, "Green synthesis of gold nanoparticles using *Arabidopsis thaliana* and *Dunaliella salina* cell cultures," Nanotechnologies in Russia 13, 539–545 (2018).
35. D. Chumakov, T. Pylaev, E. Avdeeva, L. Dykman, N. Khlebtsov, and V. Bogatyrev, "Anticancer properties of gold nanoparticles biosynthesized by reducing of chloroaurate ions with *Dunaliella salina* aqueous extract," Proceedings of SPIE 11457, e2564630 (2020).
36. A. Banerjee, R. K. Roy, S. Sarkar, J.L. López, S. Vuree, and R. Bandopadhyay, "Synthesis of hot spring origin bacterial cell wall polysaccharide-based copper nanoparticles with antibacterial property," Electronic Journal of Biotechnology 68, 11–19 (2024).
37. S. S. Evstigneeva, D. S. Chumakov, R. S. Tumskiy, B. N. Khlebtsov, and N. G. Khlebtsov, "Detection and imaging of bacterial biofilms with glutathione-stabilized gold nanoclusters," Talanta 264, 124773 (2023).
38. S. M. van de Looij, E. R. Hebels, M. Viola, M. Hembury, S. Oliveira, and T. Vermonden, "Gold nanoclusters: imaging, therapy, and theranostic roles in biomedical applications," Bioconjugate Chemistry 33(1), 4–23 (2022).

Estimating the Porosity of Nickel-Titanium (NiTi) Implants Using Optical Coherence Tomography and Machine Learning

Viktor V. Nikolaev[1], Tatiana B. Lepekhina[1], Georgii V. Malkin[1], Alexander S. Garin[1], Ekaterina S. Marchenko[1], Alexander V. Dubrov[2], Maxim D. Khomenko[2], and Yury V. Kistenev[1*]

[1] Tomsk State University, 36 Lenin Ave., 634050 Tomsk, Russian Federation

[2] NRC "Kurchatov Institute", 1 Kurchatov Sq., 123182 Moscow, Russian Federation

[*]e-mail: yuk@iao.ru

Abstract. Nickel-titanium (NiTi) implants take root well in the body and have high biocompatibility with respect to surrounding tissues. Porosity is an important parameter responsible for the biocompatibility of the material, and as a result, it is important to be able to control the material manufacturing process to achieve the required values. Destructive and non-destructive methods are currently used to analyse porosity, of which non-destructive ones are the most preferable. A method of estimating the porosity of NiTi materials using optical coherence tomography and machine learning was developed. The trained support vector machine with a radial basis function kernel classifier using the first and the second order statistics of optical coherence tomography images as a feature vector provided the classification accuracy of 95 ± 6% for two classes of NiTi materials. © 2024 Journal of Biomedical Photonics & Engineering.

Keywords: NiTi implants; optical coherence tomography; machine learning biocompatibility; porosity.

Paper #9177 received 10 Oct 2024; revised manuscript received 27 Oct 2024; accepted for publication 28 Oct 2024; published online 2 Dec 2024. doi: 10.18287/JBPE24.10.040310.

1 Introduction

Nickel-titanium (NiTi) alloys are widely utilized in medical applications due to their unique properties, such as high biocompatibility, shape memory effects, and superelasticity. These properties make NiTi a suitable material for implants in orthopedics, dentistry, and cardiology, as it can adapt to patient's anatomical features and withstand dynamic physiological loads [1]. The use of NiTi allows for the creation of implants, which are not only match the mechanical properties of natural tissues but also promote tissue regeneration [1].

Biocompatibility refers to how a material interacts with human cells and tissues without causing their significant damage. It depends on factors such as corrosion resistance and the low cytotoxicity [2]. To improve the biological response, materials must have the ability to interact favorably with the biological environment, promoting cell adhesion and proliferation [3].

An essential factor of biocompatibility is the porosity of the implant material [4, 5]. Porosity affects cell and tissue survival by providing space for cell attachment, migration, and vascularization. The strength of implant attachment increases due to bone tissue development inside the pores, while good biocompatibility is ensured by the ability of cells to adhere and spread on the material's surface, forming a monolayer. Surface roughness has a direct beneficial effect on cell morphology and proliferation, whereas a smooth surface hinders cell adhesion, reducing biocompatibility [6].

Porosity is defined as the voids within a material and is characterized by the interconnections, or throats, between these pores, and the walls or struts of the medium that form the three-dimensional structure [7]. Features of pores, throats, or struts are characterized by their size, shape, organization, density, and homogeneity. Traditionally, pore scale is delineated as macroporous, when porous widths are larger than 50 nm, mesoporous, when porous widths are between 2 nm and 50 nm, and microporous, when widths are smaller than 2 nm [8].

Pore volume is typically calculated using the density of the material (ρ_m) and the mass of the sample (m_S) [9, 10]. Eq. (1) shows these calculations of percent porosity, where V_P is the pores' volume, V_T is the total bulk volume of the material and (ε) as either a percent or ratio of V_P to V_T [5]:

$$\%\, Porosity = 100 \cdot \varepsilon = 100 \cdot \frac{V_p}{V_T} = 100 \cdot (V_T - \frac{m_s}{p_m})/V_T, \quad (1)$$

Methods allowing to measure or evaluate pores are divided on destructive and non-destructive ones [11]. Destructive methods include hydraulic, sorption, electromagnetic and ionizing techniques. For example, non-destructive methods include pneumatic and visual-optical porosity one. Using pneumatic methods, it is possible to determine the porosity, size and volume of open pores, and the specific surface area of the pores. However, they have limited applications, making visual-optical methods of pore assessment more appealing (see Table 1).

Scanning Electron Microscopy (SEM) is an electron-optical method widely used for observing and examining images of material surfaces, including medical implants, to assess their compatibility with tissues and cells. In study [12], pore size distribution was investigated using SEM images. The researchers utilized SEM images of activated carbon derived from coconut shell charcoal, with an image resolution of 1280 × 960 px. These images were processed using a program, which applies a threshold value to define areas identified as pores. This analytical approach can also be adapted to determine the pore characteristics of biomedical materials. SEM allows for the acquisition of high-quality images of porous NiTi, providing clear visualization of the structure and surface of implants produced by various methods, such as high-temperature synthesis processes and capsule-free hot isostatic pressing with argon expansion [13]. These detailed images enable a thorough analysis of pore size, distribution, and interconnectedness, which are crucial factors in assessing the biocompatibility and mechanical properties of NiTi implants.

Optical microscopy is widely used for analyzing porous structures and scaffolds, because it allows for a qualitative assessment of morphology, pore size, and pore interconnectivity. One of the advantages of this technique is its simplicity, as well as the minimal level of sample preparation required [10]. However, optical microscopy has the following limitations: it has a limited depth of focus, making it challenging to obtain high-quality and sharp images at different depths. While it allows for the visualization of pores in their entirety, evaluating porosity often requires knowledge of the depth at which these pores are located, which is not always possible with optical microscopy.

Optical Coherence Tomography (OCT) emerges as an alternative method due to its rapid measurement capabilities, minimal sample preparation, and ability to provide high-quality three-dimensional images of internal structures [14]. OCT allows for horizontal and vertical projections of the sample, giving more complete information about the diameter and size of pores.

Table 1 Comparison of methods for porosity assessment.

Technique	Advantages	Disadvantages	Ref.
Scanning Electron Microscopy (SEM)	Non-destructive; minimal preparation actions; wide-array of applications; the detailed three-dimensional and topographical imaging; easy to operate; visual estimation of interconnectivity, cross-section area, and anisotropy of the pores; greater depth of field, compared to optical microscopy.	Limited depth of focus; concerns in focusing materials with low opacity (i.e., polymers); edge effects due to scaffold preparation; the preparation of samples can result in artifacts; risk of radiation exposure; big size and high cost; black and white images.	[10, 15]
Optical microscopy	Non-destructive; low sample preparation; does not require much time; simply and not expensive.	Low opacity of most of the materials used for scaffold fabrication; difficulties in focusing 3D porous structures; smaller depth of field, compared to SEM; light reflections can mask certain features; color differentiation available; cannot go beyond around 200 nm resolution laterally and 600 to 700 nm axially.	[10]
Optical Coherence Tomography (OCT)	Non-destructive; low sample preparation; does not require much time; simply and not expensive; can produce in real time a two-dimensional image in the space (lateral coordinate, axial coordinate); real-time visualization.	Media opacities can interfere with optimal imaging.	[14]

Table 2 Chemical composition, average particle size, bulk density for powders PTM-1, PTOM-2 and PNK-OT4.

Powder	Chemical composition (impurities, wt. %)	Average particle size, μm	Bulk density, g/cm³
PTM-1 (Ti)	Ti − Bal.*, N – 0.08%, C – 0.05%, H –0.35%, Fe/Ni – 0.40%, Si – 0.10%, Cl – 0.004%	45	1.02
PTOM-2 (Ti)	Ti − Bal.*, N – 0.20%, C – 0.05%, H – 0.40%, Fe/Ni – 0.40%, Si – 1.00%, Cl – 0.004%	45	1.36
PNK-OT4 (Ni)	Ni − Bal*., Ni – 99.9%, C – 0.15%, Fe –0.0015%, Co/Zn/Cu — 0.001%, Cd/Sn/Sb – 0.0003%, Mn – 0.0005%, Pb – 0.0002%	12	1.66

* Balance (Bal.) refers to the main element that constitutes the remainder of the material after accounting for all other specified elements, it fills up the remaining percentage of the composition.

Recent publications demonstrate the effectiveness of this method for the analysis of samples porosity [16, 17]. Therefore, the use of OCT in analyzing the porosity of biomedical materials is appropriate and relevant, especially in serial production and quality control of implants.

Given the volume of data obtained during material analysis, automatic pore detection from images becomes increasingly important. Methods of mathematical morphology and image processing allow for the identification of pores and analysis of their characteristics [18]. To increase the accuracy and speed of analysis, machine learning (ML) methods are increasingly used, capable of processing large amounts of data and identifying complex patterns. ML methods, such as neural networks and other artificial intelligence algorithms, can automatically classify structures in images and quantitatively assess porosity with high accuracy, enhancing the efficiency and objectivity of the analysis.

While ML is increasingly employed to evaluate the mechanical properties of materials, its application in porosity analysis remains limited. Therefore, combining OCT with ML provides an advanced approach to effectively assess the porosity of biomedical materials. The aim of this work is to develop a predictive model for estimating the NiTi porosity using OCT and ML.

2 Materials and Methods

2.1 NiTi Preparation

To produce the porous samples, we prepared a powder mixture by combining two titanium powders, grades PTM-1 and PTOM-2, in an equal mass ratio of 1:1. This titanium powder mixture was then mixed with nickel powder of grade PNK-OT4, ensuring that the total mass of the titanium powders was equal to the mass of the nickel powder (resulting in a Ti ratio of 1:1 by weight). The powders were dried in a laboratory vacuum oven Daihan Sci (South Korea) at a temperature of 70 °C and a pressure of 0.1 MPa for 8 h, then mixed in a mixer for 8 h. The resulting powder mixture was filled into a quartz tube 400 mm long and 27 mm in diameter, which was then placed in the reactor SOUL-0,4.4/12 (Russia). The chemical composition, average particle size, and bulk density of the powders are shown in Table 2.

The next methods use for fabrication of porous NiTi shape memory alloys: element powder sintering, self-propagating high-temperature synthesis (SHS), hot isostatic pressing, capsule-free hot isostatic pressing, spark plasma sintering, metal injection molding, and mechanical alloying [19, 20].

Porous samples of NiTi were obtained using SHS method in two modes: constant and pulsating. The used quartz tubes had a length of 400 mm [21]. In the constant mode, the combustion process and synthesis reaction proceed uniformly and stably. After initiation with a molybdenum spiral at a temperature of 480 °C, the temperature in the reaction zone increased to approximately 1200 °C and is maintained at this level without significant fluctuations in temperature or reaction rate (deviations do not exceed ±10 °C). The reaction front propagated at a speed of 80 mm/s. This leads to the formation of a porous alloy with a uniform pore structure and stable characteristics.

In the pulsating mode, combustion and synthesis were characterized by periodic fluctuations in temperature and reaction rate. For obtaining a porous sample in the pulsating combustion mode, argon was used, supplied into a steel flow-through tubular reactor under a pressure of 0.1 MPa. After initiation with a molybdenum spiral at a temperature of 250 °C, the temperature in the reaction zone periodically raised to 1300 °C and drops to 900 °C, creating areas with high and low reaction intensities. The reaction front propagated with average speed of 50 mm/s. These fluctuations could cause inhomogeneities in the structure of the porous alloy, leading to variations in pore size and distribution. The SHS process is schematically shown in Fig. 1.

From the obtained cylindrical porous samples, discs with a thickness of 10 mm were cut using an ARTA-123PRO (NPK Delta-Test, Russia) wire-cut electrical discharge machine for subsequent examination by OCT method.

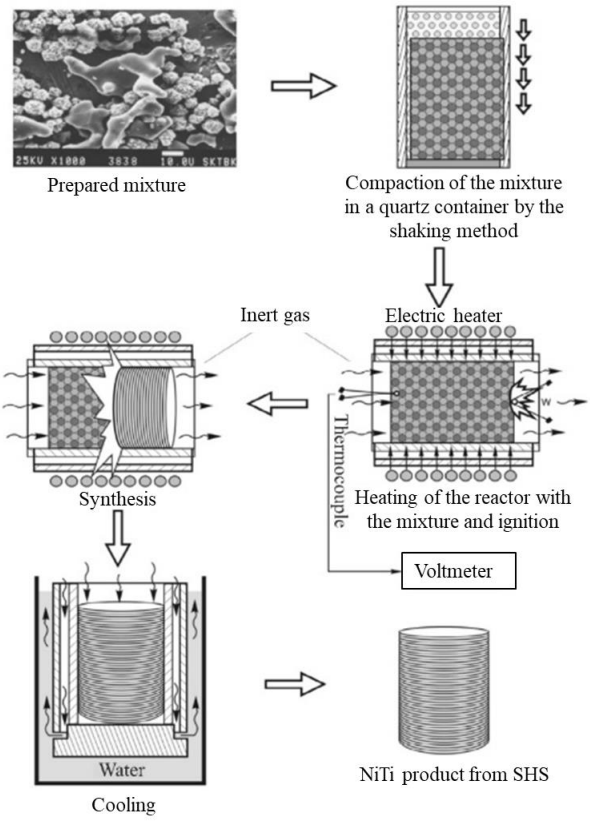


Fig. 1 Scheme for obtaining semi-finished products of porous NiTi in a flow reactor [21].

2.2 OCT Protocol

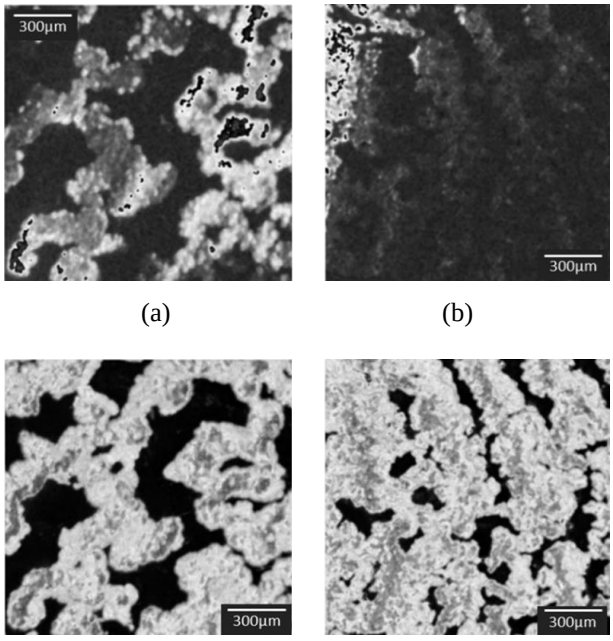
The study was conducted using OCT on the GANYMEDE−II system (Thorlabs, USA) with the basic scanning module OCTG-900. A superluminescent diode with an operating wavelength of 930 ± 50 nm, used in the GANYMEDE-II system, allows to achieve a signal penetration depth of up to 2.9 mm with an axial resolution of up to 6.0 μm. During digital data processing, depths from 200 to 400 μm were investigated.

Data processing was carried out using ThorImageOCT 5.0.1., with the following parameters: size 500 × 500 × 1024 px, field of view 3 × 3 × 2.94 mm, and pixel size 6 × 6 × 2.9 μm. The experiment was repeated with new disjoint scanning areas, which were highlighted by parallel translation along X, Y-axes and areas were measured from both sides. A total of 20 samples were measured (10 samples in each group). For each sample, 20 C-scans were measured from different non-overlapping areas (400-scans in total were measured).

Statistical analysis and data processing were carried out in Python 3.10 using libraries (numpy, scipy, matplotlib, scikit-image, scikit-learn, PIL).

3 Results

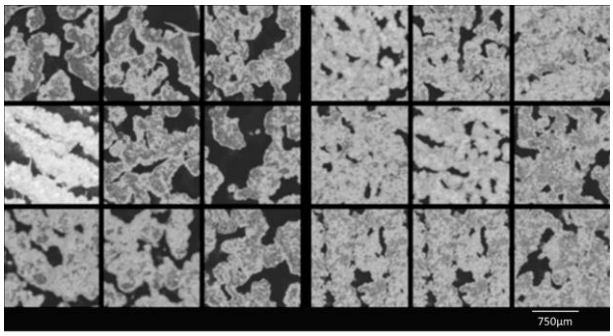
The 3D images were analyzed manually and the depth on the surface of the material was selected. After selecting the depth, images were divided on non-overlapping areas of 250 × 250 px (Fig. 2a, b) and averaging was performed by depth to reduce the noise component (Fig. 2c, d). The 95th quartile was chosen in the averaging procedure. The choice of such a procedure is due to the fact that the sample did not have a flat surface and there is an uneven distribution of intensity across the sample, as shown in Fig. 2 a, b. In addition, this procedure showed itself to be optimal in the further processing. Two examples of image processing of a porous NiTi alloy obtained by sintering, using a constant and pulsating mode, before and after averaging are shown in Fig. 2. In total, 1600 images were obtained (see the examples in Fig 3.).



(a) (b)

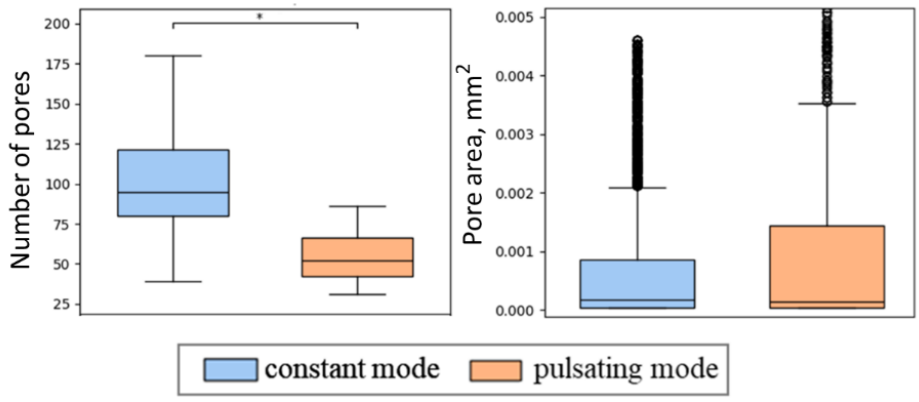
(c) (d)

Fig. 2 Examples of images of a porous NiTi alloy obtained by sintering, using (a) a constant and (b) pulsating mode, (c) before averaging and (d) after, respectively.



(a) (b)

Fig. 3 Examples of images of a porous NiTi alloy obtained by sintering, (a) using argon and (b) using pulsating mode: OCT data were from the depth of 200 μm, image size was 1.5 × 1.5 mm.



(a) (b)

Fig. 4 Distribution of samples (a) by the number of pores and (b) by the pore size. *p < 0.01 significance level between group by Mann-Whitney U-test.

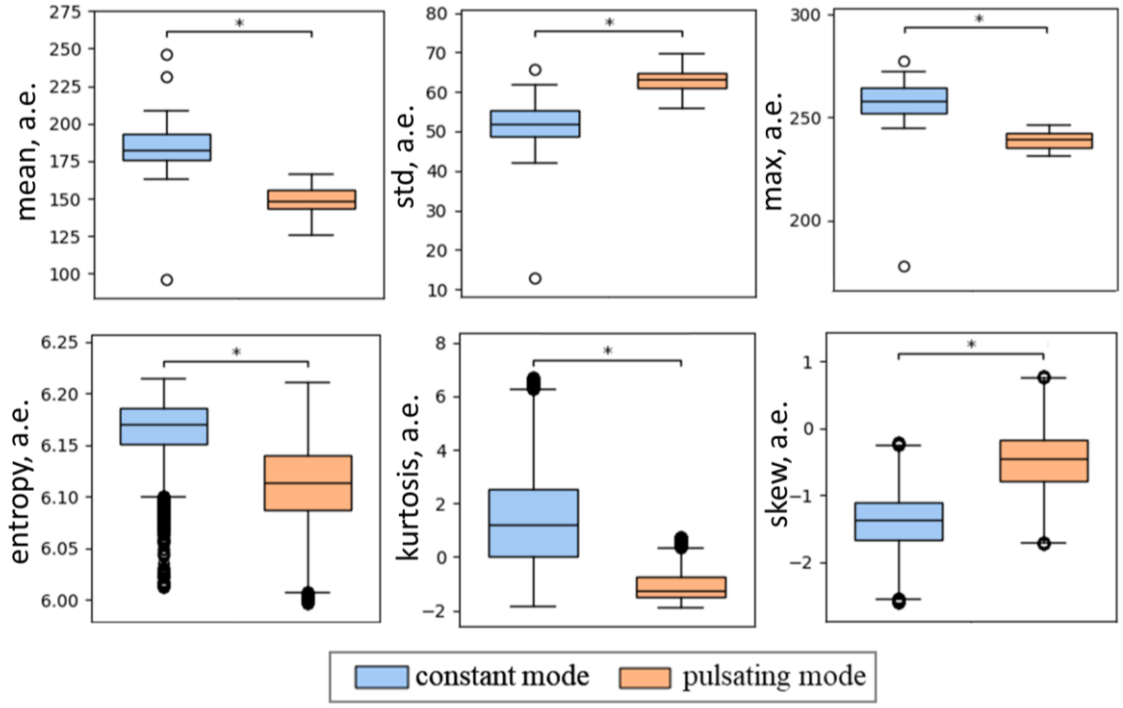


Fig. 5 Distribution of the first order statistics of OCT images. *p < 0.01 significance level between group by Mann-Whitney U-test

The next step was to calculate the number of pores and their sizes. The pore segmentation was done using the Otsu threshold, the number of regions was calculated using mathematical morphology, and the search for connected components. The pore area parameter did not show statistically significant differences in the samples, while the number of pores for the sample in the constant sintering mode category differed from the pulsating mode (see Fig. 4).

Despite their simplicity, the first- and the second-order statistics have proven to be useful for analyzing structural features in an image [22]. For the obtained data, the first- and the second-order statistics were calculated. From the first order statistics, the following characteristics were the most distinctive: mean, standard deviation, max, entropy, kurtosis and skew. For the second order statistics, the following parameters were considered: mean, standard deviation, max, Angular Second Moment (ASM), dissimilarity, entropy, energy, homogeneity, contrast. Normality was tested using the D'Agostino and Pearson tests, which verify the null hypothesis that the sample comes from a normal distribution [23, 24]. All resulting distributions were not normal. The statistical significance of differences was tested using the nonparametric Mann-Whitney test with a significance level of 0.01. All presented distributions had statistically significant differences (see box plots in Fig. 5 and Fig. 6).

The next step was to build a classifier capable of splitting the data into two classes. Support vector machine (SVM) with a linear kernel was used at this stage of analysis. The used dataset consisted of 1600 images (800 images from each class). The 5-fold cross-validation was used. According to this approach, the dataset was divided into 4 strips for training and 1 strip for testing in 80%/20% proportion. After that SVM classifier was trained and tested using this test strip. This procedure was repeated 5 times to use every strip at the test stage ones. After that, results of classifier testing were averaged.

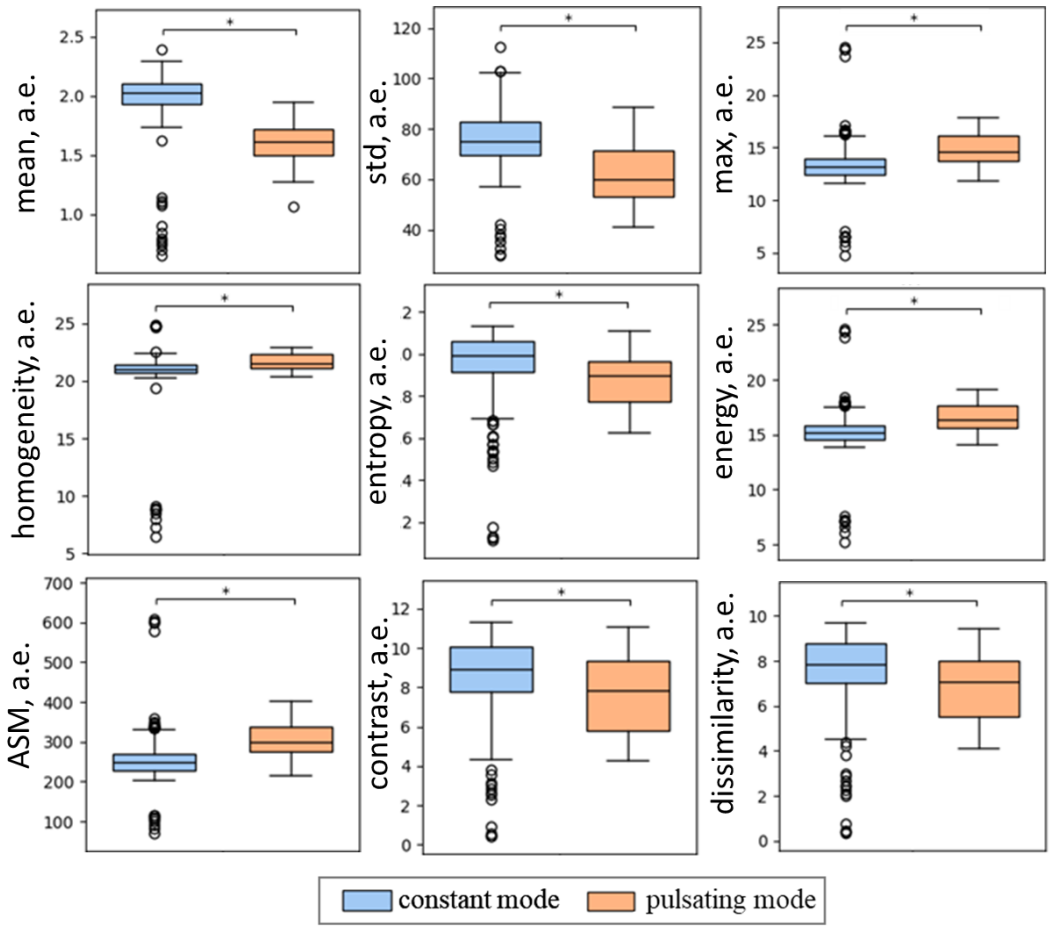


Fig. 6 Distribution of the second order statistics of OCT images. *$p < 0.01$ significance level between group by Mann-Whitney U-test.

Table 3 Accuracy of SVM classifier with a linear kernel when using the individual first order statistics.

	Kernel	Mean	Max	Std	Entropy	Kurtosis	Skew
Accuracy, % (mean ± std)	Linear	87 ± 8	61 ± 11	76 ± 7	66 ± 12	64 ± 8	61 ± 5
	*RBF	90 ± 5	63 ± 11	78 ± 8	68 ± 13	65 ± 9	64 ± 7

*RBF − Radial Basis Function.

Table 4 Accuracy of SVM classifier with a linear kernel when using the individual second order statistics.

	Kernel	Mean	Max	Std	ASM	Dissimilarity	Contrast	Energy	Entropy	Homogeneity
Accuracy, % (mean ± std)	Linear	89 ± 7	66 ± 11	77 ± 9	66 ± 12	64 ± 8	62 ± 11	66 ± 14	69 ± 14	61 ± 11
	*RBF	92 ± 4	67 ± 12	81 ± 13	68 ± 13	65 ± 9	63 ± 12	66 ± 13	70 ± 10	64 ± 10

*RBF − Radial Basis Function.

Table 5 Accuracy of SVM classifier with Radial Basis Function (RBF) kernel when using the entire group of the first-, the entire group of second-, and the combination of all statistics.

	Kernel	The entire group of the first order statistics	The entire group of the second order statistics	The combination of all statistics
Accuracy, % (mean ± std)	Linear	76 ± 17	79 ± 14	93 ± 4
	RBF	78 ± 13	85 ± 11	95 ± 6

The final classification accuracy for features in the term of individual statistics is shown in Tables 3 and 4. The classifiers performance was in the range of 61 to 92%. The next step was to combine the first and the second order statistics to achieve higher performance. The feature vector for the first-order statistics included 6 parameters, and for the second ones – 9 parameters. Combining all statistics into one feature vector yielded a final feature vector with 15 parameters. The performance of SVM classifier with linear and Radial Basis Function (RBF) kernels on test datasets is presented in Table 5.

4 Discussion

Data models for prediction of the optimal laser parameters in the additive manufacturing (AM) of NiTi shape memory alloys are intensively developed. Two multi-layer perceptron models were created to generate a nonlinear map between inputs and outputs of the AM process [25]. The coefficients of determination (R^2) are around 97–99% for the recovery ratio and transformation temperature. Artificial neural network with multilayer back propagation (BP) learning algorithm was used to predict the mechanical properties of porous NiTi shape memory alloys fabricated by press/sintering of the mixed powders [26]. In comparison with the regression models, the BP model was more effective and can be generally used in conventional press sinter investigation. A model for predicting the porosity of porous NiTi alloy based on SVM was developed [27].

The comparison of prediction values between support vector regression (SVR) and ANN-BP was conducted [28]. The mean absolute percentage error (MAPE) by SVR and ANN-BP were 0.075 and 0.41, respectively. The maximum relative error by SVR and ANN-BP were 10% and 61%, respectively. This shows that SVR has higher prediction accuracy than ANN-BP. Gaussian process regression [29], multiple linear regression, random forest [30], convolution neural network [28] were used to predict porosity in materials manufacturing.

In this work, the data model to predict the porosity of NiTi materials using optical coherence tomography and machine learning was developed. The SVM with a linear and a RBF kernel, and the first- and second-order statistics of OCT images as coordinates of a feature vector were used. Prediction efficiency was estimated using the 5-fold cross-validation scheme. Two classes of NiTi materials distinguishing accuracy was 95 ± 6% when all the first- and second-order statistics were included in data feature vector.

The next step is to develop multiclass SVM or SVR data model to predict quantitative characteristics of NITI material porosity.

5 Conclusions

The paper proposes an approach for express analysis of NiTi samples using OCT and SVM. This approach allows for rapid analysis of porous materials with high accuracy. Further development of this approach can be associated with the construction of a regression model for predicting the porosity of samples that have not yet been produced using the manufacturing process parameters. Also, the analysis of the first- and second-order statistics of OCT images of porous materials can be used to control their quality, for example, to search defects.

Acknowledgments

The investigation was supported by Russian Science Foundation with the grant № 24-63-00049, https://rscf.ru/en/project/24-63-00049/.

Data Availability Statement

The data presented in this study are available on request from the corresponding author. The data are not publicly available due to privacy.

Disclosures

The authors declare no conflicts of interest.

References

1. V. E. Gunther, V. N. Khodorenko, and Y. F. Yasenchuk, Titanium nickelide. A new generation medical material, Publishing House of MIT, Tomsk (2006). ISBN: 5-98589-020-1.
2. M. Saini, Y. Singh, P. Arora, V. Arora, and K. Jain, "Implant biomaterials: a comprehensive review," World Journal of Clinical Cases 3(1), 52–57 (2015).

3. M. Bahraminasab, B. B. Sahari, "NiTi shape memory alloys, promising materials in orthopedic applications", Shape Memory Alloys-Processing, Characterization and Applications 261–278 (2013).
4. I. V. Shishkovsky, L. T. Volova, M. V. Kuznetsov, Yu. G. Morozov, and I. P. Parkind, "Porous biocompatible implants and tissue scaffolds synthesized by selective laser sintering from Ti and NiTi," Journal of Materials Chemistry 18(12), 1309–1317 (2008).
5. J. L. Hernandez, K. A. Woodrow, "Medical applications of porous biomaterials: features of porosity and tissue-specific implications for biocompatibility", Advanced Healthcare Materials 11(9), 2102087 (2022).
6. Y. Yasenchuk, E. Marchenko, V. Gunther, A. Radkevich, O, Kokorev, S. Gunther, G. Baigonakova, V. Hodorenko, T. Chekalkin, J. Kang, S. Weiss, and A. Obrosov, "Biocompatibility and clinical application of porous tini alloys made by self-propagating high-temperature synthesis (SHS)," Materials 12(15), 2405 (2019).
7. F. J. O'Brien, "Biomaterials & scaffolds for tissue engineering," Materials Today 14(3), 88–95 (2011).
8. J. Rouquerol, D. Avnir, C. W. Fairbridge, D. H. Everett, J. M. Haynes, N. Pernicone, J. D. F. Ramsay, K. S. W. Sing, and K. K. Unger, "Recommendations for the characterization of porous solids," Pure and Applied Chemistry 66(8), 1739–1758 (1994).
9. T. M. S. Udenni Gunathilake, Y. C. Ching, K. Y. Ching, C. H. Chuah, and L. C. Abdullah, "Biomedical and microbiological applications of bio-based porous materials: a review," Polymers 9(5), 160 (2017).
10. H. J. Haugen, S. Bertoldi, "Characterization of morphology - 3D and porous structure," Characterization of Polymeric Biomaterials 21–53 (2017).
11. A. V. Medvedeva, D. M. Mordasov, and M. M. Mordasov, "Classification of methods of control of porous materials," Transactions TSTU 18(3), 749–753 (2012). [In Russian]
12. E. Widiatmoko, M. Abdullah, and A. Khairurrijal, "Method to measure pore size distribution of porous materials using scanning electron microscopy images," Aip conference proceedings. American Institute of Physics 1284(1), 23–26 (2010).
13. A. Bansiddhi, T. D. Sargeant, S. I. Stupp, and D. C. Dunand, "Porous NiTi for bone implants: a review," Acta Biomaterialia 4(4), 773–782 (2008).
14. A. Gh. Podoleanu, "Optical coherence tomography," Journal of Microscopy 247(3), 209–219 (2012).
15. O. P. Choudhary, P. Choudhary, "Scanning electron microscope: advantages and disadvantages in imaging components," International Journal of Current Microbiology and Applied Sciences 6(5), 1877–1882 (2017).
16. S. L. Campello, W. P. Dos Santos, V. F.Machado, C. C. B. O. Mota, A. S. L. Gomes, and R. E. de Souza, "Micro-structural information of porous materials by optical coherence tomography," Microporous and Mesoporous Materials 198, 50–54 (2014).
17. E. Fink, S. Celikovic, R. M. Fraga, J. Remmelgas, J. Rehrl, and J. Khinast, "In-line porosity and hardness monitoring of tablets by means of optical coherence tomography," International Journal of Pharmaceutics 666, 124808 (2024).
18. M. Ezzahmoulya, A. Elmoutaouakkila, M. Ed-Dhahraouya, H. Khallokb, A. Elouahlib, A. Mazurierc, A. ElAlbanic, and Z. Hatim, "Micro-computed tomographic and SEM study of porous bioceramics using an adaptive method based on the mathematical morphological operations," Heliyon 5(12), e02557 (2019).
19. B. Y. Tay, C. W. Goh, Y. W. Gu, C. S. Lim, M. S. Yong, M. K. Ho, and M. H. Myint, "Porous NiTi fabricated by self-propagating high-temperature synthesis of elemental powders," Journal of Materials Processing Technology, 202(1-3), 359–364 (2008).
20. M. Kaya, N. Orhan, and G. Tosun, "The effect of the combustion channels on the compressive strength of porous NiTi shape memory alloy fabricated by SHS as implant material," Current Opinion in Solid State and Materials Science, 14(1), 21–25 (2010).
21. E. S. Marchenko, Y. F. Yasenchuk, and I. A. Zhukov, "Features of the SHS of porous titanium nickelide," Educational and Methodical Manual: [for students of physics and mathematics and physics and technology specialties], Tomsk State University Publishing House, Tomsk (2021). [in Russian]
22. Y. V.Kistenev, D. A. Vrazhnov, V. V. Nikolaev, E. A. Sandykova and N. A. Krivova, "Analysis of collagen spatial structure using multiphoton microscopy and machine learning methods," Biochemistry Moscow 84, 108–123 (2019).
23. R. B. D'Agostino, "An omnibus test of normality for moderate and large sample size," Biometrika 58, 341–348 (1971).
24. R.B. D'Agostino, E. S. Pearson, "Tests for departure from normality," Biometrika 60, 613–622 (1973).
25. M. Mehrpouya, A. Gisario, A. Rahimzadeh, M. Nematollahi, K. S. Baghbaderani, and M. Elahinia, "A prediction model for finding the optimal laser parameters in additive manufacturing of NiTi shape memory alloy," The International Journal of Advanced Manufacturing Technology 105(11), 4691–4699 (2019).
26. S. Parvizi, H. R. Hafizpour, Sb.K. Sadrnezhaad, A. Akhondzadeh, and M. Abbasi Gharacheh, "Neural network prediction of mechanical properties of porous NiTi shape memory alloy," Powder Metallurgy 54(3), 450–454 (2011).
27. Q. S. Yan, "Prediction of porosity of porous NiTi alloy from processing parameters based on SVR," Advanced Materials Research 393, 231–235 (2012).
28. L. Mosser, O. Dubrule, and M. J. Blunt, "Reconstruction of three-dimensional porous media using generative adversarial neural networks," Physical Review E 96(4), 043309 (2017).

29. V. Maitra, J. Shi, and C. Lu, "Robust prediction and validation of as-built density of Ti-6Al-4V parts manufactured via selective laser melting using a machine learning approach," Journal of Manufacturing Processes 78, 183–201 (2022).
30. T. Kamal, Gouthama, and A. Upadhyaya, "Machine learning based sintered density prediction of bronze processed by powder metallurgy route," Metals and Materials International 29(6), 1761–1774 (2023).

Optical Properties of Fluorescent Tags Based on Gold Nanoparticles at Physiological Salt Content: *In Vitro* and *In Vivo* Study

Andrei Demenshin[1], Maria Istomina[2,3], and Elena Solovyeva[1*]
[1] Saint-Petersburg State University, 7/9 Universitetskaya nab., Saint Petersburg 199034, Russian Federation
[2] Institute of Experimental Medicine, Almazov National Medical Research Centre, 2 Akkuratova str., Saint-Petersburg 197341, Russian Federation
[3] Saint-Petersburg Electrotechnical University, 5 Professora Popova str., Saint-Petersburg 197376, Russian Federation
[*]e-mail: e.solovieva@spbu.ru

Abstract. The study describes the optical properties of fluorescent tags based on gold nanoparticles coated with a polymer shell with incorporated cyanine 5.5 in water and medium with a physiological salt background. The radiant efficiency was assessed by fluorescence tomography for the tag suspensions placed in a black plate and after their local subcutaneous injection into ICR mice. Partial aggregation of tags is noted, which occurs at changing water on isotonic solution, which leads to the increase of dye fluorescent intensity. *In vivo* imaging was performed in a bimodal fluorescence and computed tomography regime with varying the dose of the tags. The fluorescence enhancement 30 min after the tags injection was revealed. Computed tomography images allow reliable identification of the area of gold tags localization when their content in the injected suspension is at least 23.7 mg/mL. © 2024 Journal of Biomedical Photonics & Engineering.

Keywords: bioimaging; fluorescence tomography; computed tomography; gold nanoparticles; aggregation; cyanines.

Paper #9161 received 31 Aug 2024; revised manuscript received 22 Oct 2024; accepted for publication 6 Nov 2024; published online 3 Dec 2024. doi: 10.18287/JBPE24.10.040312.

1 Introduction

The implementation of nanomaterials in biomedicine is currently occurring at an increasing rate. Nanoparticles (NPs) of various compositions are considered to be ones of the most promising objects for a wide range of biomedical applications. In particular, many potentially biocompatible structures based on nanodiamonds [1], iron oxide [2, 3], silicon [4], silicon oxide [5, 6] and upconversion [7] nanoparticles have already been proposed for targeted drug delivery [8], instrumental diagnostics [9] and therapy [10, 11]. Some of the developments have already reached clinical trials [12–14]. Plasmonic metal NPs, primarily gold, are among the most promising candidates for solving some problems of photomedicine. On their basis, agents for contrast computed tomography (CT) [15] and photothermal therapy [16, 17] have been actively developed. In combination with molecular dyes, gold NPs can be used as fluorescent tags [18–20] and surface-enhanced Raman scattering tags [21–23]. Many relevant systems have been proposed to date, in which gold NPs are combined with cyanines [24, 25], BODIPYs [26, 27] and other dyes. The advantage of hybrid structures over molecular dyes is that they allow not only imaging of target cells, but also their treatment, i.e. theranostics.

At design of theranostic agents based on noble metal NPs, it is necessary to take into account all the features of their physical and chemical properties. In particular, chloride-induced aggregation is characteristic for almost all metal nanoparticles, which consists of the formation of NPs aggregates under a high salt background [28, 29]. Often, even stabilization of NPs by coating with various shells does not allow avoiding this effect completely. For practical purposes, nanostructures are of interest that retain colloidal stability in an aggregated state and are thus subject to injection. The aggregation of NPs affects their optical properties. As a rule, the absorption of light by gold NPs aggregates occurs at longer wavelengths compared to individual particles [30]. This can be

considered as a positive side for bioimaging, since it allows one to perform the measurements in the first transparency window of biological tissues.

It has already been noted that when developing photoactive agents based on molecules and NPs prone to aggregation, it is necessary to study their optical properties change that occurs during the aggregation [31, 32]. It is worth considering that aggregation can lead not only to an absorption wavelength shift, but also to a significant change in the intensity of the optical response. Quenching of the optical response may occur, for example, in the case of H-aggregates formation for polyaromatic dyes [33], or amplification of the optical response also may be observed, for example, the effect of aggregation-induced emission enhancement for molecular dyes [34] or the hot spots effect for plasmonic nanoparticles [35]. It is rationally to carry out a spectral evaluation of fluorophores and hybrid structures with them in conditions close to potential *in vivo* use, i.e. at physiological salt background and in the concentration range supposed for administration. This study is addressed to the evaluation of optical properties of tags based on gold NPs and cyanine 5.5 in saline solution used for injections and to testing of the tags as contrast for *in vivo* bimodal imaging by fluorescence tomography and computer tomography.

2 Materials and Methods

Gold nanoparticles of rod shape with an average aspect ratio of 2.76 were obtained by the two-stage seed-mediated method [36]. Further modification of the NPs included the coating with a polymer shell using a layer-by-layer technique accompanied with a dye incorporation. To coat the gold NPs, sodium polystyrene sulfonate (PSS) and polydiallyldimethylammonium (PDDA) chloride were used. These polymers are widely used in the fabrication of microcapsules for targeted drug delivery [37] that is the reason for their choice. Cyanine 5.5 was used as a fluorophore, the emission range of which falls within the first transparency window of biological tissues. The NPs coating with polymers was carried out sequentially in 4 stages, positively charged PDDA was used as layers 1 and 3, negatively charged PSS was used as layers 2 and 4. At each stage, NPs suspension was added dropwise to the polyelectrolyte solution under vigorous stirring, the mixture was kept for 2 h, and then the excess polymer was removed by centrifugation at 8000 rpm for 20 min. The previous study of nanorods coated via applied technique by transmission electron microscopy showed the polymer shell thickness of 2.5–3 nm [38]. The overall size of the obtained core-shell structures is about 50 nm in length and 18 nm in diameter. Cyanine 5.5 was introduced into the polymer shell by dropwise addition its solution with a concentration of 1×10^{-3} M into the NPs suspension in a ratio of 1:9 before applying the final fourth layer of polymer. Immobilization of the dye on NPs surface occurred due to non-specific adsorption proceeding during 2 h. The excess of not attached dye was removed by centrifugation at 8000 rpm for 20 min. The absorption spectra recorded for the stock solution of cyanine 5.5 and supernatant after centrifugation showed that about 40% of the added dye is retained in the polymer shell, which corresponds to ~10^5 molecules per particle since the NPs concentration in the suspension is about 3.8×10^{11} particles/mL.

UV-Vis absorption spectra were recorded on a spectrophotometer UV-1800 (Shimadzu). Spectra were acquired in the range of 200–900 nm with a step of 1 nm. Quartz cuvettes with an optical path length of 1 cm were used. The baseline was recorded with deionized water under identical conditions.

Iv vivo imaging was performed with 25–30-day-old male ICR (CD-1) mice weighing 18–20 g obtained from the vivarium of Almazov National Medical Research Centre. Imaging was performed with test and control animals. The background radiation was taken into account based on the signal from the control mouse. Fluorescence emission was measured using an IVIS spectrum CT tomograph (PerkinElmer), which also allows working in computed tomography regime. Taking into account the optical properties of the fluorophore used, imaging was performed with the filters of 675 nm for excitation and 720 nm for emission. CT images were obtained at 50 kV and 1 mA, exposure time 20 ms, 4·4 binning and increment angle of 0.5. At imaging, mice were anesthetized and injected subcutaneously with a saline suspension of NPs in a volume of 30 μL. In a dose-dependent experiment, the fluorescent tags were studied at gold concentrations of 15–45 mg/mL. The control mouse was injected subcutaneously with 30 μL of physiological solution (0.9% NaCl). The fluorescence efficiency was recorded 5 and 30 min after the tags administration, and computed tomography was performed 30 min after the administration. During the experiment, the animals were kept on a thermostatic operating table, which maintained body temperature at a level of 37.0 ± 0.5 °C (TCAT–2LV, Physitemp Instruments Inc.).

The laboratory animals were kept on a standard diet with sufficient water in accordance with veterinary legislation and in accordance with the requirements for the humane maintenance and use of animals in experimental studies (National research Council, 2011).

3 Results and Discussion

Optical properties of nanoobjects depend on their size and morphology. Gold nanoparticles are a clear example: with a change in size and shape, not only their light scattering changes, but also the absorption wavelengths and extinction coefficient. The size of gold NPs increases with their partial or complete aggregation, which can occur when the salt content in the surrounding solution changes. Fig. 1 shows the UV-Vis absorption spectra of the obtained fluorescent tags based on gold NPs in water and isotonic solution. The spectrum 2 was measured 5 min after salt addition. This time was chosen based on the time that usually passes between the dilution of nanoparticles suspension

with saline and their injection in the experiments with laboratory mice. As can be seen, the main absorption band shifts from 710 to 750 nm. This shift indicates a partial aggregation of NPs, which progresses over time, but it is not dramatic during yet in the selected time period. Nevertheless, the change in the optical properties of NPs that occurs during the environment exchange from water to salt should be taken into account when choosing the conditions for fluorescence tomography performed using them.

The preparation of core-shell nanostructures based on gold NPs modified with fluorescent dyes can only be carried out in water, since with a high salt background the stability of the NPs is significantly reduced, and they do not withstand multiple centrifugation-resuspension cycles. The transfer of NPs into a medium with physiological salt background, suitable for injection, is carried out immediately before their use by diluting the concentrated suspension with a saline solution. The degree of aggregation and the shift of the absorption band maximum, which affects the optical efficiency of the hybrid nanostructure, depend on the concentration of the gold NPs themselves in the suspension.

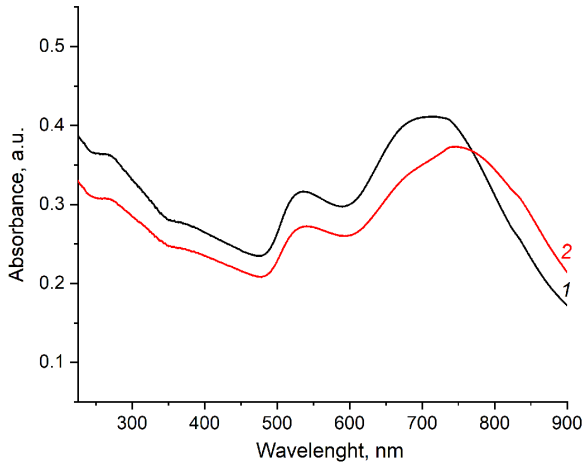


Fig. 1 UV-Vis absorption spectra of modified gold nanoparticles (1) in water and (2) isotonic solution (C_{Au} = 35 mg/L).

Gold NP-based contrast agents are used in *in vivo* experiments for injection in sufficiently high concentrations, which allow obtaining a detectable signal after natural dilution in physiological fluids. According to the literature, the concentration of suspensions based on gold NPs introduced into a laboratory animal can reach up to 33 g/L on gold [39]. The study of such concentrated and, accordingly, optically dense suspensions of gold NPs by traditional methods of absorption and fluorescence spectroscopy is extremely difficult due to the dominance of self-absorption and scattering processes. In turn, the optical scheme of signal registration in fluorescence tomography differs greatly from that implemented in conventional measurements in the cuvette holder of a spectrometer, carried out with solutions, films and solid samples. Therefore, it is advisable to evaluate the change in the optical properties of concentrated NPs suspensions when replacing water with a salt medium directly on a fluorescence tomograph. Fig. 2 shows the images of the fluorescent tags suspensions obtained in a black plate on a fluorescence tomograph before and after a two-fold dilution with a 1.8% sodium chloride solution. Since the luminosity of gold core-shell nanostructures can also vary depending on their concentration, a similar volume of distilled water was added to the well on the right as a control sample.

As can be seen, there is an increase in the signal from the fluorescent contrast by almost 40% in the isotonic solution. Comparison of radiant efficiency values from the well, to which the saline solution was added with the control well, to which water was added, shows that this observation is due to the influence of chloride background. Apparently, the plasmon resonance band of the tags shifts to the long-wavelength region as a result of aggregation and the emission of cyanine 5.5 becomes more pronounced due to the less spectral overlap with the absorption region of the gold core. It is worth noting that after aggregation, the particles do not precipitate and are suitable for injection, which was carried out on laboratory mice. Fig. 3 represents the images of mice obtained 5 and 30 min after subcutaneous injection of a suspension of gold-cyanine tags into the thigh.

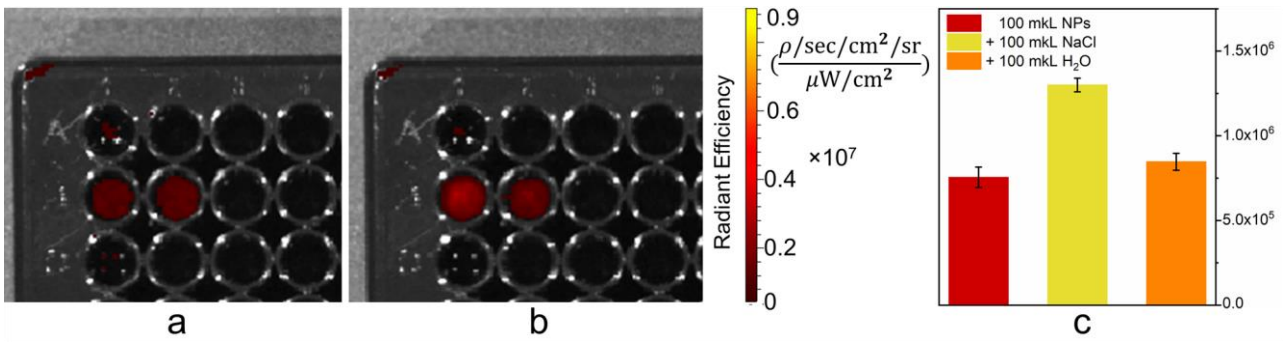
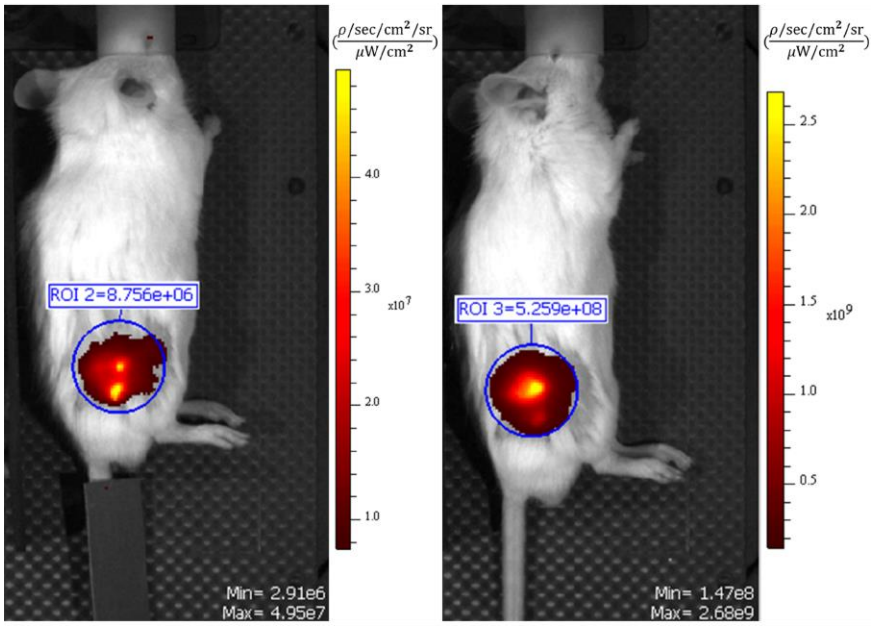


Fig. 2 Fluorescent images of the tags suspension (a) before and (b) after dilution with saline and water. (c) Radiant efficiency recorded from the test wells before and after addition of solvent.



(a) (b)

Fig. 3 Fluorescence tomography images after (a) 5 and (b) 30 min of tags subcutaneous administration.

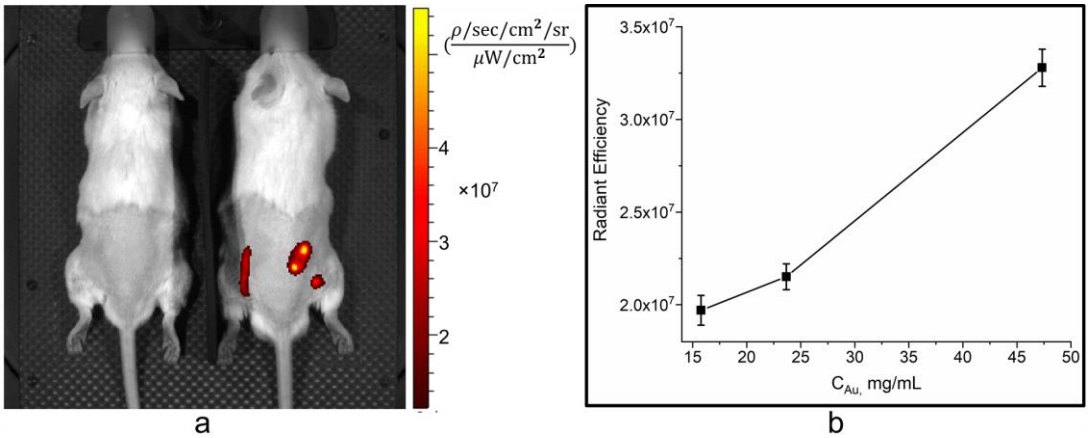


Fig. 4 (a) Fluorescence tomography images of control and injected mice after administration of tags in doses of 15.8, 23.7, and 47.3 mg/mL. (b) Dependence of the recorded radiant efficiency on the dose of gold tags administered. Error bars in graph indicate standard deviation of radiant.

Analysis of the radiant efficiency reveals that 30 min after tags injection, the signal level increases by almost two orders of magnitude. This flare-up of the introduced fluorescent tags can be associated with their interaction with the components of the subcutaneous fat tissue. The observed result is certainly extremely interesting, but requires further research.

When developing diagnostic contrasts, it is necessary to conduct dose-dependent experiments. Since hybrid nanostructures based on gold NPs and molecular fluorophores are capable of providing imaging in a bimodal mode, it is advisable to perform such experiments, scanning in both, the computer tomography and fluorescence tomography, regimes. The possibility of working with contrasts based on gold NPs in a bimodal mode has already been demonstrated previously and is one of their main advantages [40]. Fluorescence and CT images obtained with varying doses of injected contrast from 15 to 47 mg/mL on gold are shown in Figs. 4 and 5, respectively.

As can be seen, the signal intensity in both regimes increases as expected proportionally to the dose of tags admistered. At the same time, a dose of 23.7 mg/mL on gold is sufficient to obtain a contrast image.

4 Conclusions

The study highlights the physicochemical properties of hybrid tags based on gold nanoparticles with a polymer shell labeled with a fluorescent dye, which are important for their potential use for bioimaging purposes. In particular, partial aggregation of the tags is shown, which occurs when a medium in their suspension is exchanged from water to saline with a high salt content.

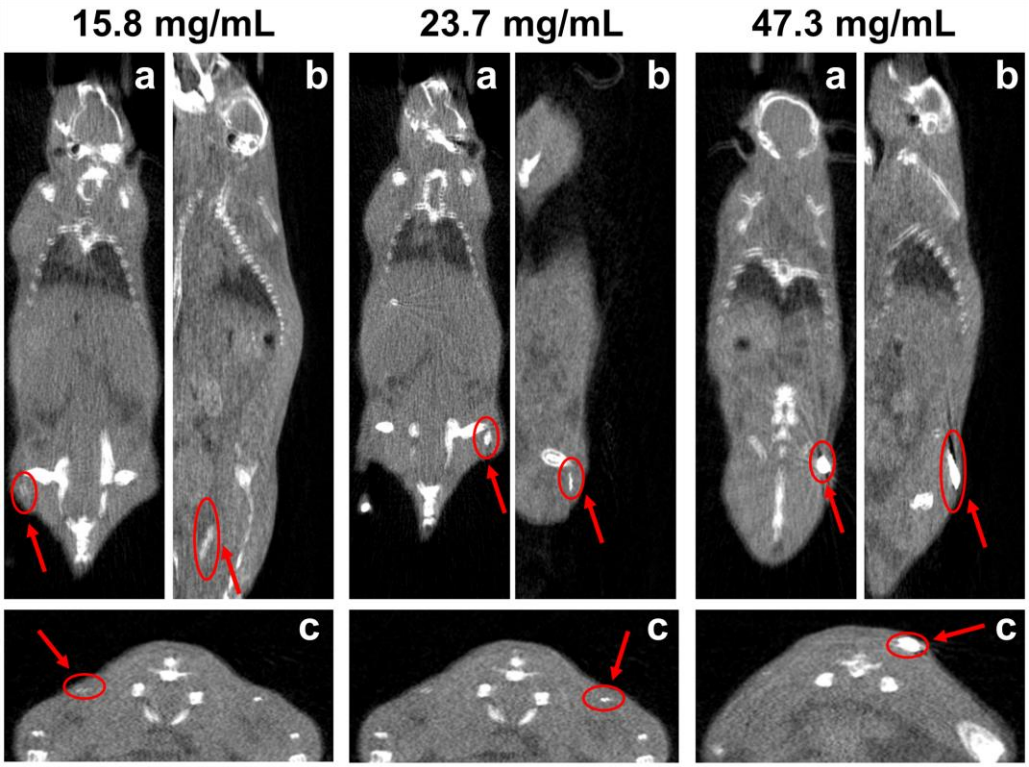


Fig. 5 *In vivo* CT images of ICR mouse after subcutaneous local injection of gold tags in three doses: (a) sagittal plane, (b) coronal plane, (c) transaxial plane. In the highlighted areas, the arrow indicates the accumulation of gold tags.

The aggregates formation causes a shift in the absorption maximum to the long-wavelength region, which is accompanied by an increase in the recorded emission intensity of cyanine 5.5.

In vivo experiments carried out on ICR mice using the gold-based tags clearly demonstrated the possibility of bimodal imaging in combined fluorescence tomography and computed tomography regime. Tags fluorescence increasing was revealed 30 min after their subcutaneous injection. The observed increase in radiative efficiency by almost two orders of magnitude is an extremely interesting effect that requires further research. CT images allow identification of the area of tags localization, the minimum tags content in the injected suspension required for acceptable contrast is of 23.7 mg/mL.

Acknowledgements

This work was funded by the Russian Science Foundation, grant № 22-73-10052. The authors acknowledge Saint-Petersburg State University for infrastructural support (Laboratory of Plasmon-Enhanced Spectroscopy and Bioimaging). The authors are grateful to the Resource Centers of SPBU: “Optical and Laser Materials Research”, “Chemical Analysis and Material Research” and “Center for Molecular and Cell Technologies” for access to equipment and for performing some measurements.

Disclosures

The authors declare no conflicts of interest.

References

1. Mumtaz, N. Hussain, S. Salam, and M. Bilal, “Multifunctional nanodiamonds as emerging platforms for cancer treatment, and targeted delivery of genetic factors and protein medications—a review,” Journal of Materials Science 57(17), 8064−8099 (2022).
2. J. Dulińska-Litewka, A. Łazarczyk, P. Hałubiec, O. Szafrański, K. Karnas, and A. Karewicz, “Superparamagnetic iron oxide nanoparticles-current and prospective medical applications,” Materials 12(4), 617 (2019).
3. R. Mahbuba, “Magnetic Resonance Imaging and Iron-oxide Nanoparticles in the era of Personalized Medicine,” Nanotheranostics 7(4), 424−449 (2023).
4. A. F. Alykova, V. G. Yakunin, V. Yu. Timoshenko, and I. N. Zavestovskaya, “Optical methods of silicon nanoparticle diagnostics for applications in biomedicine,” Journal of Biomedical Photonics & Engineering 5(2), 020304 (2019).
5. M. C. Goncalves, “Sol-gel silica nanoparticles in medicine: A natural choice. Design, Synthesis and Products,” Molecules 23(8), 2021 (2018).

6. D. V. Korolev, G. A. Shulmeyster, N. V. Evreinova, M. S. Syrovatkina, M. S. Istomina, V. N. Postnov, I. V. Aleksandrov, A. S. Krasichkov, and M. M. Galagudza, "Theranostic Platforms Based on Silica and Magnetic Nanoparticles Containing Quinacrine, Chitosan, Fluorophores, and Quantum Dots," International Journal of Molecular Sciences 23(2), 932 (2022).
7. I. Yu. Yanina, N. A. Navolokin, I. V. Vidyasheva, I. Y. Goryacheva, V. I. Kochubey, and V. V. Tuchin, "Functionalized upconversion luminescent nanoparticles for theranostics," in Diffuse Optical Spectroscopy and Imaging VII, H. Dehghani and H. Wabnitz (Eds.), 11074, 11074_43 (2019).
8. Y. Toropova, D. Korolev, M. Istomina, G. Shulmeyster, A. Petukhov, V. Mishanin, A. Gorshkov, E. Podyacheva, K. Gareev, A. Bagrov, and O. Demidov, "Controlling the Movement of Magnetic Iron Oxide Nanoparticles Intended for Targeted Delivery of Cytostatics," International Journal of Nanomedicine 16, 5651−5664 (2021).
9. N. Mhlanga, N. Mphuthi, H. Van der Walt, S. Nyembe, T. Mokhena, and L. Sikhwivhilu, "Nanostructures and nanoparticles as medical diagnostic imaging contrast agents: A review," Materials Today Chemistry 40, 102233 (2024).
10. M. Bravo, B. Fortuni, P. Mulvaney, J. Hofkens, H. Uji-I, S. Rocha, and J. A. Hutchison, "Nanoparticle-mediated thermal Cancer therapies: Strategies to improve clinical translatability," Journal of Controlled Release 372, 751−777 (2024).
11. A. B. Bucharskaya, N. G. Khlebtsov, B. N. Khlebtsov, G. N. Maslyakova, N. A. Navolokin, V. D. Genin, E. A. Genina, V. V. Tuchin, "Photothermal and Photodynamic Therapy of Tumors with Plasmonic Nanoparticles: Challenges and Prospects," Materials 15(4), 1606 (2022).
12. L. Tang, R. Zhang, Y. Wang, M. Liu, D. Hu, Y. Wang, and L. Yang, "Nanoparticle delivery for central nervous system diseases and its clinical application," Nano Research 17(7), 6305−6322 (2024).
13. Y. Liu, W. Cheng, H. Xin, R. Liu, Q. Wang, W. Cai, X. Peng, F. Yang, and H. Xin, "Nanoparticles advanced from preclinical studies to clinical trials for lung cancer therapy," Cancer Nanotechnology 14(1), 28 (2023).
14. L. Yao, D. Bojic, and M. Liu, "Applications and safety of gold nanoparticles as therapeutic devices in clinical trials," Journal of Pharmaceutical Analysis 13(9), 960−967 (2023).
15. N. Chanda, A. Upendran, E. J. Boote, A. Zambre, S. Axiak, K. Selting, K. V. Katti, W. M. Leevy, Z. Afrasiabi, J. Vimal, J. Singh, J. C. Lattimer, and R. Kannan, "Gold nanoparticle based X-ray contrast agent for tumor imaging in mice and dog: A potential nano-platform for computer tomography theranostics," Journal of Biomedical Nanotechnology 10(3), 383−392 (2014).
16. A. Bucharskaya, G. Maslyakova, G. Terentyuk, A. Yakunin, Y. Avetisyan, O. Bibikova, E. Tuchina, B. Khlebtsov, N. Khlebtsov, and V. Tuchin, "Towards effective photothermal/photodynamic treatment using plasmonic gold nanoparticles," International Journal of Molecular Sciences 17(8), 1295 (2016).
17. W. Zhang, X. Ding, H. Cheng, C. Yin, J. Yan, Z. Mou, W. Wang, D. Cui, C. Fan, and D. Sun, "Dual-Targeted Gold Nanoprism for Recognition of Early Apoptosis, Dual Model Imaging and Precise Cancer Photothermal Therapy," Theranostics 9(19), 5610−5625 (2019).
18. D. K. Tuchina, I. G. Meerovich, O. A. Sindeeva, V. V. Zherdeva, N. I. Kazachkina, I. D. Solov'ev, A. P. Savitsky, A. A. Bogdanov, and V. V. Tuchin, "Prospects for multimodal visualisation of biological tissues using fluorescence imaging," Quantum Electronics 51(2), 104−117 (2021).
19. O. Mostafa, H. M. Saleh, T. A. Salaheldin, A. K. Ibrahim, and S. A. Elfeky, "Fluorescein/gold nanoparticles conjugated EGFR antibody for imaging and P53 upregulation in hamster mucosal cells carcinoma," Journal of Drug Delivery Science and Technology 76, 103293 (2022).
20. S. K. Pirutin, M. V. Efremova, A. I. Yusipovich, V. B. Turovetskii, G. V. Maksimov, A. B. Druzhko, and A. G. Mazhuga, "Visualization and Cytotoxicity of Fluorescence-Labeled Dimeric Magnetite-Gold Nanoparticles Conjugated with Prostate-Specific Membrane Antigen in Mouse Macrophages," Bulletin of Experimental Biology and Medicine 166(3), 386−389 (2019).
21. V. O. Svinko, A. I. Shevchuk, A. N. Smirnov, D. V. Makeeva, and E. V. Solovyeva, "Gold nanostars-based labels for surface-enhanced Raman scattering imaging with red medical lasers," Opt. Spectrosc. 130(10), 1590−1595 (2022).
22. A. I. Shevchuk, V. O. Svinko, A. N. Smirnov, and E. V. Solovyeva, "SERS study of cyanine dyes: optimization of metal core and molecular label choice for plasmonic nanotags," Dyes and Pigments 216, 111329 (2023).
23. B. Andreiuk, F. Nicolson, L. M. Clark, S. R. Panikkanvalappil, Kenry, M. Rashidian, S. Harmsen, and M. F. Kircher, "Design and synthesis of gold nanostars-based SERS nanotags for bioimaging applications," Nanotheranostics 6(1), 10−30 (2022).
24. A. N. Smirnov, S. F. Aslanov, D. V. Danilov, O. Y. Kurapova, and E. V. Solovyeva, "One-Pot Synthesis of Silica-Coated Gold Nanostructures Loaded with Cyanine 5.5 for Cell Imaging by SERS Spectroscopy," Nanomaterials 13(7), 1267 (2023).
25. A. N. Smirnov, A. I. Shevchuk, A. V. Volkova, V. D. Kalganov, and E. V. Solovyeva, "Gold-silica plasmonic nanobones with tunable size and optical bimodality for bioimaging," Colloids and Surfaces A: Physicochemical and Engineering Aspects 684, 133115 (2024).

26. A. Rahman, K. Praveen, P. Panangattukara, P. Yadav, T. Goswami, A. Shanavas, H. N. Ghosh, and P. P. Neelakandan, "Gold-BODIPY Nanoparticles with Luminescence and Photosensitization Properties for Photodynamic Therapy and Cell Imaging," ACS Applied Nano Materials 5(5), 6532−6542 (2022).
27. H. Y. Lee, H. Son, J. M. Lim, J. Oh, D. Kang, W. S. Han, and J. H. Jung, "BODIPY-functionalized gold nanoparticles as a selective fluoro-chromogenic chemosensor for imaging Cu2+ in living cells," Analyst 135(8), 2022−2027 (2010).
28. S. Alizadeh, Z. Nazari, "A Review on Gold Nanoparticles Aggregation and Its Applications," Journal of Chemical Reviews 2(4), 228−242 (2020).
29. M. Chan, W. Leng, and P. Vikesland, "Surface-Enhanced Raman Spectroscopy Characterization of Salt-Induced Aggregation of Gold Nanoparticles," ChemPhysChem 19(1), 24−28 (2018).
30. L. Catanzaro, V. Scardaci, M. Scuderi, M. Condorelli, L. D'Urso, and G. Compagnini, "Surface plasmon resonance of gold nanoparticle aggregates induced by halide ions," Materials Chemistry and Physics 308, 128245 (2023).
31. D. S. Farrakhova, I. D. Romanishkin, D. V. Yakovlev, Yu. S. Maklygina, V. A. Oleinikov, P. V. Fedotov, M. V. Kravchik, L. Bezdetnaya, and V. B. Loschenov, "Correlation of spectroscopic and structural properties of indocyanine green J-aggregates," Biomedical Photonics 11(3), 4−16 (2022).
32. I. V. Klimenko, T. Yu. Astakhova, E. N. Timokhina, and A. V. Lobanov, "Molecular Aggregation of Aluminum Phthalocyanine Chloride in Organic and Water-Organic Media," Journal of Biomedical Photonics & Engineering 9(3), 030301 (2023).
33. J. Kang, O. Kaczmarek, J. Liebscher, and L. Dahne, "Prevention of H-Aggregates Formation in Cy5 Labeled Macromolecules," International Journal of Polymer Science 2010(1), 264781 (2010).
34. H. He, T. Li, L. Yao, M. Liu, H. Xia, and L. Shen, "Aggregation-induced emission enhancement (AIEE)-active donor-acceptor type fluorophores based on the 1,3-diaryl pyrazole unit: Conspicuous mechanochromic fluorescence and biosensing of iodide ions," Dyes and Pigments 203, 110309 (2022).
35. T. Haug, P. Klemm, S. Bange, and J. M. Lupton, "Hot-Electron Intraband Luminescence from Single Hot Spots in Noble-Metal Nanoparticle Films," Physical Review Letters 115(6), 067403 (2015).
36. A. Yoshida, N. Uchida, and N. Kometani, "Synthesis and spectroscopic studies of composite gold nanorods with a double-shell structure composed of spacer and cyanine dye J-aggregate layers," Langmuir 25(19), 11802–11807 (2009).
37. N. Pargaonkar, Y. M. Lvov, N. Li, J. H. Steenekamp, and M. M. De Villiers, "Controlled release of dexamethasone from microcapsules produced by polyelectrolyte layer-by-layer nanoassembly," Pharmaceutical Research 22(5), 826−835 (2005).
38. V. O. Svinko, A. N. Smirnov, A. I. Shevchuk, A. I. Demenshin, A. A. Smirnov, and E. V. Solovyeva, "Comparative study of fluorescence core-shell nanotags with different morphology of gold core," Colloids and Surfaces B: Biointerfaces 226, 113306 (2023).
39. G. Sonavane, K. Tomoda, and K. Makino, "Biodistribution of colloidal gold nanoparticles after intravenous administration: Effect of particle size," Colloids and Surfaces B: Biointerfaces 66(2), 274−280 (2008).
40. S. Kozomara, N. L. Ford, "Detectability of fluorescent gold nanoparticles under micro-CT and optical projection tomography imaging," Journal of Medical Imaging 7(2), 026002 (2020).

Effects of Illumination Angle and Different Light Sources on Acousto-Optic-based Sensing of Focused Ultrasound

Mohammadreza Omidali[1,2*], Triana Rahayu[2,3], Zuomin Zhao[1,2], Sadegh Moradi[1], and Teemu Myllylä[1,2,3]

[1] Optoelectronics and Measurement Techniques Unit, Faculty of Information Technology and Electrical Engineering, University of Oulu, 1 Pentti Kaiteran katu, Oulu 90570, Finland

[2] Infotech Oulu, University of Oulu, 1 Pentti Kaiteran katu, Oulu 90570, Finland

[3] Research Unit of Health Sciences and Technology, Faculty of Medicine, University of Oulu, 5 Aapistie, Oulu 90220, Finland

*e-mail: mohammadreza.omidali@oulu.fi

Abstract. The acousto-optic (AO) effect, characterized by the deflection and modulation of photons by ultrasound, is currently being explored to a certain degree. AO could bring together advantages of optics and acoustics particularly addressing the challenges of spatially accurate deep tissue optical sensing that arise from light scattering. Moreover, AO-based monitoring technique could offer valuable insights into the effects of focused ultrasound (FUS) in its therapeutic applications. This paper investigates different light sources (coherents and noncoherent) for use in AO. In particular, we compare tagging efficiency detected in the context of AO signal amplitude. Additionally, the impact of adjusting the angle of the light source to optimize light penetration into the focal area is examined. Experiments were performed in both transmission and reflection modes utilizing AO phantom models, with a primary emphasis on reflection mode. The findings reveal that coherent light sources produce larger but has greater standard deviation in AO signal, while light emitting diodes (LED) yield comparatively stable signals. Additionally, results from reflection mode experiments indicate an enhancement of AO signals by as much as 40% when the angle of coherent sources is adjusted from perpendicular to 45° within a phantom that simulates the optical characteristics of the average human brain. © 2024 Journal of Biomedical Photonics & Engineering.

Keywords: focused ultrasound; tagging efficiency optimization; acousto optic sensing; laser diode and LEDs; coherence & non-coherence light.

Paper #9163 received 1 Sep 2024; revised manuscript received 25 Oct 2024; accepted for publication 25 Oct 2024; published online 5 Dec 2024. doi: 10.18287/JBPE24.10.040313.

1 Introduction

Acousto-optic sensing (AOS) is a hybrid technique aiming to combine the deep penetration and high spatial resolution of ultrasound with optical sensing to overcome optical scattering limitations while maintaining the original optical contrast [1, 2]. The AO phenomenon was first demonstrated experimentally already in 1930s [3, 4], however, Marks et. al made its biomedical application possible in 1993 [5]. By utilizing non-invasive FUS transducers to modulate a specific area within a medium by acoustic waves and by illuminating that area with light, the AO effect partially modulates the light by frequency shifting. The key to achieving optimal modulating or tagging efficiency lies in ensuring that photons pass through the focal area efficiently. The separation of these modulated photons enables acoustic resolution in acoustic focus area, facilitating the retrieval of local optical properties within the focus area [1].

AOS exhibits sensitivity to both optical absorption and scattering, offering optical contrast that can dynamically capture changes in tissue properties due to

metabolic and structural alterations. When light interacts with the focal area of ultrasound wave, optical diffraction and frequency shifting occur, enabling a light detector to capture a fraction of this frequency-shifted light as it propagates out of the tissue [2, 4, 6]. The choice of ultrasonic frequencies in AOS is critical, necessitating a balance between achieving deep tissue penetration (with order of cm) and providing spatial accuracy within the mm range. However, deep tissue sensing poses challenges in detecting and separating tagged photons from untagged background photons, leading to a lower signal-to-noise ratio (SNR) in the AOS [7]. In this study, we explored both transmission and reflectance modes, but placing particular emphasis on the practicality of reflectance, similar to the settings commonly employed in human brain hemodynamic measurement by functional near-infrared spectroscopy (fNIRS), where both light source and detector are placed on the scalp commonly at 3 cm source-detector distance. Latter approach overcomes the limitations of transmittance mode, presenting a more practical solution for instance in brain monitoring applications.

In Ref. [8], the influence of varying source angles on tagging efficiency was investigated through simulations. Building on this, the present research expands the investigation experimentally by introducing additional parameters, such as FUS frequency and pressure, source-detector distances, light source angles, and the use of both coherent and non-coherent light sources. The aim is to quantify FUS-modulated light in terms of AO signal intensity under these conditions.

2 Methods

This section first presents the simulation of FUS wave propagation, followed by MC modeling to simulate the FUS-induced modulation of light. Subsequently, the experimental procedures are described in detail.

2.1 Simulations

The acoustic waves generated by FUS cause pressure changes in the medium which were simulated using the open-source MATLAB toolbox *k*-wave [9], to determine the position, size, and shape of the pressure distribution as a function of the frequencies. Using *k*-WaveArray class model [10], transducers can be defined in any shape and placed inside the computational grid anywhere without being constrained by grid points. The acoustic properties of the simulation medium are detailed in Table 1.

Table 1 Tissues' acoustic and transducer parameters.

	Acoustic Parameters [11, 12]				**Transducer Parameters**		
	V_a	ρ	α_0	y	**Frequency (MHz)**	**ROC (mm)**	**Ø (mm)**
Water	1483	999.5	0.0022	2	0.5	57.5	60
Average Brain	1552	1046	0.21	1.18	1	18.5	20

V_a = Ultrasound Velocity ($\frac{m}{s}$)
ρ = density ($\frac{kg}{m^3}$)
α_0 = Power-Law Prefactor (dB MHz^{-y} cm^{-1})
y = Power Law Exponent
Ø = Diameter
ROC = Radius of Curvature

Table 2 FUS and MC simulation parameters.

Input parameter	**Value**			
Focused area dimension (mm)	**1 MHz**		**0.5 MHz**	
	Length	**Width**	**Length**	**Width**
	9	1.3	15	2.5
SDD (mm)	30, 35			
Detector fiber diameter (mm)	0.2			
Light source angle (°) with respect to the Z-axis (depth) and X-axis (*SDD direction)	0° − perpendicular in the experiments, 20°, 45°			
Optical properties of the average brain [17, 18] (850-nm)	μ_a (mm^{-1})	μ_s (mm^{-1})	g	n
	0.037	9.5	0.82	1.38

*SDD = Source-Detector Distance

The acoustic absorption coefficient was computed according to the frequency-power law, $\alpha = \alpha_0 \omega^y$. The focal pressure distribution and focus size were examined for two transducers, with the brain modeled as an average volume submerged in water as the surrounding medium. The dimensions of the 3D simulation domain were $60 \times 60 \times 80$ mm^3, with a grid spacing of 140 μm.

MC Multi-Layer [13, 14] modeling was implemented and modified in MATLAB to model FUS-modulated light inside biotissue and calculate the tagging efficiency. The medium was represented as a cuboidal layer with dimensions of $75 \times 75 \times 25$ mm^3, and simulations were executed using the parameters outlined in Table 2. The focal area with adequate approximation, as stated in Table 2, was modeled in MC simulation as an ellipse with its length and width of focal area considered as major and minor radius, respectively. The simulation study focused on quantifying the number of photons traversing the focal area and reaching the detector. Among the photons interacting with the focal region − either through scattering or direct passage − 70% were classified as tagged photons [15]. The intensity of the photons was determined by adding the weights of all photons that reached the detector and dividing the total weight by the detector area. Simulations were performed separately and in parallel for each of the US frequencies, source angles, and source-detector distances. Upon reaching the detector, the labeled photons were recorded as modulated signals, whereas the remaining photons were classified as unmodulated signals [14]. By varying the illumination angles and source-detector distances (SDD), the optimal configuration for maximizing the tagging efficiency was established. The Monte Carlo simulation, which involved 2 billion photons and spanned 48 h, detected only a few thousand photons. This outcome is attributable to the simulation's use of a 1 mm diameter detector, reflecting the specified of the experimental fiber detector. The MC was verified by MCX results on source-detector separation versus diffuse-reflectance plot [16−18].

2.3 Measurements Setup

Polyvinyl chloride-plastisol and Titanium Dioxide Nanopowder (TiO2-5430MR) were used as the base materials for the construction of the tissue phantoms in this study. These materials were mixed in a ratio of 1 mL to 3 mg using an electromagnetic mixer and heated for twenty minutes until the oven temperature reached 200 ºC. Afterward, the magnetic stirrer was removed from the glass cup, the oven was turned off, and the mixture was allowed to cool naturally to room temperature to solidify. The optical and acoustic properties of this ultrasoft phantom closely resemble those of biological tissue, with an acoustic speed of 1.4 mm/μs and a density of 1 g/mL, which are comparable to those of soft tissues (approximately 1.5 mm/μs and 1 g/mL). Its optical absorption and reduced scattering coefficients are approximately 0.02 mm^{-1} and 1 mm^{-1}, respectively, which align well with the characteristics of brain tissue in the near-infrared wavelength range. Therefore, this phantom can effectively serve as a model for brain tissue in optical and acoustic studies of the brain [19, 20]. Transmission mode measurements were conducted on a cuboidal phantom of 3 cm × 3 cm × 7 mm, whereas reflection mode measurements were performed on a cylindrical phantom standing at 4 cm height with a radius of 5 cm.

The experimental setup for reflection mode is presented in Fig. 1(a) wherein the fibers and transducer are aligned on the XY plane, in which the FUS wave propagation is aligned with the Z-axis. Two commercially available transducers (HIFU-Siansonic) were employed in the study: the TQ60-0560, which operates at a frequency of 0.5 MHz, featuring a curvature radius of 60 mm and an active diameter of 57.5 mm, and the TQ20-1020, operating at 1 MHz, with a curvature radius of 20 mm and an active diameter of 18.5 mm. The pressure at focal area was measured using a hydrophone (NH1000, Precision Acoustics) within a water bath under controlled conditions. The lock-in amplifier (MFLI-500 kHz/5 MHz) generates an internal sinusoidal driving signal, precisely tuned to the center frequencies of the transducers (0.5260 MHz and 1.0299 MHz). This signal is amplified by the power amplifier (240L-RF10KHZ-12MHZ, 40 W) to drive the transducer. The internal sinusoidal driving signal is used as the reference throughout the lock-in detection process to detect modulated light signals. To achieve acoustic impedance matching, the phantom was positioned within a container filled with distilled water. The transducer was submerged and placed above the phantom to ensure that the focal area was located at a depth of 18 mm, which is critical for utilizing AO techniques in brain monitoring, where penetration depths on the order of centimeters are essential. The source fiber and detection fiber were located at varying distances of 30, and 35 mm on the phantom surface. This configuration was chosen to replicate penetration depth observed in the human brain, as supported by relevant literature [18, 21]. Three different light sources were employed, each varying at three angles − perpendicular, 20°, and 45° − with respect to the X-axis and Z-axis. A 100 mW long coherent (CrystaLaser, DL852-100-SO) operating at $\lambda = 852$ nm, a 150 mW laser diode (L852P150-Thorlabs) operating at $\lambda = 852$ nm, and a 400 mW high-power LED (ARE6-88D1-0GH00) provided by Broadcom Limited operating at $\lambda = 855$ nm. An adjustable attenuator and a power meter were employed to maintain a consistent optical power of 40 mW transmitted to the sample surface from the light sources through a multimode fiber cable (M76L02-Ø400). Light scattered within the sample passed through the focal area and was partially modulated by FUS. A portion of the modulated light, along with the diffuse reflectance comprising both tagged and untagged components, was transmitted through the detection fiber (M76L02-Ø400) to a fast photoreceiver (FEMTO-OE-300), which functioned as both a detector and an amplifier. The photoreceiver's output was bifurcated, with one pathway interfacing with a data acquisition (DAQ) card to record unmodulated light. Concurrently, the other pathway was routed to a lock-in amplifier to isolate the modulated light, thereby obtaining the AO signal amplitude. This extracted signal was subsequently transmitted to a computer for comprehensive analysis.

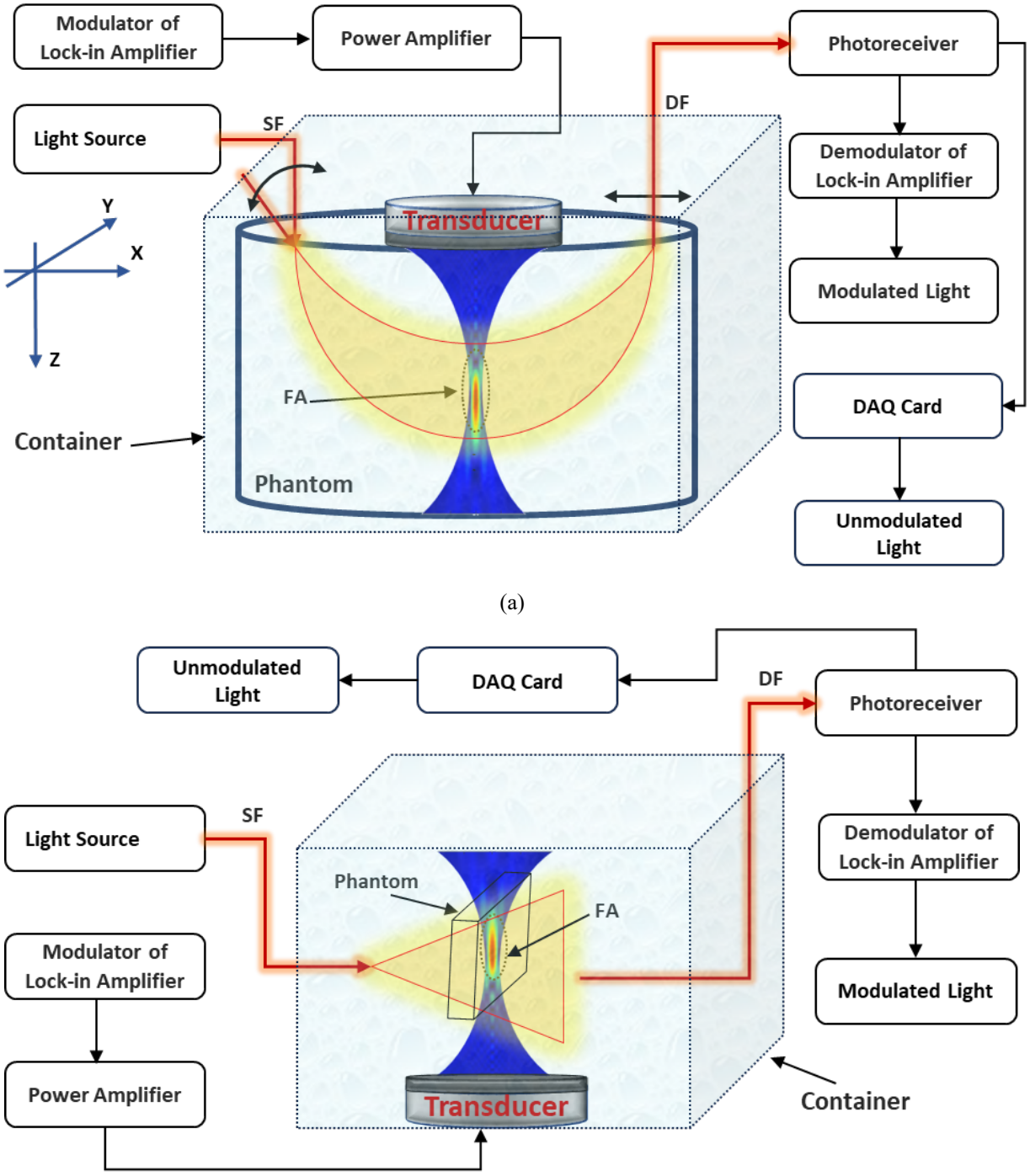


Fig. 1 Experimental configurations for detecting FUS-modulated light. The optical signal is represented by red arrows, while black arrows indicate the electrical signal. Abbreviations used are as follows: SF (source fiber), DF (detector fiber), and FA (focal area). Panel (a) illustrates the reflection mode configuration, and panel (b) depicts the transmission mode configuration.

Fig. 1(b) illustrates the transmittance setup, utilizing the same light sources and transducers as in the reflection mode, but arranged in a different configuration. The light source intensity was limited to 18 mW due to detector saturation. The transducer was fully immersed and positioned at the bottom of a cuvette measuring $23 \times 16 \times 13$ cm^3, which was filled with distilled water. A cuboidal phantom 3×3 cm^2 with 7 mm thickness in the optical transmission direction fixes inside the cuvette, ensuring the focused area aligned with the center of the phantom. The source fiber and photoreceiver fibers were axially aligned with the focal area. The rest of the detection process was the same as in the reflection mode. All measurement data presented is based on a four-minute recording, repeated three times for consistency.

3 Results

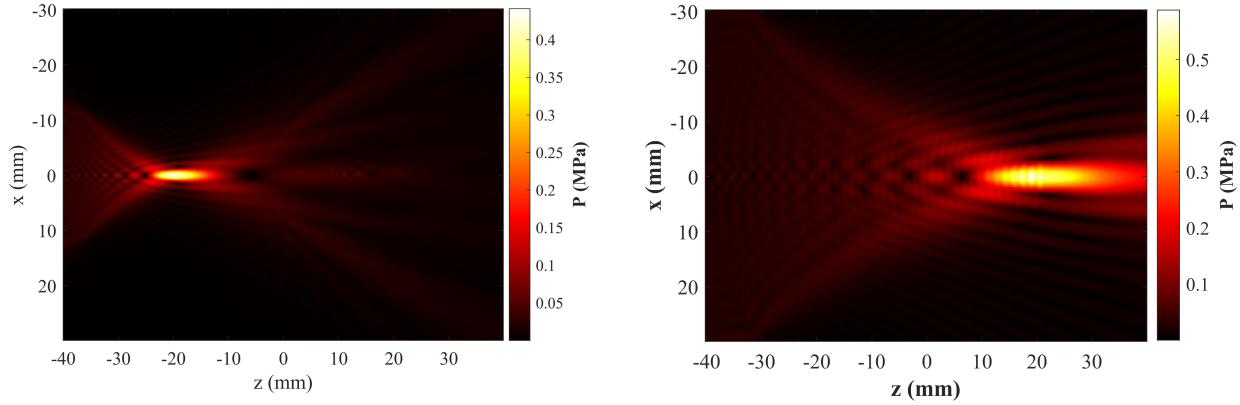
This section starts with the simulation results, followed by the presentation of the experimental outcomes, commencing with the transmission configuration and subsequently addressing the reflection mode results.

3.1 Results of Simulation

The pressure distribution generated by FUS transducers is shown in Fig. 2. The pressure amplitude exhibited a range of 0.3 to 0.5 MPa, which remains well within the permissible limits established by the FDA for medical applications [16]. At 3 dB amplitude, the focal length and width are 9 mm and 1.3 mm for 1 MHz, and 15 mm and 2.5 mm for 0.5 MHz, respectively.

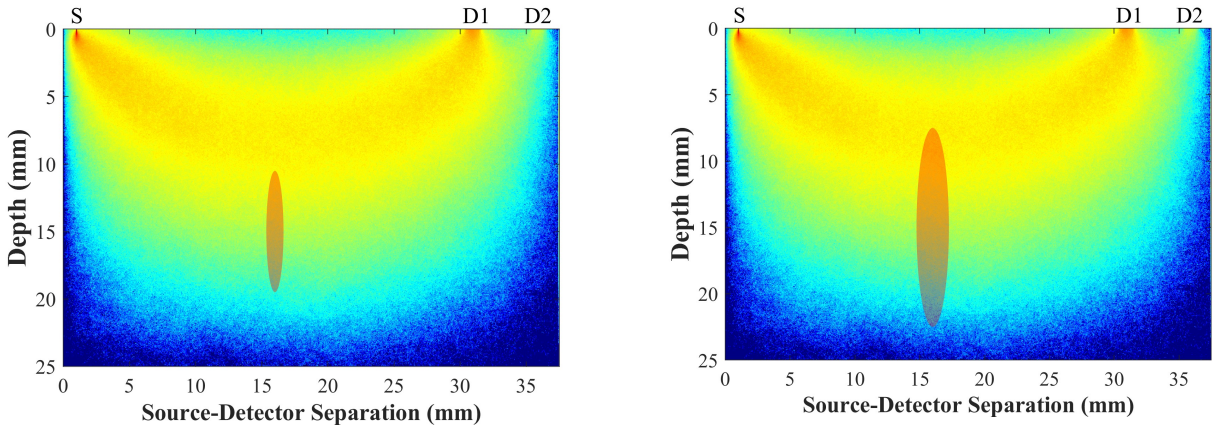
Fig. 3 shows map illustrating the trajectory of photons and the history of their intensity that clearly indicates a decrease in the number of photons reaching detectors as the distance between the source and detector increases. However, detected photons can penetrate deeper, up to about 18 mm.

Initial simulation results were presented in Ref. [8]. Fig. 4 illustrates that the tagging efficiency decreased as the FUS frequency increased from 0.5 MHz to 1 MHz; however, the number of untagged photons increased. This phenomenon occurs because, as the frequency rises, the focal area becomes smaller, limiting the number of photons that can interact with the focused region. In comparison to 1 MHz shown in Fig. 4(a) and 4(b), in 0.5 MHz, a greater number of tagged photons reached detectors D1 and D2 at the 0.5 MHz frequency, resulting in a larger accumulation of weights, as illustrated in Fig. 4(c) and 4(d). Additionally, lower FUS frequency generates larger particle displacements for the same ultrasound pressure, leading to higher tagging efficiency [15].



(a) (b)

Fig. 2 Magnitude pressure calculated for FUS propagation in the medium and pressure distribution in the focal region at two frequencies: (a) 1 MHz and (b) 0.5 MHz. The FUS source is positioned at coordinates (x, y, z) = (0, 0, 0.0399) and is directed along the +Z-axis, producing a peak pressure amplitude of approximately 0.5 MPa. The acoustic properties of the medium are specified in Table 1, with a grid spacing of 140 μm utilized in the simulation.



(a) (b)

Fig. 3 Photon trajectory mappings (logarithmic color maps) at 850 nm wavelength are depicted for two source-detector distances: S-D1: 30 mm, and S-D2: 35 mm, relative to the focus area generated by FUS. (a) At frequency of 1 MHz, while panel (b) displays them at 0.5 MHz.

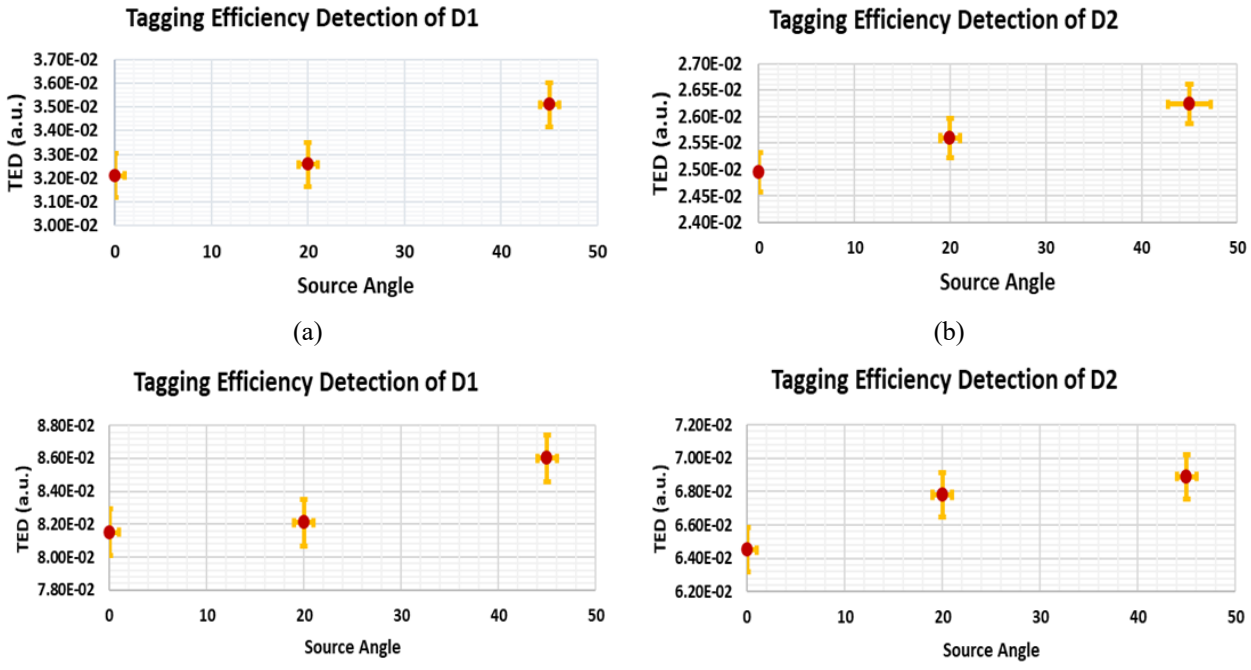


Fig. 4 Illustration of the detected tagging efficiency for three distinct angles (perpendicular, 20º, and 45º) and two SDDs. Panels (a) and (b) depict the results obtained using a 1 MHz FUS transducer, while panels (c) and (d) showcase outcomes for a 0.5 MHz frequency. The SDD is 30 mm in panels (a) and (c), and 35 mm in panels (b) and (d).

3.2 Results of Experiments

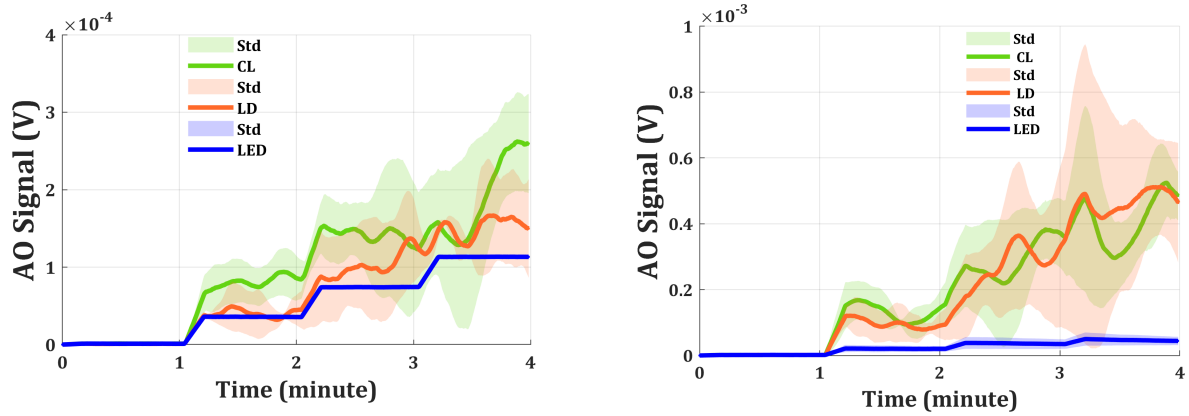
Results of AO measuring at transmission mode are presented in Fig. 5. FUS pressures in the focal region were measured ranging between 300 and 500 kPa. As FUS pressure increased, the amplitude of AO signal in both coherent and non-coherent light also increased; however, phase modulation in the coherent light introduced greater fluctuations in the signal. Upon deactivating FUS power, the AO signal rapidly diminished to levels comparable to the noise floor, primarily attributed to shot noise and environmental factors. Likewise, when the laser was turned off while maintaining FUS transducer activity, the AO signal also decreased to a similar noise level. This confirms that the AO signal arises from the interaction between ultrasound waves and light. The unmodulated light registered approximately 1 V, whereas the AO signal amplitude varied from 10^{-5} to 10^{-3} V. The amplitude of the AO signal demonstrated a proportional increase across three distinct FUS pressure levels at one-minute intervals. For coherent light sources, this increase followed a polynomial trend, whereas for noncoherent light, it demonstrated a linear relationship. Fig. 5(a) shows the AO signal generated by the 1 MHz FUS transducer, which produced lower intensity signal compared to the 0.5 MHz transducer, as illustrated in Fig. 5(b). This enhancement in light modulation at lower FUS frequencies, under constant pressure, can be attributed to the inverse relationship between particle displacement and ultrasound frequency. Furthermore, the larger focal area produced by the 0.5 MHz transducer likely increases the interaction volume between light and FUS, thereby enhancing the probability of modulated light detection.

Fig. 6 illustrates the AO signal amplitude in reflection mode, using a 1 MHz FUS transducer. In transmission mode, the LED produces an AO signal comparable with CL and LD, whereas, in reflection mode, no discernible AO signal was detected when using the LED. Examination of the SDD was conducted at 30 mm in Fig. 6(a), (b), and (c) and 35 mm in Fig. 6(d), (e), and (f). Fig. 6(a) and (d) with the source angle perpendicular to the surface of the phantom, Fig. 6(b) and (e) with a 20º angle of source illumination, and Fig. 6(c) and (f) with a 45º angle of source illumination.

Analysis of the AO signals revealed an enhancement of approximately 20% at the minimum pressure level and up to 30% at the maximum pressure level for coherent light sources when the illumination angle was adjusted from perpendicular to 20º. In contrast, at a 45º angle of illumination, the AO signal demonstrated increases of up to 40% and 60% at the minimum and maximum pressure levels, respectively. These results underscore the significant impact of illumination angle on the modulation of light in reflection mode. In the following, Fig. 7 present the results obtained using a 0.5 MHz FUS transducer. Due to the diameter of the 0.5 MHz transducer exceeding 60 mm, it was not feasible to utilize it in the reflection mode configuration.

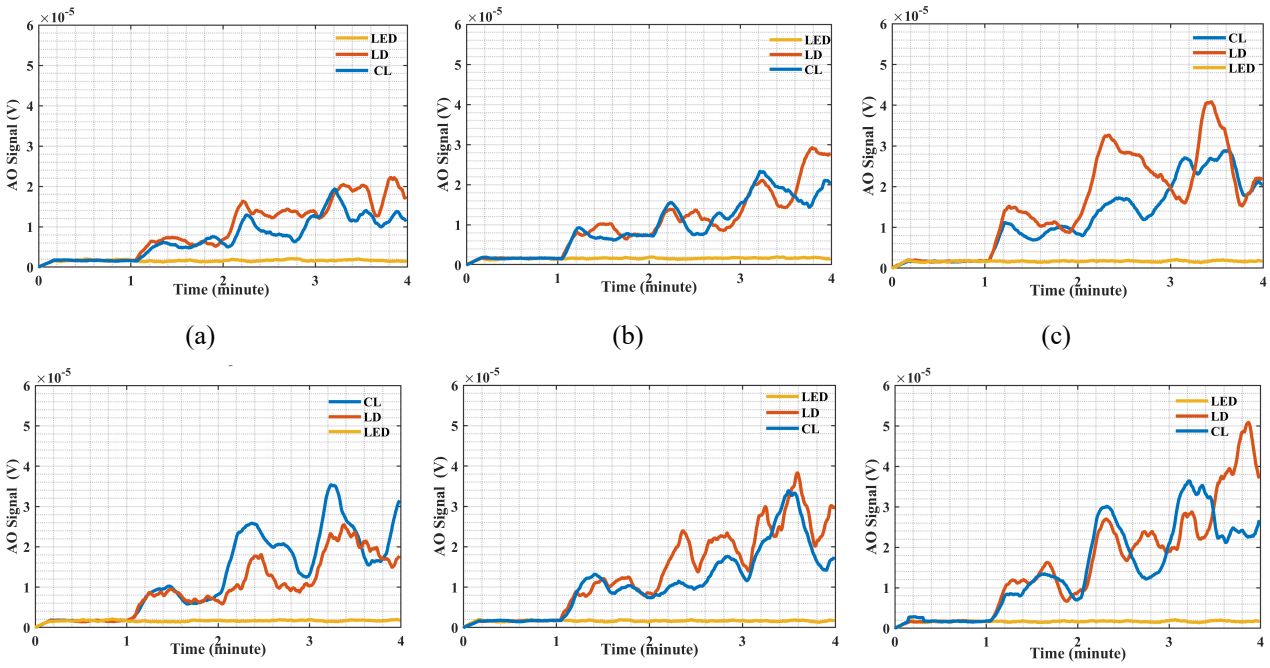
Instead, a side mode configuration was employed to assess the impact of the angle of the light source. In this arrangement, the transducer was positioned laterally relative to the phantom, with the source and detector placed above the phantom and oriented perpendicularly to each other. Similarly to the reflection mode setup with

the 1 MHz transducer, the SDDs, and the focal area were situated approximately 18 mm deep inside the tissue, as observed from the perspective of the paired fibers. As anticipated, the AO signal exhibited greater magnitude compared to the 1 MHz transducer. Analysis of the AO signals revealed a notable enhancement, with an approximate 30% increase observed at the minimum pressure level and up to a 40% increase at the maximum pressure level for coherent light sources when the illumination angle was adjusted from perpendicular to 20º. Conversely, when illuminated at a 45º angle, the AO signal displayed a remarkable increase, reaching up to 50% and 70% at the minimum and maximum pressure levels, respectively.



(a) (b)

Fig. 5 The AO signal generated by FUS, which reflects the amplitude of the AO signals in transmission configurations is presented. This data was collected in the time domain and includes measurements taken at three distinct pressure levels during the first minute of FUS inactivity. Three different light sources were utilized: a crystal laser (CL) as a long-coherent source, an LD, and an LED. The curve illustrates the AO signals, while the shaded region represents the standard deviation. (a) 1 MHz frequency FUS, and (b) 0.5 MHz frequency FUS.



(a) (b) (c)

(d) (e) (f)

Fig. 6 The amplitude of AO signals, indicating light modulated by 1 MHz FUS transducer in reflection mode. Measurements were taken at SDD of 30 mm on the bottom and 35 mm on the top. Three different light source angle configurations were used: panels (a) and (d) with the source positioned perpendicularly to the phantom surface, panels (b) and (e) with a 20° angle relative to the X-Z plane, and panels (c) and (f) with a 45° angle relative to the X-Z plane. The blue, red, and yellow curves represent AO signals for crystal laser (CL), laser diode (LD), and (LED) illumination light sources, respectively.

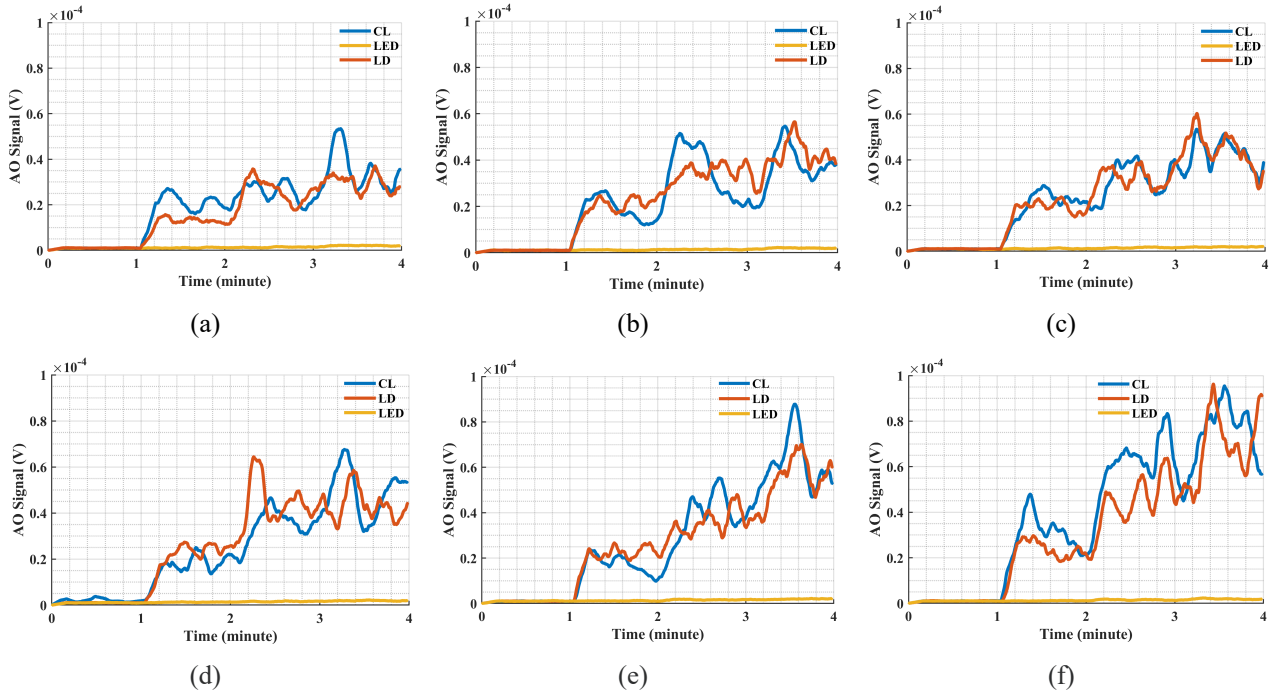


Fig. 7 The amplitude of AO signals, indicating light modulated by 0.5 MHz FUS transducer in reflection mode. Measurements were taken at SDD of 30 mm on the bottom and 35 mm on the top. Three different light source angle configurations were used: panels (a) and (d) with the source positioned perpendicularly to the phantom surface, panels (b) and (e) with a 20º angle relative to the X-Z plane, and panels (c) and (f) with a 45º angle relative to the X-Z plane. The blue, red, and yellow curves represent AO signals for crystal laser (CL), laser diode (LD), and (LED) illumination light sources, respectively.

4 Discussion and Conclusion

The numerical simulations of FUS pressure in the focal region, targeting average brain tissue, revealed pressures ranging between 300 and 500 kPa, consistent with experimental measurements. This pressure range is suitable for applications, such as, blood brain barrier (BBB) opening for brain drug delivery, as reported [22]. The results indicate that for a 0.5 MHz transducer, the focal dimensions were elongated compared to the 1 MHz transducer. This elongation is likely due to the greater transmission efficiency at lower frequencies. MC simulations of FUS-light interactions confirmed that the 0.5 MHz transducer exhibited higher tagging efficiency, attributed to the larger focal area it generated compared to the 1 MHz transducer. The close relationship between FUS pressure, frequency, and modulation efficiency was evident, with higher frequencies resulting in lower AO modulation under identical FUS pressures. This occurs because particle displacement is inversely proportional to FUS frequency [15], leading to reduced modulation amplitude at higher frequencies.

Simulation results further demonstrate that at a wavelength of 850 nm, and with FUS frequencies of 0.5 or 1 MHz, increasing the source angle from perpendicular to 45º led to increased tagging efficiency. However, increasing the SDD resulted in a decrease in tagging efficiency. Notably, the 0.5 MHz transducer consistently produced higher tagging efficiency values, trends that were corroborated by the experimental measurements.

In our study, the simulation and phantom experiments were designed with distinct objectives in mind. Although they may seem independent, they are intended to complement one another by addressing aspects of the research question. We aimed to closely match the optical properties between the phantom and the input simulation. However, due to certain practical limitations, slight differences remain. For instance, the phantom had optical absorption and scattering coefficients of approximately 0.02 mm^{-1} and 10 mm^{-1}, respectively, while the corresponding values in the simulation were 0.037 mm^{-1} and 9.5 mm^{-1}. By considering that in AO techniques the scattering coefficient plays a more critical role than the absorption coefficient, these differences can be considered small and do not have much significant influence. Furthermore, the detector size, ultrasound transducer shape, and frequencies were kept same and consistent between the simulation and the experiment. The source-detector distances were maintained at 30 mm and 35 mm in both cases. Additionally, three light source angles (0° – perpendicular in the experiments, 20°, and 45°) were investigated in the reflection mode configuration.

The numerical experiments provide a controlled, idealized environment to test theoretical assumptions, while the phantom experiments introduce more realism necessary for practical applications. Taken together, these approaches reinforce the findings: for instance, the pressure in the focal area ranged from 0.25 to 0.5 MPa in the simulations and from 0.3 to 0.5 MPa in the

experiments. Moreover, the experimental results in Fig. 6 indicate that a source angle of 45º yields the maximum AO signal, which is further supported by the simulation results in Fig. 4, showing that tagging efficiency is maximized at the same angle.

Several techniques for detecting ultrasound-modulated light have been developed, each with specific advantages and limitations. In this study, we employed a relatively low-complexity setup that is highly sensitive and can potentially be adapted for preclinical, and eventually clinical, applications. The setup's sensitivity allows it to detect FUS-modulated light in a human head model configuration. This configuration, where both the light source and detector fibers are positioned on the same side of the phantom, could be advantageous for transcranial high-intensity focused ultrasound (HIFU) therapy monitoring. The reflection setup, involving paired source and detector fibers, is convenient and adaptable for future *in vivo* and preclinical studies.

Across all measurements, increasing the FUS pressure corresponded to an increase in AO signal strength, reflecting a direct relationship between pressure at the focal point and signal amplitude. This trend is consistent with Fig. 5 to Fig. 7, which illustrate a linear relationship for non-coherent light sources and a more complex trend for coherent light sources. In transmission mode, the AO signal remained relatively stable for LED sources but exhibited significant fluctuations under coherent light, likely due to phase modulation effects. These fluctuations result from speckle patterns generated by variations in refractive index and particle displacement, leading to random phase interference. In contrast, the AO signal for LED sources remained stable, primarily due to intensity modulation. This stability can be explained by the pressure-induced density changes in the medium, which modulate the optical properties, and subsequently, the intensity of the transmitted light [1, 6, 23, 24]. Wherein, experimental results confirmed the fundamental theory of AO technique, demonstrating that in non-coherent light, FUS modulates the intensity of the light.

Although the AO technique faces challenges, particularly when compared to more mature modalities like photoacoustic imaging, it remains a promising field for development. Our results show that adjusting the source illumination angle can enhance the AO signal by up to 40% using a single detector. This study represents the first experimental investigation of the effect of source angle on FUS-modulated diffusing light aiming for brain monitoring to omptimize photon illumination and detection at the focal area. Three different source angles − perpendicular, 20º, and 45º relative to the X-Z plane − were evaluated. Specifically, coherent light at 20º angle showed 20% increase in AO intensity, while at 45º angle resulted in a 40% increase, both compared to the perpendicular angle.

In conclusion, these findings advance the understanding of AOS by demonstrating optimization of AO signal amplitude through light illumination angles and detection strategies. Future research will focus on enhancing the system's stability for planned *in vivo* experiments, in order to further develop it for selected clinical applications.

Acknowledgments

This research was funded by Infotech Oulu.

Disclosures

The authors declare that they have no conflict of interest.

References

1. L. V. Wang, "Ultrasound-mediated biophotonic imaging: a review of acousto-optical tomography and photo-acoustic tomography," Disease Markers 19(1), 123–138 (2004).
2. M. Omidali, A. Mardanshahi, M. Särestöniemi, Z. Zhao, and T. Myllylä, "Acousto−optics: recent studies and medical applications," Biosensors 13(2), 186 (2023).
3. C. V. Raman, N. S. Nagendra Nathe, "The diffraction of light by high frequency sound waves: part I," Proceedings of the Indian Academy of Sciences-Section A 2, 406–412 (1935).
4. A. Korpel, "Acousto-optics—a review of fundamentals," Proceedings of the IEEE 69(1), 48–53 (1981).
5. F. A. Marks, H. W. Tomlinson, and G. W. Brooksby, "Comprehensive approach to breast cancer detection using light: photon localization by ultrasound modulation and tissue characterization by spectral discrimination," Photon Migration and Imaging in Random Media and Tissues 1888, 500–510 (1993).
6. J. Gunther, S. Andersson-Engels, "Review of current methods of acousto-optical tomography for biomedical applications," Frontiers in Optoelectronics 10(2), 211–238 (2017).
7. A. Walther, L. Rippe, L. V. Wang, S. Andersson-Engels, and S. Kröll, "Analysis of the potential for non-invasive imaging of oxygenation at heart depth, using ultrasound optical tomography (uot) or photo-acoustic tomography (pat)," Biomedical Optics Express 8(10), 4523 (2017).
8. M. Omidali, A. Mardanshahi, Z. Zhao, D. Sonker, A. V. Bykov, and T. S. Myllylä, "Light source-detector pair positioning to optimize tagging efficiency of focused ultrasound-modulated photons in a backward detection mode," Proceedings of SPIE 12379, 359–362 (2023).
9. B. E. Treeby, B. T. Cox, "k-Wave: matlab toolbox for the simulation and reconstruction of photoacoustic wave fields," Journal of Biomedical Optics 15(2), 021314 (2010).

10. E. S. Wise, B. T. Cox, J. Jaros, and B. E. Treeby, "Representing arbitrary acoustic source and sensor distributions in fourier collocation methods," Journal of the Acoustical Society of America 146(1), 278–288 (2019).
11. F. Duck, Physical Properties of Tissues: A Comprehensive Reference Book, Academic Press (2013). ISBN: 0-12-222800-6.
12. M. A. Samoudi, T. Van Renterghem, and D. Botteldooren, "Computational modeling of a single-element transcranial focused ultrasound transducer for subthalamic nucleus stimulation," Journal of Neural Engineering 16(2), 026015 (2019).
13. L. Wang, S. L. Jacques, and L. Zheng, "MCML—monte carlo modeling of light transport in multi-layered tissues," Computers in Biology and Medicine 47(1), 131–146 (1995).
14. G. Yao, L. V. Wang, "Theoretical and experimental studies of ultrasound-modulated optical tomography in biological tissue," Applied Optics 39(4), 659–664 (2000).
15. Y. Huang, M. Cua, J. Brake, Y. Liu, and C. Yang, "Investigating ultrasound–light interaction in scattering media," Journal of Biomedical Optics 25(3), 1 (2020).
16. J. Shin, C. Kong, J. S. Cho, J. Lee, C. S. Koh, M.-S. Yoon, Y. C. Na, W. S. Chang, and J. W. Chang, "Focused ultrasound–mediated noninvasive blood-brain barrier modulation: preclinical examination of efficacy and safety in various sonication parameters," Neurosurgical Focus 44(2), E15 (2018).
17. Q. Fang, D. A. Boas, "Monte carlo simulation of photon migration in 3d turbid media accelerated by graphics processing units," Optics Express 17(22), 20178–20190 (2009).
18. T. Myllylä, M. Harju, V. Korhonen, A. Bykov, V. Kiviniemi, and I. Meglinski, "Assessment of the dynamics of human glymphatic system by near-infrared spectroscopy," Journal of Biophotonics 11(8), e201700123 (2018).
19. G. M. Spirou, A. A. Oraevsky, I. A. Vitkin, and W. M. Whelan, "Optical and acoustic properties at 1064 nm of polyvinyl chloride-plastisol for use as a tissue phantom in biomedical optoacoustics," Physics in Medicine and Biology 50(14), N141–N153 (2005).
20. A. N. Bashkatov, E. A. Genina, V. I. Kochubey, and V. V. Tuchin, "Optical properties of human skin, subcutaneous and mucous tissues in the wavelength range from 400 to 2000 nm," Journal of Physics D: Applied Physics 38(15), 2543–2555 (2005).
21. S. C. Feng, F. Zeng, and B. Chance, "Monte carlo simulations of photon migration path distributions in multiple scattering media," Photon Migration and Imaging in Random Media and Tissues 1888, 78–89 (1993).
22. W. Qiu, A. Bouakaz, E. E. Konofagou, and H. Zheng, "Ultrasound for the brain: a review of physical and engineering principles, and clinical applications," IEEE Transactions on Ultrasonics, Ferroelectrics, and Frequency Control 68(1), 6–20 (2020).
23. J. W. Goodman, Speckle phenomena in optics: theory and applications, Roberts and Company Publishers (2007).
24. D. S. Elson, R. Li, C. Dunsby, R. Eckersley, and M.-X. Tang, " Ultrasound-mediated optical tomography: a review of current methods," Interface Focus 1(4), 632–648 (2011).

Nanocomposites Based on Gold Nanostars with a Hollow Silica Shell for Controlled-Release Drug Delivery

Andrey V. Simonenko[1,2], Andrey M. Burov[1], and Vitaly A. Khanadeev[1,3*]

[1] Institute of Biochemistry and Physiology of Plants and Microorganisms, Saratov Scientific Centre of the Russian Academy of Sciences (IBPPM RAS), 13 pr. Entuziastov, Saratov 410049, Russian Federation

[2] Saratov State University, 83 Astrakhanskaya str., Saratov 410012, Russian Federation

[3] Saratov State University of Genetics, Biotechnology and Engineering named after N.I. Vavilov, 4 Stolypin av., build. 3., Saratov 410012, Russian Federation

[*]e-mail: khanadeev@gmail.com

Abstract. Recently, there has been a significant development of targeted drug delivery methods using various nanomaterials. This has opened up new opportunities for the therapeutic use of drugs with pronounced side effects. The use of targeted delivery and controlled release systems provides an opportunity to reduce the negative effect on the whole organism and improve the effectiveness of treatment. In this work, nanocomposites based on gold nanostars with a hollow organosilica shell were studied as carriers for drug delivery. Two types of drugs, docetaxel and doxorubicin, were loaded into the cavities formed after silica etching. To implement controlled unloading, the nanocomposites were coated with a molecular gate based on tetradecanol. It was found that the drug was retained in the nanocomposites until an external stimulus was received. © 2024 Journal of Biomedical Photonics & Engineering.

Keywords: gold nanostars; hollow shell; organosilica; drug delivery; docetaxel; doxorubicin; tetradecanol; cytotoxicity.

Paper #9154 received 30 Aug 2024; revised manuscript received 18 Nov 2024; accepted for publication 19 Nov 2024; published online 6 Dec 2024. doi: 10.18287/JBPE24.10.040314.

1 Introduction

Recently, the treatment of cancer has become an important area of research in the field of medicine and biotechnology [1]. One of the main methods of treating such diseases is chemotherapy using antitumor drugs [2]. For example, the drug docetaxel is a clinically proven anti-tumor agent for inhibiting breast cancer [3]. However, despite their high efficiency, antitumor drugs have many side effects, affecting not only tumor cells, but also healthy cells of the body [4]. The most common side effects include bone marrow suppression, nausea and vomiting, fatigue, and hair loss. To solve this problem, targeted drug delivery using various nanocarriers is currently of great practical interest. The use of nanocarriers helps reduce side effects and increase the effectiveness of chemotherapy due to the fact that they can be delivered directly to the tumor, minimizing their impact on other organs and tissues of the body. In addition, encapsulating the drug in a carrier helps reduce its interaction with other substances and overcome various physiological barriers [5]. Such carriers may include protein-based conjugates [6], liposomes [7], dendrimers [8], magnetic nanoparticles [9], etc. Among the numerous nanocarriers for drug delivery, it is worth noting silica nanoparticles, which have favorable physicochemical properties [10, 11]. Firstly, they have a large surface area, which ensures high drug loading. This way, more active substance can be delivered to its destination. Secondly, due to their chemical structure, silica nanoparticles are not broken down by the body's enzymes, which ensures that the drug will be delivered to the right place and maintain its effectiveness for a long time. Another important advantage of silica nanoparticles is the controlled release of drugs [12]. By using various surface modification methods, it is possible to control the rate of drug release from nanoparticles. Slow release of the drug ensures maintenance of a therapeutic concentration of the drug at the site of localization, which allows achieving maximum therapeutic effect with minimal side effects and reducing the frequency of drug administration.

In addition to chemotherapy, photothermal therapy can be used to treat tumor diseases. It is based on the use

of light-absorbing agents, which, by absorbing light, heat up and destroy cancer cells [13, 14]. Of particular interest here are gold nanoparticles that exhibit plasmon resonance. Plasmon resonance of nanoparticles can be tuned to a specific wavelength by changing the shape and size of the nanoparticles, which is important for biomedical applications. Of great interest in biomedicine is the near infrared range with wavelengths from 650 to 950 nm, called the first therapeutic "optical window" [15]. The "optical window" corresponds to the wavelength range where absorption by water and biological tissues is minimal and laser penetrating power is maximal. Therefore, non-spherical gold nanoparticles with high absorption within the "optical window" can act as effective agents for photothermal therapy on their own or even as part of composites [16]. In addition, gold is a noble and inert metal that is non-toxic and ideal for use in biomedicine. In addition, the surface of gold nanoparticles has adsorption capacity. Coating gold nanoparticles with silica shells offers an alternative strategy where drugs incorporated into the shell can be co-delivered with photothermal agents [17]. On the one hand, heating can directly destroy cancer cells. On the other hand, increasing the temperature promotes the release of the drug, thereby initiating chemotherapy. In a number of studies, gold nanostars were coated with a mesoporous silica shell and loaded with doxorubicin. After drug encapsulation, a molecular layer, such as paraffin heneicosane [18] or hyaluronic acid [19], was applied to the surface of the composite to seal the channels of the mesoporous silica shell. The drug was contained within these composites and release was initiated either by heating under laser irradiation, or by changing the pH, or by exposure to an enzyme. In addition, hollow silica shells are of great interest [20]. Due to their hollow structure, they are able to accommodate a larger number of encapsulated substances, which in turn are protected from the effects of the environment. Nanocomposites for drug delivery are also created based on the hollow shell. Various types of gold nanoparticles are used as cores. Thus, in the work [21], gold nanocages were used, which acted both as a sensitive substrate for SERS and as an effective photothermal converter for localized hyperthermic cancer therapy due to strong absorption of near-infrared light. In addition, coating the nanocages with a hollow SiO_2 shell prevents the aggregation of metal particles, preserving their optical properties. Such nanocomposites can be effectively used for drug delivery and photothermal therapy. Gold nanorods were also used as cores for the nanocomposites [22]. They were used to synthesize a hollow silica shell, which was loaded with doxorubicin and then the pores were closed. This structure allowed the drug to be preserved inside with virtually no losses. In addition, they were able to demonstrate that combined chemo-photothermal therapy was more effective in killing cancer cells than either chemotherapy or photothermal therapy alone. Also in 2021, it was shown [23] that gold nanotriangles, nanorods, and other types of particles can act as cores for the synthesis of nanocomposites with a hollow silica shell.

In this work, we synthesized nanocomposites based on gold nanostars coated with a hollow organosilica shell for drug delivery. These nanocomposites have a number of advantages, making them ideal candidates for controlled drug delivery. First, gold nanostars have wide tuning ranges of localized surface plasmon resonance [24]. Secondly, among other forms of gold nanoparticles, they are the most photostable [25]. Third, the organosilica shell contains two different functional groups: Si–OH and –SH. The thiol residue provides a more convenient way of covalently linking to target molecules: fluorescent molecules, proteins or single-stranded DNA (ssDNA) with isothiocyanate, succinimidyl ester or maleimide groups [26]. Thus, the surface of nanocomposites is convenient for functionalization. The resulting cavities were loaded with drugs: doxorubicin and docetaxel after etching the organosilica shell. The cytotoxicity of the obtained nanocomposites was also studied for their further use in biomedicine.

2 Materials and Methods

2.1 Chemicals

The following reagents were used in the synthesis without further purification: hydrogen tetrachloroaurate(III) trihydrate ($HAuCl_4*3H_2O$; 99%), sodium citrate trihydrate ($Na_3C_6H_5O_7*2H_2O$), sodium borohydride ($NaBH_4$), hydrochloric acid (HCl, high purity grade), L-ascorbic acid (99.9%), silver nitrate ($AgNO_3$; 99.9%), 3-mercaptopropyltriethoxysilane (MPTES), polysorbate 20 (Tween 20), docetaxel (DOC, purum, ≥97.0% (HPLC)) all purchased from Sigma–Aldrich (Darmstadt, Germany). Adriamycin hydrochloride (doxorubicin, DOX, 98%) purchased from Macklin (China). Polyethylene glycol thiol (Mw=5000, Creative PEGWorks, Chapel Hill, North Carolina, USA), sodium hydroxide (NaOH, analytical grade; Dia-M, Russia), 25% ammonia solution (Vekton, Russia). MilliQ ultrapure water (18 mΩ×cm; Millipore, Merck KGaA, Darmstadt, Germany) was used in all experiments. All glassware and magnets were cleaned with freshly prepared aqua regia (a mixture of HNO_3 and HCl, in a ratio of 1:3 by volume) followed by rinsing with plenty of water.

2.2 Equipment

To measure the extinction spectra of colloidal solutions of nanoparticles and nanocomposites, a high-speed spectrophotometer Specord S300 (Analytik Jena, Germany) was used. Measurements were carried out in the wavelength range of 320–1100 nm using a 2 mm thick quartz cuvette. To measure the extinction spectra of drugs, in particular docetaxel, and drug-loaded nanocomposites, a Specord 250 dual-beam spectrophotometer (Analytik Jena, Germany) was used. It is additionally equipped with a UV lamp and allows

measurements in the wavelength range of 190–1100 nm. The measurements were carried out in a 1-mm thick quartz cuvette.

To describe the morphological properties of the synthesized nanoparticles and nanocomposites, we used transmission electron microscopy (TEM) images obtained using a Libra-120 microscope (Carl Zeiss, Germany) at the Simbioz Center for the Collective Use of Research Equipment of the Institute of Biochemistry and Physiology of Plants and Microorganisms – Subdivision of the Federal State Budgetary Research Institution Saratov Federal Scientific Centre of the Russian Academy of Sciences (IBPPM RAS).

2.3 Synthesis of Gold Nanostars

Gold nanostars were synthesized from gold seeds using a two-step protocol [27]. For this purpose, in the first stage, using the citrate reduction method of $HAuCl_4$ described by Frens [28], gold nanospheres with an average diameter of 25 nm were synthesized, which were used as seeds for the synthesis of gold nanostars. To do this, 145.95 ml of water was poured into an Erlenmeyer flask and brought to a boil with a reflux water condenser while stirring on a magnetic stirrer. 1.5 ml of 1% $HAuCl_4$ and 2.55 ml of 1% sodium citrate were added. The solution was stirred for 15 min. The color of the solution changed from colorless to red. The second step involved the actual synthesis of nanostars. Briefly, to a mixture ("growth solution") containing 40 ml of water, 1 ml of 1% $HAuCl_4$, 120 µl of 1 M HCl, different amounts of a colloid of 25 nm gold nanospheres ("seeds"), 600 µl of 4 mM $AgNO_3$ and 600 µl of 100 mM ascorbic acid were quickly alternately added.

2.4 Synthesis of Organosilica Shell

The organosilica shell was synthesized using the method described in the article [26]. Briefly, after the gold nanostars were synthesized, they were coated with SH-PEG-COOH. Then, different amounts of 3-mercaptopropyltriethoxysilane (MPTES) were added to the particle colloid to synthesize shells of different thicknesses and a 25% ammonia solution as an initiator for the hydrolytic condensation reaction.

2.5 Etching of Organosilica Shell

To load the drugs into the synthesized nanocomposites, an internal cavity was created using a protocol that has been described in detail for the etching of silica nanoparticles [29]. For this purpose, the inner part of the organosilica shell was etched in an alkaline medium using NaOH with a final concentration of 0.75 M. Before etching, the organosilica-coated nanoparticles were coated with polyvinylpyrrolidone (PVP) to protect the surface. In this case, the PVP polymer performs the important function of preserving the surface of the nanoparticles, and this process is called the surface-protecting etching method. It is also important to note here that coating with PVP does not prevent the penetration of drug molecules and other substances into the nanoparticles [22, 29]. The degree of etching is defined in our work by analogy with the work [29] as a decrease in the extinction intensity at a certain wavelength in percent relative to the initial value. The fact is that during etching the colloid becomes more transparent and a decrease in extinction can be an easily measured characteristic of the etching degree. In the work of Zhang Q. et al. [29] the extinction value at a wavelength of 700 nm was used, which was convenient for silica nanospheres. In our work, starting from approximately 550 nm, the spectrum exhibits a characteristic maximum of gold nanostars, which act as nanocomposite cores. And the characteristic spectral contribution of silica is observed as a pronounced shoulder in the region of 350–600 nm. Therefore, for our nanocomposites, the degree of etching is conveniently determined by the decrease in the extinction value at a wavelength of 400 nm.

Different degrees of etching are achieved by adjusting the exposure time of nanocomposites in the NaOH solution. The longer the exposure time, the greater the etching degree. The etching degree is determined in real time by measuring the extinction using a high-speed spectrophotometer Specord S300 by the extinction value at 400 nm. To stop etching, the same volume of water is added to the colloid, which reduces the NaOH concentration. After this, the nanocomposites are washed by three-fold centrifugation at 800 g for 20 min with redispersion in water.

2.6 Drug Loading

The drugs used were doxorubicin and docetaxel. Two methods were used to load the drug. In the first method, the composite nanoparticles were concentrated to a concentration of 375 µg/ml, which was determined by drying and weighing a portion of the sample. The drug (doxorubicin or docetaxel) was then added to the nanoparticles to bring its final concentration to 200 µg/ml. The mixture was incubated for 24 h and then measurements were taken of the spectra of the colloid of nanoparticles with the drug and the supernatant after centrifugation.

The second method of drug loading was used to close the pores with a molecular gate [22]. The temperature-sensitive material 1-tetradecanol was used as such a molecular gate. This method consists of drying the particles and adding a high concentration solution of the drug to them – 8 mg/ml. The mixture was stirred while heating at 60 °C for 1 h, then tetradecanol and hot water were added successively. After this, the samples were washed from excess drugs and tetradecanol, first in hot water and then in cold water. This method allowed the tetradecanol to harden and close the pores.

2.7 Determination of the Concentration of Loaded and Released Drug

The concentration of the loaded and released drug was determined as follows. First, calibration curves were

constructed for each drug using the two-fold dilution method and the formula for the dependence of extinction on concentration was determined. Docetaxel was dissolved in ethanol and the concentration was determined by the intensity of the maximum at a wavelength of 231 nm. Doxorubicin hydrochloride was dissolved in water and the concentration was determined at a wavelength of 480 nm. After incubation of the nanocomposites with the drug, the samples were centrifuged and the concentration of the drug in the supernatant was measured. The amount of loaded drug was determined as the difference between the initial concentration and the concentration in the supernatant. The concentration of the released drug was determined similarly by measuring the concentration of the drug in the supernatant after centrifugation of nanocomposites.

2.8 Cytotoxicity Test

The toxicity test of the synthesized nanocomposites was based on measuring the metabolic activity of cells. Quantitative assessment of cell viability was measured by a spectrofluorometric method using Alamar blue reagent (Thermofisher, USA). Alamar blue is resazurin, a cell-permeable dye that can be reduced by mitochondrial dehydrogenases in living cells to the fluorescent compound resorufin. The integrated fluorescence intensity of resorufin at a wavelength of 600 nm is directly proportional to the number of cells and their metabolic activity. The Chinese hamster ovary cell line (CHO II) was chosen as the object of study. This cell line is considered one of the most sensitive cell lines for cytotoxicity studies [30]. The cells were cultured in DMEM/F-12 (1:1) nutrient medium supplemented with 20% fetal calf serum, L-glutamine and 1% penicillin in an atmosphere of 5% CO_2 at 37 °C until a monolayer was formed. When the cell monolayer reached 70–90%, the old nutrient medium was removed and a new one containing the studied nanocomposites was introduced. Cytotoxicity assessment was performed for samples of gold nanostars coated with an organosilica shell without drug loading. The preparations were preliminarily washed 3 times from the reaction mixture. Next, the solution with nanoparticles was diluted with DMEM nutrient medium to a final gold concentration of 0.8 to 25 μg/ml. The resulting solution was poured into a 96-well plate at 190 μl. The plate was placed in an Innova CO-14 CO_2 incubator (New Brunswick Scientific, USA) at 37 °C with 5% CO_2. For each obtained gold concentration, the test was performed in 4 replicates. The duration of the cytotoxicity test was chosen to be 72 h based on the observation of cell growth without nanocomposites in the wells of the plate 24, 48 and 72 h after the introduction of the seed dose. At the growth time of 72 h, the cells filled about 80% of the well bottom area, which was a favorable control for careful measurement of the cytotoxicity of the nanocomposites. After 72 h of incubation of cells with nanoparticle samples, the culture medium was removed and a resazurin solution was added to a final concentration of 0.01 mg/ml. The incubation time with the dye was 1 h. Next, spectrofluorometric measurements were performed on a Cary Eclipse microplate fluorimeter (Agilent Technologies, USA). The excitation wavelength was 530 nm. The emission wavelength range was 590–610 nm. To assess the cytotoxicity of gold nanoparticle samples, the metabolic activity value was calculated:

$$MA = \frac{I}{I_0} * 100, \quad (1)$$

where *MA* is the metabolic activity, *I* is the fluorescence intensity value of the experimental sample, I_0 is the fluorescence intensity value of the control sample.

3 Results and Discussion

3.1 Synthesis of Nanocomposites

The general scheme for the synthesis of nanocomposites based on gold nanostars with a hollow silica shell for controlled-release drug delivery is shown in Fig. 1. The first step involves the synthesis of gold nanostars. It is carried out using a seed protocol that includes the synthesis of spherical seeds and their subsequent growth, which includes the formation of sharp spikes. Next, a shell of organosilica is formed on the surface of the nanoparticles. To ensure controlled drug delivery, a cavity is created inside the organosilica shell. The resulting pores on the outside of the shell are closed with a heat-sensitive gate – tetradecanol. This system allows the drug to be kept inside the nanocomposite at room temperature. The drug is released by heating.

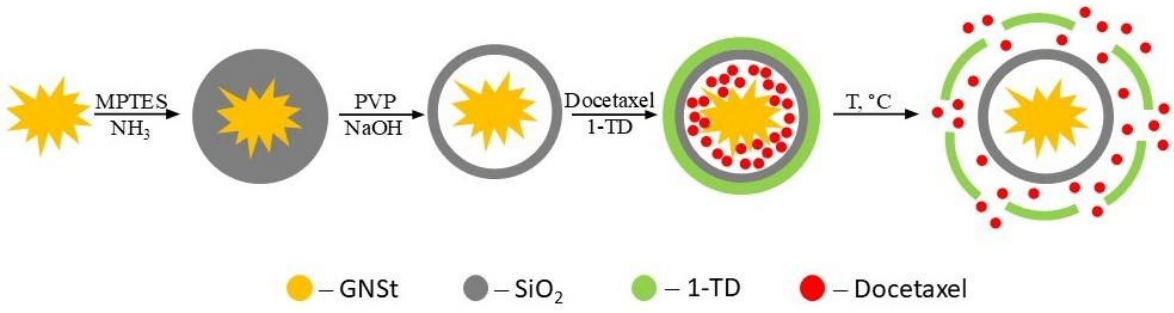


Fig. 1 Scheme for the synthesis of nanocomposites based on gold nanostars with a hollow silica shell for controlled drug delivery.

3.2 Characteristics of Gold Nanostars

By varying the amount of added 25-nm seeds, the plasmon resonance was tuned in the range from 700 to 1000 nm. When the amount of added seed solution was reduced from 400 to 150 µl per 5 ml of growth solution, the plasmon resonance shifted to a longer wavelength region of the spectrum from 758 to 853 nm (Fig. 2a). This is explained by the fact that as the number of seeds decreases, the amount of $HAuCl_4$ per nanoparticle increases. It is known that in such cases the average size of the core and the length of the spikes of nanostars increase [31]. Accordingly, the length of the spikes increases on average from 36.3 ± 6.7 nm (Fig. 2b) to 91.7 ± 15.6 nm (Fig. 2d). Also, with a decrease in the number of seeds, the diameter of the core of the nanostars increases from 52.9 ± 7.4 nm (Fig. 2b) to 86.8 ± 11.5 nm (Fig. 2d). In further experiments, nanostars with a plasmon resonance of 853 nm were used, where 150 µl of seeds per 5 ml of growth solution were added during synthesis (Fig. 2d).

3.3 Synthesis of Organosilica Shell

Using this method, 3 samples with an organosilica shell with an average shell thickness of 170 ± 24.6, 90 ± 10.2 and 28 ± 3.5 nm were synthesized (Fig. 3a–c). Spectral changes are shown in Fig. 3d. When a shell is formed on the surface of nanoparticles, a shift in plasmon resonance occurs to the long-wave region as a result of a change in the local dielectric environment of the nanoparticles. Also, with an increase in the thickness of the organosilica shell, a significant increase in the short-wave shoulder in the spectrum is observed. For all subsequent experiments on silica shell etching and drug loading, a sample of nanocomposites with a maximum silica shell thickness of 170 ± 24.6 nm was used (Fig. 3a).

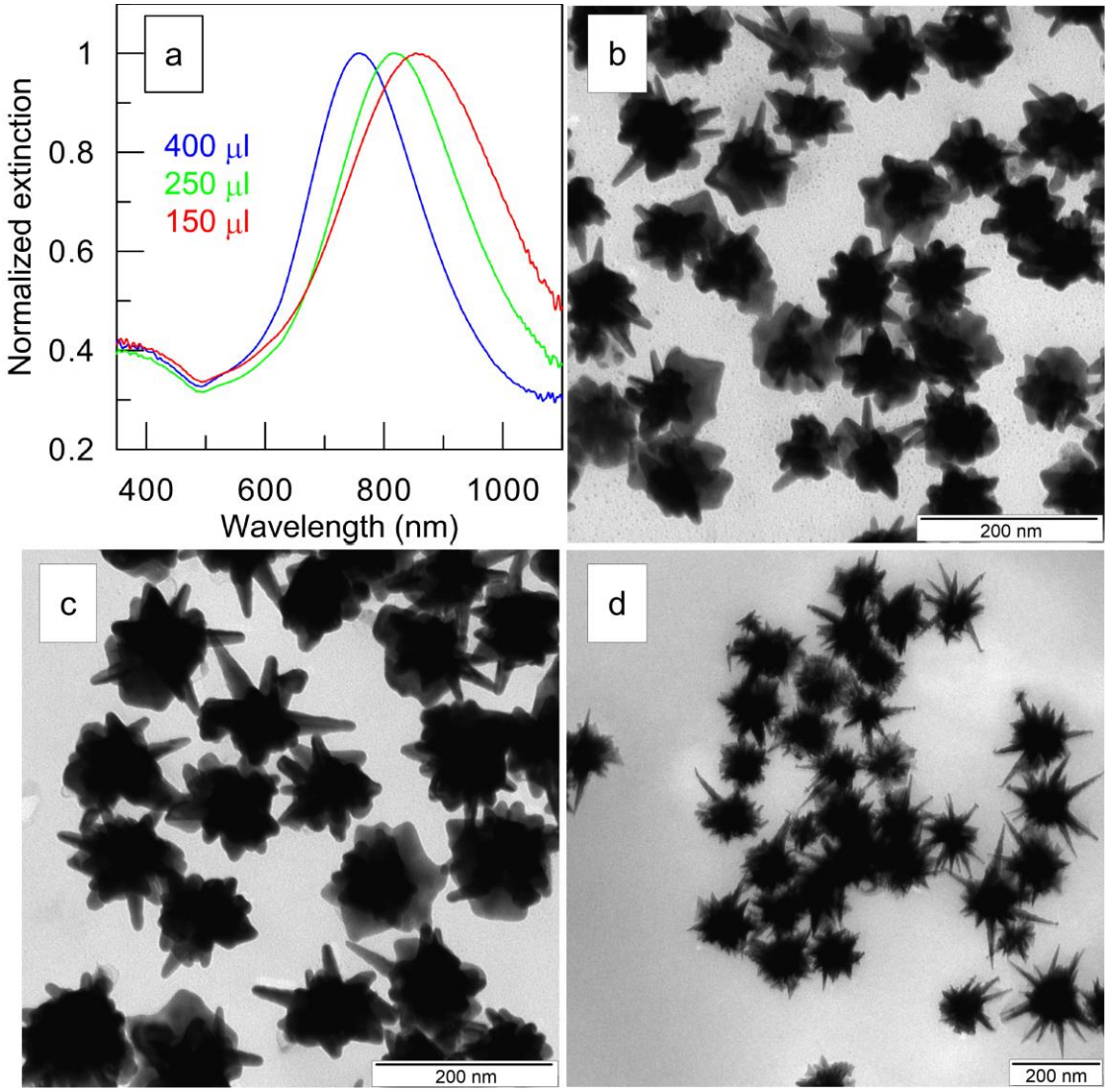


Fig. 2 (a) Extinction spectra of gold nanostar colloids after adding 400 (blue line), 250 (green line) and 150 µl (red line) of seeds to 5 ml of growth solution and TEM image of gold nanostars synthesized with the addition of (b) 400, (c) 250 and (d) 150 µl of seeds.

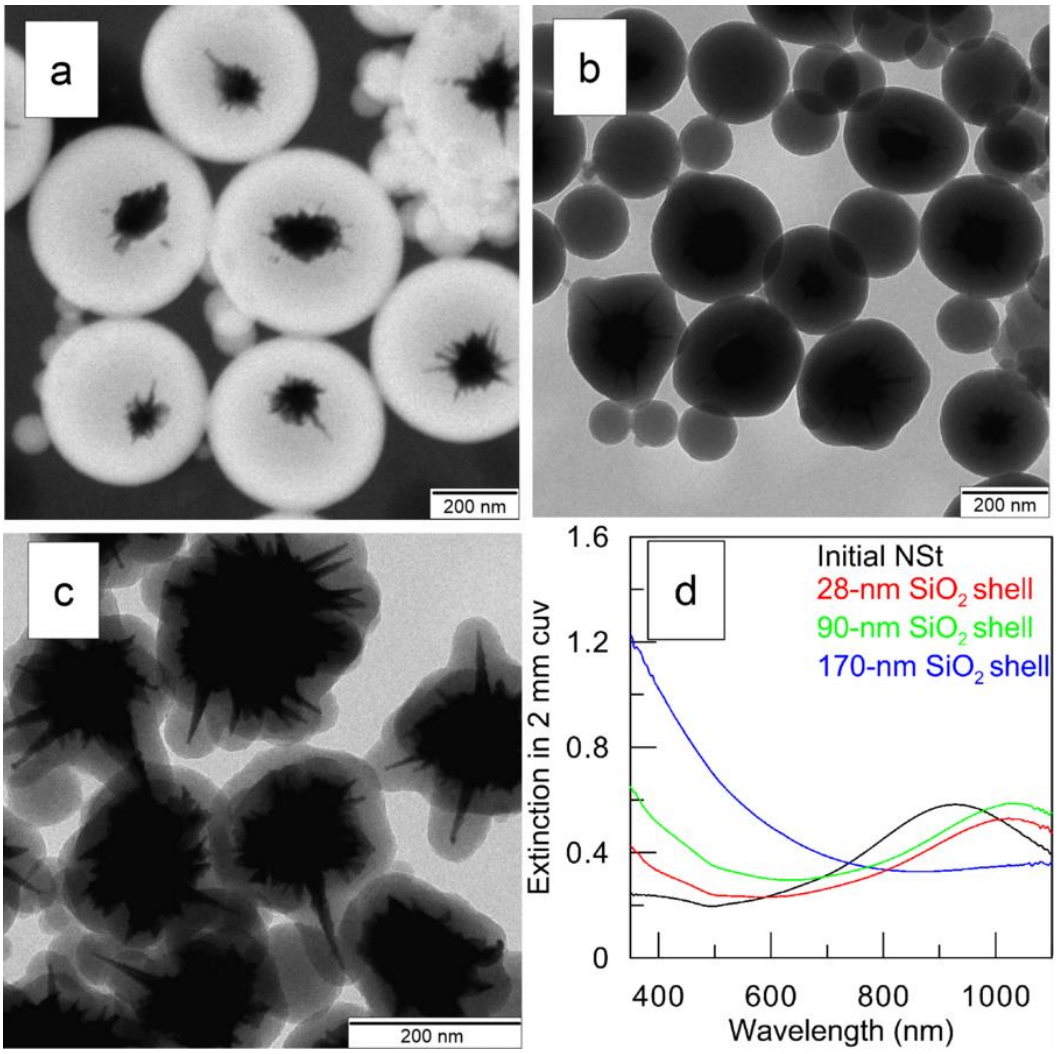


Fig. 3 TEM images of gold nanostars coated with an organosilica shell of (a) 170, (b) 90 and (c) 28 nm thickness. (d) Extinction spectra of gold nanostars before (black) and after the formation of an organosilica shell with a thickness from 28 nm (red) to 170 nm (blue).

3.4 Etching of Organosilica Shell

Three samples with different degrees of etching of the organosilica shell were obtained, when the decrease in optical density at a wavelength of 400 nm was 35, 64 and 75% (Fig. 4). These etched samples were designated as ENC1, ENC2 and ENC3, respectively.

The spectrum shows a significant decrease in the intensity of the short-wave shoulder, indicating a decrease in the amount of silica. There is also a shift in the plasmon resonance of gold nanostars toward shorter wavelengths due to a change in the local dielectric environment of the nanoparticles.

Electron microscope images confirm spectral changes (Fig. 5). With a spectrum reduction of 64% (ENC2), nanocomposites exhibit irregularities along the perimeter of the shell. Light areas also appear, indicating thinning of the shell (Fig. 5c). With further etching, the number of light areas increases and, accordingly, the amount of silica decreases (Fig. 5d).

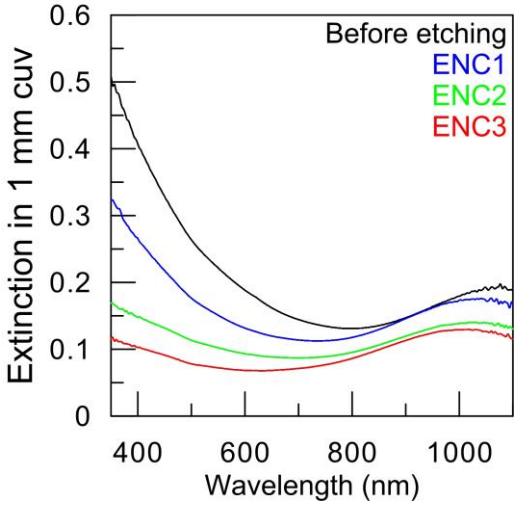


Fig. 4 Extinction spectra of gold nanostars coated with an organosilica shell before (black line) and after etching, where the extinction at 400 nm is reduced by 35% (ENC1, blue line), 64% (ENC2, green line), and 75% (ENC3, red line).

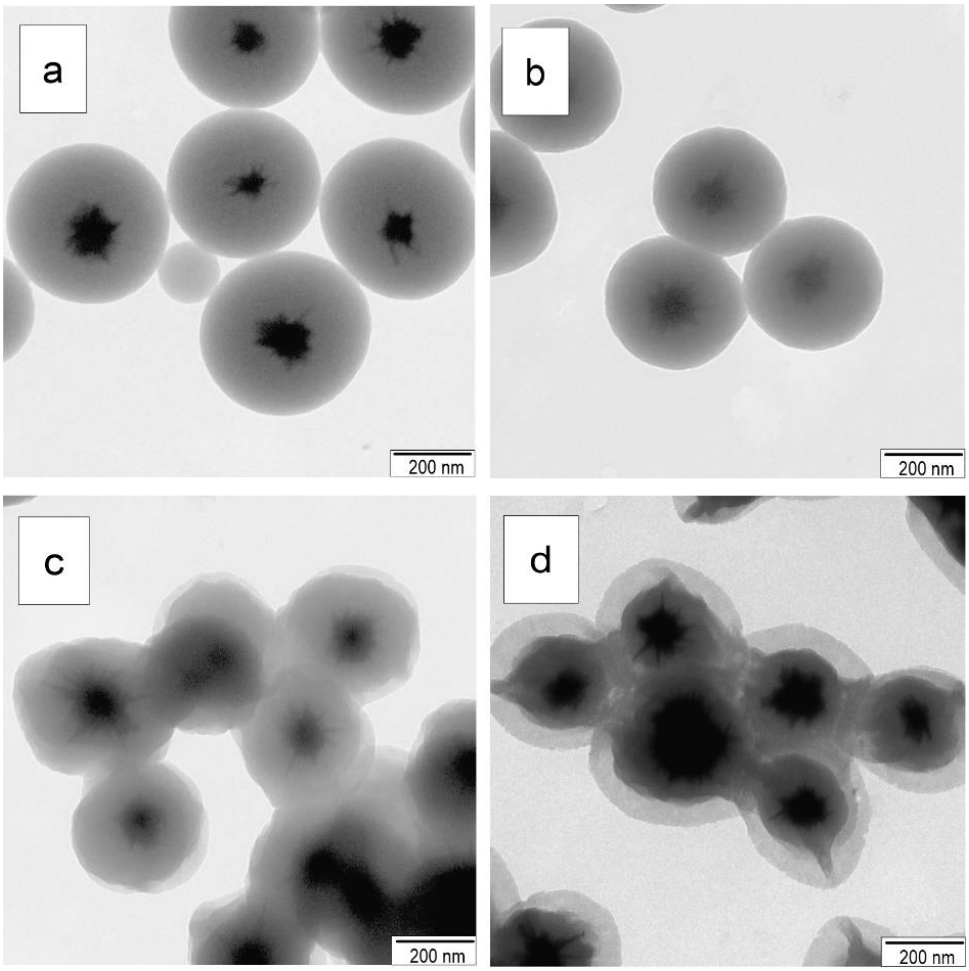


Fig. 5 TEM images of gold nanostars coated with a silica shell (a) before and after etching: (b) ENC1, (c) ENC2, and (d) ENC3.

3.5 Loading Drugs

To determine the concentration of the loaded drug, calibration curves were constructed (Fig. 6) and formulas for the dependence of concentration on the maximum absorption of a specific drug were determined. For docetaxel, the concentration was determined by the intensity of the maximum at a wavelength of 231 nm, and for doxorubicin at 480 nm. The measurements were carried out in a 1 mm thick quartz cuvette; the graphs show the values recalculated for a 10 mm cuvette.

Fig. 7 shows the extinction spectra of solutions of gold nanostars coated with a silica shell after etching (ENC1, ENC2 and ENC3) with docetaxel (Fig. 7a) and doxorubicin (Fig. 7b). Depending on the degree of shell etching, 64.5 ± 0.11 to 77.3 ± 0.6 μg/ml of docetaxel were loaded, which amounted to 32.23 ± 0.55 and 38.65 ± 0.3% of the initial drug concentration of 200 μg/ml, respectively. Doxorubicin was loaded in concentrations from 95.74 ± 0.13 to 106.25 ± 0.23 μg/ml, which amounted to 47.9 ± 0.07 and 53.1 ± 0.11% of the initial drug concentration of 200 μg/ml, respectively. The release of drugs from nanocomposites was also investigated. Without the use of a molecular gate, doxorubicin was found to be completely released from the loaded nanoparticles into solution within 30 min. Docetaxel is released from loaded nanoparticles in less than 4 h. The increase in the release time of docetaxel compared to doxorubicin may be due to the fact that it is practically insoluble in water.

A second drug loading method using tetradecanol was used to load docetaxel into nanocomposites with a maximally etched shell (ENC3, 75% extinction decrease). It was performed as described in the Materials and Methods Section. This method caused tetradecanol to solidify and close the pores, thereby preventing the drug from escaping from the particles, as confirmed by measuring the extinction of the sample over 72 h when stored at room temperature. This stability ensures that the drug remains unchanged for a long time and, therefore, increases the likelihood of its delivery to its destination. To study the controlled release of drugs, tetradecanol-coated nanocomposites were heated to 50 °C after 72 h of storage, centrifuged, and the spectrum of the supernatant was measured (Fig. 8). Within 10 min of heating, the loaded drug docetaxel was released from the particles into solution and its maximum was clearly detected in the supernatant (Fig. 8, blue line).

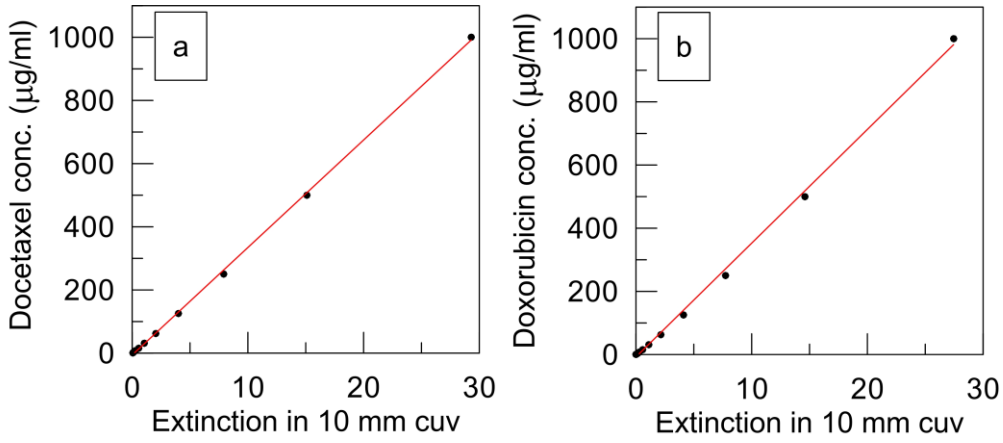


Fig. 6 Calibration curves of the dependence of the concentration of (a) docetaxel and (b) doxorubicin on the extinction value in a 10 mm cuvette at a maximum of 231 and 480 nm, respectively.

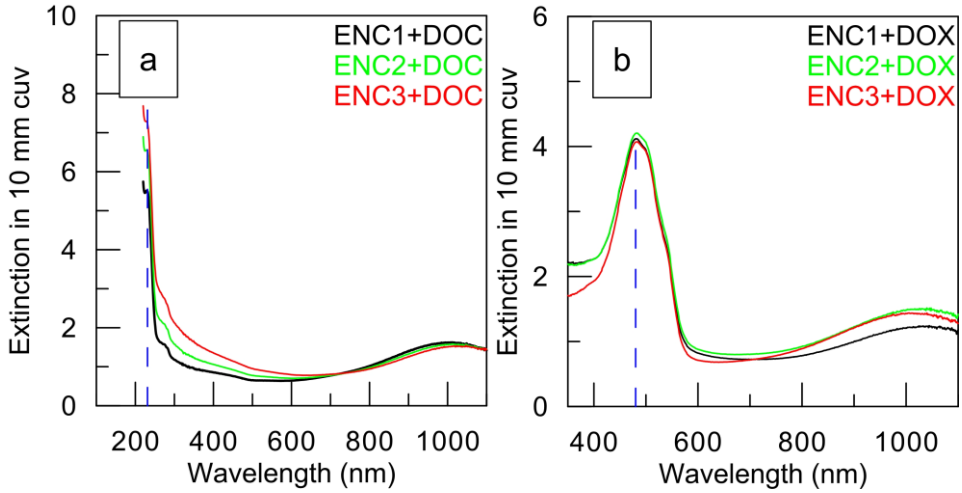


Fig. 7 Extinction spectra of colloidal solutions of gold nanostars coated with a silica shell after etching (ENC1, ENC2 and ENC3) loaded with (a) docetaxel and (b) doxorubicin, plotted for a 10 mm cuvette. The blue dotted line shows the major drug peaks: (a) 231 nm for docetaxel and (b) 480 nm for doxorubicin.

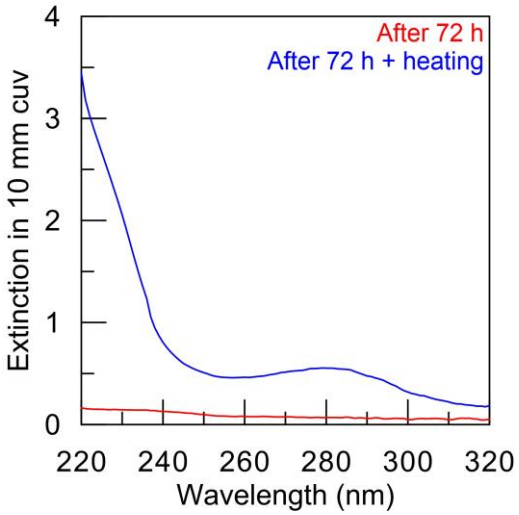


Fig. 8 Extinction spectrum of the supernatant of docetaxel-loaded nanocomposites after 72 h of incubation at room temperature without heating (red line) and after heating (blue line) plotted for a 10 mm cuvette.

3.6 Cytotoxicity Test

To test the possibility of using the synthesized nanocomposites based on gold nanostars coated with an organosilica shell in biomedicine for drug delivery, they were tested for cytotoxicity. Fig. 9 shows the results of the assessment of metabolic activity on the Chinese hamster ovary cell line (CHO II) after 72 h of incubation with the synthesized unloaded nanocomposites.

It was found that with an increase in gold concentration from 0.8 to 25 µg/ml, a decrease in metabolic activity occurs. At gold concentrations from 0.8 to 12.5 µg/ml, a sufficiently high metabolic activity was observed, above the threshold value of 70%. This indicates the absence of a cytotoxic effect of nanocomposites on the cell line. However, at a gold concentration of 25 µg/ml, the metabolic activity was 50.8 ± 5.1%, which indicates an increase in the toxicity of the obtained nanocomposites. Thus, the fabricated nanocomposites in a certain concentration range may be favorable candidates for use in biomedical drug delivery

applications, which will require further *in vitro* and *in vivo* studies.

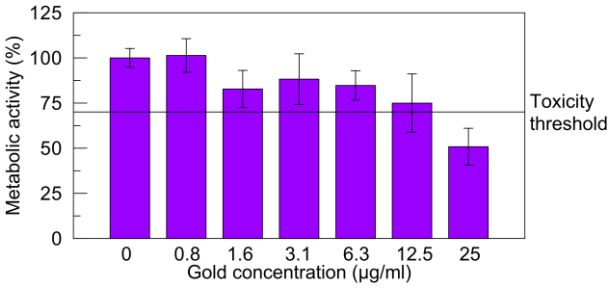


Fig. 9 Fluorometric quantification of the metabolic activity of Chinese hamster ovary cell line (CHO II) after 72 h incubation with synthesized nanocomposites based on gold nanostars coated with an organosilica shell.

4 Conclusions

This work demonstrated the development of innovative nanocomposites designed for targeted delivery of drugs. Gold nanostars, which have unique optical properties and high chemical stability, were chosen as the basis for these nanocomposites. Three samples with different degrees of etching of the organosilica shell were obtained, when the decrease in optical density at a wavelength of 400 nm was 35, 64 and 75%. Two antitumor drugs, doxorubicin and docetaxel, were loaded into the created cavity. Their amount loaded into the nanocomposites depended on the degree of etching of the shell. For example, doxorubicin was loaded from 95.74 to 106.25 μg/mL, which was 47.9 and 53.1%, respectively, of the initial concentration. Docetaxel was loaded from 64.5 to 77.3 μg/ml, which was 32.23 and 38.65% of the initial concentration. A molecular gate was used to prevent premature drug release. It prevents the release of drugs from the nanocomposite for a long time. It has been experimentally proven that docetaxel is retained inside nanocomposites for 72 h at room temperature. We also demonstrated the possibility of initiating a controlled release of the drug docetaxel from nanocomposites by heating the solution to 50 °C, which was detected spectrophotometrically by the appearance of a characteristic absorption maximum in the supernatant. It is important to note that the developed nanocomposites demonstrated low toxicity to cells at gold concentrations from 0.8 to 12.5 μg/ml. This demonstrates the safety of using these nanocomposites in biomedical applications. In conclusion, it can be said that the results of the study indicate the possibility of using the developed nanocomposites as effective carriers for drug delivery.

Author Contributions

Methodology, investigation, data curation, V.A.K., A.V.S.; writing−original draft, A.V.S.; TEM study, A.M.B.; writing−review and editing, conceptualization, project administration, funding acquisition, V.A.K. All authors have read and agreed to the published version of the manuscript.

Funding

This research was funded by the Russian Science Foundation, grant number 23-22-00354, https://rscf.ru/en/project/23-22-00354/.

Disclosures

The authors declare no conflicts of interest.

References

1. D. T. Debela, S. G. Muzazu, K. D. Heraro, M. T. Ndalama, B. W. Mesele, D. C. Haile, S. K. Kitui, and T. Manyazewal, "New approaches and procedures for cancer treatment: Current perspectives," SAGE Open Medicine 9, 20503121211034366 (2021).
2. V. Malhotra, C. P. Michael, "Classical chemotherapy: mechanisms, toxicities and the therapeutic window," Cancer Biology & Therapy 2(1), 1–3 (2003).
3. J. Crown, M. O'Leary, and W.S. Ooi, "Docetaxel and paclitaxel in the treatment of breast cancer: a review of clinical experience," The Oncologist 9, 24–32 (2004).
4. V. Malhotra, C. P. Michael, "Classical chemotherapy: mechanisms, toxicities and the therapeutic window," Cancer Biology & Therapy 2(1), 1–3 (2003).
5. S. Parvaz, R. Taheri-Ledari, M.S. Esmaeili, M. Rabbani, and A. Maleki, "A brief survey on the advanced brain drug administration by nanoscale carriers: With a particular focus on AChE reactivators," Life Sciences 240, 117099 (2020).
6. B. Ma, F. Niu, X. Qu, W. He, C. Feng, S. Wang, Z. Ouyang, J. Yan, Y. Wen, D. Xu, Y. Shao, P. X. Ma, and W. Lu, "A tetrameric protein scaffold as a nano-carrier of antitumor peptides for cancer therapy," Biomaterials 204, 1−12 (2019).
7. S. Saraf, A. Jain, A. Tiwari, A Verma, P. K. Panda, and S. K. Jain, "Advances in liposomal drug delivery to cancer: an overview," Journal of Drug Delivery Science and Technology 50(1), 1173–2247 (2020).
8. B. Surekha, N. S. Kommana, S. K. Dubey, A. V. P. Kumar, R. Shukla, and P. Kesharwani, "PAMAM dendrimer as a talented multifunctional biomimetic nanocarrier for cancer diagnosis and therapy," Colloids Surf B Biointerfaces 204, 1–25 (2021).
9. J. E. Kim, J. Y. Shin, and M. H. Cho, "Magnetic nanoparticles: an update of application for drug delivery and possible toxic effects," Archives of Toxicology 86(12), 685–700 (2012).

10. B. B. Galabova, "Mesoporous silica nanoparticles: Synthesis, functionalization, drug loading and release," Tropical Journal of Pharmaceutical Research 20(5), 1091–1100 (2021).
11. M. Vallet-Regi, M. Colilla, I. Izquierdo-Barba, and M. Manzano, "Mesoporous silica nanoparticles for drug delivery: Current insights," Molecules 23(1), 47 (2017).
12. B. Teankov, C. Voycheva, Y. Yordanov, D. Aluani, L. Spassova, D. Kovacheva, N. Lambov, and V. Tzankova, "Development and in vitro safety evaluation of pramipexole-loaded hollow mesoporous silica (HMS) particles," Indian Journal of Pharmaceutical Education and Research 33(1), 1204–1215 (2019).
13. H. S. Han, K. Y. Choi, "Advances in nanomaterial-mediated photothermal cancer therapies: toward clinical applications," Biomedicines 9(3), 305 (2021).
14. S. Duan, Y. Hu, Y. Zhao, K. Tang, Z. Zhang, Z. Liu, Y. Wang, H. Guo, Y. Miao, H. Du, D. Yang, S. Li, and J. Zhang, "Nanomaterials for photothermal cancer therapy," RSC Advances 13(21), 14443–14460 (2023).
15. M. Zhang, H. S. Kim, T. Jin, and W. K. Moon, "Near-infrared photothermal therapy using EGFR-targeted gold nanoparticles increases autophagic cell death in breast cancer," Journal of Photochemistry and Photobiology B: Biology 170, 58–64 (2017).
16. N. Khlebtsov, V. Bogatyrev, L. Dykman, B. Khlebtsov, S. Staroverov, A. Shirokov, L. Matora, V. Khanadeev, T. Pylaev, N. Tsyganova, and G. Terentyuk, "Analytical and theranostic applications of gold nanoparticles and multifunctional nanocomposites," Theranostics 3(3), 167–180 (2013).
17. R. S. Riley, E. S. Day, "Gold nanoparticle-mediated photothermal therapy: applications and opportunities for multimodal cancer treatment," Wiley Interdisciplinary Reviews Nanomedicine and Nanobiotechnology 9, e1449 (2017).
18. A. Hernández Montoto, R. Montes, A. Samadi, M. Gorbe, J. M. Terrés, R. Cao-Milán, E. Aznar, J. Ibañez, R. Masot, M. D. Marcos, M. Orzáez, F. Sancenón, L. B. Oddershede, and R. Martínez-Máñez, "Gold nanostars coated with mesoporous silica are effective and non-toxic photothermal agents capable of gate keeping and laser induced drug release," ACS Applied Materials & Interfaces 10(33), 27644–27656 (2018).
19. J. Hou, Y. Zhao, L. Sun, and X. Zou, "Fabrication of mesoporous silica-covered gold nanostars for chemophototherapy," Journal of Industrial and Engineering Chemistry 114, 115–125 (2022).
20. Y. Si, M. Chen, and L. Wu, "Syntheses and biomedical applications of hollow micro-/nano-spheres with large-through-holes," Chemical Society Reviews 45, 690–714 (2016).
21. F. Hu, Y. Zhang, G. Chen, C. Li, and Q. Wang, "Double-walled Au nanocage/SiO2 nanorattles: integrating SERS imaging, drug delivery and photothermal therapy," Small 11(8), 985–993 (2015).
22. Y. Yu, M. Zhou, W. Zhang, L. Huang, D. Miao, H. Zhu, and G. Su, "Rattle-type gold nanorods/porous-SiO2 nanocomposites as near-infrared light-activated drug delivery systems for cancer combined chemo-photothermal therapy," Molecular Pharmaceutics 16(5), 1929–1938 (2019).
23. X. Xie, M. A. van Huis, and A. van Blaaderen, "Single-step coating of mesoporous SiO2 onto nanoparticles: growth of yolk–shell structures from core–shell structures," Nanoscale 13(24), 10925–10932 (2021).
24. N. G. Khlebtsov, S. V. Zarkov, V. A. Khanadeev, and Y. A. Avetisyan, "A novel concept of two-component dielectric function for gold nanostars: theoretical modelling and experimental verification," Nanoscale 12, 19963–19981 (2020).
25. V. A. Khanadeev, A. V. Simonenko, O. V. Grishin, and N. G. Khlebtsov, "One-shot laser-pulse modification of bare and silica-coated gold nanoparticles of various morphologies," Nanomaterials 13(8), 1312 (2023).
26. Y. Cui, X.-S. Zheng, B. Ren, R. Wang, J. Zhang, N.-S. Xia, and Z.-Q. Tian, "Au@organosilica multifunctional nanoparticles for the multimodal imaging," Chemical Science 2, 1463–1469 (2011).
27. H. Yuan, C. G. Khoury, H. Hwang, C. M. Wilson, G. A. Grant, and T. Vo-Dinh, "Gold nanostars: surfactant-free synthesis, 3D modelling, and two-photon photoluminescence imaging," Nanotechnology 23(7), 075102 (2012).
28. G. Frens, "Controlled nucleation for the regulation of the particle size in monodisperse gold suspensions," Nature Physical Science 241, 20–22 (1973).
29. Q. Zhang, T. Zhang, J. Ge, and Y. Yin, "Permeable silica shell through surface-protected etching," Nano Letters 8(9), 2867–2871 (2008).
30. B. Cervantes, F. Lopez-Huerta, R. Vega, J. Hernandez-Torres, L. Garcia-Gonzalez, E. Salceda, A. L. Herrera-May, and E. Soto, "Cytotoxicity evaluation of anatase and rutile TiO2 thin films on CHO-K1 cells in vitro," Materials 9, 619 (2016).
31. B. N. Khlebtsov, E. V. Panfilova, V.A. Khanadeev, and N.G. Khlebtsov, "Improved size-tunable synthesis and SERS properties of Au nanostars," Journal of Nanoparticle Research 16, 2623 (2014).

Radiation Patterns Formed by Sapphire Capillary Needles with Different Shapes of Internal Channels

Irina A. Shikunova*, Dmitry O. Stryukov, Julia N. Zubareva, Anna S. Kucheryavenko, Vladimir N. Kurlov, and Irina N. Dolganova

Osipyan Institute of Solid State Physics Russian Academy of Sciences, 2 Academician Osipyan str., Chernogolovka, Moscow District 142432, Russian Federation

*e-mail: sh_irina@issp.ac.ru

Abstract. Compact sapphire capillary needles for laser-assisted therapy connected to optical fibers by the means of internal channel closed from one side transmit laser radiation to the tissues with minimal loss of energy and simultaneously protect the fibers. The geometry of the internal capillary channel with the curved bottom is a key factor in the formation of the output beam's shape. Various curvatures of the bottom in combination with the different angle of conical needle's tip are studied in detail. When the tissue is covered in a liquid, we have observed forming the ring radiation pattern with a sharp axial peak without additional diaphragms or spatial light modulators. Coagulation of *ex vivo* liver tissue samples using continuous laser source with 1.06 μm wavelength, offered opportunity to obtain small coagulated spots without carbonization with the diameter of at least 0.8 mm and to enlarge them evenly by tuning the source output power. © 2024 Journal of Biomedical Photonics & Engineering.

Keywords: sapphire shaped crystals; fiber optic irradiators; laser therapy; interstitial laser irradiation; microfocusing.

Paper #9174 received 7 Oct 2024; revised manuscript received 18 Nov 2024; accepted for publication 18 Nov 2024; published online 14 Dec 2024. doi: 10.18287/JBPE24.10.040315.

1 Introduction

The extensive development of laser medicine, both therapy and diagnosis, is accompanied by the search of methods and instruments for the delivering of light to tissues, which should be characterized by high efficiency and ease of use [1−6]. The instruments, based on fiber optics, have become widespread in clinics, since they allow for compact design, low losses of light propagation and the ability to access hard-to-reach tissues. Different fiber-based probes are applied for intravascular evaluation of plaques, angioplasty, lithotripsy, endoscopy, optical coherence tomography, intraoperative fluorescence diagnosis and other clinical purposes [7−11]. Among them, laser photodynamic and thermal therapy [4, 12−14] also need fiber-based light delivering instruments, which should enable predictable and reproducible exposure, mechanical and chemical stability, as well as to have a compact size. Such instruments can provide either diffused or localized light beams [15−17] and be made of single quartz fiber or special needles/sheaths combined with fibers. Their design varies significantly depending on the required radiation patterns and output beam shape applied for non-contact, contact and interstitial laser surgery and therapy. Localized irradiation is achieved by using conical distal end of a fiber with a small angle of sharpening; other devices include spheres, micro-lenses, domes, faceted shapes, gradient index lenses and tapered fibers [18−21]. The diffused beam is obtained by partial destruction of the fiber cladding, its structuring, application of diffusing sheaths, etc. [13, 14, 22−25].

Routine use of protective sheathes is due to (1) the rapid degradation of quartz during tissue ablation and coagulation, when bare fiber is in contact with tissue, and (2) the fragility of fiber tip, applied for interstitial therapy. Additional liquid or gas cooling helps to avoid carbonization of tissue, which limits further light propagation, and prevents adhering of the instrument to tissue [26−28]. Thus, with the use of increased radiation power, cooled instruments yields higher coagulation volume. Moreover, such probes, either cooled or uncooled, may provide diagnostic puncture or imaging of tissue.

It is quite attractive to assist the laser therapy and ablation with sapphire capillaries for fiber placement. Sapphire has a complex of unique properties that guarantees the absence of any degradation of the optical and mechanical properties under hard physical exposure and in chemically non-neutral environments [29−37]. Besides, it possesses high transparency in visible and near infrared ranges, which makes it suitable for light delivering and implementation of various optical diagnostic and exposure techniques. The application of sapphire for medical purposes was considered previously and has demonstrated high prospective for manufacturing of scalpels, cryosurgical and aspiration probes, along with the capillary needles for laser therapy and ablation [38−44]. Such instruments are characterized by complex shape, which can be achieved by the use of shaped crystal growth techniques [45−50]. Moreover, Stepanov/ Edge-defined Film-fed Growth (EFG) technique is the only method applicable for the manufacturing of sapphire elements with long internal channels with the diameter of 0.5−0.8 mm for fiber accommodation. These channels possess high quality of as-grown surfaces. Additionally, the closed end of the channel protects the inserted fiber from direct contact with tissues during exposure.

The closed-channel design of sapphire crystals applied for medical instruments mainly determines the radiation pattern formed by the instrument in the tissue or on its surface. The external shape of the crystal plays a significant role. Previously, it was demonstrated that a different geometry of the sapphire capillary's tip, formed either by a growing process or by additional mechanical shaping, enables changing the outer beam shape [51, 52]. In particular, it is possible to obtain sub-millimeter focusing of the radiation beam in contact with water medium using micro-focusing sapphire capillary needle [52]. However, the shape of channel bottom formed completely during the process of crystal growth also affects the radiation pattern due to its significant negative curvature.

In this paper, the impact of the channel's form on the radiation pattern is studied in details. We consider the case of a thin capillary needle for surface and interstitial laser ablation combined with quartz fiber with routine numerical aperture. Both numerically and experimentally, we observe the light propagation in tissue caused by this kind of needle with different shapes of the channel bottom. The results show the possibility of forming diffusing light beams as well as narrow collimated beams in the axial direction by choosing particular combinations of the channel's curvature and the tip's angle. Moreover, we have demonstrated the capability for forming the ring pattern with a sharp axial peak without additional diaphragms or spatial light modulators. Our findings are important for further design of sapphire capillary medical instruments and allow for effective application of the sapphire capillary needles for laser therapy and ablation.

2 Materials and Methods

2.1 Fabrication of Sapphire Needles

Sapphire capillary needles were produced by the EFG technique [33, 53−58], which relates to methods of growing shaped crystals from a melt. Sapphire needle has the form of a thin tube with monolithic end. The internal channel is completely formed during the growth process, while the end of such crystal can be additionally processed by grinding and polishing to obtain conical shape. The channel is then used for placing optical fiber connected to the light source [34, 52].

The schematic of the growing process is shown in Fig. 1A. The setup includes a growing chamber with a high purity atmosphere of argon. Temperature gradient in crystallization zone was insured by a 22-kHz induction heated graphite susceptor. A crystal shape is determined by the design of a die immersed in the Al_2O_3-melt with a temperature of over 2053 °C. Due to the capillary force, the melt rises up through the ring gap with 0.1 mm thickness inside the die. On the top, the melt forms a meniscus, locked by the edges of the die. Thus, the lateral dimensions of a crystal could only vary within a narrow range determined by the volume of the melt meniscus [54, 55]. A sapphire crystal of relatively small cross-section (with outer diameter of ~1–3 mm) grows with the pulling rate 50−150 mm/h.

The pressure inside of the melt meniscus and its height depends on growth conditions in the crystallization zone. Their changes, both abrupt and continuous, together with the specific design of the die result in the crystal's shape transition. In particular, an increase of temperature and/or pulling rate, a break and reverse of pulling, may cause closing of the channel inside the capillary needle (Fig. 1B), while its opening occurs due to the overcooling in melt meniscus, which leads to the pull-off of melt excesses and melt hooking on internal edge of the die (Fig. 1C). Thus, the actual shape of the channel's bottom depends on the combination of technological conditions and their alteration within a short time period along with the particular shape of the die.

To study the possible channel shapes, we manufactured several capillary needles with the same external and internal diameters, i.e. 1.2 and 0.5 mm, respectively. The representative images of the needle and its cross section are shown in Fig. 1D and E. The bottom of the channel has a regular geometry of an axially symmetrical body, whose form may vary from a near-to-flat surface to approximately spherical and even ellipsoidal one. For our further considerations, we choose several cases (see Fig. 1F) between the maximum and minimum possible curvatures, namely – flat bottom, spherical surfaces with the radiuses $r = 1.25, 0.5, 0.25$ mm and ellipsoidal surface with semi-axes $a_{\mathrm{el}} = 0.25$ and $b_{\mathrm{el}} = 0.5$ mm. We should note that we leave for our future studies the detailed analysis of the technical aspects and their impact on the channel shape.

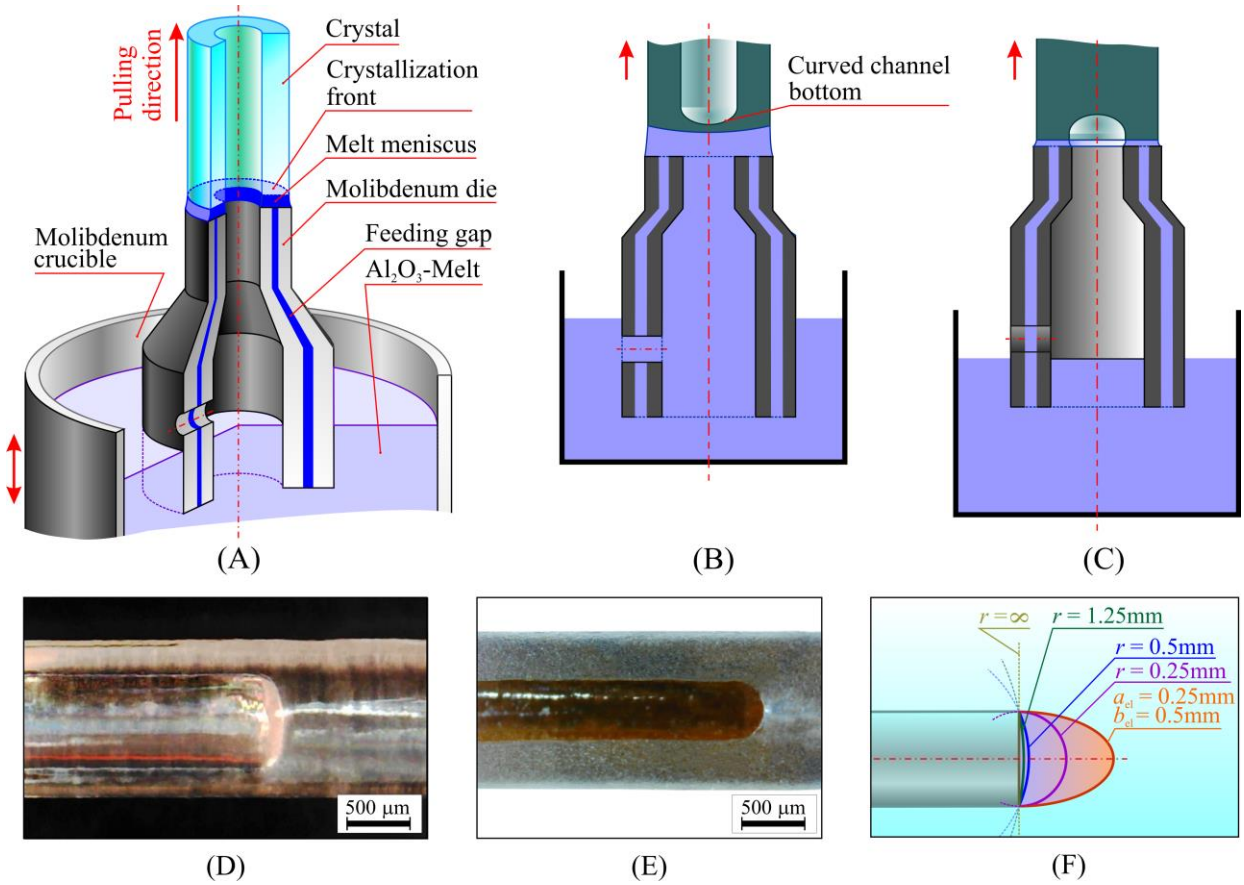


Fig. 1 (A) A schematic of EFG growth of a sapphire capillary needle; (B) "capillary to rod" transition; (C) "rod to capillary" transition; (D) image of a needle with closed channel; (E) the needle's cross section; diameters of the needle and the channel are 1.2 mm and 0.5 mm, respectively; (F) the curvature of channel bottom considered in this work; r stands for the radius of the related sphere, a_{el} and b_{el} stand for semi-axes of the related ellipsoid.

In this work, we only observe different curvature of the channel bottom and use it in numerical simulations of radiation patterns to investigate its impact on the output beam shapes.

2.2 Numerical Simulations of Radiation Patterns

The radiation patterns formed at the output end of the sapphire needles were studied numerically by means of the ray tracing approach. Namely, we use the TracePro package for the 3D numerical simulation of photons' migration. We assume that the approximations of geometrical optics are relevant, since the analysis of light–needle interaction is implemented at the scales much larger than the wavelength. In this study, the radiation wavelength λ is set to 1.06 μm, which corresponds to one of the most applicable laser sources for tissue coagulation; therefore, the refractive index n_{s} and the absorption coefficient (by power) $\mu_{\text{a,s}}$ of sapphire are considered to be 1.76 (for ordinary ray) and 10^{-6} mm^{-1}, respectively. The cylindrical part of the needle has the outer diameter $d_n = 1.2$ mm, while its conical part is characterized by the angle of sharpening 2γ, which varies in the performed numerical simulations. The channel has the diameter $d_c = 0.5$ mm and the position l_{c} inside the needle (see Fig. 2). It is filled with air ($n = 1$). The curvature of its closed end corresponds to the above-mentioned values r, a_{el} and b_{el}. In this work, multimode optical fiber with the diameter $d_{\text{f}} = 200$ μm, refractive index $n_{\text{f}} = 1.54$ and $\mu_{\text{a,f}} = 3 \cdot 10^{-6}$ mm^{-1} is considered; parameters z_{f} and 2ω denote its position inside the channel and the numerical aperture (NA), respectively. The output beams have the Gaussian shape. The radiation patterns are analyzed either in free space or in water medium featuring $n_0 = 1.33$ and $\mu_{\text{a,m}} = 0.015$ mm^{-1}, in the plane removed from the needle at a distance $L_{\text{an pl}}$. The quantitative evaluation of the laser beams in this plane is performed by means of the reduced axial energy I_{max} and full width at half maximum (FWHM) for Gaussian spatial profile, as it is illustrated in Fig. 2. The grid of rays that set Gaussian spatial profile is represented by a spatial weighting, where each ray has uniform flux and weighted position.

2.3 Tissue Samples

To study the coagulation regions in living tissues performed by the sapphire needles with a specific combination of the needle's tip and the shape of its channel, we have used the *ex vivo* samples of turkey liver.

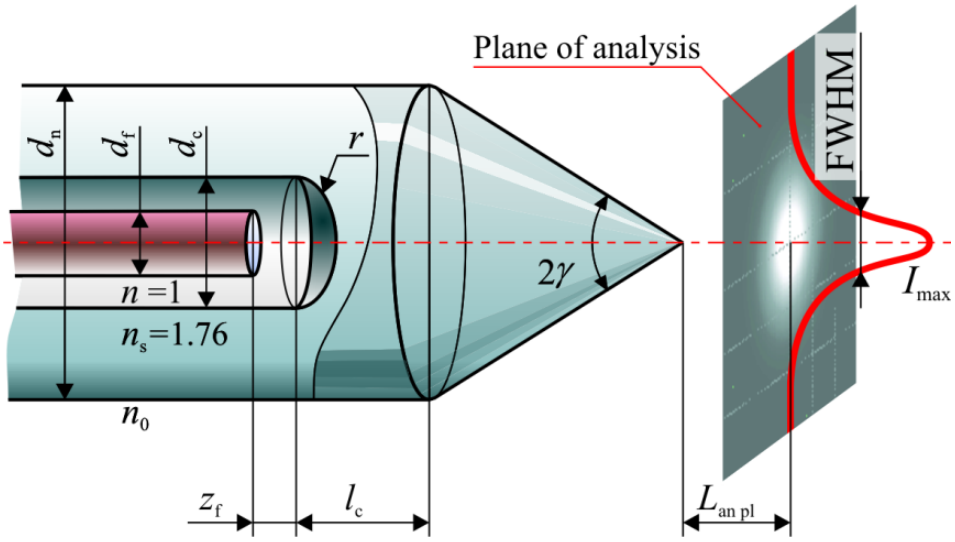


Fig. 2 The scheme of a needle and the parameters used in the numerical simulations.

Such type of tissue effectively absorbs laser radiation of the near infrared range. Before the measurements, the tissue samples with lateral dimensions 40 × 40 mm and 15 mm height were placed in a cuvette then the cuvette was filled with distilled water, covering the surface of the samples by 10 mm. The initial temperature of the samples and water was ambient (24 °C). After performing coagulation, the samples were extracted from the cuvette. The sizes of the coagulated regions were analyzed using digital camera and threshold filtering of the tissue images.

3 Results

3.1 Beam Shape in Case of Flat Needle's Tip

To analyze the output beam shapes formed by the described sapphire needles, we start with the case of the flat needle's tip ($2\gamma = 180°$) in a free space. Fig. 3 demonstrates the changes of I_{max} and FWHM right at a needle's distal end ($L_{an\ pl} = 0$), when a common quartz fiber with $2\omega = 40°$ is placed inside the needle's channel at $z_f = 0.1$ mm. It is clear that the curved bottom of the channel acts as an additional refractive interface between air and sapphire with rather high refractive index $n_s = 1.76$. It results in the nonlinear decrease of I_{max} and blurring of FWHM when the curvature of this interface changes from flat, with r tends to infinity, to ellipsoidal shape (graph point corresponded to $r = 0.125$). The equivalent radius $r = 0.125$ is valid for the referred ellipsoidal shape as all the beam's rays fall on the inner surface in the close vicinity of optical axis.

The most common case of the channel's shape obtained by the EFG technique corresponds to $r \cong d_c/2$. Therefore, for the considered geometry of the needle, we should pay special attention to the area near $r = 0.25$ mm. In its vicinity, the change of the beam parameters strongly depends on even small deviation of r, which confirms the need to consider the internal shape of the needle for appropriate planning of the tissue exposure.

Fig. 4(A–D) demonstrates the radiation patterns formed by the needle with flat end in the free space. When the bottom of the capillary channel is also flat or features slight curvature (see panels A and B), the light beam is entirely projected on the output surface of the needle and the beam shape has a regular form. The increase of the bottom's curvature leads to blurring of the beam. At the same time, the more curved channels yield the formation of the ring-like shape of the output beam due to the total internal reflection of the extreme rays from the cylindrical surface of the needle (panels C and D). Such beams are characterized by the appearance of high energy density in the axial direction.

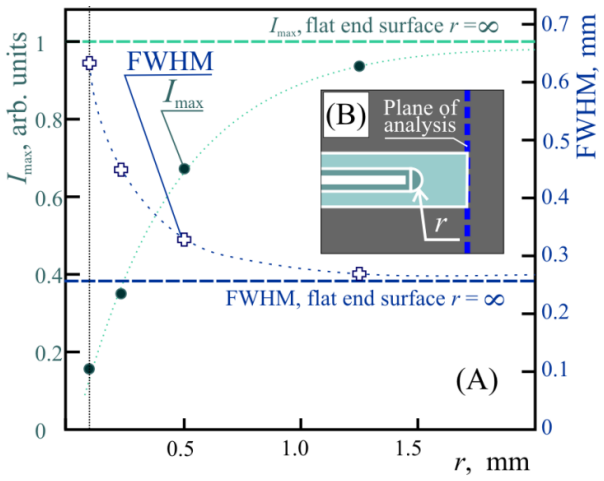


Fig. 3 (A) The change of laser beam parameters (reduced axial energy I_{max} and FWHM) depending on the curvature r of the channel; numerical simulations performed for a specific needle's form (B) and parameters $l_c = 1$ mm, $z_f = 0.1$ mm, $L_{an\ pl} = 0$ mm, $2\omega = 40°$.

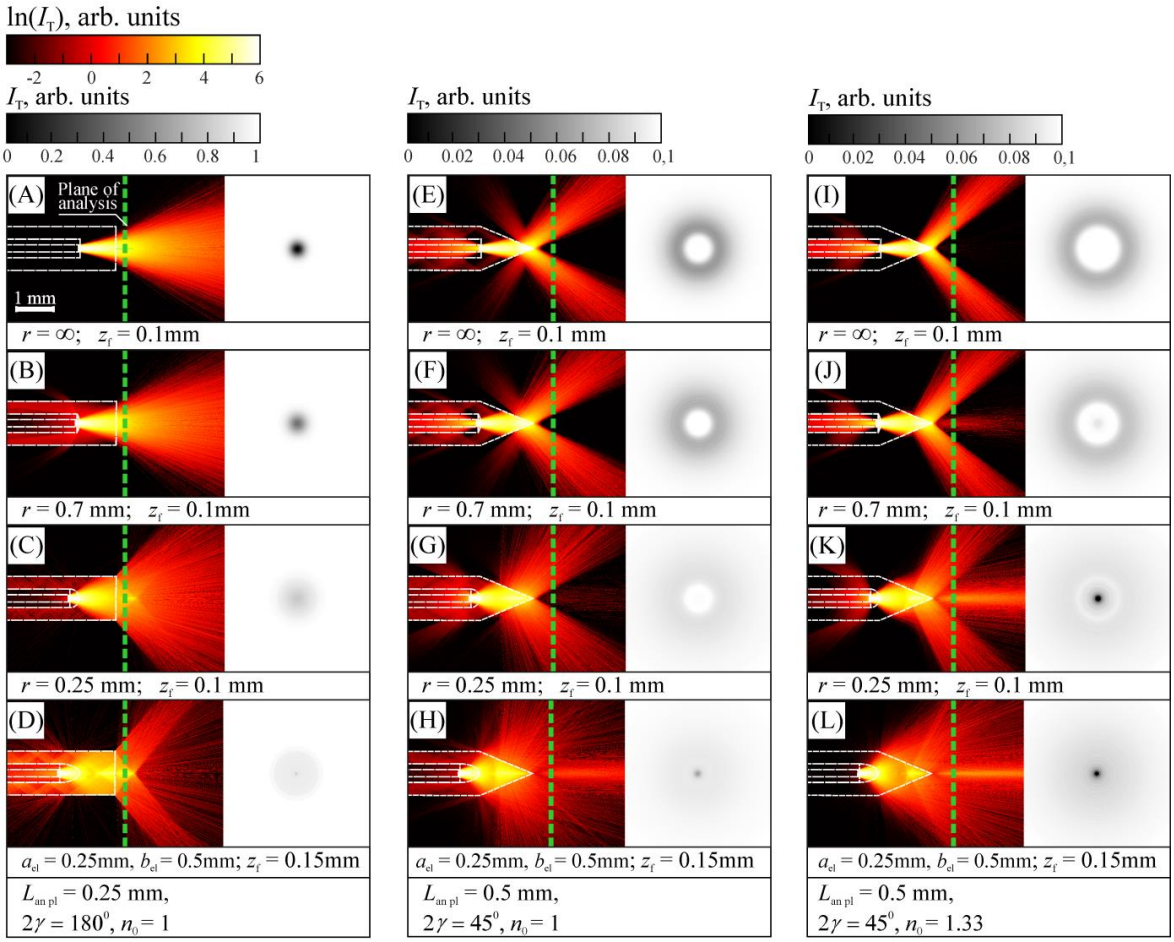


Fig. 4 Numerical simulations of the beam shapes, represented by the transmitted intensity I_T, formed by the capillary needles with different curvature of channel's bottom and the quartz fiber with $2\omega = 40°$. (A)–(D) The needle with flat tip is placed in a free space. (E)–(H) The needle with conical tip $2\gamma = 45°$ is placed in a free space. (I)–(L) The needle with conical tip $2\gamma = 45°$ is placed in a water medium.

Despite the flat end of the needle is rarely used for laser therapy, it may be applied for diagnostic sapphire probes [39, 59]. In that case, the channel's curvature may change the diagnostic precision. This fact deserves additional experimental studies, but we leave it for our future work. We account the shape of the needle's conical tip and observe the joint impact of the needle's inner and outer geometry on the beam shape in the following subsections.

3.2 Beam Shape in Case of Conical Needle's Tip

When the needle has conical tip, it can be applied for local high energy concentration of light coming out from the fiber [56, 57]. The multiple total internal reflection of beams in the cone leads to redistribution of energy and the grouping of rays in portions exceeding at different angles to the needle axis. Panels (E–L) in Fig. 4 demonstrate a representative case, when the conical tip has the angle $2\gamma = 45°$. The formation of a ring structure of the output beam shape is clearly observed. Moreover, it depends on the curvature of the channel's bottom. When the latter is flat, the axial part of the output beam is almost absent, and the beam has an obvious annular shape (see panels E and I for distribution of transmitted intensity I_T in a free space and water, respectively). The appearance and further increase of the curvature enlarge the portion of rays unreflected in the cone; thus, it enhances the beam divergence and blurs the rings in the beam shape (see Fig. 5A). Moreover, it leads to the formation of collimated and focused rays transmitted in the outer environment. One can clearly observe the central peak in the beam shapes in panels H and J–L. Obviously, this process is stronger in the medium with a higher refractive index.

The condition for the appearance of the collimated and the focused rays depends on the combination of the aperture angle $2\omega'$ of the ray refracted at the channel's bottom and the tip's angle 2γ (Fig. 5B). The aperture angle ω' depends on both the fiber NA and the curvature of the channel. It is clear that for a sharper needle the fiber should have larger NA for the same curvature of the channel. Thus, to obtain an axial beam spot for the focused tissue exposure, the particular combination of the needle and fiber should be chosen.

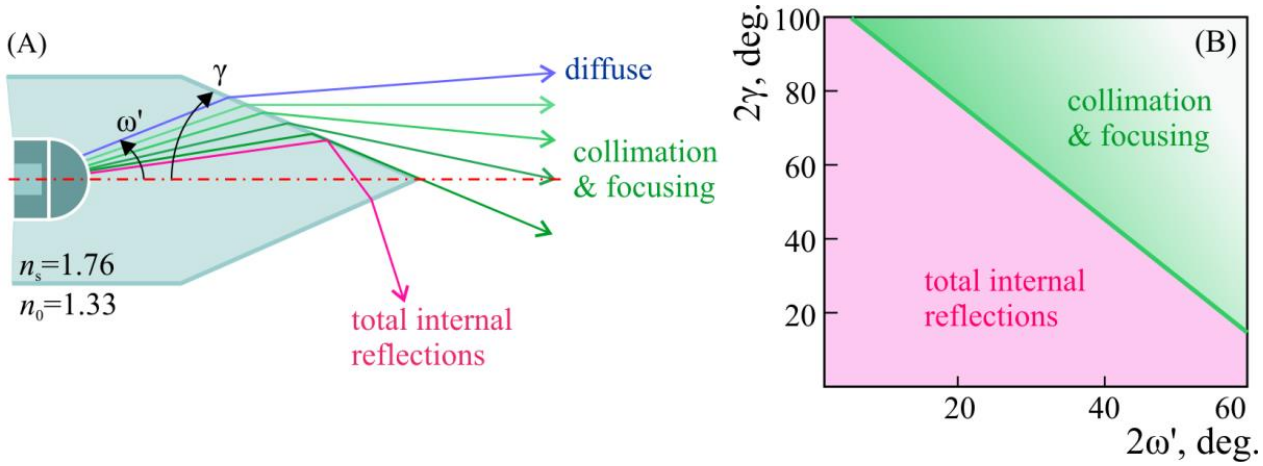


Fig. 5 Appearance of the ring-like, collimated and diffused parts of the beam shape due to different combination of the tip's angle γ and the aperture angle ω' of the ray refracted at the channel's bottom. (A) Change of the direction of the output beam due to an increase of ω'. (B) The condition for the appearance of a collimated and focused part of the beam; the needle in water environment is considered. The parameters $l_c = 1$ mm, $z_f = 0.1$ mm are considered.

3.2.1 Impact of Different Cone Angle on the Beam Shape

Fig. 6 compares the beam shapes formed by the needles with different cone angles in water medium. While rather sharp tip yields the diffuse beams (A, B) regardless of the shape of the channel bottom, large angle 2γ leads to beam focusing near the tip end (C, D). However, the ellipsoidal and flat bottoms are rarely expected during the crystal growth. Despite the analysis of beams in such extreme cases is useful, the most common hemispherical channel shape deserves special attention (Fig. 6(E–I)). Near the tip, one can observe the significant impact of the cone angle on the light distribution and, in particular, on the ability of focusing a part of the beam, which is in accordance with Fig. 5B.

Fig. 6J shows the reduced axial energy I_{max} in the representative case of the needle with $2\gamma = 45°$ and hemispherical bottom of the channel. As it is illustrated in Fig. 6G, such needle forms the collimated and focused part of the output beam. The maximal intensity in the focused part rapidly reduced with the distance $L_{an\ pl}$. Moreover, to obtain the highest I_{max} in the beam spot, one should choose the fibers with 2ω from the range of 24°–34°. The beam parameters for this needle and $2\omega = 34°$ are shown in Fig. 6K. Within the distance $L_{an\ pl}$ from 1 to 5 mm, I_{max} decreases by about 5 times and FWHM of the spot size increases from 80 to 500 μm.

The above analysis is valid for the environments with no scattering or when the needle is slightly removed from the tissue sample. Nevertheless, when the interstitial application is considered, the tissue scattering properties should be accounted. Fig. 7 shows the impact of increased scattering coefficient in the outer environment on the blurring of the focusing beam part. Therefore, a sapphire needle is more likely to form in a tissue a diffuse isotropic-like light distribution concentrated on the needle's end.

3.3 Micro-Coagulation of Tissue by Conical Needle

A complex beam shape formed by a sapphire capillary needle gives an opportunity of micro-coagulation of tissues. Since an impact of light scattering in soft tissues is significant, a small distance between the needle's tip and tissue surface should be remained to concentrate most of the beam in a small spot. We have compared experimentally the results of two positions of the needle with angle $2\gamma = 45°$ and hemispherical bottom of the channel (Fig. 8). For this aim, we prepared samples of *ex vivo* liver tissue and placed them in a cuvette filled with water. The water prevents from the dehydration of samples during experiments and also contributes to formation of strong focusing beam part. In the first position, the needle tip touched the sample surface and slightly inserted in it (Fig. 8A). In the second position, the distance between the needle and the sample was 0.5 mm. As it is shown in Fig. 8B, where alignment green beam was used, it allowed us to make a small central spot surrounded by a ring-like beam part. However, the results of numerical simulations demonstrate the blurring of this ring in the tissue volume (Fig. 8D). But the observed localization of beam power inside the tissue in these two cases (C and D) allows us to expect the possibility to perform micro-coagulation.

To study this effect experimentally, the continuous-wave laser source (LAKHTA-MILON, Milon Group, Russia) with the wavelength $\lambda = 1.06$ μm and tunable output power was used. The liver tissues were exposed by this laser for 30 s using uncovered fiber with $d_f = 300$ μm and $NA = 0.14$ and the combination of the fiber with the sapphire needle. Contact and contactless positions were considered as stated above. Panels (E–H) in Fig. 8 demonstrate the representative images of tissue samples after exposure.

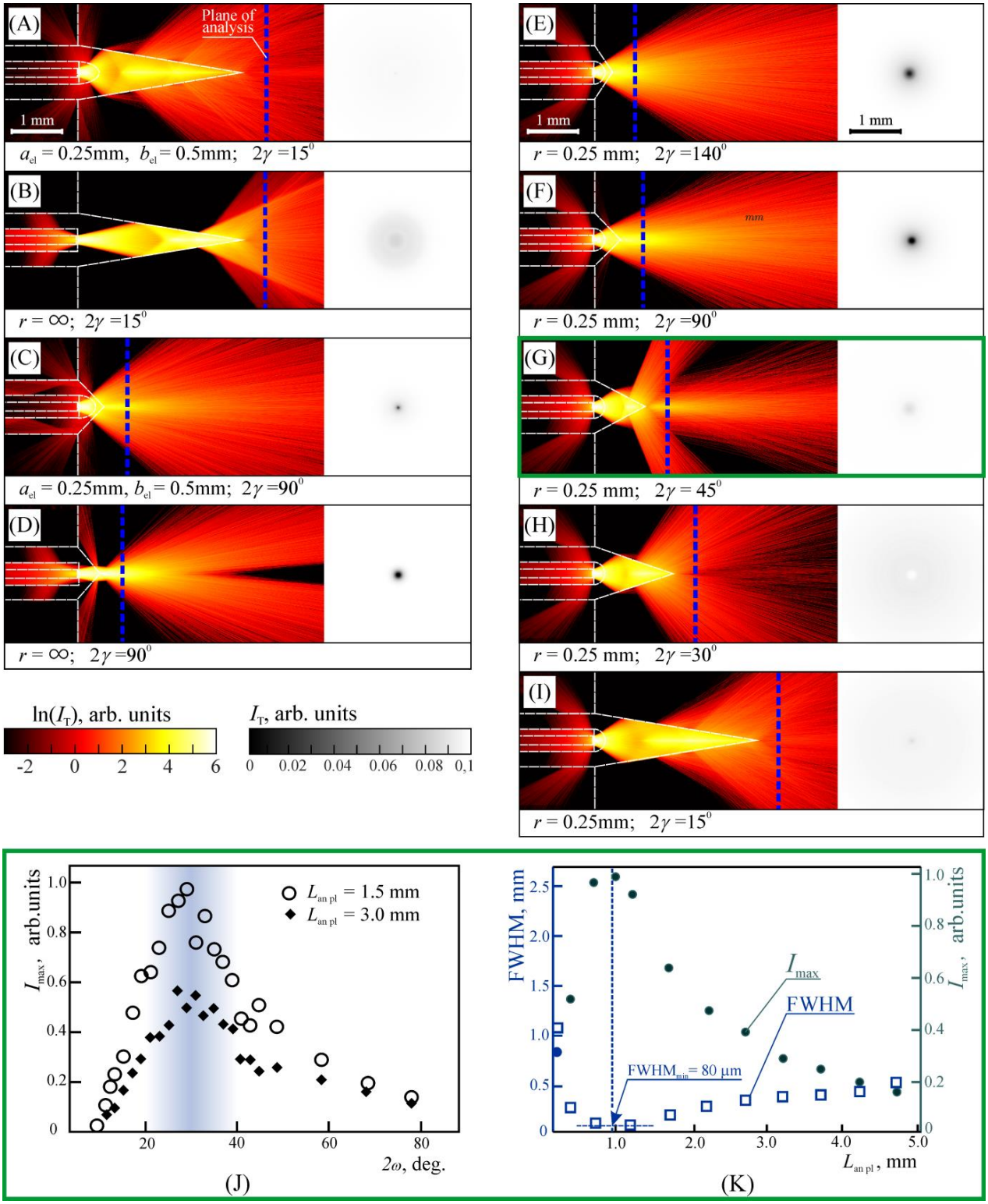


Fig. 6 Numerical simulations of the output beam shapes in water, represented by the transmitted intensity I_T, formed by the capillary conical needles and the quartz fiber with $2\omega = 40°$. On the left, the extreme cases of cone angles $2\gamma = 15°$ (A, B) and 90° (C, D) and ellipsoidal (A, C) or flat (B, D) bottom of the channel are shown. (E–I) Beam shapes produced by the needle with hemispherical bottom of the channel and various cone angles. In panels A–I, $L_{an\ pl} = 0.5$ mm, $z_f = 0.1$ mm. (J, K) Output beam parameters in case of $2\gamma = 45°$ and $r = d_c/2 = 0.25$ mm. (J) reduced axial energy I_{max} depending on different fiber NA, (K) beam parameters for $2\omega = 34°$.

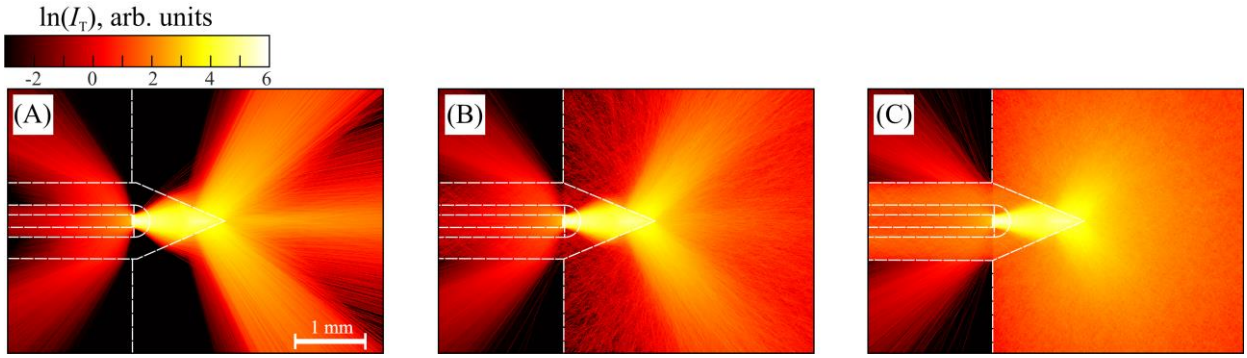


Fig. 7 Numerical simulations of the output beam shapes in the tissue (n_0=1.37) with increasing of scattering coefficient μs and decreasing of anisotropy parameter g: (A) g = 1, m_s = 1 mm^{-1}; (B) g = 0.9, m_s = 1.5 mm^{-1}; (C) g = 0.72, m_s = 3.7 mm^{-1}; the needle with cone angle $2\gamma = 45°$ and hemispherical channel's bottom is considered, 2ω=40°. Absorption is neglected in tissue.

When the uncovered fiber is used, it can lead to the carbonization (panels G and H), which was started at 8 W of laser output power for contactless position and 3 W, when the fiber is in contact with tissue. In contrast, the application of the sapphire needle prevents from tissue carbonization in the observed range of laser power, up to 10 W (panels E and F). But unlike the commonly used diffusers, which are also applied for the same purpose, the coagulation spot remains very narrow and does not exceed 1.5 mm for contactless position. In Fig. 8I, one can compare the diameters of coagulation area. It is clear that choosing the position of the sapphire needle, a rather wide range of coagulation spots from 0.8 up to 3 mm can be achieved without carbonization, including extremely small ones less than 1 mm.

4 Discussion

Sapphire capillary needles are unique instruments for surface and interstitial laser therapy. They can be combined with a wide range of light sources and fibers. Despite their small external dimensions of less than 2 mm in diameter, it is possible to manufacture such needles with different shape of their tips. In addition, the capillary channel inside the needle, which is made during the crystal growth process, may possess different bottom curvature. Therefore, the radiation patterns formed by the needles are rather different. Since sapphire has a higher refractive index than quartz, small changes of the needle's shape alter the output beam distribution more noticeably. The condition for total internal reflection inside the conical tip is satisfied for a larger number of rays. The results of this study demonstrate that for these reasons, it is possible to observe diffusing, collimated, focusing or ring-like beams formed by the sapphire needles.

While the diffusing beams are rather common in laser therapy and there are several solutions and instruments for their formation, the focusing needles are of particular interest. As we have shown, in the case of sapphire needles, partial focusing of the output beam can be achieved for a simple conical geometry of the tip, when the angle γ is chosen appropriately. In aqueous environment, this effect is more pronounced.

It permits using these needles for local exposure of small tissue area, for example, for coagulation of small metastasis and cysts [16, 60−65]. The point concentration of light near the needle's tip in aqueous solutions can be useful for optogenetics [66, 67], when local stimulation of cells and tissue areas is caused by optical radiation [8, 9]. Application of various gels, including cooling ones, in combination with needle-assisted laser therapy can reduce the localization of tissue destruction even more, when it is important to prevent damage and overheating of surrounding intact tissues. The same effect of local therapy can be achieved in low scattering tissues or hollow organs filled with saline solution.

The principal difference between glass tips, quartz fibers and sapphire needles is the significantly higher thermal conductivity of the latters, which is probably the main reason for the absence of tissue carbonization for contact mode. While coagulation of very small volumes in tissues using uncovered fiber requires exposure of laser power density at much more reduced level in comparison with the combination of the fiber with the sapphire needle, there is still a risk of spontaneous rapid accumulated overheating of fiber. The small changes in thermal conducing properties of irradiator or tissue can cause carbonization hindering the planned growth of coagulated volume. It should be mentioned that carbonization prevents from light penetration in deeper tissues; therefore, laser exposure becomes uneven and unpredictable. Additionally, it can cause damage to glass instruments or unprotected quartz fibers. The sapphire needle removes heat from the tissue more efficiently.

It is essential that the shape of the internal capillary channel plays the same important role as the tip's geometry for the formation of the complex output radiation pattern. The curvature of the channel's bottom should be taken into account, as shown by the demonstrated numerical results. In general, it increases the beam divergence before transmitting the needle's tip, and the output beam includes ring-like diffused radiation and collimated and focused rays.

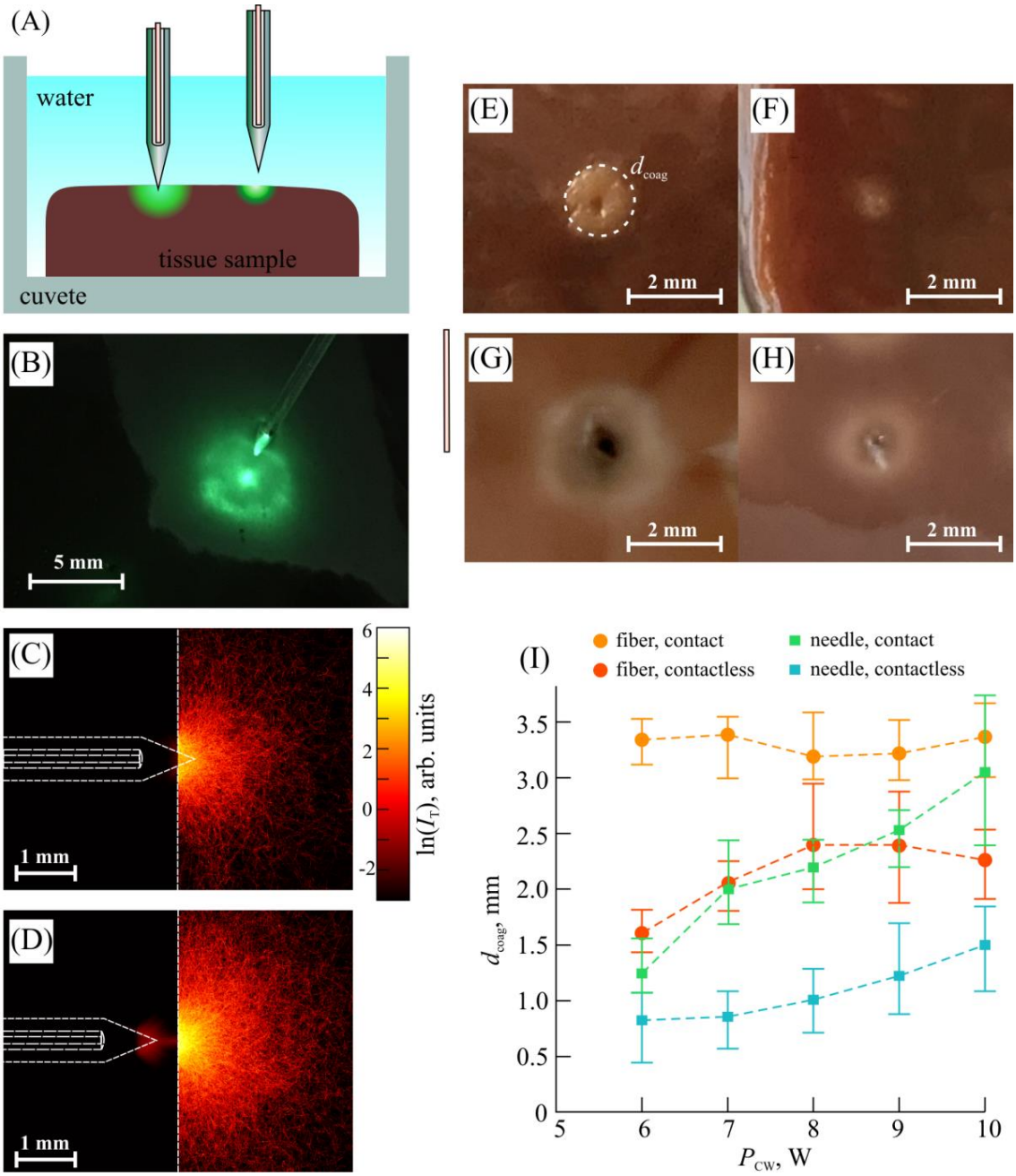


Fig. 8. Experimental study of tissue coagulation by the conical sapphire needle and continuous-wave laser source at 1.06 μm. (A) Positions of the needle during exposure. (B) The beam shape formed contactlessly by the conical needle. (C), (D) The results of numerical simulation of light transport in tissue with parameters $n_0 = 1.37$, $\mu_a = 4.0\ \text{cm}^{-1}$, $\mu_s = 52.13\ \text{cm}^{-1}$, $g = 0.77$, by the needle in two considered positions. (E–H) The representative examples of coagulation of liver tissue by 8 W output power during 30 s, performed by a combination of conical needle with quartz fiber in contact with tissue (E) and remoted from the tissue surface at 0.5 mm (F); (G), (H) – the same for the single fiber. (I) The diameters of coagulation spot d_{coag} obtained in the considered cases during 30 s of exposure; errorbars denote $\pm\sigma$ for the set of 5 measurements.

Since the bottom is produced during the crystal growth process, no additional resources are needed for shaping its curvature. Although the hemispherical shape is the most common, small deviations of the curvature can appear due to alterations of the technological growth parameters. As we have shown in the numerical simulations, the increase of the curvature results in the illumination of the larger tip's surface and in a larger coagulation region in the tissue. Therefore, it is important to estimate the channel shape before applying the needle for laser thermal therapy.

The demonstrated impact of the channel form on the beam shape is of high importance for other types of sapphire crystals with internal capillary channels, manufactured by the EFG technique, such as diagnostic probes and scalpels. For these instruments, the aperture

of the output and the detected light beams is one of the key factors for estimating their sensitivity and precision. In this regard, the channel curvature should be considered during the theoretical description of the analyzed optical response from tissues and further signal processing.

Finally, we should mention the capability of growing rather long sapphire needles up to tens of centimeters along with short compact tips. While the former can be used solely for surface or interstitial laser therapy, small cut-off tips can be integrated with endoscopes and other surgical instruments, granting the possibility to use flexible medical tools.

5 Conclusion

In this work, the formation of different beam shapes by applying conical sapphire capillary needles for laser thermal therapy was studied numerically and experimentally. The main focus was on the capillary channel inside the needles, grown by the EFG technique. We have analyzed the possible range of the curvature that can be produced in the channel's bottom during the crystal growth process. It was observed that even slight alteration of the curvature dramatically changes the output beam divergence and radiation pattern. Completely different radiation patterns can be obtained by changing the combination of the channel's curvature and the conical angle of the tip. In particular cases of the needle's geometry, the beam can possess strong collimated and focused components as well as a ring-like structure. It can be used effectively for localized coagulation of tissues. To analyze this feasibility more precisely, we have performed coagulation of *ex vivo* liver tissue with such a sapphire needle and a continuous-wave laser source (with 1.06 μm wavelength), comparing the results with the application of a single quartz fiber without a needle or other protection. We have covered the tissue samples with a layer of water for making the beam shape more pronounced. The absence of tissue carbonization along with the precise coagulation was observed for the laser power up to 10 W and application of the sapphire needle, in contrast to using single fiber. Moreover, the sapphire needle allows one to smoothly adjust the coagulation spot from 0.8 up to 3 mm by tuning the laser source power, while the carbonization of tissues appeared for a single fiber prevents this opportunity.

The results of this work revealed the need for accounting the channel shape inside the sapphire capillary needles and posed the question for further research on the crystal growth technological parameters, which have the strongest influence on the final channel's geometry.

Acknowledgments

This work was supported by the Russian Science Foundation, Project # 24-29-00424.

Disclosures

The authors declare no conflicts of interest.

References

1. M. Niemz, Laser-Tissue Interactions: Fundamentals and Applications, 4th ed., Springer, Switzerland (2019). ISBN: 9783030119164.
2. M. R. Hamblin, Y. Huang, Handbook of photomedicine, 1st ed., CRC Press, Boca Raton, FL (2013). ISBN: 9781439884706.
3. A. J. Welch, M. J. C. van Gemert (Eds.), Optical-thermal response of laser-irradiated tissue, 2nd ed., Springer Dordrecht (2011). e-ISBN: 978-90-481-8831-4.
4. G. Shafirstein, D. Bellnier, E. Oakley, S. Hamilton, M. Potasek, K. Beeson, and E. Parilov, "Interstitial photodynamic therapy—a focused review," Cancers 9(2), 12 (2017).
5. T. Vo-Dinh, Biomedical photonics handbook: therapeutics and advanced biophotonics, 2nd ed., CRC Press, Florida (2014).
6. C. M. Pacella, T. Jiang, and G. Mauri, Image-guided laser ablation, Springer, Switzerland (2020). ISBN: 9783030217471.
7. G. Keiser, F. Xiong, Y. Cui, and P. P. Shum, "Review of diverse optical fibers used in biomedical research and clinical practice," Journal of Biomedical Optics 19(8), 080902 (2014).
8. A. Tsakas, C. Tselios, D. Ampeliotis, C. Politi, and D. Alexandropoulos, "Review of optical fiber technologies for optogenetics," Results in Optics 5, 100168 (2021).
9. J. Zou, W. Li, N. Meng, J. Jiang, C. Wu, T. C. Lei, R. Sroka, and Z. Huang, "Evaluation of lensed fibers used in photodynamic therapy (PDT)," Photodiagnosis and Photodynamic Therapy 31, 101924 (2020).
10. N. Katta, A. D. Estrada, A. B. McErloy, and T. E. Milner, "Fiber-laser platform for precision brain surgery," Biomedical Optics Express 13(4), 1985–1994 (2022).
11. T. Stokbroekx, A. De Boer, R. M. Verdaasdonk, M. E. Vuylsteke, and S. R. Mordon, "Commonly used fiber tips in endovenous laser ablation (EVLA): an analysis of technical differences," Lasers in Medical Science 29(2), 501–507 (2014).
12. R. Stafford, D. Fuentes, A. Elliott, J. Weinberg, and K. Ahrar, "Laser-induced thermal therapy for tumor ablation," Critical Reviews in Biomedical Engineering 38(1), 79–100 (2010).

13. T. Vogl, R. Straub, K. Eichler, D. Woitaschek, and M. Mack, "Malignant liver tumors treated with MR imaging-guided laser-induced thermotherapy: experience with complications in 899 patients (2,520 lesions)," Radiology 225(2), 367–377 (2002).
14. A. Carpentier, R. McNichols, R. Stafford, J. Guichard, D. Reizine, S. Delaloge, E. Vicaut, D. Payen, A. Gowda, and B. George, "Laser thermal therapy: Real-time MRI-guided and computer-controlled procedures for metastatic brain tumors," Lasers in Surgery and Medicine 43(10), 943–950 (2011).
15. C. Pantaleone, S. Dymling, and J. Axelsson, "Optical fiber solutions for laser ablation of tissue and immunostimulating interstitial laser thermotherapy – Product development in the network of developers, industry and users," Photonics and Lasers in Medicine 5(1), 69–75 (2016).
16. U. Salem, V. A. Kumar, J. E. Madewell, D. F. Schomer, D. C. De Almeida Bastos, P. O. Zinn, J. S. Weinberg, G. Rao, S. S. Prabhu, and R. R. Colen, "Neurosurgical applications of MRI guided laser interstitial thermal therapy (LITT)," Cancer Imaging 19(65), 1–13 (2019).
17. J. Li, C. Shang, Y. Rong, J. Sun, Y. Cheng, B. He, Z. Wang, M. Li, J. Ma, B. Fu, and X. Ji, "Review on laser technology in intravascular imaging and treatment," Aging and Disease 2, 13(1), 246–266 (2022).
18. R. Verdaasdonk, C. Borst, "Ray tracing of optically modified fiber tips. 1: spherical probes," Applied Optics 30(16), 2159–2171 (1991).
19. K. Iwai, Y.-W. Shi, M. Endo, K. Ito, Y. Matsuura, M. Miyagi, and H. Jelinkova, "Penetration of high-intensity Er:YAG laser light emitted by IR hollow optical fibers with sealing caps in water," Applied Optics 43(12), 2568–
20. T. Watanabe, Y. Matsuura, "Side-firing sealing caps for hollow optical fibers," Lasers in Surgery and Medicine 38(8), 792–797 (2006).
21. T. Hutchens, A. Darafsheh, A. Fardad, A. Antoszyk, H. Ying, V.Astratov, and N. Fried, "Novel microsphere chain fiber tips for use in mid-infrared ophthalmic laser surgery," Optical Fibers and Sensors for Medical Diagnostics and Treatment Applications XII, 8218, 18–25 (2012).
22. L. Vesselov, W. Whittington, and L. Lilge, "Design and performance of thin cylindrical diffusers created in Ge-doped multimode optical fibers," Applied Optics 44(14), 2754–2758 (2005).
23. A. Roggan, "Laser applicators for interstitial coagulation," in Applied Laser Medicine, H.-P. Berlien, G. Müller (Eds.), Springer-Verlag, Berlin, Heidelberg and New York, 165–167 (2003).
24. V. Knappe, A. Roggan, M. Glotz, M. Müller, J.-P. Ritz, C.-T. Germer, and G. Müller, "New flexible applicatorsfor laser-induced thermotherapy," Medical Laser Application 16(2), 73–80 (2001).
25. J. C. Mizeret, H. E. Van Den Bergh, "Cylindrical fiberoptic light diffuser for medical applications," Lasers in Surgery and Medicine 19(2), 159–167 (1996).
26. B. Anvari, M. Motamedi, J. H. Torres, S. Rastegar, and E. Orihuela, "Effects of surface irrigation on the thermal response of tissue during laser irradiation," Lasers in Surgery and Medicine 14(4), 386–395 (1994).
27. B. Anvari, B. S. Tanenbaum, W. Hoffman, S. Said, T. E. Milner, L.-H. L. Liaw, and J. S. Nelson, "Nd:YAG laser irradiation in conjunction with cryogen spray cooling induces deep and spatially selective photocoagulation in animal models," Physics in Medicine & Biology 42(2), 265–282 (1997).
28. W. Whelan, D. Wyman, "Dynamic modeling of interstitial laser photocoagulation: implications for lesion formation in liver *in vivo*," Lasers in Surgery and Medicine 24, 202–208 (1999).
29. R. M. Verdaasdonk, C. F. P. van Swol, "Laser light delivery systems for medical applications," Physics in Medicine & Biology 42(5), 869−894 (1997).
30. P. Möller, L. Lindberg, P. Henriksson, B. Persson, and K. Tranberg, "Interstitial laser thermotherapy: Comparison between bare fibre and sapphire probe," Lasers in Medical Science 10(3), 193–200 (1995).
31. T. Eguro, A. Aoki, T. Maeda, A. A. Takasaki, M. Hasegawa, M. Ogawa, T. Suzuki, K. Yonemoto, I. Ishikawa, Y. Izumi, and I. Katsuumi, "Energy output reduction and surface alteration of quartz and sapphire tips following Er:YAG laser contact irradiation for tooth enamel ablation," Lasers in Surgery and Medicine 41(8), 595–604 (2009).
32. V. N. Kurlov, S. N. Rossolenko, N. V. Abrosimov, and K. Lebbou, "Shaped Crystal Growth," Chapter 5 in Crystal Growth Processes Based on Capillarity Czochralski, Floating Zone, Shaping and Crucible Techniques, Th. Duffar (Eds.), John Wiley & Sons, 277−354 (2010).
33. G. M. Katyba, K. I. Zaytsev, I. N. Dolganova, I. A. Shikunova, N. V. Chernomyrdin, S. O. Yurchenko, G. A. Komandin, I. V. Reshetov, V. V. Nesvizhevsky, and V. N. Kurlov, "Sapphire shaped crystals for waveguiding, sensing and exposure applications," Progress in Crystal Growth and Characterization of Materials 64(4), 133–151 (2018).
34. I. Dolganova, I. Shikunova, G. Katyba, A. Zotov, E. Mukhina, M. Shchedrina, V. Tuchin, K. Zaytsev, and V. Kurlov, "Optimization of sapphire capillary needles for interstitial and percutaneous laser medicine," Journal of Biomedical Optics 24(12), 1–7 (2019).
35. V. Kurlov, I. Shikunova, A. Ryabova, and V. Loschenov, "Sapphire smart scalpel," Bulletin of the Russian Academy of Sciences Physics 73(10), 1420–1423 (2009).
36. I. Shikunova, V. Volkov, V. Kurlov, and V. Loschenov, "Sapphire needle capillaries for laser medicine," Bulletin of the Russian Academy of Sciences Physics 73(10), 1345–1348 (2009).

37. I. Shikunova, D. Stryukov, S. Rossolenko, A. Kiselev, and V. Kurlov "Neurosurgery contact handheld probe based on sapphire shaped crystal," Journal of Crystal Growth 457, 265–269 (2017).
38. I. N. Dolganova, D. A. Varvina, I. A. Shikunova, A. I. Alekseeva, P. A. Karalkin, M. R. Kuznetsov, P. V. Nikitin, A. K. Zotov, E. E. Mukhina, G. M. Katyba, K. I. Zaytsev, V. V. Tuchin, and V. N. Kurlov, "Proof of concept for the sapphire scalpel combining tissue dissection and optical diagnosis," Lasers in Surgery and Medicine 54(4), 611–622 (2021).
39. I. Shikunova, I. Dolganova, G. Katyba, K. Zaitsev, and V. Kurlov, "Sapphire neurosurgical probe for aspiration of brain tumors with boundary demarcation by use of spectroscopy," Optics and Spectroscopy 126(5), 545–553 (2019).
40. I. Shikunova, I. Dolganova, A. Kuznetsov, E. Mukhina, L. Safonova, K. Zaytsev, and V. Kurlov, "Sapphire crystal cryoapplicators enabling control of cryosurgery based on light-tissue interaction," Cryobiology 92, 278 (2020).
41. I. N. Dolganova, A. K. Zotov, S. N. Rossolenko, I. A. Shikunova, S. L. Shikunov, K. B. Dolganov, K. I. Zaytsev, and V. N. Kurlov, "Manufacturing of hollow sapphire crystal with variable shapes for cryosurgical applications," Crystals 14(4), 346 (2024).
42. I. N. Dolganova, A. K. Zotov, L. P. Safonova, I. V. Reshetov, K. I. Zaytsev, and V. N. Kurlov, "Feasibility test of a sapphire cryoprobe with optical monitoring of tissue freezing," Journal of Biophotonics 16(3), e202200288 (2023).
43. G. M. Katyba, S. P. Lebedev, A. S. Kucheryavenko, I. N. Dolganova, N. V. Chernomyrdin, M. G. Burdanova, I. E. Spektor, M. Skorobogatiy, V. N. Kurlov, and K. I. Zaytsev, "Terahertz refractometry of hard-to-access objects using the sapphire endoscope suitable for harsh environments," Applied Physics Letters 124(24), 243703 (2024).
44. A. A. Platonova, P. V. Aleksandrova, A. I. Alekseeva, S. P. Kudryavtseva, A. K. Zotov, K. I. Zaytsev, K. B. Dolganov, I. V. Reshetov, V. N. Kurlov, and I. N. Dolganova, "Feasibility of monitoring tissue properties during microcirculation disorder using a compact fiber-based probe with sapphire tip," Journal of Biophotonics 17(11), e202400368 (2024).
45. H. E. LaBelle, "Growth of controlled profile crystals from the melt: Part II - Edge-defined, film-fed growth (EFG)," Materials Research Bulletin 6(7), 581–589 (1971).
46. H. E. LaBelle, "EFG, the invention and application to sapphire growth," Journal of Crystal Growth 50, 8–17 (1980).
47. N. Abrosimov, V. Kurlov, and S. Rossolenko, "Automated control of Czochralski and shaped crystal growth processes using weighing techniques," Progress in Crystal Growth and Characterization of Materials 46(1–2), 1–57 (2003).
48. P. I. Antonov, V. N. Kurlov, "New advances and developments in the Stepanov method for the growth of shaped crystals," Crystallography Reports 47(1), S43–S52 (2002).
49. V. N. Kurlov, "Sapphire: Properties, Growth, and Applications," in: Encyclopedia of Materials: Science and Technology, S. Hashmi (Ed.), Elsevier, 8259–8264 (2001).
50. P. Antonov, V. Kurlov, "A review of developments in shaped crystal growth of sapphire by the Stepanov and related techniques," Progress in Crystal Growth and Characterization of Materials 44(2), 63–122 (2002).
51. I. Dolganova, I. Shikunova, G. Katyba, A. Zotov, E. Mukhina, M. Shchedrina, V. Tuchin, K. Zaytsev, and V. Kurlov, "Optimization of sapphire capillary needles for interstitial and percutaneous laser medicine," Journal of Biomedical Optics 24(12), 128001 (2019).
52. I. Dolganova, A. Zotov, I. Shikunova, K. Zaytsev, P. Aleksandrova, E. Mukhina, and V. Kurlov, "Experimental study of pointed sapphire needles for interstitial laser therapy," Society of Photo-Optical Instrumentation Engineers, 11458, 114580E (2020).
53. I. Dolganova, I. Shikunova, A. Zotov, M. Shchedrina, I. Reshetov, K. Zaytsev, and V. Tuchin, V. Kurlov, "Microfocusing sapphire capillary needle for laser surgery and therapy: Fabrication and characterization," Journal of Biophotonics 13(10), e202000164 (2020).
54. S. Rossolenko, G. Katyba, I. Dolganova, I. Shikunova, D. Stryukov, K. Zaytsev, and V. Kurlov, "Numerical Analysis of Liquid Menisci in the EFG Technique," Chapter 3 in Crystal Growth, V. Glebovsky (Ed.), IntechOpen, London (2019).
55. S. Rossolenko, I. Shikunova, V. Kurlov, and S. Shikunov, "Growth of sapphire ribbons with capillary channels for laser spectroscopy," Inorganic Materials: Applied Research 2, 381–386 (2011).
56. R. M. Verdaasdonk, C. Borst, "Optical characteristics of sapphire laser scalpels analyzed by ray-tracing," Society of Photo-Optical Instrumentation Engineers 1420(6), 136–140 (1991).
57. I. Melnik, N. Denisov, and I. Kravchenko, "Light concentration by modified fiber tips and attached scalpel probes," Society of Photo-Optical Instrumentation Engineers 2328, 58 (1994).
58. I. Carneiro, S. Carvalho, R. Henrique, L. Oliveira, and V. V. Tuchin, "Measuring optical properties of human liver between 400 and 1000 nm," Quantum Electronics 49, 13 (2019).
59. A. K. Zotov, A. V. Pushkarev, A. I. Alekseeva, K. I. Zaytsev, S. S. Ryabikin, D. I. Tsiganov, D. A. Zhidkov, I. A. Burkov, V. N. Kurlov, and I. N. Dolganova, "Optical sensing of tissue freezing depth by sapphire cryo-applicator and steady-state diffuse reflectance analysis," Sensors 24, 3655 (2024).
60. M. Nikfarjam, V. Muralidharan, C. Malcontenti-Wilson, and C. Christophi, "Progressive microvascular injury in liver and colorectal liver metastases following laser induced focal hyperthermia therapy," Lasers in Surgery and Medicine 37, 64–73 (2005).

61. M. Havel, C. Betz, A. Leunig, and R. Sroka, "*Diode laser-induced tissue effects: in vitro tissue model study and in vivo* evaluation of wound healing following non-contact application," Lasers in Surgery and Medicine 46(6), 449–455 (2014).
62. F. Pisanello, G. Mandelbaum, M. Pisanello, I. A. Oldenburg, L. Sileo, J. E. Markowitz, R. E. Peterson, A. Della Patria, T. M. Haynes, M. S. Emara, B. Spagnolo, S. R. Datta, M. De Vittorio, and B. L. Sabatini, "Dynamic illumination of spatially restricted or large brain volumes via a single tapered optical fiber," Nature Neuroscience 20, 1180–1188 (2017).
63. J. Stujenske, T. Spellman, and J. Gordon, "Modeling the spatiotemporal dynamics of light and heat propagation for *in vivo* optogenetics," Cell Reports 12 (3), 525–534 (2015).
64. A. Shalabi, A. Ehab, S. F. Shalabi, G. Kugler, H.-J. Schäfers, and T. Graeter, "Laser assisted pulmonary metastasectomy promises a low local recurrence rate," Nature Neuroscience 14, 5988 (2024).
65. H. Fu, F. Luo, and H. Zhao, "A pilot study of minimal invasion combined PDL/Nd:YAG laser in treating facial epidermoid cyst," Journal of Cosmetic Dermatology 20(3), 2805-2809 (2021).
66. B. Spagnolo, A. Balena, R. T. Peixoto, M. Pisanello, L. Sileo, M. Bianco, A. Rizzo, F. Pisano, A. Qualtieri, D. D. Lofrumento, F. De Nuccio, J. A. Assad, B. L. Sabatini, M. De Vittorio, and F. Pisanello, "Tapered fibertrodes for optoelectrical neural interfacing in small brain volumes with reduced artefacts," Nature Materials 21, 826–835 (2022).
67. V. Emiliani, E. Entcheva, R. Hedrich, P. Hegemann, K. R. Konrad, C. Lüscher, M. Mahn, Z.-H. Pan, R. R. Sims, J. Vierock, and O. Yizhar, "Optogenetics for light control of biological systems," Nature Reviews Methods Primers 2, 55 (2022).

Phase Separation of L-Menthol an Aqueous Dispersion of Biologically Active Nanoparticles of Chitosan L- and D-Aspartate

Xenia M. Shipenok*, Aliya M. Mazhikenova, Evgeny G. Glukhovskoy, and Anna B. Shipovskaya
Saratov National Research State University named after N.G. Chernyshevsky, 83 Astrakhanskaya str., Saratov 410012, Russian Federation
*e-mail: kshipenok@gmail.com

Abstract. Phase separation in an ethanol solution of L-menthol in an aqueous dispersion of biologically active nanoparticles of chitosan L- and D-aspartate was studied. The process was found to proceed through the mechanism of selective extraction crystallization and to combine two types of phase separation (liquid-liquid and liquid-crystal). Liquid phase separation involves spontaneous dispersion of the ethanol macrophase to form a water microemulsion with hydrophobic content and subsequent coalescence of the dispersed phase. Crystalline phase separation involves L-menthol crystallization into optically anisotropic fibrillar particles. The size of microdroplets and fibrils and their packing density in the condensed phase are significantly affected by the concentration of the components and surface tension of the aqueous macrophase and the enantiomeric form of chitosan aspartate. It has been suggested that the system under study is promising for the development of new approaches to studying the fundamental principles of phase separation during intracellular communication and regulation.
© 2024 Journal of Biomedical Photonics & Engineering.

Keywords: chitosan; L- and D-aspartic acid; chitosan L- and D-aspartate; nanoparticles; L-menthol; phase separation; extraction crystallization; intracellular regulation; subcellular organization.

Paper #9184 received 23 Oct 2024; revised manuscript received 21 Nov 2024; accepted for publication 25 Nov 2024; published online 14 Dec 2024. doi: 10.18287/JBPE24.10.040316.

1 Introduction

Chiral polymeric matrices with controlled sites of complementary-specific interactions are considered as innovative substrates for the production of highly selective medicinal and pharmaceutical drugs [1–3]. To solve this task, first of all, information is necessary about stereospecific features of the chemical substance used to obtain such biomaterials, including those under model conditions of intracellular communication and regulation.

At present, nobody doubts that biochemical reactions inside cells occur in limited spaces of both membraneless and classical membrane organelles − cellular bodies in the form of a drop of liquid (bubble), formed as a result of liquid-liquid phase separation [4–6]). According to the modern concept of phase separation in cell biology, extracellular vesicles secreted by cells are key participants in intercellular communication and regulation, since they deliver proteins, lipids, nucleic acids and other signaling molecules to recipient cells, ending up in almost all body fluids [7–9]. The component composition of such liquid droplets (bubbles) is not constant and varies depending on the physical or chemical composition of their environment, as well as the local concentrations of low- and high-molecular-weight molecules present therein [10]. Moreover, *in vitro* model experiments have shown that in addition to liquid-liquid phase separation, biomacromolecules may undergo a liquid-crystal phase transition. For example, droplets of RNA-binding proteins may transform into fibrillar structures [11, 12]. The latter are almost stationary, since the exchange rate of the molecular components present therein with the surrounding volume of the solution is

extremely low. The evolution of the liquid–liquid and liquid-crystal transitions *in vitro* is accelerated for mutant variants of these proteins, some of which are known to be pathogenic [12].

An optically active system based on L-menthol and the salt form of chitosan (CS, D-glucan) with L-(D-)aspartic acid (AspA) is considered as a successful model for studying the fundamental principles of intracellular communication and regulation in both physiological and pathological cellular processes [13]. The choice in Ref. [13] of not only L-AspA, a non-essential proteinogenic amino acid [14, 15], but also its D-enantiomer for the production of chitosan aspartate (CS·L-(D-)AspA) is due to an increase in the content of D-AspA in the process of physiological aging of the body due to racemization of L-AspA [16]. The choice of L-menthol is due to its optical and biological activity [17, 18], as well as the diversity of morphostructures and supramolecular symmetries formed when varying the conditions of phase separation: from a water emulsion with hydrophobic content, whose dispersed phase is represented by nano- and microscopic droplets of the hydrophobic component [18, 19], to needle-shaped (whiskers) or lamellar crystals and ring-shaped or non-banded spherulites [13, 20].) Phase separation in an ethanol solution of L-menthol in an aqueous solution of CS·L-(D-)AspA has been established to proceed through the mechanism of extraction crystallization and to combine two types of phase separation, namely: liquid-liquid and liquid-crystal [13]. In the aqueous solution of CS·D-AspA, as well as with an increase in the concentration of the components of the optically active medium, the rate of phase separation, the size of droplets and solid-phase structures increase. It has been suggested that this process mimics the separation of liquid phases during intracellular signal transmission [4, 5].

It was also discovered that the effect of counterionic condensation occurs in the CS + AspA + H_2O system with phase segregation of the salt form of the polymer substance at the level of nano- and microparticles of CS·L-(D-)AspA [21], whose surface functionalization with a polysiloxane shell (~–Si–O–Si–~) leads to the production of a kinetically stable aqueous dispersion of CS·L-(D-)AspA·Si particles [22]. It has been established that CS·L-(D-)AspA and CS·L-(D-)AspA·Si nanoparticles are non-toxic, hemo- and biocompatible, and also exhibit a bactericidal action against *Staphylococcus aureus* 209 P and *Escherichia coli* 113-13 with the best effect for homochiral particles of D-glucan·D-AspA [22, 23]. It seems to us that a dispersion of CS·L-(D-)AspA·Si nanoparticles, like CS·L-(D-)AspA solutions, could be a promising model for studying the colloidal phase separation of biologically active substances.

The purpose of this work was to study features of crystallization of the L-menthol + ethanol system in an aqueous dispersion of CS·L-(D-)AspA·Si nanoparticles.

2 Materials and Methods

2.1 Materials

The following reagents were used: CS with a viscosity-average molecular weight of 200 kDa, a degree of deacetylation DD of 82 mol % (Bioprogress Ltd., RF), L-AspA (JSC Bioamid, RF); D-AspA (Vekton Ltd., RF), laboratory-synthesized silicon tetraglycerolate ($Si(OGly)_4$) obtained via the method described elsewhere [24], L-menthol with 99% basic substance (Alfa Aesar, Heysham, Lancs, UK), 95% ethyl alcohol (RFK Corp., Orel, RF), and distilled water. All reagents were chemical grade and used without further purification.

2.2 Preparation of Solutions and Nanoparticles

To obtain L-(D-)AspA solutions with a concentration of 0.3 g/dL, weighed portions of L- and D-AspA powders were dissolved in distilled water with stirring on a Labdevices HMS-100D heating mantle (China) at 80 °C, followed by cooling down to room temperature at 20 °C/h.

To prepare CS·L-(D-)AspA solutions, weighed portions of CS, L- or D-AspA powders were dissolved in distilled water with stirring in an Atlas reactor (Syrris, England) for 3 h at 50 °C. The concentrations of CS (C_{CS}), L- and D-AspA (C_{AspA}) were varied in a range of 0.3−1.2 g/dL, maintaining the molar ratio [Asp]/[CS] at 1.3 mol·(mol of NH_2)$^{-1}$. CS·L-(D-)AspA solutions were filtered through a Schott-160 funnel, $Si(OGly)_4$ was added thereto at a rate of ~0.08 g of precursor per 25 mL of solution, and stirred at 50 °C for 6 h, as described above. As a result, an aggregation and sedimentation stable dispersion of CS·L-(D-)AspA·Si nanoparticles was formed. A detailed procedure for functionalizing the surface of particles is given in Ref. [22].

A solution of L-menthol with a concentration of 2.5 g/dL was prepared by dissolving a sample of air-dry L-menthol in 95% ethyl alcohol for 24 h.

2.3 Methods

Gravimetric measurements were carried out on an Ohaus Discovery analytical balance (USA), weighing accuracy being ±0.01 mg.

To explore the phase separation, 3 ml of an aqueous dispersion of CS·L-(D-)AspA·Si was poured into a Petri dish 4 cm in diameter, and 1.5 ml of an ethanolic L-menthol solution was added dropwise onto the surface of the liquid medium with an automatic dispenser without stirring. The Petri dish was covered with a cover glass and left under static conditions in an air atmosphere at a temperature of 23 ± 1°C for 48 h. The phase separation process was considered complete if there were no changes in the morphostructure of the condensed phase.

The phase separation was observed both visually and on a LaboPol-2 (RF) polarization microscope (PM) with the polarizer and analyzer crossed. A halogen lamp (12 V, 30 W) served as the light source. The microscope

was focused on the site of space located at the Petri dish's center. PM-photos were obtained by a DMC 300 (3 Mpx) USB camera (Hangzhou, China). Temperature was measured using a mercury thermometer TL-5-2 (RF) with a measurement range of 0–105 °C and a division value of 0.5 °C.

Interfacial surface tension (σ, mN/m) was measured by the Wilhelmy plate lift-off method at the liquid-gas (air) interface at 24 ± 2 °C, the accuracy being 0.1 mN/m. Distilled water was used to calibrate the Wilhelmy balance. Three replicate experiments with 10 measurements each were carried out. When calculating σ values, a correction was introduced for the temperature coefficient of the surface tension of water [25].

Contact angles (θ, deg) were measured by the sessile drop method at the solid-liquid-gas interface on an Attension Theta Lite TL 100 precision optical tensiometer from Biolin Scientific (Sweden), the accuracy was 0.1 deg. An optical-quality glass slide, previously cleaned of contaminants, was used as a substrate, and distilled water was used as the base liquid. The time it took for a drop of liquid on the glass substrate to reach equilibrium was 25 s.

3 Results and Discussion

After applying the ethanol solution of L-menthol onto the surface of the aqueous dispersion of CS·L-(D-)AspA·Si nanoparticles, almost immediately there was a sharp increase in the temperature of the aqueous macrophase by 3–5 °C (depending on C_{CS} and C_{AspA}), the release of vaporous products and their condensation in volume to form a whitish fog. Fig. 1 (a–d) shows typical photos of this phenomenon when the dispersion of CS·D-AspA·Si nanoparticles is used as the aqueous phase. In parallel, turbulent movement of the liquid begins throughout the entire bulk of the ethanol macrophase and its spontaneous dispersion in the aqueous macrophase with the formation of a direct water microemulsion with hydrophobic content (Table 1, t = 0.02 h). Note that no increase in temperature, no formation of a dynamic aerosol cloud and no intense movement of ethanol layers occur if solutions of individual L-(D-)AspA and solutions of CS·L-(D-)AspA salts studied by us earlier [13] are used as the aqueous phase.

When a glass plate stored in a room atmosphere at 23 ± 1 °C is introduced into the space of the aerosol cloud, droplets of ovoid-shaped condensate appear on its surface, which quickly take a spherical shape and evaporate (Fig. 1 (e–g)).

Subsequently, a coalescence process of microdroplets proceeds due to Brownian aggregation of particles (Table 1, t = 0.5 h) and crystallization of an optically active low-molecular-weight substance into anisodiametric (fibrillar) solid-phase particles with pronounced optical anisotropy (t = 24–48 h). In addition, Janus-like objects (supramolecular structures with signs of Janus particles) are observed, especially at t = 48 h. At t = 48 h, some attenuation of the condensed phase birefringence was observed, but the effect of optical anisotropy did not completely disappear. With increasing concentrations of CS and L-(D-)AspA in the initial solution used to obtain nanoparticles, the size of spontaneously formed droplets in the liquid macrophase of the antisolvent and the length/thickness of solid-phase fibrils increase.

In the medium of individual enantiomers of L- and D-AspA, as well as in that of CS·L-(D-)AspA·Si, two types of phase separation are also observed: liquid-liquid and liquid-crystal (Table 1). However, the size of phase-separated microdroplets is significantly smaller (submicron size), the onset time of coalescence of emulsion droplets increases up to 5–6 h, and the condensed phase is mainly represented by optically isotropic needle-like crystals (thread-like whiskers) and their aggregates. A similar type of solid-phase particles was observed during the crystallization of L-menthol in the CS·L-(D-)AspA medium [13].

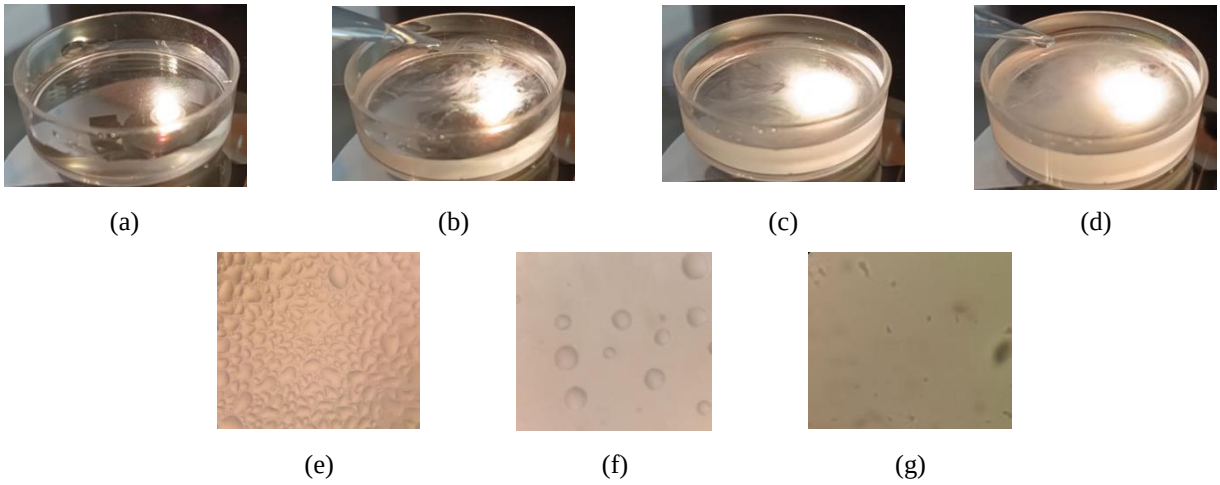
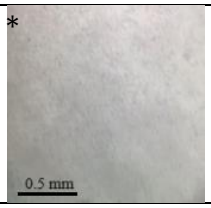
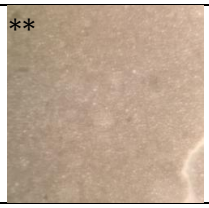
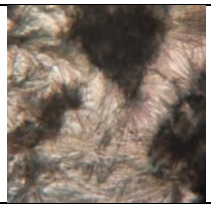
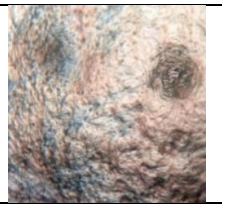
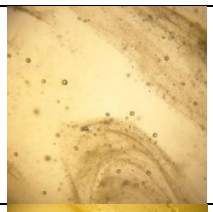
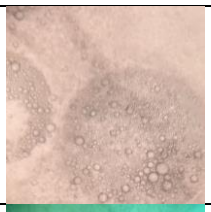
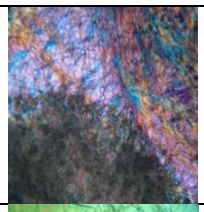
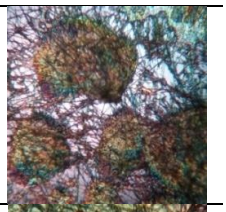
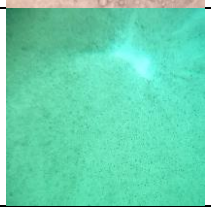
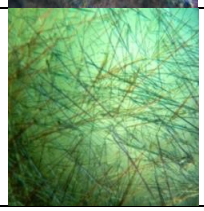
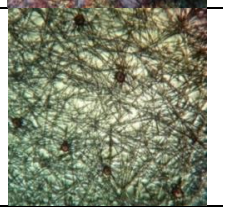
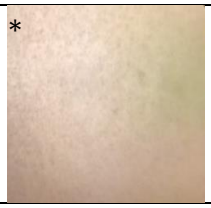
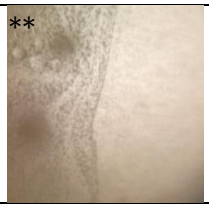
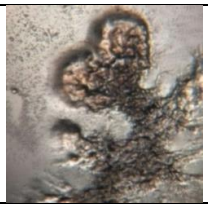
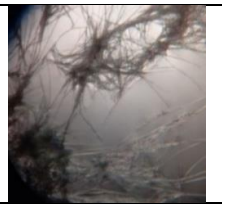
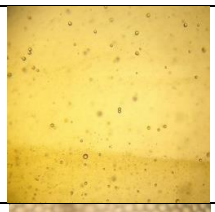
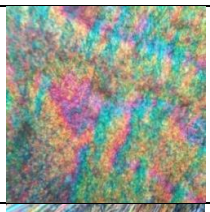
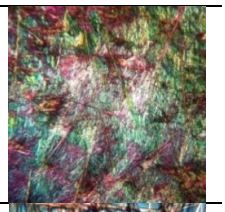
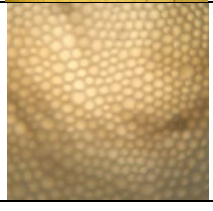
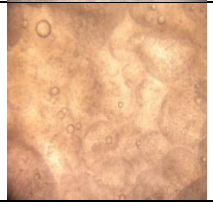
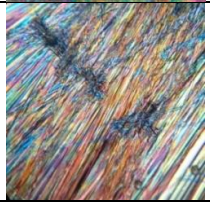
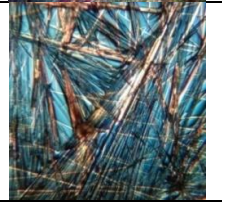


Fig. 1 Photos: Petri dishes (a) with the initial dispersion of CS·D-AspA·Si nanoparticles and the initial stage of applying the ethanol solution of L-menthol onto its surface at a contact time (t) between the ethanol and aqueous macrophases of (b) 4, (c) 10 and (d) 20 s; condensate of the aerosol cloud shown in panel (d) on the surface of a glass plate at (e) t = 0.02, (f) 0.05 and (g) 4 h; the concentration of aqueous phase components C_{CS} = 1.2 g/dL, C_{AspA} = 1.2 g/dL.

Table 1 Photos of the stages of extraction crystallization of the ethanol solution of L-menthol in the aqueous solutions of L-(D-)AspA and aqueous dispersions of CS·L-(D-)AspA·Si nanoparticles, magnification ×4.

Concentration of aqueous phase components		**PM-photos of forming droplets, fibrillar structures and their supramolecular aggregates**			
		Contact time *t*, h			
C_{CS}, g/dL	C_{AspA}, g/dL	**0.02**	**0.5**	**24**	**48**
L-AspA					
–	0.3				
CS·L-AspA·Si					
0.3	0.3				
1.2	1.2				
D-AspA					
–	0.3				
CS·D-AspA·Si					
0.3	0.3				
1.2	1.2				

*, ** Time – 0.08 and 6 h, respectively.

But the whiskers were ordered into optically anisotropic non-banded spherulites, and upon transition to the air-dry state they formed needle-shaped spherulites of a “leaked radial configuration” with macroscopic chirality. Crystallization in droplets with the formation of spherulites was not observed in the CS·L-(D-)AspA·Si medium, which is probably due to the functionalization of nanoparticles with a polysiloxane shell.

Our assessment of the influence of the AspA isomer on the observed processes showed that the rate of increase in the temperature of the aqueous macrophase when a hydrophobic weakly polar macrophase is applied onto its surface was greater when carrying out the phase separation of L-menthol in the CS·D-AspA·Si medium. In the same environment, the resulting fog was whiter, and the emulsion droplets were larger and more uniform in size. The length/thickness of the fibrils and the packing density of their supramolecular aggregates were greater than for similar structures upon crystallization in CS·L-AspA·Si. In the liquid phase of AspA enantiomers, on the contrary, the densest condensed phase was formed in the L-AspA medium. The birefringence effect was most pronounced for fibrils condensed in the CS·D-AspA·Si phase.

One of the causes for the observed nature of phase separation of an ethanol solution of L-menthol in an aqueous dispersion of CS·L-(D-)AspA·Si may be some specificity of the structural and molecular ordering of the aqueous macrophase, determined by its surface energy. Recent studies [26] have shown that in terms of surface activity, nanoparticles in dispersions behave in many ways similar to surfactant molecules, with the only difference being that the orientation of nanoparticles (especially spherical ones) relative to the surface has virtually no effect on the interfacial tension, and the adsorption energy of nanoparticles on the surface changes sharply with the wetting angle. In this regard, the surface tension and contact angle of the CS·L-(D-)AspA·Si + H_2O system were estimated.

It turned out that chitosan L-(D-)aspartate nanoparticles had surface activity and reduced the surface energy at the liquid-gas interface. At the same time, the interfacial tension of the aqueous dispersion of CS·L-AspA·Si and CS·D-AspA·Si nanoparticles non-monotonically decreases with increasing C_{CS}, and is also significantly lower than the interfacial tension of the base liquids-water, an aqueous solution of the surface-inactive L-aspartic acid and an aqueous solution of CS L-AspA (Fig. 2(a)). Probably, the compacted conformation of macrocoils in the structure of CS·L-(D-)AspA·Si nanoparticles weakens the intermolecular interactions of the components in the bulk of the aqueous macrophase and, as a result, reduces the surface adsorption energy and surface tension. The synergistic effect of increasing surface activity was more pronounced in the aqueous macrophase with CS·L-AspA·Si nanoparticles.

The formation of a drop of an aqueous dispersion of CS·L-(D-)AspA·Si nanoparticles on glass occurs in the limited wetting mode (Fig. 2(b)). The surface of the glass substrate is more lyophilic for the CS·L-AspA·Si dispersion, which explains its higher surface activity at the liquid–gas interface in comparison with CS·D-AspA·Si. At the same time, the contact angle at the solid-liquid-gas interface monotonically increases with CS concentration. Therefore, the interactions between the components of the aqueous macrophase become more preferable than the interactions of these same components with the substrate surface. This character of the $\theta = f(C_{CS})$ dependence is expressed to the greatest extent for the dispersion of CS·D-AspA·Si nanoparticles. One more discovered nontrivial effect should also be noted. Despite the fact that the σ of aqueous dispersions of both isomeric forms of chitosan aspartate nanoparticles is less than that of water, the contact angle of the aqueous dispersion of CS·D-AspA·Si is greater than that of water on the same glass substrate.

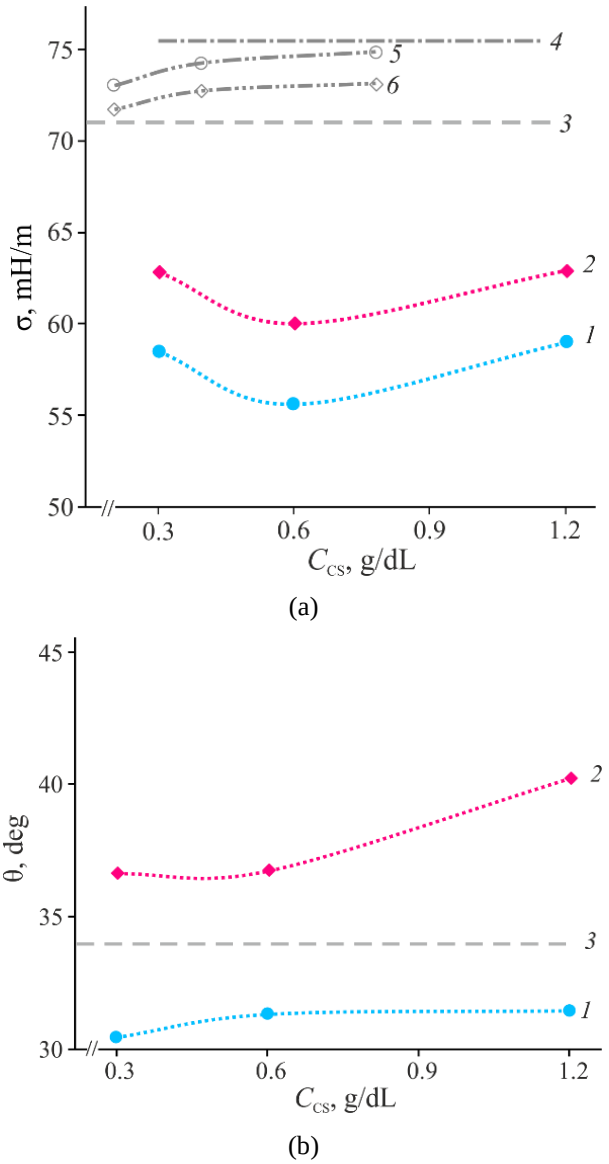


Fig. 2 (a) Surface tension and (b) contact angle of an aqueous dispersion of (*1*) CS·L-AspA·Si and (*2*) CS·D-AspA·Si nanoparticles as a function of CS concentration. The dotted line (*3*) in panels (a) and (b) shows the σ and θ values for distilled water. The dashed-dotted line (*4*) in panel (a) corresponds to the σ values of aqueous solutions of L-AspA with concentrations between 0.3–1.2 g/dl, according to Ref. [27] and the dashed-dotted curves (*5*) and (*6*) corresponds to the σ values of aqueous solutions of L-AspA and D-AspA, respectively, with concentrations between 0.2–0.8 g/dl.

4 Conclusion

The phase separation of an ethanolic L-menthol solution in an aqueous CS·L-(D-)AspA dispersion proceeds through the mechanism of selective extraction crystallization and combines two types of phase separation (liquid-liquid and liquid-crystal). At the initial stage of liquid–phase separation, the interaction of the ethanol solution of L-menthol with the aqueous dispersion of chitosan nanoparticles to spontaneously form hydrophobic droplets turns out to be the most preferable. During liquid–solid phase separation, the preferred morphostructural organization of L-menthol is optically anisotropic fibrillar particles. The formation of Janus-like objects also indicates spontaneous (controlled) phase separation. The size of microdroplets and fibrils and their packing density in the condensed phase are significantly affected by the concentration of the components of the aqueous macrophase and the enantiomeric form of chitosan aspartate. The surface properties of the initial dispersion of CS·L-(D-)AspA·Si nanoparticles have an important effect on the specific nature of phase separation in the studied system. In comparison with the base liquid (H_2O), the presence of nanoparticles in the aqueous phase not only increases surface adsorption at the liquid–gas interface, but also specifically changes the lyophilic balance of the nanodispersion components at the solid-liquid-gas interface.

The results obtained show the promise of using CS·L-(D-)AspA·Si nanoparticles in studies of biomolecular condensation and the biogenesis of membraneless/membrane organelles in physiological/pathological cellular processes and, accordingly, the development of new pharmaceutical compositions to treat specific diseases.

Acknowledgements

This research was funded by a grant from the Russian Science Foundation No. 24-16-00172, https://rscf.ru/project/24-16-00172/.

Disclosures

All authors declare that there is no conflict of interests in this paper.

References

1. H. Zhong, J. Deng "Organic polymer-constructed chiral particles: preparation and chiral applications," Polymer Reviews 62(4), 826–859 (2022).
2. L. Song, M. Pan, R. Zhao, J. Deng, and Y. Wu, "Recent advances, challenges and perspectives in enantioselective release," Journal of Controlled Release 324, 156–171 (2020).
3. H. Yu, X. Yong, J. Liang, J. Deng, and Y. Wu, "Materials established for enantioselective release of chiral compounds," Industrial and Engineering Chemistry Research 55(21), 6037–6048 (2016).
4. S. V. Nesterov, N. S. Ilyinsky, and V. N. Uversky, "Liquid-liquid phase separation as a common organizing principle of intracellular space and biomembranes providing dynamic adaptive responses," Biochimica et Biophysica Acta - Molecular Cell Research 1868(11), 119102 (2021).
5. D. M. Mitrea, R. W. Kriwacki, "Phase separation in biology; functional organization of a higher order," Cell Communication and Signaling 14(1), 1 (2016).
6. M. Feric, N. Vaidya, T. S. Harmon, D. M. Mitrea, L. Zhu, T. M. Richardson, R. W. Kriwacki, R. V. Pappu, and C. P. Brangwynne, "Coexisting liquid phases underlie nucleolar subcompartments," Cell 165(7), 1686–1697 (2016).
7. P. Robbins, A. Morelli, "Regulation of immune responses by extracellular vesicles," Nature Reviews Immunology 14, 195–208 (2014).
8. A. C. Dixson, T. R. Dawson, and D. Di Vizio, "Context-specific regulation of extracellular vesicle biogenesis and cargo selection," Nature Reviews Molecular Cell Biology 24, 454–476 (2023).
9. L. P. Bergeron-Sandoval, N. Safaee, and S. W. Michnick, "Mechanisms and consequences of macromolecular phase separation," Cell 165(5), 1067–1079 (2016).
10. L. Zhu, C. P. Brangwynne, "Nuclear bodies: the emerging biophysics of nucleoplasmic phases," Current Opinion in Cell Biology 34, 23–30 (2015).
11. A. Molliex, J. Temirov, J. Lee, M. Coughlin, A. P. Kanagaraj, H. J. Kim, T. Mittag, and J. P. Taylor, "Phase separation by low complexity domains promotes stress granule assembly and drives pathological fibrillization," Cell 163(1), 123–133 (2015).
12. Y. Lin, D. S. W. Protter, M. K. Rosen, and R. Parker, "Formation and maturation of phase-separated liquid droplets by RNA-binding proteins," Molecular Cell 60(2), 208–219 (2015).
13. A. B. Shipovskaya, N. O. Gegel, and X. M. Shipenok, "Features of L-menthol crystallization in optically active medium based on L- and D-asparaginate chitosan features of L-menthol crystallization in optically active medium based on L- and D-asparaginate chitosan," Journal of Biomedical Photonics 9(1), 010305 (2023).
14. N. J. Ayon, "Features, roles and chiral analyses of proteinogenic amino acids," AIMS Molecular Science 7(3), 229−268 (2020).
15. L. Tu, Y. K. Lin, "The origin of life and the crystallization of aspartic acid in water," Crystal Growth and Design 10(4), 1652−1660 (2010).

16. A. V. Chervyakov, N. V. Gulyaeva, and M. N. Zakharova, "D-Amino acids in normal ageing and pathogenesis of neurodegenerative diseases," Neurochemical Journal 5(2), 100−114 (2011).
17. A. G. Shtukenberg, Y. O. Punin, A. Gujral, and B. Kahr, "Growth actuated bending and twisting of single crystals," Angewandte Chemie International Edition 53(3), 672−699 (2014).
18. E. Betz-Güttner, M. Righi, S. Micera, and A. Fraleoni-Morgera, "Directional growth of cm-long PLGA nanofibers by a simple and fast wet-processing method," Materials 15(2), 687 (2022).
19. S. Kim, S. C. Peterson, "Optimal conditions for the encapsulation of menthol into zein nanoparticles," LWT 144, 111213 (2021).
20. T. Kovács, R. Szűcs, G. Holló, Z. Zuba, J. Molnár, H. K. Christenson, and I. Lagzi, "Self-assembly of chiral menthol molecules from a liquid film into ring-banded spherulites," Crystal Growth and Design 19(7), 4063−4069 (2019).
21. T. N. Lugovitskaya, A. B. Shipovskaya, S. L. Shmakov, and X. M. Shipenok, "Formation, structure, properties of chitosan aspartate and metastable state of its solutions for obtaining nanoparticles," Carbohydrate Polymers 277, 118773 (2022).
22. A. Shipovskaya, X. Shipenok, T. Lugovitskaya, and T. Babicheva, "Self-assembling nano- and microparticles of chitosan L-and D-aspartate: preparation, structure, and biological activity," Materials Proceedings 14(1), 31 (2023).
23. A. B. Shipovskaya, T. N. Lugovitskaya, and I. V. Zudina, "Biocidal activity of chitosan aspartate nanoparticles," Microbiology 92(1), 75–82 (2023).
24. E. V. Shadrina, O. N. Malinkina, T. G. Khonina, A. B. Shipovskaya, V. I. Fomina, E. Yu. Larchenko, N. A. Popova, I. G. Zyryanova, and L. P. Larionov, "Formation and pharmacological activity of silicon—chitosan-containing glycerohydrogels obtained by biomimetic mineralization," Russian Chemical Bulletin 64, 1633–1639 (2015).
25. G. Kaptay, "On the temperature dependence of surface tension: Historical perspective on the Eötvös equation of capillarity, celebrating his 175th anniversary," Advances in Colloid and Interface Science 332, 103275 (2024).
26. A. M. Emelianenko, and L. B. Boinovich, "Role of disperger particles in physical-chemical movement of nanofluids," Colloid Journal 85(6), 727–737 (2023).
27. T. N. Lugovitskaya, and A.B. Shipovskaya "Physicochemical properties of aqueous solutions of L-aspartic acid containing chitosan," Russian Journal of General Chemistry 87(4), 782–787 (2017).

Non-Contact Automatic Respiratory Rate Monitoring for Newborns Using Digital Camera Technology and Deep Learning

Huda Ali Hashim
Middle Technical University, Electrical Engineering Technical College, Doral, Baghdad, Iraq
e-mail: huda.ali@mtu.edu.iq

Abstract. In healthcare settings, particularly for newborns in the Neonatal Intensive Care Unit (NICU), continuous and accurate monitoring of respiratory rates (RR) is crucial, yet current methods often involve manual region selection, which limits their effectiveness. To address this challenge, we developed a novel approach using a low-cost digital camera for non-contact RR monitoring of ten newborns. This study leverages deep learning for automated region of interest (ROI) selection in the face and chest areas, coupled with signal decomposition techniques to reduce noise artifacts. A graphical user interface (GUI) system was also introduced to facilitate real-time RR monitoring and visualization of results. The experimental outcomes demonstrate the system's high efficacy, with the object detector achieving precision rates of 98.24% for the face region and 96.61% for the chest region. Additionally, the system recorded a low average mean absolute error (MAE) of 1.11 breaths per minute for the face and 1.03 breaths per minute for the chest, corroborated by reference ECG monitor readings. This method offers a cost-effective, non-contact, and deployable solution suitable for both clinical and home health monitoring applications. © 2024 Journal of Biomedical Photonics & Engineering.

Keywords: respiratory rate; newborns; digital camera; YOLOV4-Tiny.

Paper #9164 received 3 Sep 2024; revised manuscript received 27 Nov 2024; accepted for publication 28 Nov 2024; published online 26 Dec 2024. doi: 10.18287/JBPE24.10.040317.

1 Introduction

Monitoring respiratory rate (RR) is crucial for the preservation of newborns' lives since they have a substantial impact on the diagnosis of newborns' health in both hospital and home settings [1, 2]. The use of imperceptible vital signs may be very advantageous, especially in scientific and therapeutic contexts [3]. Hemoglobin in the blood has a higher capacity to absorb light compared to the surrounding epidermis tissue [4]. Photoplethysmograph (PPG) signals are used to assess chest function by quantifying fluctuations in blood volume in specific areas [5]. These signals indicate cyclic patterns produced by the heart's activity and breathing [6]. Contact techniques like nasal thermocouples, electronic sensors, ECGs, and oximetry probes are used to monitor respiratory signals. However, using and removing these biosensors and electrodes may harm the skin and restrict the newborn's mobility [7].

To overcome the limitations of contact techniques, researchers have developed non-contact techniques for monitoring biomedical signals. Thermal imaging detects physiological signs by observing temperature changes related to blood flow in superficial arteries [8], while radar detects chest movements in a specific region of interest (ROI) [9, 10]. However, these methods are susceptible to noise and motion artifacts, limiting mobility [11]. Furthermore, they are harmful to human health and may have a variety of biological impacts on bodily tissue [12, 13].

Video camera techniques capture and analyze biological signals from many areas of the human body. We can categorize techniques into two fundamental groups [14]: color-based techniques, also called imaging photoplethysmography (iPPG) [9, 15–17], and motion-

based techniques [8, 18]. The first category utilizes differences in pigmentation resulting from cardiorespiratory physical exertion. Though iPPG is appealing in principle, prior investigations have been influenced by various downsides for extracting respiratory signals from patients, including lighting conditions, distance, and skin color [9, 19]. Consequently, the photoplethysmography technique is unable to accurately reveal physiological indicators in regions of interest that are not well defined [8]. Using a video camera to record the motion of specific human parts, such as the chest, head, or face, is a dependable way to detect the respiratory signal [18, 20−22].

For example, Al-Naji et al. [23] proposed a non-contact method for assessing newborn respiration rates using a video camera to record chest movements or blankets in various positions. Lucy et al. [24] developed a video-based approach that correlates respiratory rates with chest-abdominal wall movements, analyzing RGB video components and applying a fast Fourier transform to the denoised signal. However, irregular vital signs due to respiratory diseases necessitate accurate ROI selection for effective monitoring, highlighting the limitations of manual methods.

Additionally, Olmi et al. [25] introduced an automatic face detection system for infants in the NICU using the aggregate channel feature technique. The Neurophysiology and Neonatology Clinical Units used newborn data to train the model. Khanam et al. [26] utilized the YOLOv3 model as an automatic face detector for monitoring newborn vital signals, ensuring accurate ROI selection for video image analysis.

Current methods for respiratory signal monitoring are often unsuitable for real-time systems due to high processing and memory demands, prompting researchers to refine their algorithms [24]. Recently, the YOLO series, particularly YOLOv4-tiny [27], has emerged as a leading solution in object detection. YOLOv4-tiny, an optimized variant of YOLOv4 [28], features a lightweight architecture with a CSPDarknet53-tiny backbone and innovative techniques to enhance detection speed and performance [29]. Unlike YOLOv3-tiny, it uses CSPBlock for feature extraction and incorporates complete intersection over union for bounding box selection [30]. Comparative studies, such as those by Hraybi et al. [31], have demonstrated YOLOv4-tiny's superior accuracy and speed over other YOLO variants in face-mask detection. Experiments show that the Yolov4_tiny model improves performance for reduced time detection while keeping the speed of the lightweight model and meeting the accuracy standard of substantial target detection models [32].

After reviewing the literature, the manual ROI selection approach was mostly used for non-contact biological sign monitoring. Furthermore, the current studies exhibit a significant research gap due to the limited exploration of non-contact vital sign monitoring in the NICU. Furthermore, some literary works employ multi-object ROI detection, necessitating computationally expensive calculations in terms of both power and time. The aforementioned limitations serve as the impetus for implementing automated ROI selection for infants. The main focus of this work is to develop a healthcare system for non-contact respiratory rate monitoring of newborns. This research investigates the appropriateness of using a deep learning model to automatically determine ROI in a healthcare system. The contributions of this study are as follows:

1. An accurate non-contact RR monitoring system was developed using digital camera technology to evaluate two experiments: the first focused on respiratory signals extracted from the face region, while the second focused on signals extracted from the chest region of newborns.
2. An automatic ROI selection technique was developed using a pre-trained deep-learning model (YOLOV4-Tiny) as a baby detector, efficiently handling various challenging scenarios and different region selections (i.e., face and chest).
3. Motion-based techniques, combined with ensemble empirical mode decomposition (EEMD), were utilized to effectively extract respiratory signals from PPG signals.
4. A Newborn's Graphical User Interface (GUI) system was implemented for monitoring the baby's status and displaying the findings of the proposed non-contact monitoring system.

2 Methods and Materials

2.1 Subjects and Experiment Setup

We conducted this study at Al-Elwiya Maternity and Teaching Hospital (AMTH) in Al Rusafa, Baghdad, Iraq. We got permission from guardians to record videos using non-contact techniques at various periods after explaining the nature of the work and the experiment's aim to collect data without touching baby newborns. We protected the baby newborns' anonymity by concealing their faces. In this work, we used an ECG monitor as reference information to compare and analyze the performance of the 2 proposed experiments in evaluating the respiratory signals of baby newborns.

We used 10 newborn babies as participants, dividing them into 2 experiments: the first involved extracting RR values from the face region, named the RRface experiment, while the second involved extracting RR values from the chest region, named the RRchest experiment. The age range of newborns was 24 to 40 weeks, and they weighed 1500 to 3100 g. Fig. 1 depicts the experimental configuration, where 2 digital cameras recorded videos of 10 baby newborns in incubators. We tripod-mounted a Canon 2000D with a resolution of 1920 width × 1080 height at 25 frames per sec (fps) to record the infants' videos at a distance of approximately 1–1.5 m. We also installed another Canon 650D camera on a tripod to record the true state of vital signs on the ECG monitor. To synchronize the information from the ECG monitor and contactless technique, recording from both cameras began simultaneously.



Fig. 1 Experimental configuration of newborn's data collection.

We stored the videos in the "MOV" format. Collecting data from newborn babies requires a significant amount of time and effort. Recording rated videos of baby newborns is extremely challenging in a hospital setting, such as the NICU. Typically, medical devices or soft layers obstruct newborn babies. To validate our work, we gathered a small database. We considered the use of video recorders when newborns were not moving, as well as the constant use of ECG monitors.

We recorded each infant 5 times in their most stable condition. We recorded each newborn's video for approximately 10 min and edited it into 10-sec segments when the monitor's readings remained stable. As a result, we captured 50 videos for each experiment.

3 System Framework

This section will provide a detailed explanation of the proposed non-contact RR values monitoring system for newborns. This will include details: an automatic ROI selection-based deep learning model for 2 regions, respiratory rate calculation, and a newborn's GUI system proposed. Fig. 2 illustrates the framework for developing non-contact automatic respiratory rate monitoring for newborns.

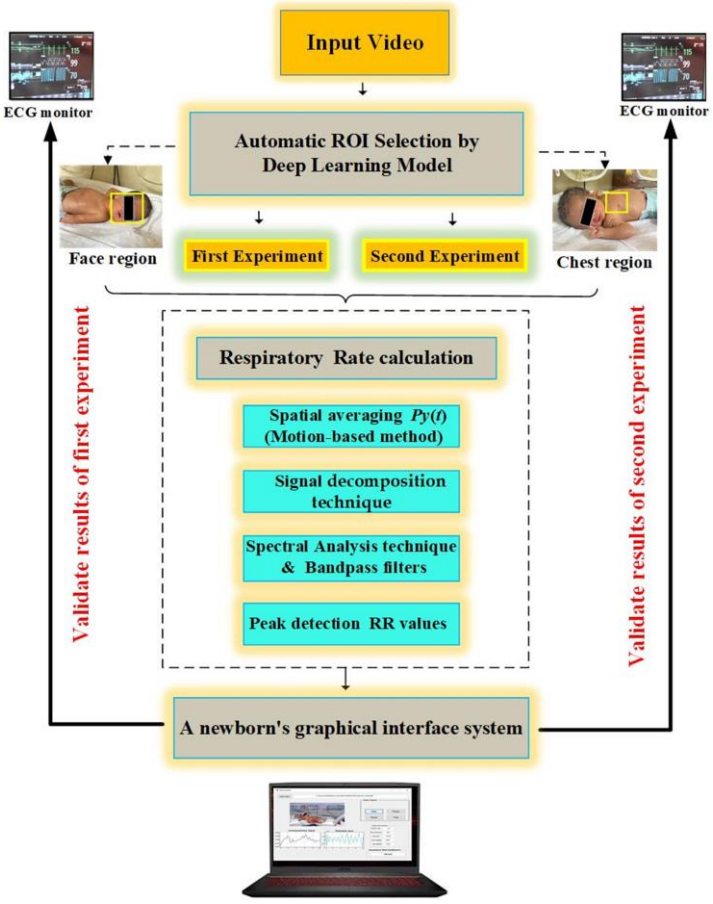


Fig. 2 The system framework of the proposed study.

3.1 Automatic Selection Model

Capturing high-quality video of newborns in healthcare units presents significant challenges due to the complexity of the environment. Traditional detection models, such as YOLOv2 and Mask-RCNN, supported by MATLAB [33], are generally effective for detecting people of all ages but fail to recognize infants within hospital settings. Also, insufficient infant-specific data may be not available [34].

Therefore, we trained a small dataset consisting of 420 images acquired from healthcare units, internet sources, and the NJN dataset [35], featuring various illumination conditions and infants in different sleeping positions.

We completed the label annotation process using the MATLAB 2023a toolbox's image-labeler function, drawing bounding boxes around each detected object. In the first experiment, we labeled the images as face regions, and in the second experiment, we labeled them as chest regions. In object detection, YOLO models predict the bounding box and category of objects in images. We assessed the accuracy of these predictions using Intersection over Union (IoU), applying a threshold of 0.5 to determine successful detections. If the intersection between the predicted bounding box and the ground truth bounding box is more than 50%, the detection is deemed successful. After label annotation, we applied data preprocessing techniques, such as rotations, scaling, and resizing images to 416 × 416 px, to enhance dataset diversity.

We trained the object detector model using pre-trained YOLOv4-Tiny weights [27], which were originally trained on the MS COCO dataset [27]. After configuring the model's parameters, we fine-tuned it using our small data. YOLOv4-Tiny outperforms other detection models in terms of accuracy and speed. The YOLOv4-Tiny's average speed is twice that of the YOLOv4 and 10 times that of the Faster-RCNN [29].

Using the Adam optimization algorithm, we set the hyperparameters to 30 epochs, a batch size of 20, and a learning rate of 0.001. The training was conducted on a system with an i7 processor, NVIDIA GeForce GTX 1060Ti GPU, and 16 GB of RAM, using a GPU execution environment to expedite the process. We split the gathered data set from the sources mentioned into 70% (294 images) for training, 15% (63 images) for validation, and 15% (63 images) for testing. Finally, we evaluated the model's performance using precision, recall, and F_1 score, by applying the following Eqs.:

$$Precision = \frac{T_p}{T_p + F_P}, \tag{1}$$

$$Recall = \frac{T_p}{T_p + F_n}, \tag{2}$$

$$F_{1\,Score} = 2 * \frac{(Precision * Recall)}{(Precision + Recall)}, \tag{3}$$

where T_p represents the number of true positive regions detected during object detection, such as the face in the first experiment and the chest in the second experiment. F_P denotes the number of false positives, T_n is the number of true negative cases, and F_n is the number of false negative instances. To evaluate the model performance, we used the mean average precision (mAP), specifically the $mAP_{(0.5)}$ refers, for computing it at an IoU threshold of 0.5. Fig. 3 illustrates the steps involved in building the automatic ROI selection-based deep learning model.

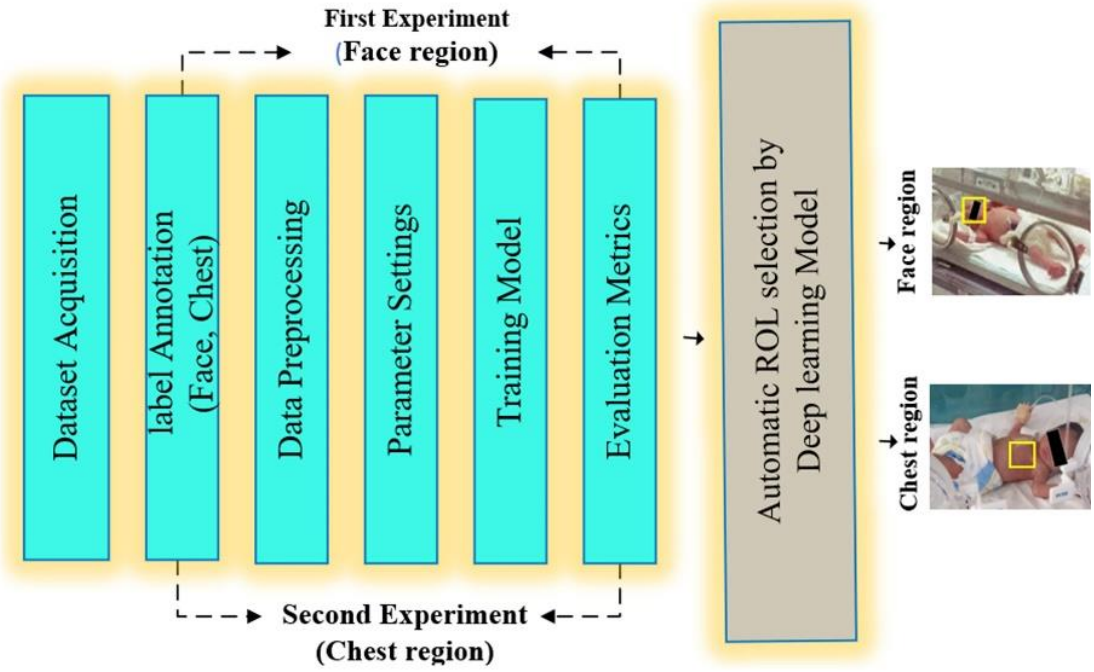


Fig. 3 Steps for building the automatic ROI selection-based deep learning model.

3.2 Respiratory Rate Calculation

In this study, we employed a motion-based technique to extract raw respiratory signals from newborns from 2 experiments (RRface and RRchest) as the first step. Respiratory activity generates a rhythmic motion in certain areas of the body, including the face, thorax, and chest regions. Therefore, in the recorder clip, spatial variations in intensity values refer to this motion. This principle allows for the calculation of the respiratory signal. As the digital camera records the video in the RGB color space, it is essential to distinguish between intensity and color information. Therefore, we transformed the RGB color space to 'YIQ' using MATLAB's built-in function 'rgb2ntsc'. Next, we calculated the raw respiratory signal from the Y channel of the YIQ color space by assessing the average brightness values of pixels within the chosen ROI, as follows:

$$p_{y(t)} = \frac{\sum_{x,y \in \text{ ROI}} p(x,y,t)}{|\text{ ROI}|}, \quad (4)$$

where $p_{y(t)}$ is the computed respiratory signal of a newborn, $p(x,y,t)$ indicates the intensity value of each pixel in the Y channel at the specified image location (x,y), and time (t), and |ROI| represents the size of ROI regions by an automatic ROI selection.

In biomedical signal processing, signal decomposition methods are used to separate a time signal into a set of interesting modes. In this work, we employed the EEMD technique for signal decomposition as the second step. This technique was improved by Wu and Huang [36], in which white noise was added to the original EMD method to restrain the mode-mixing effect. The following steps identify the signal decomposition process, which is based on EEMD.

Also, we used the Fast Fourier Transform (FFT) to transfer the respiratory signals from the time domain to the frequency domain for spectral analysis as the third step. We then implemented the appropriate band-pass filters within the frequency range of 0.3 to 1 Hz, aligning with the respiratory range of 30 to 60 breaths per min fourth step. Then, we subjected the processed data to the inverse of FFT to obtain the time-series respiratory signal accuracy.

In the fifth step, time series respiratory signals are processed by computing peaks and their locations (*locs*) between successive peaks. The built-in MATLAB function 'findpeaks' was utilized to detect peaks. Then, the total cycle length (L) between 2 peaks is calculated by applying the following Eq.:

$$L = mean\,(diff(locs)). \quad (5)$$

The number of peaks (N_P) can be retrieved by the following Eq.:

$$N_P = \frac{D}{L}, \quad (6)$$

where D is the duration time in seconds of the video.

Finally, the RR values in breaths per min (breaths/min) is calculated using Eq. (7):

$$\text{RR} = \frac{60\ N_P}{T}. \quad (7)$$

3.3 A Newborn's Graphical User Interface System

We implemented a newborn GUI system for non-contact RR monitoring using MATLAB 2023a, as shown in Fig. 4. The proposed system features a user-friendly interface that includes respiratory signal processing and displays the RR value results based on an automatic deep-learning model. It also provides an efficient environment for video uploads, along with analytical tools, including 3 axes for video selection, input signal display, and respiratory signal output. The proposed system includes 6 text fields for displaying video information and RR values. Additionally, it offers a variety of video controls, such as Start, Extract, Pause, and Reset, each designed for specific functions.

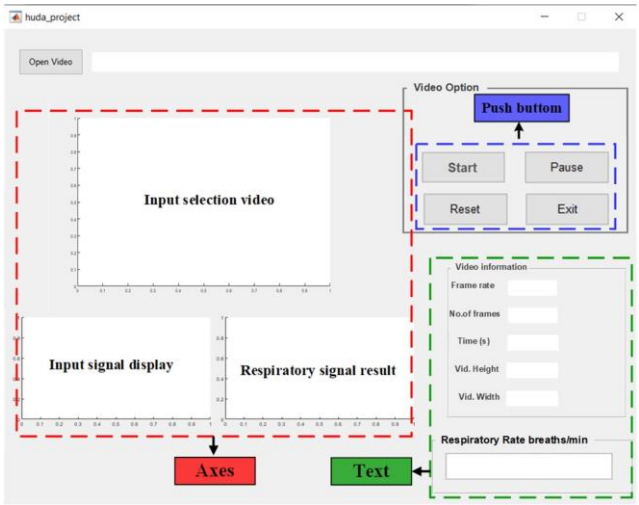


Fig. 4 A snapshot of the newborn's proposed graphical user interface.

4 Results and Analyses Experimental

4.1 Automatic Selection Model Performance

This Section evaluates the performance of the automatic ROI selection model based on the fine-tuned YOLOv4-Tiny model as a baby detector. As shown in Fig. 5, the YOLOv4-Tiny model effectively segments images, predicting bounding boxes and probabilities for each region. The model independently processes the detected face and chest regions, delivering accurate predictions with strong performance.

The results of performance metrics on the test dataset set regarding precision, recall, and F_1 score, and $mAP_{(0.5)}$ are shown in Table 1. The table demonstrates the performance results an automatic ROI selection region RRface and RRchest experiments.

The detector accuracies comparing the bounding box detected by the trained object detector with the true-label bounding box annotated (face and chest) were 96.31% for $mAP_{(0.5)}$ and 96.11% for mAP (50) for the RRface and RRchest experiments, respectively. Also, it is clearly shown from the table results that the object detector for regions (face and chest) had good performance for precision, recall, and F_1 Score for 2 experiments.

4.2 Respiratory Rate Extraction

In our experiments, we obtained raw respiratory signals for 250 frames by applying spatial averaging to the automatically detected ROIs using a motion-based method. We captured the signals for 2 distinct regions: the face and the chest. Fig. 6(a) presents the respiratory signal from the RRface experiment, while Fig. 6(b) shows the corresponding signal from the RRchest experiment.

The raw respiratory signals were subsequently decomposed using the EEMD method. The EEMD had a 10-sec window length. Fig. 7 illustrates the results of IMF decomposition for respiratory signals into IMF1, IMF2, and IMF7. Using FFT, we conducted a frequency spectral analysis of the decomposed IMFs to determine the most suitable IMF for calculating the RR values.



Fig. 5 Automatic ROI selection using the YOLOV4-Tiny deep learning model.

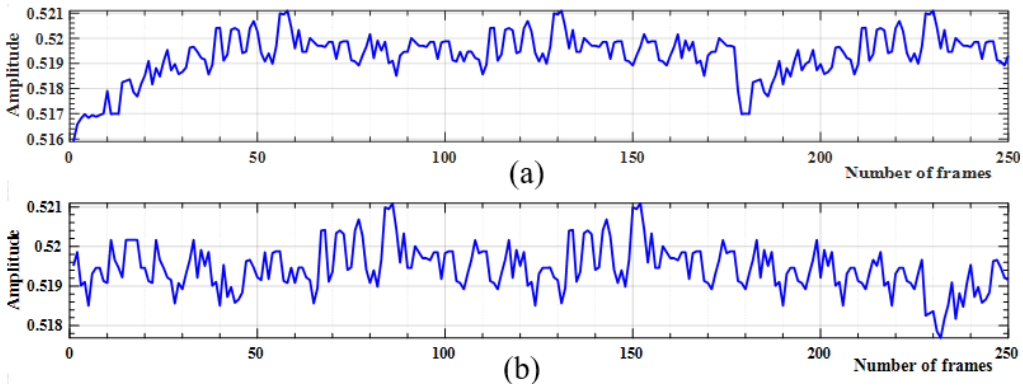


Fig. 6 Raw respiratory signals of two experiments. (a) RRface experiment; (b) RRchest experiment.

Table 1 Performance evaluation of 2 experiments.

Experiments	Select ROI region	Precision (%)	Recall (%)	F_1 Score (%)	$mAP_{(0.5)}$ (%)
First	Face	98.24	96.55	97.39	96.31
Second	Chest	96.61	98.27	97.43	96.11

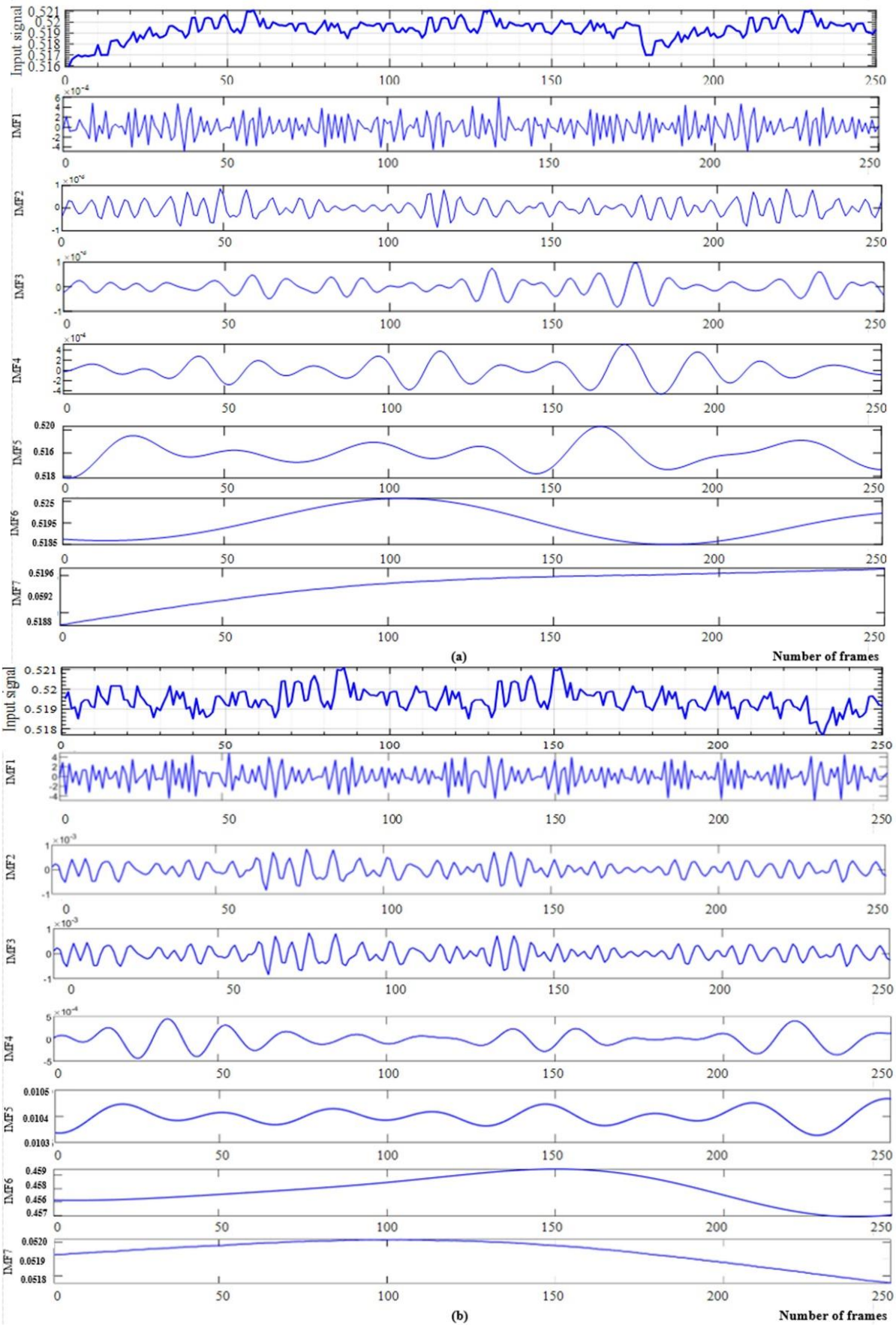


Fig. 7 IMFs component results of the raw respiratory signals. (a) RRface experiments; (b) RRchest experiment.

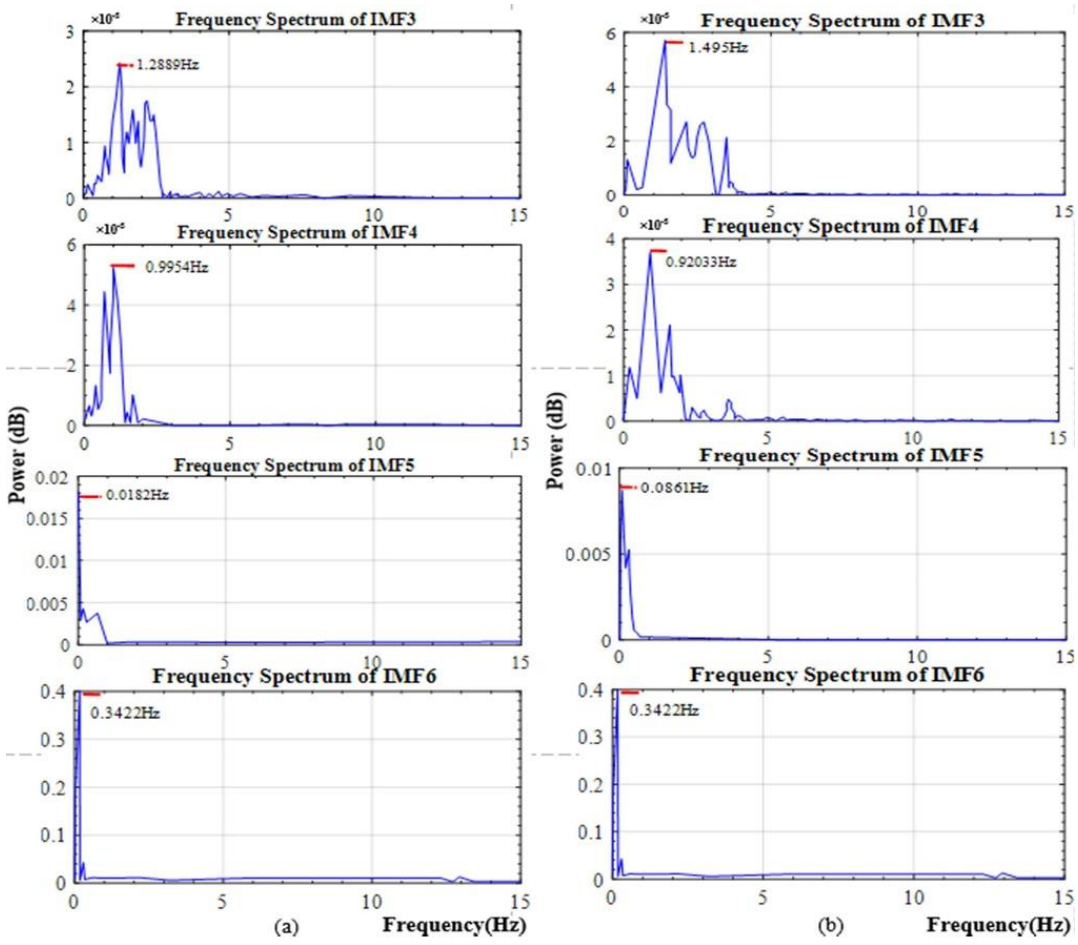


Fig. 8 Frequency spectrum analysis of IMFs. (a) RRface experiment; (b) RRchest experiment.

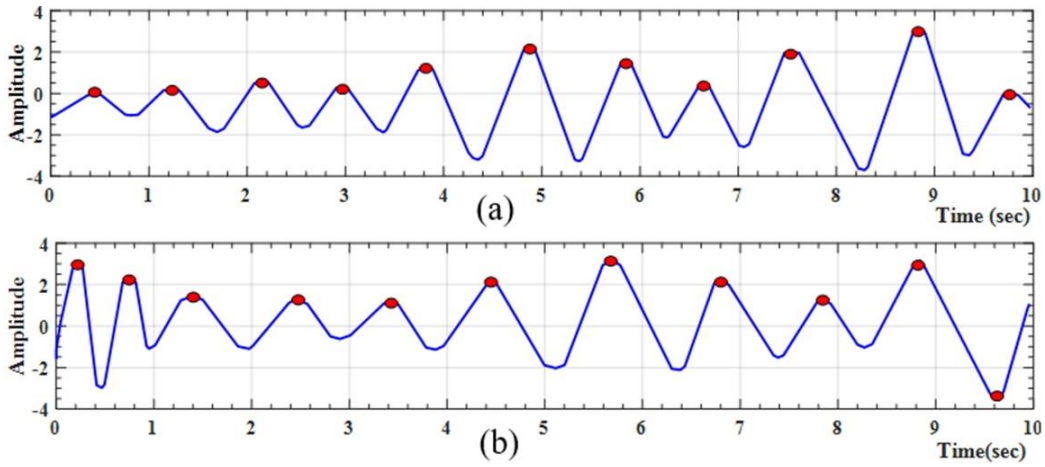


Fig. 9 Filtered respiratory signals. (a) RRface experiment; (b) RRchest experiment.

For 2 experiments, Fig. 8 displays the frequency bands of IMFs 3−6 most relevant to the respiratory range. Other spectra fall outside of this range. Typically, the breathing rate ranges between 30 and 60 breaths per min; thus, the normal frequency range of the RR measurements for newborns is approximately 0.3 Hz to 1 Hz. Therefore, we identified IMF4 (Figs. 7(a) and 8(a)) and IMF4 (Figs. 7(b) and 8(b)) for calculating the RRface experiment and the RRchest experiment, respectively.

Fig. 9(a, b) shows the results of filtered respiratory signals obtained after applying FFT, band-pass filtering, and inverse FFT, respectively. The FFT's window duration was 10 sec. The red color points indicate the peak locations of the filtered signals. The red circles indicate the peak locations of the filtered signal, as shown in Fig. 8(a) (RRface experiment) and Fig. 8(b) (RRchest experiment).

Fig. 10 shows the newborn's GUI, which includes the RR values (breaths/min) calculation from Eq. (8), the

input signal, and the filtered respiratory signal. Additionally, this proposed algorithm allows for real-time remote status monitoring of newborns and saves the RR results automatically on the computer as available medical data to aid in the future diagnosis of breathing conditions.

4.3 Statistical Analysis Measurements

To validate the performance of the proposed non-contact monitoring system from two experiments, we applied statistical analysis methods, including Pearson's correlation coefficient (PCC), Bland-Altman plots, Spearman's correlation coefficient (SCC), mean bias, and linear regression. The overall sample size was set at n = 50. Fig. 11 presents the statistical analyses for the measured readings from the RRface experiment. As shown in Fig. 10(a), the Bland-Altman analysis reveals a mean bias of −0.32 breaths/min, with 95% limits of agreement ranging from −2.75 to +2.09. The PCC and SCC between the measured and reference readings were 0.991 and 0.978, respectively. Fig. 10(b) shows that the linear regression analysis demonstrates a strong relationship between the measured readings and the linear fit, with an R^2 value of 0.9823.

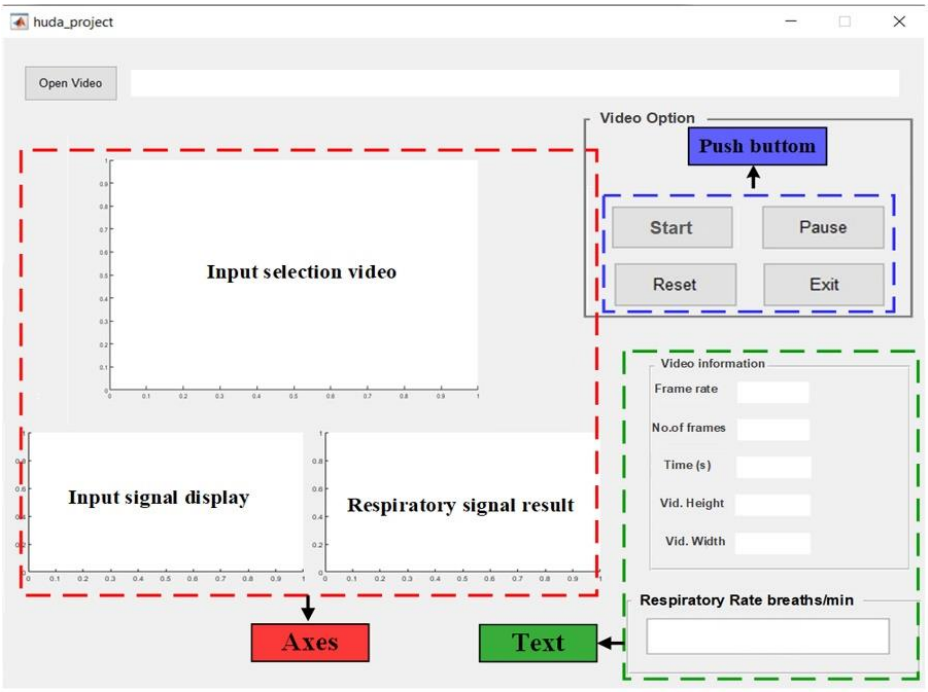
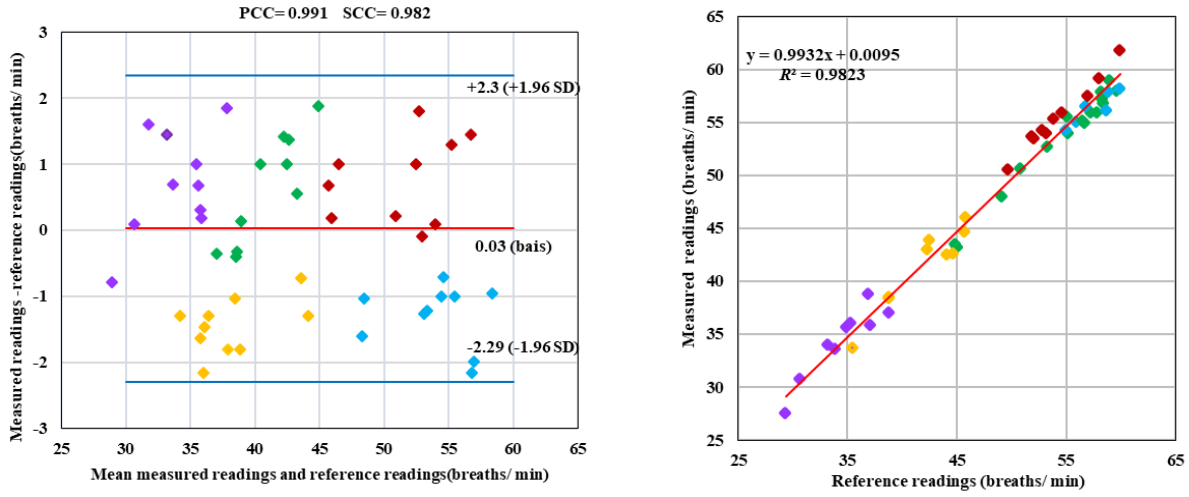


Fig. 10 Screenshot of proposed newborn's GUI.

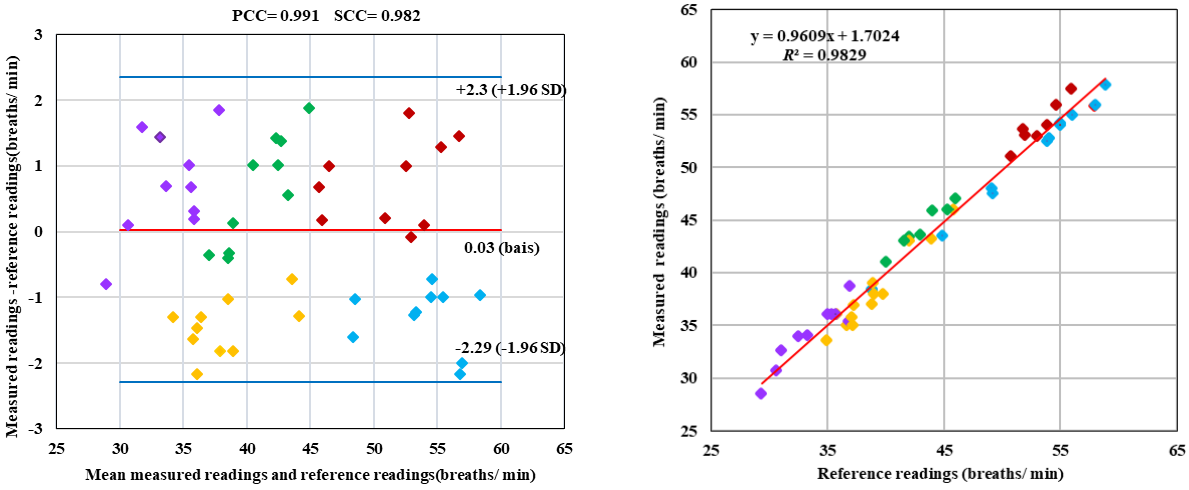


(a) (b)

Fig. 11 Statistical analyses of the RRface experiment: (a) Bland-Altman plot, (b) correlation plot. The colored dots − purple, green, orange, red, and blue − represent data visualization from the first, second, third, fourth, and fifth newborns, respectively, related to the first experiment.

In addition, Fig. 12 illustrates a statistical investigation related to measured readings from the RRchest experiment. As demonstrated in Fig. 11(a), the Bland-Altman statistics exhibit a mean bias of 0.03 breaths/min, with 95% confidence intervals ranging from −6.67 to +5.2. Also, the PCC and SCC between RR readings and reference readings were 0.991 and 0.982, respectively. As shown in Fig. 11(b), linear regression coefficients demonstrate a strong match between the measured readings and the linear fit, with R^2 = 0.983.

For each experiment, data from 5 newborns was collected, with 10 videos recorded for each newborn. To enhance data visualization, the data for each newborn were represented using uniquely colored dots, with each color corresponding to a specific newborn.



(a) (b)

Fig. 12 Statistical analyses of the RRchest experiment: (a) Bland-Altman plot, (b) correlation plot. The colored dots − purple, green, orange, red, and blue − represent data visualization from the first, second, third, fourth, and fifth newborns, respectively, related to the second experiment.

Table 2 Comparison performance of the proposed system with the techniques of previous studies.

Authors	Sensor	ROI	Technique	Region	MAE (breaths/min)	PCC, SCC
Al-Naji et al. [23]	DSLR video camera	Manually	Wavelet pyramid	Chest	1.314	0.956, 0.966
Brieva et al. [7]	digital camera EOS 1300D	Manually	Hermite	Chest	2.15	−,−
Khanam et al. [26]	digital camera Nikon D610	Automatic	EEMD	Face	2.13	0.9453, −
Jorge et al. [34]	RBG camera	−	PCA	Chest	6.9	−,−
Chen et al. [37]	Video camera	Automatic	Convolution attention network	Face	3.02	−,−
Ganfure et al. [13]	Video camera	Automatic	Lucas Kanade optical flow	Chest	15.34	−,−
Tarassenko et al. [11]	Digital camera	Manually	Auto-regressive	Face	3	−,−
McDuff et al. [38]	Digital camera of five band	Manually	ICA	Face	−	0.92, −
Brieva et al. [39]	Digital camera EOS 1300D	Automatic	Hermite Magnification	Face	1.83	0.99, 0.91
Chen et al. [4]	Canon camera	Automatic	Lomb-Scargle periodogram	Face	2.16	−,−
Al-Naji et al. [40]	Nikon D3500 camera	Manually	ICA	Face	1.44	0.872, 0.823
Our work	Canon 2000D	Automatic	EEMD	Face	1.11	0.991, 0.978
				Chest	1.03	0.991, 0.982

5 Discussion

Based on the findings obtained in this paper, it appears to be possible to remotely extract the RR values in newborns' regions (face and chest) based on non-contact automatic monitoring using a digital camera and deep learning. The YOLOV4-Tiny deep learning model enhances the system's ability to automatically select the ROI in RRface and RRchest experiments, as demonstrated in Table 1. The study utilizes the pre-trained model's important feature extraction for efficient training, significantly enhancing the model's detection speed. The most considerable challenges faced in this work can be summarized in the bellow following points:

1. The unsteady measurements of the hospital ECG monitor connected to the newborns, which were considered reference data. Consequentially, we videotaped every newborn 5 times in their most stable position.
2. Consequentially, we videotaped every newborn 5 times in their most stable position. Thus, data gathering from newborns is a time-consuming and difficult procedure.
3. Additionally, there was limited space available for camera installation, which often resulted in unequal distances between the camera and the newborns.

To assess the effectiveness of our findings from the RRface and RRchest experiments, we compared them with 10 trustworthy studies using non-contact camera-based monitoring systems. The results revealed that the proposed system performed at the minimum average MAE of 1.11 breaths/min and had high metrics in PCC and SCC of 0.991 and 0.978, respectively, for the RRface experiment. Also, we obtained the lowest minimum average MAE of 1.03 breaths/min and had excellent metrics in PCC and SCC of 0.991 and 0.982 for the RRchest experiment. From the error rate analysis above, we can deduce that the proposed algorithm based on the deep learning model significantly improves the RR evaluation accuracy compared with previous works. As a result, the proposed technique is suitable for use in hospitals or indoor healthcare monitoring.

6 Conclusions

In conclusion, this study successfully developed a non-contact automatic RR monitoring system for newborns, utilizing digital camera technology and deep learning. We introduced a fast and accurate ROI selection method based on a pre-trained YOLOV4-Tiny model to efficiently detect newborns in various challenging scenarios, with a focus on the face and chest regions. To further enhance signal quality, we employed an EEMD-based signal decomposition technique to minimize noise artifacts. Additionally, we developed a specialized GUI for newborns, providing a visual interface and comprehensive information that supports biomedical engineers in remotely monitoring vital signs in the NICU. The experimental results demonstrated a strong correlation, with PCC values of 0.991 for both RRface and RRchest, alongside low average error rates, with MAE values of 1.11 breaths/min for RRface and 1.03 breaths/min for RRchest. The system's low cost and ease of deployment make it a promising solution for real-time neonatal health monitoring. Future work will focus on enhancing system reliability by incorporating advanced signal-processing techniques and exploring a dual-camera (RGB and thermal) approach to further improve performance.

Acknowledgments

The author would like to thank the staff of the Department of Medical Instrumentation Techniques Engineering, Electrical Engineering Technical College, Middle Technical University, for their support during this work.

Disclosures

The authors have no competing interests to declare that are relevant to the content of this article.

Funding

No funding was received for conducting this study.

Author Contribution

Huda Ali Hashim: Conceptualization, Resources, Methodology, Investigation, Software, Writing - Review & Editing.

References

1. X. He, R. A. Goubran, and X. P. Liu, "Wrist pulse measurement and analysis using eulerian video magnification," 2016 IEEE-EMBS International Conference on Biomedical and Health Informatics (BHI), IEEE, 41−44 (2016).
2. A. G. Shabeeb, H. A. Hashim, and S. K. Gharghan, "Heart disease classification based on combination of PCA/ANFIS model," Research on Biomedical Engineering 40(3–4), 609–625 (2024).
3. H. A. Hashim, N. M. Ahmed, and A. G. Shabeeb, "Infant heart rate estimation based on non-contact UV photoplethysmography," Indonesian Journal of Electrical Engineering and Computer Science 31(1), 180–188 (2023).
4. M. Chen, Q. Zhu, H. Zhang, M. Wu, and Q. Wang, "Respiratory rate estimation from face videos," in 2019 IEEE EMBS International Conference on Biomedical & Health Informatics (BHI), IEEE, 1–4 (2019).
5. D. Kolosov, V. Kelefouras, P. Kourtessis, and I. Mporas, "Contactless Camera-Based Heart Rate and Respiratory Rate Monitoring Using AI on Hardware," Sensors 23(9), 4550 (2023).

6. L. Scalise, N. Bernacchia, I. Ercoli, and P. Marchionni, "Heart rate measurement in neonatal patients using a webcamera," in 2012 IEEE International Symposium on Medical Measurements and Applications Proceedings, IEEE, 1–4 (2012).
7. J. Brieva, E. Moya-Albor, O. Rivas-Scott, and H. Ponce, "Non-contact breathing rate monitoring system based on a Hermite video magnification technique," in 14th International Symposium on Medical Information Processing and Analysis 10975, 19–25 (2018).
8. A. Al-Naji, K. Gibson, S.-H. Lee, and J. Chahl, "Monitoring of cardiorespiratory signal: Principles of remote measurements and review of methods," IEEE Access 5, 15776–15790 (2017).
9. A. Al-Naji, A. G. Perera, and J. Chahl, "Remote monitoring of cardiorespiratory signals from a hovering unmanned aerial vehicle," Biomedical Engineering Online 16, 1–20 (2017).
10. W. Verkruysse, L. O. Svaasand, and J. S. Nelson, "Remote plethysmographic imaging using ambient light," Optics Express 16(26), 21434–21445 (2008).
11. L. Tarassenko, M. Villarroel, A. Guazzi, J. Jorge, D. Clifton, and C. Pugh, "Non-contact video-based vital sign monitoring using ambient light and auto-regressive models," Physiological Measurement 35(5), 807 (2014).
12. Y. Zeng, D. Yu, X. Song, Q. Wang, L. Pan, H. Lu, and W. Wang, "Camera-based cardiorespiratory monitoring of preterm infants in NICU," IEEE Transactions on Instrumentation and Measurement 73, 1–13 (2024).
13. G. O. Ganfure, "Using video stream for continuous monitoring of breathing rate for general setting," Signal, Image and Video Processing 13(7), 1395–1403 (2019).
14. J. H. Klaessens, M. Van Den Born, A. Van Der Veen, J. Sikkens-van De Kraats, F. A. Van Den Dungen, and R. M. Verdaasdonk, "Development of a baby friendly non-contact method for measuring vital signs: First results of clinical measurements in an open incubator at a neonatal intensive care unit," SPIE Proceedings 8935, 89351P (2014).
15. M.-Z. Poh, D. J. McDuff, and R. W. Picard, "Non-contact, automated cardiac pulse measurements using video imaging and blind source separation," Optics Express 18(10), 10762–10774 (2010).
16. Y. J. Chen, L.-C. Lin, S.-T. Yang, K.-S. Hwang, C.-T. Liao, and W.-H. Ho, "High-reliability non-contact photoplethysmography imaging for newborn care by a generative artificial intelligence," IEEE Access 11, 90801–90810 (2023).
17. G. Boccignone, A. D'Amelio, O. Ghezzi, G. Grossi, and R. Lanzarotti, "An evaluation of non-contact photoplethysmography-based methods for remote respiratory rate estimation," Sensors 23(7), 3387 (2023).
18. L. Svoboda, J. Sperrhake, M. Nisser, L. Taphorn, and H. Proquitté, "Contactless assessment of heart rate in neonates within a clinical environment using imaging photoplethysmography," Frontiers in Pediatrics 12, 1383120 (2024).
19. A. Al-Naji, K. Gibson, S.-H. Lee, and J. Chahl, "Real time apnoea monitoring of children using the Microsoft Kinect sensor: a pilot study," Sensors 17(2), 286 (2017).
20. L. A. M. Aarts, V. Jeanne, J. P. Cleary, C. Lieber, J. S. Nelson, S. Bambang Oetomo, and W. Verkruysse, "Non-contact heart rate monitoring utilizing camera photoplethysmography in the neonatal intensive care unit—A pilot study," Early Human Development 89(12), 943–948 (2013).
21. W. Wang, S. Stuijk, and G. De Haan, "A novel algorithm for remote photoplethysmography: Spatial subspace rotation," IEEE Transactions on Biomedical Engineering 63(9), 1974–1984 (2015).
22. H. Hashim, S. Mohammed, and S. Gharghan, "Accurate localization of elderly people based on neural and wireless sensor networks," ARPN Journal of Engineering and Applied Sciences 14(11), 3777–3789 (2019).
23. A. Al-Naji, J. Chahl, "Remote respiratory monitoring system based on developing motion magnification technique," Biomedical Signal Processing and Control 29, 1–10 (2016).
24. F. K. Lucy, K. T. Suha, S. T. Dipty, M. S. I. Wadud, and M. A. Kadir, "Video based non-contact monitoring of respiratory rate and chest indrawing in children with pneumonia," Physiological Measurement 42(10), 105017 (2021).
25. B. Olmi, C. Manfredi, L. Frassineti, C. Dani, S. Lori, G. Bertini, S. Gabbanini, and A. Lanata, "Aggregate channel features for newborn face detection in neonatal intensive care units," in 44th Annual International Conference of the IEEE Engineering in Medicine & Biology Society (EMBC), 455–458 (2022).
26. F.-T.-Z. Khanam, A. G. Perera, A. Al-Naji, K. Gibson, and J. Chahl, "Non-contact automatic vital signs monitoring of infants in a neonatal intensive care unit based on neural networks," Journal of Imaging 7(8), 122 (2021).
27. Z. Jiang, L. Zhao, S. Li, and Y. Jia, "Real-time object detection method based on improved YOLOv4-tiny," arXiv preprint arXiv:2011.04244 (2020).
28. Y. Yuliza, R. Muwardi, M. Rhozaly, L. Lenni, M. Yunita, and G. Yehezkiel, "Fast human recognition system on real-time camera," Jurnal Ilmiah Teknik Elektro Komputer dan Informatika 9(4), 895–903 (2023).
29. X. Li, J. Pan, F. Xie, J. Zeng, Q. Li, X. Huang, D. Liu, and X. Wang, "Fast and accurate green pepper detection in complex backgrounds via an improved Yolov4-tiny model," Computers and Electronics in Agriculture 191, 106503 (2021).
30. R. Zhu, L. Zhao, "Research and application of face mask detection algorithm based on YOLOV4-tiny," Academic Journal of Computing & Information Science 5(1), 64–69 (2022).
31. S. Hraybi, M. Rizk, "Examining YOLO for real-time face-mask detection," IET Conference Proceedings 2021(11), 571–575 (2022).

32. A. Bochkovskiy, C.-Y. Wang, and H.-Y. M. Liao, "Yolov4: Optimal speed and accuracy of object detection," arXiv preprint arXiv:2004.10934 (2020).
33. S. Chaichulee, M. Villarroel, J. Jorge, C. Arteta, G. Green, K. McCormick, A. Zisserman, and L. Tarassenko, "Multi-task convolutional neural network for patient detection and skin segmentation in continuous non-contact vital sign monitoring," in 12th IEEE International Conference on Automatic Face & Gesture Recognition (FG 2017), 266–272 (2017).
34. J. Jorge, M. Villarroel, S. Chaichulee, K. McCormick, and L. Tarassenko, "Data fusion for improved camera-based detection of respiration in neonates," Optical Diagnostics and Sensing XVIII: Toward Point-of-Care Diagnostics 10501, 215–224 (2018).
35. A. Y. Abdulrazzak, S. L. Mohammed, A. Al-Naji, and J. Chahl, "Real-time jaundice detection in neonates based on machine learning models," BioMedInformatics 4(1), 623–637 (2024).
36. Z. Wu, N. E. Huang, "Ensemble empirical mode decomposition: a noise-assisted data analysis method," Advances in Adaptive Data Analysis 1(01), 1–41 (2009).
37. W. Chen, D. McDuff, "Deepphys: Video-based physiological measurement using convolutional attention networks," Proceedings of the European Conference on Computer Vision (ECCV), 349–365 (2018).
38. D. McDuff, S. Gontarek, and R. W. Picard, "Improvements in remote cardiopulmonary measurement using a five band digital camera," IEEE Transactions on Biomedical Engineering 61(10), 2593–2601 (2014).
39. J. Brieva, H. Ponce, and E. Moya-Albor, "A contactless respiratory rate estimation method using a hermite magnification technique and convolutional neural networks," Applied Sciences 10(2), 607 (2020).
40. A. Al-Naji, J. Chahl, "Remote optical cardiopulmonary signal extraction with noise artifact removal, multiple subject detection & long-distance," IEEE Access (6), 11573−11595 (2018).

Light Dose and Fluorescence Imaging Depth in Dual-Wavelength PDT: a Numerical Study for Various Photosensitizer Distributions in a Layered Biotissue

Daria Kurakina*, Ekaterina Sergeeva, Aleksandr Khilov, and Mikhail Kirillin
A.V. Gaponov-Grekhov Institute of Applied Physics of the Russian Academy of Sciences, 46 Ulyanov str., Nizhny Novgorod 603950, Russian Federation
*e-mail: daria.kurakina@ipfran.ru

Abstract. Dual-wavelength photodynamic therapy (PDT) in combination with fluoescence monitoring has great potential in medical applications, in particular, in the treatment of skin diseases. In this study we conducted numerical Monte Carlo experiments in a two-layer skin model to simulate the absorbed light dose distribution for PDT with chlorin-based photosensitizers as well as to estimate the fluorescence imaging depth depending on the probing radiation wavelength and the photosensitizer (PS) in-depth distribution. The obtained dependencies provide a detailed overview of the light absorption profile and fluorescence signal formation for different PS distribution in layered biotissues, and can be used in various fluorescence based light dosimetry techniques. © 2024 Journal of Biomedical Photonics & Engineering.

Keywords: chlorin-based photosensitizers; photodynamic therapy; fluorescence imaging; light transport in biotissue; Monte Carlo simulations.

Paper #9186 received 25 Oct 2024; revised manuscript received 27 Nov 2024; accepted for publication 29 Nov 2024; published online 27 Dec 2024. doi: 10.18287/JBPE24.10.040318.

1 Introduction

Photodynamic therapy (PDT) is a modern non-invasive therapeutic method used for treatment of a wide range of tumor and non-oncologic pathologies via externally stimulated cytotoxic effects, tumor vascular damage, as well as immune responses [1−3]. PDT procedure is based on the administration of a photosensitizer (PS) and its accumulation in the target tissue followed by illumination by light of an appropriate wavelength causing production of cytotoxic agents [1−3]. The success of a PDT procedure depends on local concentration of cytotoxic agents which is affected by the PS concentration, light transport in the tissue and tissue oxygenation [4]. According to modern PDT protocols, only the PS dose administered to a patient and the light energy delivered to the surface of the biological tissue during the procedure are specified at the stage of the treatment planning [4]. This limited set of parameters does not consider such individual features as heterogeneous PS accumulation and non-uniform distribution of optical radiation in biological tissues of various localizations. Thus, in regard with the current trends towards personalized medicine, individualization of the PDT procedure scheme at the stage of its planning is an urgent problem.

For PSs with high absorption in different bands of visible spectrum, PDT can be performed at several wavelengths. Chlorin-based photosensitizers are a wide class of PDT agents with two pronounced absorption peaks located in the blue and red bands of the visible spectrum (402 and 662 nm, respectively). Optical properties of biotissues at these therapeutic wavelengths differ significantly [5]: for most biotissues subjected to PDT (superficial and mucous biotissues) both the absorption and scattering coefficients at $\lambda = 402$ nm are several times higher than those at $\lambda = 662$ nm [5−7], which leads to different penetration depth of therapeutic light for these two wavelengths and thus, to the difference in the PDT impact area. Therefore, development of multi-wavelength PDT protocols may benefit from combining the effects of exposure at several wavelengths to ensure the effect over wide depth.

Treatment of skin diseases is an essential part of PDT applications with specific requirements for light dosimetry. Skin is a layered structure with epidermal, dermal and hypodermal layers that are characterized by

specific values of thickness and optical properties. These characteristics can significantly deviate for diseased versus normal skin [8]. In the case of non-uniform tissue, determination of light fluence distribution in biotissue is a challenge. Light dosimetry problem for PDT has been studied previously using analytical or numerical approaches, however, they are mainly limited by the case of uniform biotissue [9, 10]. Direct interstitial measurements of light fluence rate [11, 12] are invasive and low informative in terms of providing volumetric information. Monte Carlo simulation technique [13] is the most promising approach for modeling the propagation of light in biotissue with complex structure. The simulation consists in tracing the large number of random photon trajectories for a given probing configuration in the medium with predefined optical properties followed by statistical processing of the obtained data. This approach makes it possible to estimate PDT impact volume for the specified optical properties of the medium, tissue geometry, and the procedure mode, by calculating the absorbed light dose distribution. In Ref. [14−15] numerical Monte Carlo simulations of fluence in multilayer skin are carried out for one [14] or several [15] wavelengths followed by its implementation into PDT pharmacokinetics mathematical model to evaluate the production of singlet oxygen. In Ref. [16], using Monte Carlo simulation of a PDT procedure, the effect of tumor density heterogeneity on the distribution of light and photodynamic dose is investigated. In paper [17], based on Monte Carlo simulation of the irradiation distribution, dose-volume histograms are obtained which demonstrate the fraction of the organ volume receiving particular level of light dose.

In order to improve the efficiency of a PDT procedure and to obtain additional information about the tissue in the course and in the follow-up of the procedure, optical imaging techniques are used [3, 18]. Fluorescence properties of most PSs make it possible to employ fluorescence imaging (FI) techniques to monitor PS distribution in tissues [19−21]. Broad-beam excited FI allows for monitoring the accumulation of PS in biological tissue prior to the PDT procedure, as well as evaluating the PS photobleaching during PDT [22, 23] that can serve as a dosimetric indicator of the procedure effectiveness [24−28]. In monitoring the PDT procedure with the chlorin-based PSs characterized by two absorption peaks, dual-wavelength fluorescence imaging allows to analyze information from different depths simultaneously due to different localization of fluorescence excited at 402 nm and at 662 nm [19−21], while the thickness of the PS distribution can be estimated by the ratio of fluorescence signals at two excitation wavelengths [29, 30].

At the same time, the question arises whether the depth from which the fluorescence is registered is the depth where it has been emitted. Due to isotropic fluorescence emission and further stochastic behavior of light in biotissue, the depth from which the fluorescence is registered in explicit dosimetry PDT systems is challenging to predict and it cannot be measured directly. The maximum depth from which the fluorescence photons are detected (further called “FI depth”) depends on the optical properties of the tissue and on the way of PS administration, being an important characteristic for further optimization of the fluorescence monitoring technique. Monte Carlo approach is widely utilized for modeling fluorescence distribution in biological media [5, 31−35]. It is a convenient tool for tracing individual trajectories of the detected fluorescence photons and it can be used to analyze their depth distribution. In Ref. [35] numerical investigation of fluorescence probing depth dependence on the source-detector separation is conducted for a configuration of a surface contact probe equipped with multiple detector fibers. However, studies of signal formation in fluorescence imaging with several excitation wavelengths are quite limited [19−21, 36, 37].

The aim of this work is to perform numerical experiments in a two-layer biotissue mimicking skin with epidermal and dermal layers to simulate the distribution of the absorbed light dose for PDT with chlorin-based photosensitizers, as well as to estimate the FI depth in dependence on the probing radiation wavelength and the PS distribution pattern.

2 Materials and Methods

2.1 Monte Carlo Simulations

2.1.1 Distribution of the Excitation Light Absorption

In this study we used our previously reported code [20] which was adopted and employed for simulation of signal formation in a system for widefield surface FI [29]. The feature of this code is that all photons are processed in parallel in contrast to a conventional MC algorithm with consequent calculations. Biotissue is considered as a slab of scattering and absorbing medium which is illuminated by a wide beam from its upper boundary $z = 0$ along z direction. The slab consists of two layers with differing optical properties: thin topical layer mimicking epidermis and thick layer mimicking dermis. To calculate a three-dimensional distribution of the absorbed dose $A(x, y, z, \lambda_{ex})$ of light with the wavelength λ_{ex}, at each *n*-th step of modeling and for each photon the absorbed fraction of the photon weight was added to the corresponding voxel of the absorption map array:

$$A^n(x, y, z, \lambda_{ex}) = A^{n-1}(x, y, z, \lambda_{ex}) + \\ + \sum_i w_i \frac{\mu_a(x, y, z, \lambda_{ex})}{\mu_a(x, y, z, \lambda_{ex}) + \mu_s(x, y, z, \lambda_{ex})}, \quad (1)$$

where w_i is the current weight of the *i*-th photon located in a voxel with the center coordinates (x, y, z) at step *n*, $\mu_a(x, y, z, \lambda_{ex})$ and $\mu_s(x, y, z, \lambda_{ex})$ are local absorption and scattering coefficients of the medium in this voxel. Eq. (1) implies that all the photons are processed in parallel and at each step of the simulations the absorbed weight fractions of all the propagating photons are

summed up within a given voxel. Local optical properties account for contribution of a background biological tissue (epidermis or dermis) and of a photosensitizer. We assumed that the background biotissue was transversely homogeneous with parameters $\mu_a^{tissue}(z,\lambda_{ex})$ and $\mu_s^{tissue}(z,\lambda_{ex})$, while non-uniformly distributed PS was manifested by the additive term to the local absorption coefficient as in Refs. [29, 38, 39]:

$$\begin{aligned}&\mu_a(x,y,z,\lambda_{ex}) = \mu_a^{PS}(x,y,z,\lambda_{ex}) + \mu_a^{tissue}(z,\lambda_{ex});\\&\mu_s(x,y,z,\lambda_{ex}) = \mu_s^{tissue}(z,\lambda_{ex}).\end{aligned} \quad (2)$$

Here $\mu_a^{PS}(x,y,z,\lambda_{ex}) = \sigma_{a,PS}(\lambda_{ex})C_{PS}(x,y,z)$ is the absorption coefficient of PS with the absorption cross-section $\sigma_{a,PS}(\lambda_{ex})$ and volume concentration distribution $C_{PS}(x,y,z)$.

To simulate the formation of fluorescence signal, we employed previously developed dual-stage algorithm [20, 29, 40]. At the first stage of Monte Carlo simulation, the map of absorbed light dose $A(x,y,z,\lambda_{ex})$ was calculated for the considered optical properties, particular PS distribution in the tissue and the irradiation wavelength. Further this map was recalculated to generate the light dose density $A^{PS}(x,y,z,\lambda_{ex})$ absorbed directly by the PS using the ratio of local PS absorption coefficient to the total one:

$$\begin{aligned}&A^{PS}(x,y,z,\lambda_{ex}) =\\&= A(x,y,z,\lambda_{ex})\frac{\mu_a^{PS}(x,y,z,\lambda_{ex})}{\mu_a^{PS}(x,y,z,\lambda_{ex})+\mu_a^{tissue}(z,\lambda_{ex})},\end{aligned} \quad (3)$$

The values of $A(x,y,z,\lambda_{ex})$ and $A^{PS}(x,y,z,\lambda_{ex})$ are measured in photons. To transform them into volumetric distributions of fractional absorbed dose one should normalize the corresponding characteristics by the value of $A_0 = N_{ph}\,\Delta V$ [photons·mm^3] where N_{ph} is the number of excitation photons and $\Delta V = \Delta x\Delta y\Delta z$ is the volume of an elementary voxel with the sizes Δx, Δy, and Δz.

For PDT planning, it is more practical to analyze one-dimension in-depth distribution of energy absorbed by a PS only (Eq. (3)) that allows to evaluate the impact depth for PDT at the particular irradiation wavelength. It can be calculated by transversal integration of the normalized PS absorption dose within an elementary layer at the depth z:

$$\begin{aligned}&\bar{A}^{PS}(z,\lambda_{ex}) = \sum_{x,y}\frac{A^{PS}(x,y,z,\lambda_{ex})}{A_0}\Delta x\Delta y =\\&= \frac{1}{N_{ph}\Delta z}\frac{\mu_a^{PS}(z,\lambda_{ex})}{\mu_a^{PS}(z,\lambda_{ex})+\mu_a^{tissue}(z,\lambda_{ex})}\sum_{x,y}A(x,y,z,\lambda_{ex})\end{aligned} \quad (4)$$

and is measured in inverse millimeters. Another key parameter that cannot be measured directly is the dimensionless fraction of energy $\bar{A}_\Sigma^{PS}(Z,\lambda_{ex})$ absorbed by the PS in a layer of a thickness Z measured from the surface of the tissue which is calculated by the integral:

$$\bar{A}_\Sigma^{PS}(Z,\lambda_{ex}) = \sum_{z=0}^{Z}\bar{A}^{PS}(z,\lambda_{ex})\Delta z. \quad (5)$$

2.1.2 Distribution of Fluorescence

At the second stage the PS absorption map $A^{PS}(x,y,z,\lambda_{ex})$ served as a distribution of fluorescence emission sources. The emission of fluorescence photons was assumed isotropic with quantum yield equal to 1 for simplicity. As we are interested not in absolute values of fluorescence but in weights distribution, the magnitude of quantum yield is not critical. In the evaluation of absolute fluorescence, real value of quantum yield amounting 0.1−0.2 [41] for chlorin-based PSs can be easily introduced by the corresponding multiplicative factor. Surface distribution of fluorescence intensity $I_{fl}(x,y,z=0,\lambda_{ex},\lambda_{em})$ [1/mm^2] can be calculated as:

$$\begin{aligned}&I_{fl}(x,y,z=0,\lambda_{ex},\lambda_{em}) =\\&= \frac{1}{N_{ph}\Delta S}\sum_{x',y',z'} I_{em}(x',y',z',x,y,z=0,\lambda_{ex},\lambda_{em}),\end{aligned} \quad (6)$$

where $I_{em}(x',y',z',x,y,z=0,\lambda_{ex},\lambda_{em})$ is the weight of fluorescence photons with the wavelength λ_{em} that are launched isotopically from the center of an elementary voxel with coordinates (x',y',z') having the initial weight equal to $A^{PS}(x',y',z',\lambda_{ex})$ and leave the biotissue through an elementary pixel $\Delta S = \Delta x\Delta y$ with coordinates (x,y) at the tissue surface $z=0$.

Along with the fluorescence signal from a distributed source, the following parameters for all detected fluorescence photons were recorded: the maximum depth z_j^{max} reached by *j*-th fluorescence photon in the medium ("FI depth") and the photon weight w_j when it exits the biotissue. The weight distribution over the FI depth $W^d(z_{max})$ for photons detected at the boundary $z=0$ from all directions and collected at the whole sample surface was binned according to the following Eq.:

$$\begin{aligned}&W^d(z_{max}) = \sum_{j=1}^{N} w_j\,\{z_j^{max}\in(z_{max},z_{max}+\Delta z]\},\\&z_{max} = k\Delta z, \qquad k = 0,\dots N_k-1,\end{aligned} \quad (7)$$

where each *k*-th bin contains the summed weight of the photons with FI depth within the bin edges $(z_{max}, z_{max}+\Delta z]$, N is the total number of fluorescence photons that have reached the tissue surface, Δz is the bin size, N_k is the total number of bins. The effective FI depth was calculated as the median value $\tilde{z}_{max}$ of the corresponding distribution $W^d(z_{max})$.

2.2 Simulation Parameters

We aim to model light distribution during a PDT procedure of various skin diseases. There are two ways in PS administration in this task. Topical application is used in lesions that affect mainly epidermis so therapeutic impact is localized above basal membrane which is almost impenetrable for a PS. In the therapy of malignant lesions deeper impact is required so intravenous injection of a PS is implemented according to the protocol. We further considered three models of in-depth PS concentration

distribution $C_{PS}(z)$ in biological tissue mimicking skin (Fig. 1) similar to those previously discussed in paper [29]: (i) boxcar PS distribution in the upper tissue layer of a given thickness d_E (a simplified topical application model assuming the PS is uniformly distributed over the whole epidermis thickness d_E); (ii) uniform PS distribution in a subsurface tissue covered by a PS-free layer of a given thickness d_E (an intravenous injection model assuming PS accumulation below epidermis due to blood flow); (iii) exponential in-depth decay of PS concentration in a two-layer tissue (a refined topical application model assuming realistic PS penetration through upper layers, i.e. stratum corneum and epidermis).

In distributions (i) and (ii), the PS absorption coefficient corresponding to the constant level of the drug concentration was denoted as $\mu_a^{PS}(\lambda_{ex})$. In distribution (iii), the PS absorption coefficient profile was set in accordance with the following Eq.:

$$\mu_{a,exp}^{PS}(z,\lambda_{ex}) = \frac{M_0(\lambda_{ex})}{d_{1/e}} \exp\left(-\frac{z}{d_{1/e}}\right), \qquad (8)$$

where $M_0(\lambda_{ex}) = \sigma_a^{PS}(\lambda_{ex}) \cdot \Xi$ is a dimensionless parameter equal to the product of the PS absorption cross-section ($\sigma_a^{PS}(\lambda_{ex})$) and the PS surface density (Ξ) at the moment of its application on the tissue, $d_{1/e}$ is a spatial scale of PS concentration decrease with depth. This model is more accurate approximation for the topical application case [42, 43] which allows for tracking the dynamics of the PS penetration if the dependence of $d_{1/e}$ on time is given.

In order to study spatial distribution of the absorbed light and the FI depth distribution in the task of dual-wavelength PDT for all PS concentration models (further denoted as Case (i), Case (ii) and Case (iii), correspondingly), we conducted simulations of light propagation at two excitation wavelengths λ_{ex} = 405 nm and 660 nm typically used in PDT with chlorin-based PSs. Fluorescence from chlorin-based PS in dual-wavelength systems is typically detected at the wavelengths red shifted from the emission peak at 665 nm to avoid a cross-talk with the reflected red-excitation light [20]. In our simulations the PS fluorescence was modeled for the emission wavelength of 760 nm equal to that in the custom-designed dual-wavelength FI setup [20].

Total amount of $N_{ph} = 10^7$ excitation photons was used in the simulations. The sample was illuminated from the top normal to the surface by a circular beam with radius of 9 mm and uniform intensity distribution. Transverse dimensions of the sample were set to 20 mm × 20 mm, its thickness was 20 mm, and the size of an elementary voxel equaled 0.25 mm × 0.25 mm × 0.01 mm. The value of d_E in the distributions (i) and (ii) varied in the range of 0.05–1 mm in accordance with the data on epidermis thickness in norm and pathology in different skin types [44–47], the value of $d_{1/e}$ in the distribution (iii) varied in the range of 0.1–1 mm. Optical properties of epidermis and dermis were set in accordance with the data in Ref. [8] and are presented in Table 1 for the considered excitation and emission wavelengths (405 nm, 660 nm, and 760 nm). The values of the PS absorption coefficient $\mu_a^{PS}(\lambda)$ in Cases (i) and (ii) corresponded to the constant concentration level of Revixan® Derma of 0.1% vol that was achieved by *in vivo* topical administration of 1 μg/g [48, 49]. The value of $M_0(\lambda_{ex})$ was chosen so that the surface absorption coefficient $\mu_{a,exp}^{PS}(0,\lambda_{ex}) = M_0(\lambda_{ex})/d_{1/e}$ was of the same order as the corresponding $\mu_a^{PS}(\lambda)$ for the first two cases. The value of scattering anisotropy factor was set as g = 0.8 for all wavelengths as we assumed that the effects of small-angle scattering related to the shape of a scattering phase function were insignificant.

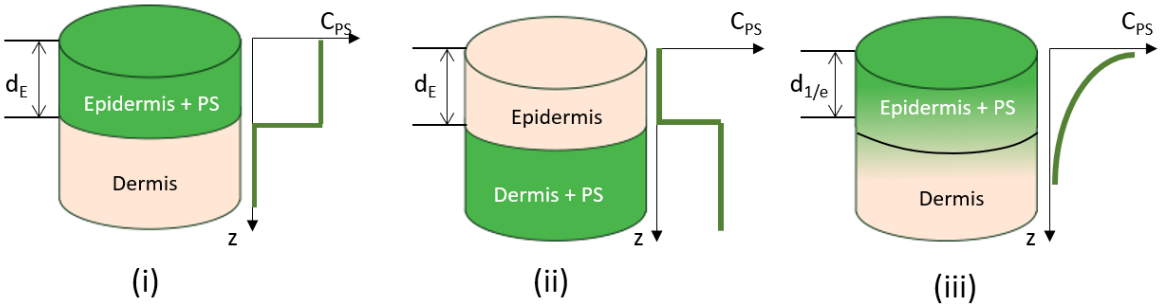


Fig. 1 Considered spatial PS distribution models with different in-depth profiles: topical application model (Case (i)), intravenous injection model (Case (ii)), refined topical application model (Case (iii)). Here d_E is the thickness of epidermis, $d_{1/e}$ is the $1/e$ scale of exponential PS concentration distribution.

Table 1 Optical properties of epidermal (E) and dermal (D) skin layers and chlorin-based PS used in simulations.

Wavelength, nm	μ_a^{PS}, mm^{-1}	M_0	μ_a^E, mm^{-1}	μ_s^E, mm^{-1}	μ_a^D, mm^{-1}	μ_s^D, mm^{-1}	g
405	0.10	0.020	1.25	50	0.9	38	0.8
660	0.02	0.004	0.26	22	0.14	14	0.8
760	0	0	0.2	14	0.13	12	0.8

3 Results and Discussion

3.1 Absorbed Light Dose Distribution

Fig. 2 shows $\log_{10}$ of normalized absorbed light dose distribution $A(x, y = 0, z, \lambda_{ex})/A_0$. The maps are plotted for a boxcar PS distribution (i) with the thickness of $d_E = 0.2$ mm and two irradiation wavelengths λ_{ex} of 405 nm and 660 nm. Due to significant dependence of skin optical properties on the wavelength (see Table 1), for $\lambda_{ex} = 405$ nm the light is primarily absorbed in superficial tissue layer, while for $\lambda_{ex} = 660$ nm deeper layer is involved. Central part of the maps represents distribution of absorbed dose over depth which can be used for planning PDT procedures with chlorin-based PS in skin.

Fig. 3a shows in-depth profiles of the PS-absorbed dose $\bar{A}^{PS}(z, \lambda_{ex})$ calculated with Eq. (4) for different thicknesses d_E of epidermis containing uniformly distributed PS and for two excitation wavelengths λ_{ex} of 405 nm and 660 nm (Case (i)). Smaller values of d_E correspond to normal thickness of epidermis while larger ones, to the cases of its pathological thickening, e.g., for actinic keratosis [44, 45]. Fig. 3b depicts the dependences of absorbed energy fraction $\bar{A}_{\Sigma}^{PS}(Z, \lambda_{ex})$ calculated with Eq. (5) for the same PS distribution. Faster accumulation of total light dose delivered with blue light compared to that for red light is shown.

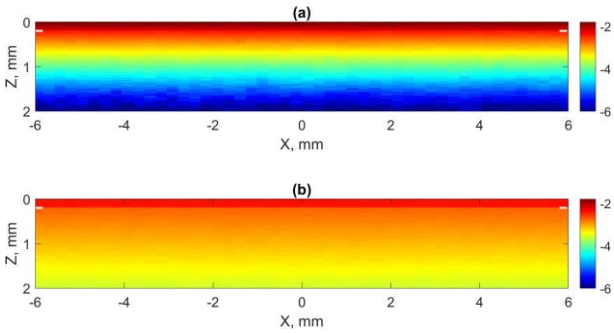


Fig. 2 Log_{10} of normalized volume density of the absorbed energy fraction $A(x, y = 0, z, \lambda_{ex})/A_0$ in the biotissue containing PS uniformly distributed in epidermis (d_E =0.2 mm) for irradiation wavelengths of (a) 405 nm and (b) 660 nm. White dashes show the boundary of the PS containing layer.

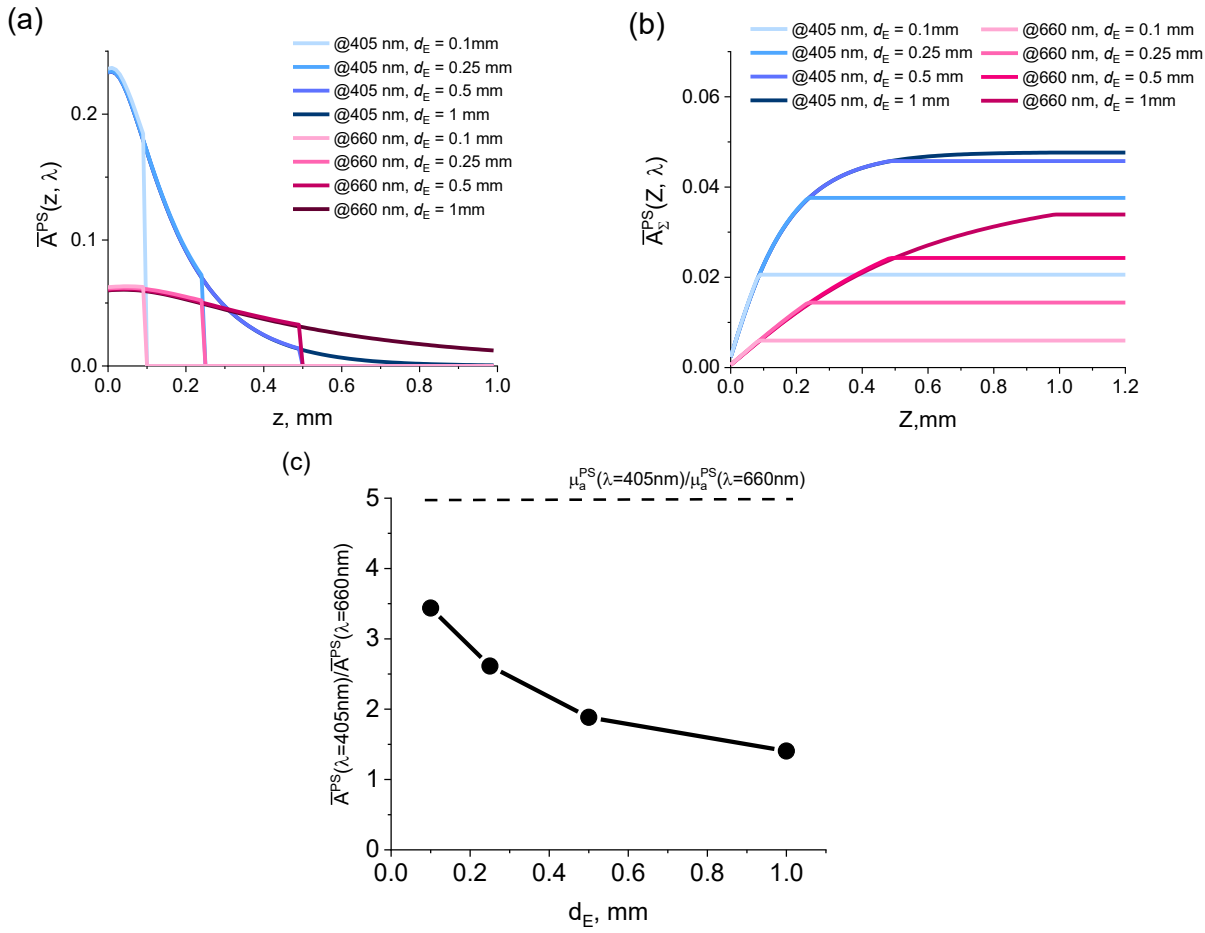


Fig. 3 (a) In-depth distribution of energy $\bar{A}^{PS}(z, \lambda_{ex})$ absorbed by a PS uniformly distributed in a topical (epidermal) layer of a thickness d_E for the irradiation wavelengths of 405 nm and 660 nm; (b) fraction of energy $\bar{A}_{\Sigma}^{PS}(Z, \lambda_{ex})$ absorbed by a PS in a superficial layer of tissue versus the layer thickness Z. (c) Ratio of total light doses absorbed at $\lambda_{ex} = 405$ nm to that absorbed at $\lambda_{ex} = 660$ nm as the function of the PS layer thickness.

For the given PS concentration total absorbed energy fraction does not exceed units of percent. Similar to the plots in Fig. 3a, Fig. 3b shows that the dose accumulation stops at the depth Z equal to the thickness of the PS-containing layer d_E. Note that the ratio of total doses absorbed at different wavelengths for the same PS distribution (Fig. 3c) is not equal to the ratio of the PS absorption coefficients at these two wavelengths ($\frac{\mu_a^{PS}(405\ nm)}{\mu_a^{PS}(660\ nm)} = 5$) and decreases with the increase of the PS layer thickness.

In Fig. 4 density profile of the PS-absorbed light dose and absorbed energy fraction are shown for Case (ii) mimicking intravenous injection with a uniformly distributed PS in a subsurface slab of biotissue covered by a PS-free layer (epidermis) of thickness d_E. The absorption profile (Fig. 4a) shows a jump at the depth equal to d_E while the curve shape is determined by the optical properties of dermal tissue. Fig. 4b demonstrates the dependences of absorbed dose $\bar{A}_\Sigma^{PS}(Z, \lambda_{ex})$ for Case (ii) showing the behavior of the curves for 405 nm and 660 nm similar to Case (i). Absorbed dose of light at the wavelength of 660 nm is comparable or even exceeds that at the wavelength of 405 nm except the case of the smallest d_E value.

The same set of curves is plotted for the case of exponential PS distribution in the two-layer biotissue (Case (iii)) for different values of $d_{1/e}$ (Fig. 5). The increase of $d_{1/e}$ mimics the dynamics of in-depth redistribution of a PS after topical application. During this process the fraction of the PS in superficial layers decreases and its fraction in deeper layers grows, however total amount of PS is constant. Despite that, total absorbed light doses that correspond to the asymptotic values in Fig. 5b decrease with $d_{1/e}$, which is caused by light attenuation. Also, the accumulated doses reach the asymptotic values faster (Fig. 5b) as compared to Case (i) with uniform PS distribution within epidermis (Fig. 3b).

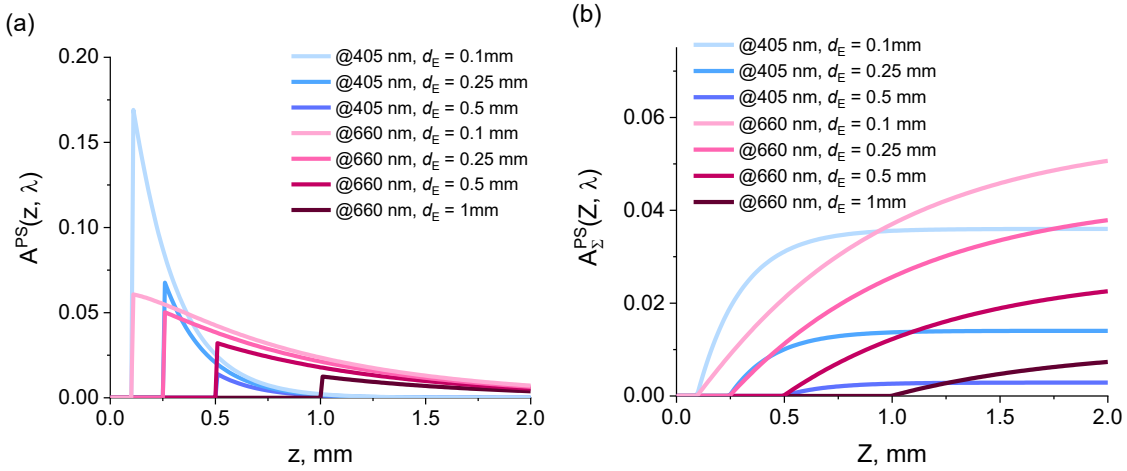


Fig. 4 (a) In-depth distribution of light dose $\bar{A}^{PS}(z, \lambda_{ex})$ absorbed by a PS uniformly distributed below a topical (epidermal) layer of a thickness d_E for the irradiation wavelengths of 405 nm and 660 nm; (b) fraction of light dose $\bar{A}_\Sigma^{PS}(Z, \lambda_{ex})$ absorbed by a PS in a superficial layer of tissue versus the layer thickness Z.

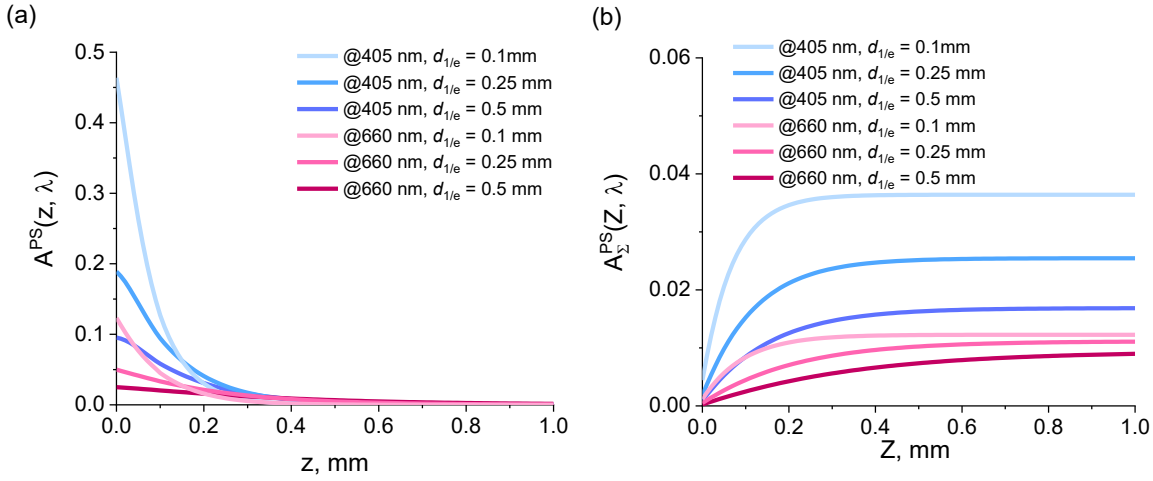


Fig. 5 (a) In-depth distribution of light dose $\bar{A}^{PS}(z, \lambda_{ex})$ absorbed by a PS distributed exponentially with different values of $d_{1/e}$ for the irradiation wavelengths of 405 nm and 660 nm; (b) fraction of light dose $\bar{A}_\Sigma^{PS}(Z, \lambda_{ex})$ absorbed by a PS in superficial layer of tissue versus the layer thickness Z.

3.2. Fluorescence Imaging Depth

Based on the PS fluorescence excitation at two wavelengths from different spectral ranges, dual-wavelength FI provides the capability to measure the PS localization depth using the ratio of the detected fluorescence signals [19, 20, 29, 38]. In order to analyze the fluorescence signal formation in dual-wavelength FI, one should figure out from which volume the signal is detected for the considered excitation wavelength. This characteristic is statistically related to the maximum depth (FI depth) reached in the medium by the photons which contribute to the detected fluorescence.

Fig. 6 shows distribution of fluorescence photon weights over maximum depths $W^d(z_{max})$ calculated with Eq. (7) for all three models of PS distribution (Cases (i)−(iii)) at two excitation wavelengths. The widths of the distributions for $\lambda_{ex} = 405$ nm and $\lambda_{ex} = 660$ nm noticeably differ which is explained by a much smaller number of absorbed photons that generate fluorescence at a large depth for blue light compared to red light. As a result, the distribution maxima for $\lambda_{ex} = 405$ nm are located closer to the tissue surface than those for $\lambda_{ex} = 660$ nm.

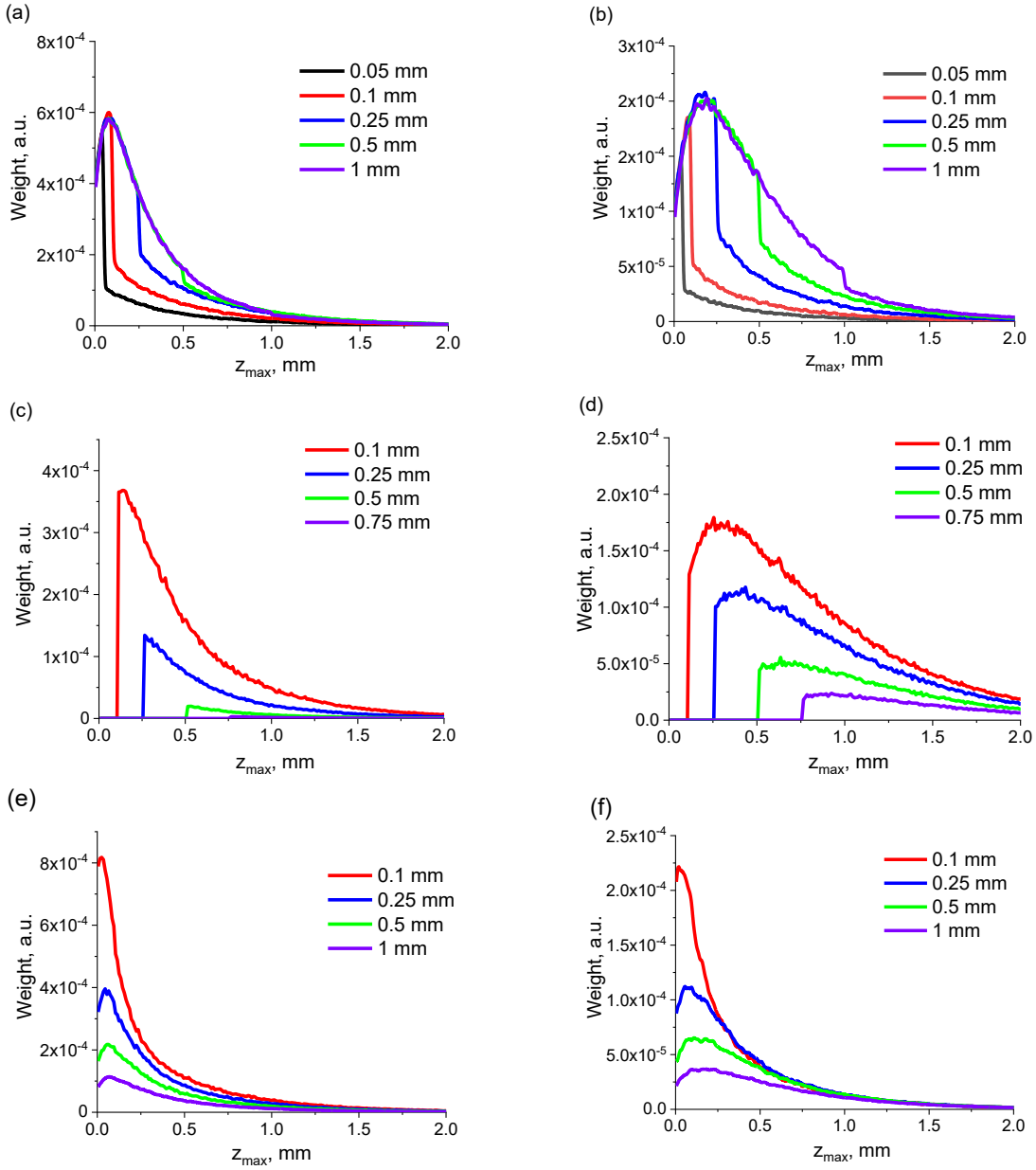


Fig. 6 Distribution of fluorescence photon weights over FI depth $W^d(z_{max})$ normalized by the number of launched photons for excitation wavelengths of 405 nm (left column) and 660 nm (right column) and for different PS distributions: (a), (b) Case (i); (c), (d) Case (ii); (e), (f) Case (iii). Colored lines correspond to different values of the epidermis thickness d_E (a)−(d), and the $1/e$ scale of exponential PS concentration distribution $d_{1/e}$ (e)−(f) indicated in the plots.

In Figs. 6a,b for the Case (i), a sharp drop is observed in the distribution profiles at values of $z_{max} = d_E$ when the PS-containing layer thickness d_E is small compared to the transport length of fluorescence light $l_{t,760} = \left(\mu_{a,760} + \mu_{s,760}(1 - g_{760})\right)^{-1}$ amounting about 0.3–0.4 mm in epidermis and dermis. This fact is explained by the presence of two diffuse fluxes of fluorescence photon: a forward flux directed inside the tissue and a backward flux directed to the front boundary of the tissue where the detector is located. Photons from the forward flux can redirect into the backward flux as the result of backscattering and vice versa. For the backward flux, the maximum depth reached by most fluorescence photons corresponds to the depth at which fluorescence emission occurred, however, there is a fraction of those travelled forward and then backscattered. For the forward flux, the maximum depth of a photon is defined by the depth at which it has changed its direction towards the detector as a result of backscattering. Thus, photons from the backward flux mostly contribute to the bins with lower index corresponding to small values of z_{max}. The bins with larger index (i.e, larger z_{max} values) collect also from the forward flux due to backscattering. The overall distribution depends on the absorption profile within PS layer and the attenuation of fluorescence photons energy along their paths. The presence of a sharp drop at $z_{max} = d_E$ is caused by disappearance of the straight backward flux contribution since only the photons with at least one backscattering can form the fluorescence signal with $z_{max} > d_E$. The number of such photons decreases with the increase of z_{max} which causes a decaying tail in the dependence. When the PS layer thickness exceeds $l_{t,760}$, the peak at the boundary $z_{max} = d$ is smoothened due to pronounced multiple scattering when the forward and the backward fluxes are mixed.

For Case (ii) of uniform PS distribution below epidermis, the dependencies in Figs. 6 c,d show the opposite trend: minimum value of z_{max} is determined by the epidermis thickness d_E. Multiple scattering is responsible for long tails in these dependencies whereas slower decay is observed for 660 nm, similar to Case (i) (Fig. 6b). In Case (iii) of exponentially decaying PS concentration, the distributions $W^d(z_{max})$ for various values of parameter $d_{1/e}$ in Figs. 6 e,f appear smooth with the maxima that are located close to the boundary for $\lambda_{ex} = 405$ nm (Fig. 6e) and are shifted to larger depths for $\lambda_{ex} = 660$ nm (Fig. 6f).

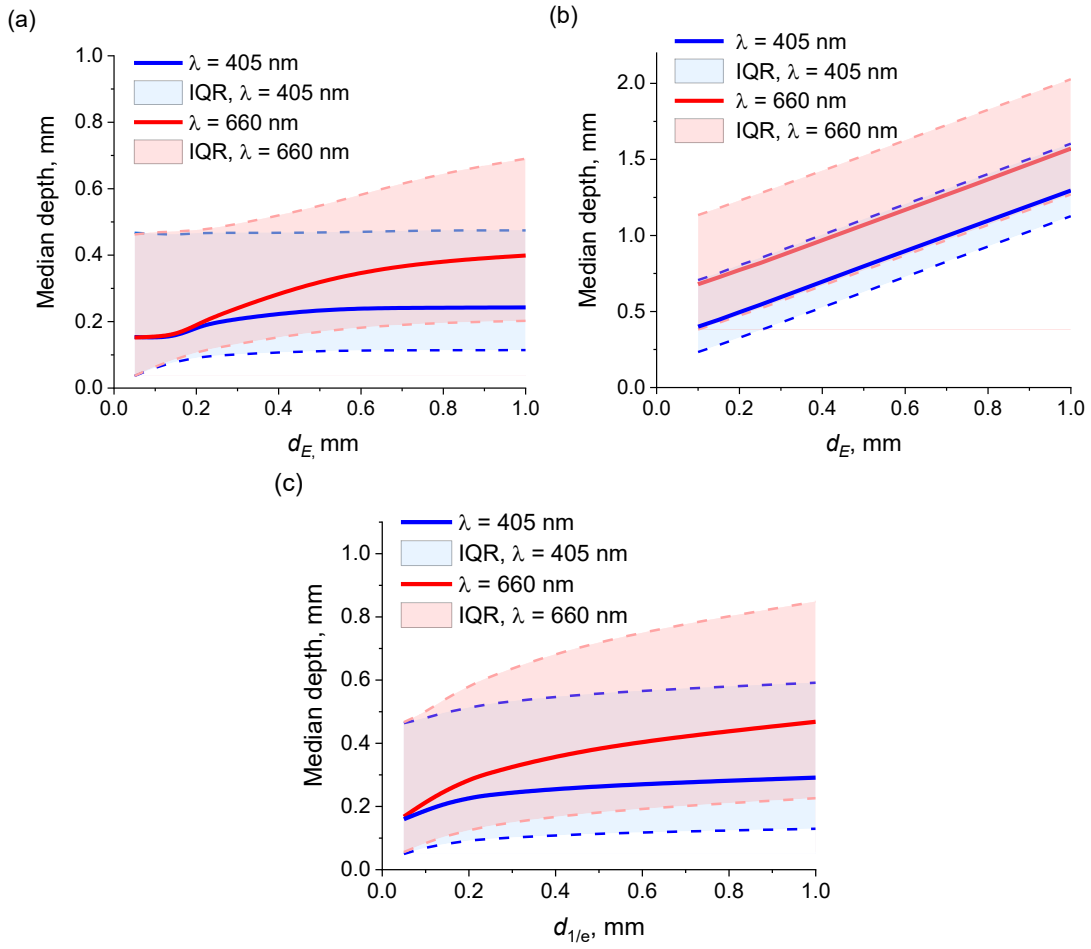


Fig. 7 The dependence of the median FI depth $\tilde{z}_{max}$ (solid lines) on the epidermis thickness d_E ((a) Case (i) and (b) Case (ii)), and on the effective thickness $d_{1/e}$ ((c) Case (iii)) for excitation wavelengths of 405 and 660 nm. Filled areas between dashed lines indicate the interquartile range (IQR) between the 25th and the 75th percentiles of z_{max} distribution shown in Fig. 6.

Fig. 7 demonstrates the dependence of the median depth $\tilde{z}_{max}$ on the characteristic scale of the PS distribution for Cases (i)−(iii). In Fig. 7a describing Case (i), the dependence of $\tilde{z}_{max}$ on the thickness d_E is not linear and it tends to an asymptotic value with the increase of d_E due to decrease in the contribution of fluorescence photons from deep layers (see Figs. 6 a,b). For $\lambda_{ex} = 405$ nm the median $\tilde{z}_{max}^{405}$ reaches its asymptotic value for the values of $d_E \approx 0.75$ mm, while for $\lambda_{ex} = 660$ nm the median $\tilde{z}_{max}^{660}$ keeps growing. The ratio $\tilde{z}_{max}^{660}/\tilde{z}_{max}^{405}$ is close to 1 at small values of d_E, however it increases with the epidermis thickness and for $d_E = 1$ mm it reaches 1.6 which characterizes the difference in the effective imaging depths in FI at these wavelengths. Fig. 7b shows the dependence of the median $\tilde{z}_{max}$ on the epidermis thickness for Case (ii). It is almost linear for both considered wavelengths in the specified range of d_E values. This is presumably due to the major role of the straight backward flux in the formation of fluorescence signal. However, in the whole range of epidermis thickness values the median value $\tilde{z}_{max}$ exceeds d_E because it is influenced by the photons emitted from the back of the dermis, not only by those from the interface. Similar to Fig. 7a, the plot in Fig. 7c describing Case (iii) shows saturating growth of the median $\tilde{z}_{max}$ with the effective PS layer thickness $d_{1/e}$, whereas $\tilde{z}_{max}^{660}/\tilde{z}_{max}^{405} > 1$ for a given value of $d_{1/e}$. Still, the ratio $\tilde{z}_{max}^{660}/\tilde{z}_{max}^{405}$ is slightly less in Case (iii) compared to Case (i) owing to higher contribution of fluorescence coming from smaller depths.

3.3 Fluorescence Imaging Depth and Fluorescence Signal Ratio

Dual-wavelength FI has been reported as a tool for estimating the PS localization depth [29]. This estimation is based on the monotonous dependence of the fluorescence signal ratio $R_\lambda = \frac{I_{fl}^{660}}{I_{fl}^{405}}$ on the characteristic thickness of a PS-containing region. I_{fl}^{660} and I_{fl}^{405} are the fluorescence signals either registered from the tissue upon excitation at the wavelengths of 660 nm and 405 nm, correspondingly, or evaluated numerically with Eq. (6). However, for the development of reconstruction techniques it is reasonable to evaluate the relation between R_λ and the FI imaging depth at both probing wavelengths, since this dependence should be more direct. The performed simulations allowed to plot the dependence of the ratio R_λ on the median depth ratio $\tilde{z}_{max}^{660}/\tilde{z}_{max}^{405}$ which characterizes the difference in the imaging volumes at two wavelengths employed in dual-wavelength FI. Fig. 8 demonstrates that the dependence of R_λ on $\tilde{z}_{max}^{660}/\tilde{z}_{max}^{405}$ is close to linear one for both cases mimicking topical administration case (Cases (i) and (iii)). Such a behavior is caused by a growing difference in FI depth at 660 nm versus 405 nm with the increase of the PS localization depth owing to the difference in the absorption dose in-depth distribution (see Figs. 3a, 5a). In Case (ii) the dependence monotonously decreases since both $\tilde{z}_{max}^{660}$ and $\tilde{z}_{max}^{405}$ linearly grow with the thickness d_E of the upper layer, however their difference becomes smaller (see Fig. 7b), while the ratio R_λ increases due to larger attenuation of blue light compared to that of red light in the PS-free epidermal layer. The dependence is shown in semilogarithmic scale and can be attributed by an inverse power law.

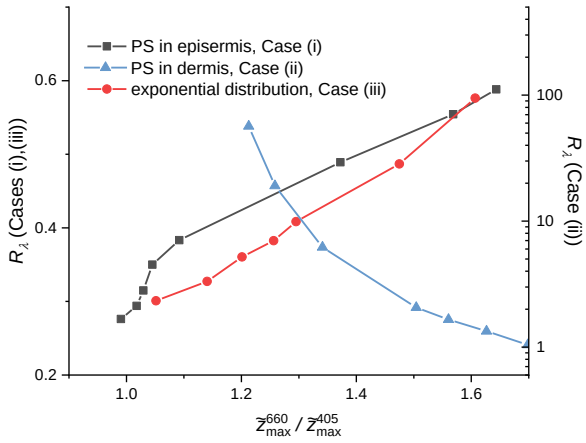


Fig. 8 Dependence of fluorescence signal ratio $R_\lambda = I_{fl}^{660}/I_{fl}^{405}$ on the ratio $\tilde{z}_{max}^{660}/\tilde{z}_{max}^{405}$ of median FI depths for different cases of PS distribution in two-layer biotissue.

4 Conclusion

In this study we have conducted numerical Monte Carlo modeling of light characteristics essential for planning and monitoring of PDT with chlorin-based PS. We compared the effect of different PS distribution models in skin on the profiles of absorbed light dose and on the FI depths in a two-layer biotissue mimicking epidermis-dermis geometry when excitation is performed at the wavelengths close to the maxima in the absorption spectrum of chlorin-based PS (405 nm and 660 nm). Profiles of PS-absorbed light dose evaluated with account of layered biotissue structure allow for more accurate estimation of the PDT procedure efficiency compared to the light dosimetry models developed for uniform biotissue. We studied fluorescence photon distribution versus the depth from which the signal is detected for different PS distributions in biotissue and for optical characteristics at particular probing and emission wavelengths. Dependence of the median FI depth on the characteristic depth of the PS distribution differs sufficiently for topical and intravenous PS administration cases: the former demonstrates asymptotic trend for both boxcar and exponential distribution of PS concentration, while the latter in nearly linear. Ratio of fluorescence signals at wavelengths of 660 nm and 405 in dual-wavelength FI as the function of the ratio of median FI depths at these wavelengths also shows opposite trends for topical and intravenous administration models: the former demonstrates slow monotonous increase while the latter

can be described by a decaying inverse power law. The obtained dependencies provide a detailed overview of the light absorption profile and fluorescence signal formation for different PS distribution in layered biotissues, which has practical value in various fluorescence-based light dosimetry techniques assisting dual-wavelength PDT.

Acknowledgements

The study has been supported by the Russian Science Foundation (Project 24-15-00175, https://rscf.ru/project/24-15-00175/).

Disclosures

The authors declare no conflicts of interest.

References

1. J. F. Algorri, M. Ochoa, P. Roldán-Varona, L. Rodríguez-Cobo, and J. M. López-Higuera, "Light technology for efficient and effective photodynamic therapy: a critical review," Cancers 13(14), 3484 (2021).
2. R. R. Allison, K. Moghissi, "Photodynamic therapy (PDT): PDT mechanisms," Clinical Endoscopy 46(1), 24 (2013).
3. J. P. Celli, B. Q. Spring, I. Rizvi, C. L. Evans, K. S. Samkoe, S. Verma, B. W. Pogue, and T. Hasan, "Imaging and photodynamic therapy: mechanisms, monitoring, and optimization," Chemical Reviews 110(5), 2795–2838 (2010).
4. B. C. Wilson, M. S. Patterson, "The physics, biophysics and technology of photodynamic therapy," Physics in Medicine & Biology 53(9), R61–R109 (2008).
5. V. V. Tuchin, Tissue Optics: Light Scattering Methods and Instruments for Medical Diagnostics, 3rd Ed., Society of Photo-Optical Instrumentation Engineers (SPIE), Bellingham, WA, USA (2015). PDF ISBN: 9781628415179.
6. A. N. Bashkatov, E. A. Genina, V. I. Kochubey, and V. V. Tuchin, "Optical properties of human skin, subcutaneous and mucous tissues in the wavelength range from 400 to 2000 nm," Journal of Physics D: Applied Physics 38(15), 2543–2555 (2005).
7. S. L. Jacques, "Optical properties of biological tissues: a review," Physics in Medicine & Biology 58(11), R37–R61 (2013).
8. E. Salomatina, B. Jiang, J. Novak, and A. N. Yaroslavsky, "Optical properties of normal and cancerous human skin in the visible and near-infrared spectral range," Journal of Biomedical Optics 11(6), 064026 (2006).
9. S. L. Jacques, "How tissue optics affect dosimetry of photodynamic therapy," Journal of Biomedical Optics 15(5), 051608 (2010).
10. J. S. Dysart, M. S. Patterson, "Photobleaching kinetics, photoproduct formation, and dose estimation during ALA induced PpIX PDT of MLL cells under well oxygenated and hypoxic conditions," Photochemical & Photobiological Sciences 5(1), 73–81 (2006).
11. A. Dimofte, J. C. Finlay, and T. C. Zhu, "A method for determination of the absorption and scattering properties interstitially in turbid media," Physics in Medicine & Biology 50(10), 2291–2311 (2005).
12. T. Johansson, M. Soto Thompson, M. Stenberg, C. A. Klinteberg, S. Andersson-Engels, S. Svanberg, and K. Svanberg, "Feasibility study of a system for combined light dosimetry and interstitial photodynamic treatment of massive tumors," Applied Optics 41(7), 1462 (2002).
13. L. Wang, S. L. Jacques, and L. Zheng, "MCML—Monte Carlo modeling of light transport in multi-layered tissues," Computer Methods and Programs in Biomedicine 47(2), 131–146 (1995).
14. N. Lopez, R. Mulet, and R. Rodríguez, "Tumor reactive ringlet oxygen approach for Monte Carlo modeling of photodynamic therapy dosimetry," Journal of Photochemistry and Photobiology B: Biology 160, 383–391 (2016).
15. B. Liu, T. J. Farrell, and M. S. Patterson, "Comparison of photodynamic therapy with different excitation wavelengths using a dynamic model of aminolevulinic acid-photodynamic therapy of human skin," Journal of Biomedical Optics 17(8), 0880011 (2012).
16. C. L. Campbell, K. Wood, C. T. A. Brown, and H. Moseley, "Monte Carlo modelling of photodynamic therapy treatments comparing clustered three dimensional tumour structures with homogeneous tissue structures," Physics in Medicine & Biology 61(13), 4840–4854 (2016).
17. J. Cassidy, V. Betz, and L. Lilge, "Treatment plan evaluation for interstitial photodynamic therapy in a mouse model by Monte Carlo simulation with FullMonte," Frontiers in Physics 3, (2015).
18. B. C. Wilson, M. S. Patterson, and L. Lilge, "Implicit and explicit dosimetry in photodynamic therapy: a New paradigm," Lasers in Medical Science 12(3), 182–199 (1997).
19. A. V. Khilov, D. A. Kurakina, I. V. Turchin, and M. Y. Kirillin, "Monitoring of chlorin-based photosensitiser localisation with dual-wavelength fluorescence imaging: numerical simulations," Quantum Electronics 49(1), 63–69 (2019).
20. A. V. Khilov, M. Y. Kirillin, D. A. Loginova, and I. V. Turchin, "Estimation of chlorin-based photosensitizer penetration depth prior to photodynamic therapy procedure with dual-wavelength fluorescence imaging," Laser Physics Letters 15(12), 126202 (2018).
21. A. V. Khilov, D. A. Loginova, E. A. Sergeeva, M. A. Shakhova, A. E. Meller, I. V. Turchin, and M. Yu. Kirillin, "Two-wavelength fluorescence monitoring and planning of photodynamic therapy," Sovremennye Tehnologii v Medicine 9(4), 96 (2017).

22. D. J. Robinson, H. S. De Bruijn, N. Van Der Veen, M. R. Stringer, S. B. Brown, and W. M. Star, "Fluorescence photobleaching of ALA-induced protoporphyrin IX during photodynamic therapy of normal hairless mouse skin: the effect of light dose and irradiance and the resulting biological effect," Photochemical & Photobiological Sciences 67(1), 140–149 (1998).
23. J. Moan, "Effect of bleaching of porphyrin sensitizers during photodynamic therapy," Cancer Letters 33(1), 45–53 (1986).
24. S. Anbil, I. Rizvi, J. P. Celli, N. Alagic, and T. Hasan, "A photobleaching-based PDT dose metric predicts PDT efficacy over certain BPD concentration ranges in a three-dimensional model of ovarian cancer," SPIE Proceedings 8568, 85680S (2013).
25. J. Tyrrell, S. Campbell, and A. Curnow, "Protoporphyrin IX photobleaching during the light irradiation phase of standard dermatological methyl-aminolevulinate photodynamic therapy," Photodiagnosis and Photodynamic Therapy 7(4), 232–238 (2010).
26. M. A. Scott, C. Hopper, A. Sahota, R. Springett, B. W. McIlroy, S. G. Bown, and A. J. MacRobert, "Fluorescence photodiagnostics and photobleaching studies of cancerous lesions using ratio imaging and spectroscopic techniques," Lasers in Medical Science 15(1), 63–72 (2000).
27. A. Johansson, F. Faber, G. Kniebühler, H. Stepp, R. Sroka, R. Egensperger, W. Beyer, and F. Kreth, "Protoporphyrin IX fluorescence and photobleaching during interstitial photodynamic therapy of malignant gliomas for early treatment prognosis," Lasers in Surgery and Medicine 45(4), 225–234 (2013).
28. M. T. Jarvi, M. S. Patterson, and B. C. Wilson, "Insights into photodynamic therapy dosimetry: simultaneous singlet oxygen luminescence and photosensitizer photobleaching measurements," Biophysical Journal 102(3), 661–671 (2012).
29. M. Kirillin, A. Khilov, D. Kurakina, A. Orlova, V. Perekatova, V. Shishkova, A. Malygina, A. Mironycheva, I. Shlivko, S. Gamayunov, I. Turchin, and E. Sergeeva, "Dual-wavelength fluorescence monitoring of photodynamic therapy: from analytical models to clinical studies," Cancers 13(22), 5807 (2021).
30. M. Kirillin, D. Kurakina, A. Khilov, A. Orlova, M. Shakhova, N. Orlinskaya, and E. Sergeeva, "Red and blue light in antitumor photodynamic therapy with chlorin-based photosensitizers: a comparative animal study assisted by optical imaging modalities," Biomedical Optics Express 12(2), 872 (2021).
31. M.-A. Mycek, B. W. Pogue (Eds.), Handbook of biomedical fluorescence, 1st ed., CRC Press, Boca Raton, FL (2003). ISBN: ISBN: 9780203912096.
32. J. Swartling, A. Pifferi, A. M. K. Enejder, and S. Andersson-Engels, "Accelerated Monte Carlo models to simulate fluorescence spectra from layered tissues," Journal of the Optical Society of America A 20(4), 714 (2003).
33. Y. H. Ong, J. C. Finlay, and T. C. Zhu, "Monte Carlo modeling of fluorescence in semi-infinite turbid media," SPIE Proceedings 10492, 104920T (2018).
34. Y. H. Ong, M. M. Kim, J. C. Finlay, A. Dimofte, S. Singhal, E. Glatstein, K. A. Cengel, and T. C. Zhu, "PDT dose dosimetry for Photofrin-mediated pleural photodynamic therapy (pPDT)," Physics in Medicine & Biology 63(1), 015031 (2017).
35. Y. H. Ong, T. C. Zhu, "Estimation of fluorescence probing depth dependence on the distance between source and detector using Monte Carlo modeling," SPIE Proceedings 11628, 116280X (2021).
36. D. Y. Churmakov, I. V. Meglinski, S. A. Piletsky, and D. A. Greenhalgh, "Analysis of skin tissues spatial fluorescence distribution by the Monte Carlo simulation," Journal of Physics D: Applied Physics 36(14), 1722 (2003).
37. A. Ustinova, I. Bratchenko, and D. Artemyev, "Monte Carlo simulation of skin multispectral autofluorescence," Journal of Biomedical Photonics & Engineering 5(2), 020306 (2019).
38. A. V. Khilov, E. A. Sergeeva, D. A. Kurakina, I. V. Turchin, and M. Yu. Kirillin, "Analytical model of fluorescence intensity for the estimation of fluorophore localisation in biotissue with dual-wavelength fluorescence imaging," Quantum Electronics 51(2), 95–103 (2021).
39. R. M. Valentine, C. T. A. Brown, H. Moseley, S. Ibbotson, and K. Wood, "Monte Carlo modeling of in vivo protoporphyrin IX fluorescence and singlet oxygen production during photodynamic therapy for patients presenting with superficial basal cell carcinomas," Journal of Biomedical Optics 16(4), 048002 (2011).
40. M. Y. Kirillin, D. A. Kurakina, V. V. Perekatova, A. G. Orlova, E. A. Sergeeva, A. V. Khilov, P. V. Subochev, I. V. Turchin, S. Mallidi, and T. Hasan, "Complementary bimodal approach to monitoring of photodynamic therapy with targeted nanoconstructs: numerical simulations," Quantum Electronics 49(1), 43–51 (2019).
41. E. Zenkevich, E. Sagun, V. Knyukshto, A. Shulga, A. Mironov, O. Efremova, R. Bonnett, S. P. Songca, and M. Kassem, "Photophysical and photochemical properties of potential porphyrin and chlorin photosensitizers for PDT," Journal of Photochemistry and Photobiology B: Biology 33(2), 171–180 (1996).
42. L. O. Svaasand, P. Wyss, M.-T. Wyss, Y. Tadir, B. J. Tromberg, and M. W. Berns, "Dosimetry model for photodynamic therapy with topically administered photosensitizers," Lasers in Surgery and Medicine 18(2), 139–149 (1996).
43. L. O. Svaasand, B. J. Tromberg, P. Wyss, M.-T. Wyss-Desserich, Y. Tadir, and M. W. Berns, "Light and drug distribution with topically administered photosensitizers," Lasers in Medical Science, 11, 261–265 (1996).

44. D. A. Lintzeri, N. Karimian, U. Blume-Peytavi, and J. Kottner, "Epidermal thickness in healthy humans: a systematic review and meta-analysis," Journal of the European Academy of Dermatology and Venereology 36(8), 1191–1200 (2022).
45. I. M. Heerfordt, C. V. Nissen, T. Poulsen, P. A. Philipsen, and H. C. Wulf, "Thickness of actinic keratosis does not predict dysplasia severity or P53 expression," Scientific Reports 6(1), 33952 (2016)
46. D. Yudovsky, L. Pilon, "Rapid and accurate estimation of blood saturation, melanin content, and epidermis thickness from spectral diffuse reflectance," Applied Optics 49(10), 1707 (2010).
47. V. V. Tuchin, "Tissue optics and photonics: biological tissue structures," Journal of Biomedical Photonics & Engineering 1(1), 3−21 (2015).
48. A. R. Kamuhabwa, R. Roelandts, and P. A. De Witte, "Skin photosensitization with topical hypericin in hairless mice," Journal of Photochemistry and Photobiology B: Biology 53(1–3), 110–114 (1999).
49. M. Gallardo-Villagrán, D. Y. Leger, B. Liagre, and B. Therrien, "Photosensitizers used in the photodynamic therapy of rheumatoid arthritis," International Journal of Molecular Sciences 20(13), 3339 (2019).

Comparison of Machine Learning Methods for the Analysis of Serum Raman Spectra in the Detection of Chronic Heart Failure

Elena Sorokina[1], Yulia Khristoforova[1*], Ivan Bratchenko[1], Maria Skuratova[2], Petr Lebedev[3], and Valery Zakharov[1]

[1] Samara National Research University, 34 Moskovskoe shosse, Samara 443080, Russian Federation
[2] Samara City Clinical Hospital №1 named after N. I. Pirogov, 80 Polevaya str., Samara 443096, Russian Federation
[3] Samara State Medical University, 159 Tashkentskaya str., Samara 443095, Russian Federation
[*] e-mail: khristoforovajulia@gmail.com

Abstract. The high sensitivity of Raman spectroscopy to the chemical composition of substances at the molecular level makes it a valuable tool for the diagnosis of chronic heart failure (CHF) through analysis of blood serum. Raman spectroscopy offers a label-free, fast detection method, with highly specific and accurate results when combined with machine learning (ML) techniques. However, it is essential to carefully choose the appropriate ML algorithm for analyzing high-dimensional spectral data to achieve reliable and correct results that are primarily based on the true chemical features and differences of the studied samples, specimens or structures as not all algorithms may deliver the high performance. In this study, we compared four approaches: (1) multivariate curve resolution alternating least squares method in combination with logistic regression (MCR-LR), (2) with linear kernel support vector machine (MCR-SVM), (3) projection on the latent structures with discriminant analysis (PLS-DA), and (4) projection on the latent structures with linear kernel support vector machine (PLS-SVM). These methods were applied to 193 Raman spectra from patients with CHF and 78 from control cases. We found that PLS-DA and PLS-SVM demonstrated the best ROC AUCs, with average value of 0.950 (0.91−0.97, 0.95 CI) and 0.99 (0.94−1.00, 0.95 CI), while MCR-LR and MCR-SVM achieved only 0.50 (0.46−0.53, 0.95 CI) and 0.59 (0.54−0.65, 0.95 CI), respectively.
© 2024 Journal of Biomedical Photonics & Engineering.

Keywords: Raman spectroscopy, spectral analysis, multivariate curve resolution alternating least squares method, projection on the latent structures with discriminant analysis, linear kernel support vector machine, chronic heart failure.

Paper #9195 received 4 Dec 2024; revised manuscript received 24 Oct 2024; accepted for publication 24 Oct 2024; published online 30 Dec 2024. doi: 10.18287/JBPE24.10.040319.

1 Introduction

Chronic heart failure (CHF) is a clinical syndrome that occurs with structural or functional abnormalities of heart that results in elevated intracardiac pressures and/or inadequate cardiac output [1]. The chronic heart failure (CHF) is diagnosed based on physical examination and a series of tests included echocardiography and electrocardiogram, and brain natriuretic peptide (BNP) or N-terminal pro-BNP (NT-proBNP) protein level, both of which tend to be elevated in people with heart failure [2]. The BNP and NT-proBNP protein level has been recommended as a biomarker for the diagnosis of CHF that allows one to predict of all stages of the CHF disease, but this diagnostic approach is time-consuming and expensive. Therefore, it is extremely important to develop rapid diagnostic techniques for CHF identification.

Today, Raman spectroscopy has become widely used in medical research for diagnostic purposes. In numerous studies, biological fluids [3, 4] and tissues [3, 5−7] are being analyzed using Raman spectroscopy to diagnose skin diseases [5], cardiovascular disorders [6, 8], cancer [7, 9], etc. The principle of the Raman spectroscopy is based on the inelastic scattering of the radiation following its interaction with the vibrational modes of molecules. The Raman spectrum registered as a result of this phenomenon consists of a set of characteristic Raman peaks that correspond to the specific molecular vibrational modes which makes it a unique "fingerprint" of a biological sample. Therefore, Raman spectrum can be analyzed to identify of the relative sample's composition and identify any changes that may occur due to disease.

In the analysis of Raman spectra, machine learning (ML) methods have been found to be useful for a variety of applications [10], including classification [5, 11], clustering [12], regression analysis [13, 14] of the experimental data. The ML applications involve creating prediction, regression and classification statistical models based on the analysis of high-dimensional spectral data, with reducing the dimensionality and identifying the significant features that can be used to interpret the physical meaning of the results. Then, ML models are validated using new spectra to ensure their performances.

The projection on latent structures (PLS) can be considered a reference classifier as it is widely employed for various biomedical applications. For example, in study by I. Behl et al. [15] Raman spectra of brush biopsies from the buccal mucosa/tongue were subjected to PLS-DA to differentiate the healthy samples from oral mucosal dysplastic lesions. S Zhu et al. [16] achieved high classification accuracies more than 85% by PLS-LDA diagnostic model based on serum SERS to diagnose pulmonary cryptococcal infection and to assess the degrees of infection. In study by Khristoforova et al. [17] PLS-DA was also used to analyze autofluorescence and Raman data of *in vivo* human skin lesions to identify amelanotic melanoma cases. However, the cited works [15−17] do not explain the choice of the currently widely used PLS-DA method. The question arises as to whether the performance will depend on the ML methods. Additionally, PLS does not essentially analyze spectra, focusing solely on the classification task. Therefore, we want to compare the PLS approach with the multivariate curve resolution alternating least squares (MCR-ALS) analysis, which is used to reconstruct the spectral profiles contributed to complex Raman spectra of biological substances. This allows for both the physical interpretation of the components that the original Raman spectra are composed of, and for classification in combination with differentiating algorithms.

In this study, we applied 4 combinations of ML algorithms: MCR-ALS analysis in combination with logistic regression and linear kernel support vector machine (SVM), and supervised PLS algorithm with discriminant analysis and linear kernel SVM to analyze Raman spectra of human serum of patients with CHF and control group. Therefore, the aim of this study is to select the efficient ML approach to determine the potential of Raman spectroscopy to identify CHF cases by analyzing the *in vitro* serum samples spectra.

2 Materials and Methods

2.1 Studied Samples

The study protocols were approved by the ethical committee of Samara State Medical University (protocol No 268, 11 September 2023). All involved subjects agreed to participate in this study by informed consent. In this study, the *in vitro* analysis of human serum was performed at Cardiology Department Samara City Clinical Hospital №1 named after N. I. Pirogov and Samara National Research University. The final diagnosis of CHF was made based on the results of an NT-proBNP test.

In this work, a total of 78 patients were included in the *in vitro* experimental study: 14 patients affected by CHF of 1 and 2 stages and 64 subjects of control group. The control group included subjects from the same Cardiology Department of Samara City Clinical Hospital №1 named after N. I. Pirogov, but with an unconfirmed diagnosis of CHF. The serum samples were collected from patients in the morning, after they had fasted. Each sample was placed in a labelled, sterile tube. The tubes were immediately frozen at −16 °C and then transferred to the laboratory for Raman analysis in the freezer. Immediately before the analysis, the samples were defrosted at room temperature. A sample of serum in a volume of 10 μl was placed on aluminum foil and allowed to air dry at room temperature until it was completely dry. In laboratory, for each sample 4−6 Raman spectra were registered from different surface points. A total of 271 Raman spectra were analyzed, including 193 spectra from CHF cases and 78 from control cases.

2.2 Experimental Setup

The experimental setup consisted of the EnSpectr R532 spectrometric system (Spektr-M, Chernogolovka, Russia)) and the ADF U300 microscope (ADF, China) with 50× LMPlan Objective. A laser with a central wavelength of 532 nm was used to acquire Raman spectra in the 89−3892 cm^{-1} region with a spectral resolution of 1.5 cm^{-1}. The laser spot size at the sample surface was approximately 5 μm. All Raman spectra were registered during 2 sec acquisition time with 10 accumulations.

2.3 Spectra Preprocessing

Statistical analysis and data processing were conducted using Python 3, including numpy, scipy, matplotlib, and scikit-learn libraries.

Before recording the Raman spectra of the dried serum samples, a background signal was recorded and then subtracted from the recorded spectrum of the serum using a built-in software algorithm. For the subsequent analysis, the spectral range of 800−1800 cm^{-1} was used, which corresponds to a discrete set of 744 parameters representing the Raman intensities, corresponding to specific values of the wavenumber.

The preprocessing algorithm includes 3 steps: baseline removal with asymmetric least squares [18, 19], smoothing by Savitsky-Golay filter (2 order of polynomial degree, 15 window width size, 0 polynomial order) [20, 21], and normalization by standard normal variation.

2.4 Machine Learning Methods

2.4.1 MCR-ALS

We used the MCR-ALS method [22] to decompose the Raman spectra, which represents a combination of contributions from Raman-active molecular components, into individual spectral components. In this context, each Raman spectrum will be just a linear combination of the spectra of "pure" spectral components:

$$X = C * S^T, \quad (1)$$

where X is a knowing matrix of serum Raman spectra, S is a matrix of derived "pure" spectral components (profiles), and C is a matrix of concentrations. Therefore, the application of MCR-ALS method for analysis of 532-nm stimulated Raman spectra of human serum allows us to recognize the spectra profiles of the most significant serum components and their contribution to the samples.

A principal component analysis (PCA) has been conducted to estimate the correct number of significant spectral components (S) into which the experimental spectral set can be resolved. When the spectra were decomposed into 8 components, the first 4 MCR components explained 97% variances of the initial Raman spectra and eigenvalues of 5, 6, 7, 8 components are strongly dropped. Additionally, we also divided the experimental set into different numbers of components to determine the optimal number. The serum spectra were divided into a different number of components to determine the optimal number. When the spectra were decomposed into 8 components, spectral profiles above the 5th order were noise-like. When the spectra were decomposed into 5 components, the concentration of 5th component was almost entirely contained within 4th component in accordance with exploratory factor analysis. Therefore, we can assume that the number of useful spectral profiles describing serum Raman spectra is 4.

To perform the decomposition of serum Raman spectra using MCR-ALS method we used MCR-ALS GUI 2.0 software [23].

2.4.2 PLS

PLS reduces the spectral dimension to a smaller number of new, orthogonal components, called latent variables (LVs). LVs are linear combinations of the original spectral data and are determined based on the variability in the spectral values. This variability correlates with the different classes of spectra, meaning that only the spectral characteristics that distinguish between the classes being studied are used. In PLS analysis, it is important to determine the correct number of LVs to avoid overfitting of the model [24]. In this study, the number of LVs was determined in accordance with several criteria. We estimated RMSE of the performed K-fold cross validation, and, in addition, we estimated, the shapes and scores of LVs to discard the LVs related to possible noise contribution and scatter of LV scores.

2.4.3 Classification Models

We analyzed various combinations of machine learning algorithms, including MCR with logistic regression (MCR-LR), MCR with linear kernel support vector machine (MCR-SVM), PLS with linear discriminant analysis (PLS-DA), and PLS with linear kernel SVM, to build classification models to distinguish CHF versus control cases. Both PLS and MCR methods allow one to reduce the dimensionality of the spectral data. Considering that data dimensionality reduction had already been performed using MCR, we decided not to combine the MCR and PLS-DA methods.

LR estimates the probability that an observation belongs to a specific class based on a linear threshold that determined by the linear discriminant function. To build the LR classification model, each registered Raman spectra of human serum is represented as a set of concentrations of statistically significant MCR components (MCR-LR).

SVM builds a hyperplane that optimally separates the cases of CHF and control groups. This algorithm assumes that the larger the distance between the hyperplane and observations from the same class, the lower the average error rate of the classifier. In this study, only a linear model was employed to construct a dividing hyperplane. Linear kernel SVM enables the extraction of the most discriminative features, based on the proximity of a predictor vector to a dividing hyperplane.

The PLS scores are traditionally combined with linear discriminant analysis, so we built PLS-DA classification model for analysis of experimental cases based on the preprocessed Raman spectra of serum. Additionally, we combined PLS with a linear kernel SVM, where the SVM algorithm was applied to the scores of the useful LVs.

The experimental set was split into a training set (80%, 220 spectra) and testing (20%, 51 spectra) set. To evaluate the reliability and the stability of the model throughout the training process, 10-fold cross-validation was used. 10-fold cross-validation approach involves dividing the training set into 10 equal sized parts (folds) with each part (fold) being used in turn as a validation part, while the other 9 folds are used to train the model.

Then, the performance results were averaged of the 10 results obtained. This allows one to ensure the stability of the model and to avoid overfitting. After training the model with 10-fold cross-validation on the training set, the final model performance was evaluated on a test set that had not been used in the training process. The diagram of the proposed analysis procedure is presented in Fig. 1.

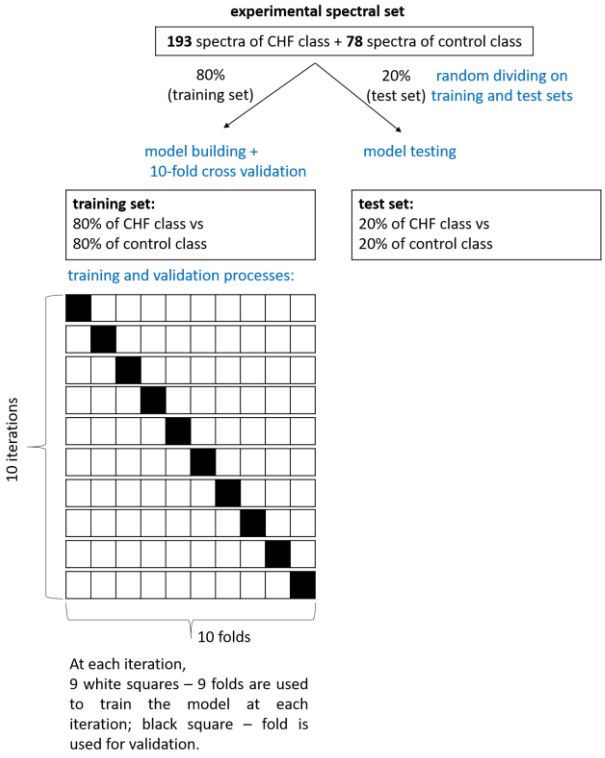


Fig. 1 Diagram of the model building procedure.

The performance of the ML algorithms for differentiating CHF cases from control serum was presented using a receiver operating characteristic (ROC) curve. For quantitative analysis, the area under the curve (AUC) was calculated. The statistical comparison between the ROC AUC values obtained using two different ML methods was conducted according to Hanley and McNeil [25].

3 Results and Discussion

3.1 Serum Raman Spectra

Fig. 2 shows the average serum Raman spectra of CHF and control cases with standard deviation. As is known, biological systems, in particular human serum, contain carotenoids, which give rise to a resonance Raman signal when excited by 532 nm laser [26]. This results in dominant carotenoid Raman bands at 1151 (ν(C-C)) and 1511 (ν(C=C)) cm^{-1}. Also, both spectra have prominent peak at 1004 cm^{-1} can be also assigned to carotenoids ($C\text{-}CH_3$ rocking vibration) and it can be overlapped with a phenylalanine band [26–28]. A deficiency of carotenoids in the blood can cause cell membranes to dry out, leading to cell rupture, fluid leakage, and disruption of cell control, ultimately causing cell death [27]. However, the exact effect of carotenoids, especially β-carotene, on cardiovascular disease remains unclear. For instance, in Ref. [29], it was found that carotenoids in blood serum have an inverse linear relationship with the prevalence of cardiovascular disease. Additionally, serum Raman spectra contains the band at 1445 cm^{-1} corresponded to $\delta(CH_2)$, $\delta(CH_3)$ in collagen and phospholipids and band at 1665 cm^{-1} corresponded to Amide I of collagen [26, 27]. The low intensity peaks are observed at extended Amide III band (1285, 1336 cm^{-1}).

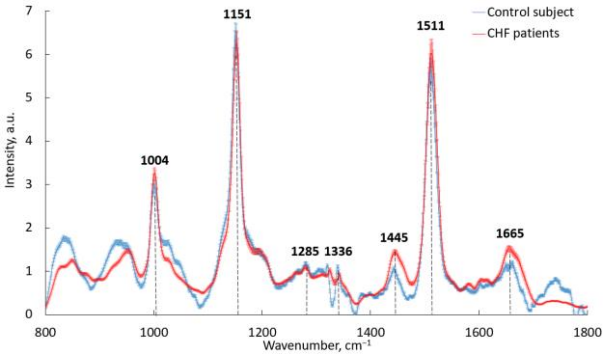


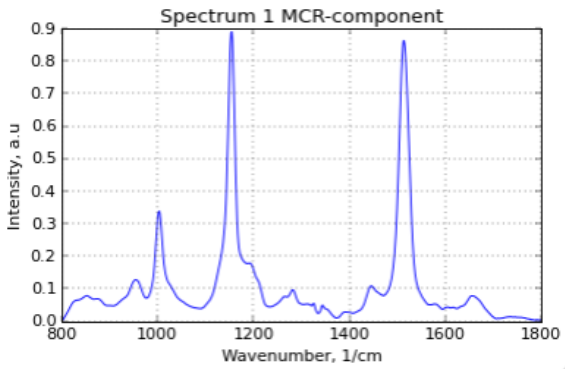
Fig. 2 The 532 nm stimulated Raman spectra of human serum. The shaded area represents the standard deviation.

3.2 MCR-ALS Analysis

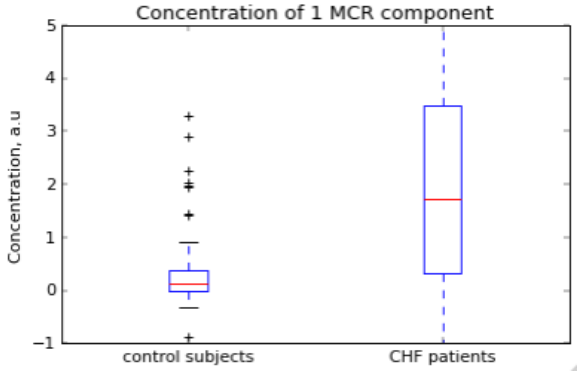
The progression of various diseases, including CHF, is accompanied by quantitative changes in the molecular components of biological tissues and fluids. The Raman spectra of serum of patients with CHF and control patients are expected to show differences in the intensities of the same set of spectral peaks. Therefore, we propose decomposing experimental set of CHF and control Raman spectra into the same spectral MCR components and analyzing the concentrations of these spectral MCR components as new features of the blood serum.

In accordance with PCA analysis 97% explained variance of the experimental data are described by the first 4 MCR components. The spectral profiles and concentrations of the obtained MCR components are presented in Fig. 3.

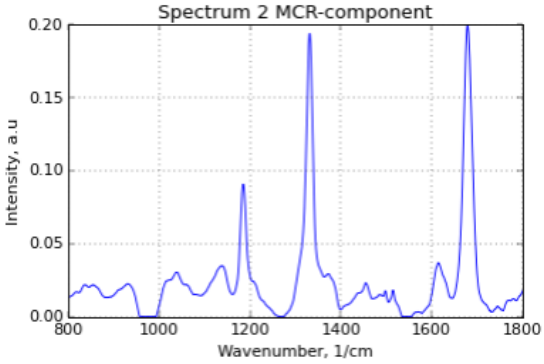
The spectral profile of the 1st MCR component shows the prominent 1004 cm^{-1}, 1151 cm^{-1} and 1511 cm^{-1} bands. This indicates that 1st MCR component mostly corresponds to a carotenoid in blood serum. In accordance with box-plot diagram (Fig. 3b), the concentration values of 1 MCR component is higher in Raman spectra of CHF patients in comparison with control group.



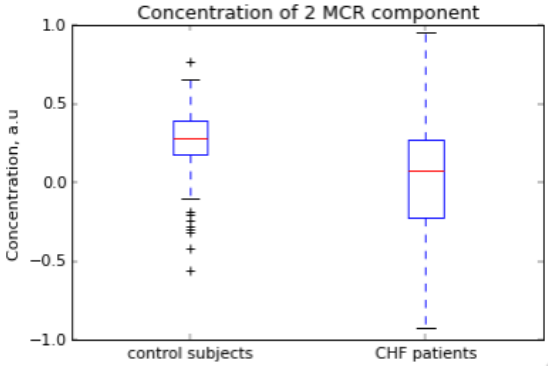
(a)



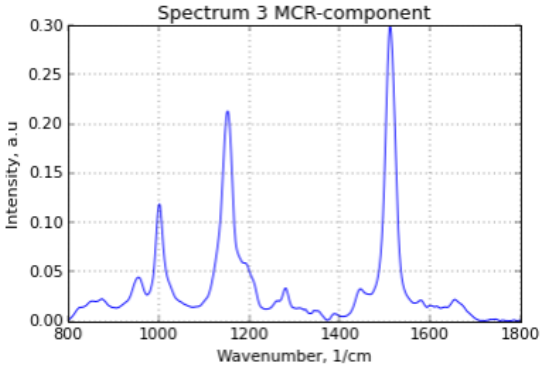
(b)



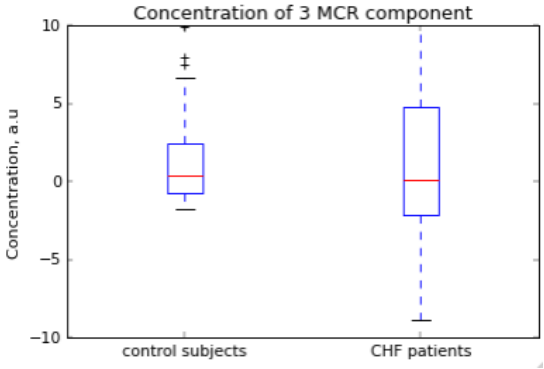
(c)



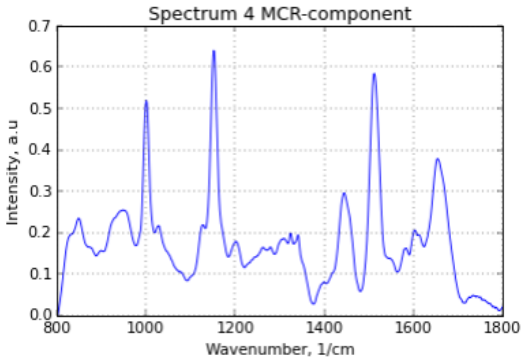
(d)



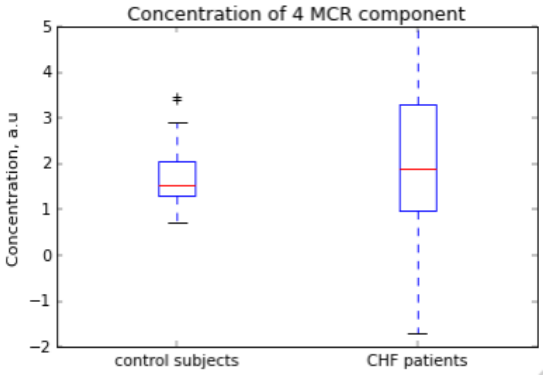
(e)



(f)



(g)



(h)

Fig. 3 MCR components extracted from the serum Raman spectra stimulated by the 532 nm laser wavelength. (a, c, e, g) The spectral profiles of the MCR components. (b, d, f, h) The relative concentrations of the MCR components.

The spectral profile of the 2nd MCR component are characterized by the 1336 cm^{-1} band associated with CH_3CH_2 in collagen, and Amide I band at 1665 cm^{-1}. Also, according to the box-plot diagram (Fig. 3d), the relative concentration values of 2nd MCR component has a shifted median and higher dispersion in the CHF group.

The spectral profile of the 3th MCR component has similar peaks to the 1st MCR components and also can be associated with protein and carotenoids contributions. The 4th MCR component represents the contribution of various proteins at 1445 cm^{-1}, 1665 cm^{-1} bands, carotenoids at 1004 cm^{-1}, 1151 cm^{-1} and 1511 cm^{-1} bands, phenylalanine at 1004 cm^{-1} band. The medians of the concentration relative values of 3th and 4th MCR components in opposite groups have close values while dispersion is higher in CHF group.

The Mann-Whitney *U*-test was used to evaluate the statistical significance of differences in relative concentration values between the CHF and control groups. It was achieved that 1st and 2nd MCR components had a statistically significant difference, with *p*-values of <0.001 and <0.0001 respectively. Therefore, to build classification models to differ CHF and control cases, we will use only the 1st and 2nd MCR components, basing the model on differences in carotenoid and protein levels.

3.3 Classification Models

To build the MCR-LR and MCR-SVM classification models, each Raman spectra of human serum is represented as a concentrations vector of 2 MCR components obtained using the MCR method. The values of 1st and 2nd MCR concentrations were used as predictor variables for 78 CHF and 271 control cases to differ them. The MCR-LR and MCR-SVM models were built to classify CHF and control cases and verified on the test set with 0.50 (0.46−0.53, 0.95 CI) and 0.59 (0.54−0.65, 0.95 CI) ROC AUC, respectively. The ROC curves of both models are presented in Fig. 4.

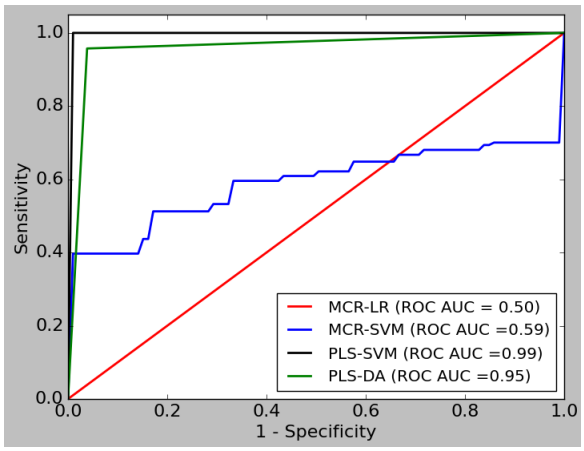
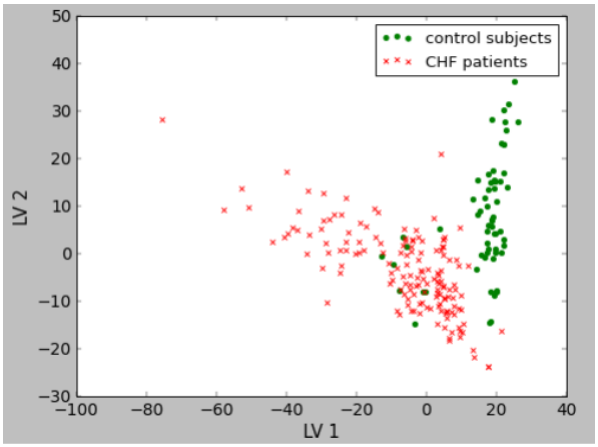


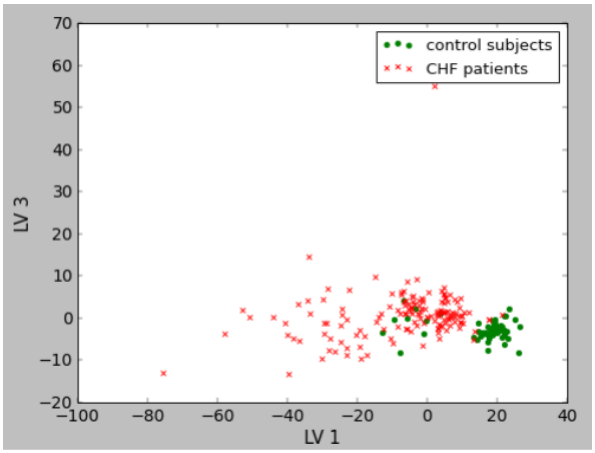
Fig. 4 ROC curves of the binary classification models.

We performed PLS analysis to enable more accurate differentiation of CHF and control cases analyzing preprocessed serum Raman spectra. To determine the optimal number of LVs for our classification model, firstly, we applied minimum of RMSE criterion. The RMSE value has decreased to 3 LVs for the training set and cross validation algorithm. In addition, scatter plots in Fig. 5 demonstrated that scores of 3 LVs allows us good separating the CHF and control cases on LV1−LV2 and LV1−LV3 plots. Therefore, analysis of estimation RMSE values and score distributions, has demonstrated that 3 PCs can be used for training a statistical PLS model in order to avoid overfitting.

The classification model based on analyses of preprocessed Raman spectra using PLS with DA achieves ROC AUC equaled to 0.95 (0.91−0.97, 0.95 CI). The corresponding ROC curve is presented in Fig. 4. The highest ROC AUC of 0.99 (0.94−1.00, 0.95 CI) was obtained when PLS was combined with the linear kernel SVM algorithm for classifying serum SERS spectra between the CHF and control groups.



(a)



(b)

Fig. 5 2D plots of the PLS scores obtained for training set: (a) LV1−LV2, (b) LV1−LV3.

In this study, comparing the ROC AUCs of MCR-LR, MCR-SVM, PLS-DA, and PLS-SVM models together, we revealed that the PLS-SVM method based on analysis of the preprocessed Raman spectra had the best performance with the largest ROC AUC (Fig. 4).

Nevertheless, it is need to estimate the statistical significance of obtained differences in ROC AUC values. The comparison of the MCR-LR and MCR-SVM models' performances equaled to 0.50 (0.46−0.53, 0.95 CI) and 0.59 (0.54−0.65, 0.95 CI) ROC AUCs, respectively, resulted in an insignificant statistical difference ($p = 0.24$). Also, ROC AUCs achieved for PLS-DA (0.95 (0.91−0.97, 0.95 CI)) and PLS-SVM (0.99 (0.94−1.00, 0.95 CI)) algorithms do not differ significantly from each other ($p = 0.09$), as they are statistically similar. However, when we compared the results obtained using different methods, we found a statistically significant improvement in the ROC AUC values for PLS compared to MCR ($p<0.001$ in all cases).

As we can see from the spectral profiles of the MCR components in Fig. 3, the MCR-ALS analysis does not allow us to reconstruct the spectral profile of individual vibrational molecular bonds. Instead, the spectral profile of each MCR component is a complex spectrum composed of a mixture of peaks corresponding to the contribution of several biomolecule groups. It is important to note that the individual MCR components are associated with real biomolecules, but their spectral profiles are not identical to those of pure substances. Therefore, a valuable application of MCR-ALS analysis is the physical interpretation of the differences and similarities between the classes being analyzed, while the extracted MCR components are not sufficient for optimal classification. The full Raman spectra analyzed using PLS and subsequently differentiating them using DA and SVM algorithms enables us to achieve a more accurate model compared to processing the spectra using MCR. PLS performs better at finding the input variables that have a closer relationship with the output variables.

Nevertheless, some studies have demonstrated successful results from the use of MCR [30] techniques for classification tasks. In our opinion, a comparison of modeling techniques for data prediction should be conducted with care, taking into account the type of the biochemical data involved.

4 Conclusions

In this study, we explore the performance of the MCR-LR, MCR-SVM, PLS-DA, and PLS-SVM machine learning algorithms in differentiating the serum Raman spectra of patients with CHF from control subjects. MCR enabled the identification of common patterns and differences in the MCR spectral components associated with the molecular components, however, it was not possible to effectively classify the CHF and control cases based on MCR components using LR and SVM. We found that PLS-DA and PLS-SVM demonstrated the best statistical significant ROC AUCs equaled to 0.95 (0.91−0.97, 0.95 CI) and 0.99 (0.94−1.00, 0.95 CI) in comparison with MCR-LR and MCR-SVM for classification of CHF and controls. Nevertheless, we MCR method allows one to extract the spectral components corresponding to different vibrational bonds which can be valuable for physical interpreting differences between the analyzed classes. Taken together, combination of Raman spectroscopy with MCR and PLS method has shown promising potential for rapid and accurate clinical diagnostics of CHF disease in the near future.

Disclosures

The authors declare no conflicts of interest.

References

1. T. A. McDonagh, M. Metra, M. Adamo, R. S. Gardner, A. Baumbach, M. Böhm, H. Burri, J. Butler, J. Čelutkienė, O. Chioncel, J. G. F. Cleland, A. J. S. Coats, M. G. Crespo-Leiro, D. Farmakis, M. Gilard, S. Heymans, A. W. Hoes, T. Jaarsma, E. A. Jankowska, M. Lainscak, C. S. P. Lam, A. R. Lyon, J. J. V. McMurray, A. Mebazaa, R. Mindham, C. Muneretto, M. Francesco Piepoli, S. Price, G. M. C. Rosano, F. Ruschitzka, A. Kathrine Skibelund, ESC Scientific Document Group, R. A. De Boer, P. Christian Schulze, M. Abdelhamid, V. Aboyans, S. Adamopoulos, S. D. Anker, E. Arbelo, R. Asteggiano, J. Bauersachs, A. Bayes-Genis, M. A. Borger, W. Budts, M. Cikes, K. Damman, V. Delgado, P. Dendale, P. Dilaveris, H. Drexel, J. Ezekowitz, V. Falk, L. Fauchier, G. Filippatos, A. Fraser, N. Frey, C. P. Gale, F. Gustafsson, J. Harris, B. Iung, S. Janssens, M. Jessup, A. Konradi, D. Kotecha, E. Lambrinou, P. Lancellotti, U. Landmesser, C. Leclercq, B. S. Lewis, F. Leyva, A. Linhart, M.-L. Løchen, L. H. Lund, D. Mancini, J. Masip, D. Milicic, C. Mueller, H. Nef, J.-C. Nielsen, L. Neubeck, M. Noutsias, S. E. Petersen, A. Sonia Petronio, P. Ponikowski, E. Prescott, A. Rakisheva, D. J. Richter, E. Schlyakhto, P. Seferovic, M. Senni, M. Sitges, M. Sousa-Uva, C. G. Tocchetti, R. M. Touyz, C. Tschoepe, J. Waltenberger, M. Adamo, A. Baumbach, M. Böhm, H. Burri, J. Čelutkienė, O. Chioncel, J. G. F. Cleland, A. J. S. Coats, M. G. Crespo-Leiro, D. Farmakis, R. S. Gardner, M. Gilard, S. Heymans, A. W. Hoes, T. Jaarsma, E. A. Jankowska, M. Lainscak, C. S. P. Lam, A. R. Lyon, J. J. V. McMurray, A. Mebazaa, R. Mindham, C. Muneretto, M. F. Piepoli, S. Price, G. M. C. Rosano, F. Ruschitzka, and A. K. Skibelund, "2021 ESC Guidelines for the diagnosis and treatment of acute and chronic heart failure," European Heart Journal 42(36), 3599–3726 (2021).
2. M. Onodera, M. Nakamura, F. Tanaka, T. Takahashi, S. Makita, T. Ishisone, Y. Ishibashi, K. Itai, T. Onoda, M. Ohsawa, K. Tanno, K. Sakata, S. Omama, K. Ogasawara, A. Ogawa, T. Kuribayashi, K. Sakamaki, and A. Okayama, "Plasma B-Type Natriuretic Peptide Is Useful for Cardiovascular Risk Assessment in Community-Based Diabetes Subjects: Comparison With Albuminuria," International Heart Journal 53(3), 176–181 (2012).
3. Y. Khristoforova, L. Bratchenko, and I. Bratchenko, "Raman-Based Techniques in Medical Applications for Diagnostic Tasks: A Review," International Journal of Molecular Sciences 24(21), 15605 (2023).

4. S. Abalde-Cela, L. Wu, A. Teixeira, K. Oliveira, and L. Diéguez, "Multiplexing Liquid Biopsy with Surface-Enhanced Raman Scattering Spectroscopy," Advanced Optical Materials 9(15), 2001171 (2021).
5. I. A. Bratchenko, L. A. Bratchenko, Y. A. Khristoforova, A. A. Moryatov, S. V. Kozlov, and V. P. Zakharov, "Classification of skin cancer using convolutional neural networks analysis of Raman spectra," Computer Methods and Programs in Biomedicine 219, 106755 (2022).
6. Y. A. Khristoforova, L. A. Bratchenko, M. A. Skuratova, E. A. Lebedeva, P. A. Lebedev, and I. A. Bratchenko, "Raman spectroscopy in chronic heart failure diagnosis based on human skin analysis," Journal of Biophotonics 16(7), e202300016 (2023).
7. L. Huang, H. Sun, L. Sun, K. Shi, Y. Chen, X. Ren, Y. Ge, D. Jiang, X. Liu, W. Knoll, Q. Zhang, and Y. Wang, "Rapid, label-free histopathological diagnosis of liver cancer based on Raman spectroscopy and deep learning," Nature Communications 14(1), 48 (2023).
8. H. Yang, C. Zhao, R. Li, C. Shen, X. Cai, L. Sun, C. Luo, and Y. Yin, "Noninvasive and prospective diagnosis of coronary heart disease with urine using surface-enhanced Raman spectroscopy," Analyst 143(10), 2235–2242 (2018).
9. H. Leng, C. Chen, R. Si, C. Chen, H. Qu, and X. Lv, "Accurate screening of early-stage lung cancer based on improved ResNeXt model combined with serum Raman spectroscopy," Journal of Raman Spectroscopy 53(7), 1302–1311 (2022).
10. N. M. Ralbovsky, I. K. Lednev, "Raman spectroscopy and chemometrics: A potential universal method for diagnosing cancer," Spectrochimica Acta Part A: Molecular and Biomolecular Spectroscopy 219, 463–487 (2019).
11. I. Matveeva, I. Bratchenko, Y. Khristoforova, L. Bratchenko, A. Moryatov, S. Kozlov, O. Kaganov, and V. Zakharov, "Multivariate Curve Resolution Alternating Least Squares Analysis of In Vivo Skin Raman Spectra," Sensors 22(24), 9588 (2022).
12. A. Ospanov, I. Romanishkin, T. Savelieva, A. Kosyrkova, S. Shugai, S. Goryaynov, G. Pavlova, I. Pronin, and V. Loschenov, "Optical Differentiation of Brain Tumors Based on Raman Spectroscopy and Cluster Analysis Methods," International Journal of Molecular Sciences 24(19), 14432 (2023).
13. S. Shafaq, M. Irfan Majeed, H. Nawaz, N. Rashid, M. Akram, N. Yaqoob, A. Tariq, S. Shakeel, A. Ul Haq, M. Saleem, M. Zaman Nawaz, and R. Zaki Abdul Bari, "Quantitative analysis of solid dosage forms of Losartan potassium by Raman spectroscopy," Spectrochimica Acta Part A: Molecular and Biomolecular Spectroscopy 272, 120996 (2022).
14. K. Bērziņš, S. D. L. Harrison, C. Leong, S. J. Fraser-Miller, M. J. Harper, A. Diana, R. S. Gibson, L. A. Houghton, and K. C. Gordon, "Qualitative and quantitative vibrational spectroscopic analysis of macronutrients in breast milk," Spectrochimica Acta Part A: Molecular and Biomolecular Spectroscopy 246, 118982 (2021).
15. I. Behl, G. Calado, A. Vishwakarma, D. Traynor, S. Flint, S. Galvin, C. M. Healy, M. L. Pimentel, A. Malkin, H. J. Byrne, and F. M. Lyng, "Classification of cytological samples from oral potentially malignant lesions through Raman spectroscopy: A pilot study," Spectrochimica Acta Part A: Molecular and Biomolecular Spectroscopy 266, 120437 (2022).
16. S. Zhu, Y. Li, H. Gao, G. Hou, X. Cui, S. Chen, and C. Ding, "Identification and assessment of pulmonary Cryptococcus neoformans infection by blood serum surface-enhanced Raman spectroscopy," Spectrochimica Acta Part A: Molecular and Biomolecular Spectroscopy 260, 119978 (2021).
17. I. Bratchenko, Y. Khristoforova, L. Bratchenko, A. Moryatov, S. Kozlov, E. Borisova, and V. Zakharov, "Optical Biopsy of Amelanotic Melanoma with Raman and Autofluorescence Spectra Stimulated by 785 nm Laser Excitation," Journal of Biomedical Photonics & Engineering 7(2), 020308 (2021).
18. P. H. C. Eilers, H. F. M. Boelens, "Baseline correction with asymmetric least squares smoothing," Leiden University Medical Centre Report 1(1), 5 (2005).
19. S. He, W. Zhang, L. Liu, Y. Huang, J. He, W. Xie, P. Wu, and C. Du, "Baseline correction for Raman spectra using an improved asymmetric least squares method," Analytical Methods 6(12), 4402–4407 (2014).
20. A. Savitzky, M. J. E. Golay, "Smoothing and Differentiation of Data by Simplified Least Squares Procedures," Analytical Chemistry 36(8), 1627–1639 (1964).
21. I. Pence, A. Mahadevan-Jansen, "Clinical instrumentation and applications of Raman spectroscopy," Chemical Society Reviews 45(7), 1958–1979 (2016).
22. J. Felten, H. Hall, J. Jaumot, R. Tauler, A. De Juan, and A. Gorzsás, "Vibrational spectroscopic image analysis of biological material using multivariate curve resolution–alternating least squares (MCR-ALS)," Nature Protocols 10(2), 217–240 (2015).
23. J. Jaumot, A. De Juan, and R. Tauler, "MCR-ALS GUI 2.0: New features and applications," Chemometrics and Intelligent Laboratory Systems 140, 1–12 (2015).
24. I. A. Bratchenko, L. A. Bratchenko, "Comment on "Combining derivative Raman with autofluorescence to improve the diagnosis performance of echinococcosis"," Spectrochimica Acta Part A: Molecular and Biomolecular Spectroscopy 252, 119514 (2021).
25. J. A. Hanley, B. J. McNeil, "A method of comparing the areas under receiver operating characteristic curves derived from the same cases," Radiology 148(3), 839–843 (1983).

26. K. Kralova, M. Kral, O. Vrtelka, and V. Setnicka, "Comparative study of Raman spectroscopy techniques in blood plasma-based clinical diagnostics: A demonstration on Alzheimer's disease," Spectrochimica Acta Part A: Molecular and Biomolecular Spectroscopy 304, 123392 (2024).
27. M. Saleem, M. Bilal, S. Anwar, A. Rehman, and M. Ahmed, "Optical diagnosis of dengue virus infection in human blood serum using Raman spectroscopy," Laser Physics Letters 10(3), 035602 (2013).
28. H. Horiue, M. Sasaki, Y. Yoshikawa, M. Toyofuku, and S. Shigeto, "Raman spectroscopic signatures of carotenoids and polyenes enable label-free visualization of microbial distributions within pink biofilms," Scientific Reports 10(1), 7704 (2020).
29. M. Wang, R. Tang, R. Zhou, Y. Qian, and D. Di, "The protective effect of serum carotenoids on cardiovascular disease: a cross-sectional study from the general US adult population," Frontiers in Nutrition 10, 1154239 (2023).
30. I. A. Matveeva, A. I. Komlev, O. I. Kaganov, A. A. Moryatov, and V. P. Zakharov, "Multidimensional Analysis of Dermoscopic Images and Spectral Information for the Diagnosis of Skin Tumors," Journal of Biomedical Photonics & Engineering 10(1), 010307 (2024).

Modern Optical Microscopy. Part 2

Darya V. Prokopova* and Svetlana P. Kotova
Lebedev Physical Institute, 221 Novo-Sadovaya str., Samara 443011, Russian Federation
*e-mail: prokopovadv@lebedev.ru

Abstract. The subject of this article which is the second part of the review published earlier, is the methods of fluoresce microscopy which make it possible to avoid the diffraction restrictions and obtain image resolution with sub-diffraction accuracy. These methods provide new opportunities for biomedical research. In the review some hybrid or mixed microscopy methods combining the capabilities of different approaches are also described.
© 2024 Journal of Biomedical Photonics & Engineering.

Keywords: optical microscopy; optical microsphere nanoscopy; fluorescence microscopy; reversible saturable optical fluorescence transition (RESOFT); Stimulated Emission Depletion (STED); single-molecule localization microscopy (SMLM); Photo-Activation Localization Microscopy (PALM); Stochastic Optical Reconstruction Microscopy (STORM); Fluorescence Photo Activation Localization Microscopy (FPALM); Total Internal Reflection Fluorescence (TIRF) microscopy; 3D nanoscopy; Double-Helix Point Spread Function (DH-PSF); tetrapod PSF; hybrid microscopy methods.

Paper #9109 received 3 Jun 2024; revised manuscript received 10 Dec 2024; accepted for publication 10 Dec 2024; published online 26 Dec 2024. doi: 10.18287/JBPE24.10.040202.

1 Introduction

Since the end of the seventeenth century, optical microscopy has become an irreplaceable tool for biologists. The problem of increasing spatial resolution beyond the diffraction limit remains relevant to the present time and is actively studied by many scientific groups [1–3]. This review covers the currently existing optical microscopy methods that provide images of better quality and higher information content. In this second part of the review the following methods are considered: the microsphere nanoscopy, fluorescence microscopy of ultrahigh resolution and hybrid systems whose design combines various approaches aimed to obtain the most complete information about the test sample. Here we will consider the possibilities, features and limitations of these methods. In the previous part of our review [4], the first one, the subject of research was the methods that have already found their application in practice. These are laser scanning confocal microscopy, near-field optical microscopy and digital holographic microscopy.

2 Optical Microsphere Nanoscopy

While studying the laser radiation scattering on quartz micro cylinders, an effect was revealed, later called “photonic nanojet”. The extensive studies of this effect, both theoretical and experimental, were carried out in the near field zone of various micro-objects. A photonic nanojet (PNJ) is a narrow light beam of high-intensity formed near the shadow surface of transparent dielectric microobjects: spheres, hemispheres, cylinders, ellipsoids. The curvature diameter of these microobjects is approximately equal to the wavelength of the incident radiation or slightly greater than it (Fig. 1) [5–7].

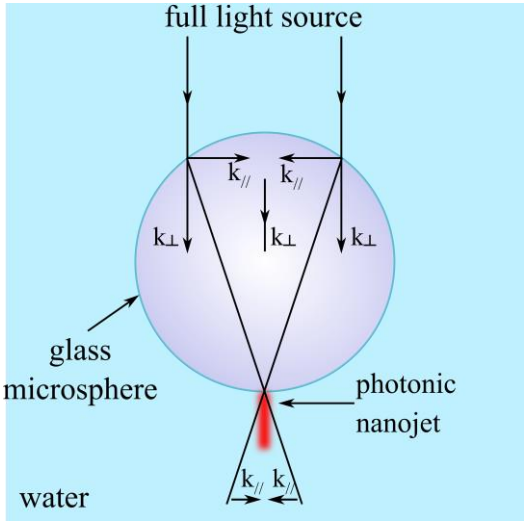


Fig. 1 Schematic diagram of the photonic nanojet emergence.

This effect originates from the interference of the scattered light wave and the wave that passed through the particle. Its peculiarity consists in the sub-wavelength dimensions of the light field localization. The length of such object is ~ 2λ by full width at half maximum (FWHM), and its width is ~ 0.5 ± 0.2λ by the same criterion. Such dimensions of the light field localization can be used in nanostructuring and nano-lithography with sub-diffraction resolution. The width and height depend on the environmental parameters. The mechanism of influence of the above-mentioned parameters on photonic nanojets and their application aimed to increase the resolution of the generated image has been circumstantially studied in the last decade [8].

To describe the structure of the light field near the illuminated spherical particle, the Mie theory is used [9, 10]. Within the framework of this theory, the field is conditionally divided into 3 components with respect to the particle: incident, internal (diffracted), and scattered. These fields are represented as a series of eigenfunctions of a ball, which are described by vector spherical harmonics. In a spherical coordinate system, vector spherical harmonics $\vec{M}^{(l)}_{hon/odd\ \ nm}$ and $\vec{N}^{(l)}_{hon/odd\ \ nm}$, are characterized by indices *m* and *n*, which determine the azimuthal and polar harmonics, respectively. The index *l* determines the type of spherical Bessel function that is included in the harmonics, and the *hon/odd* notation takes into account the parity of the harmonic with respect to a change in the azimuth angle. The coefficients of the fields expansion in the rows are found in the usual way, that is from the conditions of continuity of the tangential components of the electric field of an optical wave on the particle surface. For a homogeneous spherical non-magnetic particle with a_0 radius, with a complex refractive index $n_a = n'_a + in''_a$ and located in a non-absorbing ($n''_m = 0$) medium with a refractive index $n_m = n'_m + in''_m = n'_m$, the following expressions are found for the complex envelope of the electric fields of the scattered $\overrightarrow{E_{sc}}$ and diffracted $\overrightarrow{E_1}$ waves for the case of a flat linearly polarized monochromatic wave (azimuthal index *m=1*) incident on a particle:

$$\begin{aligned}\vec{E}_{sc}(\vec{r}) &= \sum_{n=1}^{\infty} E_n \left[i a_n(m_r, x_a) N^{(3)}_{e1n}(\vec{r}) - b_n(m_r, x_a) M^{(3)}_{o1n}(\vec{r}) \right];\\ \vec{E}_1(\vec{r}) &= \sum_{n=1}^{\infty} E_n \left[c_n(m_r, x_a) M^{(1)}_{e1n}(\vec{r}) - i d_n(m_r, x_a) N^{(1)}_{o1n}(\vec{r}) \right],\end{aligned} \quad (1)$$

where $\vec{r}$ is the radius vector of a point with spherical coordinates $\{r, \theta, \varphi\}$, $m_r = \dfrac{m_a}{m_m}$; $E_n = E_0 i^n \dfrac{2n+1}{n(n+1)}$ are the coefficients of expansion by spherical harmonics of an incident wave $\vec{E}_i = E_0 \exp\{ikr\cos\theta\}\vec{e}_x$. The amplitude of this wave E_0 is propagating along the Z axis and is polarized along the X axis. The partial coefficients of the rows (Mie coefficients) a_n, b_n, c_n, d_n depend on the relative refractive index of the particle n_r and the parameter of its optical size, i.e. diffraction parameter, and they are calculated by the recurrent schemes. In the Mie theory, the optical field inside and outside a weakly absorbing sphere illuminated by a light wave, is described by the presence of spatial focusing zones called internal and external field focuses. They are caused by the curvature of the spherical particle surface that deforms the wave front of the wave incident on the particle. The peak intensity of the field in the focusing zones depends on the particle size and can by several orders exceed its initial value, and the focuses spatial dimensions can be equal only to fractions of the wavelength of the incident radiation. Thus, a spherical microparticle behaves like a microlens that focuses light within an extremely small volume. A special combination of the particle material optical properties and its size provides a special ratio between the length and width of the waist of the radiation external focus. The focusing zone is stretched in the direction of the radiation incidence, and a light jet is formed of a narrow subwavelength size in the transverse direction. Provided that the particle is illuminated by radiation from the visible or UV range of the spectrum, then the jet transverse dimensions will be of nanometer size.

The results of experimental research on photonic nanojets created by single latex microspheres illuminated by a plane wave at a wavelength of 520 nm, are presented in Ref. [11]. The 3D structure of photonic nanojets was measured using a fast-scanning confocal microscope under detection mode. On the base of the accumulated set of 2D images, a 3D structure was reconstructed. The photonic jets were formed by polystyrene spheres of 1-, 3- and 5-μm diameters. The spheres were applied to a glass substrate placed in air or water. The experimental results were then compared with calculations carried out using the Mie theory. This work proved the existence of photonic nanojets. It was also demonstrated that several microspheres are able to form nanojets simultaneously and independently.

The use of microspheres as lenses is related to microscopy techniques based on the use of photonic nanojets with solid immersion microscopy, which was proposed in 1990 [12]. The essence of this method is to increase the microscope resolution by raising the refractive index of the medium located between the lens and sample. This is reached by placing on the surface of the sample an extra lens with a refractive index greater than the refractive index of traditional immersion media. In Ref. [12], it became possible to resolve lines of 100 nm-thickness through using a lens with $n = 2$ and radiation at a wavelength of $\lambda = 436$ nm. The disadvantage of the method is that an additional lens with a high refractive index must be in direct contact with the test sample, and therefore the field of view of the microscope is smaller than the field of view of a conventional microscope. The field of view can definitely be increased by scanning the sample, but in this case, it is impossible to observe dynamic processes in the scanned area under study. An alternative method

proposed in 2000, suggests the use of materials with a negative refractive index [13].

Paper [13] presents a theoretical approach to amplification of decaying waves and transmission of their encoded information to the far field. The main problem with this method is its limitation to a certain frequency, since materials with a negative refractive index are created in the spectrum microwave range, and to special materials required for the lens and medium.

The interest in the photonic nanojet effect is due to the potential practical applications of photonic nanojets in studying the properties and creating nanoparticles of various compositions, such as metallic, dielectric, and fluorescent materials. These nano particles can be used to create waveguides with low losses and record and store optical data with high density. When a nanoparticle enters an area of increased intensity created by a photonic nanojet formed by a dielectric sphere, backscattering occurs due to the interaction between the photon jet and the nanoparticle [10]. This will lead to a significant increase in the backscattering power of a microsphere with a diameter of 3 μm, when a nanoparticle with a diameter of 30 nm is placed in a photonic nanojet emerging from the microsphere. Despite the small size of the nanoparticle compared to the cross-sectional area of the microsphere, the backscattering characteristics change significantly compared to an isolated microsphere. This allows for a more accurate determination of the presence of certain substances at lower concentrations, making it possible to use this phenomenon for developing new methods of ultra-high-resolution optical microscopy.

The first results of research into improving the resolution of images formed in a PNJ-based microscope were published in 2004 [14]. The photonic nanojet was generated by dielectric micro-objects with a high refractive index. Since then, a number of articles have appeared on photonic nanojets and their use in microscopy [15−18]. A schematic diagram of the operation of such a system is shown in Fig. 2. Radiation from a source, such as a laser, light-emitting diode (LED) or lamp, is reflected by a beam-splitting cube and illuminates the sample (Ob). The radiation then passes through a micro lens (microobjective, MO) and microsphere (MS) before reaching the detector. Then, the micro lens displays an imaginary image of the object formed by the microsphere on the detector. For microspheres with a diameter not exceeding 10 μm, a model was created to study the dependence of photonic nanojet shape and size on the generating microobject and the illuminating beam. The study of two-layer microparticles as objects generating photonic nanojet showed that this phenomenon can be the basis for detecting inhomogeneities with nanometric sizes [15]. Experimental studies of the photonic nanojet phenomenon have also been conducted. It has been shown that not only microspheres but also hemispheres can form photonic nanojet and be used to visualize objects [16]. Between 2011 and 2012, extensive studies were conducted to establish a relationship between the parameters of photonic nanojet and illumination of the generating micro-object [18−20]. The relationship between the shape, size, and layout of photonic nanojet and the wavelength of radiation illuminating a glass sphere has been established, as has the dependence of photonic nanojet's location relative to the surface of a microsphere on the radius of curvature of an illuminating spherical wave [18]. Some unusual or extraordinary photonic nanojets have been obtained [19, 20] under illumination of glass and polymer spheres with a field that has a complex spatial distribution or polarization structure, and polymer spheres have been proposed as an alternative to glass spheres.

The simulation showed a non-monotonic dependence of the resolution obtained on the wavelength, due to the amplification of the field caused by resonances. This phenomenon can be used to visualize broadband point sources, such as dye molecules or fluorophores. In Ref. [21], the fundamental limit on resolution was determined when using photonic nanostructures, which corresponds to a transverse resolution of the order of λ/6 to λ/7. However, there are several challenges associated with the practical implementation of this method.

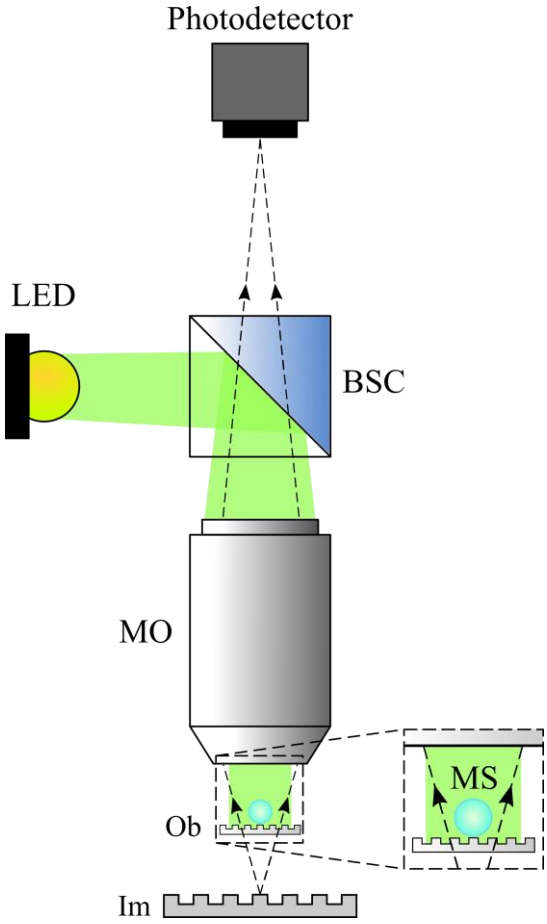


Fig. 2 Schematic diagram of the operation of a super-resolution microscope based on the use of photonic nanojets formed by transparent micro-objects. LED − light-emitting diode, BSC – beam splitter cube, MO – microobjective, Ob – sample, MS – microsphere, Im – imaginary image.

The main challenge lies in the difficulty of manufacturing and handling micro-objects. This can create obstacles for experiments, as without precise control over the microspheres processing, it will be impossible to isolate the part of the sample that researchers want to study. Another challenge is that the photonic nanostructures created by these microspheres are located very close to the surface (within a distance not exceeding λ). This issue was addressed by creating two-layer microspheres that can project photon jets up to a distance of about 4λ. These microspheres have a similar diameter to those made from a single material, but with two layers [22−26]. The two-layer microspheres are SiO_2 spheres coated with gold. This concept was applied to larger diameter microspheres [27], which demonstrated a 2.4-fold increase in the length of the generated photonic nanojet when a two-layer and single-layer microsphere were placed in the same medium and illuminated by light with the same wavelength. The development of this concept continued in the investigation of the possibility of forming photonic nanostructures using hollow microparticles [28]. Alongside studies on two-layered microspheres, various other geometries of microparticles were investigated for their potential application in generating photonic nanostructures [29] and the effect of surface roughness [30].

The second area of research conducted with microspheres focused on the possibilities of visualizing different microspheres under various conditions [31−36]. In Ref. [32], a comparison was made between the techniques of solid-state immersion microscopy and the use of microspheres, demonstrating the significant advantages of the latter method. This comparison inspired further research into the potential applications of photonics nanojet based microscopy. As a result, in Refs. [33−35] various biological samples were visualized, and in Refs. [36], this technique was used for metrological tasks.

One more problem related to these methods is the limited field of view. This can be addressed by increasing the size of the microspheres used, but this would result in a decrease in resolution. To solve this issue, several approaches have been proposed, including the formation of an array of micro-objects for monitoring the test sample [37−39] and shifting the microsphere relative to the sample, or vice versa, to scan it [40−45].

The most impressive results from this method of improving resolution are described in Ref. [46]. A technique is presented that allows for a spatial resolution comparable to that of an atomic force microscope, using microspheres made from barium titanate ($BaTiO_3$). These unique results were achieved through the use of an interferometer. Due to the use of these microspheres, the field of view for the microscope was expanded and, as a result, the scanning time for the sample was significantly decreased. The authors of this work reported a transverse resolution of 50 nm and an axial resolution of 10 nm for the created system.

The advantage of the above methods for increasing the resolution of optical microscopes by using photonic nanojets formed by micro-objects is their economic feasibility compared to analogues [47]. The scope of application for these methods is wide and includes metrology, biological observation, robotics, environmental monitoring, and others. However, due to the lack of a universal method for evaluating the resolution of these systems it is difficult to analyze the results obtained from different groups. In Refs. [21, 48] standardization of measurement processes was proposed. The following basic elements are necessary for a precise description of the method: 1) a clear description of a priori knowledge about the system, including illumination, wavelength, filtering, polarization state, and the main components of the optical system such as the lens type and post-processing stages of the resulting image; 2) obtaining images of test mires; and 3) considering gold-coated substrates or fluorescent samples as specific cases rather than general ones.

The issue of increasing the field of view of such nanoscopes also remains not finally solved yet. The works describing this problem have appeared in recent years.

All these factors prevent the classification of super-resolution nanoscopy methods based on the use of photonic nanojets formed by transparent microobjects, and their commercialization by now. Provided these issues are resolved, then micro lenses with microspheres attached to them and specialized software providing the super-resolution images will soon be available. In November 2020, OptoSigma presented a device for nanoscale imaging called OptoNano based on the principle of Optical Microsphere Nanoscopy (OMN) [23]. According to the developers, OptoNano provides a resolution as high as 137 nm with no need for sample preparation. OptoNano microscopes have not only overcome the optical limit, but also eliminated the barriers of high cost and high complexity of operations in ultra-high-resolution microscopy. This unlocks a new paradigm that allows the use of optical microsphere nanoscopy technology for users with a wide variety of training type and level: from research laboratories to biochemists and industrial enterprises managers.

The advantage of the microsphere nanoscopy method is that it does not require fluorescent labels, which can negatively affect the sample under study. There is also no need to use additional pulsed laser radiation, which can affect the sample. It can be used to study metal and silicon samples in cases where it is impossible to implement fluorescent methods. For further development of this technique, it is necessary to establish the production of special microspheres, methods for their positioning relative to the sample under study, and miniaturization of the technology. And although microsphere nanoscopy allows to overcome the diffraction limit to a lesser extent than ultrahigh-resolution fluorescent methods, it will be widely used in various fields, for example, for semiconductor control, where an ultrahigh-resolution fluorescent microscope does not work effectively [49]. A summary of the main characteristics of microsphere nanoscopy and other techniques considered in the review are presented in Table 1.

Table 1 Characteristics of modern super-resolution microscopy methods.

Technique	Resolution	Features	Advantages	Limitations
Optical microsphere nanoscopy	2D projection of the sample. Fundamental resolution limit $\Delta x = \Delta y = \lambda/6 - \lambda/7$; record value: 50 nm [46]. Commercially available solution: $\Delta x = \Delta y = 137$ nm ($\lambda = 460$ nm, $\Delta x = \Delta y = 154$ nm (white light) [23].	There is no need for special sample preparation and the use of fluorescent labels	Simple and accessible	Micro-objects of uniform size made with good accuracy are needed. A limited field of view
Stimulated Emission Depletion (STED)	2D resolution $\Delta x = \Delta y = 30 - 50$ nm Record resolution $\Delta x = \Delta y = 1$ nm [57].	The sample must contain fluorescent labels. In order for the molecules to be forced into the ground state, the sample is illuminated, in addition to exciting light, by a STED laser with a special spatial distribution of intensities in the form of a torus with zero intensity in the center.	Ultra-high resolution. Multiple types of labels can be tracked in a single experiment	Two lasers must be used to excite and quench fluorescence. Photobleaching of phosphors and phototoxic effects under intense laser exposure to the sample
Single Molecule Localization microscopy (SMLM)	2D resolution $\Delta x = \Delta y = 2.5 - 80$ nm	The sample must contain fluorescent labelsThe sample must contain fluorescent labels Stochastic activation of small groups of emitters and their separate localization. To achieve ultra-high resolution, post-processing of the obtained data is carried out, combining information about different groups into a single image of the sample. The accuracy of determining the coordinates of single molecules depends on the stability of the experimental setup and the signal-to-noise ratio	Ultra-high resolution.	Difficulty in processing images from closely spaced overlapping labels. Accuracy of determining the coordinates of single molecules depends on the stability of the experimental setup and the signal-to-noise ratio.
Total Internal Reflection Fluorescence (TIRF)	3D resolution $\Delta x = \Delta y =$ $=250 - 200$ nm Resolution $\Delta z = 100$ nm	The sample must contain fluorescent labels. Obtaining information about fluorescent labels located near the interface of media with different refractive indices.	Obtaining high-contrast images at the interface of media. Using different sources of exciting radiation	Resolution is limited by diffraction. Use of special systems for fluorescence excitation

Table 1 (Cont.)

		Short exposure time. Special image processing is required, since the intensity of the exciting radiation decreases exponentially with distance from the interface.	(lamps, lasers). Obtaining high-contrast images of cell structures located near its membrane adjacent to the cover glass of the sample under study, where total internal reflection occurs. Observation of fast processes.	(prisms or special objectives)
Nanoscopy with modified PSF	3D record resolution $\Delta x = \Delta y = \Delta z =$ =10 nm [86]. Commercially available systems: $\Delta x = \Delta y = 20 - 30$ nm $\Delta z = 50$ nm ($\Delta Z = 1$ μm) for the system N-STORM [64] with astigmatic PSF; $\Delta x = \Delta y = 20$ nm $\Delta z = 25$nm ($\Delta Z = 2{-}20$ μm) for the system SPINDLE from Double Helix Optics [100].	The sample must contain fluorescent labels. Additional elements are introduced into the microscope optical scheme to modify the PSF, and subsequent processing of the obtained images is necessary. By choosing the type of modernized PSF, it is possible to select different working depths and localization accuracies of labels in the sample	The processing provides access to 3D information with super-resolution without scanning. It is used to study samples of different nature	Special post-processing of the obtained images to determine the coordinates (x, y, z) of the emitting tags. The accuracy of determining the coordinates of a single object depends on the signal-to-noise ratio. The problem of detecting and processing superimposed images

3 Methods of Fluorescence Microscopy of Single Molecules

Fluorescence microscopy is a technique for detecting fluorescent micro-objects using an optical microscope. This method has found widespread application in materials science and the biomedical fields. The operation of a fluorescence microscope is based on the ability of atoms and molecules to absorb light quanta and transition to excited states. When a molecule returns to its ground state, it emits light or fluorescence. Absorption and fluorescence depend on the structure of an electron energy level of a molecule and are specific to each type of molecule. Biological samples fluoresce only weakly, but by using bright and diverse fluorescent molecules (fluorophores), which can stain various tissue and cell structures, fluorescence microscopy has proven to be a valuable technique in biomedical research.

In the 90s of the last century, new technologies for fluorescence microscopy were developed, such as the 4Pi and I^5M methods (mentioned in the first part of this review). These technologies provide a better resolution than diffraction limits. One method for determining the exact location of a fluorescent molecule is by suppressing the spontaneous emission of surrounding molecules, which is implemented in methods like reversible saturable optical fluorescence transition (RESOFT).

The first approach implemented in practice was the microscopy of spontaneous emission suppression, known as STED (Stimulated Emission Depletion) [50−52]. This method was developed by Stefan Hell in 1994 [50], and in 2014 he received the Nobel Prize for Chemistry for his development of the technique [53]. The first version of the STED microscope was a single-point system, which used two synchronized pulsed lasers to excite fluorescent molecules and suppress their fluorescence. When a molecule in the excited S_1 state interacts with a photon with an energy equal to the difference between the S_1 and S_0 states, it returns to its ground state (Fig. 3a). In order to force molecules to return to their ground state, the sample is additionally illuminated with a STED laser along with the exciting light. The STED laser has a special spatial distribution of intensity in the form of a torus, with zero intensity at the center. This results in only molecules located close to the region of zero intensity of the STED light emitting, narrowing the point-scattering function (Fig. 3b). Then a sequential scan of the entire sample takes place [51, 52]. The resolution achieved by the STED method is determined by an Eq.:

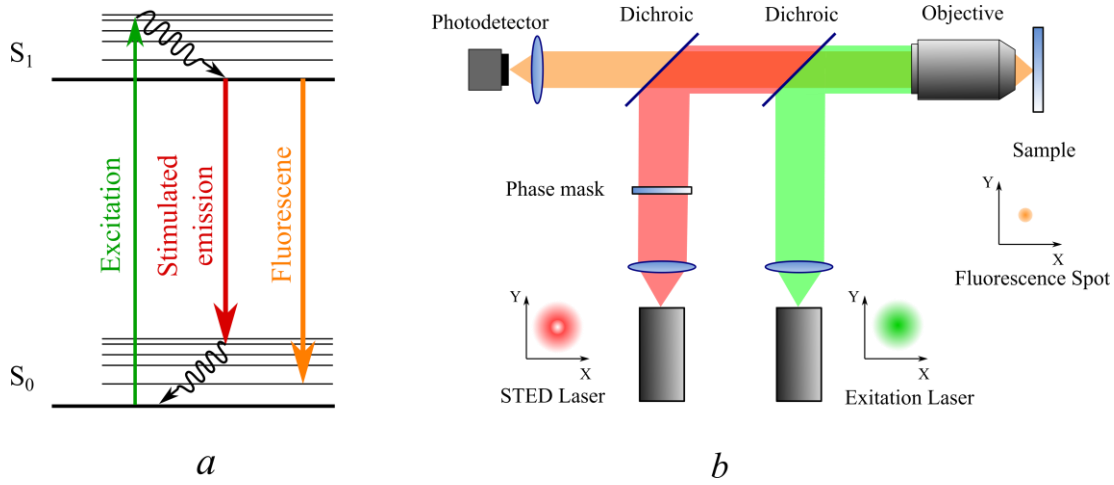


Fig. 3 STED-microscopy: (a) diagram of energy levels; (b) schematic diagram of a STED microscope, point source images obtained using confocal and STED microscopes.

$$\Delta x = \frac{\lambda}{2n\sin\alpha\sqrt{1+\frac{I_{\max}}{I_{sat}}}}, \qquad (2)$$

where $I_{\max}$ is the used intensity of the STED laser, I_{sat} is the intensity required for 50% of the forced emission. The enhancement of $I_{\max}$ to high values results in a fast photo-fading of the sample, therefore, to increase the resolution, I_{sat}, which is inversely proportional to the lifetime of the fluorophore, should be reduced. The achieved resolution in the XY- plane is 30−70 nm.

The advantage of this method lies in its high shooting speed, making it suitable for analyzing live, dynamic systems. However, creating multicolored STED microscopy can be challenging due to the undesirable overlap of wavelengths from the exciting and quenching lasers. Nevertheless, the selection of dyes allows us to solve this issue and perform two-color microscopy on living cells with a resolution of approximately 50 nm [54]. At the same time, achieving a resolution of 30−50 nm requires the use of very high intensities from a quenching STED laser, on the order of 10−100 MW/cm^2. When using a conventional STED laser that emits radiation in the red portion of the spectrum, such as 594 nm, this intense light flux can lead to rapid photobleaching of the dyes in the sample and cause phototoxic effects. These problems can be partially addressed by using pulsed lasers and time-gated detection methods (gated STED) [54]. Due to the registration of radiation with an expected lifetime of fluorescence, the intensity of the STED laser can be reduced by 3−10 times without losing resolution.

A reduction in the scanning area to smaller fields of view (subdiffractive in size) has proven to be an effective method for reducing photobleaching in STED microscopy [55]. With this approach (MINFIELD), the fluorophores inside the quenching laser ring are not exposed to the maximum light intensity, and therefore remain fluorescent for a longer period of time. In addition, when scanning an area of 200 × 200 nm^2 corresponding to a single nuclear pore, this method provides an increase in photostability of up to an order of magnitude compared to scanning the entire nucleus using the same parameters. As a result, it is possible to obtain a high-resolution or dynamic image of fluorescent proteins in the nuclear pore complex. The most incoming results were obtained in the MINSTED (the doughnut position entailing minimal STED must be identical with the fluorophore coordinate, hence the name MINSTED) and MINFLUX (or minimal fluorescence photon fluxes microscopy) systems [56−58]. The localization accuracy is about 1 nm. This high accuracy can be achieved by localizing with the movement of the quenched STED beam in the form of a ring closer to the position of the fluorophore during localization. This increases information gain per detected photon and reduces the number of photons needed to obtain high accuracy.

Thus, STED microscopy allows obtaining images of ultra-high spatial resolution, an order of magnitude higher than the diffraction limitation. It is possible to implement tracking of several types of labels in a single experiment. Unfortunately, intense laser exposure can lead to photobleaching of luminescent labels and the occurrence of phototoxic effects. These drawbacks are overcome in the MINSTED and MINFLUX methods, which are the next stage in the development of this approach and increase the resolution to the size of an individual luminescent molecule of ≈1 nm.

In parallel, at the same time, methods of single-molecule localization microscopy (SMLM methods) are being developed. These methods operate by separately registering individual fluorescent labels (such as molecules, quantum dots, or fluorescent proteins) [59−63]. There is another name for these techniques, which are also referred to as SMACM (single-molecule active control microscopy) methods. For photo-switchable fluorescent proteins that undergo a reversible transition between fluorescent and dark states, fluorescence can be induced using radiation from a light source with an intensity that is one or two orders of

magnitude lower than a STED (stimulated emission depletion) laser, approximately 1–10 kW/cm² [62]. This corresponds to typical illumination levels in confocal microscopy.

Three independent groups of researchers have worked independently on the development and implementation of these techniques, and the results of their research are currently available in the form of three microscopy techniques. These techniques include Photo-Activation Localization Microscopy (PALM) [59, 62], Fluorescence Photo Activation Localization Microscopy (FPALM) [60], and Stochastic Optical Reconstruction Microscopy (STORM) [61, 62]. Single-molecule localization techniques rely on separately detecting individual fluorescent molecules. Typically, the sample being studied contains a large number of fluorescent tags. And if they all start emitting light at the same time, their images will overlap and it will be difficult to get information about their location. Therefore, it is necessary to provide conditions for the labels to emit in sparse groups, record their images, and determine the exact location of each individual label (Fig. 4). To achieve subdiffraction accuracy in determining the coordinates of the emitting labels, the type of radiation point source hardware is taken into account. The source image is an Airy disk, and its transverse coordinates can be determined by calculating the "gravity center" of the molecule image, or by approximating the distribution of radiation intensity recorded within the source using a 2D Gaussian function. The accuracy of evaluating individual molecule coordinates depends on the stability of the experimental setup and the signal-to-noise ratio. An image of the fluorescent label or fluorophore is formed by a number of photons emitted from it. Based on this, an image consisting of N photons can be considered as N measurements of the location of the fluorophore. And each measurement has an uncertainty determined by the point spread function (PSF), leading to a localization accuracy close to:

$$\Delta x = \frac{\Delta_{PSF}}{\sqrt{N}}, \qquad (3)$$

where Δx is the localization accuracy and ΔPSF is the size of the point spread function. It is necessary in these methods to bypass the group nature of fluorescent label emission by exposing them to laser radiation in order to study the entire sample. The labels are switched from the emitting to the non-emitting state. By sorting through the combinations of "switched-on" (i.e., emitting) labels and determining their location with accuracy exceeding the diffraction limit (localization accuracy ranging from 80 nm to 2.5 nm, depending on the level of useful signal), the sample image is compiled with higher resolution in the transverse plane [59−62].

It is possible to obtain a 3D image using the microscopy technique of localization of single molecules, provided that a slight upgrade to the microscopic system is made. For example, weak cylindrical lenses can be added to the optical system [63]. As a result of using these extra cylindrical lenses, the image of the emitting molecule will depend on its position along the Z axis. The point spread function (PSF) of the system will also be modified. By analyzing the shape of the images obtained in this system, it will be possible to estimate not only the coordinates of the emitting object in the transverse directions (X and Y), but also its position in the longitudinal direction relative to the Z axis. The successful implementation of this system contributed to the fact that by the end of 2016 Nikon developed the N-STORM system, capable of building images with super resolution operating on this principle [64]. According to the manufacturer, the system provides a resolution of 20−30 nm in the transverse direction and 50 nm in the Z axis [61]. At the current stage of developing this technique, the ways to solve the issue of resolution and localization of overlapping source images are being studied. This solution is important, as it will accelerate data processing, and therefore − increase the speed of getting images with super-resolution. Currently, several algorithms for localization have been proposed that permit to resolve individual images of radiation sources even under significant overlap of their images [62, 65].

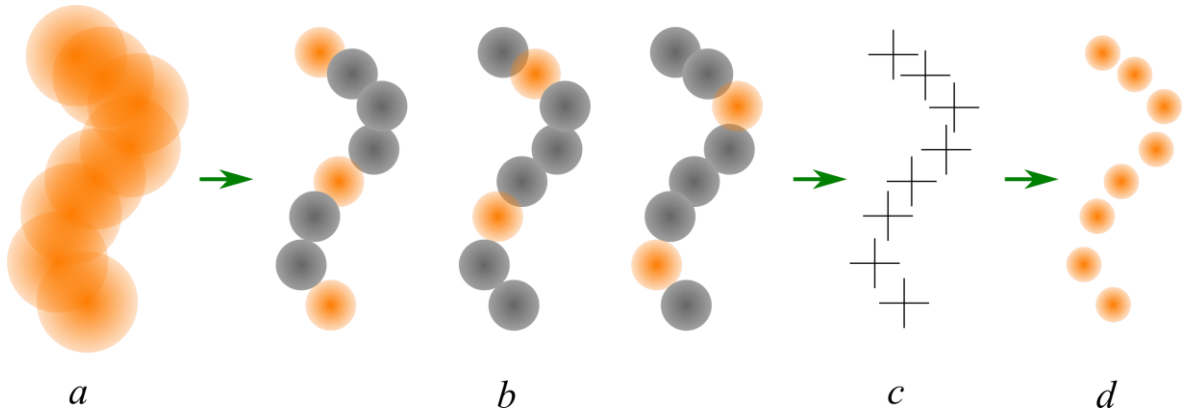


Fig. 4 Demonstration of the principle of single-molecule localization microscopy. (a) Standard fluorescence image. (b) Sequential stochastic activation of small groups of emitters and their separate localization. (c) Determining the location of individual emitters. (d) Reconstructed super-resolution image.

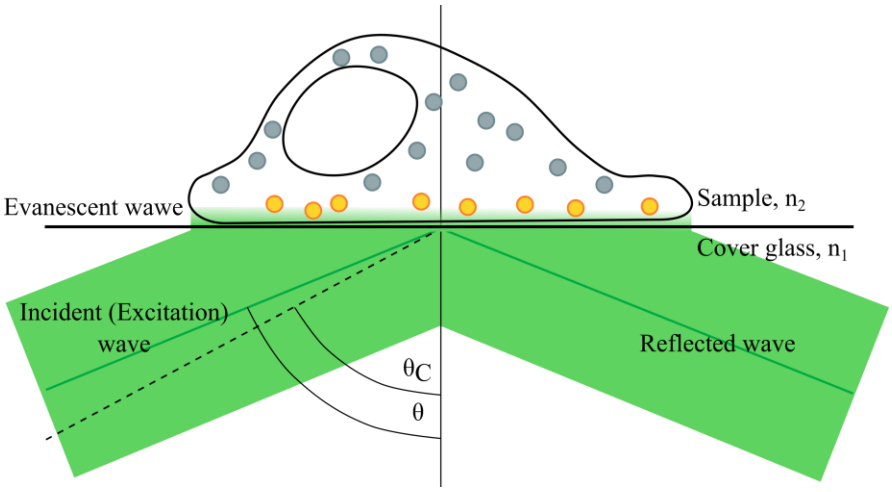


Fig. 5 Schematic diagram of total internal reflection microscopy.

The idea of separate activation, registration and subsequent processing of the received data images allows obtaining ultra-high spatial resolution in the SMLM method. However, it is necessary to choose a compromise between temporal and spatial resolution, since the accuracy of localization of single molecules depends on the stability of the experimental setup and the signal-to-noise ratio. As the ensemble of excited labels increases, difficulties arise in processing images of closely spaced and overlapping labels. Various approaches are proposed to solve this problem.

An increase in resolution can be achieved by using the phenomenon of total internal reflection. Total Internal Reflection Fluorescence (TIRF) microscopy is based on this principle. The phenomenon of total internal reflection occurs when light passes through the boundary between two media, provided that the first medium from which the light originates is denser than the second medium into which it enters. This condition is expressed as $n_1 > n_2$ where n_1 and n_2 are the refractive indexes of the two media. By increasing the angle of incident light on the interface between the two media, a critical angle of incidence can be reached, at which the angle of refraction becomes equal to $\pi/2$ and the reflected light becomes completely internal. At this point, the light no longer propagates in the second medium, but slides along the interface. The value of the critical angle depends on the refractive index of the media, and not on the wavelength of the light. In the region where the incident light experiences total internal reflection, there is a narrow area where attenuated, non-propagating (evanescent) light waves occur. These waves can excite fluorescence in a thin layer of material, as shown in Fig. 5 [66].

The size of a typical living cell is several microns. Radiation at the boundary between media with full internal reflection penetrates to a depth of about 100 nm [67]. Therefore, TIRF microscopy allows obtaining high contrast images of cell structures next to the membrane adjacent to the cover glass of the sample being studied, where total internal reflection occurs. The sample is illuminated in a thin layer, leading to the fact that there is no “illumination” of the image by fluorescence excited in structures deeper than 100 nm from the cover glass. Using TIRF microscopy, fast moving processes can be observed because the exposure time for this method is short. The intensity of light in the area of fluorescence excitation decays exponentially with distance from where the light is incident. This feature must be taken into account when evaluating fluorescence at different depths − at the surface it will be more intense than at the edges of the attenuated wave region. With an equal content of fluorochrome, this fact will require special image processing [66, 67].

As the light source for fluorescence excitation, lasers and various lamps can be used. The choice of the light source depends on the specific parameters of a particular system. The use of white light is more convenient, since any component necessary for work can be extracted from it with the help of light filters [68]. But regardless of the type of light source chosen, its rays should illuminate the sample at an angle. There are 2 main methods for illuminating a sample at an angle: using prisms or through a specialized objective. When a prism is used, the light source should be placed above the test sample and there should be a system for the prisms configuration correction for each test sample [69]. And when using special objectives, the angle of light incidence on the sample is adjusted by focusing the objective. An important parameter of the objective is its numerical aperture, since it determines the ability of the objective to illuminate the sample at a certain angle. The higher the numerical aperture value, the greater the angle of incidence. For TIRF microscopy, the value of the numerical aperture must exceed the value of the sample refractive index. For instance, in biological tasks, this requirement is met by objective with a numerical aperture (NA) of 1.4. Prism-based systems allow operating in a wide range of wavelengths, and have larger sensitivity. The systems where lenses are used are easy to handle and therefore widely used, but their capabilities regarding the field of view size and sensitivity are smaller.

The interface between the media, where complete internal reflection of light happens, is located between the cover glass and the test sample, but for solving some

specific research problems, it can be deeper. Owing to focusing in deeper layers of the sample, it became possible to see what was previously considered inaccessible for observation, for example, a membrane of a plant cell hidden under the cell wall [69]. Detection of fluorescence in various parts of the spectrum can be fulfilled automatically, the TIRF-microscopy system can be combined with the visualization of fluorescence recovery after photobleaching (FRAP) or fluorescence resonance energy transfer (FRET).

Although TIRF microscopy does not provide super-high resolution imaging, it does visualize structures at the interface with high contrast inaccessible to other approaches. This feature opens up new possibilities. The combined use of TIRF microscopy and optical tweezers opens up new possibilities for studying the physical interactions between organelles. Specifically, it allows us to study the interaction between the endoplasmic reticulum and Golgi corpuscles in plant cells [70]. Currently, the TIRF microscopy method is being used beyond biological applications in other areas. For example, it is used for visualization and study of kinetics in nanocatalysis [71]. In Ref. [72], this technique was used to study the surface dynamics of polyethylene terephthalate hydrolase. This is important for the future development of polyethylene terephthalate (PET) hydrolases.

4 Microscopy with Increased Axial Resolution by Upgrading the Point Spread Function

In the methods of fluorescence microscopy of single molecules, wide-angle microscopes and 2D camera detectors are normally used to localize molecules with an accuracy significantly exceeding the diffraction limit. Due to the limited number of photons available from each emissive label (single molecule, nanoparticle, fluorescent protein, quantum dot), these methods require a scrupulous mathematical analysis and image processing. They allow getting the information about the projections of the radiating labels location on the sample observation plane. Much more information on the test object can be obtained by extending it to the 3D localization of the emitters. While working with a 2D projection, when there is no information about the position of structures or their dynamics in the axial direction, it is easy to miss important information or make a mess of the data obtained. This prevents a correct understanding of the structure and processes taking place in the sample under study. By means of scanning, the 3D information about the test sample structure or position of a small luminous object can be obtained. And this is exactly what is done in the methods earlier described in the first part of the review: laser scanning confocal microscopy, near-field optical microscopy (by this method the information at a shallow depth can be obtained), light sheet microscopy. In order to obtain 3D information from a single 2D image, it is necessary to modify the PSF of the microscopic system so that it depended on the object position along the Z axis. Then the information about the axial object location will be encoded in its image [73]. To date, many options for the microscope PSF upgrading are known, but the schematic diagram of them is approximately the same (Fig. 6), and represents an inverted 4f microscopic system. The PSF of a standard microscope is changed by changing the phase of the electromagnetic field in the Fourier plane of the 4f system.

The most obvious and easily made PSF modification is the addition of astigmatism to the system using cylindrical lens [64]. Due to this, an astigmatic PSF can be obtained, and by the change of the source image shape, i.e., whether the ellipse is stretched along the X-axis or the Y-axis, (Fig. 7), the Z coordinate of the radiating label can be determined. However, the range for the Z coordinate estimation is limited to 1-μm depth. In section 2 the N-STORM system is described, functioning on this principle and able to restore the longitudinal coordinate with an accuracy of 50 nm.

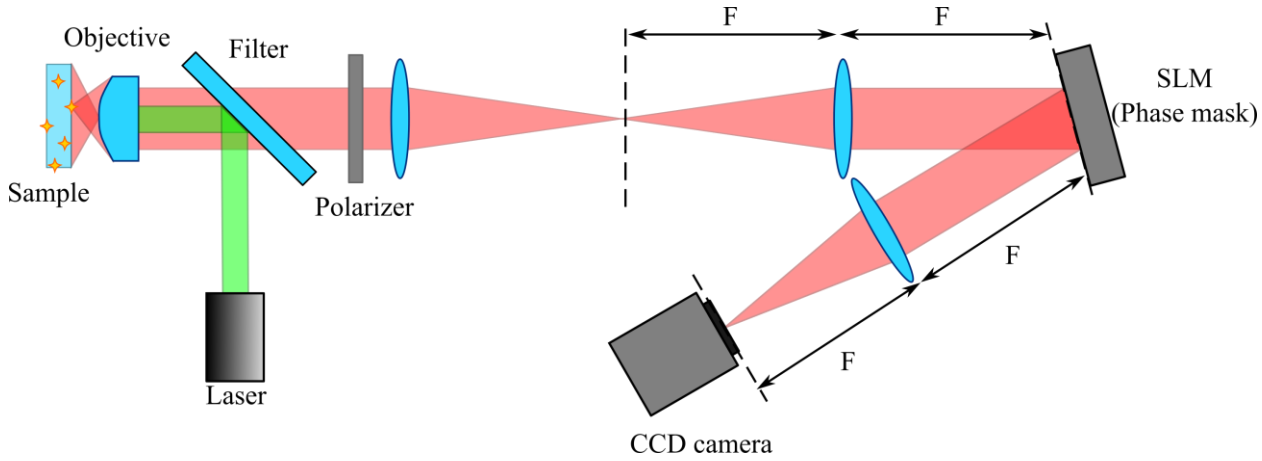


Fig. 6 Diagram of experimental setup for modifying the PSF based on spatial phase modulation of the back focal plane radiation. F – focal distance, SLM – spatial light modulator.

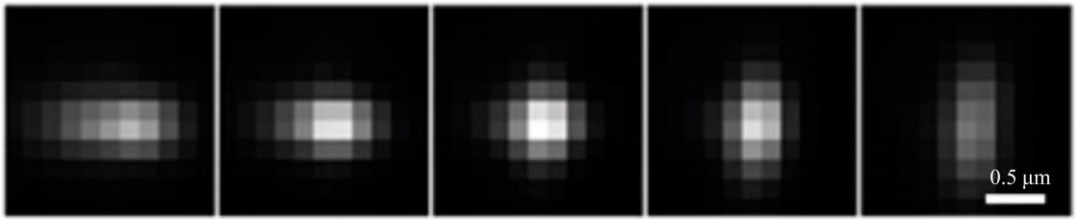


Fig. 7 Images generated due to the PSF modifying into an astigmatic PSF. Scale 0.5 μm (from Ref. [63]. Reprinted with permission from AAAS).

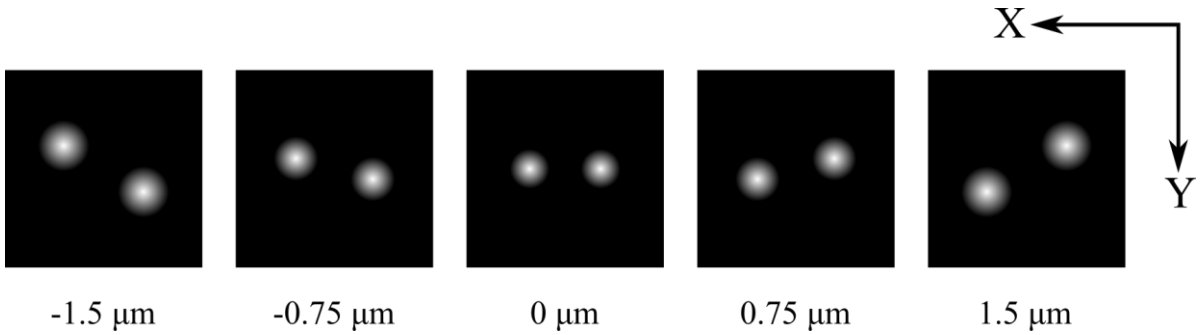


Fig. 8 Schematic images were obtained by converting PSF into an DH-PSF at different distances from the focus of the objective.

Another approach is based on the formation of a rotating light field collected from a point radiation source to determine the depth of the object by defocusing (Depth from Defocus, DFD). A rotating PSF can have various structure [74]. Thus, the PSF described in Refs. [75, 76], is a bright spot, rotating around the center under defocusing. For further processing, the easiest method is the one that allows transformation of the microscope classical PSF into two spots rotating during defocusing. In this case, it is possible to explicitly associate the longitudinal location of the radiating object with the gradient of the straight line passing through the centers of the rotating spots. The obtained two-lobe fluorescent images can be analyzed using algorithms and programs engineered for the analysis of fluorescent images, by the methods of fluorescence microscopy of single molecules described in the previous section. But these algorithms and programs should be slightly supplemented, since now it is necessary to analyze a pair of spots instead of one. To make this modification of the microscope PSF, several types of diffraction optical elements (DOE) were offered. Their development is based on various principles. A more detailed discussion of them is given below.

It was proposed in Refs. [77, 78] to use the 5 Laguerre-Gauss modes superposition in order to obtain a field with the intensity distribution in the form of 2 bright spots rotating around their common center during propagation (Fig. 8). The results of numerical modeling for a linear system along with the experimental obtaining of the proposed field using a calculated hologram are presented. A low efficiency, about 2%, is reported for this field formation. The authors draw a conclusion that the generated field can be used as a PSF system for the tasks of precise 3D-localization of luminous objects in optical microscopy. But for this, an increased energy efficiency of its formation is necessary. It is shown in Ref. [79] that using rotating fields, the depth estimation accuracy is higher than that for classical microscopes with PSF, representing the Airy function. The authors offer to modify the microscope optical system in a way providing the microscope PSF transformation into a superposition of five Laguerre-Gauss modes, the same as in Ref. [78]). As for information about the object depth, it is proposed to obtain it by defining the transfer function of the system. The transfer function, in turn, depends on the value of the defocus parameter, which is related to the position of the object, since the received image is a convolution of the object field and the transfer function. The authors of this work assert that this method of getting information about the object depth is rather complicated. For these purposes it is reasonable to use a simpler and more efficient pre-built calibration curve for the depth estimation based on the image rotation. In the article the demonstration of the proposed method is also given. In Ref. [80], a solution to the problem of low efficiency of the two-lobe field generation is proposed. The authors propose an algorithm to increase the efficiency of the field formation, with the initial distribution of intensity and phase of the field being a superposition of Laguerre-Gauss modes. During the algorithm operation, the intensity distribution is replaced by a homogeneous one within the aperture boundaries. After this the field is decomposed by Laguerre-Gauss basis functions. To improve the efficiency of the field formation, 9 planes are selected in the space where the field under study rotates in the range from −90° to 90° through 2 Rayleigh lengths, or Rayleigh ranges. In each of the planes, the intensity distribution obtained due to the Fresnel transform, is multiplied by the weight function. The weight function is

two 2D Gaussian functions, it is located at the point of the intensity maxima. Parameters of the functions included in the weight function are chosen in such a way that the width of the Gaussian functions coincides with the maxima width. The reverse Fresnel transform is carried out and the phase in the plane of the phase mask is replaced with the received one. The efficiency of the field generation using the phase mask and obtained as a result of this algorithm was 56.8% according to the modeling results and 37% according to the data received in the experiment, where the phase profile was formed with a spatial light modulator. The modified PSF of the microscope is called a Double-Helix Point Spread Function, DH-PSF.

After the publication of work [80], a series of papers followed testifying to the effectiveness of using a two-lobe field as the microscope PSF to get 3D information about the position of a small luminous object in a sample with sub-diffraction accuracy. The research described in Ref. [81], demonstrates the possibility of the DH-PSF application for visualization of weak emitters in biological systems for tracking the quantum dots motion in glycerin and in living cells. One more experimental demonstration of this mask use for precise localization of objects is given in Ref. [82]. A precise localization of the molecules of photoactivated fluorophore, DCDHF (2-dicyanoethylene-3-cyano-2,5-dihydrofuran fluorophore) residing in the polymer matrix, is carried out. The achieved accuracy is 10 nm in the transverse direction and 20 nm in the longitudinal direction for a sample of 2 μm thickness. This exceeds the diffraction limit by an order of magnitude. In Ref. [83], it is proposed to take into consideration the molecular radiation anisotropy. The polarization and intensity distribution of the field emitted by a molecule is related to its orientation in space. Disregard of this fact in designing systems for the precise localization of individual molecules, causes the errors of tens of nanometers in the localization estimation, which is unacceptable with an accuracy of the object position evaluating of 10−15 nm. The author's crew has proved that using a 2-lobe field as a function of the microscope PSF, it is possible to determine not only the exact location of the molecule, but also its orientation in space. Owing to the offered method use, the determination of the location of molecules was significantly improved: the dipole-induced location error was reduced, and the standard deviation for transverse and longitudinal localization was also lowered. The test object is localized within an elementary volume, $(\Delta x, \Delta y, \Delta z)=(5, 5, 34)$ nm; while previously proposed methods were limited to the volume $(\Delta x, \Delta y, \Delta z)=(25, 25, 116)$.

The probable wide use of two-lobe light fields in real optical systems influenced by aberrations inspired the studies of these fields for their resistance to aberrations. Thus, in Ref. [84] the influence of spherical aberration is studied, and in Ref. [85] the influence of coma and astigmatism is investigated. As a result, it became possible to develop a system capable of tracking RNA COVID-19 in a cell with an accuracy of 10 nm [86], to identify nanoscale details of the MyosinH organization in the apical complex of Toxoplasma gondii, with localization accuracy of 12 nm in the transverse direction and 22 nm in the axial direction [87], to produce 3D localization of individual atoms in an optical lattice [88], imaging of whole mammalian cells [89].

Thus, in Ref. [86] a team of authors proposed to build an "unconventional" two-lobe point spread function (unconventional DH-PSF), with the controllable parameters, such as energy efficiency, transverse size and localization accuracy of the luminous source. By changing these characteristics, it is possible to obtain a PSF with the parameters required for a specific task and a certain sample. In the work, a 2-lobe field is generated, which is later used for 3-D localization, suitable for typical background conditions of the experiment. The development of a phase element providing the "unconventional two-lobe PSF" formation is based on a regularity revealed by the authors. If optical vortices of the first order are located along the axis, then the beam energy will be divided into 2 lobes. The impact of the number of vortices on the intensity distribution was studied by the authors and it was found that with an increase in the number of optical vortices, the efficiency of the 2-lobe field formation rises. But at the same time an increase in the image transverse size is observed. For an effective localization of molecules, a high efficiency of the field formation and a small transverse size of the resulting image are obligatory, therefore it is necessary to find the optimal efficiency-and-size combination, and consequently − the optimal vortices number. The search of these optimal values was fulfilled with the same unchanged number of vortices, $N = 9$, and the distance between them changed. The aperture of the pupil also remained unchanged. The localization accuracy was estimated using the Cramér-Rao inequality. It was illustrated that the field proposed by the authors of this work gives better results than the field proposed in article [79], but the depth of field (depth of focus) here is only 1.2 μm, whereas for the field from Ref. [79] this value is 2 μm.

The capabilities of the proposed phase mask and the "unconventional two-lobe PSF" obtained with its help are demonstrated by visualizing microtubules in mice cells, fulfilled using the obtained PSF. The tubes are marked with a fluorescent dye, excited by laser radiation. The re-emitted light passes through a system where the PSF is modified by means of the calculated element, and is recorded by an EMCCD camera (Electron Multiplying Charge-Coupled Device). This method used for getting the information about the fluorescent dye molecules position in 3-D space, is called Super-resolution Photon-efficient Imaging by Nanometric Double-helix-PSF Localization of Emitters (SPINDLE). By applying this algorithm, it is possible to localize the emitting object in an elementary volume $(\Delta x, \Delta y, \Delta z) = (2.5, 3.8, 16.5)$ nm when 6000 photons from the source are detected, and in a volume $(\Delta x, \Delta y, \Delta z) = (22, 29, 52)$ nm while detecting 1100 photons from the emitter. And the background noise of 30 photons per pixel was typical.

To form a light field with the required rotation parameters and intensity distribution structure, it is reasonable to refer to the structured light fields properties. Thus, in Ref. [90] a method was proposed to obtain diffractive optical elements (DOE) for the 2-lobe light field formation, based on the spiral beam's optics [91]. A further development of the method made it possible to develop a DOE optimized for a specific system with an increased efficiency [92, 93]. This allowed for upgrade of the spatial and temporal resolution characteristics. The capabilities of the obtained system are presented in Ref. [94]. A resolution about 10 nm the for single colloidal quantum dots was achieved for all 3 spatial coordinates, and for an exposure time of about 100 ms.

An alternative method is proposed in Refs. [95, 96] for making a phase mask for the formation of fields rotating during propagation. In Ref. [95] a simple and effective method for generating rotating light fields is offered. Here a phase mask is used consisting of sectors (or spiral sections) filled with discrete phase levels ranging from 0 to 2π. The authors consider these spiral phase masks suitable for spatial modulation of light. The calculation algorithm for the mask phase was developed for a general selection of topological charges in radial and azimuthal zones, which provides controllability of the generated rotating field. The results of numerical modeling and experiments, demonstrating rotation of 3-lobe and 4-lobe fields during defocusing, are also presented. It is shown that during propagation, the dependence of the rotation angle of the field intensity distribution on the defocusing value corresponds to the arctangent function. Defocusing is understood as a displacement of the observation plane from the image plane along the axis of the beam propagation. The gradient of the linear part of the obtained dependence rises with the increase of both numerical aperture of the optics used and the number of phase levels of the spiral phase mask. The same researchers team reported on the obtainment of a phase mask capable of the formation of a two-lobe field in Ref. [96], and the algorithm for calculating the spiral phase used by this team was the same as in the previous work [95]. The rotation speed of the field being generated was controlled by variation of two main parameters of the spiral phase mask: the number of radial zones and phase difference in the neighboring sectors. Characteristics of the fields generated by these masks were studied through numerical modeling. As a result of this numerical modeling, the influence of the number of radial zones and phase gradations on the resulting fields properties was determined. To prove the revealed dependences, a full-scale experiment was carried out, and its results were consistent with the numerical modeling results

In works [97–99], for 3D localization it is proposed to use a tetrapod point spread function (Tetrapod PSF), the intensity distribution structure of which is more complex as compared to an astigmatic or double-helical PSF. The peculiarity of the tetrapod PSF is that it can provide detection of emitting objects at larger depths, compared to the above-described methods: 1 μm for astigmatic and 2 μm for double-spiral PSF. In Ref. [97] the use of tetrapod PSF is demonstrated for localization at depths of 20 μm (in the experiment carried out with a microchannel system) and 6 μm (in tracking of quantum dots attached to lipid molecules diffusing in the cellular membranes of mammalian cells). In a series of experiments at depths of 6 μm and 20 μm, the same optical system was used. The element forming the tetrapod PSF was obtained using a multi-element liquid crystal spatial light modulator (LC SLM). This enabled the researcher to dynamically control the structure of the generated field and change the PSF depending on the test sample. The phase distribution needed for the generation of tetrapod PSF was calculated using an algorithm. Accounting for the system parameters (magnification, numerical aperture, noise and signal levels), a numerical image model was constructed. The image model was used to solve the problem of finding the phase distribution in the Fourier plane that could provide the dependence of the system PSF on the depth of occurrence of the point source. This strict condition imposed on the PSF, forces researchers to solve a number of tasks for the parameter's minimization, therefore an optimization program was specially developed for these purposes.

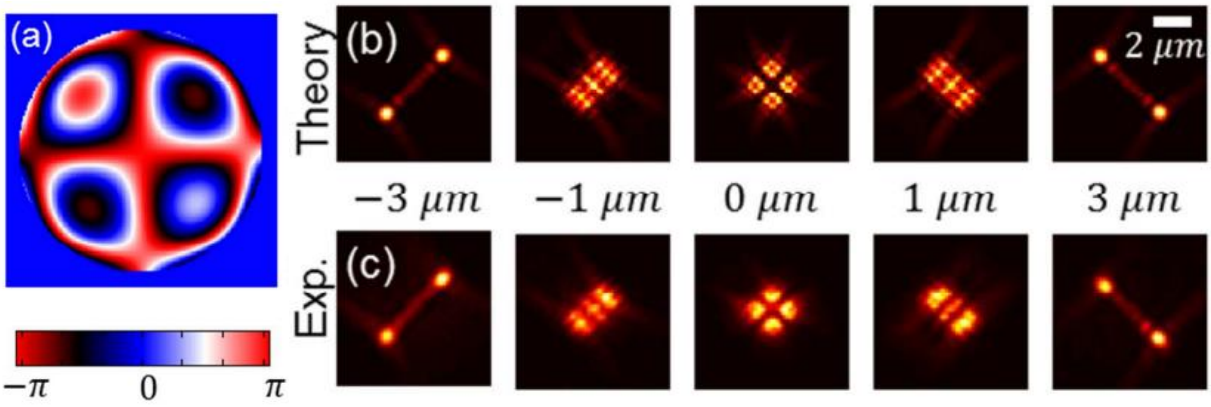


Fig. 9 (a) Phase distribution in the Fourier plane of the 4f system. Intensity distributions: (b) numerically calculated, (c) experimentally obtained (taken from Ref. [97]).

The optimization program was used for various depths of determining the point source location, from 2 to 20 μm. In the course of this program operation, a whole family of phase filters was obtained for the formation of tetrapod PSF needed for various conditions. The found PSFs consisted of 2 separate fractions, and the transverse distance between them raised while the emitter was moving away from the focal plane of the microscope lens. The type of phase distribution in the Fourier plane and the type of tetrapod PSF, found by the calculation and experimentally obtained in various sections along the Z axis, are shown in Fig. 9.

The modification of the microscopic system PSF provides new possibilities for making nanoscopes based on optical microscopes that are capable of displaying the 3D structure of the test sample. The PSF can be formed for a specific task, whether it is required to get a precise localization, ~1 nm, at a shallow depth >1 μm; or vice versa − a less accurate localization, 40−50 nm, but at a greater depth, say up to 20 μm.

However, the use of microscopes with modified PSF has its own difficulties related to various factors: post-processing of images, choice of optimal algorithms for its obtainment, selection of concentrations of fluorescent labels, resolution of images overlapped from neighboring labels, the sample drift. Nevertheless, despite the difficulties these methods show imposing results. In 2019 in the USA, the company "Double Helix Optics" was established, that made a commercial offer for the set-top box attached to microscopes [100]. With this attachment it is possible to obtain 3D images with nanometric resolution due to replaceable phase masks that provide the PSF modification of the system. The localization depth declared by the manufacturer is 20 μm, and the accuracy of coordinate's estimation is 25 nm. So, for a specific task it is possible to select a PSF required for the work in certain conditions. But manufacturers warn that the user will need to choose what is more important for him in each particular case: a larger localization depth or a higher accuracy in determining the point source location. The set of phase masks includes elements for getting DH PSF, tetrapod PSF, multi-color visualization, and elements providing larger depth. Besides, special software is also supplied complete with the set-top box for constructing a 3D image by the images obtained.

Thus, the modification of the PSF system allows one to obtain information about the position of luminous marks in 3D space from 2D images. Due to the large set of statistics, one can obtain ultra-high resolution. By choosing different types of modified PSF, one can localize one can localize luminous point sources at different depths or in a relatively thin layer, but with high accuracy. The accuracy of localization of single molecules depends on the stability of the experimental setup and the signal-to-noise ratio. The use-related approach continues to offer new DOE options for implementing 3D visualization [101] and to develop algorithms for working in a large field of view [102].

5 Hybrid Methods of Super Resolution Microscopy

Various methods of super resolution microscopy with their benefits and disadvantages have been considered in this review. Lately, works have been published describing systems where various methods are combined in order to obtain the most complete information about studied samples.

In Ref. [103], a system is described that combines the method of super resolution microscopy based on the use of photonic nanojets formed by transparent microobjects, with laser scanning confocal microscopy. To combine these two methods, the researchers placed microspheres in random order on the sample upper surface. To locate the microspheres on the sample upper surface, a solution of microspheres made of melted silicon dioxide (d = 2.5; 5; 7.5 μm, n_{sphere} = 1,47) and polystyrene (d = 5 μm, n_{sphere} = 1.62) was first poured onto the sample, and then evaporated. After the liquid component evaporation, the image of the sample was obtained with the aid of a confocal microscope using a laser light source with λ = 408 nm. In this way the image of an anode template made of aluminum oxide with holes of 25-nm diameter and a distance between them of 50 nm was recorded. In the resulting images holes are resolvable. Unfortunately, the authors did not provide any data on the intensity measurements or modulation for the fulfilled experiments, so it is problematic to compare the hybrid method with other methods and estimate the resolution. Besides, it is important to note that these impressively small-size elements were displayed with a laser light source, which provides the increased illumination power and reflected light intensity. One more quite important factor is the use of a confocal microscope, which ensures a higher resolution than a classical optical microscope due to the PSF change.

The construction of an ultra-sensitive nano immunosensor is described in Ref. [104]. The imaging system of this sensor is based on a joint use of methods of the microscope PSF modification for 3D localization of an object (the Airy disk is converted into an astigmatic PSF) and light-sheet microscopy. The researchers obtained images of plasmonic nanoimmunosensors consisting of specially processed couples of gold and silver nanoparticles of a certain size. Visualization was carried out in 1000 sections (500 sections above the focal plane and 500 − below the focal plane) with a pace of 10 nm. Basing on the difference in images of gold and silver nanoparticles, the distance between them was measured, it was 23 ± 3 nm for the concentration of 7.8 Zeptomol (zepto =10^{-21}). The distances between the nanoparticles were estimated for different virus concentrations, and measurements were carried out from 23 to 48 nm. The earlier unknown concentration of the virus has been estimated in a sample of lettuce leaves. In the future the offered method may prove to be a reliable way for the virus molecules detecting at the level of a single molecule.

Another example of combining the capabilities of light-sheet microscopy with the PSF modification is given in Ref. [105]. The tilted light sheet microscopy with 3D point spread functions (TILT 3D) combines a new approach of sample illumination with an inclined light sheet and the use of PSF operating in a wide axial range (i.e. working depth along the Z axis) for 3D super-localization of individual molecules, as well as for 3D super-resolution of visualization in thick cells. Since the axial position of a single emitting particle is encoded in its image structure, and not in the position or thickness of the light sheet illuminating the sample, the requirements to the light sheet in this approach are not so rigid, and the extremely thin beam formation is also not required. The system described in this paper is based on a standard inverted microscope and has a small number of specially manufactured parts and assemblies, which makes it quite affordable. With this device, a 3D-visualization with super resolution (~10 nm) can be performed in thick mammalian cells.

A system presented in Ref. [106], allows for 3D mapping of the sample temperature. The PSF modification into a DH-PSF makes it possible to receive 3D information. Photoluminescence of quantum dots is closely connected with temperature, and a linear dependence has been established between the change in the wavelength of the fluorescence intensity peak and the temperature change. And this dependence was used by the authors in their work. This means that quantum dots can be used as nanoscale materials for the temperature measurements, while the temperature is estimated by the photoluminescence spectrum of quantum dots inserted in the sample. In the obtained system, the radiation collected from the sample was divided into 2 recording channels, one was for determination of the spectral characteristics of their radiation, and the other – for the 3D localization of the emitting quantum dot. In the experiments a simultaneous measurement of temperature was demonstrated carried out in different points of the sample of living cancer cells of liver during the time t = 300 s.

6 Conclusion

The review presents modern methods for increasing the spatial resolution of optical microscopes. Table 1 summarizes the features of the high-resolution microscopy methods considered in this review. These methods make it possible to distinguish smaller details in the image of a sample, by an order of magnitude smaller than the diffraction limit. These approaches combine the latest scientific and technological achievements with the innovative ideas of their creators. By using the features of different methods, new opportunities are opened for studying samples. It is possible to obtain not only 3D information about the sample's structure, but also information about its spectral, thermal, and compositional properties, which is important for biomedical applications. This gives hope that the efforts of the scientific community to develop high-resolution imaging techniques will lead to the creation of more efficient and versatile microscopy methods that will allow obtaining more comprehensive information about the objects being studied.

Disclosures

The authors declare no conflicts of interest.

References

1. F.-Y. Zhu, L.-J. Mei, R. Tian, C. Li, Y.-L. Wang, S.-L. Xiang, M.-Q. Zhu, and B. Z. Tang, "Recent advances in super-resolution optical imaging based on aggregation-induced emission," Chemical Society Reviews 53(7), 3350–3383 (2024).
2. P. Gupta, N. Rai, A. Verma, and V. Gautam, "Microscopy based methods for characterization, drug delivery, and understanding the dynamics of nanoparticles," Medicinal Research Reviews 44(1), 138–168 (2024).
3. S. So, M. Kim, D. Lee, D. M. Nguyen, and J. Rho, "Overcoming diffraction limit: From microscopy to nanoscopy," Applied Spectroscopy Reviews 53(2–4), 290–312 (2018).
4. D. V. Prokopova, S. P. Kotova, "Modern optical microscopy. Part 1," Journal of Biomedical Photonics & Engineering 9(4), 040202 (2023).
5. A. Darafsheh, G. F. Walsh, L. Dal Negro, and V. N. Astratov, "Optical super-resolution by high-index liquid-immersed microspheres," Applied Physics Letters 101(14), 141128 (2012).
6. A. V. Maslov, V. N. Astratov, "Optical nanoscopy with contact Mie-particles: Resolution analysis," Applied Physics Letters 110(26), 261107 (2017).
7. Yu. E. Geints, A. A. Zemlyanov, and E. K. Panina, "Peculiarities of photonic nanojet formation from multilayer spherical microparticles," Atmospheric and Oceanic Optics 24(6), 587–592 (2011).
8. G. Huszka, M. A. M. Gijs, "Super-resolution optical imaging: A comparison," Micro and Nano Engineering 2, 7–28 (2019).
9. X. Li, Z. Chen, A. Taflove and V. Backman, "Optical analysis of nanoparticles via enhanced backscattering facilitated by 3-D photonic nanojets," Optics Express 13(2), 526–533 (2005).
10. S. Lecler, Y. Takakura, and P. Meyrueis, "Properties of a three-dimensional photonic jet," Optics Letters 30(19), 2641–2643(2005).
11. J. J. Schwartz, S. Stavrakis, and S. R. Quake, "Colloidal lenses allow high-temperature single-molecule imaging and improve fluorophore photostability," Nature Nanotechnology 5(2), 127–132 (2010).

12. S. M. Mansfield, G. S. Kino "Solid immersion microscope," Applied Physics Letters, 57(24), 2615–2616 (1990),.
13. J. B. Pendry, "Negative refraction makes a perfect lens," Physical Review Letters 85(18), 3966–3969 (2000).
14. Z. Chen, A. Taflove, and V. Backman, "Photonic nanojet enhancement of backscattering of light by nanoparticles: a potential novel visible-light ultramicroscopy technique," Optics Express 12(7), 1214–1220 (2004).
15. C. M. Ruiz, J. J. Simpson, "Detection of embedded ultra-subwavelength-thin dielectric features using elongated photonic nanojets", Optics Express 18(16), 16805–16812 (2010).
16. J. Y. Lee, B. H. Hong, W. Y. Kim, S. K. Min, Y. Kim, M. V. Jouravlev, R. Bose, K. S. Kim, I.-C. Hwang, L. J. Kaufman, C. W. Wong, P. Kim, and K. S. Kim, "Near-field focusing and magnification through self-assembled nanoscale spherical lenses," Nature 460(7254), 498–501 (2009).
17. Z. Wang, W. Guo, L. Li, B. Luk'yanchuk, A. Khan, Z. Liu, Z. Chen, and M. Hong, "Optical virtual imaging at 50 nm lateral resolution with a white-light nanoscope," Nature Communications 2(1), 218 (2011).
18. M. Kim, T. Scharf, S. Mühlig, C. Rockstuhl, and H. P. Herzig, "Engineering photonic nanojets," Optics Express 19(11), 10206–10220 (2011).
19. M. Kim, T. Scharf, M. Brun, S. Olivier, S. Nicoletti, and H. P. Herzig, "Advanced optical characterization of micro solid immersion lens," Proceedings of SPIE 8430, 84300E (2012).
20. D. Kang, C. Pang, S. M. Kim, H. S. Cho, H. S. Um, Y. W. Choi, and K. Y. Suh, "Shape-controllable microlens arrays via direct transfer of photocurable polymer droplets," Advanced Materials 24(13), 1709–1715 (2012).
21. V. N. Astratov, A. V. Maslov, K. W. Allen, N. Farahi, Y. Li, A. Brettin, N. I. Limberopoulos, D. E. W. Jr, A. M. Urbas, V. Liberman, and M. Rothschild, "Fundamental limits of super-resolution microscopy by dielectric microspheres and microfibers," Proceedings of SPIE 9721, 97210K (2016).
22. Yu. E. Geints, A. A. Zemlyanov, and E. K. Panina, "Controlling the parameters of photon nanojets of composite microspheres," Optics and Spectroscopy 109(4), 590–595 (2010).
23. Optonano Microsphere-Assisted Super-Resolution Microscopes, OptoSigma (accessed 22 May 2024). [https://www.optosigma.com/eu_en/optonano-microsphere-assisted-super-resolution-microscopes-PT-ONANO.html?___store=eu_en&___from_store=us_en].
24. D. Grojo, N. Sandeau, L. Boarino, C. Constantinescu, N. De Leo, M. Laus, and K. Sparnacci, "Bessel-like photonic nanojets from core-shell sub-wavelength spheres," Optics Letters 39(13), 3989–3992 (2014).
25. Yu. E. Geints, A. A. Zemlyanov, and E. K. Panina, "Spatial and energy characteristics of nanofields in the vicinity of isolated spherical particles," Atmospheric and Oceanic Optics 23(8), 666–674 (2010). [In Russian]
26. Yu. E. Geints, E. K. Panina, and A. A. Zemlyanov, "Comparative analysis of spatial shapes of photonic jets from spherical dielectric microparticles," Atmospheric and Oceanic Optics 25(5), 338−345 (2012).
27. Y. Shen, L. V. Wang, and J. Shen, "Ultralong photonic nanojet formed by a two-layer dielectric microsphere," Optics Letters 39(14), 4120–4123 (2014).
28. G. Gu, R. Zhou, Z. Chen, H. Xu, G. Cai, Z. Cai, and M. Hong, "Super-long photonic nanojet generated from liquid-filled hollow microcylinder," Optics Letters 40(4), 625–628 (2015).
29. T. Jalali, D. Erni, "Highly confined photonic nanojet from elliptical particles," Journal of Modern Optics 61(13), 1069–1076 (2014).
30. R. Chen, J. Lin, P. Jin, M. Cada, and Y. Ma, "Photonic nanojets generated by rough surface micro-cylinders," IEEE 28th Canadian Conference on Electrical and Computer Engineering (CCECE), 1393–1397 (2015).
31. S. Lee, L. Li, Y. Ben-Aryeh, Z. Wang, and W. Guo, "Overcoming the diffraction limit induced by microsphere optical nanoscopy," Journal of Optics 15(12), 125710 (2013).
32. A. Darafsheh, N. I. Limberopoulos, J. S. Derov, D. E. Walker, and V. N. Astratov, "Advantages of microsphere-assisted super-resolution imaging technique over solid immersion lens and confocal microscopies," Applied Physics Letters 104(6), 061117 (2014).
33. H. Yang, N. Moullan, J. Auwerx, and M.A. Gijs, "Super-resolution biological microscopy using virtual imaging by a microsphere nanoscope," Small 10(9), 1712–1718 (2014).
34. A. Darafsheh, C. Guardiola, J. Finlay, A. Cárabe, and D. Nihalani, "Simple super-resolution biological imaging," SPIE Newsroom, 29 April 2015 (accessed 27 May 2024) [https://www.spie.org/news/5912-simple-super-resolution-biological-imaging].
35. A. Darafsheh, C. Guardiola, A. Palovcak, J.C. Finlay, and A. Cárabe, "Optical super-resolution imaging by high-index microspheres embedded in elastomers," Optics Letters 40(1) 5–8 (2015),
36. H. Yang, M. A. Gijs, "Optical microscopy using a glass microsphere for metrology of sub-wavelength nanostructures," Microelectronic Engineering 143, 86–90 (2015).
37. W. Fan, B. Yan, Z. Wang, and L. Wu, "Three-dimensional all-dielectric metamaterial solid immersion lens for subwavelength imaging at visible frequencies," Science Advances 2(8), e1600901 (2016).
38. P. Ghenuche, J. de Torres, P. Ferrand, and J. Wenger, "Multi-focus parallel detection of fluorescent molecules at picomolar concentration with photonic nanojets arrays," Applied Physics Letters 105(13), 131102 (2014).
39. B. Du, Y. Ye, J. Hou, M. Guo, and T. Wang, "Sub-wavelength image stitching with removable microsphere-embedded thin film," Applied Physics A 122(1), 15 (2016),

40. L. A. Krivitsky, J. J. Wang, Z. Wang, and B. Luk'yanchuk, "Locomotion of microspheres for super-resolution imaging," Scientific Reports 3(1), 3501 (2013).
41. J. Li, W. Liu, T. Li, I. Rozen, J. Zhao, B. Bahari, B. Kante, and J. Wang, "Swimming microrobot optical nanoscopy," Nano Letters 16(10), 6604–6609 (2016).
42. F. Wang, L. Liu, H. Yu, Y. Wen, P. Yu, Z. Liu, Y. Wang, and W. J. Li, "Scanning superlens microscopy for non-invasive large field-of-view visible light nanoscale imaging," Nature Communications 7(1), 13748 (2016).
43. M. Duocastella, F. Tantussi, A. Haddadpour, R. P. Zaccaria, A. Jacassi, G. Veronis, A. Diaspro, and F. D. Angelis, "Combination of scanning probe technology with photonic nanojets," Scientific Reports 7(1), 3474 (2017).
44. G. Huszka, H. Yang, and M. A. M. Gijs, "Microsphere-based super-resolution scanning optical microscope," Optics Express 25(13), 15079–15092 (2017).
45. G. Huszka, M. A. M. Gijs, "Turning a normal microscope into a super-resolution instrument using a scanning microlens array," Scientific Reports 8(1), 601 (2018).
46. F. Wang, L. Liu, P. Yu, Z. Liu, H. Yu, Y. Wang, and W. J. Li, "Three-dimensional super-resolution morphology by near-field assisted white-light interferometry," Scientific Reports 6(1), 24703 (2016).
47. S. Perrin, P. Montgomery, and S. Lecler, "Super-resolution imaging within reach," Optical Engineering 58(5), 050501 (2019).
48. R. Horstmeyer, R. Heintzmann, G. Popescu, L. Waller, and C. Yang, "Standardizing the resolution claims for coherent microscopy," Nature Photonics 10(2), 68–71 (2016).
49. G. Wu, M. Hong, "Optical microsphere nano-imaging: progress and challenges," Engineering 36, 102–123 (2024).
50. S. W. Hell, J. Wichmann, "Breaking the diffraction resolution limit by stimulated emission: stimulated-emission-depletion fluorescence microscopy," Optics Letters 19(11), 780–782 (1994).
51. V. Westphal, S. O. Rizzoli, M. A. Lauterbach, D. Kamin, R. Jahn, and S. W. Hell, "Video-rate far-field optical nanoscopy dissects synaptic vesicle movement," Science 320(5873), 246–249 (2008).
52. S. W. Hell, K. Willig, M. Dyba, S. Jakobs, L. Kastrup, and V. Westphal, "Nanoscale resolution with focused light: STED and other RESOLFT microscopy concepts," Chapter 31 in Handbock of Biological Confocal Microscopy, 3rd Ed., Springer New York, New York, 571–579 (2006).
53. S. W. Hell, "Nanoscopy with focused light (Nobel Lecture)," Angewandte Chemie International Edition 54(28), 8054–8066 (2015).
54. F. Bottanelli, E. B. Kromann, E. S. Allgeyer, R. S. Erdmann, S. Wood Baguley, G. Sirinakis, A. Schepartz, D. Baddeley, D. K. Toomre, J. E. Rothman, and J. Bewersdorf, "Two-colour live-cell nanoscale imaging of intracellular targets," Nature Communications 7(1), 10778 (2016).
55. F. Göttfert, T. Pleiner, J. Heine, V. Westphal, , D. Görlich, S. J. Sahl, and S. W. Hell, "Strong signal increase in STED fluorescence microscopy by imaging regions of subdiffraction extent," Proceeding of the National Academy of Science of the USA 114(9), 2125–2130 (2017).
56. M. Weber, H. Von Der Emde, M. Leutenegger, P. Gunkel, S. Sambandan, T. A. Khan, J. Keller-Findeisen, V. C. Cordes, and S. W. Hell, "MINSTED nanoscopy enters the Ångström localization range," Nature Biotechnology 41(4), 569–576 (2023).
57. M. Weber, M. Leutenegger, S. Stoldt, S. Jakobs, T. S. Mihaila, A. N. Butkevich, and S. W. Hell, "MINSTED fluorescence localization and nanoscopy," Nature Photonics 15(5), 361–366 (2021).
58. J. Wang, Z. Zhang, H. Shen, Q. Wu, and M. Gu, "Application and development of fluorescence probes in MINFLUX nanoscopy (invited paper)," Journal of Innovative Optical Health Sciences 16(01), 2230011 (2023).
59. H. Shroff, H. White, and E. Betzig, "Photoactivated localization microscopy (PALM) of adhesion complexes," Current Protocols in Cell Biology 41(1), 4.21.1–4.21.27 (2008).
60. M. J. Rust, M. Bates, and X. Zhuang, "Sub-diffraction-limit imaging by stochastic optical reconstruction microscopy (STORM)," Nature Methods 3(10), 793–796 (2006).
61. E. Betzig, G. H. Patterson, R. Sougrat, O. W. Lindwasser, S. Olenych, J. S. Bonifacino, M. W. Davidson, J. Lippincott-Schwartz, and H. F. Hess, "Imaging intracellular fluorescent proteins at nanometer resolution," Science 313(5793), 1642–1645 (2006).
62. R. Piestun, A. Basic, 3D localization and imaging of dense arrays particle, 14/777361 Patent Number, Date of Patent: 19 May 2020, USA.
63. B. Huang, W. Wang, M. Bates, and X. Zhuang , "Three-dimensional super-resolution imaging by stochastic optical reconstruction microscopy," Science 319(5864), 810–813 (2008).
64. N-STORM Super-Resolution Microscope System (accessed 30 May 2024). [https://www.microscope.healthcare.nikon.com/en_EU/products/super-resolution-microscopes/n-storm-super-resolution].
65. A. J. Barsic, Localization of Dense Clusters of Nanoscale Emitters for Super-resolution Microscopy, Doctoral Thesis, University of Colorado at Boulder, 145 (2014).
66. G. Huszka, M. A. M. Gijs, "Super-resolution optical imaging: A comparison," Micro and Nano Engineering 2, 7–28 (2019).
67. B. Hecht, H. Heinzelmann, and D. W. Pohl, "Combined aperture SNOM/PSTM: best of both worlds?," Ultramicroscopy 57 (2–3), 228–234 (1995).

68. A. L. Mattheyses, S. M. Simon, and J. Z. Rappoport, "Imaging with total internal reflection fluorescence microscopy for the cell biologist," Journal of Cell Science 123(21), 3621–3628 (2010).
69. M. L. Martin-Fernandez, C. J. Tynan, and S. E. D. Webb, "A 'pocket guide' to total internal reflection fluorescence," Journal of Microscopy 252(1), 16–22 (2013).
70. I. Sparkes, R. R. White, B. Coles, S. W. Botchway, and A. Ward, "Using optical tweezers combined with total internal reflection microscopy to study interactions between the er and golgi in plant cells," in The Plant Endoplasmic Reticulum, C. Hawes, V. Kriechbaumer (Ed.), 1691, 167–178 (2018).
71. C. Yan, X. Mei, X. Gong, and W. Xu, "Practical applications of total internal reflection fluorescence microscopy for nanocatalysis," Industrial Chemistry & Materials 2(1), 85–99 (2024).
72. A. P. Rennison, A. Nousi, P. Westh, R. Marie, and M. S. Møller, "Unveiling PET Hydrolase Surface Dynamics through Fluorescence Microscopy," ChemBioChem 25(5), e202300661 (2024).
73. A. von Diezmann, Y. Shechtman, and W. E. Moerner, "Three-dimensional localization of single molecules for super-resolution imaging and single-particle tracking," Chemical Reviews 117(11), 7244–7275 (2017).
74. M. D. Lew, S. F. Lee, M. Badieirostami, and W. E. Moerner "Corkscrew point spread function for far-field three-dimensional nanoscale localization of pointlike objects," Optics Letters 36(2), 202–204 (2011),
75. S. Prasad, "Rotating point spread function via pupil-phase engineering," Optics Letters 38(4), 585–587 (2013).
76. A. Greengard, Y. Schechner, and R. Piestun, "Depth from diffracted rotation," Optics Letters 31(2), 181–183б (2006).
77. A. Greengard, Y. Y. Schechner, and R. Piestun, "Depth from rotating point spread functions," Proceedings of SPIE 5557, 91–97 (2004),
78. A. Von Diezmann, Y. Shechtman, and W. E. Moerner "Three-dimensional localization of single molecules for super-resolution imaging and single-particle tracking," Chemical Reviews 117 (11), 7244–7275 (2017).
79. S. R. P. Pavani, R. Piestun, "High-efficiency rotating point spread functions", Optics Express 16(5), 3484–3489 (2008).
80. M. D. Lew, M. A. Thompson, M. Badieirostami, and W. E. Moerner, "In vivo three-dimensional superresolution fluorescence tracking using a double-helix point spread function," Proceedings of SPIE 7571, 75710Z (2010).
81. S. R. P. Pavani, M. A. Thompson, J. S. Biteen, S. J. Lord, N. Liu, R. J. Twieg, R. Piestun, and W. E. Moerner, "Three-dimensional, single-molecule fluorescence imaging beyond the diffraction limit by using a double-helix point spread function," Proceedings of the National Academy of Sciences 106(9), 2995–2999 (2009).
82. M. P. Backlund, M. D. Lew, A. S. Backer, S. J. Sahl, G. Grover, A. Agrawal, R. Piestun, and W. E. Moerner, "The double-helix point spread function enables precise and accurate measurement of 3D single-molecule localization and orientation," Proceedings of SPIE 8590, 85900L (2013).
83. S. Ghosh, G. Grover, R. Piestun, and C. Preza, "Effect of double-helix point-spread functions on 3D imaging in the presence of spherical aberrations," Proceedings of SPIE 7904, 79041D (2011),
84. Z. Cao, K. Wang, "Effects of astigmatism and coma on rotating point spread function," Applied Optics 53(31), 7325–7330 (2014).
85. A. R. Roy, J. Wang, M. Han, H. Wang, L. Möckl, L. Zeng, W. E. Moerner, and L. S. Qi, "Multicolor super-resolution imaging to study human coronavirus RNA during cellular infection," Biophysical Journal 122(3), 16a (2023)
86. G. Grover, R. Piestun, "New approach to double-helix point spread function design for 3D super-resolution microscopy," Proceedings of SPIE 8590, 85900M (2013).
87. A. Balaji, L. S. Zarko, P. D. Dahlberg, J. C. Boothroyd, and W. E. Moerner, "Revealing the 3D nanoscale organization of MyosinH in the apical complex of toxoplasma gondii through single-molecule localization microscopy with the double-helix point spread function," Biophysical Journal 123(3), 30a–31a (2024).
88. T. Legrand, F.-R. Winkelmann, W. Alt, D. Meschede, A. Alberti, and C. A. Weidner, "Three-dimensional imaging of single atoms in an optical lattice via helical point-spread-function engineering," Physical Review 109(3), 033304 (2024).
89. Y. Nakatani, W. Colomb, S. Gaumer, and A.-K. Gustavsson, "3D super-resolution imaging of mammalian cells using long axial range double-helix point spread functions," Biophysical Journal 123(3), 434a–435a (2024).
90. V. G. Volostnikov, E. N. Vorontsov, S. P. Kotova, N. N. Losevskiy, and D. V. Prokopova, "Diffractive elements based on spiral beams as devices for determining the depth of bedding of radiation sources," Bulletin of the Russian Academy of Sciences: Physics 80(7), 766–769 (2016).
91. E. Abramochkin, V. Volostnikov, "Spiral-type beams," Optics Communications 102(3–4), 336–350 (1993).
92. D. V. Prokopova, E. N. Vorontsov, S. P. Kotova, N. N. Losevsky, S. A. Samagin, I. T. Mynzhasarov, A. A. Gorshelev, I. Y. Eremchev, and A. V. Naumov, "Improving the energy efficiency of diffraction optical elements for 3d nanoscopy," Bulletin of the Russian Academy of Sciences: Physics 83(12), 1453–1458 (2019).
93. D. V. Prokopova, S. P. Kotova "Phase diffraction optical elements with enhanced efficiency for nanoscopy," Photonics Russia 14(2), 170–182. (2020).
94. I. Yu. Eremchev, D. V. Prokopova, N. N. Losevskii, I. T. Mynzhasarov, S. P. Kotova, and A. V. Naumov, "Three-dimensional fluorescence nanoscopy of single quantum emitters based on the optics of spiral light beams," Physics-Uspekhi 65(06), 617–626 (2022).

95. M. Baranek, Z. Bouchal, "Rotating vortex imaging implemented by a quantized spiral phase modulation," Journal of the European Optical Society-Rapid Publications 8, 13017 (2013).
96. M. Baranek, Z. Bouchal, "Optimizing the rotating point spread function by SLM aided spiral phase modulation", Proceedings of SPIE 9441, 94410N (2014).
97. Y. Shechtman, L. E. Weiss, A. S. Backer, S. J. Sahl, and W. E. Moerner, "Precise three-dimensional scan-free multiple-particle tracking over large axial ranges with tetrapod point spread functions," Nano Letters 15(6), 4194–4199 (2015).
98. Y. Shechtman, A.-K. Gustavsson, P. N. Petrov, E. Dultz, M. Y. Lee, K. Weis, and W. E. Moerner, "Observation of live chromatin dynamics in cells via 3D localization microscopy using Tetrapod point spread functions," Biomedical Optics Express 8(12), 5735–5748 (2017).
99. Y. Shechtman, S. J. Sahl, A. S. Backer, and W. E. Moerner, "Optimal point spread function design for 3D imaging," Physical Review Letters 113(13), 133902 (2014).
100. Double Helix Optics (accessed 3 June 2024). [https://www.doublehelixoptics.com/].
101. F. Wang, H. Liu, Y. Tan, J. Gu, X. Miao, Y. Xiao, C. Wang, J. Li, Z. Wang, and Y. Zhang, "2π double-helix point spread function based on ring segmentation method for nanoparticle tracking technique," Optical Engineering 63(10), 105107 (2024).
102. D. Xiao, R. Kedem Orange, N. Opatovski, A. Parizat, E. Nehme, O. Alalouf, and Y. Shechtman, "Large-FOV 3D localization microscopy by spatially variant point spread function generation," Science Advances 10(10), eadj3656 (2024).
103. Y. Yan, L. Li, C. Feng, W. Guo, S. Lee, and M. Hong, "Microsphere-coupled scanning laser confocal nanoscope for sub-diffraction-limited imaging at 25 nm lateral resolution in the visible spectrum," ACS Nano 8(2), 1809–1816 (2014).
104. S. K. Chakkarapani, Y. Sun, and S. H. Kang, "Ultrasensitive norovirus nanoimmunosensor based on concurrent axial super-localization of ellipsoidal point spread function by 3D light sheet microscopy," Sensors and Actuators, B: Chemical 284, 81–90 (2019).
105. A. Gustavsson, P. N. Petrov, M. Y. Lee, Y. Shechtman, and W. E. Moerner, "3D single-molecule super-resolution microscopy with a tilted light sheet," Nature Communications 9(1), 123 (2018).
106. J. Yang, B. Q. Li, R. Li, and X. Mei, "Quantum 3D thermal imaging at the micro-nanoscale," Nanoscale 11(5), 2249–2263 (2019).

Laser-Stimulated Release of Methylene Blue from Porous Silicon Nanocontainers

Alexandr A. Bubnov[1*], Gleb N. Abrashitov[2], and Victor Yu. Timoshenko[1,2,3]
[1] National Research Nuclear University MEPhI Moscow Engineering Physics Institute Moscow, 31 Kashirskoe str., Moscow 115409, Russian Federation
[2] Lomonosov Moscow State University, GSP-1 Leninskie Gory, Moscow 119991, Russian Federation
[3] P.N. Lebedev Physical Institute, Russian Academy of Sciences, GSP-1, 53 Leninsky Prospekt, Moscow 119991, Russian Federation
*e-mail: bubnov96@mail.ru

Abstract. Aqueous suspensions of nanocontainers consisting of porous silicon (PSi) nanoparticles with Methylene blue (MB) loading were investigated by means of the optical spectroscopy and infrared thermometry under laser irradiation. The photothermal conversion efficiency and kinetics of the MB release from those nanocontainers based on PSi without additional oxidation and after thermal oxidation (ox-PSi) were analyzed to establish an influence of the oxidation of PSi on MB release. The optical spectroscopical study of the loaded nanocontainers showed a strong absorption band of MB at 600−700 nm, while the absorption bands of PSi and, especially, ox-PSi were relatively weak in this spectral region, indicating a high degree of the MB loading for both types of NPs. The MB release from nanocontainers in an aqueous medium was monitored by measuring the MB photoluminescence in the spectral region of 700−800 nm when excited by a continuous wave laser at a wavelength of 660 nm. The MB release from the nanocontainer based on PSi NPs was found to be significantly promoted by nanosecond laser irradiation at 532 nm because of the laser induced heating of PSi NPs. To assess possible applications of the MB release and photoheating, in vitro experiments were carried out with unicellular organisms of Paramecium caudatum, and their results confirmed the effect of spatially localized photoheating of MB-loaded PSi NPs under pulsed laser irradiation, which enhanced the MB release. The obtained results indicate new possibilities for the controlled drug release using PSi NPs and may be useful for biomedical applications as antibacterial treatment and combination therapy of cancer.
© 2024 Journal of Biomedical Photonics & Engineering.

Keywords: porous silicon; nanoparticles; nanocontainers; Methylene blue; laser irradiation; photoluminescence; photoheating.

Paper #9129 received 12 Jul 2024; revised manuscript received 4 Sep 2024; accepted for publication 24 Sep 2024; published online 25 Oct 2024. doi: 10.18287/JBPE24.10.040305.

1 Introduction

Nowadays, different types of nanoparticles (NPs) are extensively examined as carriage systems for drug delivery and controlled release in various biomedical applications, e.g. cancer therapy, treatment of cardiovascular diseases, and many others (see for examples [1, 2]). Porous silicon (PSi) NPs are advantageous as a nanocontainer for drugs because they can bind different molecular drugs and at the same time have biodegradability and low toxicity properties [3−6]. While both porous silicon oxide (silica) and PSi can be used for nanocapsulation and delivery of different drugs [1, 2], PSi-based NPs have a significant advantage over porous silica because the formers absorb visible and

near-IR radiations and then they can be directly used as an efficient light absorber for photohyperthermia applications [6]. This property allows us to use PSi NPs as a nanocontainer for the release of a drug triggered by photoheating [7].

Methylene blue (MB) is a dye that absorbs and emits light in the red and near-IR ranges of the spectrum, respectively, and is widely used in medicine for diagnostics and treatment of different diseases [8, 9]. It is worth noting the toxicity of MB when ingested in high concentrations [10, 11]. However, one can use nontoxic NPs as nanocontainers to control the MB concentration in an area of interest in the body. To stimulate the MB release from a nanocontainer the following different stimulus can be applied: laser radiation exposure, oxidation and dialysis [12, 13]. The laser-induced release of nanocapsulated MB can be combined with generation of reactive oxygen species during photoexcitation of MB at 660 nm and it can be used for the photodynamic therapy of cancer [14, 15].

The purpose of this our work was to study nanocontainers made of PSi and thermally oxidized PSi in aqueous suspensions to enhance the controlled release of MB when irradiated with continuous and nanosecond pulsed laser radiation.

2 Materials and Methods

PSi layers were formed by using a procedure of the electrochemical etching (anodization) of boron-doped c-Si wafers with a resistivity of 20 mΩ·cm in HF (48%):C_3H_7OH solution (1:1) at a current density of 50 mA/cm^2 and etching time of 1 h. The procedure allowed us to obtain mesoporous PSi with pore sizes from 2 to 50 nm and mean porosity of about 70%, as determined by using the low-temperature nitrogen sorption analysis and gravimetric measurements, respectively (see for details Refs. [16, 17]). Free-standing PSi films were obtained by applying a short pulse of the anodic current with density of 500 mA/cm^2, followed by rinsing them in deionized water and drying in air. Suspensions of PSi NPs in isopropanol were prepared by high-energy ball-milling of the dried PSi films using a planetary mill with zirconia milling balls. The rotation speed and duration of the milling were 800 rpm and 30 min, respectively. The final concentration of PSi NPs in isopropanol suspension was about 35 mg/mL.

The size and morphology of PSi NPs were analyzed by means of the scanning electron microscopy (SEM) with a Tescan MAIA 3 SEM (Tescan, Czech Republic) apparatus. Fig. 1 shows typical SEM image of PSi NPs. As can be seen from the SEM image, the average size of PSi nanoparticles is of the order of 100 nm, and their shape is irregular due to the mesoporous structure and the mechanical grinding used.

The prepared NP suspension was divided in two parts. The first part was centrifuged in an Eppendorf centrifuge 5804 (10000 rpm, duration 5 min) to remove isopropanol and the resulting precipitate was then mixed with 1 ml of deionized water to produce a concentrated aqueous suspension of PSi NPs. To load MB to the prepared PSi NPs, the corresponding suspension of the latter (0.5 mL, 35 mg/mL) was mixed with an aqueous solution of MB (0.5 mL, 11 mg/mL), followed with stirring for 12 h (rotation speed 110 rpm). The next step was done to separation of the nanocontainers from free MB molecules using centrifugation for 10 min at 10000 rpm, followed by washing the resulting drug-filled nanocontainers with water (1 mL). Due to the high concentration of the resulting suspension, the washing was carried out 3 times. The prepared concentrated suspension of MB-loaded PSi (PSi-MB) nanocontainers were then diluted by deionized water to study the optical and photothermal properties as well the MB release.

The second part of the NP suspension in isopropanol was dried in air at room temperature. After that, the dried PSi NPs were thermally oxidized in an oven at 550 °C for 12 h. Then, the thermally oxidized PSi (ox-PSi) NPs were mixed with distilled water and the obtained suspension was sonicated in an ultrasonic bath for 10 min at room temperature. To load MB into ox-PSi NPs, we applied the above-described procedure of the sorption of MB in a concentrated solution followed by three times rinsing in water, as was used for PSi NPs. The resulting MB-loaded ox-PSi (ox-PSi-MB nanocontainers) were then diluted with water for further analysis and experiments.

Diluted aqueous suspensions of PSi and ox-PSi NPs without loading and MB-loaded were transferred to quartz cuvettes with an optical path length of 10 mm for analysis by means of the optical absorption spectroscopy in the wavelength range from 400 to 900 nm using a UV752P (Wincom Ltd., China) spectrophotometer.

Photoluminescence (PL) of the prepared aqueous suspensions of nanocontainers was measured under excitation by a continuous wave (CW) semiconductor laser with a wavelength of 660 nm. The PL spectra were recorded using a compact Mightex CCD spectrometer equipped with an optical fiber at the input. To suppress the excitation line, a homemade interference filter was used, which was based on a one-dimensional photonic crystal made of a multilayer PSi film (the photonic band gap at 670 nm with a width of about 60 nm), as shown in Fig. 2.

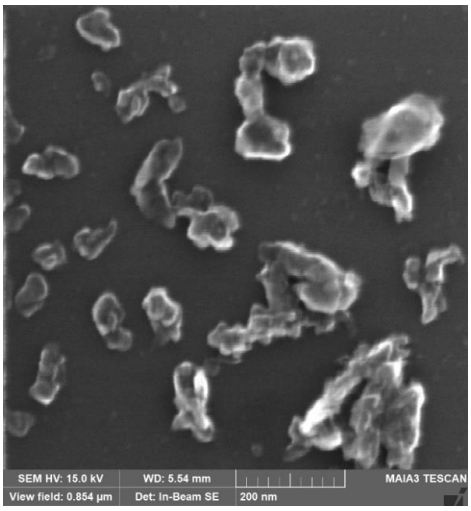


Fig. 1 SEM image of PSi NPs.

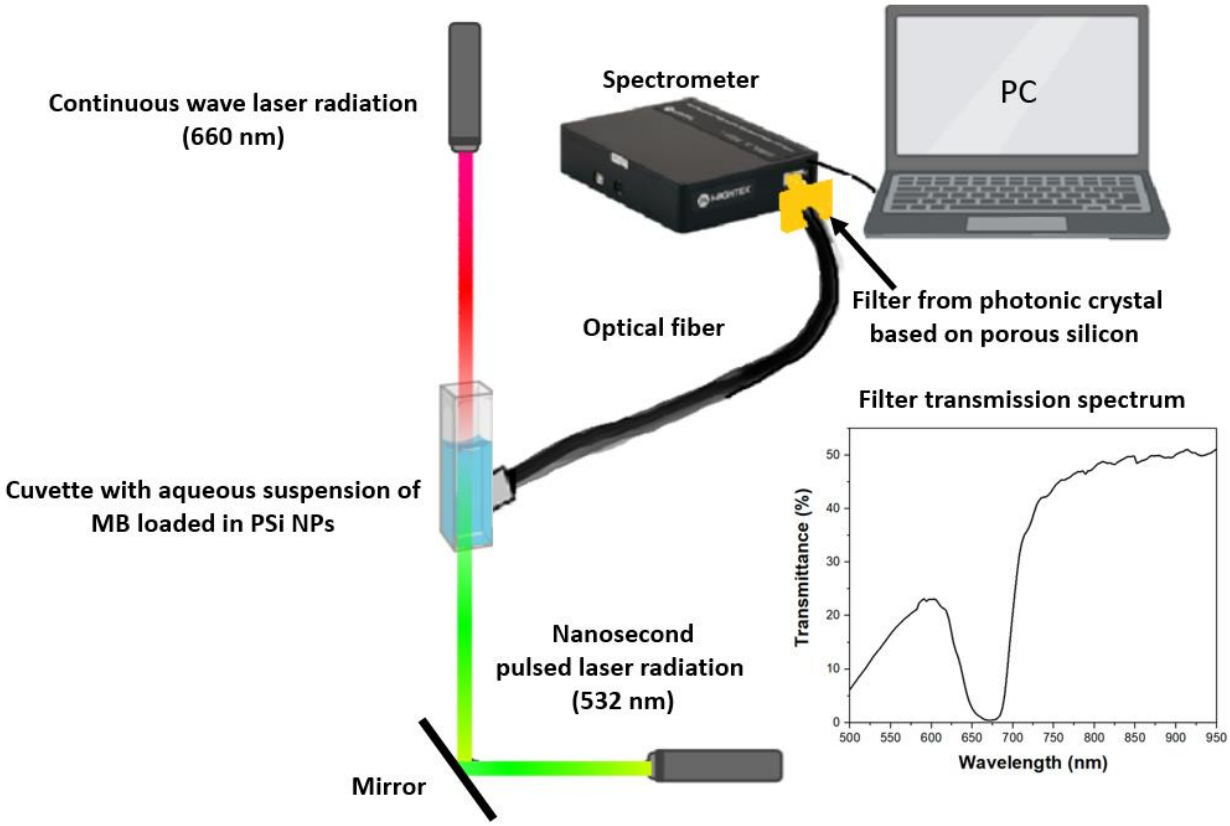


Fig. 2 Schematic representation of the experimental setup for laser irradiation and PL measurements of aqueous suspensions of MB-loaded nanocontainers.

The MB release from PSi nanocontainers was monitored by irradiating the corresponding aqueous suspension (1 mL, 0.1 mg/mL) by a CW laser at 660 nm with the maximal power of about 250 mW under ambient conditions. The collimated laser beam was 4 mm in diameter. The same setup was used for experiments with nanosecond laser irradiation by an AFPL-532-15 diode-pump solid state laser (wavelength of 532 nm, pulse duration of about 15 ns, repetition rate of 4.5 kHz, maximum average power of about 20 mW, laser spot diameter of 2 mm). A schematic representation of the experimental setup is shown in Fig. 2.

Additionally, a thermal imaging camera FLIR C3 with an accuracy of 0.01 °C and sampling rate of 9 Hz was used to monitor temperature of the aqueous suspension of nanocontainers under the influence of laser irradiation.

To assess the biomedical potential of PSi NPs containing MB, we used a model of the unicellular organism *Paramecium caudatum*. The cells were kept in an aqueous solution at a temperature of 24 °C, pH-level of about 7.0 in daylight for 12 h. The cells were fed daily. The last feeding was 2 h before the experiment and was not carried out until the end of the study. Seven groups of cells were used in the experiment (each group with a volume of 1 ml and an average concentration of about 400 cells/mL). The number of cells in each group was determined by analyzing the corresponding video image, while the cell movement was recorded using an Olympus SZ6 binocular stereoscopic microscope. The video was processed by using an open-source Fiji platform with the cell counting plug in Ref. [18]. The main criterion for cell mobility, and therefore their viability, was the average speed of cell movement.

3 Results and Discussion

Fig. 3a shows the extinction spectra of dilute aqueous suspensions of PSi and ox-PSi nanoparticles. The observed monotonic decrease in the extinction with increasing wavelength is explained by the interband absorption of light in silicon (Si) nanocrystals, which are contained in both types of the samples studied [19]. The significantly weaker absorption for the ox-PSi sample compared to the non-oxidized one is obviously due to a large fraction of silicon dioxide, transparent in the visible and near-infrared region, in the first sample.

Fig. 3b shows spectra of the extinction for MB solution as well as for as-prepared suspensions of PSi and ox-PSi NPs loaded with MB. The extinction spectrum of MB consists of two peaks with maxima at ~610 and 664 nm, which are associated with the light absorption by dimeric and monomeric states of MB molecules, respectively [20]. While the spectra for PSi-MB and ox-PSi-MB suspensions are quite similar in the absorption region of MB (550−700 nm), the absorption background for ox-PSi-MB is less pronounced than for the PSi-MB sample. It can be explained by the weaker absorption of ox-PSi NPs compared to the PSi ones.

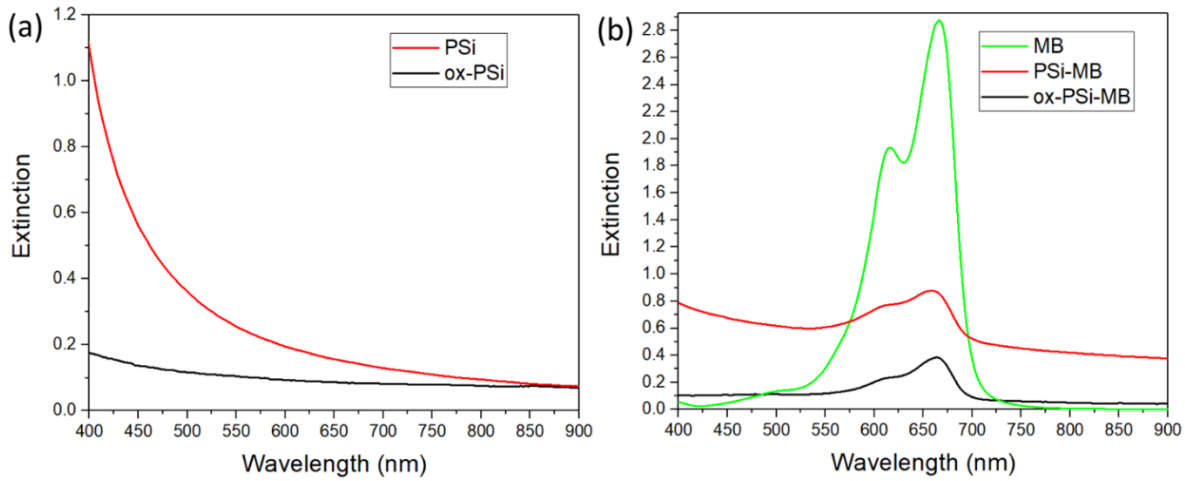


Fig. 3 Extinction spectra of the following samples in aqueous media: (a) suspensions of PSi (red line) and ox-PSi (black line) NPs with concentrations of 0.2 and 0.4 mg/mL, respectively; (b) solution of MB with concentration of 22.6 μM (green line) and as-prepared suspensions of PSi-MB (red line) and ox-PSi-MB (black line) NPs with concentration of 0.1 and 0.02 mg/mL, respectively.

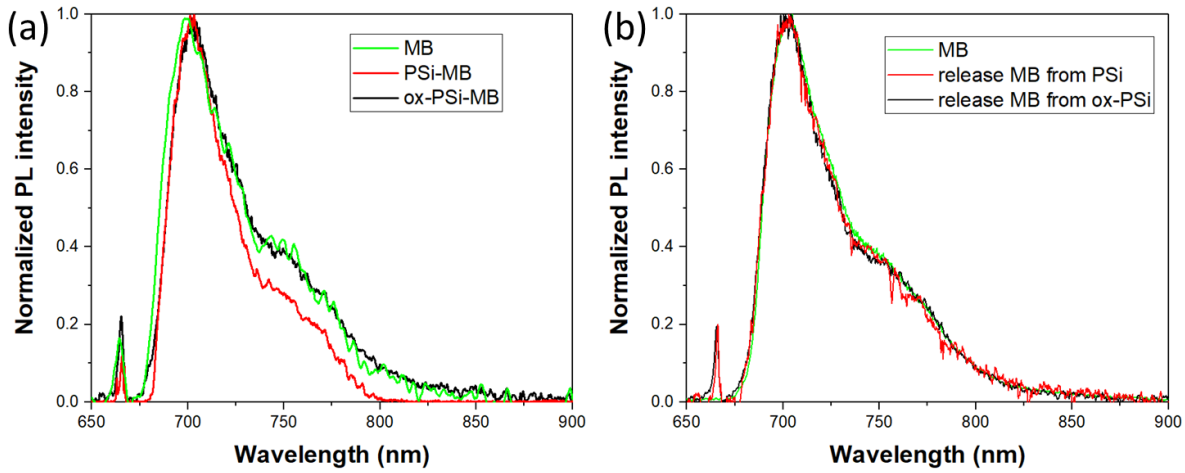


Fig. 4 Normalized PL spectra of the following samples in aqueous media: (a) 0.3 μM MB solution (green line), PSi-MB (red line) and ox-PSi-MB (black line) NP suspensions with concentration of 0.1 and 0.2 mg/mL, respectively; (b) intentionally dissolved MB (green line) and released solutions from PSi-MB (red line) and ox-PSi-MB (black line) NP suspensions. Sharp peaks at a wavelength of 660 nm correspond to the scattered exciting laser radiation, those contribution in the detected signal was suppressed by the used interference filter.

Also, it is worth noting that the extinction spectra of MB-loaded nanocontainer suspensions consist of contributions of both encapsulated and spontaneously released free MB molecules. Since it was difficult to separate these contributions in the total absorption during storage in water for various time scales, we mostly investigated the MB release from nanocontainers by using PL spectroscopy.

Fig. 4a shows the PL spectra of a MB solution and as-prepared aqueous suspensions of PSi-MB and ox-PSi-MB NPs. The spectra consist of a main peak at a wavelength of ~700 and a shoulder at ~750 nm, which are typical for MB solution in water [20]. For the nanocontainers containing MB, a shift of the main peak maximum by about 3 nm towards longer wavelength is observed that can be explained by re-absorption of MB fluorescence due to the elastic light scattering in the NP suspension, as previously reported for suspensions of metal oxide NPs [21, 22]. At the same time, the PL spectra of released MB solutions coincide with the spectrum of free MB molecules in water (Fig. 4b).

To investigate the kinetics of MB release from the NP-based nanocontainers during the CW laser irradiation at 660 nm we analyzed changes in the intensity of MB fluorescence at a wavelength of 700 nm. Fig. 5a shows transients of the normalized change in the PL intensity, which are described by the following Eq.:

$$\Delta I_{PL}(t) = \frac{I_{PL}(t) - I_{PL}(0)}{I_{PL}(0)}, \quad (1)$$

where $I_{PL}(t)$ and $I_{PL}(0)$ are the PL intensities of MB at the analyzed time and at the initial time, respectively.

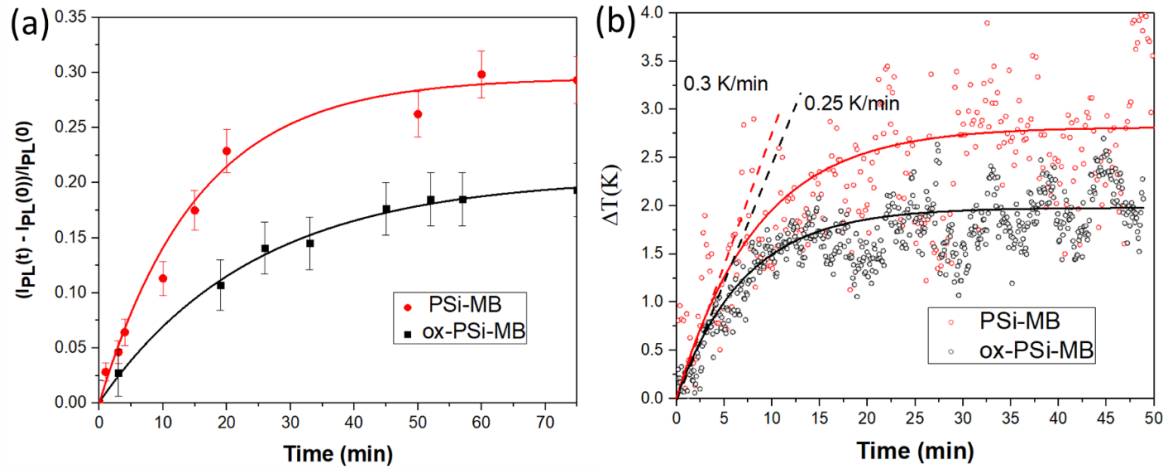


Fig. 5 (a) Transients of the normalized increase of the PL intensity of MB measured at 700 nm for aqueous suspension of PSi-MB (red line) and ox-PSi-MB (black line) nanocontainers with concentration of about 0.5 mg/mL; (b) time dependences of the temperature rise in the same suspension of PSi-MB (red circles) and ox-PSi-MB (black circles) nanocontainers, while the red and black lines are fits by using a solution of the heat balance equation. The CW laser irradiation was done with a wavelength of 660 nm and intensity of 1.2 W/cm^2.

Immediately after the beginning of MB release, the PL intensity transients were well described by the following Eq.:

$$I_{PL}(t) = I_{PL}^{max} \cdot [1 - \exp(-t/\tau)], \qquad (2)$$

where I_{PL}^{max} and τ are the maximal intensity of the MB fluorescence and characteristic time of the release rate, respectively.

As can be seen from Fig. 5a the MB release rate is faster and the relative increase of the PL intensity, i.e. the amount of released MB is larger for PSi-MB NPs, than the corresponding values in the case of ox-PSi-MB. According to the data of PL monitoring shown in Fig. 5a, the total amount of MB release is at about 30 and 18% for nanocontainers from PSi and ox-PSi, respectively. The fact can be associated with stronger binding of MB molecules to the thermally oxidized internal surface of ox-PSi NPs than it is in PSi ones.

It is worth noting that due to the light absorption both in MB and NPs the used CW laser irradiation at 660 nm led to photoheating of the analyzed aqueous media, as shown in Fig. 5b. Differences in maximum heating temperatures indicate different heating rates. By analyzing the temperature rise for the initial stage of photoheating we can evaluate the photoheating conversion efficiency (PCE) with the following Eq. [23]:

$$\eta \approx \frac{C_w \cdot m_w}{I_0 - I_t} \cdot \frac{dT}{dt}, \qquad (3)$$

where I_0 is the incident laser power, I_t is the laser power transmitted through the solution of NPs, m_w and C_w are the mass and specific heat capacity of the photoheated solution, respectively, $\frac{dT}{dt}$ is the initial rate of temperature rise. It should be noted that a more detailed analysis of the thermal balance under continuous laser irradiation gives a temperature rise, which can be fitted by a function like that described by Eq. (2) (see, for example, Ref. [23]).

Using the measured initial photoheating rates (see Fig. 5b) and Eq. (3), the PCE values for PSi-MB and ox-PSi-MB nanocontainers under CW laser excitation at 660 nm are estimated at about 10.4 and 8.5%, respectively. The PCE values for nanocontainers based on PSi and ox-PSi NPs are explained by the strong light absorption by MB, while the contribution of the light absorption by PSi and, especially, ox-PSi are relatively weak at this wavelength (see Fig. 3b). In addition, the same PCE for both types of nanocontainers indicates an almost equally high level of their MB load.

To stimulate release of MB from PSi-MB nanocontainers we have additionally used nanosecond laser irradiation with a wavelength of 532 nm, which was absorbed better in PSi compared to the red light, and the obtained results are shown in Fig. 6. While the CW laser irradiation at 660 nm of PSi-MB suspension led to a steady state level of the PL intensity for the irradiation time of 20−30 min, the additional simultaneous irradiation by nanosecond laser pulses resulted in a significant increase of the MB luminescence intensity and, then, the MB release (Figs. 6 a, b). The effect can be explained by local photoheating of the PSi NPs under the well absorbed pulsed laser radiation, which creates temperature gradients nearby those NPs resulting a stimulus for additional MB release from the pores. The PCE values evaluated from the initial transients of the temperature increase were about 0.22 and 0.42 for the irradiation with the CW laser at 600 nm and pulsed laser at 532 nm, respectively. The PCE increase by 2 times for the latter is obviously related to 2 times stronger absorption of the green light than the red radiation by PSi NPs (see Fig. 2a). Also, it is worth noting that the total temperature increase in the aqueous suspension of nanocontainers after the combined CW and pulsed laser irradiation was about 6.5 °C that was about 2 times larger than for the CW irradiation (Fig. 6c).

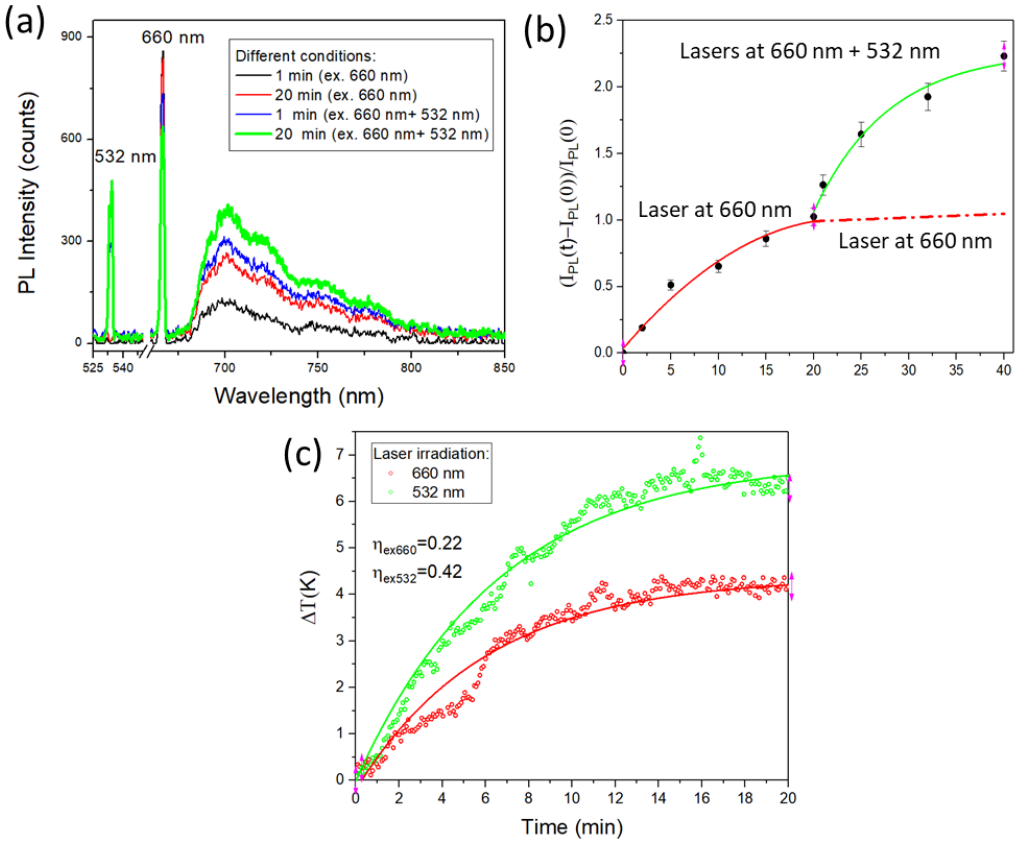


Fig. 6 (a) PL spectra of aqueous suspension of PSi-MB nanocontainers under irradiation by CW laser at 660 nm (black and red lines) followed with additional irradiation with nanosecond pulsed laser at 532 nm (blue and green lines); (b) transients of the normalized increase of the PL intensity of MB at 700 nm under CW laser radiation at 660 nm (red line) followed with simultaneous pulsed laser radiation at 532 nm (green line); (c) time dependences of the temperature increase in aqueous suspension of PSi-MB NPs under CW laser radiation at 660 nm (red circles) and pulsed laser radiation at 532 nm (green circles), while red and green lines are fits by using a solution of the heat balance equation.

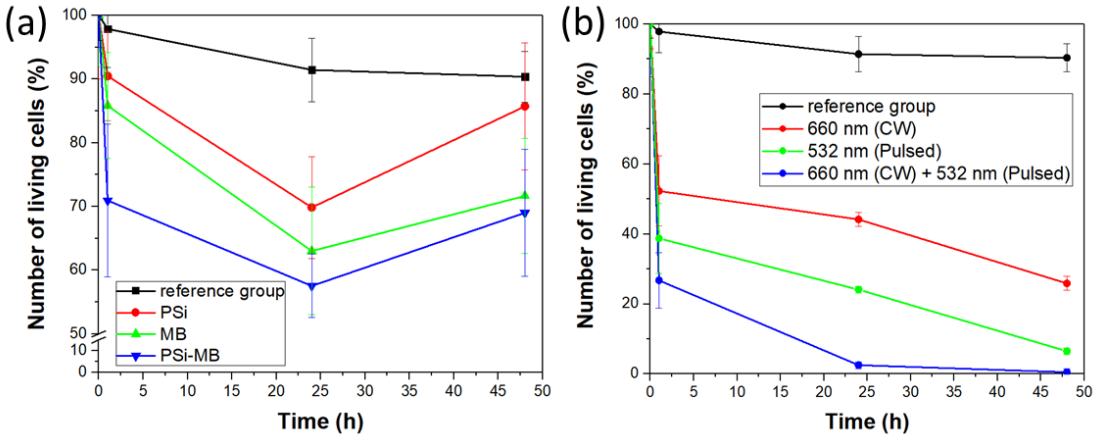


Fig. 7 Time dependences of the relative number of living *Paramecium caudatum* cells for the following groups: (a) reference (black color), PSi NP suspension (red line), MB solution (green line), PSi-MB nanocontainers (blue line); (b) reference (black line), PSi-MB nanocontainers (0.001 mg/mL) under CW laser irradiation at 660 nm (red line), nanosecond pulsed laser radiation at 532 nm (green line) and simultaneous irradiation with CW laser at 660 nm and nanosecond pulsed laser at 532 and (blue line).

The corresponding pulsed photoinduced heating of PSi-MB nanocontainers was obviously even higher that should strongly promote local temperature gradients and thus the MB release under pulsed irradiation at 532 nm.

To assess prospects of a biomedical application of MB-loaded nanocontainers we carried out *in vitro* experiments by using a model of the unicellular organisms *Paramecium caudatum*, which represent

suspension cells sensitive to local hyperthermia and toxic species like cancer cells [24, 25]. This model was previously successfully tested for laser induced photoheating with Si-based NPs [23]. Fig. 7 shows dependence of the cell viability during time after adding PSi NPs, MB solution and PSi-MB nanocontainers without laser irradiation (Fig. 7a) and for cells with added PSi-MB nanocontainers under CW and pulsed laser irradiation (Fig. 7b) as well as for the corresponding reference groups. A decrease in the number of living cells by 25−30% was observed for 24 h after administration of pure PSi NPs. Further, due to cell proliferation, the number of organisms in the suspension was partially restored (see Fig. 7a). The observed toxicity of PSi NPs was significantly lower than that for PSi-MB nanocontainers (blue curve in Fig. 7a), while free MB solution with the same MB concentration led to the similar toxic effect (green curve in Fig. 7a).

Fig. 7b shows a sharp decrease in the number of living cells during one hour just after laser irradiation for all groups. The effect was especially pronounced after the simultaneous irradiation by CW and nanosecond lasers. In this case, the cell viability during the first hour was only about 20%. In addition, the number of living cells was 2−3% within 24 h after irradiation and decreased to almost zero the next day. If the sample was only irradiated by CW laser at 660 nm it was observed a sharp decrease of the number of living cells by 50% and the further rate of cell loss slowed down. The decrease in the rate of cell death could be due to the competing process of cell proliferation.

4 Conclusions

The optical and photothermal properties of nanocontainers based on PSi NPs filled with MB molecules were studied and the obtained results showed the influence of the oxide fraction in PSi NPs as well the role of pulsed laser irradiation on the MB release. It has been established the values of PCE under CW laser irradiation at 660 nm were quite similar for PSi NPs without special oxidation and for ox-PSi NPs obtained after additional thermal oxidation at 550 °C. Despite of this, the MB release was almost two times better from the PSi-MB NPs than that from ox-PSi-MB ones. The fact can be explained by stronger binding of MB molecules with the surface of thermally oxidized PSi NPs. To increase further the MB release from PSi-MB NPs the nanosecond pulsed laser irradiation at 532 nm was rather efficient. The estimated enhancement of the MB release was about 2.3 times compared to the case of CW irradiation by the laser at 600 nm. This enhancement can be explained by local photoheating of PSi NPs by nanosecond laser pulses that induces local temperature gradients nearby those NPs, which promote the MB release from their pores. Also, the PCE value of MB-loaded PSi NPs under laser radiation at 532 nm was found to be larger by 2 times compared to the CW laser irradiation at 660 nm. Therefore, the pulsed laser induced photoheating can be efficiently combined with MB release from PSi-based nanocontainers. The combine effect of the photoheating and MB release was checked out by using in vitro experiment with unicellular organisms *Paramecium caudatum*. The pulsed laser irradiation of the cells with added PSi-MB nanocontainers resulted in almost complete cell death. This fact is explained by considering the laser stimulated MB release from PSi NPs due to their photoheating, which leads to the spatial-localized photohyperthermia combined with increased MB concentration. The obtained results indicate that PSi NPs can be considered as promising nanocontainers for MB with possibility to control the drug realize by using additional oxidation of PSi NPs as well the pulsed laser irradiation as an external stimulus.

Acknowledgements

The authors acknowledge Dr. A. Yu. Kharin and Ms. A. S. Eremina for the assistance with SEM measurements and sample preparation, respectively. The work was partially supported by the grant FSWU-2023-0070 of Ministry of Science and Higher Education of the Russian Federation.

Disclosures

The authors declare that they have no conflict of interest.

Data Availability Statement

The data presented in this study are available on request from the corresponding author.

References

1. O. Afzal, A. S. A. Altamimi, M. S. Nadeem, S. I. Alzarea, W. H. Almalki, A. Tariq, B. Mubeen, B. N. Murtaza, S. Iftikhar, N. Riaz, and I. Kazmi, "Nanoparticles in Drug Delivery: From History to Therapeutic Applications," Nanomaterials 12(24), 4494 (2022).
2. A. Yusuf, A. R. Z. Almotairy, H. Henidi, O. Y. Alshehri, and M. S. Aldughaim, "Nanoparticles as Drug Delivery Systems: A Review of the Implication of Nanoparticles' Physicochemical Properties on Responses in Biological Systems," Polymers 15(7), 1596 (2023).
3. J.-H. Park, L. Gu, G. Von Maltzahn, E. Ruoslahti, S. N. Bhatia, and M. J. Sailor, "Biodegradable luminescent porous silicon nanoparticles for in vivo applications," Nature Mater 8(4), 331–336 (2009).

4. S. M.Haidary, E. P.Córcoles, and N. K. Ali, "Nanoporous Silicon as Drug Delivery Systems for Cancer Therapies," Journal of Nanomaterials 2012(1), 830503 (2012).
5. J. Salonen, "Drug delivery with porous silicon," in Handbook of Porous Silicon, L. Canham (Ed.), 2 ed., Springer, Cham, 1377–1390 (2018). Online ISBN: 978-3-319-71381-6.
6. V. Yu. Timoshenko, "Porous silicon in photodynamic and photothermal therapy," in Handbook of Porous Silicon, L. Canham (Ed.), 2 ed., Springer, Cham, 1461−1469 (2018).
7. K. Tamarov, W. Xu, L. Osminkina, S. Zinovyev, P. Soininen, A. Kudryavtsev, M. Gongalsky, A. Gaydarova, A. Närvänen, V. Timoshenko, and V.-P. Lehto, "Temperature responsive porous silicon nanoparticles for cancer therapy – spatiotemporal triggering through infrared and radiofrequency electromagnetic heating," Journal of Controlled Release 241, 220−228 (2016).
8. T. Cwalinski, W. Polom, L. Marano, G. Roviello, A. D'Angelo, N. Cwalina, M. Matuszewski, F. Roviello, J. Jaskiewicz, and K. Polom, "Methylene blue-current knowledge, fluorescent properties, and its future use," Journal of Clinical Medicine 9(11), 3538 (2020).
9. L. Abraham, A. Rai, K. Burde, and V. Naikmasur, "Methylene blue as a diagnostic aid in the early detection of potentially malignant and malignant lesions of oral Mucosa," Ethiopian Journal of Health Sciences 26(3), 201−208 (2016).
10. M. Bužga, E. Machytka, E. Dvořáčková, Z. Švagera, D. Stejskal, J. Máca, and J. Král, "Methylene blue: a controversial diagnostic acid and medication?," Toxicology Research 11(5), 711−717 (2022).
11. S. Li, Y. Cui, M. Wen, and G. Ji, "Toxic effects of Methylene blue on the growth, reproduction and physiology of Daphnia magna," Toxics 11(7), 594 (2023).
12. A. S. Altowyan, A. Toghan, H. A. Ahmed, R. A. Pashameah, E. A. Mwafy, S. H. Alrefaee, and A. M. Mostafa, "Removal of methylene blue dye from aqueous solution using carbon nanotubes decorated by nickel oxide nanoparticles via pulsed laser ablation method," Radiation Physics and Chemistry 198, 110268 (2022).
13. M. Chen, C. T. Jafvert, "Application of cross-linked stearic acid nanoparticles with dialysis membranes for methylene blue recovery," Separation and Purification Technology 204, 21−29 (2018).
14. W. Tang, H. Xu, R. Kopelman and M. A. Philbert, "Photodynamic characterization and in vitro application of methylene blue-containing nanoparticle platforms," Photochemistry and Photobiology 81(2), 242–249 (2005).
15. X. Xu, H. Mao, Y. Wu, S. Liu, J. Liu, Q. Li, M. Yang, J. Zhu, S. Zou, and F. Du, "Fabrication of methylene blue-loaded ovalbumin/polypyrrole nanoparticles for enhanced phototherapy-triggered antitumour immune activation," Journal of Nanobiotechnology 20, 297 (2022).
16. M. A. Konoplyannikov, A. S. Eremina, Yu. V. Kargina, I. M. Le-Deygen, A. Yu. Kharin, T. Yu. Bazylenko, G. M. Yusubalieva, V. A. Revkova, O. N. Matchuk, I. A. Zamulaeva, M. R. Abramova, S. L. Kotova, P. S. Timashev, V. P. Baklaushev, and V. Yu. Timoshenko, "Mesoporous silicon nanoparticles loaded with salinomycin for cancer therapy applications," Microporous and Mesoporous Materials 328, 111473 (2021).
17. A. S. Eremina, Yu. V. Kargina, A. Yu. Kharin, D. I. Petukhov, and V. Yu. Timoshenko, "Mesoporous silicon nanoparticles covered with PEG molecules by mechanical grinding in aqueous suspensions," Microporous and Mesoporous Materials 331, 111641 (2022).
18. J. Schindelin, I. Arganda-Carreras, E. Frise, V. Kaynig, M. Longair, T. Pietzsch, S. Preibisch, C. Rueden, S. Saalfeld, B. Schmid, J.-Y. Tinevez, D. J. White, V. Hartenstein, K. Eliceiri, P. Tomancak, and A. Cardona, "Fiji: an open-source platform for biological-image analysis," Nature Methods 9(7), 676–682 (2012).
19. D. Kovalev, H. Heckler, G. Polisski, and F. Koch, "Optical properties of Si nanocrystals", Physica Status Solidi (B) 215(2), 871–932 (1999).
20. É. G. A. De Miranda, V. H. Toledo, C. G. Dos Santos, F. Costa, M. Diaz-Lopez, T. B. De Queiroz, O. R. Nascimento, and I. L. Nantes, "Organic matrix-entrapped methylene blue as a photochemical reactor applied in chemical synthesis and nanotechnology," Journal of Photochemistry and Photobiology A: Chemistry 444, 115015 (2023).
21. H. M. Dao, C. Whang, V. K. Shankar, Y. Wang, I. A. Khan, L. A. Walker, I. Husain, S. I. Khan, S. N. Murthy and S. Jo, "Methylene blue as a far-red light-mediated photocleavable multifunctional ligand," Chemical Communications 56(11), 1673−1676 (2020).
22. F. Pahang, P. Parvin, H. Ghafoori-Fard, A. Bavali, and A. Moafi, "Fluorescence properties of methylene blue molecules coupled with metal oxide nanoparticles," OSA Continuum 3(3), 688−697 (2020).
23. A. A. Bubnov, V. S. Belov, Y. V. Kargina, G. V. Tikhonowski, A. A. Popov, A. Yu. Kharin, M. V. Shestakov, A. M. Perepukhov, A. V. Syuy, V. S. Volkov, V. V. Khovaylo, S. M. Klimentov, A. V. Kabashin, and V. Yu. Timoshenko, "Laser-Ablative Synthesis of Silicon–Iron Composite Nanoparticles for Theranostic Applications," Nanomaterials 13(15), 2256 (2023).
24. S. Krenek, T. U. Berendonk, and T. Petzoldt, "Thermal performance curves of Paramecium caudatum: A model selection approach," European Journal of Protistology 47(2), 124–137 (2011).
25. G. A. Gruzdev, O. V. Karpukhina, V. G. Yakunin, A. N. Inozemtsev, V. P. Savinov, V. Yu. Timoshenko, and A. A. Kamensky, "Effect of Low-Temperature Atmospheric Pressure Plasma on Paramecium caudatum Cell Culture," Moscow University Biological Sciences Bulletin 76(4), 244–248 (2021).

Evaporation Peculiarities of Soft Biological Tissues in the Process of Automated 2D-Scanning of CO_2 Laser Radiation

Alexander K. Dmitriev, Alexey N. Konovalov*, Vladimir N. Kortunov, and Valery A. Ulyanov
NRC "Kurchatov Institute",1 Academician Kurchatov Sq., 1123182 Moscow, Russian Federation
*e-mail: ank27.ift@mail.ru

Abstract. The peculiarities of laser evaporation of soft biological tissues in the process of two-dimensional scanning of continuous CO_2 laser radiation were studied experimentally and numerically. Samples from agar and pig heart muscle in vitro were used as soft biotissue models. The depth of evaporation and the peculiarities of the formed surface of the evaporated zone were studied for different regimes of exposure: radiation power, scanning speed of the laser beam, filling density of the scanned zone. A semi-empirical model of laser evaporation of soft biological tissues with high water content is proposed based on the energy balance and the evaporative mechanism of biotissue removal. Studies have shown good agreement between experimental data and data obtained based on the proposed model. © 2024 Journal of Biomedical Photonics & Engineering.

Keywords: CO_2 laser; automated scanning; precision evaporation; biomodel; robot-assist surgery.

Paper #9115 received 7 Jun 2024; revised manuscript received 1 Oct 2024; accepted for publication 1 Oct 2024; published online 10 Nov 2024. doi: 10.18287/JBPE24.10.040307.

1 Introduction

The use of robotic and automated devices and systems in surgery is one of the promising areas for developing and improving the current medical technologies [1−3]. This approach reduces the risks of the human factor, decreases the time of surgical intervention, increases the efficiency and safety of treatment, and allows for rapid postoperative rehabilitation of patients.

High-precision and low-trauma laser surgical interventions have led to widespread devices based on CO_2 lasers with scanning systems. These devices make the process of exposure to laser radiation automatic [4]. CO_2 lasers still remain the most common in global medical practice and are most commonly used for the so-called ablative (local evaporation of tissue) or non-ablative (local heating of tissue) laser skin resurfacing [5, 6]. This technology is considered the gold standard in dermatological surgery. Currently, active research is being conducted on the use of scanning laser systems in relation to the problems of obtaining precision cuts of complex shapes of a given depth and evaporation of a given area of arbitrary shape on the biotissue surface. The scanning systems can effectively control the parameters of laser radiation in the impact zone. They provide high speed and accuracy, safety and reproducibility of operations using CO_2 lasers [7]. This significantly expands the possibilities and prospects for their use in surgery.

One of the directions in the development of robot-assisted laser surgery is predictive modeling for the purpose of preoperative planning [8, 9]. Planning is based on the selection of the optimal modes of automated laser exposure, ensuring high efficiency of the laser procedure. These approaches to carrying out precision and low-trauma laser operations are based on experimental and numerical modeling of laser irradiation processes using various *in vivo* or *ex vivo* biomodels. Ref. [10] suggests selecting the modes and predicting the depth of automated laser incision of soft tissues by means of an experimental database. To this end, they used *ex vivo* chicken muscle tissue. The obtained accuracy of the depth of the cut reached accuracy of ±100 μm. In Refs. [11, 12], to achieve a given depth of laser evaporation of soft and bone tissues, it is proposed to use simplified mathematical models for predicting the depth of the cut using experimental data on animal tissues. Ref. [13] proposed a method for simulating the removal of the superficial tumors while minimizing the damage to the healthy tissue with the help of a laser beam whose profile corresponds to the 3D shape of the pathological tissue. It is noted in Refs. [9, 14] that in the long term, the development of the robot-assisted laser surgery will

require developing predictive models of the interaction between laser radiation and various types of tissues.

An analysis of modern trends in the development of laser surgery shows that the creating of models of laser evaporation of biological tissue is urgent task due to development of robotic automated surgical complexes [9, 14]. There are numerous works devoted to modeling laser thermal and destructive effects on biological tissue. Usually such studies investigate the threshold conditions for laser destruction of biological tissue [15] and the features of its thermal damage [16], describe the formation of temperature fields during laser action and explosive boiling of interstitial fluid [17−19], and the generation of laser-induced mechanical stresses [20]. The overwhelming majority of studies are devoted to laser evaporation of biotissues in the short-pulse mode. There are much fewer works that study the effect of continuous laser radiation on biotissues. There are also few works that model the depth of cut and the depth of evaporation of the tissue zone during two-dimensional scanning of continuous laser radiation. There are known works [10, 12], which propose a completely empirical approach to predicting the depth of automated linear cutting of soft biotissues by continuous CO_2 laser radiation. Samples from agar and chicken muscle tissue were used as biomodels. This approach is based on a linear approximation of experimental data by the parameter of the input energy and the exposure time. These works do not analyze the features of the influence of the laser beam scanning speed. There is also no physical model that would allow the surgeon to predict the result of cutting and evaporation of a two-dimensional tissue zone in relation to a laser installation that has its own specific parameters of the laser beam and scanning system (spot diameter, scanning speed, etc.).

The purpose of this work is an experimental and numerical study of the efficiency and characteristics of the evaporation of soft biological tissues in the process of automated two-dimensional scanning of CO_2 laser radiation. A physical evaluation model of the depth of the evaporated region of soft biological tissue with high water content is proposed depending on the modes of two-dimensional laser scanning and the parameters of the laser beam.

2 Methods and Materials

For automated surface laser evaporation of biomodels, we used a setup consisting of a laser unit, an articulated-mirror manipulator and a 2-coordinate galvanic *Galvo Scanner*, Model *JS*1105 (*Sino-Galvo Technology Co.*, China) coupled to it. The setup is based on the *C*-20*A* single-mode CO_2 laser (*Coherent*, USA) with a power up to 20 W. A detailed description of the setup is given in Ref. [21].

The scanner control unit and the specially developed software make it possible to set any shape of the evaporation area within 20 × 20 mm, the speed of the laser beam within 1–50 mm/s, and the required filling density of the evaporated surface by laser hatching. The surface scanning area is a set of parallel lines (hereinafter, 'hatching lines'). The required density of filling the evaporated area of the surface by laser hatching was secured by changing the distance between the hatching lines.

The samples based on *Difco*™ agar and pig heart muscle tissue *in vitro* were used as biomodels. Biotissues were used within 48 h *post mortem.* The samples were stored at the temperature of 0–4°C with constant humidity. The heart muscle was used for the following reasons. Firstly, it is known that pig tissues are most similar in their parameters to human ones and are used in modeling surgical processes. Secondly, relatively large areas of tissue that would be homogeneous could be found quite easily in the heart muscle. Other soft tissues are much less homogeneous. For example, skeletal muscles often contain ligaments, fat, vessels, and tendons. This would significantly complicate the experiments and analysis of the data obtained. For experiments with agar, the prepared samples contained 15% agar mass fraction and 85% water fraction. These samples simulated soft water-containing tissues. The cross sections of biomodels were studied under a digital USB microscope (magnification 10x−200x, resolution 1600 × 1200, China).

In experiments on automated evaporation of the biomodel surface areas, a single scan of the rectangular area measuring 8.5 mm × 11.6 mm was performed (the lens focal length = 50 mm). The radiation was focused onto the surface of the biomodel. The focal spot size was 175 μm at the 86% level. During the experiments, some exposure and scanning modes were changed: the power of laser radiation (2–5 W), the speed of the laser beam (from 2 mm/s to 20 mm/s), the density of filling the evaporated area of the surface of the biotissue by hatching. The distance between the hatching lines ranged from 75 to 450 μm.

3 Results

Laser evaporation of the surface of agar samples was studied in accordance with the filling density of the hatching and scanning speed. At low filling density of the scanned area, the surface of the evaporated zone has a sawtooth shape. At a high filling density of the area (the distance between the hatching lines equal to or less than the width of the evaporated channel), the surface of the evaporated region of the sample is smoother and more uniform than at a low filling density. A similar result is achieved by decreasing the scanning speed at a fixed distance between the hatching lines. Fig. 1 shows cross sections of agar samples after evaporation for scanning speeds of 12.5 mm/s, 9 mm/s and 4.5 mm/s and the distance between hatching lines of 450 μm. As follows from the figure, at the scanning speed of 12.5 mm/s, the surface has a sawtooth shape, whereas at the scanning speed of 4.5 mm/s, the surface becomes smoother. This is due to the fact that as the scanning speed decreases, the width of the evaporated channel increases, since the thermal front has time to spread over a greater distance. As a result, the evaporated surface is smoothed due to the overlap of adjacent hatching channels. This is similar to what happens when the distance between the hatches is reduced.

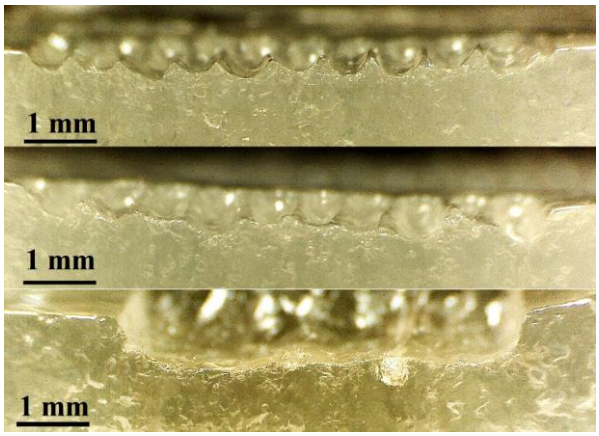


Fig. 1 Cross section of the evaporated zone in the agar samples under various single-pass scanning modes: P = 4 W; the distance between hatching lines = 450 μm; the scanning speed (top to bottom): 21; 14.5, and 7.4 mm/sec.

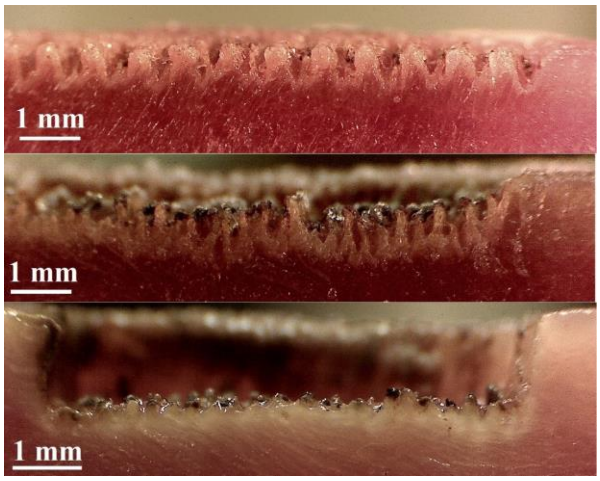


Fig. 2 Cross section of the evaporated zone of the cardiac muscle at P = 3.6 W: (a) d = 0.445 mm, V = 7 mm/s, (b) d = 0.150 mm, V = 7 mm/s, (c) d = 0.75 mm, V = 11.3 mm/s.

The experiments have also demonstrated that the depth of the evaporated zone increases both with increased hatching density and with decreased scanning speed. This is due to the fact that the energy input per unit area increases both at a lower scanning speed and at a filling density with hatching.

A similar picture was observed when evaporating the biomodels based on the cardiac muscle (Fig. 2). The main difference was that with denser hatching, the surface of the evaporated hangar area is significantly greater even compared to the heart muscle. This may be caused by the fact that when melting, agar acquires a smoother surface. Secondly, there is a change in the color of the tissue in the vaporized area on the surface of the heart muscle samples, which is caused by coagulation and carbonization of the tissue at high temperatures. For the agar samples, this effect was not observed.

In the general case, the surface of the evaporated zone of biomodels is uneven due to scanning and the peculiarities of the thermophysical processes in the irradiation zone. In the evaporated zone, a change in depth is observed from a certain minimum value H_{min} to a maximum H_{max} (Fig. 3). It is clear that the average value of the depth <H> of the evaporated zone is determined by the average value of the deposited energy by laser radiation (for more details, see Section "Model of soft tissue evaporation"). Due to the difficulty of determining <H> from the photographs of cross sections, we characterized the result of evaporation during laser scanning by the maximum depth H_{max}.

Fig. 4 shows the relationship between H_{max} and the scanning speed V for different biomodels. As can be seen from the figure, the depth of evaporation of agar and the cardiac muscle is almost the same. This was to be expected, since the determining factor in such biomodels is the absorption of radiation by water at the wavelength of 10.6 μm. The agar-based samples present a fairly good model of soft tissue from the point of view of assessing the effectiveness of laser evaporation.

Fig. 5 shows the relationship between the evaporation depth and the laser radiation power. The obtained data fits well with the linear relationship. This suggests that the determining factor is the input laser energy.

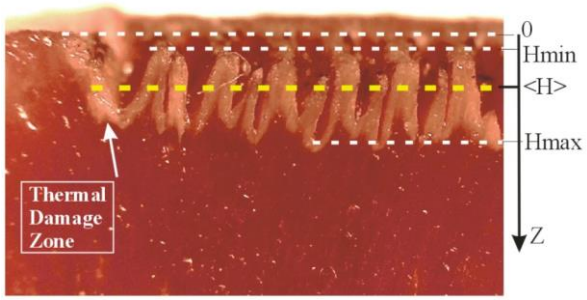


Fig. 3 Cross section of the evaporated zone of the cardiac muscle at P = 3.55 W, V = 3.5 mm/sec, d = 0.445 mm.

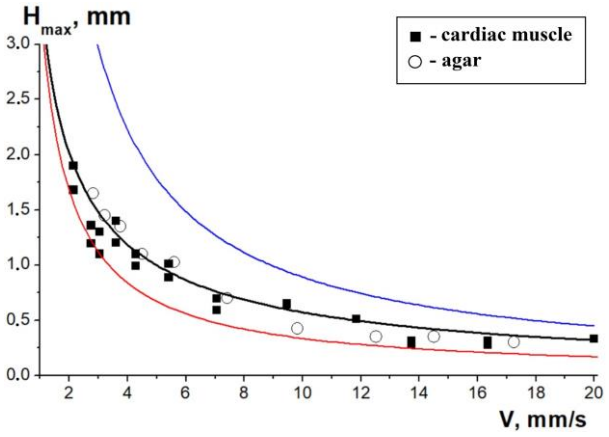


Fig. 4 The relationship between the evaporation depth of biomodels and the scanning speed V, d = 0.445 mm. The red curve is the average depth <H>, the blue curve is without taking into account thermal conductivity, the black curve is taking into account thermal conductivity (χ = 1.2 10^{-7} m^2/s).

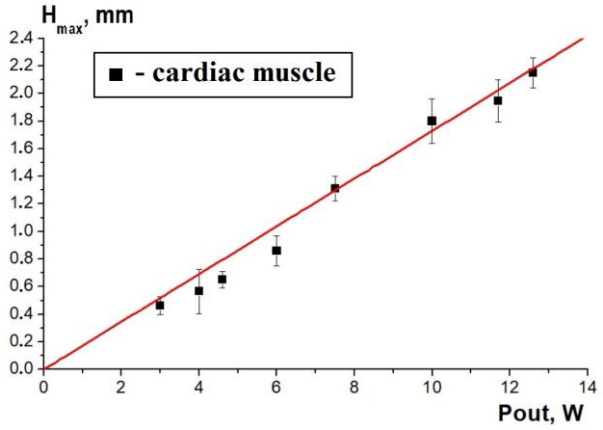


Fig. 5 The relationship between evaporation depth of cardiac muscle H_{max} and the radiation power. V = 15 mm/s, d = 0.15 mm. The red line represents the calculated linear relationship between the average evaporation depth of cardiac muscle and the power according to Eq. (7).

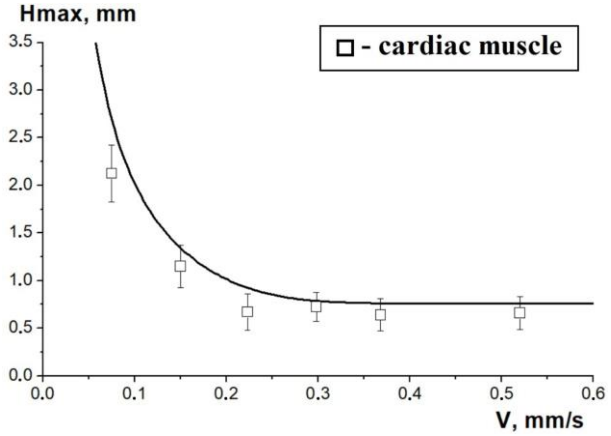


Fig. 6 The relationship between H_{max} and distance d between the hatching lines at the scanning speed of 7 mm/s. The black curve represents calculation taking into account thermal conductivity (χ = 1.2 10^{-7} m^2/s).

Fig. 6 shows the relationship between the maximum evaporation depth H_{max} and distance d between the hatching lines at the scanning speed of 7 mm/s. A rapid increase in the evaporation depth is observed with decreased distance d. As d increases, there is no change in the evaporation depth. This is due to the fact that at large distances d, scanning turns into separate cuts whose depth is constant and depends only on the scanning power and speed.

4 Model of Soft Tissue Evaporation

For soft biotissues with high water content (70−80% and more), we propose a semi-empirical model that allows determining the depth of the evaporated area of biotissue during laser scanning with continuous CO_2 laser radiation. This model assumes that the process of biotissue evaporation by continuous radiation occurs far beyond the threshold of the onset of evaporation. In this case, the intensity of the laser energy input is such that the interstitial water reaches the boiling point and higher. This leads to its intensive evaporation, accompanied by microexplosions with the mass removal from the impact zone. The model is based on the energy balance, taking into account that almost all the energy of laser radiation input into the tissue is spent on the vaporization of the water contained in it.

To justify this assumption, we will conduct some assessments. First, let us make an assessment of the threshold at which water begins to boil. The rate of temperature rise in the center of the laser spot at the initial moment of time, when the thermal conductivity is negligible, can be defined as:

$$\frac{dT}{dt} = \frac{P\mu_a}{\pi\rho C r_0^2}, \quad (1)$$

where $P = P_0 \cdot (1-R)$, P_0 – laser radiation power, R – reflection coefficient from the tissue surface, r_0 is the radius of the laser beam, ρ, C, μ_a density, specific heat and absorption coefficient for biotissue.

In this paper, only soft tissues with high water content are considered. In this regard, for further estimations we will take the values of thermophysical characteristics for water: $\rho = 10^3$ kg/m^3 and C = 4200 J/kg. The presented model does not take into account light scattering, since the determining factor in the propagation of 10 μm radiation in soft tissues is the high absorption of water. In this regard, to estimate the absorption of soft tissue, we will use the absorption coefficient for water μ_a = 792 cm^{-1} [22].

The rate of temperature rise during the passage of a laser beam with scanning speed V can be approximately estimated as follows:

$$\frac{dT}{dt} = \frac{\Delta T}{2r_0/V} = \frac{P\mu_a}{\pi\rho C r_0^2}. \quad (2)$$

From this relationship, we obtain the water boiling (ΔT = 100 °C) threshold power for a given scanning speed:

$$P_{th} = \frac{\pi\rho C r_0 V \Delta T}{2\mu_a}. \quad (3)$$

From Eq. (3) we obtain that at the scanning speed of 10 mm/s and the beam radius of 90 μm, the power threshold for boiling point is 11 mW. This estimate is made under the assumption that during the time $2r_0/V_0$, the thermal front propagates over a distance that is significantly shorter than $1/\mu_a$. This is true for the scanning speed $V_0 >> 2r_0\chi\mu_a^2$ = 27 cm/s. At speeds lower than this value, the thermal front spreads over the distance of $\Delta z = (\chi 2r_0/V_0)^{0.5}$ in the time interval of $2r_0/V_0$. From energy considerations it is easy to obtain the boiling threshold for this case:

$$P_{th} = \frac{\pi\rho C r_0 V \Delta T}{2}\left(\frac{1}{\mu_a} + \sqrt{\frac{2r_0}{V}\chi}\right). \quad (4)$$

At V = 10 m/s and r_0 = 90 μm, the threshold power will be P_{th} = 39 mW. The estimates have shown that for both high and low scanning speeds, the water boiling power threshold is significantly smaller than 1 W.

Thus, when soft biological tissues are exposed to radiation power of one W or above at the wavelength of 10.6 μm, the temperature in the exposure zone quickly reaches the boiling point. Upon reaching this temperature, the process of intense evaporation of water begins. The excess energy deposited in the laser radiation zone is no longer spent on heating but on the vaporization process. This is accompanied by micro-explosions and the removal of vapor-droplet mixture from the impact zone [23, 24]. In this model, we also assume that the mechanical energy associated with the removal of mass from the impact zone is negligible (this will be shown below after obtaining the estimates of the evaporation depth). Thus, for this model, it is assumed that the removal of tissue volume is determined solely by vaporization.

Using this assumption, it is possible to obtain the average depth of the evaporated zone when scanning a laser beam. Let laser scanning be carried out at the speed V of the rectangular zone of dimensions $L \times M$, along the face of length M. Let the distance between the hatching lines be d. In this case, the total scanning time will be $\Delta t = (M\cdot(L/d)+L)/V$. From the condition that all the adsorbed energy is spent on evaporation, it turns out:

$$P\Delta t = \rho QLM\langle h\rangle, \tag{5}$$

where $\langle h\rangle$ is the average depth of the evaporated zone and $Q = 2.26\cdot10^6$ J/kg represents specific heat of vaporization. Assuming that $M >> d$, we obtain the average depth of the evaporated zone:

$$\langle h\rangle = \frac{P}{\rho QVd}. \tag{6}$$

It is clear that when $d >> r_0$, the result of scanning will not be an evaporated layer of tissue, but individual cuts in the area of the rectangular scanning zone. In this case, the average depth taken over the scanning area $L \times M$ will also be equal to $\langle h\rangle$.

Let us assume that all the evaporated tissue of layer $\langle h\rangle$ was removed from the impact zone at speed u. Then the mechanical energy will be equal to $E_m = \rho\langle h\rangle M\cdot Lu^2/2$. The energy delivered to the biological tissue when scanning the area $M\cdot L$ is equal to $E_{las} = P\,\Delta t$. The ratio of the mechanical energy of mass removal to laser energy, taking into account Eq. (6) will be: $E_m/E_{las} = u^2/(2Q)$. Even if we take a sufficiently high mass removal rate of 10 m/s (the characteristic velocity of 1–3 m/s [23, 24]) for estimation, we obtain a fairly small value of $E_m/E_{las} = 3.8\cdot10^{-5}$ ratio of the mechanical energy to the delivered laser energy during evaporation of layer $\langle h\rangle$.

Thus, the accepted approximation that mechanical energy of mass removal and thermal energy can be neglected is satisfied quite well. Fig. 5 shows the linear dependence of $\langle h\rangle$ on the radiation power at a scanning speed of 15 mm/s and the distance between lines d = 0.15 mm. The figure demonstrates a fairly good agreement with the experiment. At the same time, the value of the average evaporation depth $\langle h\rangle$ is not quite suitable for characterizing the scanning result with relatively sparse hatching ($d > r_0$). For example, photographs of sections of an evaporated myocardial sample show explicit laser cuts (Fig. 2 and Fig. 3). A simple calculation of one value $\langle h\rangle$ is not very informative in cases where the average evaporation depth $\langle h\rangle$ is less than or comparable to the cutting depth. Fig. 4 shows the evaporation depth as a function of scanning speed at radiation power P = 3.55 W and d = 0.445 mm. The difference between the calculated curve of the average evaporation depth (Eq. (6)) and the measured values is quite strong. This is due to the fact that the measurements were taken not for the average evaporation depth but for the maximum depth H_{max} that is observed in the scanning area. With a relatively sparse hatching, this value H_{max} is greater than the average evaporation value over the entire scanning area.

To describe of this process in more detail, the shape of the channel during cutting and the overlap of these cuts with each other at $d < r_0$ must be taken into account. This can also be done under the assumption that all energy goes into evaporation. Let us consider a single cut of length M, which is obtained when a laser beam passes at a speed V.

Then, pertaining to energy, we find that the energy deposited during the passage of the laser beam at distance M was spent on evaporating water with volume $M\cdot S_0$, where S_0 is the cross-section area of the resulting channel. Thus we get:

$$S_0 \equiv \int_{-\infty}^{\infty} h(x)dx = \frac{P}{V\rho Q}, \tag{7}$$

where $h(x)$ is the shape of the cross-section of a separate cut.

In our model, the depth of the evaporated zone is determined by the absorbed energy. Therefore, at high scanning speeds, when the thermal front extends over a distance significantly less than the beam radius during $2r_0/V$, the depth $h(x)$ will repeat the shape of the laser beam profile. If the laser beam has a Gaussian shape, then $h(x)$ will also have a Gaussian shape:

$$h(x) = H_0 e^{-\left(\frac{x}{r_0}\right)^2}. \tag{8}$$

From energy considerations it is easy to obtain that:

$$H_0 = \frac{P}{\sqrt{\pi}V\rho Q r_0}. \tag{9}$$

According to energy considerations, the resulting shape of the evaporated layer will be the sum of depths $h(x)$ for all hatching lines of the evaporated zone $L\times M$ that are located equidistantly with a period d:

$$H(x) = \sum_{k=0}^{N} h(x - kd), \quad (10)$$

where $N = int(L/d)$ is the number of hatching lines in the evaporated zone (*int* is the integer part of the division).

Knowing the profile of an individual cut $h(x)$, it is easy to calculate the profile of the entire evaporated zone for different scanning parameters. Fig. 7 shows shapes $H(x)$ of the evaporated layers at various distances between the hatches at the scanning speed of 7 mm/s with the Gaussian shape of a single laser channel.

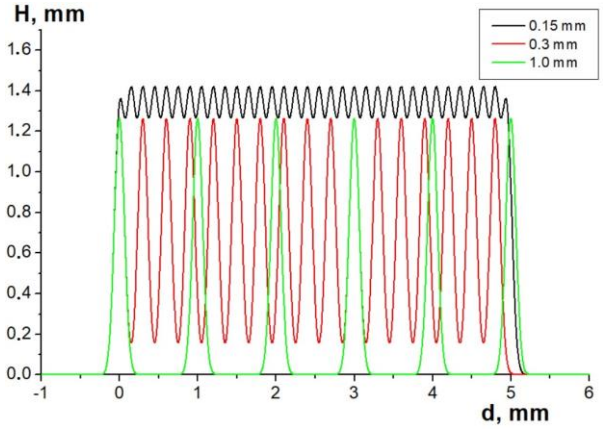


Fig. 7 Shapes $H(x)$ of the evaporated layers at various distances between hatches. V = 7 mm/s.

These dependencies can find the average depth and maximum depth in the evaporation zone. Numerical modeling has shown that the average depth $<H>$ calculated as the average of function $H(x)$ coincides with the average depth calculated using the simplified model (Eq. (6)). Fig. 4 shows the relationship between the maximum evaporation depth (blue line) and the scanning speed at the distance between the hatching lines of 0.445 mm. As can be seen from the figure, the calculated value H_{max} significantly exceeds the experimentally measured value. This is due to the fact that a Gaussian function with a half-width equal to the radius of the laser beam was taken as the profile of a single cut $p(x)$. In reality, this is not true, since during the movement of the beam over a distance equal to the diameter of the laser spot, the thermal front spreads over the distance of $\Delta x = (\chi 2r_0/V_0)^{0.5}$. As a result, the width of the evaporation zone can differ from the diameter of the laser beam. The lower the scanning speed, the wider the evaporation zone will be due to heat propagation.

Taking into account this factor, we assumed that in the presence of thermal conductivity, the profile of a single cut also retains the Gaussian shape, but the half-width of the Gaussian profile r_{eff} due to heat transfer depends on the scanning speed as follows:

$$r_{eff} = r_0 + \sqrt{\frac{2r_0}{V}\chi}. \quad (11)$$

By substituting the value of the effective radius r_{eff} in Eq. (8) instead of r_0, we can recalculate the maximum evaporation depth as a function of speed. Fig. 1 shows the relationship between H_{max} (black line) and the scanning speed when thermal conductivity is considered. Here we can see a fairly good agreement with the experimental data.

Fig. 6 shows the relationship between H_{max} and distance d between the hatching lines at the scanning speed of 7 mm/s in the presence of thermal conductivity. The peculiarities of the dependence of H_{max} on parameter d are explained by the fact that at large distances d, individual tissue cuts occur and their depth is determined only by profile $h(x)$. With denser hatching, profiles $h(x)$ overlap and the depth increases due to the summation of profiles for individual cuts (Eq. (10)).

As can be seen from Fig. 6, the calculated curve of H_{max} versus d also correlates well the experiment. Thus, the proposed model demonstrates a good agreement with the experiment on the maximum evaporation depth of soft tissues.

For the tasks of precision low-trauma surgery, an important parameter is not only the depth of a single removed layer, but also the accuracy with which the tissue is removed to a given depth. It is clear that when the biological tissues are evaporated using the scanning method, the surface of the evaporated zone is uneven, which is primarily caused by the scanning method itself in the form of serial tissue cuts. This can be seen in photographs of the sections of the evaporated zone of the myocardial samples. It is clear that at sufficiently large distances between the hatching lines, there will be a maximum surface roughness that will represent individual cuts. As the model shows, when the distance between strokes decreases, the cutting zone of individual strokes overlaps and the surface is smoothed due to the summation of individual cut profiles (Eq. (10)). This is clearly demonstrated in Fig. 1 that shows the profiles of the evaporated zone obtained by calculation (Fig. 7).

Let us take the surface roughness $\Delta H = H_{max} - H_{min}$ as a characterizing parameter, where H_{min} is the minimum depth in the evaporation zone. Fig. 8 shows the relationship between the roughness of the evaporated zone and the scanning speed at d = 0.445 mm. The same figure shows the calculation curve, which is also in good agreement with experiment.

At the same time, the experiments on cardiac muscle have shown that the magnitude of roughness as $\Delta H = H_{max}–H_{min}$ at smaller parameters d remains quite large, while the model predicts a fairly rapid decrease in roughness with decreased distance d. For example, as shown in Fig. 7, the surface roughness at d = 0.15 mm is ΔH = 150 μm, while the experiments give the roughness of about 400–600 μm (see Fig. 2b). Apparently, this is due to the fact that the roughness of the evaporated zone is determined by other factors that are not taken into account in the model. Firstly, the amount of roughness may strongly depend on the shape of profile $h(x)$ of the individual cut. The model uses a Gaussian profile shape. The superposition of several sequential Gaussian profiles leads to noticeable smoothing due to the Gaussian tail.

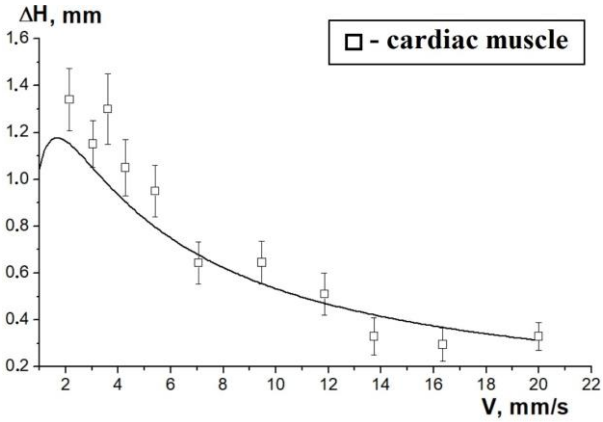


Fig. 8 The relationship between the roughness of the evaporated zone and the scanning speed at d = 0.445 mm. The black curve is the calculation.

With the shape of a separate channel $h(x)$ with sharper boundaries, such smoothing will no longer be observed. Secondly, the removal of tissue from the impact zone occurs by micro-explosions due to local overheating of water that are accompanied by tissue ruptures. This may lead to additional roughness of the resulting surface. Therefore, description of the roughness at small values of d requires a separate consideration.

It should be noted that almost all soft tissues with high water content have similar characteristics [25, 26]: density, heat capacity, thermal diffusivity, absorption coefficient at a wavelength of 10.6 μm. Such closeness of characteristics is due to the high water content. These characteristics can directly affect the threshold for the onset of laser evaporation. But in our work, we study evaporation under conditions significantly exceeding this threshold. Under such conditions, the main role in the energy balance is played by the evaporation of water, which is 70−80% or more. In this regard, the resulting evaluation formulas do not contain any specific characteristics of the biotissue except for density and thermal diffusivity.

However, tissues with a high water content may differ in mechanical and strength properties. Note that the tensile strength of soft water-containing tissues can vary from 0.01 MPa to 10 MPa. For example, the tensile strength of heart muscle is 0.04 MPa, while the strength of cartilage tissue, which also belongs to tissues with a high water content (80%), is up to 10 MPa [27, 28]. Experiments on biomodels of agar and heart muscle showed good agreement with the calculation. Therefore, it can be assumed that the proposed model can be used to estimate the depth of evaporation of other soft tissues with high water content and low tensile strength. The relationship between the mechanical and strength properties of tissues and the depth of evaporation by continuous laser radiation can be the subject of separate studies.

5 Conclusions

The features of laser evaporation of biomodels based on agar and pig tissues *in vitro* during two-coordinate scanning of continuous CO_2 laser radiation at the wavelength of 10.6 μm have been investigated both experimentally and numerically. The evaporation depth and the features of the formed surface of the evaporated area were studied for different impact modes: (1) radiation power, (2) scanning speed of the laser beam, and (3) hatching filling densities of the scanned area. It has been shown that the evaporation depth of the agar samples with 85% water practically coincides with the depth of evaporation of pig tissue samples. The agar samples can serve as good biomodels in evaluating the effectiveness of laser layer-by-layer evaporation of soft tissues. The proposed semi-empirical model of laser evaporation of soft biological tissues with high water content is based on the energy balance and the evaporative mechanism of biological tissue removal. The model allows calculating the average depth of the evaporated zone, as well as the depth of individual cuts and the unevenness of the fabric surface with a sufficiently low density of filling the scanning zone with hatching. The study has demonstrated a good correlation between the experimental data and the data obtained with the proposed model.

The study was carried out within the state task of the NRC “Kurchatov Institute”.

Disclosures

The authors declare that they have no conflict of interest.

References

1. G. Maza, A. Sharma, “Past, present, and future of robotic surgery,” Otolaryngologic Clinics of North America 53(6), 935–941 (2020).
2. J. Han, J. Davids, H. Ashrafian, A. Darzi, D. S. Elson, and M. Sodergren, “A systematic review of robotic surgery: From supervised paradigms to fully autonomous robotic approaches,” Robotics Computer Surgery 18(2), e2358 (2022).
3. I. O. Gritskov, A. A. Vitoslavskii, K. A. Kryazheva, A. O. Vasil’ev, K. B. Kolontarev, and D. Yu. Pushkar’, “Robotic systems in surgery,” Biomedical Engineering 55(5), 365–369 (2022).

4. Y. Y. Juo, A. Abiri, J. Pensa, S. Sun, A. Tao, J. Bisley, W. Grundfest, and E. Dutson, "Center for advanced surgical and interventional technology multimodal haptic feedback for robotic surgery," 17 Chapter in Handbook of Robotic and Image-Guided Surgery, M. H. Abedin-Nasab (Ed.), Elsevier, 285−301 (2020). ISBN: 978-0-12-814245-5.
5. U. Paasch, M. Haedersdal, "Laser systems for ablative fractional resurfacing," Expert Review of Medical Devices 8(1), 67–83 (2011).
6. A. Aslam, T. S. Alster, "Evolution of laser skin resurfacing: from scanning to fractional technology," Dermatologic Surgery 40(11), 1163–1172 (2014).
7. R. Colasanti, L. Giannoni, S. Dallari, V. Liverotti, D. Aiudi, A. Di Rienzo, F. Rossi, and M. Iacoangeli, "Application of a scanner-assisted carbon dioxide laser system for neurosurgery," World Neurosurgery 153, e250–e258 (2021).
8. A. R. Padalhin, "Lasers and robots: recent developments in transoral laser and transoral robotic surgery," Medical Lasers 9(2), 103–109 (2020).
9. H. C. Lee, N. E. Pacheco, L. Fichera, and S. Russo, "When the end effector is a laser: a review of robotics in laser surgery," Advanced Intelligent Systems 4(10), 2200130 (2022).
10. A. Acemoglu, L. Fichera, I. E. Kepiro, D. G. Caldwell, and L. S. Mattos, "Laser incision depth control in robot-assisted soft tissue microsurgery," Journal of Medical Robotics Research 02(03), 1740006 (2017).
11. S. Stopp, D. Svejdar, E. Von Kienlin, H. Deppe, and T. C. Lueth, "A new approach for creating defined geometries by navigated laser ablation based on volumetric 3-d data," IEEE Transactions on Biomedical Engineering 55(7), 1872–1880 (2008).
12. L. Fichera, D. Pardo, P. Illiano, J. Ortiz, D. G. Caldwell, and L. S. Mattos, "Online estimation of laser incision depth for transoral microsurgery: approach and preliminary evaluation," Robotics Computer Surgery 12(1), 53–61 (2016).
13. G. Ma, R. Prakash, B. Mann, W. Ross, and P. Codd, "3D Laser-and-tissue agnostic data-driven method for robotic laser surgical planning," in 2023 IEEE/RSJ International Conference on Intelligent Robots and Systems (IROS), Detroit, MI, USA (2023).
14. D. A. Hashimoto, G. Rosman, D. Rus, and O. R. Meireles, "Artificial intelligence in surgery: promises and perils," Annals of Surgery 268(1), 70–76 (2018).
15. F. Partovi, J. A. Izatt, R. M. Cothren, C. Kittrell, J. E. Thomas, S. Strikwerda, J. R. Kramer, and M. S. Feld, "A model for thermal ablation of biological tissue using laser radiation," Lasers in Surgery and Medicine 7(2), 141–154 (1987).
16. A. L. McKenzie, "A three-zone model of soft-tissue damage by a CO 2 laser," Physics in Medicine & Biology 31(9), 967–983 (1986).
17. A. M. Sagi-Dolev, "Heating of biological tissue by laser irradiation: temperature distribution during laser ablation," Optical Engineering 31(7), 1425 (1992).
18. G. L. LeCarpentier, M. Motamedi, L. P. McMath, S. Rastegar, and A. J. Welch, "Continuous wave laser ablation of tissue: analysis of thermal and mechanical events," IEEE Transactions on Biomedical Engineering 40(2), 188–200 (1993).
19. R. Dua, S. Chakraborty, "A novel modeling and simulation technique of photo–thermal interactions between lasers and living biological tissues undergoing multiple changes in phase," Computers in Biology and Medicine 35(5), 447–462 (2005).
20. V. Venugopalan, N. S. Nishioka, and B. B. Mikić, "Thermodynamic response of soft biological tissues to pulsed infrared-laser irradiation," Biophysical Journal 70(6), 2981–2993 (1996).
21. A. K. Dmitriev, A. N. Konovalov, V. N. Kortunov, and V. A. Ulyanov, "Diagnostics of layer-by-layer biotissue evaporation in the process of two-coordinate scanning by a laser beam for precision surgery," Journal of Biomedical Photonics & Engineering 9(2), 020302 (2023).
22. G. M. Hale, M. R. Querry, "Optical constants of water in the 200-nm to 200-μm wavelength region," Applied Optics 12(3), 555 (1973).
23. V. M. Gordienko, A. N. Konovalov, Yu. Ya. Putivskii, N. N. Kurochkin, and V. I. Savin, "Investigation of the dynamics of laser-induced explosive boiling of water using the autoheterodyning scheme," High Temperature 36(5), 789−795 (1998) [in Russian].
24. A. K. Dmitriev, A. N. Konovalov, V. N. Kortunov, and V. A. Ulyanov, "Doppler diagnostics of laser evaporation of biological tissues," Journal of Laser Applications 34, 041201 (2022).
25. V. Tuchin (Ed.), "Tissue Optics. Light Scattering Methods and Instruments for Medical Diagnosis," SPIE (2007). PDF ISBN: 9780819481061.
26. K. Giering, O. Minet, I. Lamprecht, and G. Müller, "Review of Thermal Properties of Biological Tissues," in Laser-Induced Interstitial Thermotherapy, G. Muller, A. Roggan (Eds.), SPIE Press, Washington, USA, 45−65 (1995).
27. J. T. Walsh, T. F. Deutsch, "Pulsed CO2 laser ablation of tissue: effect of mechanical properties," IEEE Transactions on Biomedical Engineering 36(12), 1195−1201 (1989).
28. V. A. Berezovskii, N. N. Kolotilov, Biophisisheskie characteristiki tkanei cheloveka. Spravochnik, Kiev, Naukova dumka, (1990) [in Russian]. ISBN: 5120013740.

Inactivation of Bacteria in Biofilms by Shock Waves

Sergey Letuta, Azamat Ishemgulov*, Olga Davydova, and Maxim Grigoriev
Orenburg State University, 13 Pobedy av., Orenburg 460018, Russian Federation
*e-mail: azamat.ischemgulov@yandex.ru

Abstract. The processes of destruction of biofilms and inactivation of bacteria under the influence of shock acoustic waves and photodynamic treatment were studied. Shock waves were generated by locally heating the medium with nanosecond pulses of focused laser radiation. The radiation energy was converted into heat in the process of nonradiative relaxation of the excited states of organic dye molecules dissolved in the medium. The processes of biofilm removal and destruction of the extracellular matrix by shock waves are discussed. The low efficiency of inactivation of bacteria in biofilms by shock acoustic waves with peak pressure commensurate with the threshold of tensile strength of the cell wall material has been experimentally proven.
© 2024 Journal of Biomedical Photonics & Engineering.

Keywords: bacterial films; shock waves; inactivation of microorganisms.

Paper #9172 received 3 Oct 2024; revised manuscript received 18 Nov 2024; accepted for publication 18 Nov 2024; published online 3 Dec 2024. doi: 10.18287/JBPE24.10.040311.

1 Introduction

The high survival rate of microbes in human and animal organisms, in reservoirs, in soil and other natural environments, is largely due to their ability to unite into communities called biofilms. The principles of formation and the main stages of development of bacterial films were formulated several decades ago [1], and it is now reliably established that this is the main form of existence of microorganisms [2]. The development of pathologies in organisms and the spread of many dangerous infectious diseases are directly related to the emergence and growth of biofilms [3–4].

In the middle of the last century, antibiotics appeared in drug therapy, the use of which dramatically increased the effectiveness of treatment. Antibiotics have been and remain the main and in-demand means of fighting bacteria, and their potential is far from being exhausted. At the same time, every year there are reports of an increase in the number of strains that develop immunity to antibiotic therapy. Most researchers associate the phenomenon of antibiotic resistance precisely with the formation of biofilms [5–7]. Therefore, it is important to have in your arsenal a variety of ways and techniques to combat pathogens in biofilms, to which they will not be able to develop resistance.

In Refs. [8–9], using the example of planktonic microorganisms, the possibility of effective destruction of bacteria by shock waves or by the combined action of shock waves with photodynamic treatment was demonstrated. Depending on the conditions of wave generation and media treatment modes, it is possible to inactivate pathogenic microorganisms with almost 100% effectiveness. The purpose of this work is to apply methods of inactivation of planktonic microorganisms for bacteria in biofilms and to compare the effectiveness of bacterial damage in solutions and in biofilms.

2 Methods

2.1 Biofilms

The object of the research was biofilms of the Gram-negative rod-shaped bacterium *Pseudomonas aeruginosa*, known for its high resistance to antibiotics. To obtain monomicrobial biofilms of *P. aeruginosa*, a suspension of cells was prepared according to the McFarland turbidity standard 0.5, which in a volume of 1 ml was mixed in a sterile Petri dish with 20 ml of cetrimide broth and cetrimide agar (Russia), taken in a ratio of 1:1, and incubated for 24 h at a temperature of 37 °C. The quality of the biofilm was assessed by the evenly distributed blue-green staining of the nutrient medium with a pigment produced by *P. aeruginosa*. Using a 5 mm diameter punch, identical blocks were cut out of a jelly-like but sufficiently dense agar substrate with a biofilm formed on its surface.

A biofilm block on an agar substrate was placed in a saline solution with erythrosine concentration of 0.5 mM, positioned with a surface with cells frontally in relation to the influencing factor (shock waves, light) and the survival of bacteria after the action of shock waves and

photodynamic treatment was studied. Depending on the mode of mechanical action or irradiation of biofilms, a certain number of planktonic bacteria appeared in solutions. To estimate the number of such bacteria, an aliquot of a solution with a volume of 100 µl was selected, diluted 10^4 times, and followed by seeding and counting of individual colonies. *P. aeruginosa* cells were seeded on cetrimide agar in Petri dishes in at least 3 repetitions, followed by incubation for 24 h at a temperature of 37 °C.

To assess the survival of bacteria in biofilms after exposure to shock waves or radiation, the block was placed in 1 ml of saline solution after treatment, pipetted for 1 min and indexed (1 min). The resulting suspension of cells was diluted 10^7 times, seeded on cetrimide agar and colony-forming units (CFU) were counted after incubation at a temperature of 37 °C for 24 h in at least 3 repetitions.

2.2 Generation and Registration of Shock Waves

A saline solution with erythrosine was poured into a rectangular quartz cuvette measuring 5 × 20 × 30 mm and irradiated through its end wall. The source of excitation was a pulsed YAG:Nd laser (SolarLS, Belarus). Using a cylindrical lens, the laser radiation was focused in solution into an extended area of 3.0 × 0.3 mm directly along the boundary of the end wall. Parameters of the exciting pulse: λ = 532 nm, pulse duration 10 ns, power density was adjusted within 0.1−20 MW/cm^2. Depending on the concentration of the dye and the pumping energy of the laser, the exciting radiation diverging after focusing penetrated deep into the solution at a distance of no more than 10 mm. Shock waves appeared in the area of the lens constriction as a result of a rapid local increase in the temperature of the medium during nonradiative relaxation of the excited electronic states of erythrosine molecules.

A probing beam of a low-power He-Ne laser (632 nm) was used to register the emerging waves. The probing beam crossed the cuvette in the transverse direction at an adjustable distance from the end wall (Fig. 1), fell into the entrance slit of the monochromator with a width of 0.5−0.8 mm and further into the photodetector (PMT). At the moment when the probing beam is crossed by a shock wave, refraction occurs and the amount of light entering the photodetector changes. The wave profile is recorded on the monitor screen, reflecting the change in the density of the medium during the propagation of the disturbance. The equipment for generating and studying shock waves is described in detail in Ref. [8].

Knowing the distance from the lens constriction to the probing beam, the wave propagation velocity was determined, which at a temperature of 22 °C turned out to be equal to 1495 ± 30 m/s, which coincides with the speed of sound in saline solution. By the angle of deflection of the beam at the moment of intersection with an acoustic wave, using the empirical Eq. [10]

$$n = 1.332 + 0.322(\rho - 1)$$

for the relationship of the refractive index with the density of a liquid, the change in the density of the medium during the passage of the wave was estimated and the peak pressure was determined. At an excitation power density of 15 MW/cm^2, the peak pressure was approximately 25−30 MPa, which is commensurate with the tensile strength σ_{ts} of the cell wall material in wet σ_{ts} ~ 20 MPa [11], which has a polymer structure. In all experiments, the results of which are presented below, the peak wave pressure was 25−30 MPa.

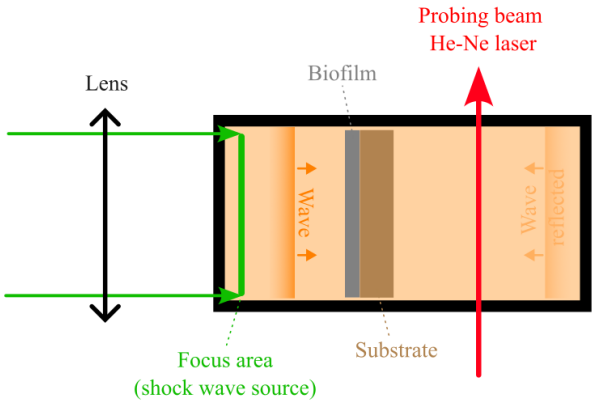


Fig. 1 Experimental registration of shock waves (a cuvette with a sensitizer solution and a biofilm is shown, top view). The focus area of the YAG:Nd laser radiation is located at the left end wall. Shock waves move from left to right. In their path there is a biofilm on a substrate, and then a probing beam of a He-Ne laser, under refraction of which registers the wave.

2.3 Photo- and Thermal Sensitizer

The choice of erythrosine as a photo- and heat sensitizer is due to its physical and chemical characteristics. In erythrosine molecules, the quantum yield of φ_T in the triplet state in aqueous solutions is close to unity [12], therefore it is characterized by high photodynamic activity [13−14]. In erythrosine solutions, the energy of laser radiation is very efficiently converted into heat, which is also associated with a high value of the φ_T value. Indeed, with a quantum yield of φ_T ~ 0.99 and a rate constant [12] of the intersystem crossing $S_1 \rightarrow T_1$, almost every molecule after excitation in the baseband $S_0 \rightarrow S_1$ passes into a triplet T_1 state in about 1 ns. If the power density of the exciting radiation is $P \geq 1$ MW/cm^2, and the dye concentration is 0.5 mM, then after 1 ns all molecules in the excitation zone turn out to be in a metastable triplet T_1 state. The absorption spectra of $S_0 \rightarrow S_1$ and $T_1 \rightarrow T_m$ in erythrosine strongly overlap; therefore, exciting radiation is absorbed in the $T_1 \rightarrow T_m$ band. Relaxation of high triplet T_m states mainly occurs nonradiatively, which ensures local heating of the medium. The lifetime of high triplet T_m states does not exceed several picoseconds [15−16], therefore, during the exciting pulse (τ = 10 ns), each molecule can repeatedly absorb exciting quanta, performing cyclic

$T_1 \leftrightarrow T_m$ or $T_1 \rightarrow T_m \rightarrow S_1 \rightarrow T_1$ transitions, each of which is accompanied by heat release.

Erythrosine is highly soluble in water and saline, has an absorption maximum in the region of 532 nm and a large molar extinction coefficient ($\varepsilon \sim 10^5$ $M^{-1}sm^{-1}l$). Note that instead of erythrosine, any other compounds can be used that effectively absorb exciting radiation, are photodynamic active and provide rapid local heating of the medium.

3 Results and Discussions

3.1 Impact of Shock Waves on Biofilms

The results of an experimental study of the impact of shock waves on bacteria in biofilms grown on a jelly-like agar substrate are shown in Fig. 2. First, the shock wave was fixed in erythrosine saline solution without biofilm at a distance of about 9 mm from the lens constriction. Then, at a distance of about 7 mm from the front wall (from the focus of the lens), a biofilm on a substrate (a fragment measuring 5 × 30 mm) was placed in a cuvette and the shock wave was again recorded under the same excitation and registration conditions. The profile of the shock wave at a distance of 9 mm from the lens band is shown in Fig. 2a. It can be seen that after installing the biofilm, the area under the curve reflecting the wave profile decreases by about 25%.

After exposure to an incident shock wave, the biofilm together with the jelly-like substrate become a source of secondary waves. Fig. 2b shows direct and reflected waves from the back wall of the cuvette in saline solution with dye before (blue line) and after (red line) placing the biofilm in the cuvette. In the recorded wave profile, in addition to changing the amplitude, a structure appears due to the generation of secondary waves by the biomaterial after exposure to direct and reflected acoustic waves. The presented data serve as a convincing illustration of the effects of direct and reflected shock waves on biofilm.

A shock wave at high peak pressure and a short front, acting on the biofilm-agar substrate, causes significant changes in the latter – from ablation of the biomaterial to bacterial damage in the biofilm. Ablation should be understood as the separation of a fragment of biofilm, in some cases together with the substrate, at the time of direct impact of the shock wave. At the same time, it must be borne in mind that shock waves are nonlinear waves of finite amplitude, and the current arising behind such a wave cannot be neglected. According to the wave profile in Fig. 2 it can be seen that it consists of a compression zone and a dilution zone.

Individual fragments of biofilms formed as a result of ablation have macroscopic dimensions of ~ 0.5 mm and are visually observed. The ablation mechanism is determined by the parameters of the shock wave (laser pumping energy, pulse duration, shock wave front and peak pressure, etc.), as well as the properties of the biofilm-agar substrate material (composition, structure, morphology, nature of interaction with the shock wave, distribution of absorbed energy, etc.). Establishing a specific ablation mechanism is a separate task, beyond the scope of this work. Here, it is important to reliably establish the fact that the threshold for destruction of the structure under the influence of a shock wave and destruction of the object under study is exceeded, regardless of the initiated physical processes. The formation of biofilm fragments significantly affects the result of bacterial inactivation under the action of shock waves and photodynamic treatment.

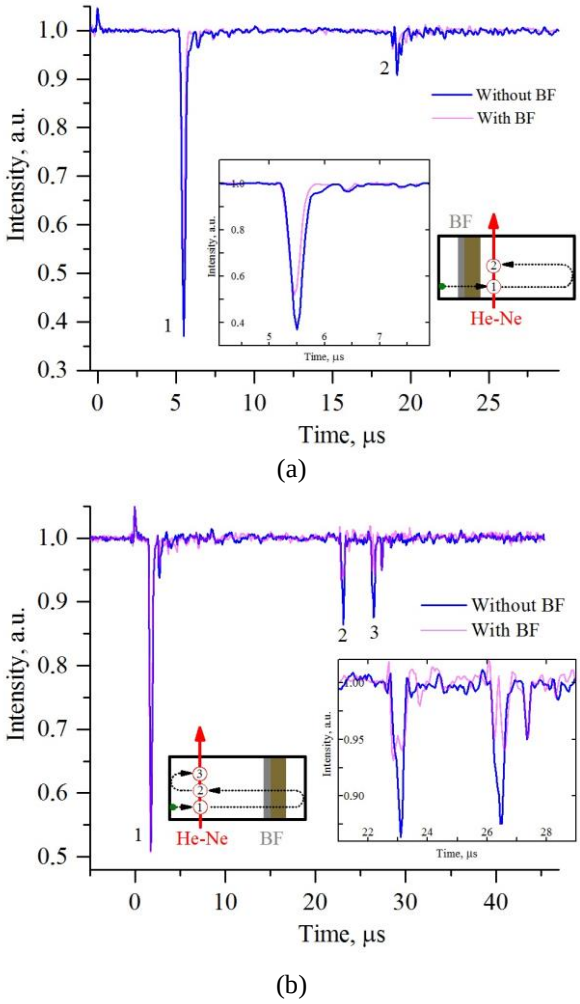


Fig. 2 The experimental scheme and the results of the interaction of shock waves with a biofilm. Direct and reflected waves are shown at different positions of the biofilm (BP) and the probing beam (He-Ne). (a) The change in the intensity of the shock wave after passing through the biofilm. (b) Direct (1) and reflected (2, 3) waves before (blue line) and after (red line) biofilm placement.

A shock wave with a high peak pressure and a short front, acting on a biofilm at an agar substrate, causes significant changes in the latter – from the ablation of biomaterial to damage to bacteria in the biofilm. Ablation should be understood as the separation of a biofilm fragment, in some cases together with the substrate, at the time of direct impact of the shock wave. Also, it must be borne in mind that shock waves are nonlinear waves of

finite amplitude, and the stream arising behind such a wave cannot be neglected. According to the wave profile shown in Fig. 2 it can be seen that it consists of a compression zone and a dilution zone.

Individual fragments of biofilms formed as a result of ablation have macroscopic dimensions of ~ 0.5 mm and are visible visually. The ablation mechanism is determined by the shock wave parameters (laser pumping energy, pulse duration, shock wave front and peak pressure, etc.), as well as the properties of the material biofilm-agar substrate (composition, structure, morphology, nature of interaction with the shock wave, distribution of absorbed energy, etc.). Elucidation of the specific ablation mechanism is a separate task beyond the scope of this work. Here it is important to reliably establish the fact that the threshold of destruction of the biofilm under the influence of a shock wave was exceeded, regardless of the initiated physical processes. The formation of biofilm fragments significantly affects the result of bacterial inactivation under the action of shock waves and photodynamic treatment.

3.2 Bacterial Survival after Exposure to Shock Waves and Radiation

When the biofilm is immersed in a cuvette, some bacteria of the peripheral layer enter the saline solution and eventually enter the planktonic state. Before exposure to the biofilms to shock waves and photodynamic radiation, the samples were kept in solution for about 5 min to achieve dynamic equilibrium in the biofilm-saline system. After mixing, an aliquot in a volume of 100 µl was taken from this suspension, which was dissolved in 1 mL of saline solution and sown in a volume of 20 µl on a Petri dish with cetrimide agar as a control sample. Before each exposure to the next series of pulses, a new biofilm on an agar substrate was placed in the cuvette, the procedure was repeated and the number of bacteria in the control samples was determined. The number of CFU bacteria in saline solution above the surface of the biofilm was estimated before and after exposure to shock waves and light, as well as the number of surviving bacteria in biofilms.

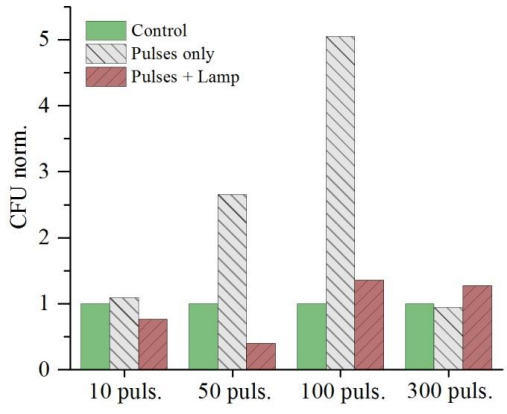


Fig. 3 Histograms of CFU bacteria in saline solution after exposure to shock waves and photodynamic treatment.

Histograms of CFU bacteria in saline solution after exposure to 10, 50, 100 and 300 shock waves and irradiation with visible light from a KGM-150 incandescent lamp through a SZS-22 light filter for 15 min are shown in Fig. 3. Unexpected was the increase in the number of viable bacteria in solution above the surface of the biofilm after exposure to 10, 50 and 100 shock waves. At the same time, the obtained result is in good agreement with the data of the work [17], where the dispersion of biofilms formed on medical catheters with the release of bacteria into the bacterial environment was observed. The increase in the number of bacteria in the solution seemed unexpected because earlier in Refs. [8−9] a decrease in the CFU of planktonic microorganisms was established after the effect of acoustic waves on bacteria in solutions.

The explanation of the obtained result is possible on the basis of modern ideas about the structure of biofilms. Microorganisms in a biofilm exist and are grouped differently from bacteria in a culture medium or saline solution. In biofilms, this is an interacting community of microorganisms, which are usually grouped into microcolonies surrounded by a protective matrix [18]. The process of interaction of shock waves with a biomaterial can be represented as follows. First, as a result of ablation, the most loosely bound biofilm fragments (sometimes together with an agar substrate) up to 1 mm in size are separated from the block. In the future, two competing processes are developing. On the one hand, shock waves destroy the binding matrix of the formed fragments (probably, protecting bacteria from mechanical damage is one of the important functions of the matrix) mechanically separating bacterial viable cells, which form new colonies after sowing. On the other hand, the waves damage the resulting planktonic microorganisms. According to the data presented in Fig. 3, if the number of shock waves is less than 300, the number of bacteria appearing in the solution as a result of the destruction of the matrix of biofilm fragments is greater than those affected by shock waves.

With an increase in the number of shock waves from 300 to 1000, the picture changes – the number of CFU decreases. Obviously, under the conditions of our experiments, after exposure to about 200−300 waves, biofilm fragments are almost completely destroyed, and subsequently the formed planktonic bacteria are damaged by shock waves, as demonstrated in Refs. [8−9].

At the same time, the permeability of bacterial membranes increases [19−21] and the probability of penetration of erythrosine (an effective anionic photosensitizer [22]) into cells increases. The basis for this assumption is a sharp decrease in CFU after irradiation of saline solution with bacteria with light with a wavelength that coincides with the absorption spectrum of erythrosine. There is a pronounced antibacterial photodynamic effect, a prerequisite for which is the penetration of a photosensitizer into cells [23−24]. Fig. 3 shows that the number of CFU bacteria of *P. aeruginosa* in the presence of erythrosine decreases significantly after photodynamic irradiation of samples treated with

shock waves. Changes in the permeability of biofilms treated with shock waves were previously observed in the work of [25], which showed an increase in the efficiency of damage to S. aureus bacteria by antibiotics in biofilms on titanium discs. Authors [17] observed a significant increase in the ability of human neutrophils to kill *S. epidermidis* bacteria in the planktonic state and within biofilms on catheters after exposure to shock waves. It should be noted that without photodynamic treatment, an increase in the permeability of bacterial membranes after exposure to acoustic waves can also stimulate an increase in CFU of microorganisms [26]. The wave creates micro-vortices in the environment surrounding the cell, ensuring effective mixing of nutrients and changing their concentration in the cytoplasm, initiating the process of cell division [27].

The threshold for destruction of biofilms on a substrate under the action of shock waves depends on the growing conditions of the biomaterial and its structure. In some samples, the number of planktonic bacteria in solution above the biofilm surface increased up to 1000 shock waves (Fig. 4). But in all the samples studied, the most rapid decrease in the number of viable bacteria in biofilms occurred after exposure to about 200 pulses.

Fig. 4 shows graphs of comparative changes in the number of viable bacteria remaining in biofilms and in solution above the film surface after exposure to different numbers of shock waves. As you can see, the dependencies are not symmetrical. In the range from 10 to 200 waves, there is a rapid decrease in the number of viable bacteria in biofilms due to ablation of the biomaterial and the transition of the formed fragments into solution. In the future, up to 1000 pulses, the decrease in the number of bacteria in biofilms, if it occurs, is very slow. The relatively slow growth in the number of microorganisms in the solution is due not only to the specifics of crushing fragments of biomaterial, but also to the competition of the processes of release of bacteria and their destruction by shock waves.

A slow decrease in the number of viable bacteria in biofilms in the range of 200−1000 pulses indicates that shock waves with peak pressure commensurate with the strength threshold of the cell membrane are capable of damaging planktonic bacteria (Fig. 3), but practically have no effect on microbes in biofilms. There are known works [28] in which a clear dose-dependent antibacterial effect is described, for the manifestation of which at least 1000 pulses were required. In our experiments, such an effect was not detected; a statistically significant decrease in the number of bacteria in the biofilm was observed with 200–250 pulses.

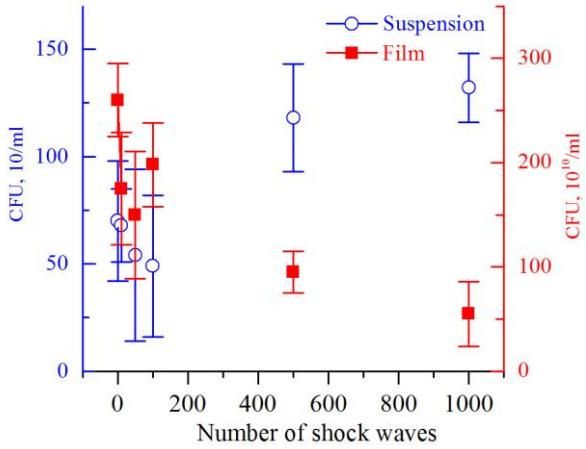


Fig. 4 CFU of bacteria in the biofilm after shock wave irradiation (red line), and bacteria in suspension beyond the biofilm (blue line).

4 Conclusion

The exact mechanisms of the impact of shock waves on biofilms remain to be elucidated. Our work shows that shock acoustic waves with a peak pressure close to the tensile strength threshold of the cell wall material are capable of destroying the peripheral layer of the biofilm by the ablation mechanism, mechanically separating the formed fragments into viable bacteria, and damaging planktonic microorganisms. At the same time, the relatively low efficiency of bacterial damage in biofilms by such shock waves has been experimentally illustrated. Probably, the elastic protective matrix of biofilms protects bacteria from mechanical damage. The manifestation of the antibacterial photodynamic effect suggests that after treatment with shock waves, the structure of the biofilm is disrupted and the penetration of the photosensitizer into deeper layers of the film is facilitated.

Funding

This work was supported by the Ministry of Education and Science of Russia (Project № 075-15-2024-550).

Disclosures

The authors declare no conflicts of interest.

References

1. S. Sharma, J. Mohler, S. D. Mahajan, S. A. Schwartz, L. Bruggemann, and R. Aalinkeel, "Microbial Biofilm: A Review on Formation, Infection, Antibiotic Resistance, Control Measures, and Innovative Treatment," Microorganisms 11(6), 1614 (2023).
2. A. Zhao, J. Sun, and Y. Liu, "Understanding bacterial biofilms: From definition to treatment strategies," Frontiers in Cellular and Infection Microbiology 13, 1137947 (2023).
3. A. G. Abdelhamid, A. E. Yousef, "Combating Bacterial Biofilms: Current and Emerging Antibiofilm Strategies for Treating Persistent Infections," Antibiotics 12(6), 1005 (2023).

4. D. Liu, Q. Huang, W. Gu, and X. Zeng, "A review of bacterial biofilm control by physical strategies," Critical Reviews in Food Science and Nutrition 62(13), 3453–3470 (2022).
5. J. Khan, S. M. Tarar, I. Gul, U. Nawaz, and M. Arshad, "Challenges of antibiotic resistance biofilms and potential combating strategies: a review," 3 Biotech 11(4), 169 (2021).
6. J. P. Sahoo, A. P. Mishra, K. C. Samal, and A. K. Dash, "Insights into the antibiotic resistance in Biofilms – A Review," Environment Conservation Journal 22(3), 59–67 (2021).
7. S. P. Songca, Y. Adjei, "Applications of Antimicrobial Photodynamic Therapy against Bacterial Biofilms," International Journal of Molecular Sciences 23(6), 3209 (2022).
8. S. N. Letuta, S. N. Pashkevich, A. T. Ishemgulov, and A. N. Nikiyan, "Inactivation of Planktonic Microorganisms by Acoustic Shock Waves," Russian Journal of Physical Chemistry A 95(4), 848–854 (2021).
9. S. N. Letuta, A. T. Ishemgulov, A. N. Nikiyan, D. A. Razdobreev, L. V. Galaktionova, D. V. Dorofeev, and D. E. Tsurko, "Mechanisms of Damage in Salmonella typhimurium and Staphylococcus aureus upon Pulse Photoexcitation of Molecular Sensitizers," Biophysics 67(3), 419–426 (2022).
10. H. S. Yadav, D. S. Murty, S. N. Verma, K. H. C. Sinha, B. M. Gupta, and D. Chand, "Measurement of refractive index of water under high dynamic pressures," Journal of Applied Physics 44, 2197–2200 (1973).
11. H. H. Tuson, G. K. Auer, L. D. Renner, M. Hasebe, C. Tropini, M. Salick, W. C. Crone, A. Gopinathan, K. C. Huang, and D. B. Weibel, "Measuring the stiffness of bacterial cells from growth rates in hydrogels of tunable elasticity," Molecular Microbiology 84(5), 874–891 (2012).
12. K. K. Rohatgi-Mukherjee, Fundamentals of Photochemistry, Wiley Eastern Ltd., New Delhi, Bangalore, Bombay (1978). ISBN: 9780470265475.
13. L. M. Tokubo, P. L. Rosalen, J. De Cássia Orlandi Sardi, I. A. Freires, M. Fujimaki, J. E. Umeda, P. M. Barbosa, G. O. Tecchio, N. Hioka, C. F. De Freitas, and R. S. Suga Terada, "Antimicrobial effect of photodynamic therapy using erythrosine/methylene blue combination on Streptococcus mutans biofilm," Photodiagnosis and Photodynamic Therapy 23, 94–98 (2018).
14. C. Fracalossi, J. Y. Nagata, D. S. Pellosi, R. S. S. Terada, N. Hioka, M. L. Baesso, F. Sato, P. L. Rosalen, W. Caetano, and M. Fujimaki, "Singlet oxygen production by combining erythrosine and halogen light for photodynamic inactivation of Streptococcus mutans," Photodiagnosis and Photodynamic Therapy 15, 127–132 (2016).
15. S. Tobita, Y. Kaisu, H. Kobayashi, and I. Tanaka, "Study of higher excited singlet states of zinc(II)-tetraphenylporphin," The Journal of Chemical Physics 81(7), 2962−2969 (1984).
16. H.-B. Lin, M .R. Topp, "Low quantum-yield molecular fluorescence. Aromatic hydrocarbons in solution at 300 K," Chemical Physics Letters 48(2), 251−255 (1977).
17. D. P. Gnanadhas, M. Elango, S. Janardhanraj, C. S. Srinandan, A. Datey, R. A. Strugnell, J. Gopalan, and D. Chakravortty, "Successful treatment of biofilm infection using shock waves combined with antibiotic therapy," Scientific Reports 5, 17440 (2015).
18. B. W. Peterson, Y. He, Y. Ren, A. Zerdoum, M. R. Libera, P. K. Sharma, A.-J. Van Winkelhoff, D. Neut, P. Stoodley, H. C. Van Der Mei, and H. J. Busscher, "Viscoelasticity of biofilms and their recalcitrance to mechanical and chemical challenges," FEMS Microbiology Reviews 39, 234–245 (2015).
19. S. Lee, A. G. Doukas, "Laser-generated stress waves and their effects on the cell membrane," IEEE Journal of Selected Topics in Quantum Electronics 5(4), 997–1003 (1999).
20. N. S. Soukos, S. E. Mulholland, S. S. Socransky, and A. G. Doukas, "Photodestruction of human dental plaque bacteria: enhancement of the photodynamic effect by photomechanical waves in an oral biofilm model," Lasers in Surgery and Medicine 33(3), 161–168 (2003).
21. P. E. Huber, P. Pesterer, "In vitro and in vivo transfection of plasmid DNA in the Dunning prostate tumor R3327-AT1 is enhanced by focused ultrasound," Gene Therapy 7, 1516−1525 (2000).
22. S. Wood, D. Metcalf, D. Devine, and C. Robinson, "Erythrosine is a potential photosensitizer for the photodynamic therapy of oral plaque biofilms," Journal of Antimicrobial Chemotherapy 57(4), 680–684 (2006).
23. J. Ghorbani, D. Rahban, S. Aghamiri, A. Teymouri, and A. Bahador, "Photosensitizers in antibacterial photodynamic therapy: an overview," Laser Therapy 27(4), 293–302 (2018).
24. A. K. Surur, A. B. De Oliveira, S. R. De Annunzio, T. M. Ferrisse, and C. R. Fontana, "Bacterial resistance to antimicrobial photodynamic therapy: A critical update," Journal of Photochemistry and Photobiology B: Biology 255, 112905 (2024).
25. A. Milstrey, S. Rosslenbroich, J. Everding, M. J. Raschke, R. G. Richards, T. F. Moriarty, and J. Puetzler, "Antibiofilm efficacy of focused high-energy extracorporeal shockwaves and antibiotics in vitro," Bone & Joint Research 10(1), 77–84 (2021).
26. S. Gu, Y. Zhang, and Y. Wu, "Effects of sound exposure on the growth and intracellular macromolecular synthesis of E. coli k-12," PeerJ 4, e1920 (2016).
27. Y. Chisti, "Sonobioreactors: Using ultrasound for enhanced microbial productivity," Trends in Biotechnology 21(2), 89–93 (2003).
28. L. Gerdesmeyer, C. Von Eiff, C. Horn, M. Henne, M. Roessner, P. Diehl, and H. Gollwitzer, Antibacterial effects of extracorporeal shock waves," Ultrasound in Medicine & Biology 31(1), 115–119 (2005).